ADVANCED FUNCTIONAL MATERIALS
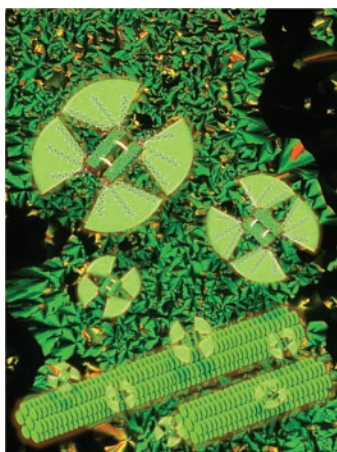
ADVANCED
FUNCTIONAL
MATERIALS

ADVANCED FUNCTIONAL MATERIALS

www.afm-journal.de

Liquid Crystals

(2Z,2′Z)-2,2′-(1,4-phenylene)bis(3-(3,4,5-tris(dodecyloxy)phenyl)acrylonitrile) (GDCS) molecules self-assemble into supramolecular disks consisting of a pair of molecules in a side-by-side disposition assisted by secondary bonding interactions of the lateral polar cyano group, which, in turn, constitute the hexagonal columnar LC structure. As demonstrated on page 61 by Dongho Kim, Soo Young Park, and co-workers, uniaxially aligned liquid crystal (LC) and crystalline GDCS microwires with enhanced fluorescence and semiconductivity are successfully fabricated by using a micromolding in capillaries (MIMIC) process.
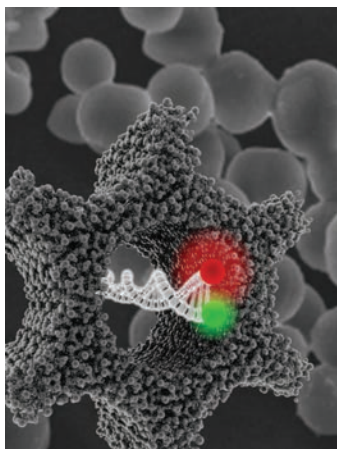
Biomedical Applications

Mesoporous silica particles represent a novel, highly versatile class of drug-delivery systems. On page 106, Thomas Bein, Christoph Bräuchle, and co-workers utilize these materials as a host for the incorporation of short oligonucleotides as model gene therapeutics. The diffusion of a labelled oligonucleotide through a nanometer-sized silica pore is shown. Organic functionalization of the silica pore system offers a means to control oligonucleotide mobility and stability.

Organic Single Crystalline Lasers

On page 33, Jing Feng, Hong-Bo Sun, and co-workers report the use of an interference ablation method to fabricate an organic single-crystalline distributed feedback laser. Organic single crystals are difficult to treat using traditional fabrication methods because of their fragility and sensitivity to organic solvents and this method resolves these difficulties. The method may be applied to fabricate high-quality organic devices based on the single-crystalline materials.
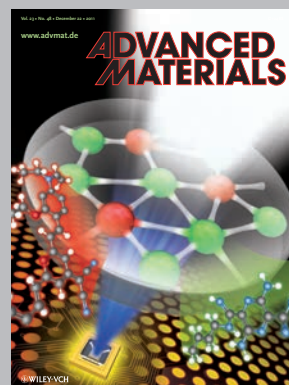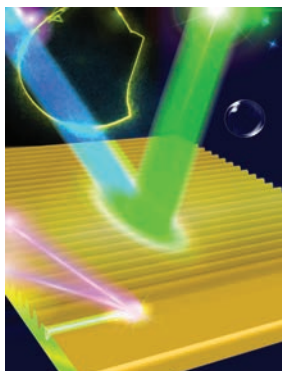
Advanced Materials has been bringing you the best in materials research for over twenty years.

With its increased ISI Impact Factor of 10.857, Advanced Materials is one of the most influential journals in the field. Publishing every week, Advanced Materials now brings you even more of the latest results at the cutting edge of materials science.

www.advmat.de
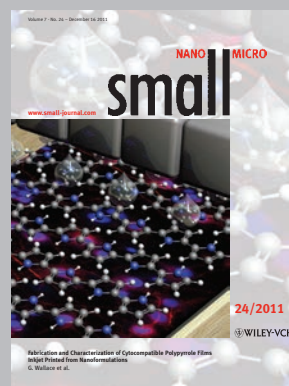
Small is the very best interdisciplinary forum for all experimental and theoretical aspects of fundamental and applied research at the micro and nano length scales.

With an ISI impact Factor of 7.333 and publishing every two weeks in 2011 with papers online in advance of print, Small is your first-choice venue for top-quality communications, detailed full papers, cutting-edge concepts, and in-depth reviews of all things micro and nano.

www.small-journal.com
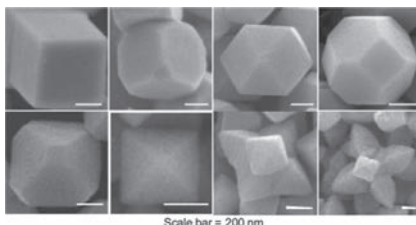
CONTENTS

EDITORIAL

FEATURE ARTICLE

Nanostructures

Crystal Morphology Control: In this article, the syntheses of Au, Cu_2O, and Ag_2O nanocrystals with shape evolution are described. As an example, the images show submicrometer-sized Cu_2O crystals with cubic, truncated cubic, cuboctahedral, truncated octahedral, octahedral, and hexapod structures that can be synthesized systematically. These crystals with sharp faces are ideal for the examination of their facet-dependent properties.

FULL PAPERS

Photonic Crystals
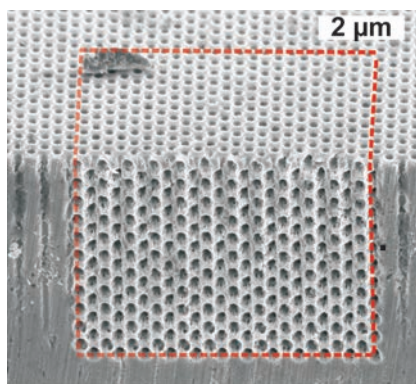
Three-dimensional silicon photonic band gap crystals with a diamond-like symmetry are fabricated by complementary metal oxide–semiconductor compatible methods. These "inverse woodpiles" consist of two perpendicular sets of pores etched consecutively after careful alignment. The crystals are analyzed in detail regarding pore depth, radius, tapering, shape, and alignment. Optical reflectivity demonstrates that the crystals are of high quality.

Lasers
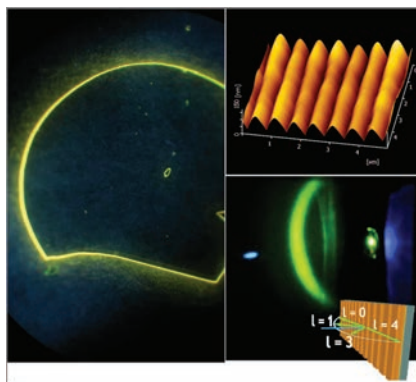
Distributed feedback lasing is produced from high-mobility organic thin-film single crystals. High-quality 1D distributed feedback resonators are constructed in 2,2′-bithiophene,5,5′-bis([1,1′-biphenyl]-4-yl) (BP2T) single-crystalline thin-film materials by an extremely simple method – laser interference ablation. This method does not involve chemical solution and avoids the need for good-quality end facets of crystals.

FULL PAPERS

The efficacy of covalently immobilized **Subtilisin A** on the exploratory behavior, settlement, and adhesion of the major marine fouling pest *Balanus amphitrite* is systematically tested. The coating is suggested as the first step towards the development of a nontoxic, clear anti-fouling and fouling-release coating that could have uses within both medical fields and the marine industry.
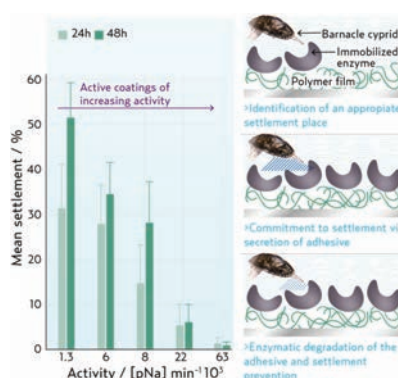
Antifouling Coatings

M. Tasso, S. L. Conlan, A. S. Clare,*
C. Werner* 39–47

Active Enzyme Nanocoatings Affect Settlement of *Balanus amphitrite* Barnacle Cyprids

---

Perfluorophenyl-functionalized tetrathienothiophene (DFP-TTA) exhibits n-channel transport with a mobility as high as 0.30 cm^2 V^{-1} s^{-1} and an on-off ratio of 1.8×10^7. The large TTA core size and good solid state packing in combination with optimum film growth conditions enhance electron transport in DFP-TTA thin-film transistors.

Organic Electronics

J. Youn, P.-Y. Huang, Y.-W. Huang, M.-C. Chen,* Y.-J. Lin, H. Huang, R. P. Ortiz, C. Stern, M.-C. Chung, C.-Y. Feng, L.-H. Chen, A. Facchetti,* T. J. Marks* 48–60

Versatile α,ω-Disubstituted Tetrathienoacene Semiconductors for High Performance Organic Thin-Film Transistors

---

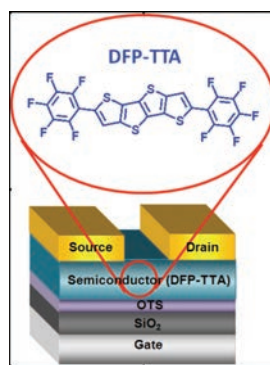A new dicyanodistyrylbenzene-based liquid-crystalline material [(2Z,2′Z)-2,2′-(1,4-phenylene)bis(3-(3,4,5-tris(dodecyloxy)phenyl)acrylonitrile) (GDCS)] shows intense green/yellow fluorescence in the liquid/solid crystal state. The aggregation-induced enhanced emission and two-color luminescence behaviors are promoted by intra- and intermolecular actions, which are caused by the dipolar cyanostilbene unit. The aligned microwires of GDCS are fabricated by micromolding in capillaries for enhanced electrical conductivity.
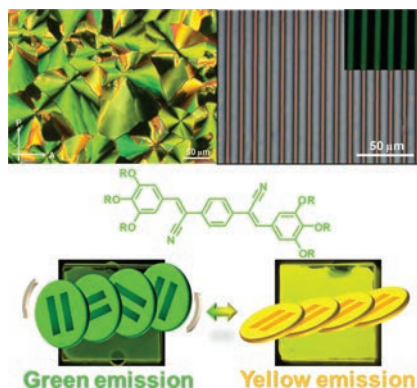
Liquid Crystals

S.-J. Yoon, J. H. Kim, K. S. Kim, J. W. Chung, B. Heinrich, F. Mathevet, P. Kim, B. Donnio, A.-J. Attias, D. Kim,* S. Y. Park*.......................................61–69

Mesomorphic Organization and Thermochromic Luminescence of Dicyanodistyrylbenzene-Based Phasmidic Molecular Disks: Uniaxially Aligned Hexagonal Columnar Liquid Crystals at Room Temperature with Enhanced Fluorescence Emission and Semiconductivity

---

The role of moisture in the switching characteristics of oxide-based, gapless-type atomic switches is clarified. A certain amount of residual water exists in the oxide layer, forming a hydrogen-bond network at grain boundaries. Its stability has an impact on the ionization of Cu at the anode interfaces and the migration of Cu ions in the oxide layer, which plays a major role in determining the operation – important findings for the microscopic understanding of the switching behavior of oxide-based atomic switches.
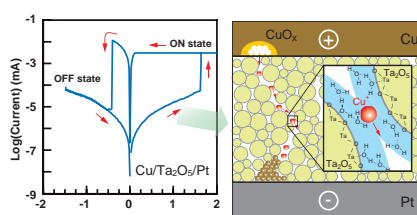
Atomic Switches

T. Tsuruoka,* K. Terabe, T. Hasegawa, I. Valov, R. Waser, M. Aono 70–77

Effects of Moisture on the Switching Characteristics of Oxide-Based, Gapless-Type Atomic Switches

FULL PAPERS

High-oxygen-content strong oxidizers are encapsulated within mild oxidizer particles. This approach enables the use of hygroscopic materials by stabilizing them within a matrix. When mixed with nanoaluminum these formulations illicit very violent reactions, which significantly outperform the single metal oxide system in both pressurization rate and peak pressure.
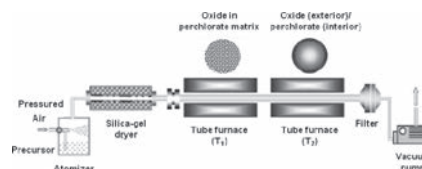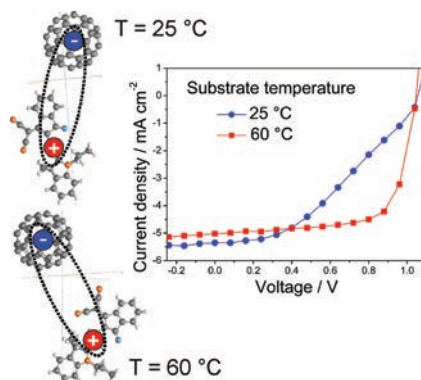
Substrate heating and post-annealing techniques are used to control the orientation of dye molecules in thermally vacuum-deposited planar heterojunction merocyanine/C$_{60}$ solar cells. Favorable molecular orientation at the heterointerface substantially improves the exciton dissociation efficiency, resulting in up to 100% improvement of the fill factor.
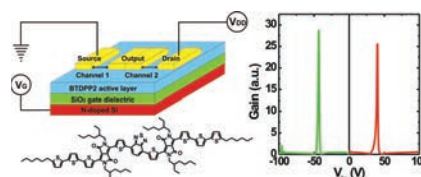
An inverter is fabricated from solution-processed small molecules containing a diketopyrrolopyrrole core (BTDPP2) using a simple thermally evaporated electrode pattern. The device architecture is composed of two BTDPP2 ambipolar transistors connected in parallel. The inverter displays gain values exceeding 25 when operated under both p-type and n-type regimes.
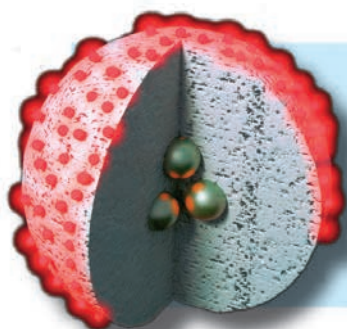
FULL PAPERS

Template-free SBA-15 type mesoporous silica particles are loaded with siRNA and dsDNA. The particles' uptake capability is controlled by an organic surface functionalization and the dynamics of the intact oligonucleotides inside the functionalized nanochannels are determined. The study demonstrates the potential of mesoporous silica as an alternative means for gene delivery. Such alternatives are urgently needed since the delivery of oligonucleotides to their target sites still represents a major hurdle in the application of gene therapy.
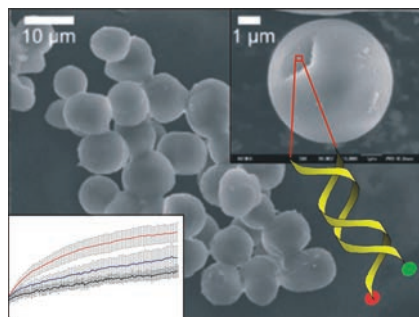
Biomedical Applications

T. Lebold, A. Schlossbauer, K. Schneider, L. Schermelleh, H. Leonhardt, T. Bein,* C. Bräuchle*...............................106–112

Controlling The Mobility Of Oligonucleotides In The Nanochannels Of Mesoporous Silica

---

A novel method for the fast, one-step growth of large-area, homogeneous, high-quality epitaxial graphene (EG) on SiC(0001) is presented. An infrared CO_2 laser (10.6 μm) is used as the heating source, enabling in situ patterning. A number of experimental techniques, such as scanning electron microscopy, X-ray photoelectron spectroscopy, depth profiling methods, and Raman spectroscopy, are employed to present an in-depth analysis of the quantitative and qualitative features of the EG grown by the current method.
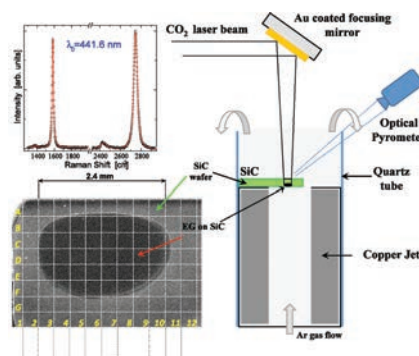
Graphene

S. N. Yannopoulos,* A. Siokou,* N. K. Nasikas, V. Dracopoulos, F. Ravani, G. N. Papatheodorou 113–120

CO_2-Laser-Induced Growth of Epitaxial Graphene on 6H-SiC(0001)

Uniform embryoid bodies (EBs) with controlled sizes are formed in the pores of an alginate inverse opal scaffold and then recovered after disintegration of the scaffold. The EBs maintain their viability and undifferentiated state, and they are able to differentiate into specific lineages upon stimulation.
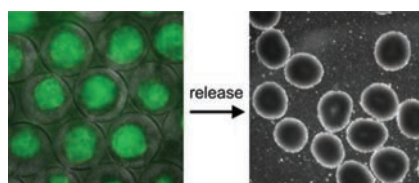
Scaffolds

Y. Zhang, Y. Xia* 121–129

Formation of Embryoid Bodies with Controlled Sizes and Maintained Pluripotency in Three-Dimensional Inverse Opal Scaffolds

---

Near infrared (NIR)-sensitive poly-(DL-lactic-co-glycolic) acid (PLGA) microcapsules with programmed release properties are generated by controlling the capsule morphology. The effect of PLGA microcapsule morphology on their NIR responsiveness is illustrated.
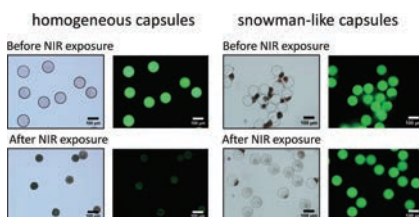
Drug Delivery

M. H. Lee, K. C. Hribar, T. Brugarolas, N. P. Kamat, J. A. Burdick, D. Lee* 131–138

Harnessing Interfacial Phenomena to Program the Release Properties of Hollow Microcapsules

FULL PAPERS

Sensitized triplet–triplet annihilation in multicomponent organic systems in solution allows efficient up-conversion at the solar-irradiance power density, but loses efficiency in the solid state. It is demonstrated that this limitation can be avoided by incorporating suitable dyes into polymer nanoparticles, which can be used for drop-cast films or as dopants for solid matrices.
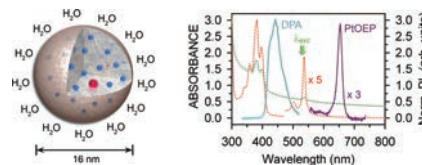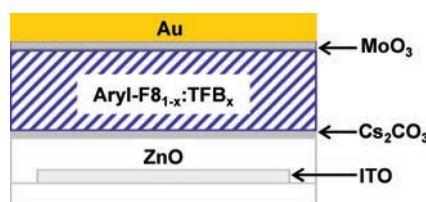
Charge-carrier balance and color purity is achieved in an arylated polyfluorene-based blue-emitting light-emitting diode (LED) by use of a macromolecular additive. This additive provides excellent control over current density while keeping the optical properties of emissive materials intact. Luminance efficiency of up to 5.9 cd A^{-1} along with a pure blue emission is achieved in the blend instead of 1.2 cd A^{-1} in the homopolymer-based LED.
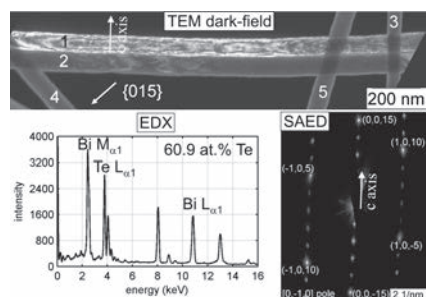
Stoichiometric, single-crystalline Bi$_2$Te$_3$ nanowires with diameters of 50–80 nm are grown by potential-pulsed electrochemical deposition in a nanostructured Al$_2$O$_3$ matrix. X-ray diffraction, electron diffraction, and high-accuracy energy-dispersive X-ray spectroscopy unambiguously prove that, for the first time, single-crystalline, stoichiometric Bi$_2$Te$_3$ nanowires are grown that allow transport in the basal plane without being affected by grain boundaries.
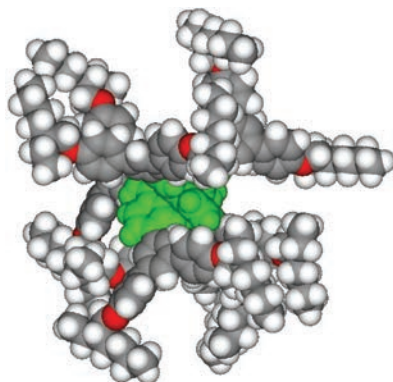
High phosphorescence efficiency can be combined with non-dispersive charge transport in doubly dendronized iridium(III) complex-cored dendrimers for organic light-emitting diodes. The double dendrons give the macromolecule a more spherical shape, reducing energetic disorder in the film and hence improving charge transport, as well as increasing photoluminescence quantum yield.

Nanostructures

A new silica-protected calcination process is developed for the synthesis of mesoporous hollow spheres of small-grain-size anatase TiO$_2$ with controllable crystallinity, high surface area, and excellent dispersity in water. The mesoporous TiO$_2$ shells show significantly enhanced photocatalytic activity towards degradation of organic molecules.
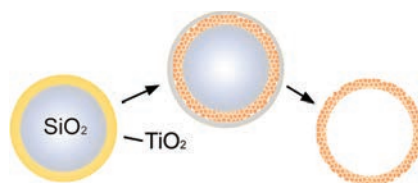
Mesoporous Anatase Titania Hollow Nanostructures though Silica-Protected Calcination

Organic Field-Effect Transistors

To produce flexible organic electronics, understanding the effects of strain on the device performance is critical. A comprehensive study of seven polymer dielectrics with two organic semiconductors is presented. The novel influence of both dielectric and organic semiconductor structure is described.
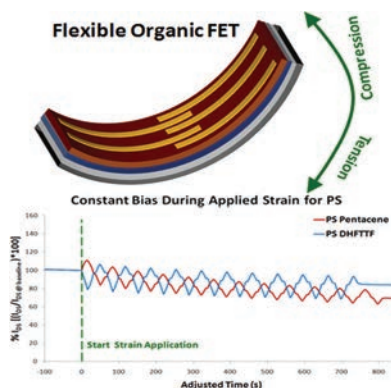
Mechanistic Considerations of Bending-Strain Effects within Organic Semiconductors on Polymer Dielectrics

Magneto-Sensitive Materials

Magnetic memory materials can remember a magnetic field strength, H_{def}, at which they were deformed recently. In cyclic, magneto-mechanical tests, a linear correlation is found between H_{def} and the magnetic field strength, H_{sw}, at which the magnetic memory effect occurred. This correlation impressively demonstrates excellent magnetic memory properties.
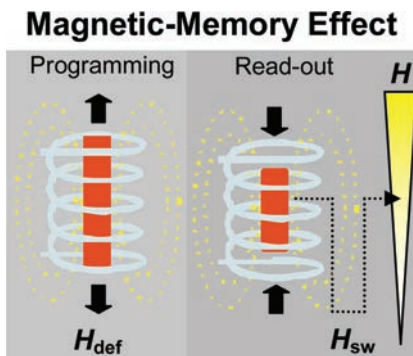
Magnetic Memory Effect of Nanocomposites

Ferroelectric Switching

Field dependence of domain-switching speeds is estimated over five orders of magnitude at temperatures of 5.4–280 K from domain-switching current transients in Pb(Zr$_{0.4}$Ti$_{0.6}$)O$_3$ thin films. By using Merz's equation and nucleation-rate limited models, an ultimate domain-switching current density of 1.4×10^8 A cm^{-1} and nucleation time of 0.47 ps at the highest field of 0.20 MV cm^{-1} are extracted.

Sub-Picosecond Processes of Ferroelectric Domain Switching from Field and Temperature Experiments

FULL PAPERS

Highly Efficient Organic THz Generator
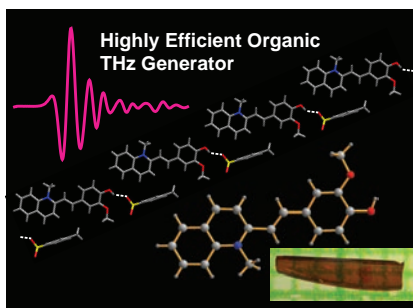
Highly efficient ionic electro-optic quinolinium single crystals with a high order parameter and a large macroscopic optical nonlinearity exhibit more than three times higher THz generation efficiency than benchmark organic phenolic polyene crystals and are almost one order of magnitude higher than inorganic standard ZnTe crystals pumped by near-infrared Ti:sapphire femtosecond laser pulses at 836 nm.
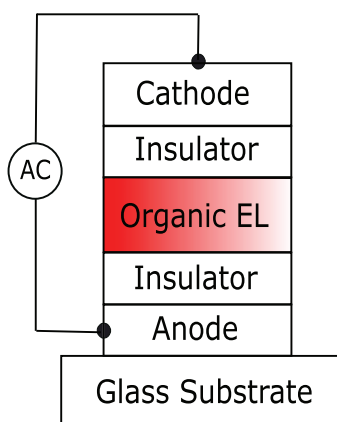
A novel approach for alternating current (AC)-driven organic light-emitting devices, which uses the concept of molecular doping in organic semiconductors is reported. Doped charge-transport layers are used for generation of charge carriers within the device. Bright luminance of up to 1000 cdm^{-2} is observed under AC bias. The luminance observed is attributed to charge-carrier generation and recombination within the device without injection of charge carriers through external electrodes.

Small Ag nanoparticles and large Ag spheres are simultaneously sputtered uniformly onto the side surface and the top ends of cone-shaped ZnO-nanorods fabricated by ZnO-seed-induced electrodeposition, respectively. The as-prepared 3D hybrid surface-enhanced Raman spectroscopy substrate manifests high detection sensitivity to rhodamine and a detection limit as low as 10^{-11} M to polychlorinated biphenyl 77—one of the highly toxic persistent organic pollutants.

ADVANCED
FUNCTIONAL
MATERIALS

www.afm-journal.de

Materials
Views
www.MaterialsViews.com

EDITORIAL

More Fundamental Understanding In Materials Science

In his recent MaterialsViews.com column (http://mvie.ws/t8hLq), Geoff Ozin wonders what happened to fundamental research without the drive towards immediate application:

> Nowadays, in the area of materials research, however, scientists have to pin applications on their materials which aren't ready for them. It's not enough to just study an interesting material – now you must put it into a solar cell (and probably not a very good one because it takes years to develop these things) or claim that it is good for "drug delivery" or a "sensor" or a "battery" or a "white light emitting diode".

We've noticed this trend too in the last couple of years. Traditionally, *Advanced Functional Materials* papers have included lots of device data and applications because the longer full paper format allows room for going into additional detail about a materials system than a communication. However, it seems like engineering device performance increases is more and more becoming the focus. Similarly, many more papers promise immediate applications, when a closer look reveals that there would still be a lot of steps from lab to technology.

Is Prof. Ozin right? As a community, are we in danger of losing touch with the fundamentals of materials science research?

One of the greatest strengths of materials science is its immense applicability. Without this, the explosion in materials science research–and in research funding–over the last decade would not have been possible. The importance of materials science research for creating new, innovative, and practical solutions to real-world problems should not be ignored.

But, in the long run, are we leaning too far towards devices and applications, incremental improvements, and device engineering in favor of fundamental research? And how will that affect the development of materials science in the next decade, as we try to develop smarter, more efficient, more functional materials?

This isn't to say that we should forgo devices, applications, and the real-world applicability that makes materials science so interesting. But, maybe we can strive for more of a balance between development of new materials and systems and their understanding.

The ideal result would combine both: increased understanding of an interesting materials science problem that could lead to practical applications.

Therefore, in addition to being novel, important, and of broad interest, I'd like to propose an additional criterion for *Advanced Functional Materials* for authors, reviewers, and editors to consider:

Does the reported research advance our fundamental understanding of the materials science involved?

Or, if you prefer, *Why does this interesting material* function *the way it does?*

A solar cell might not have the highest reported efficiency to date, but what if we learn something new about how the chemistry and physics interact within the cell? We might be years away from optical computing, but finding out more about the interactions between light and matter may be another step towards that goal.

I'd like to come back in a year and say that, in 2012, *Advanced Functional Materials* published more high-risk research and emphasized more fundamental understanding of materials science. I'd be interested in hearing what you think. You can send me an email at materialsdave@wiley.com, or message me on Twitter (twitter.com/materialsdave) or Google+(profiles.google.com/materialsdave).

P.S. *Advanced Healthcare Materials* was published as a special focus section in *Advanced Materials* in 2011 and will be a new journal from January 2012. *Advanced*
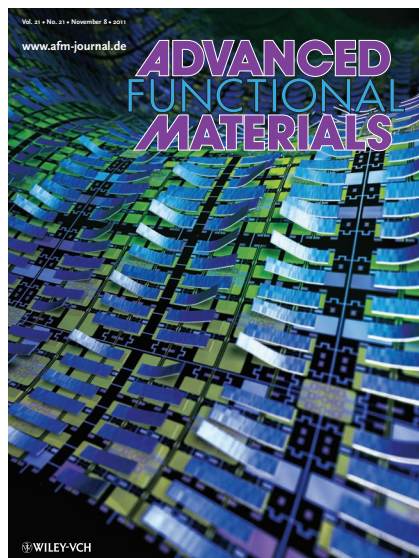
Dave Flanagan

ADVANCED HEALTHCARE MATERIALS

Healthcare Materials is an interdisciplinary forum for peer-reviewed papers on materials science aimed at promoting human health, covering all aspects of materials science in medicine and biotechnology. It contains a mix of Communications, Full Papers, Review Articles, Progress Reports, Research News, and Essays on cutting-edge research areas such as biomaterials for drug-delivery systems, cancer therapy, tissue engineering, imaging, biosensors and diagnostic tools, personalized medicine, bioelectronics, and implantable devices. Find out more at www.advhealthmat.de.

One more thing: As studies of light–matter interactions continue to push into uncharted territory, *Advanced Materials* is launching *Advanced Optical Materials,* a new topical section dedicated to breakthrough discoveries and

ADVANCED OPTICAL MATERIALS

fundamental research in photonics, plasmonics, metamaterials, and all important aspects of this burgeoning research field. It will include Communications, Full papers, and Reviews. Look for the first edition in Spring 2012. For more information, visit www.advopticalmat.de.

FEATURE ARTICLE

Shape-Controlled Synthesis of Polyhedral Nanocrystals and Their Facet-Dependent Properties

Michael H. Huang* and Po-Heng Lin

Growth of inorganic polyhedral nanocrystals with excellent morphology control presents significant synthetic challenges, especially when the development of synthetic schemes to make nanocrystals with systematic shape evolution is desired. Nanocrystals with fine size and shape control facilitate formation of their self-assembled packing structures and offer opportunities for examination of their facet-dependent physical and chemical properties. In this Feature Article, recent advances in the synthesis of nanocrystals with systematic shape evolution are highlighted. The reaction conditions used to achieve this morphology change offer insights into the growth mechanisms of nanocrystals. A novel class of polyhedral core–shell heterostructures fabricated using structurally well-defined nanocrystal cores is also presented. Facet-dependent photocatalytic activity, molecular adsorption, and catalytic and electrical properties of nanocrystals have been examined and are discussed. Nanomaterials with enhanced properties and functionality may be obtained through continuous efforts in the synthesis of nanocrystals with well-defined structures and investigation of their plane-selective properties.

1. Introduction

Widespread interest and development in the growth of inorganic nanostructures is associated with the possibility of observing their size- and shape-dependent optical, electronic, magnetic, and catalytic properties. A wide variety of methods has been developed for the solution-phase synthesis of colloidal nanoparticles with size, shape, and composition control.[1–4] The preparation of metal nanocrystals such as Au, Ag, Pd, Pt, and Fe polyhedral nanoparticles with well-defined structures has been reported.[5–14] Similarly, growth of nanocrystals with polyhedral morphologies has been achieved for some semiconductors such as Cu_2O, PbS, and PbSe.[15–23] Review articles desribing synthetic routes towards the growth of shape-controlled metal and semiconductor nanocrystals and their property characterization are available.[24–29] The ability to synthesize metal and semiconductor nanocrystals with good size and shape uniformity is not only critical for their property characterization, the nanocrystals may also readily form self-assembled superlattice structures with novel collective properties.[6,15,22,30–35] Large supercrystals

constructed from the regular assembly of polyhedral nanocrystal building blocks can also be fabricated by controlling the solvent-evaporation conditions.[36–38]

An interesting development in the shape-controlled synthesis of metal and semiconductor/metal oxide nanocrystals is achieving their systematic shape evolution. With precise variation in the reaction conditions, nanoparticles possessing cubic crystal structures may grow into cubic, octahedral, and rhombic dodecahedral structures.[14,17,18,32,39–46] Their intermediate structures such as cuboctahedral structure and extended growth structures such as hexapods can also be synthesized. While individual particle shapes may be more readily obtained, relatively few nanocrystal systems have been demonstrated to yield systematic shape evolution. Thus, it remains challenging to expand the range of nanocrystal compositions at this level of morphology control. The ability to synthesize nanocrystals with systematic shape evolution offers opportunities to examine their facet-dependent properties with greater reliability, because the nanoparticles are prepared under similar solution conditions. Facet-dependent properties of nanocrystals are interesting and potentially important in developing better nanomaterials for various applications.

Another recent development in nanocrystal growth is the utilization of polyhedral nanoparticles as cores for the formation of core–shell heterostructures with structurally well-defined shell morphology.[47–55] Triangular core–shell nanoplates have also been synthesized.[56,57] Due to a lattice mismatch problem, these core–shell nanostructures are mostly limited to bimetallic systems.[58] Heterojunctions, rather than complete core–shell structures, are frequently formed for metal–semiconductor[59–67] and oxide–chalcogenide systems.[68–73] Thus, the preparation of these core–shell heterostructures with semiconductor components represents a new and challenging direction for nanomaterials research. These types of heterostructures may provide enhanced functionality such as efficient charge-carrier separation and allow facet-dependent property investigation.[74] Recently, $Au–Cu_2O$ core–shell heterostructures with structurally well-defined cores and shells have been fabricated using a variety of gold-nanocrystal cores such as octahedra and rhombic dodecahedra.[75,76] This represents one of the first metal–semiconductor systems with both polyhedral core and shell components. Cubic and octahedral Cu_2O nanocrystals can also serve as templates for the generation of $Cu_2O–Cu_2S$ core–shell

Prof. M. H. Huang, P.-H. Lin
Department of Chemistry
National Tsing Hua University
Hsinchu 30013, Taiwan 101, Section 2, Kuang Fu Road,
Hsinchu 30013, Taiwan
E-mail: hyhuang@mx.nthu.edu.tw

Materials
Views
www.MaterialsViews.com

ADVANCED
FUNCTIONAL
MATERIALS
www.afm-journal.de

FEATURE ARTICLE

cubes and octahedra with and without the incorporation of gold nanocrystal cores.[77]

In this Feature Article, metal and metal oxide nanocrystals synthesized with systematic shape evolution are highlighted. Some of the illustrated examples are taken from our own research. Because nanoparticles with different morphologies and surface facets are produced from essentially the same solution conditions, their syntheses offer unique opportunities to consider factors affecting the particle shape. Time-dependent microscopy investigation during the growth process provides insights into the growth mechanisms of nanocrystals with shape control. This mechanistic analysis is also presented. Examples of bimetallic and metal–semiconductor core–shell heterostructures with structurally well-defined cores and shells are introduced next. Finally, the facet-dependent chemical and physical properties of these polyhedral nanocrystals and core–shell heterostructures are discussed. These include their photocatalytic, catalytic, electrical, and molecular adsorption properties.[14,41–43,52,75–84] Dramatic differences in these properties have been observed for nanocrystals with distinctly different surface facets. Nanostructures with enhanced properties can be fabricated through excellent control of nanocrystal morphologies.

2. Shape-Controlled Synthesis of Polyhedral Nanocrystals

2.1. Metal Nanocrystals

Song et al. have prepared gold nanocrystals with shape evolution from octahedra to truncated octahedra, cuboctahedra, and cubes by rapid reduction of $HAuCl_4 \cdot 3H_2O$ in refluxing 1,5-pentanediol and PVP, or poly(vinyl pyrrolidone).[39] Adjustment of the added amount of $AgNO_3$ resulted in the formation of these gold nanocrystals with sizes of ≈100 nm. Yang et a. have used a similar polyol synthesis approach to make silver nanocrystals with shapes varying from cubes to cuboctahedra, truncated octahedra, and octahedra.[85] A solution of $AgNO_3$ and $CuCl_2$ dissolved in 1,5-pentanediol and a separate solution of PVP dissolved in 1,5-pentanediol were injected into a hot (≈180 °C) 1,5-pentanediol solution in a flask at different rates. By collecting products after different reaction times, cubes were first synthesized, followed by nanocrystals with progressively larger fractions of {111} facets. Park et al. have observed the shape transformation of rhombic dodecahedral gold nanoparticles by collecting samples at various reaction times.[86] A mixture of $HAuCl_4$, N,N-dimethylformamide (DMF), PVP, and water was placed in a sealed vial and heated in an oil bath at 120 °C. DMF served as both a solvent and a reducing agent. At lower water content, rhombic dodecahedra were formed first. By increasing the reaction time, rhombicuboctahedra and octahedra were generated.

It is desirable to prepare gold nanocrystals in aqueous solution, because the particle surfaces can be readily modified, including linkages to various biomolecules. We have used a hydrothermal synthesis approach to make monodisperse octahedral gold nanocrystals from an aqueous solution of $HAuCl_4$, trisodium citrate, and cetyltrimethylammonium bromide (CTAB) surfactant.[6] A [CTAB]/[$HAuCl_4$] molar ratio of 60 was
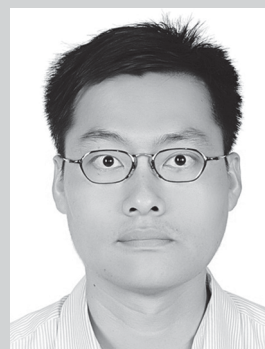
Michael H. Huang obtained his BA in chemistry in 1994 from Queens College, City University of New York and his PhD in 1999 from the University of California, Los Angeles. He was a postdoctoral fellow at UC Berkeley and then at UCLA from 1999 to 2002, working with Prof. Peidong Yang and Prof. Jeffrey I. Zink. He joined the Department of Chemistry at National Tsing Hua University in 2002 as an Assistant Professor. In 2006, he was promoted to Associate Professor and since 2010, he has been a Professor in the same department. His research interests include the shape-controlled synthesis of metal and semiconductor nanocrystals and their property characterization.

used. By heating the mixture at 110 °C for 6, 12, 24, 48, and 72 h, gold octahedra with approximate sizes of 30, 60, 90, 120, and 150 nm can be obtained. These monodisperse gold octahedra can spontaneously self-assemble into long-range ordered packed structures upon water evaporation. High-quality gold octahedra can be produced, but the reaction time is long.

By using a seed-mediated growth method, we have prepared gold nanocrystals with systematic shape evolution from truncated cubic to cubic, trisoctahedral, and rhombic dodecahedral structures in aqueous solution for the first time.[32] These particle shapes are important for the subsequent fabrication of core–shell heterostructures. Gold seed particles with sizes of a few nm were first made by mixing a solution of $HAuCl_4$ and cetyltrimethylammonium chloride (CTAC) surfactant with an ice-cold $NaBH_4$ solution. The seed particle solution was then added to a growth solution containing CTAC, water, $HAuCl_4$, NaBr, and ascorbic acid. A small amount of this solution was then transferred to a second growth solution. After reaction at room temperature for just 15 min, the desired nanocrystals were formed in the final solution. The combination of using CTAC surfactant and a very small amount of NaBr to control the bromide concentration in the growth solution was found to be critical to the formation of gold nanocubes. An increase in the volume of ascorbic acid added to the growth solution enables this nanocrystal shape evolution from nanocubes to trisoctahedra and finally rhombic dodecahedra. **Figure 1** shows scanning electron microscopy (SEM) images of these nanocrystals viewed from two different orientations and the corresponding drawings of the particles to illustrate this morphological evolution process. A nanocube is bounded by six {100} facets. A rhombic dodecahedral nanocrystal is bounded by twelve {110} rhombic faces. A trisoctahedral gold nanocrystal has been determined to expose mainly high-index {221} surfaces.[87,88] Nanocubes and rhombic dodecahedra with controlled sizes of 30–75 nm were synthesized by adjusting the volume of the seed solution added to the growth solution.
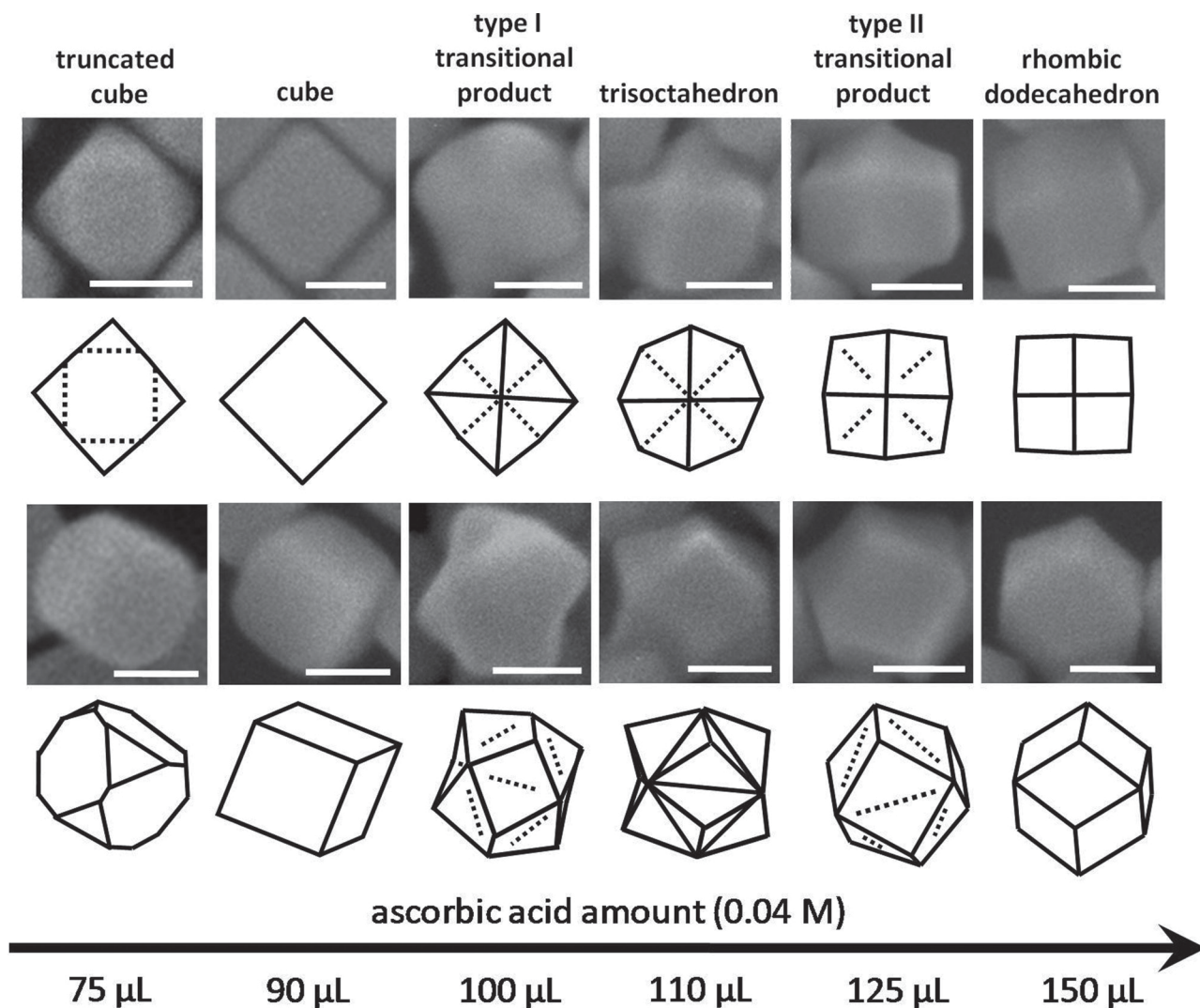
Figure 1. SEM images and the corresponding drawings showing the morphological evolution of the gold nanocrystals synthesized by varying the amount of ascorbic acid added to the reaction solution. All scale bars represent 50 nm. Reproduced with permission.[32] Copyright 2010, American Chemical Society.

Synthetic methods enabling a systematic shape evolution of gold nanocrystals from cubic to octahedral and cubic to rhombic dodecahedral structures have been demonstrated. It would be nice to develop a simple method that connects octahedral and rhombic dodecahedral structures. Recently, we have developed a seed-mediated and iodide-assisted method for the synthesis of monodisperse gold nanocrystals with systematic shape evolution from rhombic dodecahedral to octahedral structures.[40] It turns out that the procedure is very similar to that employed for the synthesis of cubic to rhombic dodecahedral gold nanocrystals. By progressively increasing the volume of KI used in a growth solution while keeping the amount of added ascorbic acid constant, nanocrystals with morphologies varying from rhombic dodecahedral to rhombicuboctahedral, edge- and corner-truncated octahedral, corner-truncated octahedral, and octahedral structures were synthesized. Particle growth is complete in 15 min at room temperature. **Figure 2** presents SEM images of the products synthesized. The nanocrystals are monodisperse in

size and readily form self-assembled structures on substrates. By simply adjusting the volume of gold-seed solution added to a growth solution, particle sizes of the octahedral gold nanocrystals can be tuned with average opposite corner-to-corner distances of 42, 48, 54, 60, 68, 93, 107, and 125 nm. Thus, octahedral gold nanocrystals can also be prepared over a large size range without using the hydrothermal synthesis method.

2.2. Metal Oxide Nanocrystals

It is also desirable to synthesize metal oxide and chalcogenide nanocrystals with similar systematic shape evolution. Materials with a cubic crystal structure should be required. Again this subsection only focuses on nanomaterials with systematic shape evolution. Yang et al. have prepared separate Pb and Te precursor solutions and injected the two solutions at different molar ratios to control the nanocrystal morphology.[44] The Pb solution

Materials
Views
www.MaterialsViews.com

ADVANCED
FUNCTIONAL
MATERIALS
www.afm-journal.de

FEATURE ARTICLE
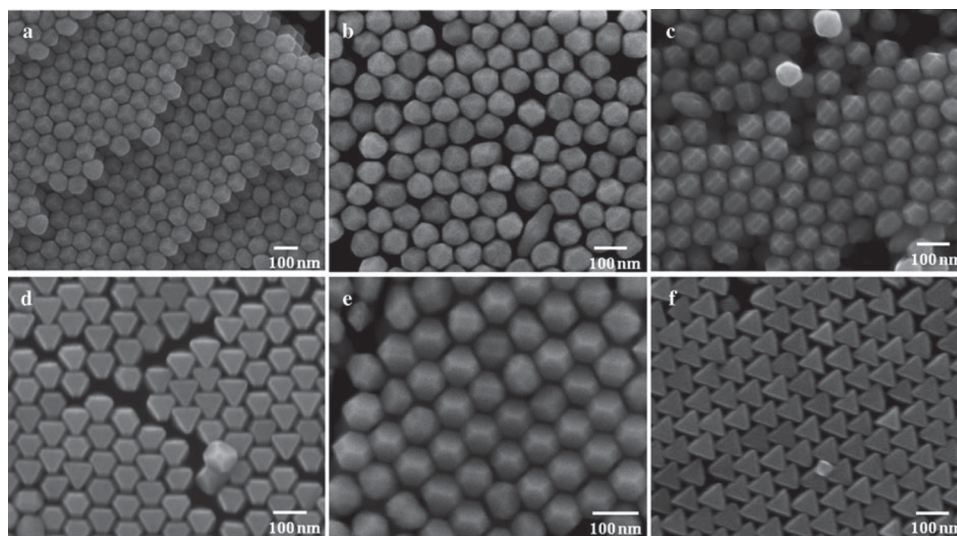
Figure 2. SEM images of the gold nanocrystals synthesized by progressively increasing the amount of added KI. a) Rhombic dodecahedra. b) Rhombicuboctahedra. c) Edge- and corner-truncated octahedra. d,e) Corner-truncated octahedra self-assembled into two different orientations. f) Octahedra. Reproduced with permission.[40]

contained lead acetate and oleic acid in trioctylphosphine (TOP) or diphenyl ether, and the Te solution contained dissolved Te powder in TOP. The two solutions heated to 250 °C were injected and the mixture was maintained at 170–180 °C for 3–4 min. At a Pb:Te precursor molar ratio of 5:1, PbSe octahedra were obtained. Changing the Pb:Te precursor molar ratio to 1:5 gave nanocubes. At intermediate molar ratios, cuboctahedra were collected.

We have developed aqueous solution methods for the syntheses of cuprous oxide and silver oxide nanocrystals with systematic shape evolution from cubic to octahedral and hexapod structures. A seed-mediated synthesis approach was first developed to grow monodisperse Cu_2O nanocubes with progressive increasing sizes of 40, 65, 100, 230, and 420 nm.[16] Six vials of aqueous solution of $CuSO_4$, sodium dodecyl sulfate (SDS) surfactant, sodium ascorbate, and NaOH were prepared. The 40-nm nanocubes formed in the second vial were added to the next vial to grow into larger nanocubes, and the process was repeated. Next, a direct method for the formation of cuprous oxide nanocrystals with shape evolution from cubic to octahedral structures was developed.[41,42] Perfectly cubic, truncated cubic, cuboctahedral, truncated octahedral, octahedral, and hexapod crystals can be synthesized directly in an aqueous solution of $CuCl_2$, NaOH, SDS surfactant, and hydroxylamine ($NH_2OH \cdot HCl$) reductant.[42] This particle morphology evolution is achieved by simply increasing the volume of hydroxylamine added to the reaction mixture. Products were collected after reaction at room temperature for 2 h. It is expected that $Cu(OH)_2$ precipitate and $Cu(OH)_4^{2-}$ ions form readily upon the addition of NaOH and are quickly reduced to Cu_2O by NH_2OH. **Figure 3** gives the SEM images of the Cu_2O crystals. The hexapods represent a progressive structural evolution beyond the octahedral structure with each corner of an octahedron developing into a square pyramidal branch enclosed by the {111} surfaces. The particle size distribution is fairly large, so it is still desirable to modify the reaction conditions to improve the size homogeneity and reduce their dimensions. The high morphological uniformity of these Cu_2O

crystals is reflected by their X-ray diffraction (XRD) patterns. Nanocubes show an exceptionally strong (200) reflection peak and an extremely weak (111) reflection peak. The intensity of
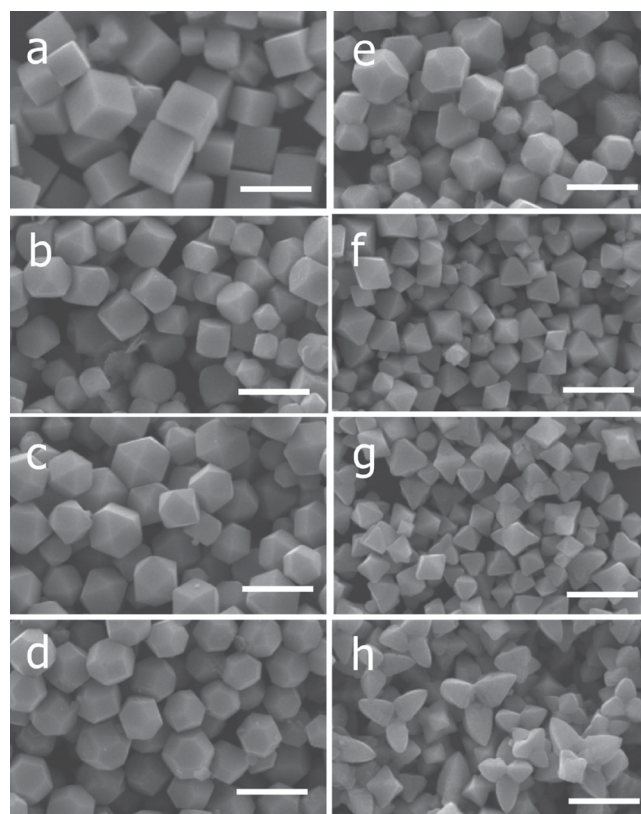
Figure 3. SEM images of the Cu_2O nanocrystals with various morphologies: a) cubes, b) truncated cubes, c) cuboctahedra, d,e) truncated octahedra, f) octahedra, g) short hexapods, and h) extended hexapods. Scale bar = 1 μm. Reproduced with permission.[42] Copyright 2009, American Chemical Society.

the (111) peak increases progressively as nanocrystals with more fractions of {111} faces are formed. The (111) peak dominates for octahedra and hexapods.

Ag$_2$O has the same cuprite crystal structure as that of Cu$_2$O. Very few reports have described the synthesis of Ag$_2$O crystals with morphology control. The preparation of polyhedral Ag$_2$O nanocrystals is more challenging than it appears, because a simple reaction of AgNO$_3$ and NaOH yields irregularly shaped particles. We have successfully developed a facile method for the synthesis of Ag$_2$O crystals with systematic shape evolution from cubic to edge- and corner-truncated cubic, rhombicuboctahedral, edge- and corner-truncated octahedral, octahedral, and hexapod structures by mixing AgNO$_3$, NH$_4$NO$_3$, and NaOH at molar ratios of 1:2:11.8.[43] By changing their molar ratios and AgNO$_3$ concentration in the final solution, octapods and elongated hexapods can also be prepared. **Figure 4** summarizes the different reaction conditions employed and the products formed. Systematic shape evolution

of the nanocrystals is achieved by progressively increasing the volume of 0.1 M AgNO$_3$ solution added. A sufficient volume of 2.0 M NaOH solution (i.e., 22.5 to 180 μL depending on the particle shape) was first added to a mixture of AgNO$_3$ and NH$_4$NO$_3$ solution to promote the formation of Ag(NH$_3$)$_2^+$ complex ions. Further, the addition of NaOH leads to the formation of AgOH, which can easily dehydrate to give Ag$_2$O. This strategy enables the growth of Ag$_2$O nanocrystals with a high degree of morphology control. The following reactions take place to form Ag$_2$O:

$$NH_4NO_3 + NaOH \rightarrow NH_3 + H_2O + Na^+ + NO_3^- \qquad (1)$$

$$AgNO_3 + 2NH_3 \leftrightarrow Ag(NH_3)_2^+ + NO_3^- \qquad (2)$$

$$Ag(NH_3)_2^+ + NaOH \leftrightarrow AgOH + 2NH_3 + Na^+ \qquad (3)$$

$$2AgOH \leftrightarrow Ag_2O + H_2O \qquad (4)$$
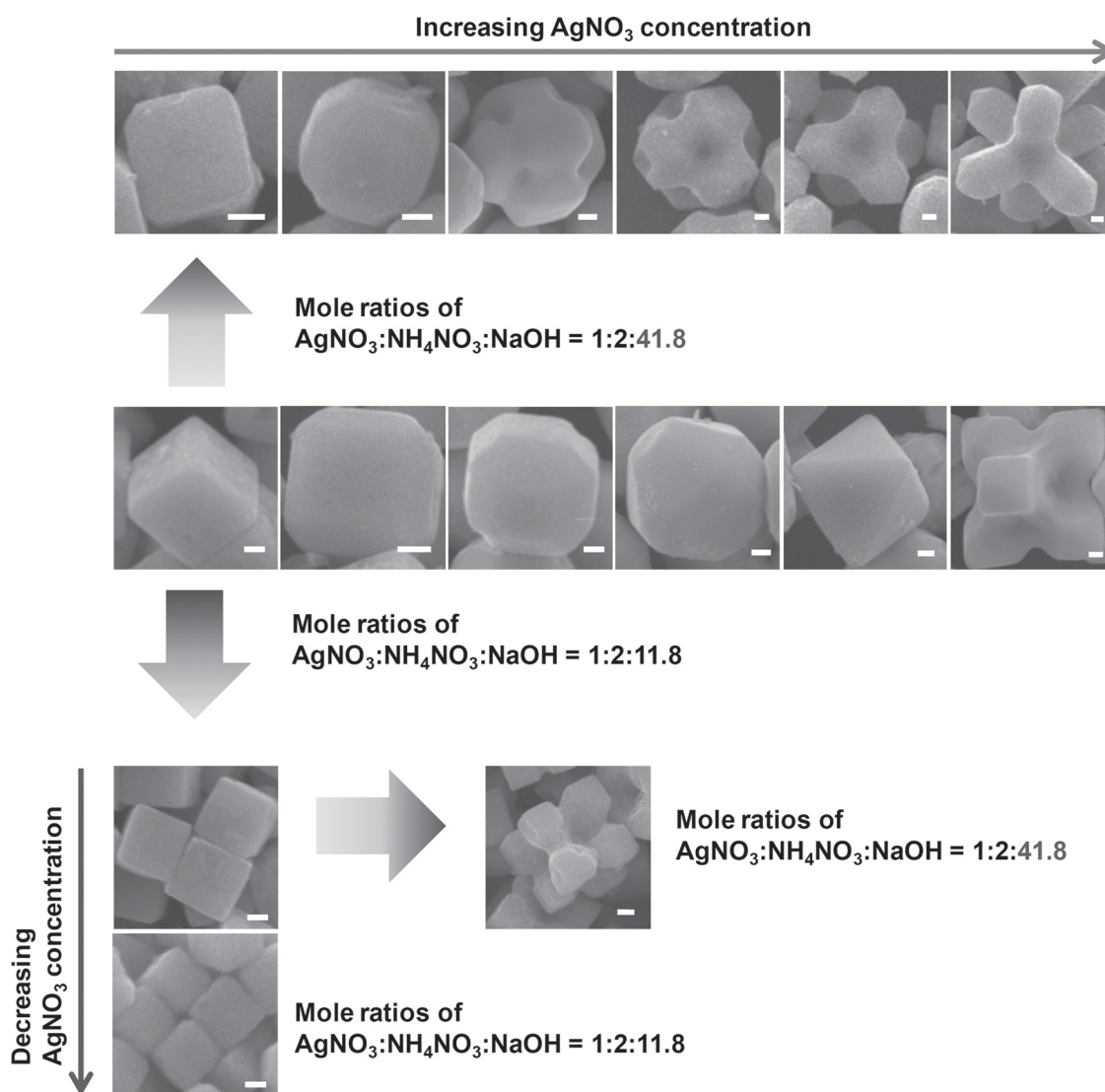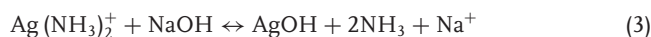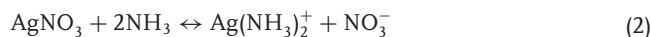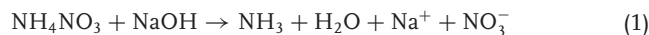
Figure 4. Schematic summary of the different experimental conditions used to obtain Ag$_2$O crystals with a variety of particle shapes. All scale bars represent 100 nm. Reprinted with permission.[43]

Materials
Views
www.MaterialsViews.com

ADVANCED
FUNCTIONAL
MATERIALS
www.afm-journal.de

2.3. Insights of the Growth Mechanisms from the Synthesis of Nanocrystals with Systematic Shape Evolution

Our series of work on the growth of Au, Cu_2O, and Ag_2O nanocrystals with systematic shape evolution offers interesting and important insights into the growth mechanisms of nanocrystals and factors governing their morphology. For the synthesis of Au nanocrystals with shape evolution from cubic to trisoctahedral and rhombic dodecahedral structures, the amount of surfactant used has been kept constant. It is the variation of ascorbic acid that controls the final geometries of the nanoparticles. For the growth of rhombic dodecahedral to octahedral Au nanocrystals, again the amount of surfactant used was kept the same. Adjustment of the volume of KI introduced resulted in the particle shape evolution. Iodide with its lower reduction potential can act as a reducing agent to modulate the precursor reduction rate.[40] To make Cu_2O nanocrystals with shape variation from cubic to cuboctahedral, octahedral and hexapod structures, the amount of surfactant we used was also kept constant. The gradual increase in the volume of $NH_2OH \cdot HCl$ introduced enables the transformation of nanocrystal morphology. A typical notion in the literature links the formation of different polyhedral nanocrystals to selective surfactant or polymer capping on certain crystal planes. Preferential halide ion adsorption on certain planes has also been suggested. Further crystal growth on these planes is inhibited, but growth on other crystal planes or along other directions is promoted. However, such mechanism cannot explain why the use of the same amount of surfactant and almost identical solution conditions still leads to the growth of Au and Cu_2O nanocrystals exposing exclusively {100}, {111}, and {110} surface planes for cubes, octahedra, and rhombic dodecahedra, respectively. In the case of Ag_2O nanocrystal growth with shapes varying from cubic to octahedral and hexapod structures, surfactant was not even added. Tuning of the reduction rates through adjustment of the concentration of the reducing agent in the reaction mixture seem to be the correct explanation for achieving the systematic shape evolution of Au and Cu_2O nanocrystals in our studies. In the growth of Au nanocrystals with shape evolution from cubic to rhombic dodecahedral structures, the concentrations of bromide and chloride ions in the solution are the same, so preferential adsorption of halide ions on certain crystal planes cannot be the cause of this shape transformation.[32] For the synthesis of Ag_2O crystals with shape evolution, formation of $Ag(NH_3)_2^+$ species is critical since its reaction with NaOH has an equilibrium constant of just 0.34. Direct reaction between $AgNO_3$ and NaOH has a large equilibrium constant (i.e., 5×10^8). In this sense, a slower reaction rate enables this particle shape evolution. These examples illustrate that although surfactant and other capping molecules may frequently be needed in the synthesis of nanocrystals for size and shape control, the control of reduction rate or reaction rate (for precipitation reactions) may be more critical and should be carefully considered in the expla-

Figure 5. Selected TEM images of the intermediate nanostructures observed during the growth of a) octahedral gold nanocrystals and b) Au–Pd core–shell heterostructures. Final products are also shown. The scale bar is equal to 20 nm for panel (b). a) Reproduced with permission.[40] b) Reproduced with permission.[52] Copyright 2010, American Chemical Society.

nation of growth mechanism and the design of experiments to achieve particle shape control.

Another issue relating to the growth mechanism of polyhedral nanocrystals is how nanocrystals are actually formed. R values have been used to describe the formation of particles with particular shapes.[89] R values typically refer the relative growth rate along the [100] directions to that along the [111] directions. Use of R values suggests that nucleation seed particles grow to their final sizes with a fair degree of maintenance of their initial shapes. Through investigation of intermediate structures formed during the growth of octahedral gold nanocrystals at around room temperature, we found that twisted or wormlike structures are produced at the very early stage (see **Figure 5**a).[40] These structures then concentrate toward the center. The central portion becomes a single crystal and grows in size by incorporating the surrounding twisted structures or particles. The initially formed single nanocrystals (for example, at 4 min) then undergo a fairly long period of surface reconstruction to evolve into their final octahedral shape. A similar growth process with surrounding twisted structures at the very early stage and a period of surface reconstruction has been observed in the growth of Pd shells on cubic Au cores and the formation of Au microplates (see Figure 5b).[52,90] Thus, such a growth mechanism of metal nanocrystals should be general. Intermediate structures examined in the growth of Cu_2O nanocrystals also suggest a long period of surface reconstruction before establishing the final particle morphologies.[41] The observations indicate that nanocrystals do not really grow following relative growth rates along different directions, as predicted by the R values.

3. Synthesis of Core–Shell Heterostructures

Many kinds of core–shell heterostructures including bimetallic, metal–semiconductor, and semiconductor–semiconductor systems have been reported. However, few papers have described the use of polyhedral nanocrystals as cores to make core–shell heterostructures with controlled shell geometry. Almost all the
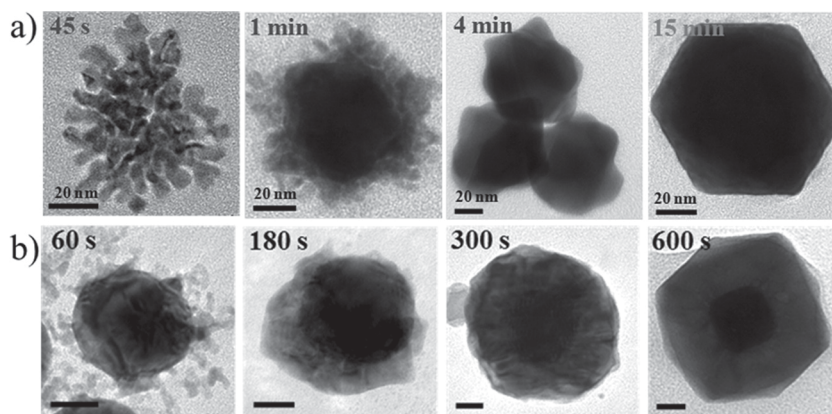
studies on the growth of core–shell nanocrystals using polyhedral cores involve bimetallic systems. This is because the crystal packing structures (face-centered cubic unit cells for many metals) and lattice matching are favorable. As an example, Yang et al. have used Pt nanocubes for the overgrowth of Pd shells with shell morphologies varying from cubic to cuboctahedral and octahedral structures.[47] Cubic Pt seeds were added to a heated solution containing tetradecyltrimethylammonium bromide (TTAB), ascorbic acid, and K_2PdCl_4 to make the binary metal nanocrystals. After the formation of cubic Pd shells, the shell morphology can be altered by increasing the amount of NO_2 added to form cuboctahedra and octahedra. In another study, Tian et al. have synthesized Au@Pd nanocubes using 30-nm octahedral Au nanocrystals as the cores.[48] The Au cores were added to a solution of H_2PdCl_4, ascorbic acid, and CTAB.

We have recently reported the synthesis of tetrahexahedral (THH) Au–Pd core–shell nanocrystals using gold nanocubes as the cores.[52] The gold nanocubes were prepared by the seed-mediated growth approach.[32] In a typical synthesis of the Au–Pd core–shell nanocrystals, CTAC, deionized water, Au nanocube solution, and H_2PdCl_4 solution were introduced into a sample vial. The vial was kept in a water bath set at 31 °C. Then ascorbic acid was added and the mixture was stirred. The solution color quickly turned brown and then gray by keeping the vial undisturbed in the water bath for 30 min. The THH nanocrystals were found to be bound by high-index {730} facets. Interestingly, the same THH nanocrystals can be prepared using rhombic dodecahedral and octahedral gold nanocrystal cores of similar sizes (see **Figure 6**). It is important to note that the cores and the shells are exactly oriented such that their respective lattice planes are aligned along the same directions. Au and Pd have a lattice mismatch of 4.61%. As the conformal shell growth increases in thickness, lattice strain can develop. The shell surface planes may become less regular on the atomic scale and the THH morphology with all high-index facets forms in response to the build-up of this lattice strain.
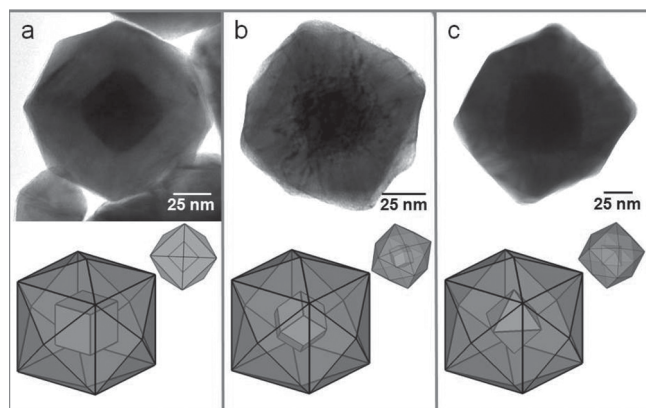
Figure 6. TEM images of single THH Au–Pd core–shell nanocrystals synthesized using a) cubic, b) rhombic dodecahedral, and c) octahedral gold nanocrystals as the structure-directing cores. Schematic drawings are also provided. The smaller drawings show the exact viewing directions corresponding to the respective TEM images. The lattice directions of the cores match those of the shells in all the cases. Reprinted with permission.[52] Copyright 2010, American Chemical Society.

We have found that CTAC is important for the formation of the THH Au–Pd nanocrystals. The role of chloride is likely related to the oxidative etching of Pd surface for the emergence of {730} faces via the following redox reaction:

$$2Pd + O_2 + 8Cl^- + 4H^+ \leftrightarrow 2PdCl_4^{2-} + 2H_2O \qquad (5)$$

For metal–semiconductor composites, heterojunctions, rather than core–shell structures, are typically produced. Thus, it is still quite challenging to form structurally well-defined semiconductor shells enclosing polyhedral metal nanoparticle cores. We have described the fabrication of Au–Cu_2O core–shell heterostructures using gold nanoplates, nanorods, octahedra, and highly faceted nanoparticles as the structure-directing cores for the overgrowth of Cu_2O shells by a facile aqueous solution approach.[75] The gold nanoparticle cores guide the growth of Cu_2O shells with morphological and orientation control. In a typical synthesis of the Au–Cu_2O core–shell heterostructures, water, $CuCl_2$ solution, SDS surfactant, Au nano-core solution, and NaOH were introduced into a sample vial in the order listed. After adding $NH_2OH \cdot HCl$ as the reducing agent, the solution color became yellow and finally light brown by aging the mixture for 2 h. By simply varying the amount of $NH_2OH \cdot HCl$ used in the reaction mixture, Au–Cu_2O core–shell structures with systematic morphological evolution can be achieved. **Figure 7** presents the SEM images of the heterostructures synthesized by varying the volume of 0.2 M $NH_2OH \cdot HCl$ used from 0.15 to 0.25, 0.45, and 0.65 mL. Truncated cubes, cuboctahedra, truncated octahedra, and octahedra were synthesized using octahedral gold nanocrystal cores. Unusual stellated icosahedra were obtained with the use of highly faceted particle cores. Each of the twenty triangular faces of the particle develops into a triangular pyramid. The stellated icosahedra are formed as a result of the interpenetrated growth of truncated cubes. When penta-twinned gold nanorods were used as cores to grow into core–shell structures, pentagonal prisms can be converted to form star columns by increasing the volume of $NH_2OH \cdot HCl$ added.

Cross-sectional TEM images reveal the exact orientation relationship between the cores and the shells, such that the {100} and {111} planes of Au and Cu_2O are parallel to each other. The lattice mismatch between the (111) planes of Au and the (111) planes of Cu_2O is about 4.5%, and 4.7% between the (200) planes of Au and the (200) planes of Cu_2O. These lattice mismatch percentages are considered rather large for epitaxial growth of core–shell structures. Despite the presence of a significant mismatch between Au and Cu_2O lattice planes, Au–Cu_2O core–shell heterostructures with excellent interfacial epitaxial growth can still be prepared. The (111) planes of Cu_2O were found to grow epitaxially on the {111} facets of gold for most of the cases examined, while the (200) planes of Cu_2O can grow over the {200} facets of gold to form the interfaces. In addition to the use of octahedral gold nanocrystal cores, we have also reported the employment of rhombic dodecahedral and highly edge- and corner-truncated octahedral gold nanocrystal cores with entirely or significant {110} faces as the structure-directing cores for the fabrication of Au–Cu_2O core–shell heterostructures.[76] By increasing the volume of reductant added, Au–Cu_2O face-raised cubes, cuboctahedra, and octahedra were synthesized. Transmission electron microscopy (TEM) characterization indicates a fixed core–shell orientation

Materials
Views
www.MaterialsViews.com

ADVANCED
FUNCTIONAL
MATERIALS
www.afm-journal.de

FEATURE ARTICLE
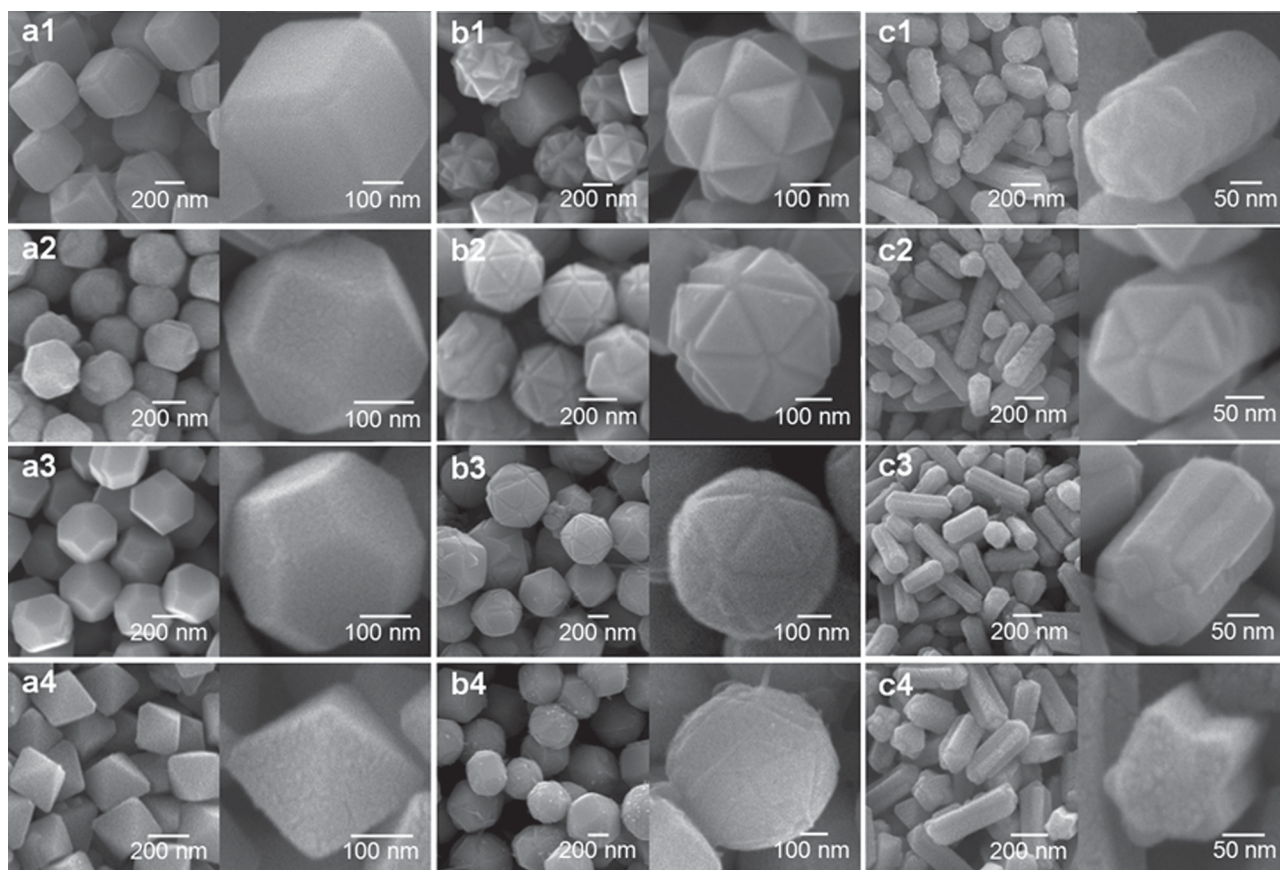
Figure 7. SEM images showing the systematic morphological evolution of the Au–Cu$_2$O core–shell heterostructures. By gradually increasing the volume of 0.2 M NH$_2$OH·HCl used in the synthesis of Au–Cu$_2$O core–shell heterostructures from 0.15 to 0.25, 0.45, and 0.65 mL, a1) truncated cubes, a2) cuboctahedra, a3) truncated octahedra, and a4) octahedra were synthesized using octahedral Au nanocrystal cores. b1) Stellated icosahedra were prepared with the use of highly faceted particle cores and the addition of 0.15 mL of 0.2 M NH$_2$OH·HCl. b2) Truncated stellated icosahedra were produced by adding 0.25 mL of NH$_2$OH·HCl. For further suppression of the formation of the triangular faces, the same 0.25 mL of NH$_2$OH·HCl was added, but b3) 0.5 and b4) 0.75 mL of 1 M NaOH need to be used. c1–c4) Pentagonal prisms were converted to form star columns by increasing the volume of NH$_2$OH·HCl added, (i.e. 0.15, 0.25, 0.45, and 0.65 mL). Reproduced with permission.[75] Copyright 2009, American Chemical Society.

relationship. The {100}, {110}, and {111} facets of the gold cores align parallel to the corresponding faces of the Cu$_2$O shells.

4. Facet-Dependent Properties

Metal and semiconductor nanocrystals and microcrystals with well-defined facets have been demonstrated to exhibit facet-dependent catalytic, photocatalytic, molecular adsorption and atom-deposition properties. These properties are all related to their surface chemistry. Thus, the ability to control the morphology of polyhedral nanocrystals should allow examinations of these important properties with greater certainty. Nanocrystals with enhanced properties may be selectively prepared.

Somorjai et al. have synthesized cubic and cuboctahedral Pt nanoparticles with average sizes of 12–14 nm using TTAB surfactant and compared their activity toward benzene hydrogenation.[80] The catalytic selectivity was found to be highly shape-dependent. Both cyclohexane and cyclohexene product

molecules were formed on cuboctahedral Pt nanoparticles, but only cyclohexane was produced using cubic Pt nanocatalysts. Choi et al. have used cubic, cuboctahedral, and octahedral Cu$_2$O crystals to exploit preferential adsorption of SDS surfactant on the {111} planes of Cu$_2$O microcrystals through the plane-selective deposition of gold nanoparticles.[82] In the presence of SDS, gold nanoparticles were found to exclusively deposit on the {100} faces of the Cu$_2$O crystals. Preferential adsorption of SDS on the {111} faces can effectively inhibit nucleation of gold on these planes. It is likely that SDS being a negatively charged surfactant interacts more strongly with copper atom-terminated {111} surfaces of Cu$_2$O. We have recently shown that rhombic dodecahedral gold nanocrystals are better and more sensitive substrates for surface-enhanced Raman spectroscopic detection of thiophenol than gold nanocubes and octahedra do.[91] This is attributed to stronger molecular interactions of thiophenol with the {110} planes of gold.

We have also demonstrated highly facet-dependent photocatalytic and electrical properties of Cu$_2$O nanocrystals. To see the relative photocatalytic activities of different sharp-faced
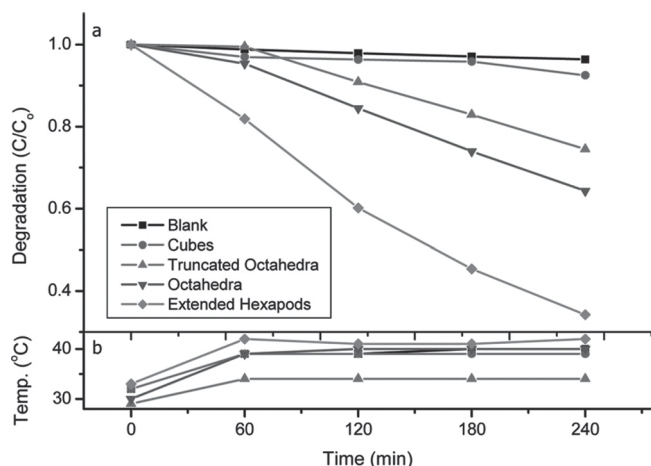
Figure 8. A plot of the extent of photodegradation of methyl orange versus time for the various Cu$_2$O nanostructures is shown. The blank sample did not contain Cu$_2$O crystals but only the methyl orange solution. A temperature change of the solution over this time period is also given. Reproduced with permission.[42] Copyright 2009, American Chemical Society.

Cu$_2$O nanostructures synthesized, methyl orange, a negatively charged molecule, was used for the photodecomposition experiments. **Figure 8** gives a plot of the extent of photodegradation of methyl orange versus time for the various Cu$_2$O nanostructures used.[42] Octahedra and the extended hexapods with entirely {111} facets exhibited moderately good photocatalytic activity towards the photodegradation of methyl orange, while perfect cubes with entirely {100} faces were practically not active. The catalytic activity of the {111} faces is attributed to the presence of surface copper atoms as revealed by the surface plane models of Cu$_2$O, making the {111} faces more positively charged. This facilitates adsorption of molecules carrying negative charges such as methyl orange and SDS. The electrically neutral or less-charged {100} faces cannot interact well with charged molecules and are catalytically inactive. Remarkably, solutions containing positively charged molecules such as methylene blue can repel crystals with {111} surfaces and make a significant amount of the crystals floating to the top surface of the solution after stirring the nanocrystal solutions for tens of minutes. The cubes are insensitive to the molecular charge and can stay in the solution. Similar behavior has been observed for Ag$_2$O nanocrystals with the same cuprite crystal structure.[43] Electrostatic repulsion force is believed to cause this effect for the octahedra and hexapods. Interestingly, Au–Cu$_2$O core–shell octahedra were found to display a better photocatalytic activity toward the photodegradation of methyl orange than pristine Cu$_2$O octahedra did, while sharp-faced core–shell cubes bound by only {100} faces were still inactive.[76,78] The photocatalytic enhancement is attributed to more efficient charge separation of photogenerated charge carriers with electrons migrating to the gold cores. This investigation reveals

that photocatalytic enhancement of Au–Cu$_2$O core–shell heterostructures only occurs with Cu$_2$O crystals exposing proper surface facets.

Cu$_2$O nanocrystals have also been shown to exhibit strongly facet-dependent electrical behavior, and that the gold nanocrystal cores can further enhance the electrical conductivity of the conductive facets.[78] **Figure 9** offers the schematic drawing of two oxide-free tungsten probes attached to a nanomanipulator installed inside a scanning electron microscope making contacts to a single Cu$_2$O nanocrystal for current–voltage (I–V) measurements. In one set of measurements, pristine Cu$_2$O octahedra bound by {111} facets were found to be 1100 times more conductive than pristine Cu$_2$O cubes enclosed by {100} faces, which are barely conductive. A 10 000-fold increase in conductivity over a cube has been recorded for an octahedron. Remarkably, core–shell octahedra are far more conductive than pristine octahedra. As shown in Figure 9, a core–shell octahedron quickly reaches a current of 1000 nA at 1.9 V, while it needs an applied voltage of ≈5 V for a pristine octahedron to get to this current value. The same facet-dependent electrical behavior can still be observed on a single truncated octahedral nanocrystal exposing both {111} and {100} facets. This example illustrates the importance of shape control of nanocrystals and core–shell heterostructures. Similar facet-dependent electrical properties may be observable in other semiconductor nanocrystals and should be measured when it is possible.

5. Conclusions

In this Feature Article, the growth of some metal and semiconductor nanocrystals with systematic shape evolution is described. Nanocrystals with cubic, cuboctahedral, truncated octahedral, rhombic dodecahedral, hexapod, and other symmetrical structures have been synthesized. In particular, we have shown that Au, Cu$_2$O, and Ag$_2$O nanocrystals can be prepared with a high degree of morphology control. The polyhedral Au nanocrystals can also serve as structure-directing cores for the fabrication of Au–Pd and Au–Cu$_2$O core–shell heterostructures. Shape evolution of the Cu$_2$O shells can be easily achieved. These studies offer important insights into the growth mechanisms of nanocrystals, because the solution conditions are almost the same in the synthesis of these nanocrystals with systematic shape evolution. Reaction or reduction rate, rather than plane-selective
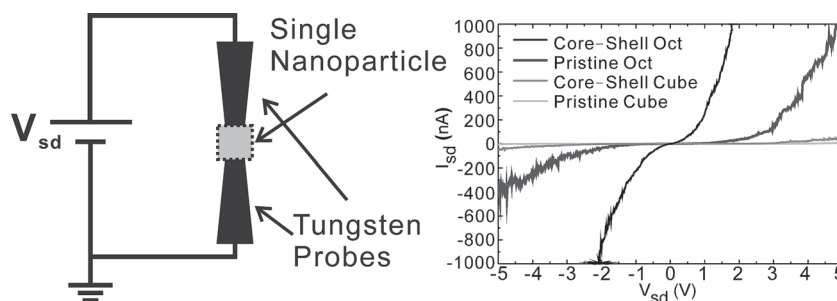
Figure 9. A schematic drawing for the electrical conductivity measurements of pristine Cu$_2$O and Au–Cu$_2$O core–shell cubes and octahedra and the recorded I–V curves. Reproduced with permission.[78] Copyright 2011, American Chemical Society.

www.MaterialsViews.com

ADVANCED
FUNCTIONAL
MATERIALS

www.afm-journal.de

FEATURE ARTICLE

adsorption of surfactant molecules or halide ions, was found to be the factor controlling the final particle morphology. Examination of intermediate products collected during particle growth reveals the formation of extensive twisted or wormlike structures at the very early stage. These nanostructures then concentrate toward the center to form a single crystal. Continuous incorporation of these external nanostructures, followed by a substantial period of surface reconstruction, yields the final product shape. This growth mechanism was found to be general. Cu_2O nanocrystals exhibit highly facet-dependent photocatalytic activity and electrical conductivity. Octahedra exposing {111} facets are photocatalytically active and electrically conductive, while nanocubes bound by {100} facets are inactive and not conductive. Enhanced photocatalytic and electrical conductivity performance has been recorded for Au–Cu_2O core–shell octahedra.

Despite the success in the shape-controlled synthesis of nanocrystals, illustrated here, this high level of morphology control is still quite challenging for many semiconductor systems with cubic crystal structures. Fabrication of metal–semiconductor and semiconductor–semiconductor core–shell heterostructures with both polyhedral core and shell morphology remain a daunting task. However, we have seen that nanocrystals with enhanced catalytic and electrical properties may be obtained through excellent control of their surface facets and shapes. For the discovery of new materials properties, we need to continue our efforts in the shape-controlled synthesis of nanocrystals of other compositions, particularly oxides and chalcogenides. Their facet-dependent properties should be measured. These nanocrystals should ultimately be important for various applications with enhanced properties.

Acknowledgements

[1] X. Wang, J. Zhuang, Q. Peng, Y. Li, *Nature* **2005**, *437*, 121–124.
[2] Y. Yin, A. P. Alivisatos, *Nature* **2005**, *437*, 664–670.
[3] B. Lim, M. Jiang, J. Tao, P. H. C. Camargo, Y. Zhu, Y. Xia, *Adv. Funct. Mater.* **2009**, *19*, 189–200.
[4] Y. Xiong, Y. Xia, *Adv. Mater.* **2007**, *19*, 3385–3391.
[5] M. L. Personick, M. R. Langille, J. Zhang, N. Harris, G. C. Schatz, C. A. Mirkin, *J. Am. Chem. Soc.* **2011**, *133*, 6170–6173.
[6] C.-C. Chang, H.-L. Wu, C.-H. Kuo, M. H. Huang, *Chem. Mater.* **2008**, *20*, 7570–7574.
[7] G. H. Jeong, M. Kim, Y. W. Lee, W. Choi, W. T. Oh, Q.-H. Park, S. W. Han, *J. Am. Chem. Soc.* **2009**, *131*, 1672–1673.
[8] Y. Ma, Q. Kuang, Z. Jiang, Z. Xie, R. Huang, L. Zheng, *Angew. Chem. Int. Ed.* **2008**, *47*, 8901–8904.
[9] M. Tsuji, Y. Maeda, S. Hikino, H. Kumagae, M. Matsunaga, X.-L. Tang, R. Matsuo, M. Ogino, P. Jiang, *Cryst. Growth Des.* **2009**, *9*, 4700–4705.
[10] W. Niu, L. Zhang, G. Xu, *ACS Nano* **2010**, *4*, 1987–1996.
[11] W. Niu, Z.-Y. Li, L. Shi, X. Liu, H. Li, S. Han, J. Chen, G. Xu, *Cryst. Growth Des.* **2008**, *8*, 4440–4444.
[12] H. Lee, S. E. Habas, S. Kweskin, D. Butcher, G. A. Somorjai, P. Yang, *Angew. Chem. Int. Ed.* **2006**, *45*, 7824–7828.
[13] C.-Y. Chiu, Y. Li, L. Ruan, X. Ye, C. B. Murray, Y. Huang, *Nature Chem.* **2011**, *3*, 393–399.
[14] Y.-X. Chen, S.-P. Chen, Z.-Y. Zhou, N. Tian, Y.-X. Jiang, S.-G. Sun, Y. Ding, Z. L. Wang, *J. Am. Chem. Soc.* **2009**, *131*, 10860–10862.
[15] K. X. Yao, X. M. Yin, T. H. Wang, H. C. Zeng, *J. Am. Chem. Soc.* **2010**, *132*, 6131–6144.
[16] C.-H. Kuo, C.-H. Chen, M. H. Huang, *Adv. Funct. Mater.* **2007**, *17*, 3773–3780.
[17] M. J. Siegfried, K.-S. Choi, *J. Am. Chem. Soc.* **2006**, *128*, 10356–10357.
[18] X. Liang, L. Gao, S. Yang, J. Sun, *Adv. Mater.* **2009**, *21*, 2068–2071.
[19] Z. Peng, Y. Jiang, Y. Song, C. Wang, H. Zhang, *Chem. Mater.* **2008**, *20*, 3153–3162.
[20] M. S. Bakshi, P. Thakur, S. Sachar, G. Kaur, T. S. Banipal, F. Possmayer, N. O. Peterson, *J. Phys. Chem. C* **2007**, *111*, 18087–18098.
[21] W. Lu, J. Fang, Y. Ding, Z. L. Wang, *J. Phys. Chem. B* **2005**, *109*, 19219–19222.
[22] Y. Wang, Q. Dai, B. Zou, W. W. Yu, B. Liu, G. Zou, *Langmuir* **2010**, *26*, 19129–19135.
[23] N. Wang, X. Cao, L. Guo, S. Yang, Z. Wu, *ACS Nano* **2008**, *2*, 184–190.
[24] T. K. Sau, A. L. Rogach, *Adv. Mater.* **2010**, *22*, 1781–1804.
[25] T. K. Sau, A. L. Rogach, F. Jäckel, T. A. Klar, J. Feldmann, *Adv. Mater.* **2010**, *22*, 1805–1825.
[26] D. Wang, Y. Li, *Adv. Mater.* **2011**, *23*, 1044–1060.
[27] C.-H. Kuo, M. H. Huang, *Nano Today* **2010**, *5*, 106–116.
[28] Y.-w. Jun, J.-s. Choi, J. Cheon, *Angew. Chem. Int. Ed.* **2006**, *45*, 3414–3439.
[29] M. Grzelczak, J. Pérez-Juste, P Mulvaney, L. M. Liz-Marzán, *Chem. Soc. Rev.* **2008**, *37*, 1783–1791.
[30] L. Liu, Z. Zhuang, T. Xie, Y.-G. Wang, J. Li, Q. Peng, Y. Li, *J. Am. Chem. Soc.* **2009**, *131*, 16423–16429.
[31] T. Huang, Q. Zhao, J. Xiao, L. Qi, *ACS Nano* **2010**, *4*, 4707–4716.
[32] H.-L. Wu, C.-H. Kuo, M. H. Huang, *Langmuir* **2010**, *26*, 12307–12313.
[33] A. R. Tao, D. P. Ceperley, P. Sinsermsuksakul, A. R. Neureuther, P. Yang, *Nano Lett.* **2008**, *8*, 4033–4038.
[34] Z. Quan, J. Fang, *Nano Today* **2010**, *5*, 390–411.
[35] M.-P. Pileni, *Acct. Chem. Res.* **2007**, *40*, 685–693.
[36] S. Disch, E. Wetterskog, R. P. Hermann, G. Salazar-Alvarez, P. Busch, T. Brückel, L. Bergström, S. Kamali, *Nano Lett.* **2011**, *11*, 1651–1656.
[37] Z. Zhu, H. Meng, W. Liu, X. Liu, J. Gong, X. Qiu, L. Jiang, D. Wang, Z. Tang, *Angew. Chem. Int. Ed.* **2011**, *50*, 1593–1596.
[38] S. Xie, X. Zhou, X. Han, Q. Kuang, M. Jin, Y. Jiang, Z. Xie, L. Zheng, *J. Phys. Chem. C* **2009**, *113*, 19107–19111.
[39] D. Seo, J. C. Park, H. Song, *J. Am. Chem. Soc.* **2006**, *128*, 14863–14870.
[40] P.-J. Chung, L.-M. Lyu, M. H. Huang, *Chem. Eur. J.* **2011**, *17*, 9746–9752.
[41] C.-H. Kuo, M. H. Huang, *J. Phys. Chem. C* **2008**, *112*, 18355–18360.
[42] J.-Y. Ho, M. H. Huang, *J. Phys. Chem. C* **2009**, *113*, 14159–14164.
[43] L.-M. Lyu, W.-C. Wang, M. H. Huang, *Chem. Eur. J.* **2010**, *16*, 14167–14174.
[44] T. Mokari, M. Zhang, P. Yang, *J. Am. Chem. Soc.* **2007**, *129*, 9864–9865.
[45] Y. Sui, W. Fu, H. Yang, Y. Zeng, Y. Zhang, Q. Zhao, Y. Li, X. Zhou, Y. Leng, M. Li, G. Zou, *Cryst. Growth Des.* **2010**, *10*, 99–108.
[46] D.-F. Zhang, H. Zhang, L. Guo, K. Zheng, X.-D. Han, Z. Zhang, *J. Mater. Chem.* **2009**, *19*, 5220–5225.
[47] S. E. Habas, H. Lee, V. Radmilovic, G. A. Somorjai, P. Yang, *Nature Mater.* **2007**, *6*, 692–697.

[48] F.-R. Fan, D. Y. Liu, Y.-F. Wu, S. Duan, Z.-X. Xie, Z.-Y. Jiang, Z.-Q. Tian, *J. Am. Chem. Soc.* **2008**, *130*, 6949–6951.

[49] M. Tsuji, R. Matsuo, P. Jiang, N. Miyamae, D. Ueyama, M. Nishio, S. Hikino, H. Kumagae, K. S. N. Kamarudin, X.-L. Tang, *Cryst. Growth Des.* **2008**, *8*, 2528–2536.

[50] F. Wang, L.-D. Sun, W. Feng, H. Chen, M. H. Yeung, J. Wang, C.-H. Yan, *Small* **2010**, *6*, 2566–2575.

[51] Y. Ding, F. Fan, Z. Tian, Z. L. Wang, *J. Am. Chem. Soc.* **2010**, *132*, 12480–12486.

[52] C.-L. Lu, K. S. Prasad, H.-L. Wu, J.-a. A. Ho, M. H. Huang, *J. Am. Chem. Soc.* **2010**, *132*, 14546–14553.

[53] M. Jiang, B. Lim, J. Tao, P. H. C. Camargo, C. Ma, Y. Zhu, Y. Xia, *Nanoscale* **2010**, *2*, 2406–2411.

[54] F. Wang, C. Li, L.-D. Sun, H. Wu, T. Ming, J. Wang, J. C. Yu, C.-H. Yan, *J. Am. Chem. Soc.* **2011**, *133*, 1106–1111.

[55] Y. Xiang, X. Wu, D. Liu, X. Jiang, W. Chu, Z. Li, Y. Ma, W. Zhou, S. Xie, *Nano Lett.* **2006**, *6*, 2290–2294.

[56] C. Xue, J. E. Millstone, S. Li, C. A. Mirkin, *Angew. Chem. Int. Ed.* **2007**, *46*, 8436–8439.

[57] B. Lim, J. Wang, P. H. C. Camargo, M. Jiang, M. J. Kim, Y. Xia, *Nano Lett.* **2008**, *8*, 2535–2540.

[58] J. Zhang, Y. Tang, K. Lee, M. Ouyang, *Science* **2010**, *327*, 1634–1638.

[59] T. Mokari, E. Rothenberg, I. Popov, R. Costi, U. Banin, *Science* **2004**, *304*, 1787–1790.

[60] Z. Sun, Z. Yang, J. Zhou, M. H. Yeung, W. Ni, H. Wu, J. Wang, *Angew. Chem., Int. Ed.* **2009**, *48*, 2881–2885.

[61] W. Shi, H. Zeng, Y. Sahoo, T. Y. Ohulchanskyy, Y. Ding, Z. L. Wang, M. Swihart, P. N. Prasad, *Nano Lett.* **2006**, *6*, 875–881.

[62] T. Mokari, C. G. Sztrum, A. Salant, E. Rabani, U. Banin, *Nature Mater.* **2005**, *4*, 855–863.

[63] J. Yang, H. I. Elim, Q. Zhang, J. Y. Lee, W. Ji, *J. Am. Chem. Soc.* **2006**, *128*, 11921–11926.

[64] H. Gu, R. Zheng, X. Zhang, B. Xu, *J. Am. Chem. Soc.* **2004**, *126*, 5664–5665.

[65] H. Yu, M. Chen, P. M. Rice, S. X. Wang, R. L. White, S. Sun, *Nano Lett.* **2005**, *5*, 379–382.

[66] S. E. Habas, P. Yang, T. Mokari, *J. Am. Chem. Soc.* **2008**, *130*, 3294–3295.

[67] C. Wang, C. Xu, H. Zeng, S. Sun, *Adv. Mater.* **2009**, *21*, 3045–3052.

[68] H. McDaniel, M. Shim, *ACS Nano* **2009**, *3*, 434–440.

[69] G. Zhu, Z. Xu, *J. Am. Chem. Soc.* **2011**, *133*, 148–157.

[70] K.-W. Kwon, M. Shim, *J. Am. Chem. Soc.* **2005**, *127*, 10269–10275.

[71] R. Buonsanti, V. Grillo, E. Carlino, C. Giannini, M. L. Curri, C. Innocenti, C. Sangregorio, K. Achterhold, F. G. Parak, A. Agostiano, P. D. Cozzoli, *J. Am. Chem. Soc.* **2006**, *128*, 16953–16970.

[72] S. Kudera, L. Carbone, M. F. Casula, R. Cingolani, A. Falqui, E. Snoeck, W. J. Parak, L. Manna, *Nano Lett.* **2005**, *5*, 445–449.

[73] T. Teranishi, Y. Inoue, M. Nakaya, Y. Oumi, T. Sano, *J. Am. Chem. Soc.* **2004**, *126*, 9914–9915.

[74] L. Amirav, A. P. Alivisatos, *J. Phys. Chem. Lett.* **2010**, *1*, 1051–1054.

[75] C.-H. Kuo, T.-E. Hua, M. H. Huang, *J. Am. Chem. Soc.* **2009**, *131*, 17871–17878.

[76] W.-C. Wang, L.-M. Lyu, M. H. Huang, *Chem. Mater.* **2011**, *23*, 2677–2684.

[77] C.-H. Kuo, Y.-T. Chu, Y.-F. Song, M. H. Huang, *Adv. Funct. Mater.* **2011**, *21*, 792–797.

[78] C.-H. Kuo, Y.-C. Yang, S. Gwo, M. H. Huang, *J. Am. Chem. Soc.* **2011**, *133*, 1052–1057.

[79] Y. Bi, S. Ouyang, N. Umezawa, J. Cao, J. Ye, *J. Am. Chem. Soc.* **2011**, *133*, 6490–6492.

[80] K. M. Bratlie, H. Lee, K. Komvopoulos, P. Yang, G. A. Somorjai, *Nano Lett.* **2007**, *7*, 3097–3101

[81] M. J. Siegfried, K.-S. Choi, *J. Am. Chem. Soc.* **2006**, *128*, 10356–10357.

[82] C. G. Read, E. M. P. Steinmiller, K.-S. Choi, *J. Am. Chem. Soc.* **2009**, *131*, 12040–12041.

[83] A.-X. Yin, X.-Q. Min, Y.-W. Zhang, C.-H. Yan, *J. Am. Chem. Soc.* **2011**, *133*, 3816–3819.

[84] Y. Zhang, B. Deng, T. Zhang, D. Gao, A.-W. Xu, *J. Phys. Chem. C* **2010**, *114*, 5073–5079.

[85] A. Tao, P. Sinsermsuksakul, P. Yang, *Angew. Chem. Int. Ed.* **2006**, *45*, 4597–4601.

[86] D. Y. Kim, S. H. Im, O. O. Park, Y. T. Lim, *CrystEngComm* **2010**, *12*, 116–121.

[87] Y. Ma, Q. Kuang, Z. Jiang, Z. Xie, R. Huang, L. Zheng, *Angew. Chem. Int. Ed.* **2008**, *47*, 8901–8904.

[88] Y. Yu, Q. Zhang, X. Lu, J. Y. Lee, *J. Phys. Chem. C* **2010**, *114*, 11119–11126.

[89] Z. L. Wang, *J. Phys. Chem. B* **2000**, *104*, 1153–1175.

[90] W.-L. Huang, C.-H. Chen, M. H. Huang, *J. Phys. Chem. C* **2007**, *111*, 2533–2538.

[91] H.-L. Wu, H.-R. Tsai, Y.-T. Hung, K.-U. Lao, C.-W. Liao, P.-J. Chung, J.-S. Huang, I-C. Chen, M. H. Huang, *Inorg. Chem.* **2011**, *50*, 8106–8111.

FULL PAPER

Inverse-Woodpile Photonic Band Gap Crystals with a Cubic Diamond-like Structure Made from Single-Crystalline Silicon

J. M. van den Broek,* L. A. Woldering, R. W. Tjerkstra, F. B. Segerink, I. D. Setija, and W. L. Vos

Three dimensional photonic band gap crystals with a cubic diamond-like symmetry are fabricated. These so-called inverse-woodpile nanostructures consist of two perpendicular sets of pores in single-crystal silicon wafers and are made by means of complementary metal oxide–semiconductor (CMOS)-compatible methods. Both sets of pores have high aspect ratios and are made by deep reactive-ion etching. The mask for the first set of pores is defined in chromium by means of deep UV scan-and-step technology. The mask for the second set of pores is patterned using an ion beam and carefully placed at an angle of 90° with an alignment precision of better than 30 nm. Crystals are made with pore radii between 135–186 nm with lattice parameters $a = 686$ and $c = 488$ nm such that $a/c = \sqrt{2}$; hence the structure is cubic. The crystals are characterized using scanning electron microscopy and X-ray diffraction. By milling away slices of crystal, the pores are analyzed in detail in both directions regarding depth, radius, tapering, shape, and alignment. Using optical reflectivity it is demonstrated that the crystals have broad reflectivity peaks in the near-infrared frequency range, which includes the telecommunication range. The strong reflectivity confirms the high quality of the photonic crystals. Furthermore the width of the reflectivity peaks agrees well with gaps in calculated photonic band structures.

1. Introduction

Photonic crystals are metamaterials with periodic variations of the dielectric function on length scales comparable to the wavelength of light. These dielectric composites are of keen

J. M. van den Broek, Dr. L. A. Woldering,
Dr. R. W. Tjerkstra, Prof. W. L. Vos
Complex Photonic Systems (COPS)
MESA+ Institute for Nanotechnology
University of Twente
7500 AE Enschede, The Netherlands
E-mail: j.m.vandenbroek@utwente.nl
F. B. Segerink
Optical Sciences (OS)
MESA+ Institute for Nanotechnology
University of Twente
7500 AE Enschede, The Netherlands
Dr. I. D. Setija
ASML Netherlands B.V., 5504 DR Veldhoven, The Netherlands

interest for scientists and engineers because they offer exciting ways to manipulate photons.[1,2] Of particular interest are three-dimensional (3D) photonic crystals possessing a photonic band gap; a frequency range where no photon modes exist at all. Photonic band gap materials possess great potential to drastically change the rate of spontaneous emission and to achieve localization of light.[3–5] Control over spontaneous emission is important for many applications, such as miniature lasers,[6] light-emitting diodes,[7] and solar cells.[8,9]

Different types of 3D photonic crystals have been conceived.[10–13] Of special interest are those that potentially provide large 3D photonic band gaps. Such structures offer ultimate control of light in all three dimensions simultaneously and therefore many research groups are pursuing their fabrication.[14–20] A promising class of 3D photonic crystals has a diamond-like symmetry.[21] Among these diamond structures, inverse-woodpile photonic crystals are of particular interest[10] because of their conceptual ease of fabrication and a broad photonic band gap that is robust to disorder and fabrication imperfections.[22–24] These crystals consist of two perpendicular arrays of cylindrical pores containing air in a high-refractive-index material, see **Figure 1**A. The predicted band gap of inverse-woodpile photonic crystals has a broad relative bandwidth of more than 25%.[10,23,25] We have chosen single-crystalline silicon as a high-refractive-index material since it is conveniently available in high purity. Many techniques for the fabrication of electronical and mechanical components in silicon are available, which eases the integration of photonics and electronics with silicon.[26]

Herein we report the fabrication and characterization of inverse-woodpile photonic crystals in monocrystalline silicon. The nanostructures consist of two separate sets of pores that run in perpendicular directions; see Figure 1A for a schematic illustration. Pores run along the x (first set) and z axis (second set), and are aligned in such a way that the second pore set is centered between the pores that run in the first direction, see Figure 1B. Therefore, the resulting structure has a network

**ADVANCED
FUNCTIONAL
MATERIALS**

www.afm-journal.de

Materials Views

www.MaterialsViews.com

FULL PAPER

Figure 1. A) Schematic illustration of a cubic inverse-woodpile structure. The structure consists of two perpendicular pore sets parallel to the *x* and *z* axis. This perspective view shows that the pores overlap, thereby creating a topologically connected structure. B) Schematic drawing of an inverse-woodpile photonic crystal viewed along the *z* axis. Each pore set forms a centered rectangular lattice with lattice parameters $a/c = \sqrt{2}$ and Miller indices (*hkl*) = (110). The axes of the cylinders running in the *x* direction are centered between rows of cylinders of the other set. C) Dispersion relations of light calculated for an inverse-woodpile structure consisting of a high-index material with $\varepsilon = 12.1$ (silicon) and air. The wavevector runs between high-symmetry points in the first Brillouin zone as is shown in the inset. The band gap (gray bar) of a cubic inverse-woodpile photonic crystal [(*R/a*) = 0.245 and $a/c = \sqrt{2}$] has a broad relative bandwidth of 25.4%. D) Calculated frequency and relative band gap width versus normalized pore radius (*R/a*). The band gap has a maximum width of 25.4% at a central frequency (*a/λ*) = 0.581 for (*R/a*) = 0.245.

topology which is favorable for the desired formation of a photonic band gap.[27] The pores form a centered rectangular lattice in which the lattice parameters *a* and *c* have a ratio $a/c = \sqrt{2}$; this ensures that the 3D crystal structure is cubic with a diamond-like symmetry. Each array of pores forms an (*hkl*) = (110) face.

By varying the relative pore radius *R/a*, the volume fraction of the constituent materials can be tuned and hence the photonic interaction strength. For high-index materials with a dielectric function of silicon, inverse-woodpile structures develop a band gap as shown in Figure 1C. For (*R/a*) = 0.245 the photonic band gap has a maximum width, as shown in Figure 1D. We investigate whether it is feasible to consecutively etch pores in two different, orthogonal directions in single-crystalline silicon wafers by means of complementary metal oxide–semiconductor (CMOS)-compatible methods such as reactive-ion etching.[28]

2. Fabrication of 3D Structures From 2D Structures

A scanning electron microscopy (SEM) image of a cleaved 2D silicon photonic crystal is shown in **Figure 2**A. The structure consists of the first set of pores that is etched parallel to the *x*

axis using reactive-ion etching with a Bosch process.[29] The pores have a depth of 5550 ± 130 nm and a radius at half-depth of 159 ± 7 nm, which corresponds to a high aspect ratio of 17.5 ± 1.2. We have managed to realize nanostructures with even higher aspect ratios up to 21.6, as shown in the inset of Figure 2A. Near the top of the pores, some "scallops" appear as remnants from the Bosch process. The pores are smooth over a large depth of 5000 nm with a low tapering of 0.2 ± 0.1°, which makes these structures highly suited to optical applications such as photonic crystals. The pores are nearly identical over the extent of the 2D array, which is important to reduce unwanted light scattering.[30] Therefore, such 2D structures are excellent starting points for the fabrication of 3D inverse-woodpile crystals.

To vary the center frequency and the bandwidth of the photonic gap, it is desirable to control the pore radii of the photonic crystal.[10,25] In the present study, we aimed to make crystals with a band gap near $\lambda = 1550$ nm, which is one of the wavelengths used in telecommunication. For this we need values for (*a/λ*) = 0.581 and (*R/a*) = 0.245. We have managed to vary the pore radii by controlling the etching procedure, in particular the protective-step duration and capacitively coupled plasma power (CCP). By doing so, we have varied the value of *R* between 135 ± 7 and 186 ± 9 nm, which corresponds to (*R/a*) = 0.198–0.271, see Appendix A in the Supporting Information. This range of (*R/a*) was chosen because a width of the band gap of at least 50% of the maximum width is maintained, see Figure 1D.[23] As a result of this control over pore radii, the center of the band gap systematically shifts from (*a/λ*) = 0.40–0.69, see Figure 1D, which is a favorably large tuning range for optical applications.[31,32]

Figure 3A shows a photograph of part of a silicon wafer with 12 identical patterns in the chromium mask on the surface of the wafer. The large colorful squares are patterns with dimensions of 4.0×4.0 mm², which corresponds to approximately 5900×8300 unit cells. The squares can easily be seen by the naked eye. Since the lattice parameters are equal for each mask, the abundance of colors is caused by diffraction of different grating modes under illumination with white light.

After reactive-ion etching of the first set of pores, the chromium mask was removed. For the next fabrication step the 2D photonic crystal was cleaved along the 2D (*hk*) = [10] direction of the crystal, which corresponds to a cleavage along the *xy* plane. Figure 3B shows a photograph of a cleaved piece of silicon of 10×20 mm² on which the blue segment of 4.0×2.5 mm² indicates where the pores were etched to form a 2D photonic crystal. Even though the large 2D crystal has been cleaved, it retains a large surface of some 5100×5900 uniform unit cells.

www.MaterialsViews.com

ADVANCED
FUNCTIONAL
MATERIALS
www.afm-journal.de

FULL PAPER
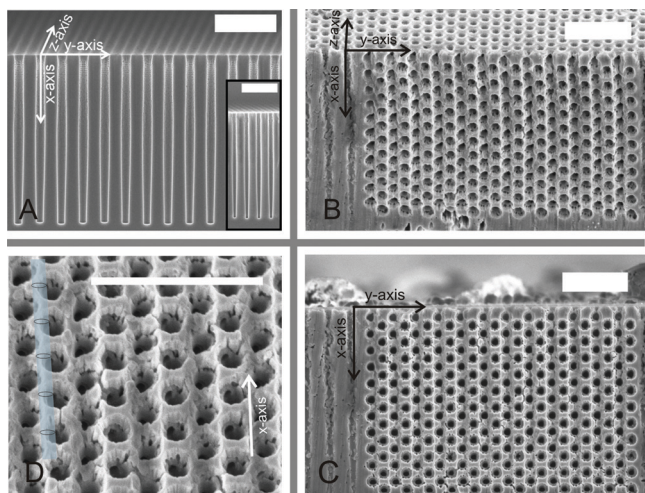
Figure 2. A) SEM image of a cross-section of a 2D photonic crystal in silicon. Smooth pores in a pattern as shown in Figure 2B are etched along the x axis. The depth of the pores is 5550 ± 130 nm and their radius is 159 ± 7 nm; the aspect ratio is 17.5. The inset shows etched pores with a high aspect ratio of 21.6. B) SEM image of a tilted 3D inverse-woodpile photonic band gap crystal in silicon realized by reactive-ion etching. Both the front and the top surfaces of an inverse-woodpile structure with pore radii R = 145 ± 9 nm. The 3D inverse woodpile is surrounded by the parental 2D crystal. C) The same structure tilted to show the front surface. D) Zoom-in of the (x–y) face of the inverse woodpile structure. z-directed pores etched perpendicular to the plane of the figure are clearly visible. The white arrow marks a place where two perpendicular pores cross each other. In all images the scale bar represents 2 µm.

To confirm that the processed wafers remain as single-crystalline silicon, we performed X-ray diffraction measurements on both an etched and a pristine wafer. The two diffraction patterns shown in **Figure 4** reveal one sharp diffraction peak at a diffraction angle of 2θ = 69.23 ± 0.02°, which corresponds to the (hkl) = 400 Bragg reflection. Using Bragg's law ($n\lambda = 2d \sin\theta$) we find the atomic lattice parameter to be d = 5.424 ± 0.002 Å, which is in excellent agreement with the literature.[33] From the observation of only one narrow diffraction peak, we conclude that both the silicon substrate and the silicon 2D photonic crystal are single-crystalline. Moreover, it confirms the orientation of the
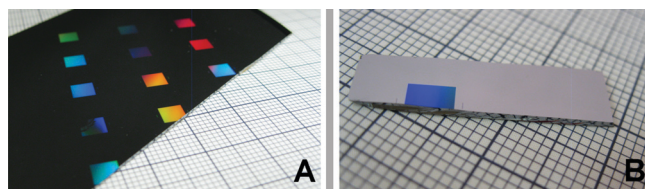
Figure 3. A) Color photograph of part of a silicon wafer containing a 50-nm chromium mask before etching. Twelve identical patterns were made in the chromium by deep UV scan-and-step lithography. The large colored areas are patterns with dimensions of 4.0 mm × 4.0 mm that show bright colors because of diffraction of different grating modes under white light illumination. B) Color photo of a large etched silicon 2D photonic crystal, cleaved to 4.0 × 2.5 mm², which contains approximately 5100 × 5900 unit cells. The uniform blue luster is caused by surface grating, and confirms that the high-quality crystal is uniform over its whole extent. The chromium mask has already been removed from this structure.
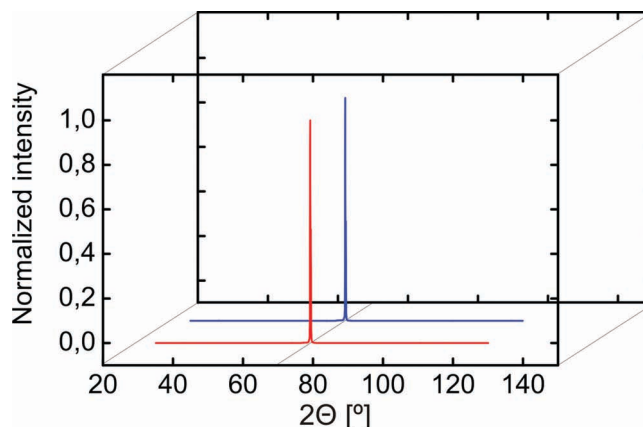
Figure 4. X-ray diffraction patterns of an etched (red) and a pristine silicon wafer (blue). Both patterns show one very sharp diffraction peak at 2θ = 69.23° which is the (hkl) = (400) single-crystal Bragg diffraction peak.

atomic crystal with respect to the photonic-crystal structure. An advantageous feature of our fabrication method over many previous methods that employ deposition[13,14,19] is that we realize nanostructures in crystalline silicon of high purity and high density instead of in a polycrystalline material. As a result, the density of chemical impurities in our structures is much lower, which serves to avoid spurious optical absorption. Moreover, the high index medium in our crystals is 100% densified. Thus the refractive index is maximal, which is favorable optimize the photonic interaction strength, whereas the index is lower in deposited structures.[34] Furthermore, the refractive index is well-defined, which is useful for a physical interpretation of experimental results and for the design of functional crystals.

After precisely aligning a second mask at 90° to a 2D array of pores[35] as shown in Figure 2A, we have managed to etch pores in the z direction. Thereby we realized seven individual 3D inverse-woodpile structures. An example is shown in Figure 2C, which shows the (x–y) face or (hkl) = 110 face of the inverse woodpile. On the left side of the picture we see several pores running in the x direction that were used to carefully align the second mask. The 3D crystal extends to over 5 × 7 µm², which is limited by our current mask-writing capabilities. By using e-beam or deep UV scan-and-step lithography, the areal extents of the crystal could be greatly increased. Nevertheless, the current crystal size is already sufficiently large for successful optical experiments, see Section 4.

Figure 2B shows the same crystal in an oblique perspective to show both (y–z) and (x–y) faces (110 and $1\bar{1}0$). We see that the lattice parameters and orientations of the structures in both faces are well matched. Indeed the lattice parameters for the (x–y) face are a = 693 ± 22 nm and c = 491 ± 19 nm, very close to those for the (y–z) face. The figure also clearly shows that all intended pores have been etched, in other words, the patterns are complete.

Figure 2D shows a zoom-in of the (x–y) face of the 3D crystal. It is clear that the second set of pores has been etched in between the first set of pores, as intended (see Figure 1A). Therefore, this result confirms our starting hypothesis that etching a second set of pores is feasible through a structure that consists of both pores and silicon; apparently, the air–silicon

FULL PAPER
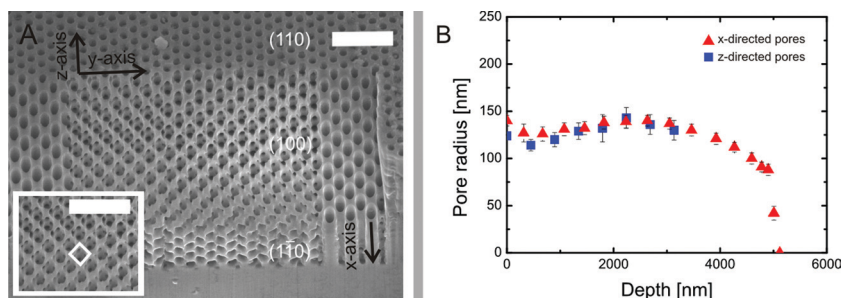
Figure 5. A) SEM of a 3D inverse-woodpile structure with pore radius $R = 139 \pm 8$ nm and displacement $\Delta y = 14 \pm 11$ nm. The 3D crystal is embedded in the large 2D crystal that was defined by the first pattern. On the right side of the figure a part of the original shape of the 2D crystal is seen. A triangular-prism-shaped part of the crystal is removed to give a view of a (100) plane in the photonic crystal. The structure that is etched in two directions possesses a surface area of 10×11 unit cells, with a depth of at least seven unit cells. The inset shows a magnified view of the (100) plane in a 3D inverse-woodpile structure. The white rhombic window indicates the square lattice in which the pores penetrate the (100) plane. The scale bar represents 2 μm. B) Pore radius as a function of pore depth, measured on the sample that is shown in Figure 5A. The pores running in the x direction were first etched and the second pore set was etched in the z direction. Both pore sets have the same pore radius up to a depth of 3.1 μm and thus equal tapering.

interfaces deflect the etching ions by only a small angle. We conclude that structures as shown in Figure 2 are successfully double-etched inverse-woodpile crystals.

In the ideal structure, the pores along the z axis are centered between the pores along the x axis. Positioning of the two pore sets with respect to each other introduces the possibility of unwanted structural displacements. From Figure 2B, we derive that the set of z-directed pores is displaced by only $\Delta y = 17 \pm 12$ nm from the first set of x-directed pores. In the 3D structure shown in **Figure 5**A, the displacement along the y axis is only $\Delta y = 14 \pm 11$ nm. For at least seven individual inverse-woodpile crystals the maximum displacement is $\Delta y <$ 30 nm, which is an excellent alignment of the two pore sets, see Appendix A in the Supporting Information. These are exciting results, since it has previously been predicted that a photonic band gap retains 90% of its width for a displacement of less than 10%, or $\Delta y \leq 69$ nm for our lattice parameters.[24] Moreover, these excellent alignments confirm that our method to pattern nanostructures on two inclined planes is indeed successful.[35]

3. Internal Structure

To investigate the detailed structure inside our inverse-woodpile crystals, we irreversibly opened several of the structures using focused-ion-beam milling, and characterized the results using SEM.[24] In this way, we investigated the dimensions of the pores as a function of depth, as well as the angular alignments of the pore sets relative to each other. Both aspects are crucial for the band gap of the photonic structure.[23]

Figure 5A shows an inverse-woodpile structure ($R = 139 \pm 8$ nm) of which we milled away part of the crystal. To this end, we milled at an angle of 45° to both the x–y ($1\bar{1}0$) and y–z (110) faces. As a result, we obtained a (100) face of the crystal that is viewed face-on in Figure 5A. In this face, the pattern of pores is clearly square as illustrated with the rhombic window,

which confirms that our 3D structures are truly cubic as intended.

One of the most challenging steps of our fabrication route is to etch the second set of pores in the macroporous 2D crystals. During this etching, the second pore set penetrates the first pore set in multiple places. Since this etching procedure is different from etching bulk silicon,[23,28] the result could give rise to a different pore radius or different pore shapes. In Figure 5B, the pore radius of both pore sets visible in Figure 5A is plotted versus the pore depth. The average radius of the first set of x-directed pores is $R_1 = 139 \pm 8$ nm, as determined at half pore depth. The pore radius of the second set of z-directed pores is measured to a maximum depth of 3 μm as limited by the focused ion milling. The mean pore radius at a depth of 3 μm is $R_2 = 134 \pm 9$ nm, which corresponds to an aspect ratio of >11.7. Thus, the radius of both sets are very close within $\Delta R =$ 5 nm, as was designed. Moreover, Figure 5B shows that the pore radius versus depth agrees very closely for both pore sets. This is an important result that indicates that the dimensions of the second pore set can be controlled with high precision. Another important consequence of this result is that the band-width of the photonic band gap is maintained. Previously, it was calculated that the relative width of the band gap remains more than $(\Delta\omega/\omega) = 20\%$ if the pore radii differ by as much as 12 nm.[23] Therefore, we conclude that our fabrication accuracy is sufficient to maintain the broad gap.

In Figure 5B the radii of both pore sets are plotted as a function of depth. From this result we can determine the tapering of the pores, that is, how conelike a pore is instead of purely cylindrical. Tapering of the first pore set was determined between a depth of 1 μm from the bottom and 1 μm from the top. In the bottom micron there was enhanced tapering, and the upper micron was excluded due to the presence of etch scallops[29] near the top. The latter is avoided in optical applications by focusing light to the center of the pores, see Section 4. The pores show the common behavior that the pore radii slightly increase with depth, before decreasing.[29] For the first pore set, tapering is $\tau = 0.1 \pm 0.2°$. For the second pore set tapering was determined to be $\tau = 0.1 \pm 0.2°$ for a depth between 1 μm from the top to a depth of 3 μm. In comparison with focused-ion-beam milling[20] the z-directed macropores etched through the macroporous silicon (Figure 5B) have much lower tapering. With ion milling we observed that the tapering of silicon and gallium phosphide yield a similar tapering to that obtained in bulk gallium phosphide was $8 \pm 4°$.[20] We propose that etching ions are less prone to become deflected from side walls than milling ions[24] and that the gaseous etching products are less prone to become redeposited than ion-milling debris.[20] Thus it seems reasonable that the plasma-etching process yields deeper pores with less tapering than does focused-ion-beam milling. The tapering of the pores influences the effective size of a photonic band gap.[23] It has been calculated that at $\tau = 0.125°$ tapering the band gap extends over 24.5 unit cells which

Materials
Views
www.MaterialsViews.com

ADVANCED
FUNCTIONAL
MATERIALS
www.afm-journal.de

FULL PAPER

is sufficient for most nanophotonic applications, since a 20% wide gap corresponds to a minimum optical size of five cells. Therefore, in our crystal the tapering of the pores is clearly sufficiently low for band gap applications.

Apart from translational alignments, other fabrication errors will also give rise to deviations of the angular misalignments. There are three deviations from angular alignments that can occur, as summarized in Appendix A in the Supporting Information. Deviations of angular alignments may occur when the 2D crystal is not placed perpendicular with respect to the incoming ions during reactive-ion etching of the second pores. From Figure 5A we determined the α angular alignment on the (100) face for our crystal to be $\alpha \ll 1°$. The angles β and γ were measured on the $(1\bar{1}0)$ face of the crystal, and are equal to $\beta \leq 0.008 \pm 0.001°$ and $\gamma = 0.6 \pm 0.2°$. A relative width of the photonic band gap of more than $(\Delta\omega/\omega) = 21\%$ remains if the angular alignment of α is better than $\alpha < 5°$. For an angular alignment of β or γ better than β or $\gamma < 0.6°$, the structure remains periodic over large extents in excess of 150 lattice spacings c. Therefore, we conclude that all deviations of the angular alignments are well within the margins.[23]

4. Nanophotonic Functionality

To verify the nanophotonic functionality of our inverse woodpile crystals, we have performed reflectivity measurements perpendicular to the (x–y) face of the 3D crystal with polarized light parallel to the x axis. **Figure 6** shows the measured reflectivity versus frequency measured on an inverse-woodpile crystal with $R_1 = 186 \pm 9$ nm and $(R/a) = 0.271$. A broad reflectivity peak is observed between 6500–9000 cm^{-1} with a high reflectivity of 62% centered at 7500 cm^{-1} (or $\lambda = 1300$ nm). This broad band covers several telecommunication bands. This distinct peak was

observed in the same frequency range for all polarizations over the entire 3D crystal surface.[31] The stop band corresponds to the stop gap in the Γ–Z direction (gray bar in Figure 6), which is part of the 3D photonic band gap.

The maximum reflectivity is likely limited by surface roughness that scatters light in directions not collected by the objective. This assertion is supported by the observation of a lower reflectivity on crystal surfaces that were less well polished. The finite thickness of the crystals could also reduce the reflectivity. Nevertheless, peaks up to 80% have been observed on other crystals.[31] These strong peaks indicate that the crystals are sufficiently extended to show clear photonic crystal behavior. Moreover, it confirms that little light is scattered away by unavoidable deviations from perfect periodicity.[30] The peak in Figure 6 is broad with a full width at half maximum of 2000 cm^{-1}, in good agreement with the theoretical stop gap in the Γ–Z direction (gray bar). The large relative width of $(\Delta\omega/\omega) = 27\%$ confirms that the crystal interacts strongly with light. The band gap is theoretically expected between 6800 and 8670 cm^{-1} (hatched gray bar). Therefore, we conclude that our CMOS-compatible fabrication process is compatible with nanophotonic applications.

One of the main driving forces for the fabrication of photonic crystals is the realization of advanced waveguides and cavities inside the photonic crystals.[1,2,4] Therefore we briefly discuss the prospects for such functionalities in inverse-woodpile crystals. A waveguide can be made by choosing not to etch one (or more) pores in the crystal. A preliminary experiment using focused-ion-beam milling revealed a promising structure.[36] Moreover, theoretical studies have confirmed that one absent pore has waveguiding capabilities.[37] A cavity is expected to appear at the intersection of two orthogonal waveguides that each consist of an absent pore. Theoretical calculations showed that near such an intersection light is confined within a small volume of order λ^3.[38]

5. Conclusion

We have fabricated 3D photonic band gap crystals with a cubic diamond-like symmetry in a two-step process. These so-called inverse-woodpile nanostructures consist of two perpendicular sets of pores. The photonic band gap crystals were made in single-crystal silicon by using CMOS-compatible methods. Both sets of pores were made by deep reactive-ion etching and have high aspect ratios. The second set of pores etched in macroporous silicon have an aspect ratio of >11.7. The mask for the first set of pores was defined in chromium by means of deep UV scan-and-step technology. The mask for the second set of pores was also defined in chromium and carefully placed at an angle of 90° with respect to the direction of the first set of pores. The alignment precision of the second set of pores was better than 30 nm. The second mask was patterned using a focused ion beam. We characterized the crystals using scanning electron microscopy and X-ray diffraction. We have made crystals with pore radii between 135 and 186 nm, with lattice parameters $a = 686$ nm and $c = 488$ nm. By milling away slices of crystal, we analyzed the pores in both directions in detail regarding depth, radius, tapering, shape, and alignment. We demonstrate by means of optical reflectivity that our crystals have broad
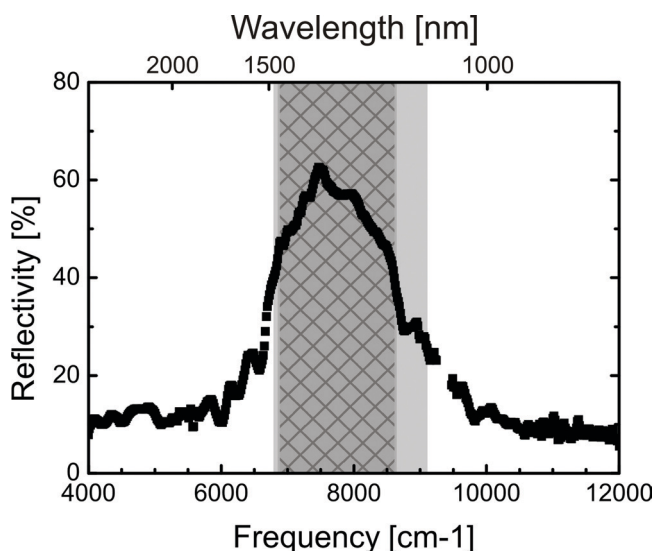
Figure 6. Optical reflectivity as function of frequency for a crystal with $R = 186 \pm 9$ nm measured on the (y–z) plane with polarized light. A strong reflectivity peak of 62% appears. The width of 2000 cm^{-1} is in very good agreement with the calculated stop gap Γ–Z direction (gray bar). The hatched bar indicates the range of the calculated 3D photonic band gap.

reflectivity peaks in the near-infrared frequency range which includes the telecommunication range. The strong reflectivity confirms the high quality of the crystals. The widths of the reflectivity peaks agree well with the calculated photonic band structures.

6. Experimental Section

We used single-crystal silicon wafers (p-type, <100> oriented, double side polished) with a diameter of 200 mm that were coated with a 50 nm thick chromium layer. On each wafer 60 segments were patterned with deep UV step-and-scan lithography (ASML PAS5500/700).[39] The mask we used contained a pattern consisting of a centered rectangular lattice of circular pores with lattice parameters $a = 686$ nm, $c = 488$ nm, and diameter 290 nm. This pattern was chosen because of its predicted broad band gap in the near-infrared.

The patterned wafer was cleaved into pieces of approximately 2×2 cm^2. Each piece was mounted on a 100 mm p-type silicon dummy wafer and placed in a reactive-ion-etching machine (Adixen Alcatel AMS100SE). Arrays of pores were etched by an optimized reactive-ion-etching process that yields deep nanopores, as described in detail elsewhere.[29] In brief, the etching process is a deep reactive-ion etching (DRIE) process based on the Bosch protocol.[28,40] This process consists of two alternating steps, where the first step is an etching step using 62 sccm SF$_6$ and the second step uses 200 sccm C$_4$F$_8$ to laminate the pore walls with a polymer layer as protection. In earlier work we found that increasing the time duration of the protective step reduces the sidewall erosion.[36] The time duration of the protective step was varied between 2 and 3 s, and the duration of the etching step was 3 s. In all experiments the number of lamination and etching steps was 180. During the etching process the substrate temperature was kept at 10 °C, and the inductively coupled plasma power (ICP) was set to 1500 W. We find that increasing the capacitively coupled plasma power raises the sidewall erosion.[36] We set the CCP to 160 or 200 W (10 ms on, 90 ms off), see **Table 1**. By varying the protective-step duration and the CCP, seven different etching experiments were successfully performed.

After etching the first set of pores, the chromium mask was removed using a commercially available aqueous Cr etching solution (LSI Selectipur®). To obtain a 3D structure, a mask was placed on the cross-section of the 2D structure as described in detail elsewhere.[35] In brief, a crystal was cleaved to approximately $0.5 \times 0.5 \times 7$ mm^3, rotated by 90° and glued in slots in a silicon holder wafer using photoresist (Olin 908/35). The 2D photonic crystal and the holder wafer were coated with a 50-nm thick chromium layer using electron gun evaporation (Balzers BAK 600). The desired pattern was written in the chromium with a focused ion beam (FEI Nova 600 dual beam apparatus). In the future, the second pattern could also be written by, for instance, e-beam or deep UV step-and-scan lithography. The second mask had the same structure as the first mask. The second pattern contained typically 12×12 unit cells, and was limited by the practical settings of the ion-beam workstation. The second set of pores was etched in the same way as the first set of pores. The sample was released from the holder wafer by dissolving

the photoresist with ethanol. The chromium mask was removed with chromium etch in the same way as the first mask.

To characterize the samples, we cleaved 2D samples to obtain cross-sections of the pores. The cross-sections were characterized with an SEM (LEO 1550 high-resolution) instrument. Pore depth and pore radius at half of the depth were measured. Data from up to 10 pores per image were analyzed and averaged. The top view and side view of the 3D inverse-woodpile structures were also characterized with SEM. In addition, we sacrificed a few crystals to investigate the interior. To this end, several inverse woodpile crystals were opened slice by slice by focused-ion-beam milling to analyze the internal 3D structures using SEM, similar previous reports,[24] see Appendix A in the Supporting Information. The error margins of all experiments are determined by the uncertainty in the measurements and the calibration accuracy (2% relative) of the SEM.

In these first experiments the pure processing time for one individual silicon bar containing eight equal crystals is 30 hours. For two silicon bars with different pore radii the time was 52 hours. Since the processing time per silicon bar decreases with an increasing number of samples, we feel that it would be reasonable to further reduce the processing time by making the crystals in larger batches.

Wide-angle X-ray diffraction analysis was performed on a powder diffractometer (Nonius PDS120) equipped with a CPS120 detector, using a mean wavelength of $\lambda = 1.54184$ Å from a Cu $\kappa\alpha$ generator. The X-ray beam was collimated to a spot of 0.5×0.5 mm^2 with a maximum flux of 2×10^6 counts s^{-1}. Both an etched and a pristine sample were studied to compare possible effects of the etching.

Optical-reflectivity experiments were performed with a dedicated reflectivity setup that employed a super continuum white-light source (Fianium SC-450-2) combined with a Fourier-transform spectrometer (Biorad FTS 6000). The polarized light beam was focused to a diameter of 1 μm[41] on the crystal with a 74× reflecting objective with a numerical aperture of 0.65 (Ealing). The polarization of the reflected light was analyzed. The reflectivity was calibrated by measuring reference spectra before and after the measurements with a gold mirror.

Supporting Information

Supporting Information is available from the Wiley Online Library or from the author.

Acknowledgements

Table 1. Summary of parameter settings used for etching.

Parameter	Setting
Etching step	62 sccm 3 s SF$_6$
Protective step	200 sccm 2–3 s C$_4$F$_8$
CCP power	160–200 W (10 ms on, 90 ms off)
ICP power	1500 W
Total etch duration	180 cycles
Substrate temperature	10 °C

[1] *Photonic Crystals and Light Localization in the 21st Century*, (Ed: C. M. Soukoulis), Kluwer, Amsterdam, **2001**.

[2] J. D. Joannopoulos, S. G. Johnson, J. N. Winn, R. D. Meade, *Photonic Crystals: Molding the Flow of Light*, 2nd ed., Princeton University Press, Princeton, **2008**.

[3] V. P. Bykov, *Sov. Phys. JETP* **1972**, *35*, 269.

[4] E. Yablonovitch, *Phys. Rev. Lett.* **1987**, *58*, 2059.

[5] S. John, *Phys. Rev. Lett.* **1987**, *58*, 2486.

[6] O. Painter, R. K. Lee, A. Scherer, A. Yariv, J. D. O'Brien, P. D. Dapkus, I. Kim, *Science* **1999**, *284*, 1819.

[7] H.-G. Park, S.-H. Kim, S.-H. Kwon, Y.-G. Ju, J.-K. Yang, J.-H. Baek, S.-B. Kim, Y.-H. Lee, *Science* **2004**, *305*, 1444.

[8] M. Grätzel, *Nature* **2001**, *414*, 338.

[9] A. Mihi, H. Miguez, *J. Phys. Chem. B* **2005**, *109*, 15968.

[10] K. M. Ho, C. T. Chan, C. M. Soukoulis, R. Biswas, M. Sigalas, *Solid State Commun.* **1994**, *89*, 413.

[11] C. López, *Adv. Mater.* **2003**, *15*, 1679.

[12] M. Maldovan, E. L. Thomas, *Nat. Mater.* **2004**, *3*, 593.

[13] J. F. Galisteo López, M. Ibisate, R. Sapienza, L. S. Froufe-Pérez, Á. Blanco, C. López, *Adv. Mater.* **2011**, *23*, 30.

[14] S. Y. Lin, J. G. Fleming, D. L. Hetherington, B. K. Smith, R. Biswas, K. M. Ho, M. M. Sigalas, W. Zubrzycki, S. R. Kurtz, J. Bur, *Nature* **1998**, *394*, 251.

[15] K. Wang, A. Chelnokov, S. Rowson, P. Garoche, J. M. Lourtioz, *J. Phys. D* **2000**, *33*, L119.

[16] J. Schilling, R. B. Wehrspohn, A. Birner, F. Müller, R. Hillebrand, U. Gösele, S. W. Leonard, J. P. Mondia, F. Genereux, H. M. van Driel, P. Kramper, V. Sandoghdar, K. Busch, *J. Opt. A: Pure Appl. Opt.* **2001**, *3*, S121.

[17] J. Schilling, J. White, A. Scherer, G. Stupian, R. Hillebrand, U. Gösele, *Appl. Phys. Lett.* **2005**, *86*, 011101.

[18] S. Takahashi, M. Okano, M. Imada, S. Noda, *Appl. Phys. Lett.* **2006**, *89*, 1231061.

[19] M. Hermatschweiler, A. Ledermann, G. A. Ozin, M. Wegener, G. von Freymann, *Adv. Funct. Mater.* **2007**, *17*, 2273; I. Staude, M. Thiel, S. Essig, C. Wolff, K. Busch, G. von Freymann, M. Wegener, *Opt. Lett.* **2010**, *35*, 1094.

[20] R. W. Tjerkstra, F. B. Segerink, J. J. Kelly, W. L. Vos, *J. Vac. Sci. Technol. B* **2008**, *26*, 973.

[21] K. M. Ho, C. T. Chan, C. M. Soukoulis, *Phys. Rev. Lett.* **1990**, *65*, 3152.

[22] A. Chutinan, S. Noda, *J. Opt. Am. B* **1999**, *16*, 240.

[23] L. A. Woldering, A. P. Mosk, R. W. Tjerkstra, W. L. Vos, *J. Appl. Phys.* **2009**, *105*, 093108.

[24] J. Schilling, A. Scherer, *Photonic Nanostruct. Fundam. Appl.* **2005**, *3*, 90.

[25] R. Hillebrand, S. Senz, W. Hergert, U. Gösele, *J. Appl. Phys.* **2003**, *94*, 2758.

[26] S. Roehl, A. Lin, M. Panicia, *Opt. Photon. News.* **2011**, *22*, 3, 25.

[27] E. N. Economou, M. M. Sigalas, *Phys. Rev. B* **1993**, *48*, 13434.

[28] B. Wu, A. Kumar, S. Pamarthy, *J. Appl. Phys.* **2010**, *108*, 051101.

[29] L. A. Woldering, R. W. Tjerkstra, H. V. Jansen, I. D. Setija, W. L. Vos, *Nanotechnology* **2008**, *19*, 145304.

[30] A. F. Koenderink, A. Lagendijk, W. L. Vos, *Phys. Rev. B* **2005**, *72*, 153102.

[31] S. R. Huisman, R. V. Nair, L. A. Woldering, M. D. Leistikow, A. P. Mosk, W. L. Vos, *Phys. Rev.* **2011**, *83*, 205313.

[32] M. D. Leistikow, A. P. Mosk, E. Yeganegidastgerdi, S. R. Huisman, A. Lagendijk, W. L. Vos, **2011**, Arxiv.org/abs/1106.1681.

[33] W. C. O'Mara, in *Handbook of Semiconductor Silicon Technology*, William Andrew Inc., **1990**, p. 349.

[34] J. E. G. J. Wijnhoven, L. Bechger, W. L. Vos, *Chem. Mater.* **2001**, 4486.

[35] R. W. Tjerkstra, L. A. Woldering, J. M. van den Broek, F. Roozeboom, I. D. Setija, W. L. Vos, *J. Vac. Sci. Tech. B* **2011**, in press.

[36] L. A. Woldering, Ph.D. Thesis, University of Twente, The Netherlands **2008**.

[37] H. P. Uranus, H. W. J. M. Hoekstra, W. L. Vos, presented at the 9th International Symposium on Modern Optics and Its Applications (ISMOA), Institut Teknologi Bandung, Indonesia, August **2009**.

[38] L. A. Woldering, A. P. Mosk, W. L. Vos, private communication.

[39] W. Bogaerts, R. Baets, P. Dumon, V. Wiaux, S. Beckx, D. Taillaert, B. Luyssaert, J. van Campenhout, P. Bienstman, D. van Thourhout, *J. Lightwave Technol.* **2005**, *23*, 401.

[40] F. Laermer, A. Schilp, *US Patent, 5501893*, **1996**.

[41] G. Ctistis, A. Hartsuiker, E. van der Pol, J. Claudon, W. L. Vos, J.-M. Gérard, *Phys. Rev. B* **2010**, *82*, 195330.

ADVANCED FUNCTIONAL MATERIALS

ORGANIC SINGLE CRYSTALLINE LASERS

On page 33, Jing Feng, Hong-Bo Sun, and co-workers report the use of an interference ablation method to fabricate an organic single-crystalline distributed feedback laser. Organic single crystals are difficult to treat using traditional fabrication methods because of their fragility and sensitivity to organic solvents and this method resolves these difficulties. The method may be applied to fabricate high-quality organic devices based on the single-crystalline materials.

FULL PAPER

Distributed Feedback Lasers Based on Thiophene/Phenylene Co-Oligomer Single Crystals

Hong-Hua Fang, Ran Ding, Shi-Yang Lu, Jie Yang, Xu-Lin Zhang, Rui Yang, Jing Feng,* Qi-Dai Chen, Jun-Feng Song, and Hong-Bo Sun*

Organic crystals have great potential for the applications in laser devices. This article presents an effective approach for fabrication of distributed feedback single crystal lasers. With the laser interference ablation method, high quality grating structures have been fabricated on the organic single-crystalline thin film materials. The relationship between the depth, periodicity, and laser fluence is discussed. The optical properties, such as photoluminescence, and diffractive properties are studied in detail. With the appropriate period, strong laser emission has been observed from these devices. Distributed feedback lasing is demonstrated from the laser interference ablated organic single crystals for the first time.

1. Introduction

Organic solid state lasers have attracted considerable attentions because they have the potential to be tunable, flexible, biocompatible, and easily integrated into plastic optoelectronics.[1–8] Optically pumped laser has been reported in a very broad range of conjugated polymers and oligomers. However, for the electrically pumped organic lasers, there still exist many challenging problems to be resolved.[5,9–11] One is that the organic devices have been damaged before the injected current reaches the expected threshold current density (kA/cm² range) for electrically driven lasing due to the low charge carrier mobilities of the disordered amorphous materials. In the view of carrier transport and charge injection, single crystalline organic semiconductors are recognized as potential building blocks for electrically pumped organic lasers. The long-range order and high chemical purity in crystals make them intrinsically excellent in charge-carrier transport properties, whose mobility could be significantly increased by three orders or more from their amorphous phase to the single-crystal phase

without any serious luminescence efficiency decrease.[12–15] Notable achievements on the amplified spontaneous emission (ASE) have been attained in a large number of crystalline materials.[16–22] For a laser device, resonator structure is necessary to apply the positive optical feedback, which may reduce the lasing threshold significantly. Within this framework, several attempts were made to construct a resonator for crystals. Examples include the use of naturally formed cleaved facet as Fabry-Pérot resonator,[23–24] or the microcavities fabricated with electron-beam (EB) lithography and reactive ion etching.[25–27] With the help of these resonators, the lasing threshold could be reduced to half or a fifth of the values observed for the bulk crystals.

As counterpart of cavity resonators, diffractive resonators, such as distributed feedback (DFB),[28–32] are extensively investigated. They can be readily incorporated into planar organic semiconductor waveguides and allow surface emission. These kinds of resonators have witnessed the great success in the polymer materials. A variety of fabrication schemes have been demonstrated to construct the DFB cavities, such as UV embossing, nanoimprint lithography, soft lithography, liquid imprinting, micromolding. Unfortunately, most of these methods are limited to organic crystals, because they are generally sensitive to solvent and the fragility makes them difficult to handle. As a dry method, laser ablation has been reported to process the organic materials. Although it has been used to fabricate polymer/amorphous organic DFB lasers,[32–33] organic crystal DFB laser has not been reported, as far as we know.

In this work, we have achieved distributed feedback laser based on the organic single-crystalline thin film materials. Diffractive resonators in the high-quality thin film crystals could be easily fabricated with a one-step, noncontact, and dry method – ultraviolet (UV) laser interference ablation (LIA). Different periodic gratings with optical quality could be directly formed in the crystals by changing the incident angle of the interference beam. With the help of the right periodic structures, distributed feedback (DFB) resonators were constructed in the crystals to provide the feedback. In particular, we observed laser emission with threshold of $E_{th} = 25$ μJ cm^{-2} in the distributed feedback resonators. More important, this method avoids both the dissolution of organic crystals and the need of good-quality end facets. This is a crucial aspect for future implementations of high-yield production.

H.-H. Fang, R. Ding, S.-Y. Lu, J. Yang, X.-L. Zhang, R. Yang, Prof. J. Feng, Dr. Q.-D. Chen, Prof. J.-F. Song, Prof. H.-B. Sun
State Key Laboratory on Integrated Optoelectronics
College of Electronic Science and Engineering
Jilin University
2699 Qianjin Street, Changchun, 130012, China
E-mail: jingfeng@jlu.edu.cn; hbsun@jlu.edu.cn
S.-Y. Lu, Prof. H.-B. Sun
College of Physics
Jilin University
119 Jiefang Road, Changchun, 130023, China

ADVANCED
FUNCTIONAL
MATERIALS
www.afm-journal.de

Materials
Views
www.MaterialsViews.com

FULL PAPER

2. Experimental Design

Figure 1 shows the experimental setup for the fabricating the DFB structures. Firstly, UV-curable adhesive NOA61 resist was spin-coated to form about 100 nm thickness film on the cleaned substrate. Then, the grown crystal plates were transferred from the quartz tube onto the substrate. The crystals were then adhered onto the substrate under the UV irradiation. After that, the prepared samples were exposed to the interference pattern of high power laser and their surfaces were structured by two-beam laser interference patterning to achieve line-like patterns on the surface. Their depth and periodicity are controlled by the laser fluence and the angle between the interfering laser beams. Under the UV excitation, the fluorescence from the crystals is waveguided in the higher refractive index organic thin film crystals and gets scattered by the periodic corrugations. If the period of the corrugations is suitable, the scattered light from each corrugation can combine through constructive interference to create a "Bragg scattered" wave that also propagates within the film but in a different direction. The DFB lasing occurs when the wavelength λ of the light satisfies the Bragg expression,[4]

$$2n_{\mathrm{eff}}\Lambda = m\lambda \tag{1}$$

where Λ is the periodicity of the grating, m is the order bragg refection, and n_{eff} is the effective refractive index of the waveguide, which is a geometrical average of the refractive indices of the layers of the waveguide and can be calculated through a solution of the Helmholtz wave equation for a planar multilayer structure.
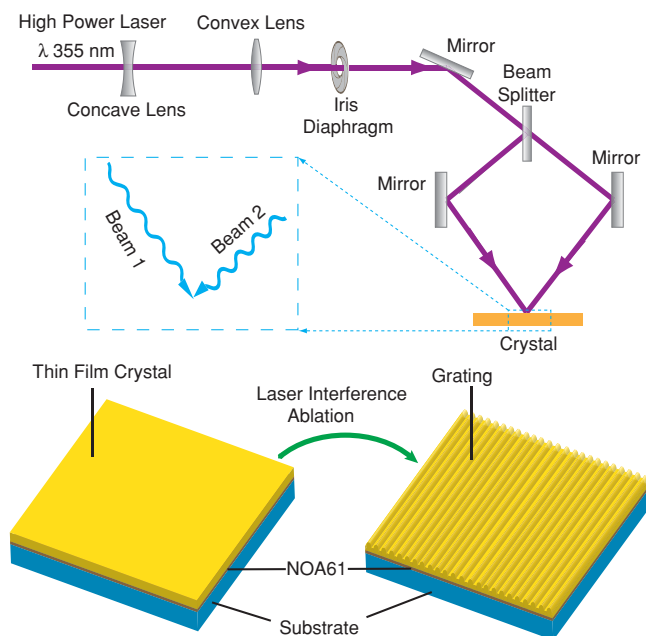
Figure 1. Schematics of experimental setup for the laser interference ablation (LIA). A 10 ns pulsed Nd:YAG laser (Quanta-Ray, Spectra Physics) with wavelength of 355 nm is used as the laser source. The primary laser beam was split into two coherent light beams (beams 1 and 2). The interference between beam 1 and 2 formed a grating pattern on the crystal surface. The main fabrication process for the crystals include: growth of thin film single crystal, transfer the crystals onto the substrate, LIA.

3. Results and Discussion

3.1. The Characteristic of Grown Thin-Film Crystals

Amongst organic molecular semiconductors thiophene/phenylene co-oligomers are counted as promising materials because of their unique optoelectronic properties.[14,34–36] Herein, crystals of a high hole mobility (0.66 cm² V⁻¹ s⁻¹) co-oligomers,[37] 2,2′-bithiophene,5,5′-bis([1,1′-biphenyl]-4-yl) (BP2T, see its structural formula in inset of **Figure 2**a) was used. The single crystals were grown by physical vapor transport in a flowing stream of argon (Figure S1 in the Supporting Information). This enabled the BP2T single crystals to grow as large as 5 mm × 5 mm with thickness varying from 200 nm to 10 μm. Figure 2a shows the photograph of a typical thin plate crystal under the daylight. The smooth surface morphology shown in the scanning electron microscopy (SEM) image (Figure 2c) suggests the high quality of grown crystals. The slab planes exhibit molecular-scale flatness with steps of about 2.58 nm (approximately 1 step per 2–5 μm), as confirmed by atomic force microscope (AFM) observations presented in Figure 2d. This step size is about half the lattice constant (Figure 2e) of 5.3 nm for c-axis of a BP2T crystal (i.e., the length of a single molecule). In the crystals of BP2T, molecules stand nearly perpendicular to the bottom crystal plane (i.e., the ab-plane), which was confirmed by the X-ray diffraction pattern (Figure S2 in the Supporting Information). According to the Bragg equation we can calculate that the thickness of one BP2T molecular layer is 2.54 nm, which corresponds to the height of one step in the AFM image. The emissions in the crystals, therefore, tend to be propagated as a waveguide mode along the slab crystal plane. As shown in the Figure 2b, orange fluorescence emitted only from the edges of the crystal without any emission from inside at all. This shows that the excellence of the waveguide properties of BP2T crystals. If the effective refractive index of the slab crystal is periodically modulated, both distributed feedback and output coupling of the waveguide mode could be supported by Bragg scattering, then distributed feedback lasing may occur from these structured crystals.

3.2. Fabrication of Grating on the Crystals

For the fabrication of grating on the crystal surface, the primary laser beam (355 nm) was split into two coherent light beams. Interference between the beams formed a grating pattern (Figure 1) on the crystal surface. The period (d) of the grating pattern is determined by the wavelength (λ) of the light and the half angle (θ) between the two incident beams through the relationship $d = \lambda/2\sin(\theta)$. During laser interference patterning, the high-energy nanosecond laser selectively ablates the crystal surface. The crystal located at the bright fringes of the interference pattern is "vaporized" and removed, while the materials at the dark fringes remains unchanged, forming the grating structures on the crystal surface. **Figure 3**a, b shows the scanning electron microscopy (SEM) images of cross section of an ablated crystal after direct laser interference ablation. The surface ablation depth (Δh) was approximately 230 nm, that is,
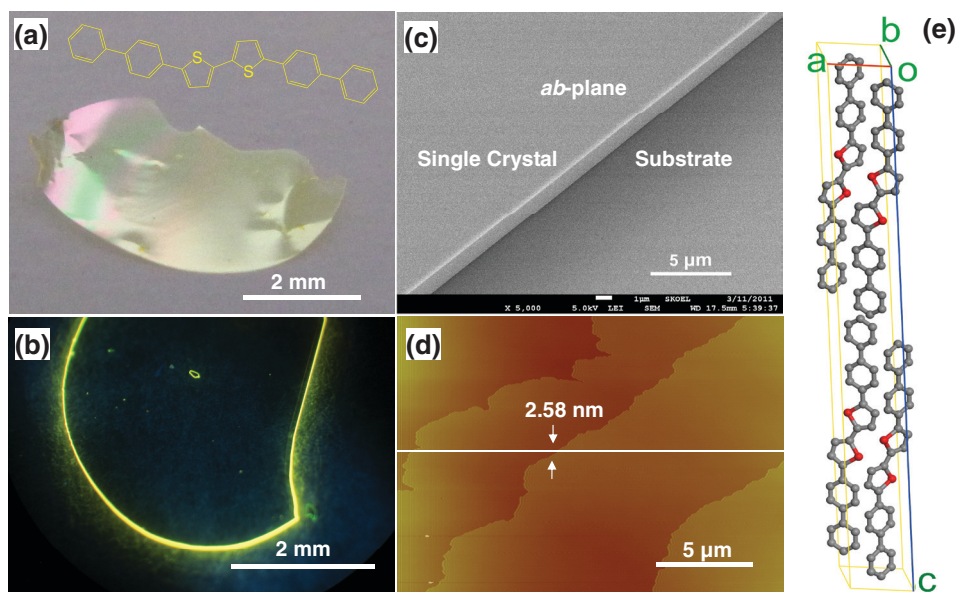
Figure 2. a) Global view of a BP2T single crystal under the daylight. Inset: chemical structure of BP2T. b) Fluorescence photograph of BP2T crystal under the UV light irradiation. c) Scanning electron microscope image of BP2T crystal. The ab-plane parallels the substrate plane. d) The surface profile investigated by the AFM; and their cross-section analyses. e) Crystal packing of BP2T.

much deeper than that of conventional DFB gratings fabricated on the polymers.

Experiments show that the pulse energy must exceed a certain threshold to achieve the removal of the materials at the bright interference fringes. Variations of the laser-beam intensity and processing time will result in change of the duty circle and depth of the gratings (Figure S3 in Supporting Information). Figure 3c shows an AFM image of the grating structure (period of about 800 nm). The modulation depth is deeper than 200 nm. The modulation depth could be controlled by adjusting the laser-beam intensity. Figure 3d shows the ablation depth as a function of the laser fluence. Each data point was obtained by averaging the ablation depth over the whole measurement area (5 μm × 5 μm). The insets show three profiles of the patterned BP2T crystal, which can be found that the higher the laser fluence, the smaller the width, as well as the depth. It should be noted that the ablation threshold is dependent on the crystallographic orientation. For example, the threshold is below 0.26 W/cm² when grating vector is parallel to the a-axis, while the threshold is much higher than this value. By controlling the laser fluence and processing time, well structured gratings can be produced.

3.3. Optical Properties of Crystal Gratings

In order to study the ablation effect on the optical properties of the crystals, the absorption spectra and photoluminescence quantum yield (QY) the crystals before and after ablation processes were comparably investigated. The results of the absorbance measurements are presented in the Supporting Information, Figure S6. Using fluence 0.3 W/cm², no significant absorption changes are detected. The QY for the ablated and unablated crystals, determined with an integrating sphere, are 55% and 59%, respectively. Considering the measurement error, it shows that no evident decrease in QY during the ablation process. Thus we conclude that the optical properties of the crystal are not significantly harmed by the ablation process. **Figure 4**a shows the spectrum detected at normal to the waveguide plane of the crystal with and without the fabricated gratings. It is clear that the presence of the grating structure drastically modifies the spontaneous emission. Bragg-scattered spontaneous emission from the BP2T crystal waveguide appears as two relatively narrow features in the output spectrum below threshold when collecting light scattered at the angle of normal incidence. The dip corresponds to the optical stop band of the one dimensional grating.

A He-Ne laser (633 nm) was employed to irradiate the grating (period 800 nm, depth 200nm). Its wavelength does not exhibit any absorption. The incident angle of the beam was adjusted to have the maximum intensity of the first diffracted line. Figure 4b present the diffraction pattern when illuminated under the He–Ne laser. Two diffraction orders (0 and ±1) can be clearly seen on the screen. The zero-order transmitted (I_0) and the first-order diffracted (I_1) lines of the reading beam, were used for the calculation of the diffraction efficiency (DE), DE = I_1/I_0. The sinusoidal phase grating model was adopted for the theoretical diffraction efficiency analysis.[38] The experimental DE is about 27%, which is about 80% of that of theory value (33.8%). Under the white illumination, we can see the white spot in the centre of the screen which corresponds to image of the grating in zero order of spectrum (Figure 4c). Diffracted color patterns are formed on the left and right, corresponding to a spectral composition of the light. These excellent diffraction properties demonstrates the optical-quality of the fabricated gratings, showing great potential for high quality DFB lasers.

**ADVANCED
FUNCTIONAL
MATERIALS**

www.afm-journal.de

*Materials
Views*

www.MaterialsViews.com
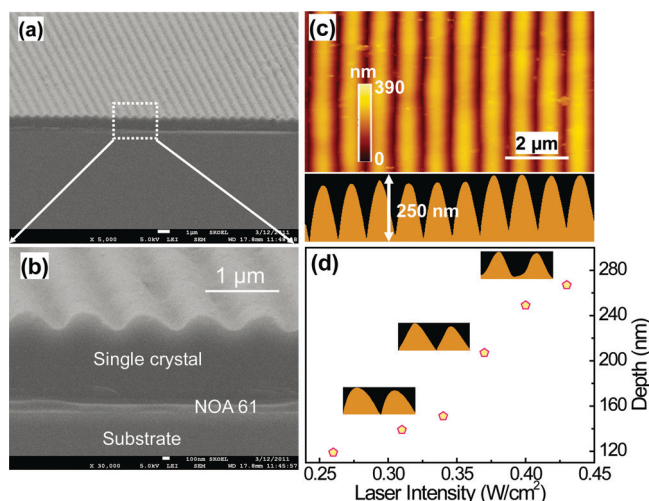
Figure 3. a) Image of thin film crystals fabricated with 800 nm period grating. b) Enlarged SEM image of side view. c) AFM images for the topographies of laser interference ablation of BP2T crystals with laser fluences 0.4 Wcm^{-2}. d) The ablation depth as a function of laser fluence. The insets are AFM profile images for representative data points.

3.4. Lasing Performance

The device (crystal thickness 1 µm, modulation depth 115 nm, period 640 nm) was excited by the 400 nm femtosecond pump beam and the emission was collected by an optical fiber connected to a spectrograph (**Figure 5**a). The emission spectra were then recorded as a function of increasing pump power. As the excitation pump energy is increased above a critical threshold, strong yellow–green emission consisting of two arc lines can be observed. Figure 5b shows photographs of one of the arc lines emitted from the device, which is at an angle of 30° normal to the plane of the crystal. Most of the laser energy is focused in the center area of the spot. The wavelength emission is centered at 565 nm with full width at half maximum (FWHM) of ~1.5 nm (**Figure 6**a). PL intensity of emission of a device as a function of the incident laser energy intensity is shown in Figure 6b. The threshold is determined to 25 µJ/cm^2, which is 3 times lower than that (~75 µJ/cm^2) of unablated crystal, and more lower that the uniformly ablated crystal (described in the Supporting Information, Figure S7).

To further confirm that it is DFB lasing, we have calculated the Bragg diffraction wavelength λ_{Bragg}. The refractive indices of BP2T thin crystals are estimated on the basis of both the thin-film interference in the reflectance spectrum and crystal thickness (details can be found in Figure S4 and S5, Supporting Information). The calculation of n_{eff} is based on three-layer planar waveguide model, in which $n_{crystal} = 1.80$, $n_{NOA61} = 1.56$, $n_{quartz} = 1.46$, $n_{air} = 1$. We obtain $n_{eff} = 1.73$ at 565 nm for TE$_1$ mode and the $m = 4$. This was in good agreement with the observed lasing wavelength, considering measurement error of the refractive indices and the thickness of the crystal layer.

The lasing wave are simultaneously diffracted by the grating, where the outcoupled angle of lasing wavelength is defined:

$$n_{eff}\Lambda(\sin\alpha + \sin\theta) = l\lambda / = 0, 1, 2 \tag{2}$$

Combination of Equation (1) and (2) yields an expression for θ:[39]

$$\sin\theta = \frac{2l}{m} - 1, \; \theta \in \left[-\frac{\pi}{2}, \frac{\pi}{2}\right] \tag{3}$$

Here, l is the diffracted order and m is the order bragg refection. The observed emissions in the Figure 5b (at an angle of 30° normal to the plane of the waveguide) is consistent with the lasing beam $l = 1$ or 3.

4. Conclusions

In summary, we have fabricated high quality distributed feedback resonators in organic single-crystalline thin film materials for the first time. Strong lasing emissions have been observed
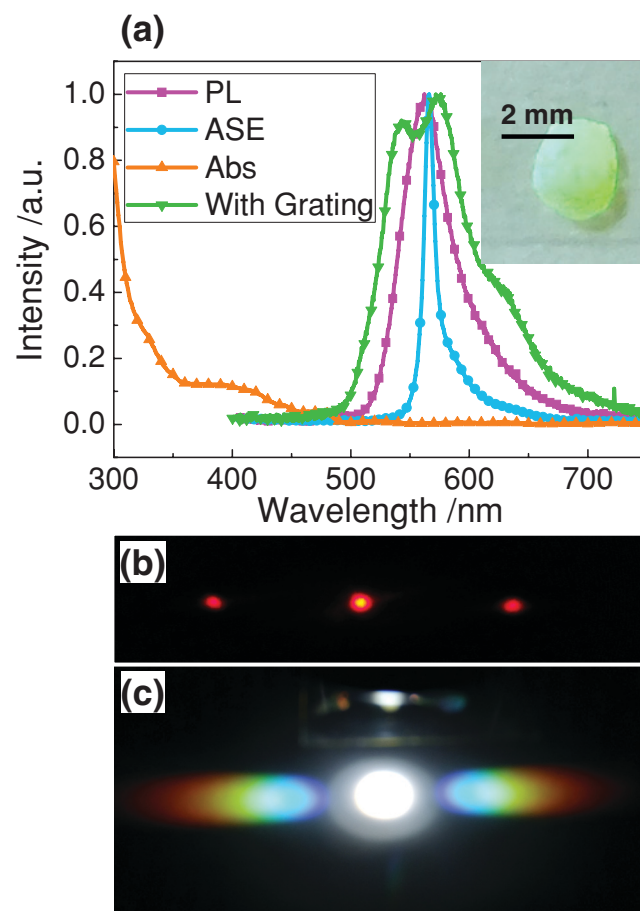
Figure 4. a) The absorption (Abs), photoluminescence spectra (PL), Bragg-scattered spontaneous emission (with grating) and amplified spontaneous emission (ASE) spectra of BP2T crystals. The photoluminescence spectra and the Bragg-scattered spontaneous emission are detected at an angle normal to the plane of crystals. The FWHM for ASE spectrum is 9 nm. Inset: Iridescence color caused by the diffraction of the fabricated grating (800 nm period) in the crystal. Diffraction patterns of the prepared grating (800 nm period) irradiated by He-Ne laser beam (b) and white light (c).
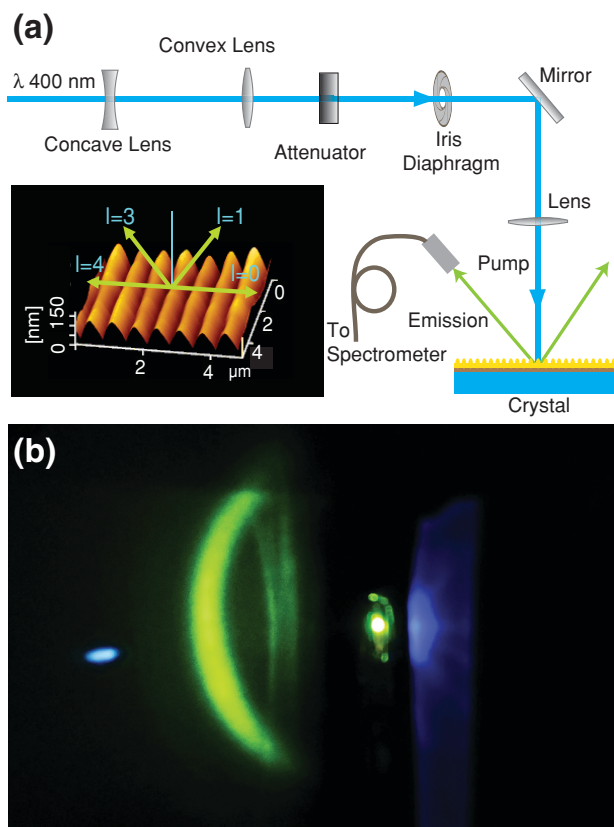
Figure 5. a) Experimental setup used for characterization of organic single crystal lasers. Inset: AFM images of the DFB and the sketch of directions of out-of-plane scattering for DFB structures of m = 4. b) Photographs of the operating single crystal laser based on 1D DFB structure.

Figure 6. a) Measured spectra of the lasing emission of the laser at different pump fluence, showing a center wavelength of about 565 nm and a linewidth of about 1.5 nm. b) Output intensity as a function of the pump fluence, indicating a pump threshold of about 25 μJ cm^{-2}.

from these devices. The lasing threshold in DFB resonators is reduced by a factor of 3 in comparison with the ASE threshold value of the BP2T film. The laser interference ablation method proved a dry, low-cost and single-step technique, consisting of short-time exposure of high power laser, enables mass fabrication of high quality single-crystal lasers based on DFB mechanisms for active photonic devices. The combination of high gain and high mobility organic crystals with laser interference ablation techniques is a promising approach to organic semiconductor lasers.

5. Experimental Section

Crystal Growth and Preparation: The materials of BP2T were purchased from Lumtec Corp., and was used without further purified. The single crystals were grown in a horizontal physical vapor transport apparatus. A quartz boat loaded with the BP2T powder was put into the center of a quartz tube, which was inserted into the high temperature zone of the tube furnace. An initial sublimation temperature at about 380 °C was employed, while deposition temperature was set at 340 °C. High-purity nitrogen was adopted as carrier and to prevent the organic materials from being oxidized, and the gas flowing rate was kept at 100 mL/min. The grown single crystals were hanged inside the growth tubes, and could be taken out with tweezers easily. Then the high quality crystals were chosen and adhered onto the substrate on which there is a layer of UV-curable adhesive NOA61 resist (~100 nm thickness).

Laser Inference Ablation: In the experiment, A Nd-YAG nanosecond-pulsed laser (Quanta-Ray Lab, Spectra Physics) was employed as the coherent light source for the interference ablation. 355 nm radiations were used, which is the third harmonic of its fundamental wavelength (1064 nm). The laser power could be adjusted through the controller of the laser and is monitored by a high damage threshold power meter. An electromechanical shutter controls the exposure time. The samples were loaded on the stage and exposed to the pulsed interference pattern. All the experiments are performed in an ambient atmosphere environment. A beam expander was used in the experiment so as to achieve uniform fluence in the central patterned area.

Lasing Characteristics: The second harmonic generation (400nm) of a regenerative amplifier (Spitfire, Spectra Physics) was used as the pump source. The spot size of the pump laser on the samples was estimated to be about 1 mm in radius. The pump pulse energy is controlled by sending the laser beam through an attenuator wheel. The emitted light was detected by the optical fiber and then dispersed to the spectrometer connected with CCD.

Instrumentation: SEM images were obtained from a Jeol-7500F microscope. Samples were coated with approximately 5–10 nm of gold before imaging. The film thicknesses for BP2T crystals were measured using a profilometer (Dektak 150), atomic force microscope (Nanoscope IIIa scanning probe microscope and Nanonavi), and the previously described SEM instrument. X-ray diffraction was carried out on a Rigaku R-AXIS RAPID diffractometer (D/max-rA, using Cu Kα radiation of wavelength 1.542 Å). Optical absorption data were

FULL PAPER

collected with a Shimadzu UV-3600 spectrophotometer equipped with an integrating sphere (in order to eliminate the scattering effect). The photoluminescence quantum yields of the crystals were measured in an integrated sphere.

Supporting Information

Supporting Information is available from the Wiley Online Library or from the author.

Acknowledgements

[1] F. Hide, M. A. Diaz-Garcia, B. J. Schwartz, M. R. Andersson, Q. Pei, A. J. Heeger, *Science* **1996**, *273*, 1833.
[2] N. Tessler, *Adv. Mater.* **1999**, *11*, 363.
[3] M. D. McGehee, A. J. Heeger, *Adv. Mater.* **2000**, *12*, 1655.
[4] I. D. W. Samuel, G. A. Turnbull, *Chem. Rev.* **2007**, *107*, 1272.
[5] J. Clark, G. Lanzani, *Nat. Photonics* **2010**, *4*, 438.
[6] H. Coles, S. Morris, *Nat. Photonics* **2010**, *4*, 676.
[7] S. Kena-Cohen, S. R. Forrest, *Nat. Photonics* **2010**, *4*, 371.
[8] H. H. Fang, B. Xu, Q. D. Chen, R. Ding, F. P. Chen, J. Yang, R. Wang, W. J. Tian, J. Feng, H. Y. Wang, H. B. Sun, *IEEE J. Quantum Electron.* **2010**, *46*, 1175.
[9] B. K. Yap, R. D. Xia, M. Campoy-Quiles, P. N. Stavrinou, D. D. C. Bradley, *Nat. Mater.* **2008**, *7*, 376.
[10] I. D. W. Samuel, E. B. Namdas, G. A. Turnbull, *Nat. Photonics* **2009**, *3*, 546.
[11] H. Kim, N. Schulte, G. Zhou, K. Mullen, F. Laquai, *Adv. Mater.* **2011**, *23*, 894.
[12] T. Oyamada, H. Uchiuzou, S. Akiyama, Y. Oku, N. Shimoji, K. Matsushige, H. Sasabe, C. Adachi, *J. Appl. Phys.* **2005**, *98*, 074506.
[13] T. Takenobu, S. Z. Bisri, T. Takahashi, M. Yahiro, C. Adachi, Y. Iwasa, *Phys. Rev. Lett.* **2008**, *100*, 066601.
[14] S. Z. Bisri, T. Takenobu, Y. Yomogida, H. Shimotani, T. Yamao, S. Hotta, Y. Iwasa, *Adv. Funct. Mater.* **2009**, *19*, 1728.
[15] K. Sawabe, T. Takenobu, S. Z. Bisri, T. Yamao, S. Hotta, Y. Iwasa, *Appl. Phys. Lett.* **2010**, *97*, 043307.
[16] H. Yanagi, T. Ohara, T. Morikawa, *Adv. Mater.* **2001**, *13*, 1452.
[17] M. Ichikawa, R. Hibino, M. Inoue, T. Haritani, S. Hotta, T. Koyama, Y. Taniguchi, *Adv. Mater.* **2003**, *15*, 213.
[18] W. J. Xie, Y. P. Li, F. Li, F. Z. Shen, Y. G. Ma, *Appl. Phys. Lett.* **2007**, *90*, 141110.
[19] R. Kabe, H. Nakanotani, T. Sakanoue, M. Yahiro, C. Adachi, *Adv. Mater.* **2009**, *21*, 4034.
[20] H. H. Fang, Q. D. Chen, R. Ding, J. Yang, Y. G. Ma, H. Y. Wang, B. R. Gao, J. Feng, H. B. Sun, *Opt. Lett.* **2010**, *35*, 2561.
[21] H. H. Fang, Q. D. Chen, J. Yang, H. Xia, B. R. Gao, J. Feng, Y. G. Ma, H. B. Sun, *J. Phys. Chem. C* **2010**, *114*, 11958.
[22] H. H. Fang, Q. D. Chen, J. Yang, H. Xia, Y. G. Ma, H. Y. Wang, H. B. Sun, *Opt. Lett.* **2010**, *35*, 441.
[23] M. Ichikawa, R. Hibino, M. Inoue, T. Haritani, S. Hotta, K. Araki, T. Koyama, Y. Taniguchi, *Adv. Mater.* **2005**, *17*, 2073.
[24] T. Yamao, K. Yamamoto, Y. Taniguchi, T. Miki, S. Hotta, *J. Appl. Phys.* **2008**, *103*, 093115.
[25] F. Sasaki, S. Kobayashi, S. Haraichi, S. Fujiwara, K. Bando, Y. Masumoto, S. Hotta, *Adv. Mater.* **2007**, *19*, 3653.
[26] S. Fujiwara, K. Bando, Y. Masumoto, F. Sasaki, S. Kobayashi, S. Haraichi, S. Hotta, *Appl. Phys. Lett.* **2007**, *91*, 021104.
[27] F. Sasaki, M. Mori, S. Haraichi, Y. Ido, Y. Masumoto, S. Hotta, *Org. Electron.* **2010**, *11*, 1192.
[28] J. R. Lawrence, G. A. Turnbull, I. D. W. Samuel, *Appl. Phys. Lett.* **2003**, *82*, 4023.
[29] D. A. Acevedo, A. F. Lasagni, C. A. Barbero, F. Mucklich, *Adv. Mater.* **2007**, *19*, 1272.
[30] E. B. Namdas, M. Tong, P. Ledochowitsch, S. R. Mednick, J. D. Yuen, D. Moses, A. J. Heeger, *Adv. Mater.* **2009**, *21*, 799.
[31] W. Y. Lai, R. D. Xia, Q. Y. He, P. A. Levermore, W. Huang, D. D. C. Bradley, *Adv. Mater.* **2009**, *21*, 355.
[32] T. Zhai, X. Zhang, Z. Pang, F. Dou, *Adv. Mater.* **2010**, *23*, 1860.
[33] M. Stroisch, T. Woggon, U. Lemmer, G. Bastian, G. Violakis, S. Pissadakis, *Opt. Express* **2007**, *15*, 3968.
[34] R. Hibino, M. Nagawa, S. Hotta, M. Ichikawa, T. Koyama, Y. Taniguchi, *Adv. Mater.* **2002**, *14*, 119.
[35] S. Hotta, M. Goto, R. Azumi, M. Inoue, M. Ichikawa, Y. Taniguchi, *Chem. Mater.* **2004**, *16*, 237.
[36] T. Yamao, Y. Sakurai, K. Terasaki, Y. Shimizu, H. Jinnai, S. Hotta, *Adv. Mater.* **2010**, *22*, 3078.
[37] M. Ichikawa, H. Yanagi, Y. Shimizu, S. Hotta, N. Suganuma, T. Koyama, Y. Taniguchi, *Adv. Mater.* **2002**, *14*, 1272.
[38] J. W. Goodman, *Introduction to Fourier optics*, Roberts & Company Publishers, Greenwood Village, USA **2005**.
[39] *Integrated Optics: Theory and Technology*, 5th edition, Springer-Verlag: Berlin Haeidelberg, **2002**.

Active Enzyme Nanocoatings Affect Settlement of *Balanus amphitrite* Barnacle Cyprids

Mariana Tasso, Sheelagh L. Conlan, Anthony S. Clare,* and Carsten Werner*

Balanus amphitrite cyprids produce complex adhesive substances that enable their attachment to surfaces and impart a strong detachment resistance from most immersed substrata. The colonization of man-made structures by barnacle cyprids and other marine organisms is a troublesome and costly phenomenon, for which controlling strategies are actively sought. In this work, we expand previous investigations about the susceptibility of cyprid adhesives to unpurified proteases in solution by evaluating the interplay between these secreted biomolecules and a surface-confined purified protease. The strategy involved the covalent immobilization of the enzyme Subtilisin A to maleic anhydride copolymer thin films through the spontaneous reaction of anhydride moieties with lysine side chains. This enabled the production of bioactive layers of tunable enzyme surface concentration and activity, which were utilized to systematically evaluate the effect of the immobilized enzyme on cyprid settlement and exploratory behavior. Surfaces of increasing enzyme activity displayed a gradual decrease in cyprid settlement levels (approaching inhibition) as well as an increase in post-settlement adhesion failure (evidenced by significant numbers of detached metamorphosed individuals). High activities of the bound enzyme also affected pre-settlement behavior of cyprids, reducing the velocity and total distance moved while increasing the amount and speed of meander compared to the controls. The here-reported low enzyme surface concentrations found to be remarkably effective at reducing cyprid settlement hold promise for the use of immobilized enzymes in the control of marine biofouling.

1. Introduction

Biofouling describes the undesirable accumulation of organic material and organisms, from unicellular to invertebrate species, on man-made surfaces.[1] Biofouling is a worldwide problem affecting a multitude of industrial processes and products, including food processing, medical devices, membrane separation, cooling systems, and ships' hulls. In the marine environment alone, more than 4000 species of marine organisms are recognized as responsible for biofouling.[2] Marine biofouling has been attacked from different fronts, from deterring organisms as they settle using biocides[1,3] to more elaborate and environmentally-friendly options based on the principle of 'non-stick' or 'fouling-release' surfaces, which do not jeopardize marine life.[4–7]

Several marine organisms use proteinaceous adhesives to attach to surfaces.[8] Proteolytic enzymes are effective agents against settlement of marine bacteria, algae and invertebrates, their proposed mode-of-action being the enzymatic degradation of the proteinaceous components of the adhesives.[9–14] To date, research has focused on either the use of commercial preparations of proteases, which include up to 80% additives (such as sorbitol and calcium formate)[14] or the incorporation of pure or commercial preparations into potential antifouling paints and coatings.[15,16] Where commercial preparations are employed, biological results are compromised by the spurious effects of non-enzymatic components and, in general, by the limited knowledge of the actual surface concentration and activity of the enzyme. Hence, it is difficult to draw conclusions about the impact of the soluble or matrix-incorporated enzyme on the observed biological response.

Balanus amphitrite is a sub-tropical sessile crustacean considered to be a serious pest due to its rapid colonization of immersed man-made objects and its widespread geographical distribution throughout the sub-tropics.[17,18] Barnacle cypris larvae explore a surface by 'walking' using their paired antennules bearing the attachment discs. In this exploratory phase, cyprids are capable of detaching, leaving behind deposits of temporary adhesive 'footprints'[17] that subsequently act as signaling molecules to induce the settlement of additional

S. L. Conlan, Prof. A. S. Clare
School of Marine Science and Technology
University of Newcastle upon Tyne
NE1 7RU Newcastle, UK
E-mail: a.s.clare@ncl.ac.uk
Dr. M. Tasso, Prof. C. Werner
Max Bergmann Center of Biomaterials Dresden
Leibniz Institute of Polymer Research Dresden
01069 Dresden, Germany
E-mail: werner@ipfdd.de
Prof. C. Werner
Institute of Biomaterials and Biomedical Engineering
University of Toronto
M5S 3G9 Toronto, Canada
Dr. M. Tasso
Chemical Engineering Department
Northeastern University
02115 Boston, MA, USA

ADVANCED
FUNCTIONAL
MATERIALS
www.afm-journal.de

Materials
Views
www.MaterialsViews.com

FULL PAPER

cyprids.[19] On finding a suitable surface, the commitment to settlement is accompanied by the release of proteinaceous cement (cyprid permanent cement) that embeds the paired antennules and cures within one to three hours to form a discrete matrix.[17] The attached individual subsequently metamorphoses and develops into the calcified adult barnacle.[17] As an adult, a third, discrete adhesive is produced, which is renewable and has 90% protein content.[18] The adult cement forms a thin disc between the basis of the adult barnacle and the surface to which it is attached.[18]

Cyprid temporary adhesive, required for exploration and settlement by the larvae, is composed primarily of protein[19,20] and is sensitive to hydrolysis by proteolytic serine proteases.[9,14] Aldred et al.[9] demonstrated that the mode-of-action of Alcalase® (a commercial preparation containing the protease Subtilisin A) in preventing cyprid settlement was to degrade the proteinaceous temporary adhesive rather than deterring them from settling. The degradation of footprints was observed by atomic force microscopy: footprints disappeared entirely within 30 min of exposure to the enzyme. Conversely (as also observed by Pettitt et al.[14]), cyprid permanent cement, while initially susceptible, became resistant to attack by Alcalase® within 15 h of release onto the substratum.

In this work, we aim to determine the susceptibility of the adhesives produced by *Balanus amphitrite* cyprids to the purified enzyme Subtilisin A bound to polymer nanocoatings. Subtilisin A (or Subtilisin Carlsberg; EC 3.4.21.62) is a well-studied serine protease with high specificity for the hydrolysis of proteins in aqueous media.[21] The extracellular alkaline protease is produced by *Bacillus licheniformis,* has an average molecular weight of 27,280 Da, and comprises 274 amino acids.[22] The protease was covalently-bound to poly(ethylene-*alt*-maleic anhydride) copolymer films via the spontaneous reaction of anhydride moieties with the lysine amine groups of the protein.[23] Previous work showed that these bioactive layers were effective at reducing the adhesion strength of spores of the green alga *Ulva linza* and cells of the diatom *Navicula perminuta* in a manner that correlated with the enzyme surface concentration and activity.[24] The present study differs from the work carried out on algae in that the functional surfaces presented to barnacle, *Balanus amphitrite,* cypris larvae were of reduced enzyme content, activity and thickness. Nevertheless, the immobilized enzyme was able to interfere with settlement of cyprids and their permanent fixation to the surface, whereas algal attachment was not prevented. As for algae, a correlation between the protein content of the cyprid adhesive(s) and the efficacy of the immobilized enzyme is indicated.

2. Results

2.1. Characterization of the Bioactive Nanocoatings

The maleic anhydride (MA) copolymer thin films that provide a platform for the immobilization of the protease Subtilisin A have been extensively characterized regarding their physicochemical properties, both in dry and swollen states.[25–28] The structure and properties of enzyme-containing MA copolymer films were recently investigated as a function of the polymer carrier features and of the enzyme concentration used during the immobilization process.[23,24]

In this work, enzyme-containing coatings were developed that permitted a reduction in enzyme surface concentration and activity (compared to those described previously[23,24]) by using enzyme concentrations in solution from 0.01 to 3 mg ml^{-1} for enzyme immobilization to poly(ethylene-*alt*-maleic anhydride) films. **Scheme 1** depicts the layered structure of the bioactive surfaces, shows the enzyme layer thickness as a function of the enzyme concentration in solution ([Es]) used for immobilization, and includes two AFM amplitude images of the coatings of lowest and highest enzyme layer thickness. **Figure 1** shows the activity and surface concentration of these bioactive layers in relation to [Es] and to the incubation time in artificial seawater (ASW*). The activity of the immobilized catalyst increased with the protein content on the surface and appeared more depleted than the latter after 48 h incubation in ASW* (e.g., for [Es] = 3 mg ml^{-1}, the residual activity after incubation is 14% whereas the residual protein content reaches 46% -if the means are considered-; similarly for [Es] = 0.25 mg ml^{-1}). Absorbance spectroscopy measurements of the incubation solutions after 48 h revealed the absence of active enzyme in the media (lack of absorbance at 405 nm when in the presence of 50 vol% 0.2 mM Suc-AAPF-pNA in PBS). Furthermore, the determination of protein concentration via absorbance spectroscopy at 280 and 555 nm (back-calculation of the protein content from the fluorophore concentration) yielded values below 200 ng ml^{-1}, i.e. below the detection limit of the equipment (NanoDrop ND-1000, Wilmington, Delaware, USA), suggesting the decrease in activity is likely due to denaturation processes occurring during incubation in salty media, and not to leaching.

The thickness of the enzyme layer bound to PEMA films (Scheme 1) displayed an increase as the [Es] increased, which is consistent with the protein content data. Thickness was in the range 1–4 nm, indicating the presence of a monolayer (mean diameter of Subtilisin A is 4.5 nm).[29]

Static water contact angle measurements of non-aged samples, confirmed the hydrophilicity of the enzyme-containing nanolayers, with water contact angles of 30° ± 5° for the active coatings and of 45° ± 8° for the denatured ones (PEMA control = 27° ± 5°). AFM measurements of non-aged samples yielded RMS roughness values of 0.55 ± 0.2 nm without statistical differences between active and denatured coatings (PEMA control = 0.61 ± 0.16 nm).

2.2. Cyprid Settlement Assay

2.2.1. Inhibitory and Antifouling Effect of Subtilisin A in Solution

The effect of 0, 0.5, 1, or 1.5 µg ml^{-1} Subtilisin A in 'Tropic Marin' artificial seawater (ASW) on cyprid settlement onto MA surfaces after 24 and 48 h is presented in **Figure 2**. PEMA and poly(octadecene-*alt*-maleic anhydride) (POMA) films without bound enzyme were considered for these assays. Settlement was inhibited on POMA coatings at all [Es] and incubation times tested. Settlement levels on PEMA coatings were

www.MaterialsViews.com

ADVANCED
FUNCTIONAL
MATERIALS
www.afm-journal.de

FULL PAPER
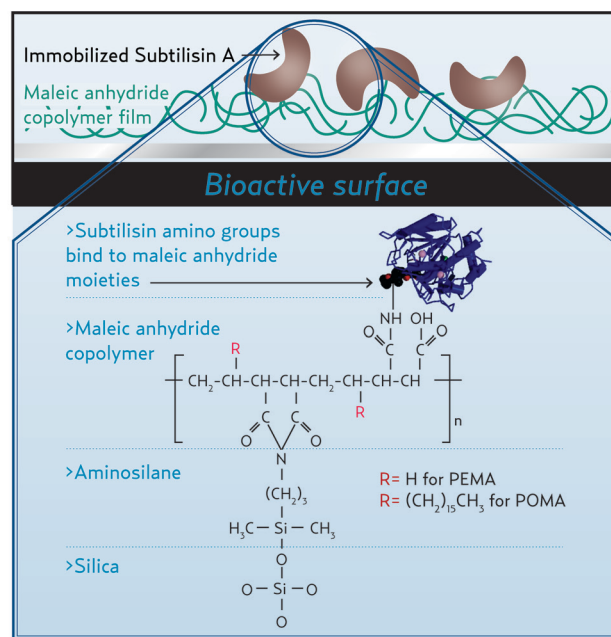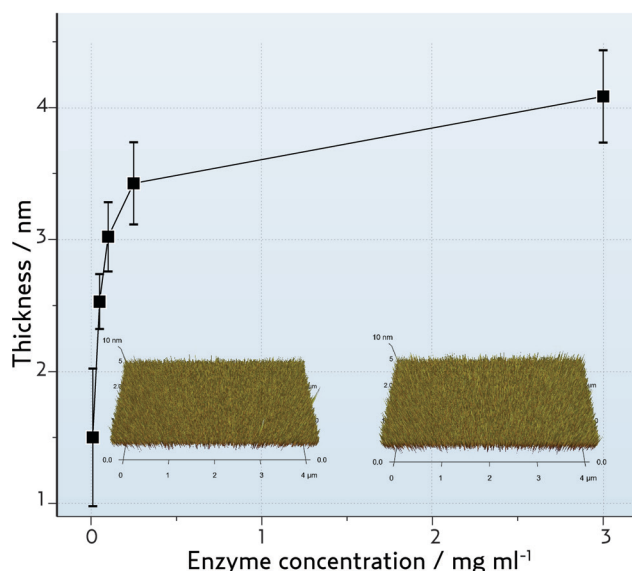
Scheme 1. Right panel: Schematic representation of the bioactive surfaces utilized in this work showing the enzyme surface immobilization strategy. Left panel: Thickness of Subtilisin A bound to PEMA films as a function of the enzyme concentration in solution used during immobilization. Values are mean ± SD. The two AFM amplitude images correspond to the coatings of lowest (left) and highest (right) enzyme layer thickness
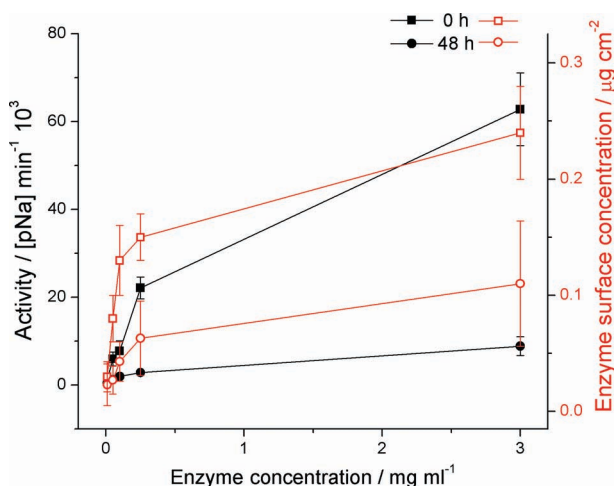
Figure 1. Activity (filled symbol) and surface concentration (unfilled symbol) of Subtilisin A bound to PEMA films as a function of the enzyme concentration in solution used during immobilization. Values (mean ± SD) with and without incubation in artificial seawater for 48 h are presented

2.2.2. Antifouling Potential of Immobilized Subtilisin A

Barnacle cyprids of *Balanus amphitrite* were exposed to bioactive PEMA coatings of increasing activity and to the respective denatured controls for 24 and 48 h to determine settlement levels of these organisms on the test surfaces. The mean settlement of cyprids displayed a significant
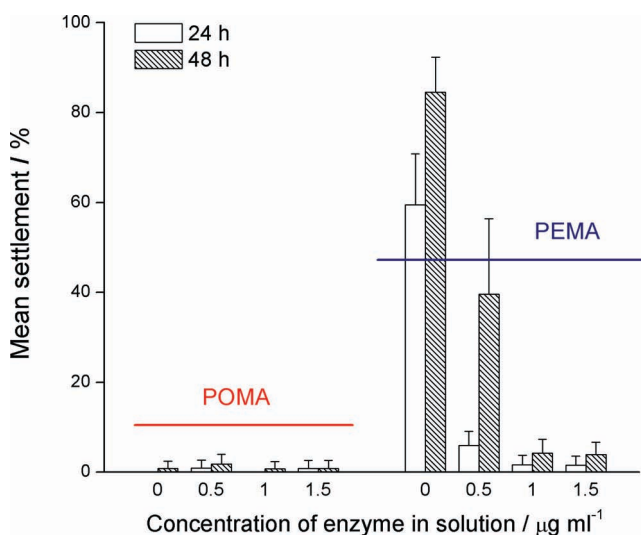
Figure 2. Mean settlement of *Balanus amphitrite* cyprids to POMA and PEMA films in the presence of 0 (control), 0.5, 1, and 1.5 µg ml^{-1} Subtilisin A in 'Tropic Marin' artificial seawater. Settlement is expressed as a percentage of the total number of cyprids dispensed on each sample. White bars show settlement after 24 h, dark bars after 48 h. $N = 6$; error bars = + 95% confidence error intervals.

particularly high in the absence of Subtilisin A in solution. When exposed to 1 and 1.5 µg ml^{-1} enzyme in solution, settlement on PEMA coatings was significantly reduced at both 24 and 48 h compared to the control ($p \leq 0.001$), whereas for 0.5 µg ml^{-1} enzyme, settlement was only significantly reduced at 24 h ($p \leq 0.01$). Based on the observed inhibitory character of the POMA films ($p = 0.82$), the further evaluation of the bioactive coatings with barnacle cyprids was restricted to the use of PEMA as platform for enzyme immobilization.

ADVANCED
FUNCTIONAL
MATERIALS
www.afm-journal.de

Materials
Views
www.MaterialsViews.com

FULL PAPER

Figure 3. A) Mean settlement of barnacle cyprids onto PEMA active coatings of increasing activity and the corresponding denatured controls. Settlement is expressed as a percentage of the total number of cyprids dispensed on each sample. Settlement on the control PEMA coating was $43 \pm 9.5\%$ after 24 h and $63.6 \pm 7.5\%$ after 48 h. B) Percentage of cyprids metamorphosed and thereafter detached for PEMA active coatings of increasing activity and the corresponding denatured controls. The percentage of detached cyprids is calculated as the relative fraction of detached individuals to the total number of settled on each surface. The percentage of detached cyprids onto the PEMA control was 0% after 24 and 48 h. White bars show settlement after 24 h, dark bars after 48 h. $N = 12$ (active coatings) or 6 (denatured coatings); error bars = + 95% confidence error intervals.

($p = 0.036$) trend with respect to increasing the enzyme surface activity (**Figure 3**A). At both incubation times, the number of settled cyprids decreased with increasing activity; the cutoff activity for action being of the order of 50 [pNa] min^{-1} 10^3. The denatured coatings were extensively fouled at both incubation times, with no significant differences observed ($p \geq 0.121$). Excluding the case of the coating of lowest activity, a significant difference in settlement between active and denatured coatings of the same enzyme surface concentration was observed after both incubation times ($p < 0.05$), clearly highlighting the inhibitory effect displayed by the immobilized active enzyme.

The active immobilized enzyme not only inhibited settlement, but also caused a fraction of settled (and metamorphosed) cyprids to detach from the surface (Figure 3B). The percentage of detached cyprids (relative to the total number of settled individuals) on the active coatings was significantly higher than on the denatured controls for the two highest activities ($p \leq 0.043$). Attachment of cyprids to the denatured coatings was strong: less than 1% of the attached and metamorphosed cyprids subsequently detached from these surfaces in clear opposition to the pattern observed for the active surfaces. The number of detached individuals from the active slides displayed an apparent increase with increasing enzyme surface activity, but the differences were not significant ($p \geq 0.05$). However, even at the lowest activity tested (i.e. 1.3 [pNa] min^{-1} 10^3), the relative number of detached individuals was higher than from the PEMA control (0% at both times). It was noteworthy that detached juveniles had a normal basis and were found to behave as normal without any sign of compromise in their health and viability (95% surviving after 14 days incubation with some being able to re-attach to glass surfaces during the course of their maintenance).

2.2.3. Comparison Between Immobilized Enzyme and Equivalent Amount of Enzyme in Solution

The amount of enzyme immobilized on the coating having the highest activity (i.e., 63 [pNa] min^{-1} 10^3) compares to 1 µg ml^{-1} of enzyme in solution. Although the amount of enzyme is the same in both cases, the activity of the soluble enzyme is higher (750 [pNa] min^{-1} 10^3) than the activity of the immobilized enzyme (essentially due to the random immobilization strategy employed). Unlike previous observations with spores of the green alga *Ulva* and the diatom *Navicula*,[24] immobilizing the enzyme did not enhance the antisettlement effect compared to the equivalent amount of enzyme in solution at any of the considered incubation times ($p \geq 0.05$) (**Figure 4**).

2.2.4. Tracking

As shown in **Figure 5**A, surface-bound enzyme reduced the total distance moved by cyprids, although only the sample of highest activity was significantly different from the blank PEMA control ($p = 0.005$). Similar effects were observed for the mean velocity (Figure 5B, $p < 0.001$). The mean angular velocity of cyprids increased significantly at the highest activity (Figure 5D, $p = 0.000$), as did their meander (Figure 5C, $p = 0.000$). The total turn angle, however, was not significantly different between treatments (data not shown, $p = 0.326$).

3. Discussion

Our reported study aimed at exploring the antifouling potential of a surface-confined purified protease against *Balanus amphitrite* barnacle cyprids. The bioactive coatings tested had a similar structure but lower enzyme surface concentration, thickness, and activity than those employed in previous

www.MaterialsViews.com

ADVANCED
FUNCTIONAL
MATERIALS
www.afm-journal.de

FULL PAPER
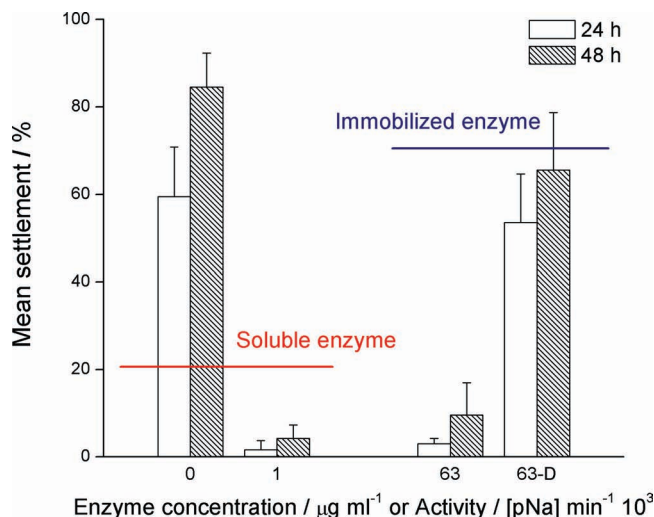
Figure 4. Mean settlement of barnacle cyprids onto PEMA coatings exposed to 0 and 1 μg ml^{-1} Subtilisin A in solution and onto PEMA coatings with bound active and denatured (-D) enzyme. The amount of bound enzyme is equivalent to 1 μg ml^{-1}. Settlement is expressed as a percentage of the total number of cyprids dispensed onto each sample. White bars show settlement after 24 h, dark bars after 48 h. $N = 6$; error bars = +95% confidence error intervals

investigations with marine algae.[24] Preliminary assays with barnacle cyprids revealed that changing the surface activity from 63 to 489 [pNa] min^{-1} 10^3 (same activity range as tested for algae) had no influence on cyprid settlement after 48 h (see supporting information, Figure S1). This result prompted us to lower the surface activity of the immobilized enzyme to the range 1.3–63 [pNa] min^{-1} 10^3, hypothesizing a dependence between surface activity and cyprid settlement could thus be made evident. The resulting bioactive coatings were essentially monolayers (thickness of the immobilized enzyme layer between 1 and 4 nm; values in the range of the average diameter of the enzyme molecule (4.5 nm)[29]). The layers exhibited an increase in enzyme surface concentration and activity for increasing concentrations of the enzyme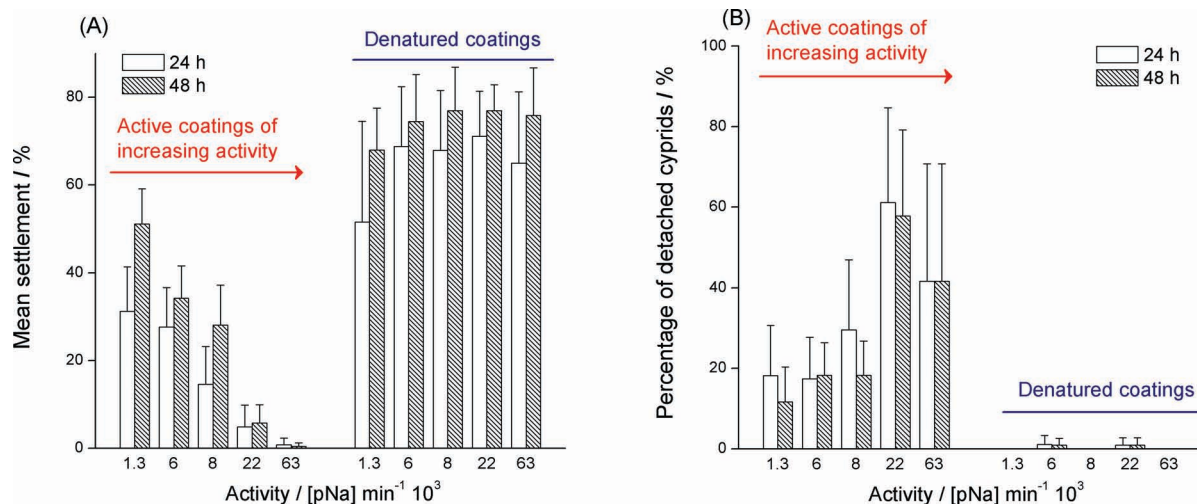 in solution used during immobilization. Exposure of the bioactive layers to artificial seawater (ASW*) for 48 h decreased both activity and protein concentration on the surfaces. If any enzyme was released from the surface into the supernatant, it was inactive and hence did not contribute to the digestion of the adhesive substances secreted by cyprids during exploration and settlement. Denaturation and autolysis processes might explain these findings, which stress the need to further improve the stability of the layers, e.g. by oriented immobilization strategies.

In the whole range of enzyme surface concentrations tested, nanorough, hydrophilic bioactive layers were obtained whose surface roughness and wettability were essentially independent of the protein content on the surface. This invariance in surface roughness and wettability over a range of enzyme surface activity is crucial to narrowing the spectrum of variables that might affect cyprid settlement and adhesion strength[17,30–34] and to analyze the cyprid-surface interaction mainly in terms of the activity of the immobilized enzyme.
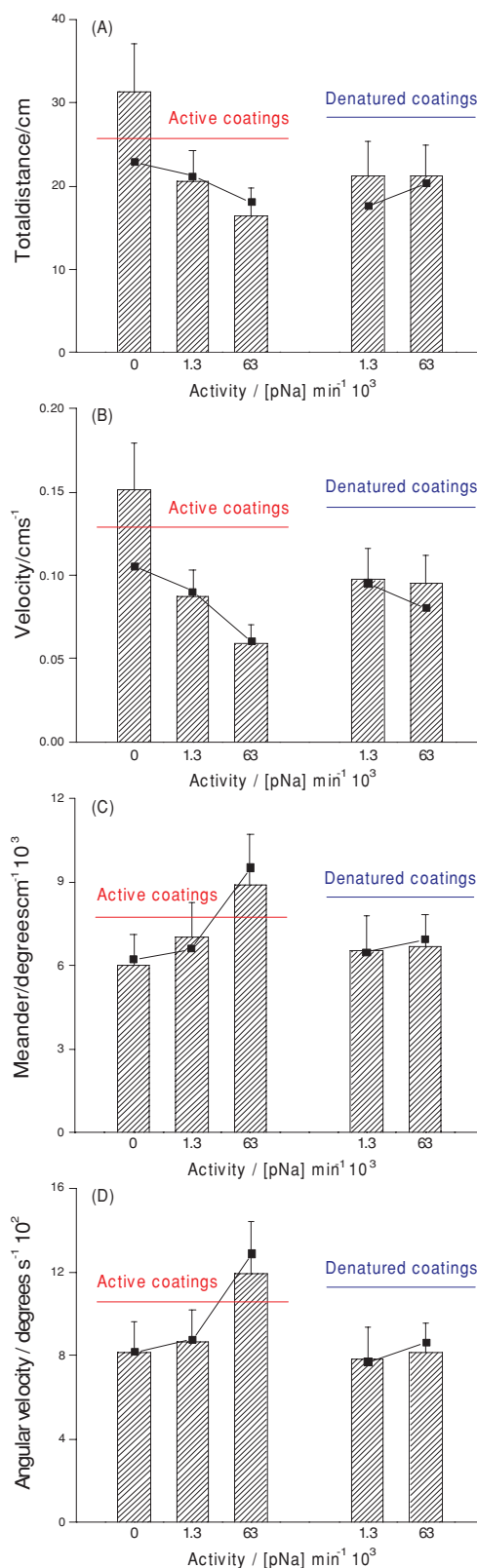
Figure 5. A) Total distance moved, B) velocity, C) meander, and D) angular velocity for barnacle cyprids exposed to active and denatured enzyme coatings of different activities. Bars show means + 95% confidence error. The line connects medians.

The evaluation of the effect of increasing concentrations of enzyme in solution ([Es]) on cyprid settlement using MA coatings revealed the highly-inhibitory character of POMA films in contrast to the highly-inductive character of its counterpart PEMA. The inhibition of settlement observed for POMA films in the absence of enzyme seemed to have pre-determined the results found at other [Es]. As these coatings were not leached prior to the assays, the release of inhibitory compounds from POMA coatings cannot be excluded. However, the leaching of inhibitory compounds appears unlikely because the chemicals used for the preparation of POMA surfaces were the same as for PEMA surfaces (for which no sign of inhibition was observed). The settlement inhibition found on POMA films may instead be associated with other surface-related inhibitory features, such as their more hydrophobic character and/or different surface charge density.[31–33] In a comparative assay using immobilized Subtilisin A on POMA films, in both active and denatured forms, plus POMA and acid-washed glass controls (**Figure 6**), all tested POMA-based surfaces were inhibitory to settlement regardless of whether the enzyme was immobilized to the POMA surface or not, or whether the bound-enzyme was active or not. As with the enzyme in solution, the settlement-inhibitory properties of the POMA layer may still have been 'recognizable' by cyprids, even when an enzyme monolayer (thickness = 2.7 ± 0.4 nm) was immobilized onto it in either active or denatured form. These observations illustrate the 'determining' effect of the polymer carrier used for immobilization, not only on the properties of the bound catalyst but also on the resulting biological response.

For PEMA films, barnacle settlement was found to be dependent on [Es]. The strong inductive character of the PEMA control ([Es] = 0) vanished at [Es] ≈ 1 μg ml^{-1}, revealing that relatively low [Es] are effective at deterring settlement of barnacle cyprids onto PEMA even after 48 h incubation. These findings are in agreement with previous studies by Pettitt et al.[14] showing that Alcalase® (a commercial preparation whose active component is Subtilisin A) had a minimum inhibitory concentration of 1.1 μg ml^{-1} for barnacle cyprid settlement onto polystyrene well plates. The enzyme in solution might degrade the temporary adhesive used by cyprids during exploration, hence making it difficult for them to commit to settlement. The enzyme is also known to target the cyprid permanent cement (prior to curing), as demonstrated by Aldred et al.[9] for Alcalase.

Compared to previous work carried out with marine algae using immobilized Subtilisin A,[24] enzyme surface concentrations and activities that proved effective against barnacle cyprid settlement were much lower, suggesting that cyprid adhesive(s) is more sensitive to the immobilized protease. Subtilisin A bound to PEMA films steadily decreased the number of settled cyprids on the surfaces with increasing surface concentration and activity. The denatured controls were all highly-fouled, settlement effects therefore being dependent on the presence of active enzyme. An enzyme surface activity of ca. 50 [pNa] min^{-1} 10^3 reduced settlement levels to ca. 5%; any further increase in surface activity had no further influence (see supporting information). The activity levels of the bound enzyme that significantly reduced cyprid settlement were substantially lower than the levels needed for *Ulva linza* zoospores (ca. 300 [pNa] min^{-1} 10^3)[24] or for *Navicula perminuta* diatom cells. No clear explanation for this difference in sensitivity can be offered based on available knowledge of cyprid adhesives. The cyprid 'temporary adhesive', involved in exploratory behavior,[9,17,19,20] and the cyprid cement, which fixes the larva permanently to the substratum, are proteinaceous.[17] The temporary adhesive is thought to comprise a glycoprotein–the settlement-inducing protein complex–which has 15% N-linked glycans, very similar to the 17% N-linked glycan[35] composition reported for *Ulva* sp.. On the other hand, the adhesive secreted by *Navicula* is largely polysaccharide with minor fractions of protein.[36,37] So while a higher protein content could explain a greater sensitivity of both cyprid adhesives to Subtilisin A compared to *Navicula* adhesive, and of cyprid cement compared to *Ulva* adhesive, this explanation is unlikely to hold for the comparison of cyprid temporary adhesive to *Ulva* adhesive. Furthermore, recent work from Barlow et al.[38] on adult cement has shown around 50% of the adhesive to be made up of amyloid-like β-sheet proteins. Subtilisin A is highly effective in breaking down amyloid[39,40] and while the available evidence suggests that the cyprid permanent cement and adult cement differ,[9,18,41] the pronounced effect of Subtilisin A on cyprid permanent adhesion may point to amyloid content in cyprid cement.

Together with the reduction in cyprid settlement at increasing enzyme activity, an increasing number of individuals failed to permanently attach to the bioactive layers. Individuals that committed to settlement, secreted adhesives, and initiated metamorphosis most likely had their adhesion strength weakened by the surface-bound enzyme, which ultimately resulted in their detachment. This observation was supported by the near absence (<3%) of detached cyprids from the denatured controls. Detached individuals had a shape indicative of late stage metamorphosis, suggesting that adhesive failure may have occurred during the movements associated with molting the cyprid exuvium. The lack of macroroughness or topographic features that could have strengthened the attachment of cyprids may have
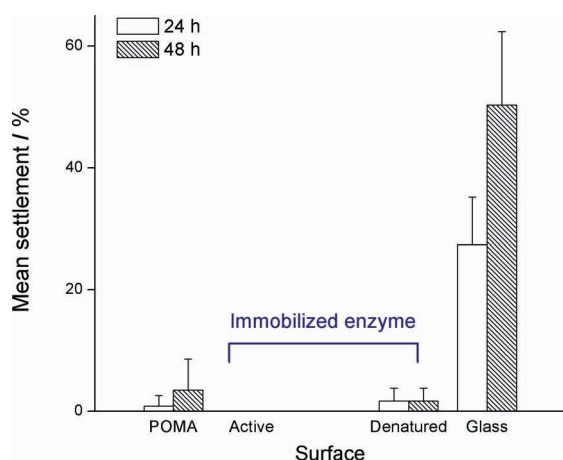
Figure 6. Mean settlement of barnacle cyprids onto conditioned POMA, POMA + bound Subtilisin A with activity 59.2 ± 11 [pNa] min^{-1} 10^3 (Active), its denatured control (Denatured), and acid-washed glass. Settlement is expressed as a percentage of the total number of cyprids dispensed on each sample. White bars show settlement after 24 h, dark bars after 48 h. N = 6, error bars = + 95% confidence error intervals.

www.MaterialsViews.com

**ADVANCED
FUNCTIONAL
MATERIALS**

www.afm-journal.de

FULL PAPER

also facilitated adhesive failure.[30] These individuals were found to have mostly (ca. 80%) flat bases, suggesting contact with the surface during final stage metamorphosis (individuals that molt in the water column show abnormal rounded bases (SLC personal observation)). Detached individuals behaved as normal without any sign of compromise in their health or viability.

The enzyme-containing PEMA surfaces tested appear to affect the consolidation of adhesion of barnacle cyprids to the substrate without permanently interfering with earlier behaviors (i.e. commitment to settlement and metamorphosis) nor with the viability after detachment. These facts point to the non-biocidal character of the bioactive PEMA layers, a highly-appreciated feature in environmentally-friendly strategies for fouling control.

When comparing immobilized with soluble enzyme at equal amount, a similar antifouling response was obtained although the activity of the soluble enzyme is higher (ca. one order of magnitude) than that of the immobilized enzyme. The localization of the immobilized enzyme at the interface between adhesive and surface might have counterbalanced its lower activity levels when compared to equal amount of enzyme in solution. Possibly, the time-scale of the settlement process in barnacle cyprids is long enough to allow the kinetically less-favored immobilized enzyme to act effectively on the secreted adhesives and/or to hinder the mechanisms of recognition of substrate ligands required for successful settlement to occur.

Finally, when evaluating the behavioral pattern of cyprids exposed to the coatings of highest and lowest surface activity (and the corresponding controls), the observed reduction in total distance moved and velocity in all tested coatings compared to the blank control (PEMA) suggests that this effect was, at least in part, due to the presence of protein on the surface (i.e. enzyme in active or denatured form). Mean angular velocity and meander were significantly increased in the highest activity coating compared to all other treatments, clearly showing that cyprid behavior was affected by the bound enzyme. This differs from the effect of soluble Alcalase reported by Aldred et al.,[9] where relatively high concentrations of the commercial enzyme preparation had no effect on behavior. The increase in meander is usually due to increased searching behavior, but observations by eye suggested that some cyprids altered their swimming behavior adopting a corkscrew-like pattern, while others were relatively inactive, which on balance may explain the reduced 'total distance moved'. In either case, cyprids experiencing natural hydrodynamic conditions rather than the static conditions of the settlement assays, would likely return to the plankton and, as future adhesion is not compromised, could attach to a more favorable surface.

4. Conclusions

The covalent immobilization of the protease Subtilisin A to PEMA copolymer films provided a suitable platform for the evaluation of the interplay between the bound enzyme and the adhesive substances secreted by *Balanus amphitrite* barnacle cyprids. The bound enzyme appeared to affect the consolidation of adhesion of cyprids to the bioactive layers in a manner that depends upon the surface activity. The postulated

mode-of-action is based on the proteolytic degradation of the adhesive substances secreted upon attachment that eventually results in the detachment of already metamorphosed individuals without further effects on their health or viability. Changes in the swimming behavioral pattern of cyprids exposed to high activities of the bound enzyme were also demonstrated. Since the strong effects observed on settlement and adhesion strength of barnacle cyprids were gained by using low amounts of immobilized enzyme, the present study may prove valuable in the design of antifouling surfaces that seek to incorporate active, non-biocidal agents.[42]

5. Experimental Section

Reagents: Poly(octadecene-*alt*-maleic anhydride) (POMA) (MW = 30,000–50,000) was purchased from Polysciences Inc. (Warrington, USA). Poly(ethylene-*alt*-maleic anhydride) (PEMA) (MW = 125,000) was purchased from Aldrich (Munich, Germany). Subtilisin Carlsberg, or Subtilisin A (alkaline protease from *Bacillus licheniformis*; type VIII; E.C. no.: 3.4.21.62), *N*-succinyl-Ala-Ala-Pro-Phe-pNa (Suc-AAPF-pNA), citric acid, 5 M sodium hydroxide solution (for molecular biology), phosphate buffered saline (PBS) tablets, and sodium bicarbonate were purchased from Sigma-Aldrich (St. Louis, USA). Tetrahydrofuran, sodium sulphate, and dimethylsulfoxide (DMSO) were obtained from Fluka (Steinheim, Germany). Hydrogen peroxide solution (35 vol%, not stabilized), calcium chloride, and magnesium chloride hexahydrate were purchased from Merck (Darmstadt, Germany). Ammonium hydroxide solution (28–30 wt%), toluene and acetone were obtained from Acros Organics (Geel, Belgium). Potassium chloride and sodium chloride were purchased from Riedel-de Haen (Seelze, Germany). Ethanol and paraffin wax were obtained from VWR International (Fontenay sous Bois, France). 3-aminopropyldimethylethoxysilane (97 vol%) was obtained from ABCR GmbH (Karlsruhe, Germany). 5-(and-6)-carboxytetramethylrhodamine, succinimidyl ester (5(6)-TAMRA, SE) mixed isomers was acquired from Invitrogen (Eugene, Oregon, USA). PD-10 desalting columns packed with Sephadex G-25 medium were obtained from GE Healthcare (Buckinghamshire, UK). Glass coverslips (hydrolytic class 1) were purchased from Menzel-Gläzer (Braunschweig, Germany). Ultrasonically cleaned microscope Nexterion Glass B slides were obtained from SCHOTT (Jena, Germany). The Petri dishes (Steriplan) employed in the tracking experiments were from Duran Group (Mainz, Germany). P 96-well plates (Rotilabo, F-profile) were obtained from Carl Roth GmbH (Karlsruhe, Germany). Quadriperm dishes were from Greiner Bio-One Ltd. (Stonehouse, UK). De-ionized double distilled water was obtained from a Milli-Q Gradient A10 water purification system (Millipore (Molsheim, France)). 'Tropic Marin' artificial seawater (ASW) from Tropic Marine Centre (Chorleywood, UK) was used at pH 8.0 and 3.3 w/v% salinity in all biological assays. Unless otherwise stated, all chemicals were of the highest available grades.

Preparation of Bioactive Nanocoatings: Poly(ethylene-*alt*-maleic anhydride) (PEMA) and poly(octadecene-*alt*-maleic anhydride) (POMA) copolymer thin films were prepared as previously described.[23,26] Briefly, glass and silicon coverslips (for the characterization assays) or ultrasonically cleaned microscope glass slides and glass dishes (for the biological assays) were sonicated in water and ethanol for 30 min, then oxidized in a mixture of water:hydrogen peroxide:ammonia (volume ratio 5:1:1) at 70 °C for 10 min, dried at 120 °C for 1 h and subsequently modified with 3-aminopropyldimethylethoxysilane by exposure to the compound in vapor phase overnight. The aminosilane-modified samples were thereafter rinsed in toluene, dried at 120 °C for 1 h and spin-coated with PEMA (0.15 wt% in THF:acetone (weight ratio 2:1)) or POMA (0.08 wt% in THF) solutions. Stable covalent binding of the maleic anhydride copolymer film was achieved by annealing at 120 °C for 2 h to generate imide bonds with the underlying aminosilane layer.

Covalent immobilization of Subtilisin A onto freshly prepared PEMA copolymer films was carried out by exposing the polymer layers to varying concentrations of the enzyme in solution ([Es]). Enzyme immobilization proceeded as disclosed in previous work[23,24] although departing from much lower enzyme concentrations (Subtilisin A was dissolved in PBS, pH = 8.6 (adjusted with 1 and 5 M sodium hydroxide solutions) at concentrations between 0.01 and 3 mg ml^{-1}). The reduction in the enzyme concentrations used for immobilization was motivated by the lack of a settlement trend with regard to enzyme surface activity in the same activity range considered for marine algae (Figure S1, Supporting Information). After overnight exposure to the enzyme solution, samples were rinsed 10 times with distilled water and were thereafter either used for assays or denatured. Denaturation of the active enzyme-containing coatings was achieved by heating the samples at 120 °C for 45 min.

Characterization of the Bioactive Nanocoatings: The characterization of the bioactive coatings utilized in the biological assays with barnacle cyprids followed Tasso et al.[23,24] and involved the determination of immobilized protein amount, enzyme layer thickness, catalytic activity, stability upon incubation in aqueous media (aging), and surface roughness and wettability.

Briefly, the thickness of the immobilized enzyme layer was determined by single-wavelength ellipsometry (SE400, Sentech Instruments GmbH, Berlin, Germany) of freshly-prepared coatings (to avoid dehydration) using a five-layer model approximation (silicon/silicon dioxide/maleic anhydride bound to aminosilane/enzyme/air) and a refractive index for the enzyme layer of 1.375[43] (N = samples per condition = 4; m = measurements per sample = 6). The surface concentration (i.e. amount of immobilized enzyme per unit area) of aged and non-aged coatings was evaluated by confocal Laser Scanning Microscopy (cLSM) (TCS SP5, Leica Microsystems, Wetzlar, Germany) using immobilized TAMRA-labeled Subtilisin A and the previously-determined surface concentration of the highest surface concentration coating (0.24 ± 0.03 µg.cm^{-2}[23]) as scaling factor (N = 4; m = 3). The activity of the enzyme-containing coatings was determined by following the conversion of the substrate Suc-AAPF-pNA into peptides and phenylnitroaniline (pNa) through absorbance spectroscopy (TECAN Magellan GENios, Tecan, Austria) at 405 nm (N = 5; m = 1). The stability of the enzyme-containing coatings was assessed by evaluating the residual activity and surface concentration of the bioactive layers after incubation in artificial sea water (ASW*) for 48 h at room temperature (see a previous report[24] for the composition of ASW*). Atomic Force Microscopy (AFM) (MFP-3D, Asylum Research, Santa Barbara, USA; scan size = 4 µm) in tapping mode was employed to determine the surface root mean square (RMS) roughness of the coatings as freshly-prepared (N = 2; m = 2). Static water contact angles (OCA30, Dataphysics Instruments GmbH, Filderstadt, Germany) of active and control coatings were measured in air using de-ionized water and utilized as an indicator of the surface wettability (N = 4; m = 3). All characterization experiments (except for AFM) were run twice on independent sample batches.

Balanus amphitrite (syn. *Amphibalanus amphitrite*[44]) cyprids: Adult, brood stock barnacles, supplied by Duke University Marine Lab, were maintained as per Hellio et al.[45] Nauplii were cultured and grown to the cyprid stage as per Hellio et al.[45] Cyprids were stored for 3 days at 6 ± 1 °C in 0.2 µm filtered natural seawater prior to all assays.

Settlement Assay: The settlement assays with barnacle cyprids concentrated on the effects of both soluble and surface-bound enzyme on cyprid settlement. The general methodology of the 'barnacle drop settlement assay' was as described elsewhere.[46] Enzyme immobilization was performed in situ and immediately before the assays to ensure the properties of the biolayers were as characterized.

Assays determining the effect of soluble enzyme used the base maleic anhydride (MA) coatings exposed to the enzyme buffer (PBS; pH = 8.6) overnight. Slides were then placed into Quadriperm dishes and exposed to a 1.5 ml drop of 0, 0.5, 1 or 1.5 µg ml^{-1} of active enzyme in 'Tropic Marin' artificial seawater (ASW) with 40 cyprids in each drop. Dishes were incubated in the dark at high humidity and at 28 °C. Settlement and mortality were enumerated at 24 and 48 h.

The assays with immobilized enzyme used freshly-prepared active and denatured samples (as previously described). These slides were carefully dipped into paraffin wax along each edge of the slide to confine cyprids to the central area of enzyme immobilization. This resulted in 3 distinct areas: the central area with immobilized enzyme, the interface wax-immobilized enzyme, and the wax area itself. Twelve (active coatings) or six (denatured and PEMA control coatings) replicates of each concentration were thus produced. Surfaces were thereafter placed in Quadriperm dishes and exposed to a 1.5 ml drop of ASW containing 40 cyprids. Dishes were treated as in the previous experiment. At the end of each incubation period (24 and 48 h), the total number of settled cyprids was determined and their location noted (i.e. central, interfacial or wax area). Any individuals that had settled on the wax were excluded from data analysis. Larvae that did not settle after the 48 h experimental period were observed for signs of abnormal behavior. During the experiments, a number of settled individuals were found to detach from the bioactive surfaces after having partially or fully metamorphosed. These detached individuals were carefully removed after the 48 h enumeration and kept for 2 weeks in ASW with two weekly changes of water and feeding (*Tetraselmis suecica*), at which time any dead individuals were noted.

Settlement results are presented as mean percent settlement (i.e. mean number of settled cyprids expressed as a percentage of the total number of dispensed cyprids) with 95% confidence intervals. Normality of the distribution was assessed by means of an Anderson Darling normality test (Minitab v15.1.0.0, Minitab Ltd., Coventry, UK). Settlement data were analyzed for statistical differences using the Kruskal-Wallis method and a post-hoc Dunn's test (GraphPad Prism v5.0, GraphPad Software, San Diego, USA).

Tracking Assay: Tracking using EthoVision 3.1 software (www.noldus.com) was carried out as per Marechal et al.[47] Thirty 3-day-old cyprids were tracked for 5 min each on active layers (activities 1.3 and 63 [pNa] min^{-1} 10^3) and the respective denatured and PEMA controls. Total distance moved, linear velocity, meander, total turn angle and angular velocity were analyzed. Normality of the data was evaluated using Anderson Darling (Minitab). Normal data underwent a one-way ANOVA followed by post-hoc Tukey's test (Minitab). Otherwise, a Kruskall Wallis test was carried out with a post-hoc Dunn's test (GraphPad Prism v5.0).

Supporting Information

Supporting Information is available from the Wiley Online Library or from the author.

Acknowledgements

www.MaterialsViews.com

ADVANCED
FUNCTIONAL
MATERIALS
www.afm-journal.de

FULL PAPER

[1] D. M. Yebra, S. Kiil, K. Dam-Johansen, *Prog. Org. Coat.* **2004**, *50*, 75–104.

[2] P. Majumdar, E. Lee, N. Patel, K. Ward, S. J. Stafslien, J. Daniels, B. J. Chisholm, P. Boudjouk, M. E. Callow, J. A. Callow, S. E. M. Thompson, *Biofouling* **2008**, *24*, 185–200.

[3] A. Negri, P. Marshall, *J. Environ. Manage.* **2009**, *90*, S31–S40.

[4] C. Anderson, M. Atlar, M. Callow, M. Candries, A. Milne, R. L. Townsin, *J. Mar. Design Operat.* **2003**, 11–23.

[5] M. E. Callow, J. A. Callow, *Biologist* **2002**, *49*, 1–5.

[6] P. S. Murthy, V. P. Venugopalan, K. V. K. Nair, T. Subramoniam, in *Marine and Industrial Biofouling* (Eds: H.-C. Flemming, P. S. Murthy, R. Venkatesan, K. E. Cooksey), Springer-Verlag, Berlin, Germany **2009**, p. 233.

[7] E. Ralston, G. Swain, *Bioinsp. Biomim.* **2009**, *4*, 015007–015015.

[8] J. B. Kristensen, R. L. Meyer, B. S. Laursen, S. Shipovskov, F. Besenbacher, C. H. Poulsen, *Biotech. Adv.* **2008**, *26*, 471–481.

[9] N. Aldred, I. Y. Phang, S. L. Conlan, A. S. Clare, G. J. Vancso, *Biofouling* **2008**, *24*, 97–107.

[10] T. M. Dugdale, R. Dagastine, A. Chiovitti, P. Mulvaney, R. Wetherbee, *Biophys. J.* **2005**, *89*, 4252–4260.

[11] C. Leroy, C. Delbarre, F. Ghillebaert, C. Compere, D. Combes, *Biofouling* **2008**, *24*, 11–22.

[12] S. M. Olsen, L. T. Pedersen, M. H. Laursen, S. Kiil, K. Dam-Johansen, *Biofouling* **2007**, *23*, 369–383.

[13] J. H. Paul, W. H. Jeffrey, *Appl. Environ. Microbiol.* **1985**, *50*, 431–437.

[14] M. E. Pettitt, S. L. Henry, M. E. Callow, J. A. Callow, A. S. Clare, *Biofouling* **2004**, *20*, 299–311.

[15] S. Dobretsov, H. Xiong, Y. Xu, L. A. Levin, P.-Y. Qian, *Mar. Biotechnol.* **2007**, *9*, 388–397.

[16] Y. D. Kim, J. S. Dordick, D. S. Clark, *Biotechnol. Bioeng.* **2001**, *72*, 475–482.

[17] N. Aldred, A. S. Clare, *Biofouling* **2008**, *24*, 351–363.

[18] K. Kamino, in *Biological Adhesives* (Eds: A. M. Smith, J. A. Callow), Springer-Verlag, Heidelberg, Germany **2006**, Ch. 8.

[19] A. S. Clare, R. K. Freet, M. McClary Jr., *J. Mar. Biol. Assoc.* **1994**, *74*, 243–250.

[20] K. Matsumura, M. Nagano, Y. Kato-Yoshinaga, M. Yamazaki, A. S. Clare, N. Fusetani, *Proc. R. Soc. Lond. B* **1998**, *265*, 1825–1830.

[21] N. D. Rawlings, A. J. Barrett, in *Methods in Enzymology*, vol. 244 (Ed: A. J. Barrett), Academic Press, New York, USA **1994**, p. 19.

[22] F. S. Markland, E. L. Smith, in *The Enzymes*, Vol. 3 (Ed: P. D. Boyer), Academic Press, New York and London, USA **1971**, p. 561.

[23] M. Tasso, A. L. Cordeiro, K. Salchert, C. Werner, *Macromol. Biosci.* **2009**, *9*, 922–929.

[24] M. Tasso, M. E. Pettitt, A. L. Cordeiro, M. E. Callow, J. A. Callow, C. Werner, *Biofouling* **2009**, *25*, 505–516.

[25] T. Osaki, C. Werner, *Langmuir* **2003**, *19*, 5787–5793.

[26] T. Pompe, S. Zschoche, N. Herold, K. Salchert, M.-F. Gouzy, C. Sperling, C. Werner, *Biomacromolecules* **2003**, *4*, 1072–1079.

[27] T. Pompe, L. Renner, M. Grimmer, N. Herold, C. Werner, *Macromol. Biosci.* **2005**, *5*, 890–895.

[28] P. Uhlmann, S. Skorupa, C. Werner, K. Grundke, *Langmuir* **2005**, *21*, 6302–6307.

[29] D. J. Neidhart, G. A. Petsko, *Protein Eng.* **1988**, *2*, 271–276.

[30] N. Aldred, A. Scardino, A. Cavaco, R. de Nys, A. S. Clare, *Biofouling* **2010**, *26*, 287–299.

[31] N. J. O'Connor, D. L. Richardson, *J. Exp. Mar. Biol. Ecol.* **1994**, *183*, 213–225.

[32] D. Rittschof, J. D. Costlow, in *Topics in Marine Biology, Proceedings of the 22nd European Marine Biology Symposium* (Ed: J. D. Ros), Instituto de Ciencias del Mar, Barcelona, Spain **1989**, p. 411.

[33] D. Roberts, D. Rittschof, E. Holm, A. R. Schmidt, *J. Exp. Mar. Biol. Ecol.* **1991**, *150*, 203–221.

[34] J. F. Schumacher, N. Aldred, M. E. Callow, J. A. Finlay, J. A. Callow, A. S. Clare, A. B. Brennan, *Biofouling* **2007**, *23*, 307–317.

[35] M. S. Stanley, M. E. Callow, J. A. Callow, *Planta* **1999**, *210*, 61–71.

[36] A. Chiovitti, T. M. Dugdale, R. Wetherbee, in *Biological Adhesives* (Eds: A. M. Smith, J. A. Callow), Springer-Verlag, Heidelberg, Germany **2006**, Ch. 5.

[37] P. J. Molino, R. Wetherbee, *Biofouling* **2008**, *24*, 365–379.

[38] D. E. Barlow, G. H. Dickinson, B. Orihuela, J. L. Kulp, III, D. Rittschof, K. J. Wahl, *Langmuir* **2010**, *26*, 6549–6556.

[39] J.-J. Wang, R. Borwornpinyo, N. Odetallah, J. C. H. Shih, *Enzyme Microb. Technol.* **2005**, *36*, 758–765.

[40] R.-L. Hsu, K.-T. Lee, J.-H. Wang, L. Y.-L. Lee, R. P.-Y. Chen, *J. Agric. Food Chem.* **2009**, *57*, 503–508.

[41] M. Schmidt, A. Cavaco, N. Gierlinger, N. Aldred, P. Fratzl, M. Grunze, A. S. Clare, *J. Adhes.* **2009**, *85*, 139–151.

[42] I. Banerjee, R. C. Pangule, R. S. Kane, *Adv. Mater.* **2011**, *23*, 690–718.

[43] C. Werner, K.-J. Eichhorn, K. Grundke, F. Simon, W. Grählert, H.-J. Jacobasch, *Colloids Surf., A* **1999**, *156*, 3–17.

[44] A. S. Clare, J. T. Høeg, *Biofouling* **2008**, *24*, 55–57.

[45] C. Hellio, J.-P. Marechal, B. Véron, G. Bremer, A. S. Clare, Y. Le Gal, *Mar. Biotechnol.* **2004**, *6*, 67–82.

[46] Y. Tang, J. A. Finlay, G. L. Kowalke, A. E. Meyer, F. V. Bright, M. E. Callow, J. A. Callow, D. E. Wendt, M. R. Detty, *Biofouling* **2005**, *21*, 59–71.

[47] J.-P. Marechal, C. Hellio, M. Sebire, A. S. Clare, *Biofouling* **2004**, *20*, 211–217.

ADVANCED
FUNCTIONAL
MATERIALS

www.afm-journal.de

Materials
Views

www.MaterialsViews.com

FULL PAPER

Versatile α,ω-Disubstituted Tetrathienoacene Semiconductors for High Performance Organic Thin-Film Transistors

Jangdae Youn, Peng-Yi Huang, Yu-Wen Huang, Ming-Chou Chen,* Yu-Jou Lin, Hui Huang, Rocio Ponce Ortiz, Charlotte Stern, Ming-Che Chung, Chieh-Yuan Feng, Liang-Hsiang Chen, Antonio Facchetti,* and Tobin J. Marks*

Facile one-pot [1 + 1 + 2] and [2 + 1 + 1] syntheses of thieno[3,2-*b*]-thieno[2′,3′:4,5]thieno[2,3-*d*]thiophene (tetrathienoacene; TTA) semiconductors are described which enable the efficient realization of a new TTA-based series for organic thin-film transistors (OTFTs). For the perfluorophenyl end-functionalized derivative DFP-TTA, the molecular structure is determined by single-crystal X-ray diffraction. This material exhibits n-channel transport with a mobility as high as 0.30 cm^{2}V^{-1}s^{-1} and a high on-off ratio of 1.8×10^7. Thus, DFP-TTA has one of the highest electron mobilities of any fused thiophene semiconductor yet discovered. For the phenyl-substituted analogue, DP-TTA, p-channel transport is observed with a mobility as high as 0.21 cm^{2}V^{-1}s^{-1}. For the 2-benzothiazolyl (BS-) containing derivative, DBS-TTA, p-channel transport is still exhibited with a hole mobility close to 2×10^{-3} cm^{2}V^{-1}s^{-1}. Within this family, carrier mobility magnitudes are strongly dependent on the semiconductor growth conditions and the gate dielectric surface treatment.

1. Introduction

Organic semiconductors have attracted growing attention over the past decade due to their potential application in organic thin-film transistors (OTFTs) for low cost/printable electronics, such as flexible displays, RF-ID components, and e-papers.[1–12] Compared with well-known organic semiconductors, such as pentacenes[13–15] and anthradithiophene derivatives,[16–18] fused-thiophenes[19–21] offer the attraction of relatively higher ambient stability originating from large band gaps, and good charge transport properties, reflecting extensive molecular conjugation and strong intermolecular S•••S interactions which promote close molecular packing. Several fused thiophene derivatives have already been demonstrated to have good p-type charge transport performance (**Figure 1**). For example, those with three fused thiophene units, compounds **1**[22] and **2**,[23] and those with four thiophene-fused units, **3**,[19] **4**,[24] **5**,[25] and **6**[26] exhibit hole mobilities up to 0.42, 0.89, 0.14, 0.06, 0.70, and 2.75 cm^2 V^{-1} s^{-1}, respectively. Furthermore, five-ring fused pentacene analogs **7**[27] and **8**[28] achieve hole mobilities of 0.51, and 1.7 cm^2 V^{-1} s^{-1}, respectively. Relative to p-type fused thiophenes, the potential of n-type fused thiophene-based semiconductors has not been fully explored until recently, and then only for a limited range of materials.[29–31] One approach to realizing electron transport in organic semiconductors is to functionalize p-type semiconductors with strong electron-withdrawing substituents, such as perfluoroaryl,[32] carbonyl[33] groups. Previously we investigated perfluorophenyl substituted dithieno[2,3-b:3′,2′-d]thiophene (**DFP-DTT; 9**) and perfluorobenzoyl (C$_6$F$_5$CO) substituted DTTs (**FBB-DTT; 10** and **DFB-DTT; 11**). All three of these new DTTs exhibit decent electron mobilities, as high as 0.07, 0.03, and 0.003 cm^2 V^{-1} s^{-1}, respectively, for vapor-deposited films.

Dr. J. Youn, Dr. H. Huang, Dr. R. P. Ortiz, Dr. C. Stern,
Prof. A. Facchetti, Prof. T. J. Marks
Department of Chemistry and the Materials Research Center
Northwestern University
2145 Sheridan Rd., Evanston, IL 60208-3113, USA
E-mail: a-facchetti@northwestern.edu; t-marks@northwestern.edu
Dr. P.-Y. Huang, Y.-W. Huang, Prof. M.-C. Chen, Y.-J. Lin,
M.-C. Chung, C.-Y. Feng
Department of Chemistry
National Central University
Jhong-Li 32054, Taiwan
E-mail: mcchen@ncu.edu.tw

Dr. R. P. Ortiz
Department of Physical Chemistry
University of Malaga
29071, Malaga, Spain
L.-H. Chen
Process Technology Division
Display Technology Center
Industrial Technology Research Institute
Chung Hsing Rd., Chutung, Hsinchu, Taiwan 31040, R.O.C.

www.MaterialsViews.com

ADVANCED
FUNCTIONAL
MATERIALS
www.afm-journal.de

FULL PAPER
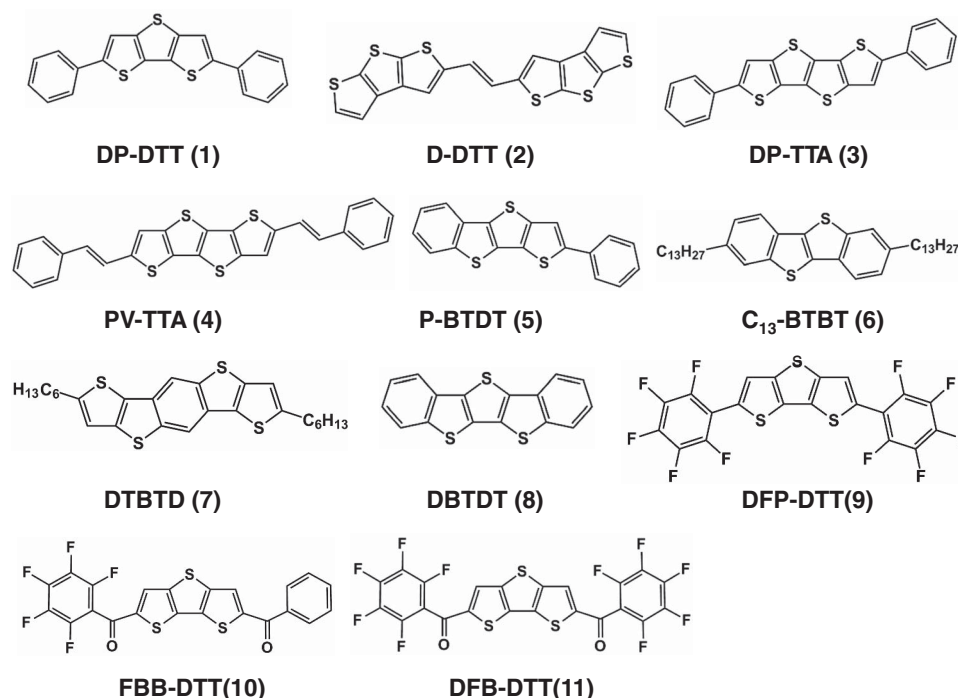
Figure 1. Several examples of fused thiophene organic semiconductors.

Following a molecular design strategy analogous to DTTs, the fused tetrathiophene-based tetrathienoacene (TTA) system, end-functionalized with electron-withdrawing groups, is investigated in this contribution to better understand correlations between molecular structure and n-type TFT performance (**Figure 2**). To the best of our knowledge, the first example of a TTA-based small molecule semiconductor with a p-channel mobility of 0.14 cm^2 V^{-1} s^{-1} was reported by Y. Liu et al. in 2009.[19] The second TTA, end-capped with styrenyl groups, was reported by the same team in 2010 with a mobility of 0.06 cm^2 V^{-1} s^{-1}.[24] Recently a dicyanomethylene substituted fused tetrathienoquinoid was reported with a good mobility of 0.9 cm^2 V^{-1} s^{-1} after solution processing.[34] Since then, no other TTA-based small molecules have been reported, due to synthetic difficulties in accessing the tetrathiophene core, which was obtained in only 15 ~ 26% overall yield from reaction of 3-bromothiophene and 3-bromothieno[3,2-b]thiophene.[19]

To address this issue, we report here facile "one-pot" [1 + 1 + 2] and [2 + 1 + 1] syntheses of TTA. Compared to the previous synthetic routes, this one-pot synthesis offers a more efficient route to obtain tetrathiophene cores at a low cost. Furthermore, we show that TTA can also be generated in a reverse [2 + 1 + 1] order, unprecedented in TTA chemistry. With the help of electron-withdrawing groups, this TTA core is shown to achieve good n-type charge transport in OTFT devices. The perfluorophenyl end-functionalized derivative **DFP-TTA** exhibits n-channel transport with a mobility as high as 0.30 cm^2 V^{-1} s^{-1}, rendering it one of the highest performing n-type semiconductors among fused thiophenes reported to date. Two other TTA derivatives are synthesized to better understand molecular structure-device performance relationships. Phenyl-substituted derivative **DP-TTA** and the 2-benzothiazolyl (BS-) containing derivative **DBS-TTA** exhibit p-channel transport with mobilities as high as 0.21 cm^2 V^{-1} s^{-1} and 0.002 cm^2 V^{-1} s^{-1}, respectively. Materials properties such as crystal structure, HOMO-LUMO localization/energetics, and film microstructure are discussed and compared/contrasted with the DTT analogs (Figure S1). In addition, film growth conditions including substrate temperature, and dielectric surface treatment are investigated and shown to strongly influence TFT device response in a readily understandable way.
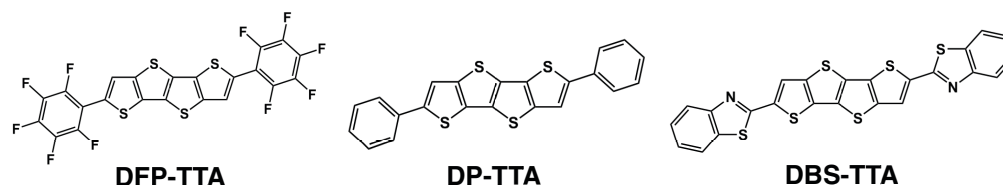
Figure 2. Chemical structures of the tetrathienoacene (**TTA**) derivatives synthesized in this study.

**ADVANCED
FUNCTIONAL
MATERIALS**
www.afm-journal.de

Materials Views
www.MaterialsViews.com

One pot [1 + 1 + 2]

One pot [2 + 1 + 1]
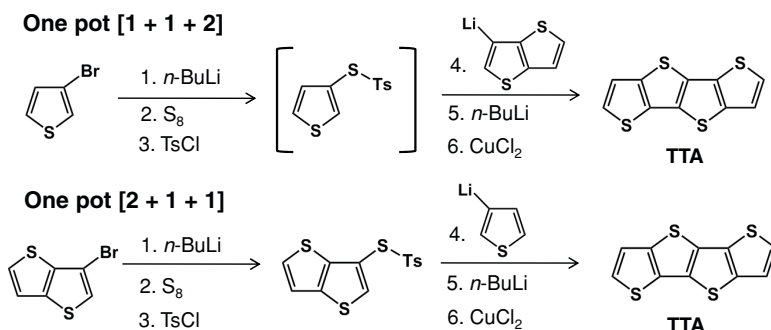
Scheme 1. One-pot [1 + 1 + 2] and [2 + 1 + 1] synthetic routes to the **TTA** core.

2. Results and Discussion

In this section we first describe the synthesis of the new semiconductors, followed by molecular characterization. Next, we examine details of the solid state packing, and the microstructure of the vapor-deposited films based on X-ray diffraction data. Finally, we discuss thin-film transistor characterization and correlate the results with semiconductor film morphology, such as crystalline domain size, surface coverage, and nucleation density at the semiconductor-dielectric interfacial region.

2.1. Synthesis

Since the key building block in this investigation is the tetrathiophene-fused core, a one-pot [1 + 1 + 2] synthesis of TTA was first explored. Our new approach originates from inexpensive, commercially available materials and dispenses with the requirement of expensive bis(phenyl-sulfonyl)sulfide, which is conventionally used in the fused-thiophene syntheses,[35–37] and the results for TTA derivatives are much shorter synthetic times with comparable yields. For this one-pot synthesis, 3-bromothiophene is first lithiated with *n*-BuLi, followed first by S$_8$ and then by TsCl addition, as shown in **Scheme 1**. Next, the mixture is treated with 3-lithiumthienothiophene,

generated in situ from 3-bromothienothiophene, synthesized as shown in Scheme S1.[37,38] Without product isolation, the crude mixture is subsequently dilithiated with *n*-BuLi and ring closure is achieved with CuCl$_2$ to afford TTA in >27% yield. An alternative/reversed one-pot [2 + 1 + 1] synthesis of TTA was also explored and offers a comparable yield (~22%).[39] For comparison, TTA was prepared following the known fused thiophene synthetic route in which 3-bromothiophene is first ring-fused,[40] and then brominated to give 2,3,5,6-tetrabromothieno[3,2-*b*]thiophene, then double ring-fused, following a known TTA synthetic route,[41] to afford tetrathienoacene in an total yield of 16% (**Scheme 2**). Undoubtedly, the latter route is much more time-consuming and labor-intensive compared to the one-pot synthetic route developed here.

Since perfluorophenyl functionalization is likely to result in good candidates for n-channel semiconductors, the synthesis of C$_6$F$_5$-functionalized TTA (**DFP-TTA**) was explored and achieved in a yield of 75% via Stille coupling (**Scheme 3**). For comparison, **DP-TTA** was also prepared via Stille coupling and the yield is comparable to the Suzuki coupling approach (Scheme 3). More conjugated benzothiazolyl substituents, in addition to contributing the electron-withdrawing capacity of the carbonyl group (C = O), tend to form planar molecular structures,[42] thus possibly resulting in lower-lying LUMOs, and hence possible n-channel transport. Therefore, 2-benzothiazolyl (BS-) end-capped **DBS-TTA** was prepared and achieved in a yield of ~51% by refluxing 2-aminobenzenethiol with **TTA**-(COCl)$_2$. The later was generated in situ by refluxing **TTA**-(COOH)$_2$[41] with SOCl$_2$ in situ as shown in **Scheme 4**.

2.2. Semiconductor Thermal and Optical Properties

The three TTA-based materials synthesized in this study are thermally stable and lack any detectable phase transitions at low
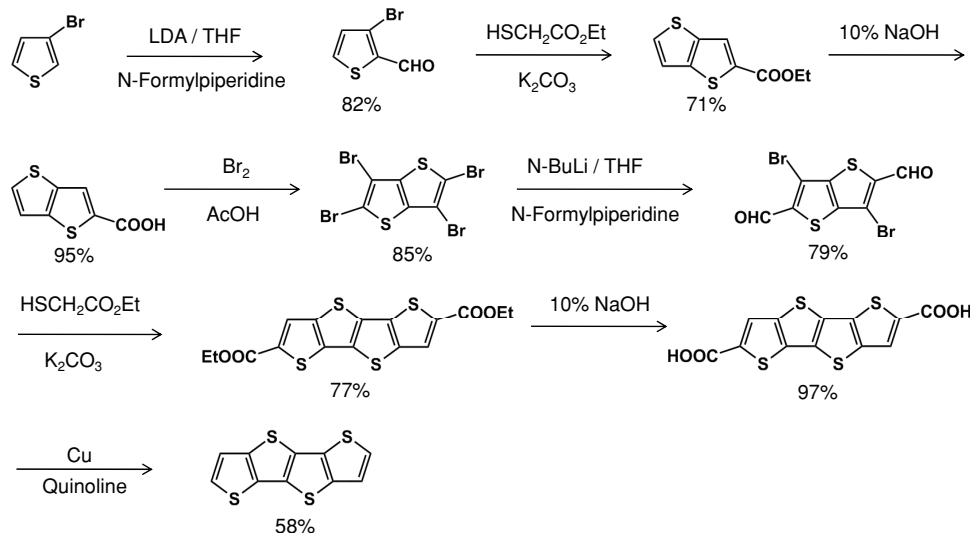
Scheme 2. Synthesis of tetrathienoacene from 3-bromothiophene.
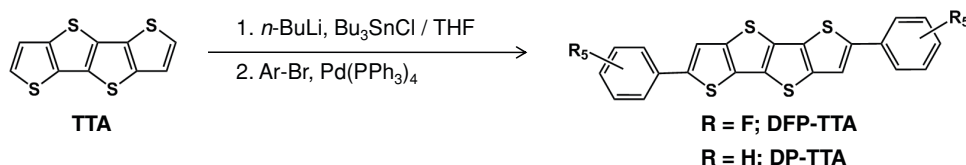
Scheme 3. Synthetic route to **DFP-TTA** and **DP-TTA**.

temperatures, indicating they are suitable for TFT fabrication. As might be expected, the highest molecular weight compound, **DBS-TTA**, exhibits the highest melting point and TGA weight loss temperature. For **DFP-TTA** and **DP-TTA**, differential scanning calorimetry (DSC) does not reveal obvious endothermic features at temperatures below 280 °C. The thermogravimetric analysis data indicate weight loss (5%) only on heating above 330 °C, as summarized in **Table 1**. Note that the present TTA compounds have significantly higher melting points and higher weight loss temperatures in comparison to their DTT analogs, **DFP-DTT, DP-DTT**, and **DBS-DTT** (Figure S1). Interestingly, with perfluorophenyl groups end-capping the TTA core, **DFP-TTA** has a lower melting point and a lower weight loss temperature than its nonfluorinated analogue, **DP-TTA**, and exhibits higher volatility, doubtless due to the perfluoroaryl substituents.[30,31]

The optical absorption spectra of the TTA compounds in o-$C_6H_4Cl_2$ are significantly red-shifted versus their DTT analogs as shown in **Figure 3**, verifying the smaller band gaps of TTA compounds than their DTT analogs. As expected, the benzothiazolyl-substituted derivative, **DBS-TTA**, exhibits the smallest energy gap among the compounds in this study, arguing that the

delocalization extends from the TTA (or DTT) core to the two benzothiazolyl substituents. Interestingly, derivatives with C_6F_5- substituents exhibit slightly blue-shifted absorptions versus those with C_6H_5 substituents in both the TTA and DTT series, as seen in **DFP-TTA** ($\lambda_{max} \sim 384$ nm) vs. **DP-DTT** ($\lambda_{max} \sim 389$ nm) and **DFP-DTT** ($\lambda_{max} \sim 367$ nm) vs. **DP-DTT** ($\lambda_{max} \sim 373$ nm). The HOMO-LUMO energy gaps calculated from the onset of the optical absorption (2.6–3.1 eV) increase in the order: **DBS-TTA < DP-TTA < DFP-TTA** as well as **DBS-DTT < DP-DTT < DFP-DTT**, as shown in Table 1.

These results seem contradictory at first glance considering well-known electron-withdrawing group (EWG) effects that typically red-shift absorption maxima in optical spectra.[43–50] However, the present DPV and DFT studies (See more below) reveal that the electron-withdrawing C_6F_5 group lowers both the HOMO and LUMO, also consistent with known EWG effects. Moreover, the HOMO levels of **DFP-TTA** and **DFP-DTT** are lowered versus **DP-TTA** and **DP-DTT** with respect to their LUMOs. Consequently, the energy gaps for C_6F_5- substituted derivatives **DFP-TTA** and **DFP-DTT** become slightly larger, thereby explaining the slightly blue-shifted absorption maxima.
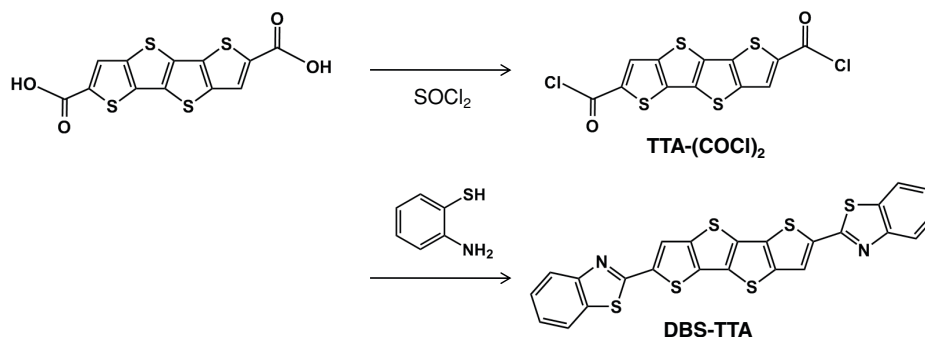
Scheme 4. Synthetic route to **DBS-TTA**.

Table 1. Thermal, optical, and electrochemical comparison of the properties of TTA and DTT compounds.

Compound	DSC Tm(°C)	TGA (°C, 5%)	UV–vis[b] λmax (nm)	Reduction Potential (V)[c]	Oxidation Potential (V)[c]	ΔEgap(eV) (Optical)[b]	(DPV)[c]
DFP-TTA	280	330	384	−1.66	1.46	2.93	3.12
DP-TTA	280[a]	371	389	−1.94	1.15	2.87	3.09
DBS-TTA	442	443	426,451	−1.48	1.35	2.60	2.83
DFP-DTT	258	270	367	−1.62	1.64	3.06	3.26
DP-DTT	290	394	373	−1.95	1.21	3.02	3.16
DBS-DTT	262	388	417,441	−1.46	1.47	2.69	2.93

[a]see ref. 19; [b]in o-$C_6H_4Cl_2$; [c]by DPV in o-$C_6H_4Cl_2$ at 25 °C (using ferrocene/ferrocenium as internal standard, set at +0.60 V).

FULL PAPER
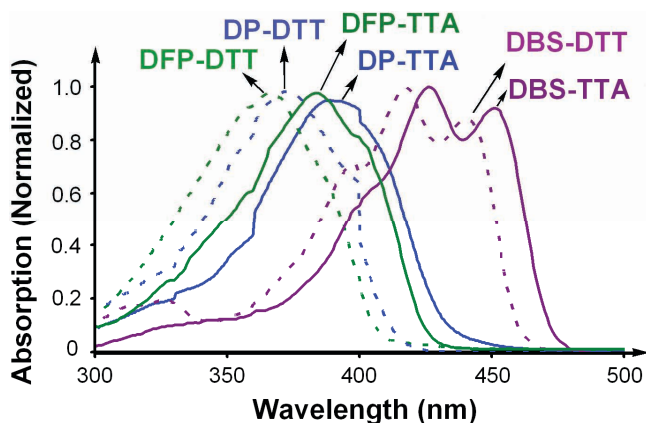
Figure 3. Optical spectra of **TTA** compounds (solid lines) and **DDT** compounds (dashed lines) in o-$C_6H_4Cl_2$ solution.

Figure 4. The electrochemically-derived HOMO and LUMO energy levels of TTA and DTT molecules.

The photooxidative stability of the present TTA derivatives was investigated by monitoring the absorbance decay at λ_{max} in aerated $CHCl_3$ solutions exposed to white light (fluorescent lamp) at room temperature. Under these conditions over the course of 3 days, no decomposition is observed for any of these compounds, demonstrating the photo-oxidative stability of these materials.

2.3. Electrochemical Characterization

Differential pulse voltammograms (DPVs) of the TTA compounds were recorded in dichlorobenzene at 25 °C, and the resulting reductive and oxidative potential data are summarized in Table 1.[51] The electrochemically-derived HOMO levels of the TTAs are significantly up-shifted versus their DTT analogs as shown in **Figure 4**. More π-electron delocalization is observed for the fused-tetrathiophene TTA system than for the DTTs, and the HOMO-LUMO energy gaps of the TTAs obtained from the DPV data are smaller than those of their DTT analogs. For C_6F_5- substituted **DFP-TTA**, the electron affinity increases with the larger number of fluoroaryl rings, and fluoroaryl substitution in **DFP-TTA** strongly lowers both the HOMO and LUMO energies versus those in **DP-TTA**. Similar trends are observed for **DFP-DTT** compared to its nonfluorinated derivative **DP-DTT**. The DPV of **DFP-TTA** exhibits an oxidative peak at +1.46 V and a reductive peak at −1.66 V (using ferrocene/ferrocenium as the internal standard, set at +0.60 V). For comparison, the oxidation and reduction potentials of **DP-TTA** (E_{ox} = +1.15 V, E_{red} = −1.94 V) are shifted to more negative values, which can be attributed to the electron-withdrawing effects of the perfluorophenyl substituents. Similarly, the benzothiazolyl substitution in compound **DBS-TTA** (E_{ox} = +1.35 V, E_{red} = −1.48 V) strongly shifts the HOMO and LUMO energies to higher values compared to **DP-TTA**, and induces the most extensive π-electron delocalization within the TTA series, and also has the smallest band gap. The HOMO-LUMO energy gaps obtained from the DPV data are 3.12 eV for **DFP-TTA**, 3.09 eV for **DP-TTA**, and 2.83 eV for **DBS-TTA** (assuming ferrocene/ferrocenium oxidation at 4.8 eV).[52,53] Overall, the electrochemically-derived HOMO-LUMO energy gaps can be ranked in
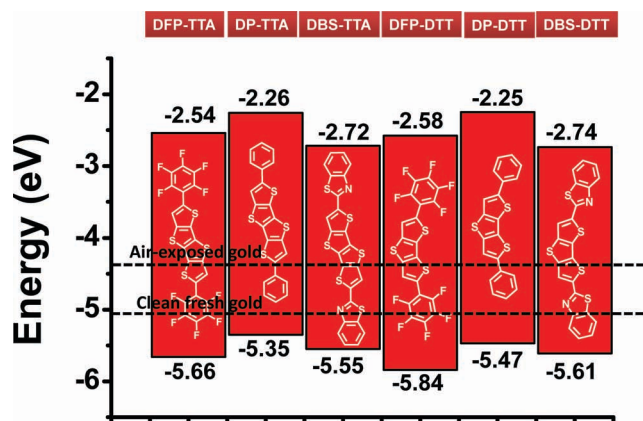
the order **DBS-TTA** < **DP-TTA** < **DFP-TTA** (as well as **DBS-DTT** < **DP-DTT** < **DFP-DTT**; Table 1, Figure 4), which is consistent with the values obtained from optical spectroscopy.

It is interesting to highlight the different effects of the two electron-deficient end-groups on the HOMO and LUMO energies. While the perfluorophenyl substituents lower both frontier orbital energies due to almost identical contribution of the perfluorophenyl units to both HOMO and LUMO orbitals (Figure S2), benzothianolyl substitution lowers the LUMO energy to a far greater extent than the HOMO. Note that despite the fact that both substituents are formally electron-withdrawing groups, the nature of their effects differs substantially; for the perfluorophenyl substituents a σ-(-I) isomeric effect is expected versus a π-mediated mesomeric (-M) electron-withdrawing effect for the benzothianolyl substitution.[54] These different effects explain the rather different modulations of the frontier MO energies, and may result in very different electrical behavior. Furthermore, if we analyze the theoretical charge distributions on both neutral **DFP-TTA** and **DBS-TTA** molecules (see Figure S2 in Supporting Information) we observe that the atoms bearing the greatest negative charge in **DBS-TTA** are the nitrogen atoms, with negative charges of −0.518 e. each. Furthermore, the sulfur atoms in the benzothianolyl group bear a much less positive charge than in the corresponding thiophene rings (Figure S2), underscoring the electron-deficient character of the lateral substituent sulfur atoms. These two electron-deficient atoms are involved to a greater extent in the LUMO (as evidenced in the frontier orbital topologies in Figure S2) than in the HOMO, which explains the unequal destabilization of both frontier orbitals as discussed above. In contrast, the negative charge on the electron-withdrawing perfluorophenyl substituents is localized on the fluorine atoms, which are equally involved in both the HOMO and LUMO topologies (Figure S2), in agreement with the equal stabilization of both orbitals discussed above.

2.4. Semiconductor Solid State and Thin-Film Structure

Thin films of the new semiconductors were vapor-deposited with the goal of investigating the thin-film microstructure

www.MaterialsViews.com

ADVANCED
FUNCTIONAL
MATERIALS
www.afm-journal.de

FULL PAPER

and morphology for TFT device fabrication. The morphology/ TFT properties of the TTA films were investigated on doped Si (gate)/SiO$_2$ (gate insulator) substrates with several different gate dielectric surface treatments. Hexamethyldisilazane (HMDS)-modified substrates were prepared by exposing the Si/SiO$_2$ substrates to HMDS vapor for 7 days in a nitrogen atmosphere to yield a trimethylsilyl-coated surface. Octadecyltrichlorosilane (OTS)-modified substrates were fabricated by immersion of the Si/SiO$_2$ substrates in 3.0 mM hexane solutions of the silane reagent in air for 1 hour after 10 hours of solution aging under 55–60% of relative humidity. All substrates were characterized by advancing aqueous contact angle measurements, which indicate increasing hydrophobicity in the order: SiO$_2$ (28°) < HMDS (95°) < OTS (104°). Additionally, the surface roughnesses were evaluated by tapping mode atomic force microscopy (AFM), revealing a root-mean square (RMS) roughness of 0.15 nm for SiO$_2$, 0.20 nm for HMDS, and 0.35 nm for OTS. All semiconductor films (~50 nm thick) were vapor-deposited while maintaining the substrates at the temperatures (T$_D$s) of 25, 50, and 110 °C, and with a film growth rate of 0.1 Å/s. All films were characterized by θ–2θ X-ray diffraction (XRD) scans and tapping mode AFM.

Before discussing the XRD results for the TTA films, it is useful to begin by correlating film X-ray θ–2θ scan data with a compound of known crystal structure. This initial examination allows a much more thorough analysis of the molecular ordering in the solid film. The perfluorinated TTA derivative DFP-TTA crystallizes in the monoclinic space group P2$_1$/c. The unit cell packing viewed perpendicular to the molecular stacking direction is illustrated in **Figure** 5B, and along the c-axis in Figure 5C.

Similar to other fused thiophenes, the unit cell of **DFP-TTA** exhibits a commonly observed herringbone packing motif with cell parameters, a = 28.500 Å, b = 3.9449 Å, c = 11.3467 Å, α = 90.00°, β = 91.014°, γ = 90.00°, and Z = 2 (Figure 5). The fluorinated phenyl moiety is slightly twisted from the plane of the fused tetrathiophene core, with a dihedral angle of 10.2° (Figure 5B). The cofacial stacking distance between TTA cores is 3.59 Å (Figure 5B), and the shortest intermolecular sulfur•••sulfur contact is 3.58 Å (Figure 5C). This planar molecular structure, short packing distances, and high crystal density (2.086 gcm^{-3}) suggest ideal conditions to achieve significant charge transport in solid films. In general, DFP-DTT[30] exhibits a very similar crystal structure to **DFP-TTA**. This latter molecule also has a typical herringbone packing with cell parameters, a = 11.7702 Å, b = 37.048 Å, c = 3.8830 Å, α = 90.00°, β = 90.000°, γ = 90.00°, and Z = 4 (Figure S3) and the perfluorophenyl groups are slightly twisted by 11.1° from the DTT core plane (Figure S3B). The stacking distance between planar DTT cores is 3.60 Å (Figure S3B) with a shortest intermolecular sulfur-to-sulfur distance of 3.48 Å (Figure S3C). In addition, the slipping angle of the **DFP-DTT** stack is 68° similar to 65° in **DFP-TTA**. It is well known that the herringbone motif is the result of pulling two adjacent molecular stacks together with a roll angle in the opposite direction.[55] When the slipping angle is larger, the overlap of the π-conjugated cores is substantially increased along the stacking direction. Since their slipping angle is almost identical, the degree of spacial overlap between adjacent π-conjugated cores depends on the core sizes of molecules. The effect of the greater core size in the **DFP-TTA** versus that in **DFP-DTT** is reflected in more efficient charge transport properties for the corresponding thin film transistors (see more below).

With the crystal structure data in hand, it is straightforward to simulate the XRD powder pattern and therefore assign the reflections observed in the thin film XRD measurements. Thus, d spacings calculated from the XRD data, and the molecular
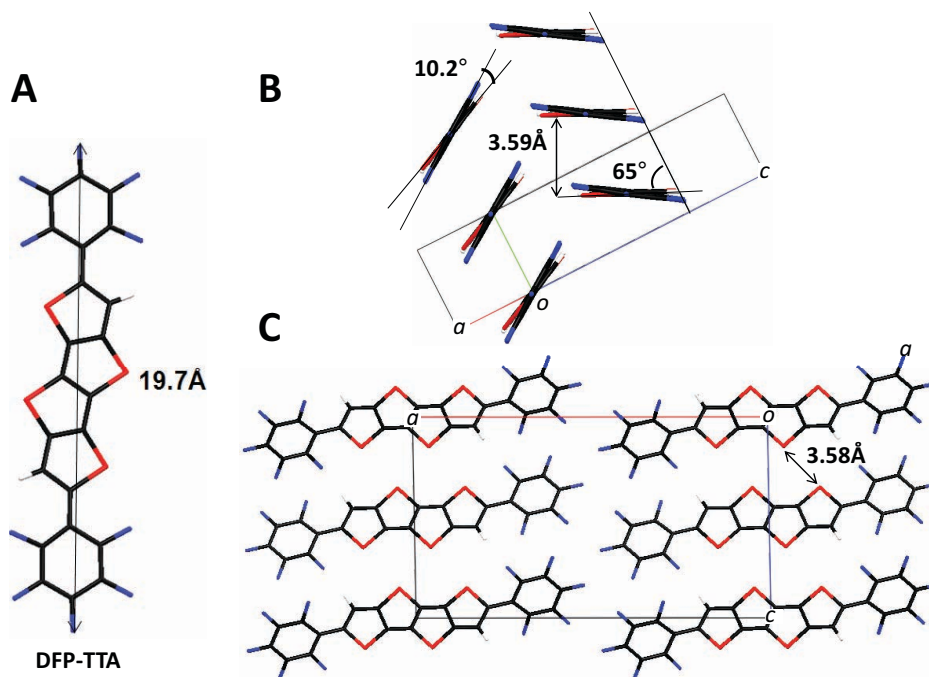
Figure 5. Crystal structure of DFP-TTA (A) molecular length of DFP-TTA = 19.7 Å, (B) slipping angle of adjacent TTA cores = 65°; cofacial distance between TTA cores = 3.59 Å; torsion angle between core and perfluorophenyl plane = 10.2° (C) the shortest intermolecular sulfur - sulfur distance = 3.58 Å.

Table 2. Film microstructural parameters for TTA and DTT molecular systems.

Compound	Substrate temperature (°C)	2θ (°)	d-spacing (A) Film XRD	Molecular length (A)	
				DFT calc.	Single crystal data
DFP-TTA	25,50	4.3	20.7	19.8	19.7
DP-TTA	25,50	4.6	19.4	17.3	NA[a]
DBS-TTA	25, 50, 110	3.8	23.3	22.8	NA
DFP-DTT	25,50	4.7	18.8	17.5	17.4
DP-DTT	25,70	2.6	16.9	17.0	NA
DBS-DTT	25, 70, 90	4.2	21.0	20.5	NA

[a]Not available

lengths computed from the geometry optimization and the single-crystal structure analysis are summarized in **Table 2**. **Figure 6** shows a graphical comparison of the experimental and simulated data, with a 2θ scan of a **DFP-TTA** film grown at $T_D = 50$ °C on an OTS-coated substrate, and a powder pattern generated from the single-crystal data. The (h 0 0) reflection family is particularly pronounced, from (1 0 0) to (6 0 0). The (1 0 0) reflection in the film XRD is observed at $2\theta = 4.25°$, corresponding to a d spacing of 20.7 Å (Table 2), approximately the length of the unit cell a axis. This indicates that the films are highly textured and that **DPF-TTA** molecules in the films are predominantly aligned with their long molecular axes along the substrate normal; that is, film growth is favored in the a direction. It is also apparent that higher deposition temperatures (T_D) make this a-directional alignment even more favorable, as indicated by sharpening and increased intensity of the (h 0 0) reflections in the θ–2θ scans of the corresponding films of the same thickness (Figure S4, Supporting Information).

In general, both TTA and DTT molecular types appear to be aligned approximately vertically at the semiconductor-dielectric interface since none of the d spacings is smaller than molecular lengths (Table 2). The slight estimated size difference between TTA and DTT may reflect the intrinsic inaccuracies of the method. This edge-on type molecular arrangement is well known to promote optimum charge transport in organic TFT devices. Over the entire T_D range examined here, the TTA films deposited on OTS substrates exhibit reflections having the same 2θ values (Figure S4). As the deposition temperature (T_D) is increased, the peaks become sharper and their intensities increase. The consistency in reflection positions indicates the presence of a single polymorph and growth orientation across the T_D range. The increase in relative intensity of the higher order peaks on going from room temperature to higher growth temperatures indicates enhanced long range order. The effect of surface treatment is not as obvious as the effect of substrate temperature on the XRD data (Figure S5).

2.5. Organic Thin Film Transistor Fabrication and Characterization

Thin film transistors were fabricated in bottom gate-top contact configurations. Highly doped p-type (100) silicon wafers were used as gate electrodes as well as substrates, and 300 nm thermally grown SiO_2 on the Si was used as the gate insulator.

Organic semiconductor thin films (50 nm) were vapor-deposited onto the Si/SiO_2, HMDS-treated, and OTS-treated substrates as described previously. Then, 50 nm gold source and drain electrodes were vapor-deposited at 2×10^{-6} Torr through a shadow mask in a high vacuum deposition chamber. Devices were fabricated with typical channel lengths of 100 μm and a channel width of 2000 μm. Current–voltage (I–V) transfer and output plots were measured for each device under vacuum and in air. To illustrate the precision of each measurement, the reported data are an average of at least five devices tested on different regions of the semiconductor film. Key device performance parameters such as field-effect carrier mobility (μ), threshold voltage (V_T), and on-to-off current ratio (I_{on}/I_{off}), were extracted using standard procedures.[56] The results are summarized in **Table 3**.

DFP-TTA and **DFP-DTT** exhibit good n-type charge transport. **DFP-TTA** exhibits electron mobility $\mu_e = 0.30$ cm^2 V^{-1} s^{-1} and $I_{on}/I_{off} = 2.9 \times 10^7$ for films grown on an OTS-coated substrate at 25 °C (**Figure 7**A, B). **DFP-DTT** exhibits $\mu_e = 0.05$ cm^2 V^{-1} s^{-1} and $I_{on}/I_{off} = 10^7$ for films grown on an HMDS-coated substrate at 25 °C.[25] The relatively low electron injection barriers evident in the HOMO-LUMO energy diagram (Figure 4) doubtless contribute to this high n-type charge transport. As discussed in the single-crystal structural analysis, the differences in core sizes
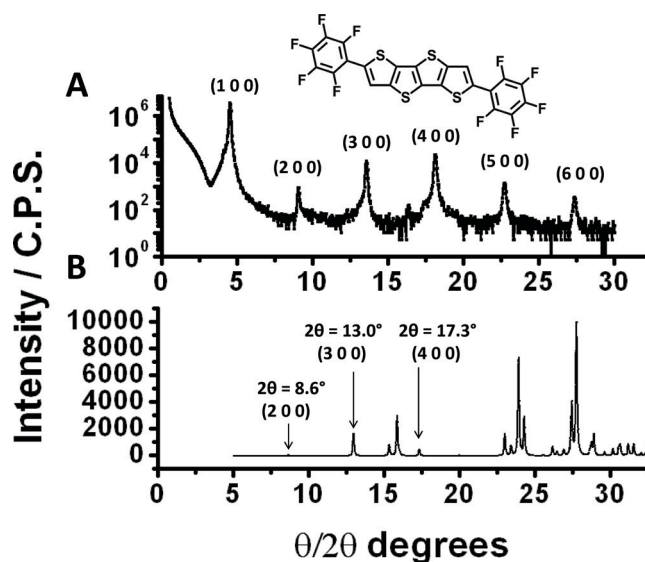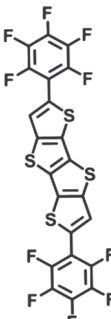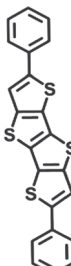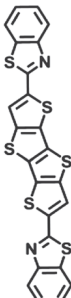
Figure 6. Comparison of the θ–2θ XRD scan of a **DFP-TTA** film grown at 50 °C on an OTS-coated substrate (A) with the simulated powder pattern (B).

Table 3. TFT device performance of TTA materials in this study.

Compound	Substrate Temperature T_D (°C)	Substrate Surface Treatment	Carrier Sign	Vacuum Mobility μ (cm^2 V^{-1} s^{-1})[a]		Vacuum Threshold Voltage V_T (V)	Vacuum I_{on}/I_{off}	Air Mobility μ (cm^2 V^{-1} s^{-1})		Air Threshold Voltage V_T (V)	Air I_{on}/I_{off}
DFP-TTA	25	Bare	N	$(6.7 \pm 1.0) \times 10^{-3}$	(7.7×10^{-3})[b]	72 ± 14	$(4.1 \pm 1.9) \times 10^{4}$	NA[c]			
		HMDS	N	0.04 ± 0.01	(0.05)	56 ± 7	$(3.2 \pm 0.2) \times 10^{6}$	NA			
		OTS	N	0.29 ± 0.01	(0.30)	56 ± 5	$(1.8 \pm 1.5) \times 10^{7}$	NA			
	50	Bare	N	$(7.6 \pm 0.0) \times 10^{-3}$	(7.6×10^{-3})	47 ± 0	$(5.3 \pm 0.0) \times 10^{7}$	NA			
		HMDS	N	0.05 ± 0.02	(0.08)	57 ± 5	$(2.8 \pm 1.1) \times 10^{7}$	NA			
		OTS	N	0.03 ± 0.00	(0.03)	44 ± 2	$(3.4 \pm 2.0) \times 10^{5}$	NA			
DP-TTA	25	Bare	P	0.04 ± 0.00	(0.04)	$-(19 \pm 0)$	$(1.5 \pm 0.0) \times 10^{6}$	0.04 ± 0.00	0.04	$-(17 \pm 1)$	$(4.7 \pm 2.7) \times 10^{5}$
		HMDS	P	0.07 ± 0.00	(0.07)	$-(17 \pm 0)$	$(3.3 \pm 0.0) \times 10^{6}$	0.08 ± 0.01	0.09	$-(18 \pm 2)$	$(1.3 \pm 0.2) \times 10^{6}$
		OTS	P	0.11 ± 0.01	(0.11)	$-(13 \pm 4)$	$(4.3 \pm 4.0) \times 10^{7}$	0.11 ± 0.02	0.13	$-(19 \pm 6)$	$(4.8 \pm 0.2) \times 10^{6}$
	50	Bare	P	0.05 ± 0.01	(0.06)	$-(19 \pm 4)$	$(1.9 \pm 1.2) \times 10^{5}$	0.04 ± 0.00	0.05	$-(16 \pm 2)$	$(1.3 \pm 0.5) \times 10^{5}$
		HMDS	P	0.10 ± 0.00	(0.10)	$-(10 \pm 1)$	$(4.0 \pm 3.6) \times 10^{6}$	0.10 ± 0.01	0.11	$-(14 \pm 1)$	$(2.4 \pm 1.3) \times 10^{6}$
		OTS	P	0.21 ± 0.00	(0.21)	$-(22 \pm 0)$	$(1.1 \pm 0.0) \times 10^{6}$	0.16 ± 0.05	0.19	$-(25 \pm 13)$	$(1.1 \pm 1.0) \times 10^{7}$
DBS-TTA	25	Bare	P	$(2.3 \pm 0.4) \times 10^{-5}$	(2.8×10^{-5})	$-(25 \pm 4)$	$(8.3 \pm 8.2) \times 10^{3}$	$(1.2 \pm 0.1) \times 10^{-5}$	(1.3×10^{-5})	$-(15 \pm 0)$	$(2.0 \pm 1.0) \times 10^{2}$
		HMDS	P	$(2.6 \pm 0.4) \times 10^{-4}$	(3.0×10^{-4})	$-(42 \pm 3)$	$(3.7 \pm 2.4) \times 10^{4}$	$(2.9 \pm 0.5) \times 10^{-4}$	(3.4×10^{-4})	$-(34 \pm 2)$	$(3.1 \pm 1.6) \times 10^{3}$
		OTS	P	$(4.1 \pm 0.9) \times 10^{-4}$	(5.0×10^{-4})	$-(45 \pm 4)$	$(5.7 \pm 1.9) \times 10^{3}$	$(4.2 \pm 0.6) \times 10^{-4}$	(4.8×10^{-4})	$-(41 \pm 5)$	$(5.7 \pm 2.5) \times 10^{3}$
	50	Bare	P	$(2.3 \pm 0.1) \times 10^{-5}$	(2.4×10^{-5})	$-(31 \pm 2)$	$(1.0 \pm 0.8) \times 10^{4}$	$(1.0 \pm 0.1) \times 10^{-5}$	(1.1×10^{-5})	$-(10 \pm 4)$	$(2.6 \pm 0.2) \times 10^{2}$
		HMDS	P	$(6.7 \pm 2.1) \times 10^{-4}$	(8.5×10^{-4})	$-(42 \pm 6)$	$(1.5 \pm 0.9) \times 10^{5}$	$(6.8 \pm 0.5) \times 10^{-4}$	(7.3×10^{-4})	$-(39 \pm 4)$	$(2.7 \pm 1.6) \times 10^{4}$
		OTS	P	$(8.6 \pm 0.3) \times 10^{-4}$	(8.8×10^{-4})	$-(44 \pm 11)$	$(4.2 \pm 3.0) \times 10^{4}$	$(7.3 \pm 0.8) \times 10^{-4}$	(8.2×10^{-4})	$-(40 \pm 8)$	$(2.4 \pm 0.2) \times 10^{4}$
	110	Bare	P	$(5.0 \pm 0.3) \times 10^{-4}$	(5.5×10^{-4})	$-(32 \pm 4)$	$(1.3 \pm 0.4) \times 10^{4}$	$(4.1 \pm 0.3) \times 10^{-4}$	(4.4×10^{-4})	$-(22 \pm 3)$	$(2.2 \pm 1.1) \times 10^{3}$
		HMDS	P	$(1.6 \pm 0.1) \times 10^{-3}$	(1.7×10^{-3})	$-(34 \pm 4)$	$(4.1 \pm 1.8) \times 10^{4}$	$(1.3 \pm 0.0) \times 10^{-3}$	(1.4×10^{-3})	$-(36 \pm 1)$	$(5.8 \pm 2.9) \times 10^{3}$
		OTS	P	$(1.8 \pm 0.5) \times 10^{-3}$	(1.9×10^{-3})	$-(12 \pm 5)$	$(5.9 \pm 2.6) \times 10^{4}$	$(2.1 \pm 0.2) \times 10^{-3}$	(2.3×10^{-3})	$-(29 \pm 3)$	$(1.5 \pm 0.1) \times 10^{4}$

[a]The average values obtained for at least 5 devices; [b]The maximum mobility recorded; [c]Not active.

of **DFP-DTT** (Figure 5B) versus **DFP-TTA** (Figure S3B) can be correlated with the lower mobility of **DFP-DTT**. DFT calculations predict the reorganization barrier for electron transport in the case of **DFP-DTT** to be 0.33 eV, slightly greater than the corresponding one for tetrathienoacene derivative **DFP-TTA**, 0.28 eV (Table S2). This factor, among others, likely contributes to the mobility differences in these two bis(perfluorophenyl) derivatives.

In marked contrast to the above **DFP-TTA** and **DFP-DTT** results, neither **DBS-TTA** nor **DBS-DTT** exhibit the anticipated

FULL PAPER
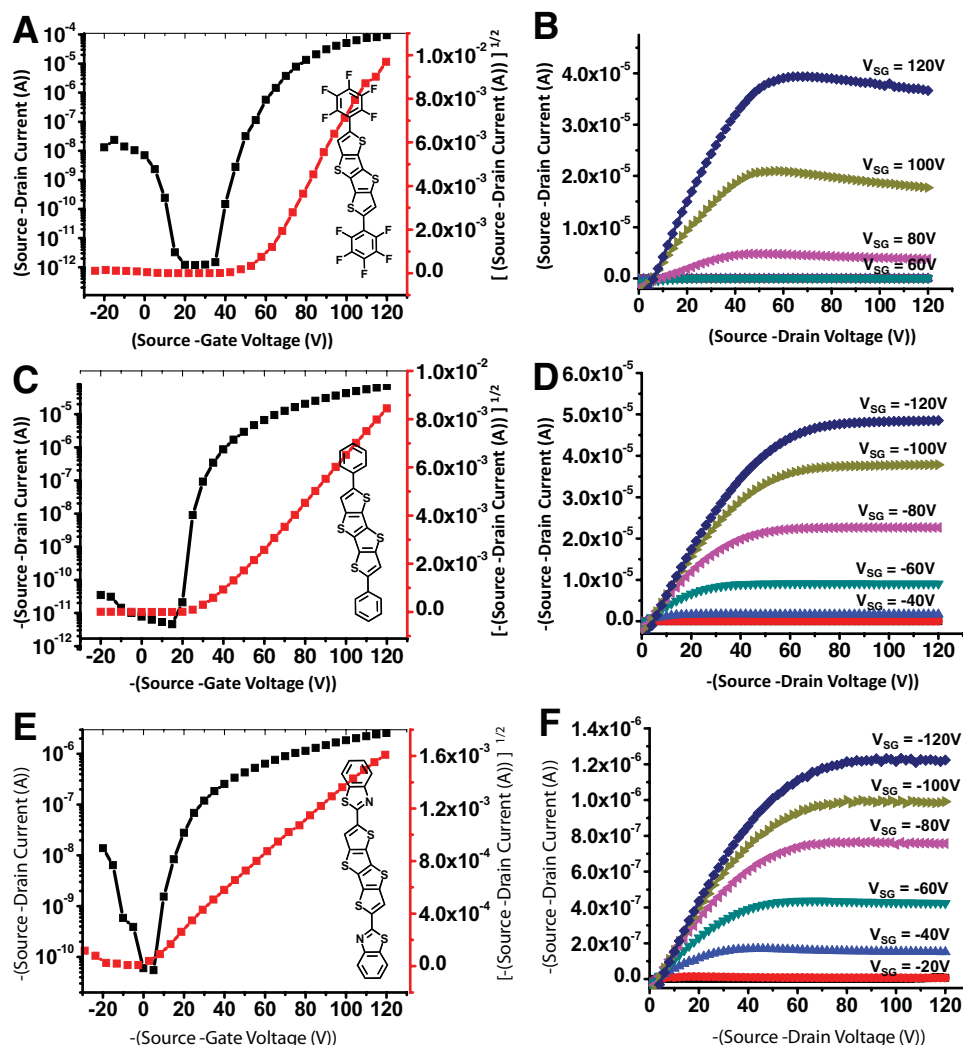
Figure 7. Transfer and output plots of OTFT devices fabricated from TTA films grown on an OTS-coated substrate: (A) transfer plot; (B) output plot. **DFP-TTA**, substrate temperature = 50 °C, $\mu = 0.30$ cm^2 V^{-1} s^{-1}, $V_T = 60$ V, $I_{on}/I_{off} = 2.9 \times 10^7$ in vacuum. (C) transfer plot; (D) output plot. **DP-TTA**, substrate temperature = 50 °C, $\mu = 0.21$ cm^2 V^{-1} s^{-1}, $V_T = -22$V, $I_{on}/I_{off} = 1.1 \times 10^6$ in vacuum (E) transfer plot; (F) output plot. **DBS-TTA**, substrate temperature = 110 °C. $\mu = 1.9 \times 10^{-3}$ cm^2 V^{-1} s^{-1}, $V_T = -5$ V, $I_{on}/I_{off} = 4.7 \times 10^4$ in vacuum. Channel width = 2000 μm, channel length = 100 μm.

n-type charge transport, despite having the lowest-lying LUMOs in this series. Instead, they exhibit p-type charge transport. Thus, **DBS-TTA** achieves $\mu = 0.0019$ cm^2 V^{-1} s^{-1} and $I_{on}/I_{off} = 4.7 \times 10^4$ on OTS-coated substrates for $T_D = 110$ °C (Figure 7E, F), and **DBS-DTT** exhibits $\mu = 0.01$ cm^2 V^{-1} s^{-1} and $I_{on}/I_{off} = 10^5$ for films grown on HMDS-coated substrates at 90 °C.[30] To understand the reversed polarity of the charge transport in these perfluorophenyl and benzothianolyl derivatives, we optimized the molecular geometries of the corresponding radical anions using DFT computation, and their charge distributions are shown in Figure S6. Upon injection of an electron into **DBS-TTA**, 63% of the charge is localized in the external electron-withdrawing groups while only 37% of the remaining charge is delocalized over the conjugated tetrathienoacene skeleton. In contrast, the negative charge on **DFP-TTA** is more uniformly distributed, with the external electron-withdrawing substituents bearing ca. 44% of the charge and the central conjugated fused

unit the remaining 56%. The more evenly delocalized charge in the perfluorophenyl derivative likely stabilizes the injected charge to a greater extend, thus facilitating electron transport even though the **DBS-TTA** LUMO energy is lower in energy. These contrasting results can be ascribed to the different nature (σ-inductive vs. π-mesomeric) of the two electron-withdrawing substituents, as discussed above. The situation for the **DBS-TTA** radical cation is very different, and we find that the positive charge is evenly distributed, with ca. 47% located in the external substituent groups and the remaining 53% on the conjugated tetrathienoacene core (Figure S6), probably favoring hole transport within the thin film. The theoretical calculations also show that **DBS-TTA** has the smallest reorganization energy within the series (Table S2), with the reorganization energy for hole transport less than that for electron transport (0.214 eV vs. 0.282 eV, respectively). Note that the present results for **DBS-TTA** and **DBS-DTT** are in accord with other observations

Materials Views
www.MaterialsViews.com

ADVANCED
FUNCTIONAL
MATERIALS
www.afm-journal.de

FULL PAPER

that appending electron-withdrawing thiazole units to oligothiophene skeletons seldom enhances electron mobility.[57] In fact, as shown here for **DBS-TTA** vs. **DP-TTA**, lower hole mobilities are usually obtained versus the corresponding oligothiophenes.

As expected from the HOMO-LUMO energy diagram (Figure 4), **DP-TTA** and **DP-DTT** exhibit good p-type charge transport. Since the work function of the gold electrode is about −5.0 eV, these materials have the lowest hole injection barrier in the series: **DFP-TTA** (0.66 eV) < **DBS-TTA** (0.55 eV) < **DP-TTA** (0.35 eV) and **DFP-DTT** (0.84 eV) < **DBS-DTT** (0.61 eV) < **DP-DTT** (0.47 eV). As a result, **DP-TTA** exhibits $\mu = 0.21$ cm^2 V^{-1} s^{-1} and $I_{on}/I_{off} = 1.1 \times 10^6$ on OTS-coated substrates at 50 °C (Figure 7C, D). Note that **DP-DTT** grown at 70 °C exhibits $\mu = 0.42$ cm^2 V^{-1} s^{-1} and $I_{on}/I_{off} = 5 \times 10^6$ on OTS-coated substrates.[22]

The effect of substrate temperature and surface treatment are also well reflected in the device performance. As the film crystallinity is enhanced by increasing the substrate temperature, the device performance is substantially enhanced. For **DP-TTA** devices, the parameters $\mu = 0.11$ cm^{2}V^{-1} s^{-1} and $I_{on}/I_{off} = 2.8 \times 10^7$ for room temperature growth change to $\mu = 0.21$ cm^2 V^{-1} s^{-1} and $I_{on}/I_{off} = 1.1 \times 10^6$ for films grown at 50 °C on OTS-coated substrates. For **DBS-TTA** devices, $\mu = 5.0 \times 10^{-4}$ cm^2 V^{-1} s^{-1} and $I_{on}/I_{off} = 3.8 \times 10^4$ for room temperature growth changes to $\mu = 1.9 \times 10^{-3}$ cm^2 V^{-1} s^{-1} and $I_{on}/I_{off} = 4.7 \times 10^4$ for 110 °C growth on OTS-coated substrates.

Organic self-assembled monolayer (SAM) treatment of gate dielectric surfaces is known to enhance TFT performance by minimizing surface charge traps and by increasing the microstructural order of semiconductor growth.[58] Thus, growth on HMDS and OTS SAM-treated Si/SiO$_2$ substrates yields significantly enhanced device performance than on bare Si/SiO$_2$ substrates. OTS surface treatment particularly enhances OTFT performance versus the other treatments for the TTA semiconductors. For example, **DFP-TTA** devices exhibit $\mu = 0.30$ cm^2 V^{-1} s^{-1} and $I_{on}/I_{off} = 2.9 \times 10^7$ on OTS for 25 °C growth, but $\mu = 0.05$ cm^2 V^{-1} s^{-1} and $I_{on}/I_{off} = 3.1 \times 10^6$ on HMDS, compared to $\mu = 0.0077$ cm^2 V^{-1} s^{-1} and $I_{on}/I_{off} = 2.7 \times 10^4$ on bare SiO$_2$. **DP-TTA** and **DBS-TTA** OTFTs follow the same pattern. One possible explanation for the superior device performance on OTS SAMs versus HMDS SAMs is the high structural quality of the OTS SAMs. If long alkyl chains in OTS molecules are tightly packed and vertically aligned, the SAM has order approaching in-plane crystallinity which enhances the interconnectivity of initial semiconductor film growth as well as the film crystallinity.[59–61] To understand the origin of these device performance variations induced by substrate temperature during semiconductor growth and dielectric surface treatment, the surface morphology of semiconductor films was next examined by tapping mode AFM.

2.6. Semiconductor Film Morphology and TFT Performance

The surface morphology of organic semiconductor thin films is often used to evaluate crystalline microstructure based on grain sizes. The highest carrier mobilities are generally obtained for films having the appropriate balance of large grain size and space-filling grain connectivity. AFM images of the TTA films clearly reflect the influence of surface morphology

on device performance. The most distinctive effect on surface morphology is substrate temperature (T_D; Figures S7, S8, S9). As the substrate temperature is increased, semiconductor molecules diffuse more rapidly, and are captured in islands facilitating grain growth. Therefore, films deposited at higher temperatures exhibit larger grain sizes. For example, 50 nm thick **DFP-TTA** films have small ball-shaped grains with diameters of 100 nm − 200 nm for room temperature growth and become web-like 2–3 µm long wire meshes in films grown at 50 °C (Figure S7). **DP-TTA** films exhibit the largest grain sizes in the series. While small gains with 100–200 nm diameters grow at room temperature, the grains grow in pentacene-like ordered crystalline structures[62–64] with 2–3 µm diameters as the substrate temperature is increased to 50 °C (Figure S8). **DBS-TTA** exhibits relatively small grains compared to **DFP-TTA** and **DP-TTA**, reflecting the highest molecular weight and melting temperature in the series. These grains evolve from small facets with 20–40 nm diameters to 200–300 nm wide balls at 110 °C growth temperature (Figure S9). XRD data shown in Figure S4 verify that the crystallinity increases along with these film morphology changes. TFT parameters summarized in Table 3 indicate corresponding device performance enhancement as well.

While bulk film morphology evolution satisfactorily explains the effects of substrate temperature on semiconductor film crystallinity, it does not correlate well with dielectric surface treatment. Thus, 50 nm thick TTA film morphologies do not vary greatly for the three different types of substrates. Even the XRD data do not exhibit significant differences related to surface treatment (Figure S5). If the bulk film morphologies are similar, the key factors defining device performance on these three substrates may involve variations in the interface microstructure. To investigate possible differences in molecular level interface microstructure, the surface morphologies of the TTA semiconductor films having submonolayer thicknesses were next investigated on these three substrates.

AFM images of sub-monolayer TTA films grown on the different substrates clearly explain the origin of the device performance differences as a function of dielectric surface treatment (**Figure 8**). In general, TTA semiconductors grow in large, widely spaced domains on bare Si/SiO$_2$ along with large empty boundary regions. On the other hand, these materials form small grains with greater nucleation densities on HMDS and OTS SAMs, resulting in tightly integrated film structures. The most densely populated small grains grow on OTS-coated Si/SiO$_2$ and the SAM plays an important role in modulating charge transport. **DFP-TTA** forms the most densely populated film structure on the OTS SAM (Figure 8A). This tightly integrated initial semiconductor film growth structure achieves the highest n-type device performance on OTS SAM-deposited gates. Note that **DP-TTA** films exhibit smaller, but densely populated grains on OTS SAMs compared with the HMDS SAMs and the bare SiO$_2$ surface (Figure 8B). **DBS-TTA** also exhibits the same trend with widely dispersed grain patches on bare SiO$_2$ (Figure 8C). In contrast, **DBS-TTA** forms webs of microwire structures on HMDS and OTS SAMs. However, the wire diameters are much smaller on OTS SAMs than on HMDS SAMs. These tightly integrated initial semiconductor layers

**ADVANCED
FUNCTIONAL
MATERIALS**

www.afm-journal.de

FULL PAPER

*Materials
Views*

www.MaterialsViews.com
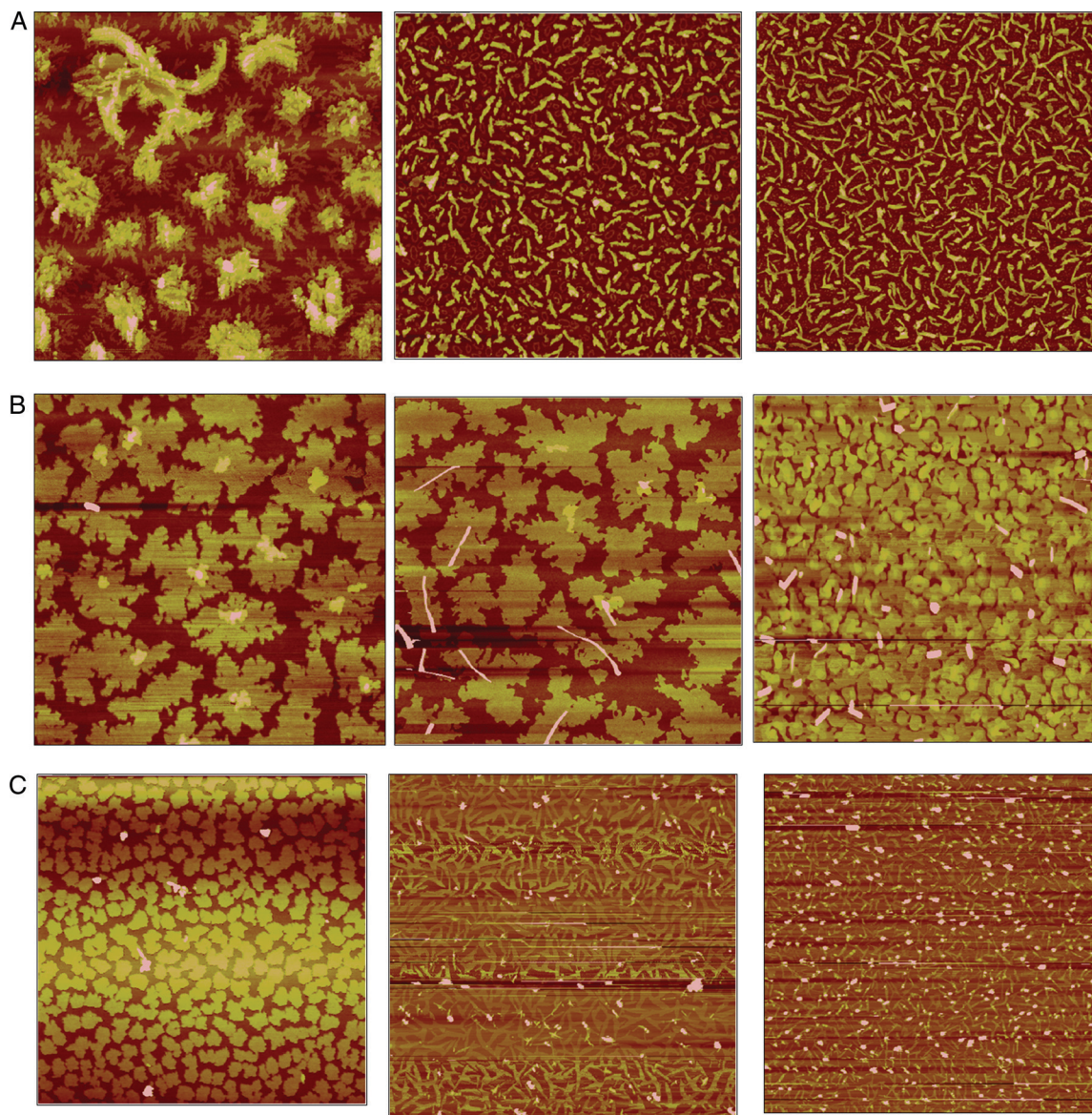
Figure 8. Sub-monolayer (1.5 nm) film morphologies of TTA films on the three different Si/SiO$_2$ substrates indicated. A. **DFP-TTA** grown at 25 °C, B. **DP-TTA** grown at 50 °C, C. **DBS-TTA** grown at 110 °C (tapping mode, topography, 10 μm × 10 μm).

composed of small but highly crystalline grains must have enhanced charge transport on OTS SAMs to achieve the best device performance among the substrates examined here. In short, interface semiconductor film microstructures, very different from bulk film morphologies, indicate that the superior device performance for growth on OTS SAMs originates from well-connected as well as highly crystalline initial semiconductor film growth in the dielectric-semiconductor interfacial region.

3. Conclusions

In this contribution, we established that tetrathiophenes with proper electron-withdrawing functional groups offer

considerable potential as versatile n-type organic semiconductors. The TTA building block can now be obtained via an efficient one-pot synthetic route and the first TTA-based n-channel molecule is one result of this study. Enlarged TTA cores are effective in reducing the bandgap and introducing n-type properties. Solid-state packing motifs revealed in single crystal analysis, substrate temperature dependence of film growth, and semiconductor–gate dielectric interface morphology are all shown to be critically important factors in optimizing TFT performance. We believe the newly designed one-pot synthetic routes offer a scalable way to produce practical building blocks for n-type organic semiconductors, and are now currently pursuing these molecular design strategies further by incorporating other building blocks into perfluorophenyl-functionalized molecular structures.

Supporting Information

Acknowledgements

[1] X. W. Zhan, A. Facchetti, S. Barlow, T. J. Marks, M. A. Ratner, M. R. Wasielewski, S. R. Marder, *Adv. Mater.* **2011**, *23*, 268.

[2] T. J. Marks, *MRS Bull.* **2010**, *35*, 1018.

[3] H. Yan, Z. H. Chen, Y. Zheng, C. Newman, J. R. Quinn, F. Dotz, M. Kastler, A. Facchetti, *Nature* **2009**, *457*, 679.

[4] M. L. Tang, S. C. B. Mannsfeld, Y. S. Sun, H. A. Becerril, Z. N. Bao, *J. Am. Chem. Soc.* **2009**, *131*, 882.

[5] N. Kobayashi, M. Sasaki, K. Nomoto, *Chem. Mater.* **2009**, *21*, 552.

[6] Y. Didane, G. H. Mehl, A. Kumagai, N. Yoshimoto, C. Videlot-Ackermann, H. Brisset, *J. Am. Chem. Soc.* **2008**, *130*, 17681.

[7] S. Subramanian, S. K. Park, S. R. Parkin, V. Podzorov, T. N. Jackson, J. E. Anthony, *J. Am. Chem. Soc.* **2008**, *130*, 2706.

[8] M. L. Tang, A. D. Reichardt, N. Miyaki, R. M. Stoltenberg, Z. Bao, *J. Am. Chem. Soc.* **2008**, *130*, 6064.

[9] C. Kim, A. Facchetti, T. J. Marks, *Science* **2007**, *318*, 76.

[10] A. R. Murphy, J. M. J. Frechet, *Chem. Rev.* **2007**, *107*, 1066.

[11] B. A. Jones, A. Facchetti, M. R. Wasielewski, T. J. Marks, *J. Am. Chem. Soc.* **2007**, *129*, 15259.

[12] J. E. Anthony, *Chem. Rev.* **2006**, *106*, 5028.

[13] D. H. Kim, D. Y. Lee, H. S. Lee, W. H. Lee, Y. H. Kim, J. I. Han, K. Cho, *Adv. Mater.* **2007**, *19*, 678.

[14] Y. N. Li, Y. L. Wu, P. Liu, Z. Prostran, S. Gardner, B. S. Ong, *Chem. Mater.* **2007**, *19*, 418.

[15] T. W. Kelley, P. F. Baude, C. Gerlach, D. E. Ender, D. Muyres, M. A. Haase, D. E. Vogel, S. D. Theiss, *Chem. Mater.* **2004**, *16*, 4413.

[16] M. C. Chen, C. Kim, S. Y. Chen, Y. J. Chiang, M. C. Chung, A. Facchetti, T. J. Marks, *J. Mater. Chem.* **2008**, *18*, 1029.

[17] M. M. Payne, S. R. Parkin, J. E. Anthony, C. C. Kuo, T. N. Jackson, *J. Am. Chem. Soc.* **2005**, *127*, 4986.

[18] J. G. Laquindanum, H. E. Katz, A. J. Lovinger, *J. Am. Chem. Soc.* **1998**, *120*, 664.

[19] Y. Liu, Y. Wang, W. P. Wu, Y. Q. Liu, H. X. Xi, L. M. Wang, W. F. Qiu, K. Lu, C. Y. Du, G. Yu, *Adv. Funct. Mater.* **2009**, *19*, 772.

[20] H. H. Fong, V. A. Pozdin, A. Amassian, G. G. Malliaras, D. M. Smilgies, M. Q. He, S. Gasper, F. Zhang, M. Sorensen, *J. Am. Chem. Soc.* **2008**, *130*, 13202.

[21] K. Xiao, Y. Q. Liu, T. Qi, W. Zhang, F. Wang, J. H. Gao, W. F. Qiu, Y. Q. Ma, G. L. Cui, S. Y. Chen, X. W. Zhan, G. Yu, J. G. Qin, W. P. Hu, D. B. Zhu, *J. Am. Chem. Soc.* **2005**, *127*, 13281.

[22] Y. M. Sun, Y. W. Ma, Y. Q. Liu, Y. Y. Lin, Z. Y. Wang, Y. Wang, C. G. Di, K. Xiao, X. M. Chen, W. F. Qiu, B. Zhang, G. Yu, W. P. Hu, D. B. Zhu, *Adv. Funct. Mater.* **2006**, *16*, 426.

[23] L. Tan, L. Zhang, X. Jiang, X. D. Yang, L. J. Wang, Z. Wang, L. Q. Li, W. P. Hu, Z. G. Shuai, L. Li, D. B. Zhu, *Adv. Funct. Mater.* **2009**, *19*, 272.

[24] Y. Liu, C. A. Di, C. Y. Du, Y. Q. Liu, K. Lu, W. F. Qiu, G. Yu, *Chem.-Eur. J.* **2010**, *16*, 2231.

[25] J. Youn, M. C. Chen, Y. J. Liang, H. Huang, R. P. Ortiz, C. Kim, C. Stern, T. S. Hu, L. H. Chen, J. Y. Yan, A. Facchetti, T. J. Marks, *Chem. Mater.* **2010**, *22*, 5031.

[26] H. Ebata, T. Izawa, E. Miyazaki, K. Takimiya, M. Ikeda, H. Kuwabara, T. Yui, *J. Am. Chem. Soc.* **2007**, *129*, 15732.

[27] P. Gao, D. Beckmann, H. N. Tsao, X. L. Feng, V. Enkelmann, M. Baumgarten, W. Pisula, K. Mullen, *Adv. Mater.* **2009**, *21*, 213.

[28] J. H. Gao, R. J. Li, L. Q. Li, Q. Meng, H. Jiang, H. X. Li, W. P. Hu, *Adv. Mater.* **2007**, *19*, 3008.

[29] Y. Suzuki, E. Miyazaki, K. Takimiya, *J. Am. Chem. Soc.* **2010**, *132*, 10453.

[30] C. Kim, M. C. Chen, Y. J. Chiang, Y. J. Guo, J. Youn, H. Huang, Y. J. Liang, Y. J. Lin, Y. W. Huang, T. S. Hu, G. H. Lee, A. Facchetti, T. J. Marks, *Org. Electron.* **2010**, *11*, 801.

[31] M. C. Chen, Y. J. Chiang, C. Kim, Y. J. Guo, S. Y. Chen, Y. J. Liang, Y. W. Huang, T. S. Hu, G. H. Lee, A. Facchetti, T. J. Marks, *Chem. Commun.* **2009**, 1846.

[32] M. H. Yoon, A. Facchetti, C. E. Stern, T. J. Marks, *J. Am. Chem. Soc.* **2006**, *128*, 5792.

[33] J. A. Letizia, A. Facchetti, C. L. Stern, M. A. Ratner, T. J. Marks, *J. Am. Chem. Soc.* **2005**, *127*, 13476.

[34] Q. Wu, R. Li, W. Hong, H. Li, X. Gao, D. Zhu, *Chem. Mater.* **2011**, *23*, 3138.

[35] X. N. Zhang, A. P. Cote, A. J. Matzger, *J. Am. Chem. Soc.* **2005**, *127*, 10502.

[36] F. Allared, J. Hellberg, T. Remonen, *Tetrahedron Lett.* **2002**, *43*, 1553.

[37] Y. Mazaki, K. Kobayashi, *Tetrahedron Lett.* **1989**, *30*, 3315.

[38] J. T. Henssler, A. J. Matzger, *Org. Lett.* **2009**, *11*, 3144.

[39] For comparison, a recent new TTA synthetic route [19] reports that no product is obtained if the synthesis is attempted in a reverse order.

[40] J. Frey, A. D. Bond, A. B. Holmes, *Chem. Commun.* **2002**, 2424.

[41] M. Q. He, F. X. Zhang, *J. Org. Chem.* **2007**, *72*, 442.

[42] Y. C. Chang, Y. D. Chen, C. H. Chen, Y. S. Wen, J. T. Lin, H. Y. Chen, M. Y. Kuo, I. Chao, *J. Org. Chem.* **2008**, *73*, 4608.

[43] S. Barlow, S. A. Odom, K. Lancaster, Y. A. Getmanenko, R. Mason, V. Coropceanu, J. L. Bredas, S. R. Marder, *J. Phys. Chem. B* **2010**, *114*, 14397.

[44] M. H. Yoon, S. A. DiBenedetto, M. T. Russell, A. Facchetti, T. J. Marks, *Chem. Mater.* **2007**, *19*, 4864.

[45] Y. Ie, M. Nitani, M. Ishikawa, K. Nakayama, H. Tada, T. Kaneda, Y. Aso, *Org. Lett.* **2007**, *9*, 2115.

[46] M. H. Yoon, S. A. DiBenedetto, A. Facchetti, T. J. Marks, *J. Am. Chem. Soc.* **2005**, *127*, 1348.

[47] P. Magnus, K. S. Matthews, *J. Am. Chem. Soc.* **2005**, *127*, 12476.

[48] A. Kunai, J. Ohshita, T. Iida, K. Kanehara, A. Adachi, K. Okita, *Synth. Met.* **2003**, *137*, 1007.

[49] J. Ohshita, H. Kai, A. Takata, T. Iida, A. Kunai, N. Ohta, K. Komaguchi, M. Shiotani, A. Adachi, K. Sakamaki, K. Okita, *Organometallics* **2001**, *20*, 4800.

[50] G. Daminelli, J. Widany, A. Di Carlo, P. Lugli, *J. Chem. Phys.* **2001**, *115*, 4919.

[51] Measured with a Pt working electrode in an o-dichlorobenzene solution using 0.1 mol dm^{-3} Bu$_4$NPF$_6$ as the supporting electrolyte.

[52] N. Jun-ichi Nishida, D. Kumaki, S. Tokito, Y. Yamashita, *J. Am. Chem. Soc.* **2006**, *128*, 9598.

[53] Y. Sakamoto, T. Suzuki, M. Kobayashi, Y. Gao, Y. Fukai, Y. Inoue, F. Sato, S. Tokito, *J. Am. Chem. Soc.* **2004**, *126*, 8138.

[54] J. Casado, V. Hernandez, M. C. R. Delgado, R. P. Ortiz, J. T. L. Navarrete, A. Facchetti, T. J. Marks, *J. Am. Chem. Soc.* **2005**, *127*, 13364.

[55] M. D. Curtis, J. Cao, J. W. Kampf, *J. Am. Chem. Soc.* **2004**, *126*, 4318.

[56] S. M. Sze, Ed. *Semiconductor Devices: Physics and Technology*, Wiley, New York **1985**.

[57] R. Ponce Ortiz, A. Facchetti, T. J. Marks, *Materials.* **2010**, *3*, 1533.

[58] Y. D. Park, J. A. Lim, H. S. Lee, K. Cho, *Mater. Today* **2007**, *10*, 46.

[59] Y. Ito, A. A. Virkar, S. Mannsfeld, J. H. Oh, M. Toney, J. Locklin, Z. A. Bao, *J. Am. Chem. Soc.* **2009**, *131*, 9396.

[60] A. Virkar, S. Mannsfeld, J. H. Oh, M. F. Toney, Y. H. Tan, G. Y. Liu, J. C. Scott, R. Miller, Z. Bao, *Adv. Funct. Mater.* **2009**, *19*, 1962.

[61] H. S. Lee, D. H. Kim, J. H. Cho, M. Hwang, Y. Jang, K. Cho, *J. Am. Chem. Soc.* **2008**, *130*, 10556.

[62] A. A. Virkar, S. Mannsfeld, Z. A. Bao, N. Stingelin, *Adv. Mater.* **2010**, *22*, 3857.

[63] P. Coppo, S. G. Yeates, *Adv. Mater.* **2005**, *17*, 3001.

[64] H. Klauk, M. Halik, U. Zschieschang, F. Eder, G. Schmid, C. Dehm, *Appl. Phys. Lett.* **2003**, *82*, 4175.

Materials
Views

www.MaterialsViews.com

ADVANCED
FUNCTIONAL
MATERIALS

www.afm-journal.de

FULL PAPER

Mesomorphic Organization and Thermochromic Luminescence of Dicyanodistyrylbenzene-Based Phasmidic Molecular Disks: Uniaxially Aligned Hexagonal Columnar Liquid Crystals at Room Temperature with Enhanced Fluorescence Emission and Semiconductivity

Seong-Jun Yoon, Jong H. Kim, Kil Suk Kim, Jong Won Chung, Benoît Heinrich, Fabrice Mathevet, Pyosang Kim, Bertrand Donnio, André-Jean Attias, Dongho Kim,* and Soo Young Park*

A new dicyanodistyrylbenzene-based phasmidic molecule, (2Z,2′Z)-2,2′-(1,4-phenylene)bis(3-(3,4,5-tris(dodecyloxy)phenyl)acrylonitrile), GDCS, is reported, which forms a hexagonal columnar liquid crystal (LC) phase at room temperature (RT). GDCS molecules self-assemble into supramolecular disks consisting of a pair of molecules in a side-by-side disposition assisted by secondary bonding interactions of the lateral polar cyano group, which, in turn, constitute the hexagonal columnar LC structure. GDCS shows very intense green/yellow fluorescence in liquid/solid crystalline states, respectively, in contrast to the total absence of fluorescence emission in the isotropic melt state according to the characteristic aggregation-induced enhanced emission (AIEE) behavior. The AIEE and two-color luminescence thermochromism of GDCS are attributed to the peculiar intra- and intermolecular interactions of dipolar cyanostilbene units. It was found that the intramolecular planarization and restricted molecular motion associated with a specific stacking situation in the liquid/solid crystalline phases are responsible for the AIEE phenomenon. The origin of the two-color luminescence was elucidated to be due to the interdisk stacking alteration in a given column driven by the specific local dipole coupling between molecular disks. These stacking changes, in turn, resulted in the different degree of excited-state dimeric coupling to give different emission colors. To understand the complicated photophysical properties of GDCS, temperature-dependent steady-state and time-resolved PL measurements have been comprehensively carried out. Uniaxially aligned and highly fluorescent LC and crystalline microwires of GDCS are fabricated by using the micromolding in capillaries (MIMIC) method. Significantly enhanced electrical conductivity (0.8×10^{-5} S·cm^{-1}/3.9×10^{-5} S·cm^{-1}) of the aligned LC/crystal microwires were obtained over that of multi-domain LC sample, because of the almost perfect shear alignment of the LC material achieved in the MIMIC mold.

1. Introduction

In the past years, molecular design of conjugated organic materials has normally been limited to the rather simple molecular orbital engineering of their primary chemical structure.[1] Recently, however, engineering of molecular stacking arrangement in addition to molecular orbital control is getting more important related to the practical solid-state applications in optoelectronic devices.[2,3] Therefore, intermolecular secondary bonding interactions,[4] such as π–π stacking, hydrogen bonding, dipole interactions, and van der Waals forces, which directly control the molecular stacking to generate various supramolecular, mesomorphic, and crystalline organizations, are drawing ever-increasing attention. Thus, fine-tuning of the intermolecular interaction by rational molecular design is an essential and promising approach to control the optoelectronic characteristics of functional molecular solids. In fact, we could develop molecular stacking engineering for the fluorescence modulation of π-conjugated molecular crystals by introducing a pair of dipolar cyano groups into the conjugated distyrylbenzene molecular structures (see **Figure 1**a for the molecular structure of DCS).[5,6]

S.-J. Yoon, Dr. J. H. Kim, Dr. J. W. Chung, Prof. S. Y. Park
Center for Supramolecular Optoelectronic Materials and
WCU Hybrid Materials Program
Department of Materials Science and Engineering
Seoul National University, ENG 445, Seoul 151-744, Korea
E-mail: parksy@snu.ac.kr
Dr. B. Heinrich, Dr. B. Donnio
Institut de Physique et Chimie des Matériaux de Strasbourg (IPCMS)
UMR 7504, CNRS-Université de Strasbourg
67034 Strasbourg Cedex 2, France

Dr. K. S. Kim, P. Kim, Prof. D. Kim
Spectroscopy Laboratory for Functional π-Electronic
Systems and Department of Chemistry
Yonsei University
Seoul 120-749, Korea
E-mail: dongho@yonsei.ac.kr
F. Mathevet, A. J. Attias
Laboratoire de Chimie des Polymères-UMR 7610 Université Pierre et
Marie Curie, 75252 Paris Cedex 5, France

FULL PAPER
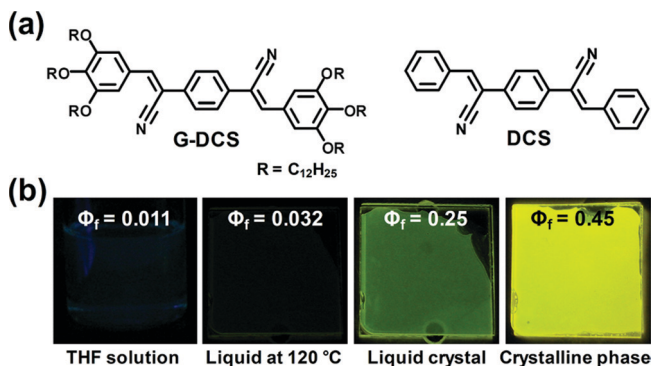
Figure 1. a) Molecular structures of GDCS and DCS. b) Fluorescence images of GDCS in THF solution, liquid state at 120 °C, LC state at 30 °C, and crystalline state under 365 nm UV light, respectively.

Highly fluorescent molecular crystals of DCS derivatives uniquely showed piezochromic, thermochromic, and solvent-induced luminescence switching, attributed to the different modes of local dipole coupling (antiparallel or head-to-tail coupling of CN dipoles) augmented by various reconfigurable secondary bonding interactions including C–H···N and C–H···O hydrogen bonds. In this work, we further aimed at extending the molecular stacking engineering of DCS derivatives to the liquid-crystalline state, which would pave the way to the innovative applications in molecular electronics, particularly by using the fluidic nature of the liquid-crystalline state to fabricate a highly ordered and patterned molecular assembly. In particular, highly fluorescent[7,8] and semiconducting[9,10] liquid crystals (LCs) incorporating very unique and specific intermolecular interaction of DCS units was targeted in this work. To this end, we have considered introducing a phasmidic mesogenic structure (e.g., polycatenar)[11] into the DCS core to enable mesomorphic organization into the highly functional self-assembled architecture.

Briefly, we have synthesized a new DCS-based liquid-crystalline material, (2Z,2′Z)-2,2′-(1,4-phenylene)bis(3-(3,4,5-tris(dodecyloxy)phenyl)acrylonitrile), GDCS, which forms a hexagonal columnar LC phase at room temperature (RT). Most uniquely, GDCS exhibited very high fluorescence quantum yields in the crystalline (Φ_F = 0.45) and LC (Φ_F = 0.25) states, due to the characteristic aggregation-induced enhanced emission (AIEE) process, as well as thermochromic two-color luminescence switching. In this work, we have comprehensively explored the structural, optical, and photophysical properties of this highly fluorescent phasmidic LC molecule to gain a deep insight into the structure–property relationship, as an extended effort towards molecular stacking engineering. In addition, we could fabricate uniaxially aligned LC microwires of GDCS, which showed an enhanced electrical conductivity by using the micromolding in capillaries (MIMIC) method.

2. Results and Discussion

We have designed the chemical structure of GDCS, which adopts the hexacatenar platform with dicyanodistyrylbenzene
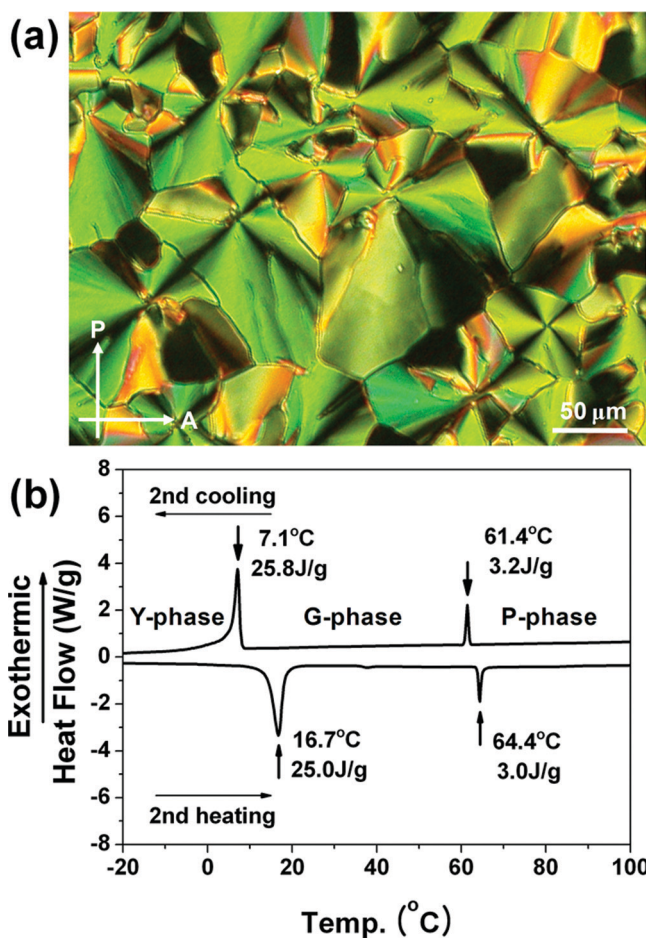
Figure 2. a) Pseudo focal-conic fan-shaped texture of GDCS observed by POM in the Col$_h$ phase at 40 °C on the cooling process. b) DSC trace of GDCS on heating/cooling rate of 10 °C per minute.

core (Figure 1a). The terminal trisdodecyloxy fragments are directly attached to the dicyanodistyrylbenzene core to facilitate a mesomorphic organization. GDCS was synthesized by Knoevenagel reaction of 3,4,5-tris(dodecyloxy)benzaldehyde and (4-cyanomethyl-phenyl)-acetonitrile in a good yield. Full synthetic details, ^{1}H NMR and mass spectroscopy, and the elemental analysis are described in the Experimental Section.

The mesomorphic properties of GDCS were investigated using polarized optical microscopy (POM) and differential scanning calorimetry (DSC). Typical pseudo focal-conic fan-shaped texture of a hexagonal columnar (Col$_h$) phase was enantiotropically observed by POM, in both heating and cooling cycles (**Figure 2**a). The phase-transition temperature and related enthalpy values are depicted in the DSC trace (Figure 2b). GDCS melts to the Col$_h$ phase at about 17 °C and isotropizes at about 64 °C at a heating rate of 10 °C per minute. On cooling, the LC phase is maintained below RT until partial crystallization occurs. This phase transition from the hexagonal columnar LC to the crystalline phase at near RT appears kinetically limited by the balance of noncovalent secondary bonding interactions mediated by the compact phasmidic molecular structure. Actually, the transformation of GDCS LC into the crystalline phase over several hours at RT was observed, which

accompanied a characteristic fluorescence color change from green (λ_{max} = 538 nm) to yellow (λ_{max} = 558 nm) (Figure 1b). This temporal mesomorphic property at RT is very unique and certainly plays a beneficial role in the fabrication and application of GDCS.

To gain further insight into the actual structure of mesomorphic organization of GDCS molecules bringing about two-color luminescence switching, we have carefully analyzed the molecular stacking structures using X-ray diffraction (XRD) measurements. The XRD pattern of GDCS in the LC state shows a distinct diffraction peak corresponding to the (100) reflection of the Col_h structure with typical two-dimensional (2D) XRD pattern of a Col_h phase (**Figure 3**a), as was similarly observed in the related functional phasmidic compounds.[12] In addition, the (100) reflection peak was shifted to the small-angle region and the intensity increased with decreasing temperature (see the Supporting Information (SI) for the XRD patterns depending on the temperature at the cooling process). The XRD data and the structural information of GDCS in the LC phase are summarized in **Table 1**. In order to propose a possible model for

Table 1. Structural data of GDCS from XRD experiments.

State	T [°C]	d_{obs} [Å]	d_{calc} [Å]	hkl	Lattice const. [Å]	
Liquid crystal	60	30.4	30.4	100	a = 35.1	
	50	30.7	30.7	100	a = 35.5	Col_h
	40	31.4	31.4	100	a = 36.2	
	30	32.0	32.0	100	a = 37.0	

the molecular organization within the columns of GDCS, the molecular length of GDCS was calculated using the Gaussian 09 software[13] (**Figure 4**a). According to the molecular length and the cross-sectional area of a column (s = 1186 Å²) in LC state at 30 °C, we could deduce that a pair of GDCS molecules were coupled to form a slice of a column ("molecular disk"), driven by the specific secondary bonding interactions between them.[5,6] GDCS includes two large local dipole moments due to the C≡N units in their molecular structure. Among others, the intermolecular head-to-tail coupling of local dipoles is operating for the formation of molecular disk, due to the spatial restriction induced by phasmidic polycatenar structure (see Figure 7 for the coupling scheme). We could verify that the number of molecules per slice is about two, through the density calculation method based on the XRD data.[14] The density of GDCS in the LC state at 30 °C was calculated to be 0.46Z, where Z is the number of molecules per unit cell. Then, the Z value must be around 2, which means that a slice of column is comprised of two molecules, if the density values of organic mesomorphic materials are assumed to be close to 1 g cm⁻³. Like for other polycatenar LCs, hexacatenars in particular,[12] the columnar cross-section area of GDCS increased with decreasing
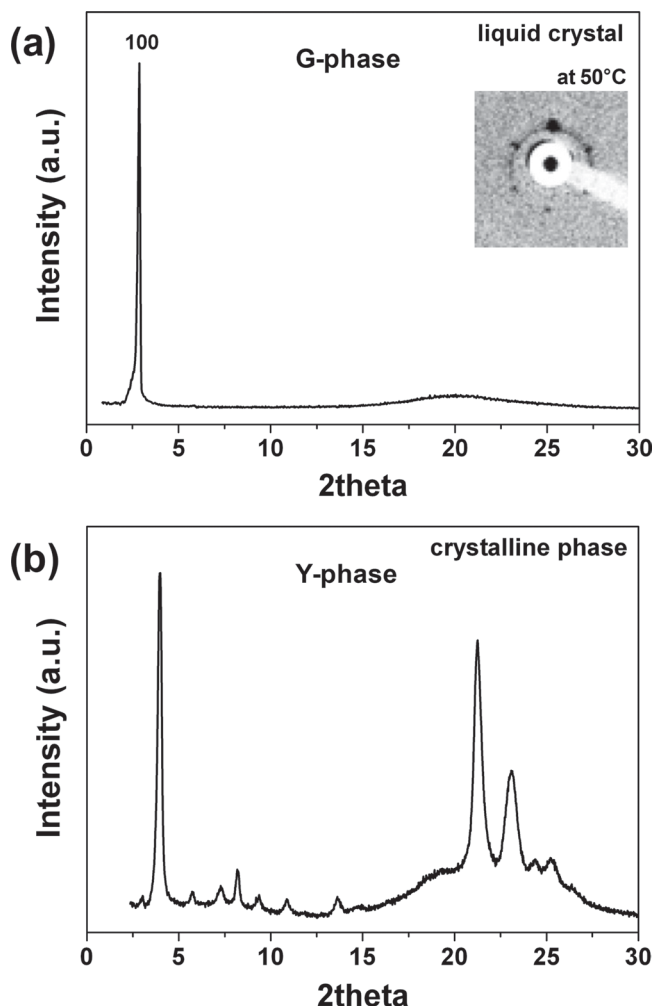
Figure 3. X-ray powder diffraction patterns of GDCS: a) Col_h phase. The inset shows the 2D XRD pattern of GDCS oriented LC phase at 50 °C. b) Crystalline phase.
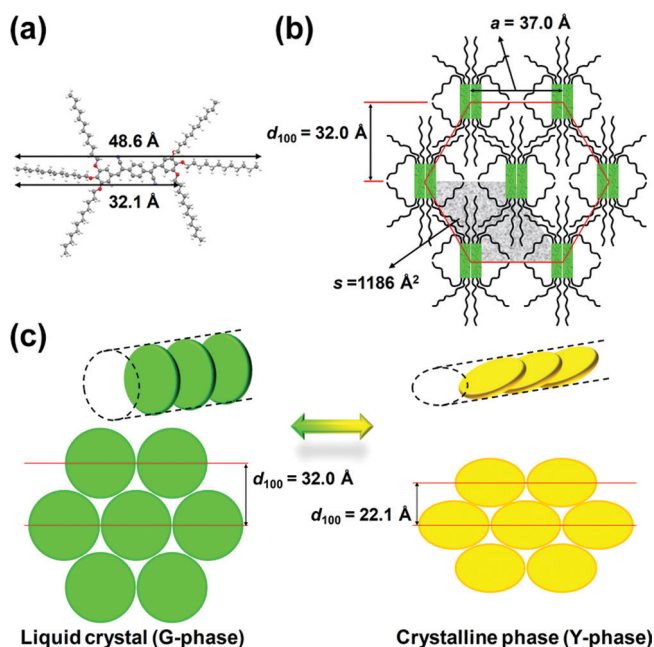
Figure 4. a) Calculated optimized molecular structure of GDCS. b) Organization structure of hexagonal columnar phase of GDCS LC state at 30 °C. c) Organization structure change during the crystallization process.

ADVANCED
FUNCTIONAL
MATERIALS
www.afm-journal.de

Materials
Views
www.MaterialsViews.com

FULL PAPER
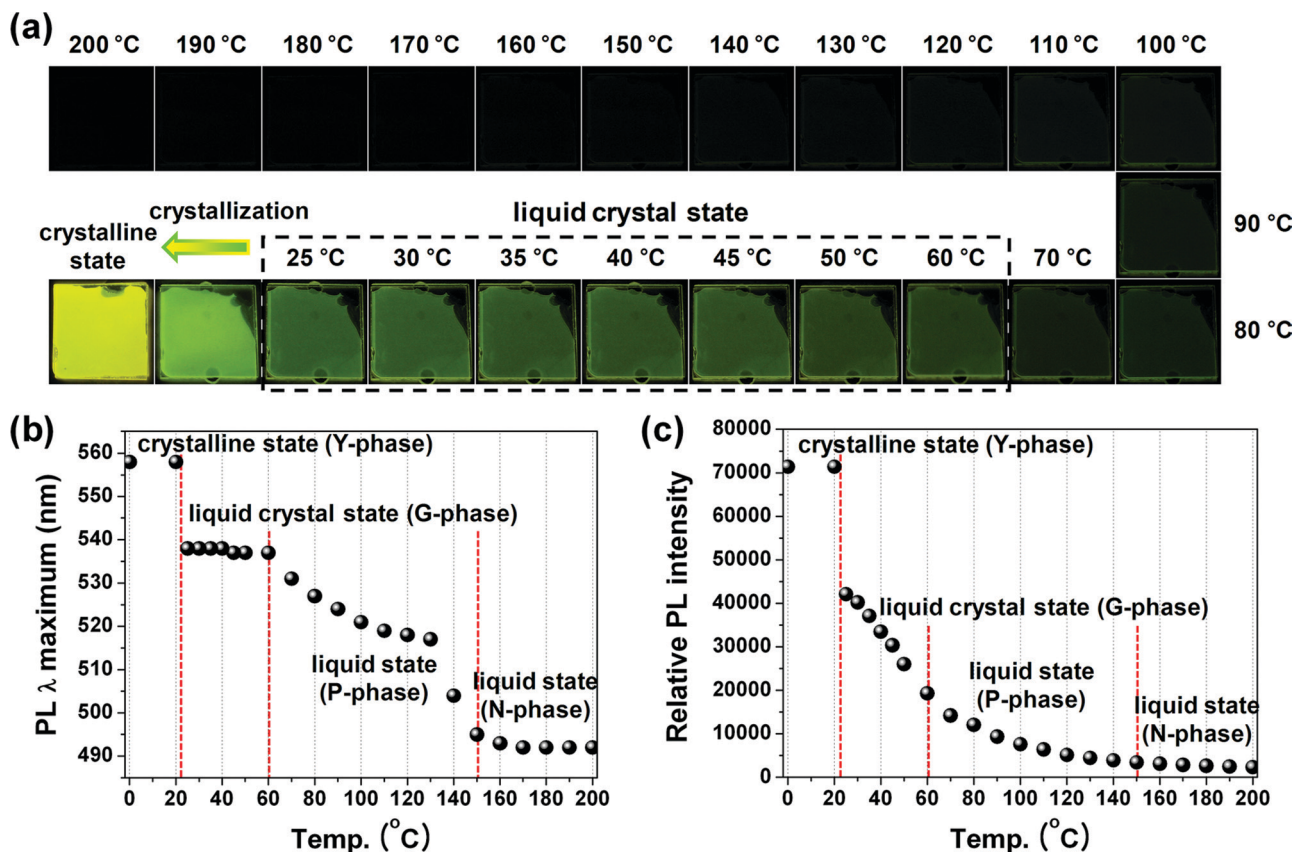
Figure 5. a) Photos of GDCS in condensed state during the cooling process from 200 °C to RT under 365 nm UV light. b) PL wavelength maximum shift behavior and c) PL intensity change behavior depending on the temperature at the cooling process.

temperature, as shown in Table 1, which is most likely due to the relaxation of the inner columnar cores undulations, resulting in the compensation of interfacial areas between cores and chains.[15] It is clearly shown that the proposed organization structure in the LC state is well matched with the lattice parameters of Col_h of GDCS, as illustrated in Figure 4b. It is to be noted that the circular molecular disks (consisting of a pair of GDCS molecule) in the G-phase (vide infra) are thus stacked flat on each other in a column. The XRD pattern of GDCS recorded at lower temperature (Y-phase, vide infra) contains several peaks both in wide- and small-angle regions, indicative of crystallization (Figure 3b). First, the stacking of molecular disks in a column seems to get slanted, as can be deduced from the diffraction peak shift in the small-angle region corresponding to d_{100} (from 32.0 Å to 22.1 Å) (see Figure 4c for the organization structure change). The newly generated diffraction peaks in the wide-angle region (20 ~ 25 °) of the crystalline state XRD pattern specifically indicate the intra-column inter-disk stacking interactions, which are distinct from the LC state (vide infra for the detailed discussion).

Like other dicyanodistyrylbenzene derivatives reported previously by us,[5,6] GDCS exhibits a great increase of fluorescence efficiency from the practically nonfluorescent THF solution ($\Phi_F = 1.1 \times 10^{-2}$) to the strongly fluorescent LC ($\Phi_F = 0.25$) and crystalline ($\Phi_F = 0.45$) phase due to the characteristic AIEE process, as demonstrated in Figure 1b. In the emission spectra,

the peak maximum of the crystalline phase is bathochromically shifted to 558 nm with respect to that of solution at 479 nm. Interestingly, GDCS exhibits remarkable thermochromic luminescence behavior in the condensed state. **Figure 5a** shows the evolution of photoluminescence (PL) images of GDCS during the cooling process from 200 °C to RT. The changes in PL maximum wavelength and relative PL intensity as a function of temperature are summarized in Figure 5b and Figure 5c (see the SI for the PL spectra depending on the temperature). These temperature-dependent PL changes in the whole range of different condensed states can be interpreted by dividing them into four distinct regions as follows. First, in the case of a high-temperature liquid state (200 ~ 150 °C), which is to be called nonfluorescent/N-phase, there appears no distinct change in the PL intensity and PL maximum wavelength ($\lambda_{max} = 492$–495 nm) as the temperature decreases. This is most probably due to the dominance of a thermally activated non-radiative decay process.[16] Secondly, in the lower-temperature liquid state (150 ~ 60 °C), denoted as planarization/P-phase, a gradual bathochromic shift of PL maximum wavelength (λ_{max}, from 495 nm to 537 nm) with simultaneously increased PL intensity was observed with decreasing temperature. In this temperature range, it is most likely that the intramolecular planarization is induced by deactivation of intramolecular torsional motion via decreasing the thermal energy and increasing the medium viscosity. Therefore, a substantial increase of the

www.MaterialsViews.com

ADVANCED
FUNCTIONAL
MATERIALS
www.afm-journal.de

FULL PAPER

molecular conjugation effected by planarization is responsible for the bathochromic shift and enhanced emission in this temperature range. Thirdly, in the LC state (60 °C ~ RT) (green/G-phase), GDCS revealed a gradually increasing PL intensity but with constant PL maximum wavelength (λ_{max} = 537–538 nm) as the temperature decreases. The intramolecular planarization and dimeric coupling to molecular disk is already complete in this LC region to give an invariant PL maximum wavelength. However, the relative rotational motions of the molecular disks in a given column are still temperature dependent in this liquid-crystalline G-phase. Consequently, with decreasing temperature, enhanced emission characteristic was observed due to the motional restriction of molecular disks (by reducing the nonradiative decay constant, vide infra) implemented by the formation of the well-ordered mesomorphic organization structure and the increased medium viscosity. Finally, the liquid-crystalline G-phase was transformed into a crystalline yellow/Y-phase at sufficiently low temperature or over several hours at RT with PL maximum wavelength shift from 538 nm to 558 nm and a remarkable increase of the PL intensity. The further PL enhancement is originating from the complete restriction of the molecular disks' rotational motions, together with the favorable intra-column inter-disk slanted stacking interactions, as identified by XRD data (vide infra for the detailed discussion about PL wavelength shift).

We have further investigated photophysical properties of GDCS in different phases to explore the relaxation dynamics of GDCS. Femtosecond fluorescence up-conversion and time-correlated single-photon counting (TCSPC) measurements were conducted. In THF solution, GDCS shows an ultrafast deactivation process with an average fluorescence lifetime (τ_{av}) of 11.4 ps, which is well correlated with the nonfluorescent behavior (see the SI for the fluorescence spectrum and decay profile). **Figure 6** shows the fluorescence decay profiles of GDCS in different condensed states depending on the temperature. At the temperature range from 130 °C to 30 °C (from the liquid P-phase to the liquid-crystalline G-phase),[17] the fluorescence decay time was gradually increased with decreasing temperature (τ_{av}, from 0.126 ns to 0.907 ns), in accordance with the fluorescence enhancement behavior. Subsequent crystallization to crystalline Y-phase, however, the fluorescence lifetime τ_{av}
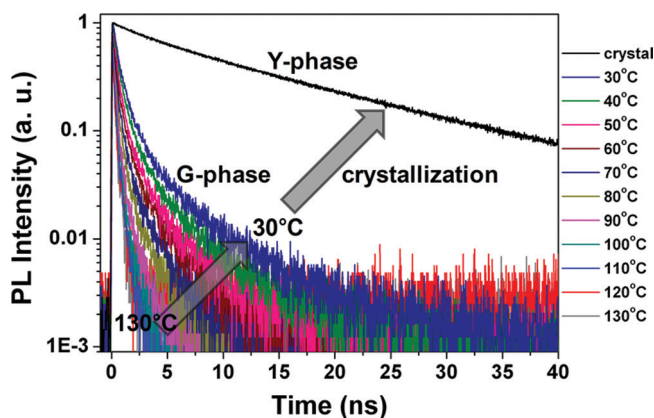
Figure 6. Fluorescence decay profiles of GDCS in condensed state depending on the temperature at the cooling process from 130 °C to RT.

Table 2. Emission properties of GDCS.

Phase	T [°C]	Φ_F[a)	τ_{av} [ns]	k_r[b)/10^9 [s^{-1}]	k_{nr}[b)/10^9 [s^{-1}]
Solution	RT	0.011	11.4×10^{-3}	0.96	87
	130	0.028	0.126	0.23	7.7
	120	0.032	0.140	0.23	6.9
	110	0.040	0.142	0.28	6.8
P-phase (liquid)	100	0.048	0.157	0.30	6.1
	90	0.059	0.181	0.33	5.2
	80	0.076	0.235	0.32	3.9
	70	0.090	0.297	0.30	3.1
	60	0.12	0.389	0.31	2.3
G-phase (liquid crystal)	50	0.16	0.496	0.33	1.7
	40	0.21	0.710	0.30	1.1
	30	0.25	0.907	0.28	0.82
Y-phase (crystal)	RT	0.45	13.1	0.034	0.042

[a)]Calculated using the crystalline state Φ_F value as a reference; [b)]Calculated using the following equations: $k_r = \Phi_F/\tau_F$, $k_{nr} = (1-\Phi_F)/\tau_F$.

was discontinuously increased to 13.1 ns. Such unique emission properties of GDCS in different condensed states are summarized in **Table 2**. Both the steady-state and time-resolved PL changes of GDCS in different condensed phases compared to those in solution, as described above, are attributed to the formation of specific supramolecular stacking architectures associated with the unique electronic and geometric characteristics of the dicyanodistyrylbenzene molecules. Actually, the dicyanodistyrylbenzene molecule is known to assume twisted molecular geometry in isolated state due to the steric factor of C≡N substituent,[5,6] which allows a torsion-induced nonradiative deactivation process. Therefore, a relatively higher nonradiative rate constant ($k_{nr} = (1-\Phi_F)/\tau_F = 8.7 \times 10^{10}$ s^{-1}) than radiative rate constant ($k_r = \Phi_F/\tau_F = 9.6 \times 10^8$ s^{-1}) of GDCS in THF solution (see Table 2) is mainly a consequence of the nonplanarity and torsional relaxation of GDCS molecule in the isolated state. On the other hand, in the case of the crystalline Y-phase of GDCS, the nonradiative rate constant ($k_{nr} = 4.2 \times 10^7$ s^{-1}) is three orders of magnitude smaller than that in solution, while the radiative rate constant ($k_r = 3.4 \times 10^7$ s^{-1}) is only one order of magnitude smaller than that in solution to give the peculiar AIEE effect.[5] As shown in Table 2, the PL quantum yield and lifetime of GDCS condensed states (liquid P- and liquid-crystalline G- phases) are also gradually increased during the cooling process. However, it is important to note that the nonradiative rate constant (k_{nr}) gradually decreases with temperature, while the radiative rate constant (k_r) remains unchanged. This observation clearly indicates that the substantial reduction of the nonradiative deactivation pathways is effected via intramolecular planarization and reduced molecular motion in the P- and G-phases of GDCS.

On the other hand, the liquid-crystalline G- to crystalline Y-phase transition, which actually generated slanted stacking of molecular disks and inter-disk ordering as evidenced by the XRD study (vide supra), is originating from the additional
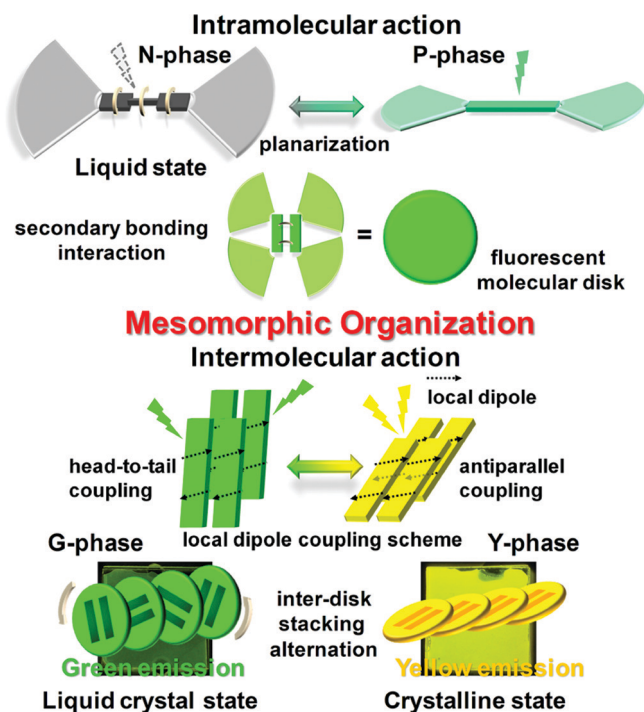
Figure 7. Schematic representation of the hierarchical mesomorphic organization of GDCS molecule concurrent with the intra- and intermolecular actions related to the emission characteristics.

intermolecular electronic interaction other than the one for making molecular disk. Most specifically, the slanted stacking of molecular disks and their intra-column inter-disk crystallization are simultaneously achieved by the antiparallel coupling of the pairs of local dipoles located on different molecular disks (see **Figure 7** for the stacking alternation scheme). Consequently, different from P- and G- phases, the crystalline Y-phase of GDCS uniquely shows strong characteristics of excited-state dimeric coupling,[18] which can be inferred from the longer wavelength and lifetime of the emission ($\lambda_{em, max}$ = 558 nm, τ_{av} = 13.1 ns). It should also be noted that the radiative rate constant (k_r) of crystalline Y-phase is only one eighth of the liquid-crystalline G-phase, indicating the presence of inter-disk excitonic interactions. Attributed to the even larger decrease of the nonradiative

rate constant (k_{nr}) (one twentieth via total confinement of molecular motion), however, the fluorescence quantum yield increases upon phase transition from G- to Y-phase (Φ_F from 0.25 to 0.45).

To gain unambiguous insight into this G- to Y-phase transition, we have performed a global analysis with the whole temporally and spectrally resolved PL signals in the liquid-crystalline G-phase and the crystalline Y-phase (**Figure 8**). In both cases, three decay-associated spectra (DAS) were obtained, due to the perturbation in the molecular stacking structures and thus the imperfection of intermolecular electronic interaction mode attributed to the soft mesogenic medium of long alkyl chains. The liquid-crystalline G-phase of GDCS exhibits a pronounced 500-nm-centered emission with a lifetime of 0.3 ns, which originates from the individual planar GDCS molecular disk without excited-state delocalization. Only a small portion of GDCS molecular disks in the liquid-crystalline G-phase showed rather weak intermolecular interactions, which are responsible for the 520-nm-centered emission with a lifetime of 1 ns and the 550-nm-centered emission with a lifetime of 6 ns. In its crystalline Y-phase, however, the 560-nm-centered emission with a much longer lifetime of 17 ns is dominant, suggesting a strongly coupled excimeric interaction between the molecular disks. Although insignificant, the presence of a 520-nm-centered emission with a lifetime of 0.3 ns and a 550-nm-centered emission with a lifetime of 4 ns, indicates a loss of excited-state delocalization by some loose intermolecular stacking components in the soft paraffinic medium even in the Y-phase crystal.

Figure 7 comprehensively depicts the hierarchical mesomorphic organization of the GDCS molecule together with the characteristic PL behavior of the GDCS material. In the liquid state, GDCS is assumed to be a molecular "torsion spring" with a large nonradiative decay constant. With decreasing temperature, GDCS gradually gains the molecular planarity due to the restricted thermal energy, which brings about the substantial reduction of the nonradiative decay channels and thus the enhanced PL emission (liquid P-phase). Subsequently, a highly fluorescent molecular disk consisting of a pair of GDCS molecules is spontaneously formed by the head-to-tail coupling of polar cyano groups. In the liquid-crystalline G-phase, molecular disks are closely packed to construct the hexagonal columns (Col_h) with rather weak intra-column inter-disk interaction to give out green emission. Finally, the slanted stacking of molecular disks in a given column and also the inter-disk crystallization are simultaneously driven by the inter-disk antiparallel coupling of local dipoles in different disks to complete G- to Y- transition.

To fully exploit such LC properties of GDCS, we have briefly investigated the strategy for the actual device fabrication. In general, a mechanical rubbing method is routinely applied for the realization of the uniaxial orientation of columnar LC materials.[10a,12d] Aiming at the uniaxial orientation and the spatial pattering simultaneously, however, the MIMIC method,[19] one of soft lithography techniques, has been employed herein to
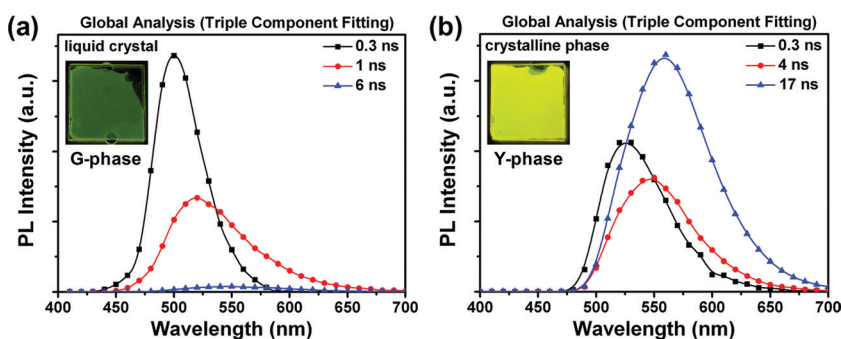
Figure 8. Decay-associated PL spectra of GDCS in a) the LC state, and b) the crystalline state. Insets show the fluorescence images of GDCS in the LC and the crystalline phase under 365 nm UV light, respectively.

www.MaterialsViews.com

ADVANCED
FUNCTIONAL
MATERIALS
www.afm-journal.de

FULL PAPER
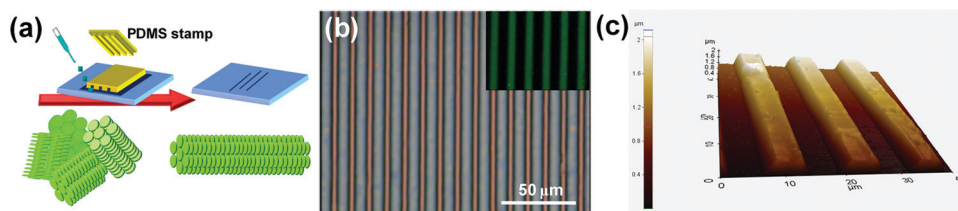
Figure 9. a) Schematic illustration of micromolding in capillaries for the alignment of the columnar LC material. b) Optical microscopy image of the patterned GDCS LC microlines. Inset shows the fluorescence image under 365 nm UV light. c) AFM image of the patterned GDCS LC microlines.

fabricate aligned liquid-crystalline G- and crystalline Y-phase microwires of GDCS.

Figure 9a shows a schematic illustration of the MIMIC process for molding of the GDCS molecule. In the first place, the GDCS molecule was heated to the liquid-crystalline G-phase ($T = 60\ °C$) and was introduced into the micrometer-sized rectangular capillary channels, which were formed by the conformal contact of a patterned poly(dimethylsiloxane) (PDMS, Sylgard 184, Dow Corning) mold and a glass substrate. After cooling down to the RT and removal of the mold, we could obtain well-aligned liquid-crystalline G-phase microwires of GDCS, as shown in the optical microscopy image of Figure 9b, because the MIMIC processes induced an almost perfect shear alignment of the LC material. The aligned liquid-crystalline G-phase microwires of GDCS exhibited intense green fluorescence, as shown in the inset photograph of Figure 9b. This G-phase microwire of GDCS showed almost perfect birefringence under cross-polarized condition, indicating that the aligned microwire had a monodomain structure (see the SI for the POM image with cross-polarization alternation). The atomic force microscopy (AFM) image of this G-phase microwires clearly shows the well-defined pattern morphology with the dimensions of 7.5 μm width and 0.8 μm height (Figure 9c).

Current–voltage (*I–V*) measurements were carried out in order to investigate the conductivity of GDCS in different phases and also the alignment effect of the MIMIC process. We have fabricated the gap-type bottom-contact planar two-electrode (gold, thickness of 50 nm) device for the *I–V* measurement. For the liquid-crystalline G-phase, a polydomain device of GDCS, the spin-cast film was fabricated on the electrode-deposited glass substrate from 1,2-dichloroethane solution of GDCS. By annealing at 70 °C and cooling down to RT, the polydomain structure of liquid-crystalline G-phase was spontaneously formed on the device framework (see the SI for the image of the liquid-crystalline G-phase polydomain). On the other hand, the uniaxially aligned G-phase microwires of GDCS were conveniently coated across the electrode channel of the device by using the MIMIC process. **Figures 10**a and b depict *I–V* curves for GDCS in different phases and alignments. It is shown that the electrical conductivity increased from $0.2 × 10^{-5}$ S cm^{-1} in the polydomain G-phase to $0.8 × 10^{-5}$ S cm^{-1} in monodomain G-phase due to the favorable alignment effect of GDCS LC via the MIMIC process. After a phase transition from the liquid-crystalline G-phase to the crystalline Y-phase of aligned GDCS microwires, the conductivity was even further enhanced to the value of $3.9 × 10^{-5}$ S cm^{-1}, according to the increased intra-column inter-disk interactions (Figure 10b). It is noteworthy that the uniaxial orientation and

the spatial patterning of highly fluorescent RT LC material was successfully achieved in this work by using the MIMIC process to give a good semiconducting property comparable with one of the well-known organic semiconductors, poly(3-hexylthiophene) (P3HT) ($\sigma = 6.7 × 10^{-5}$ S cm^{-1}).[20]

3. Conclusions

We have synthesized and fully characterized a novel dicyano-distyrylbenzene-type LC molecule (GDCS) exhibiting highly enhanced fluorescence emission in the RT liquid-crystalline
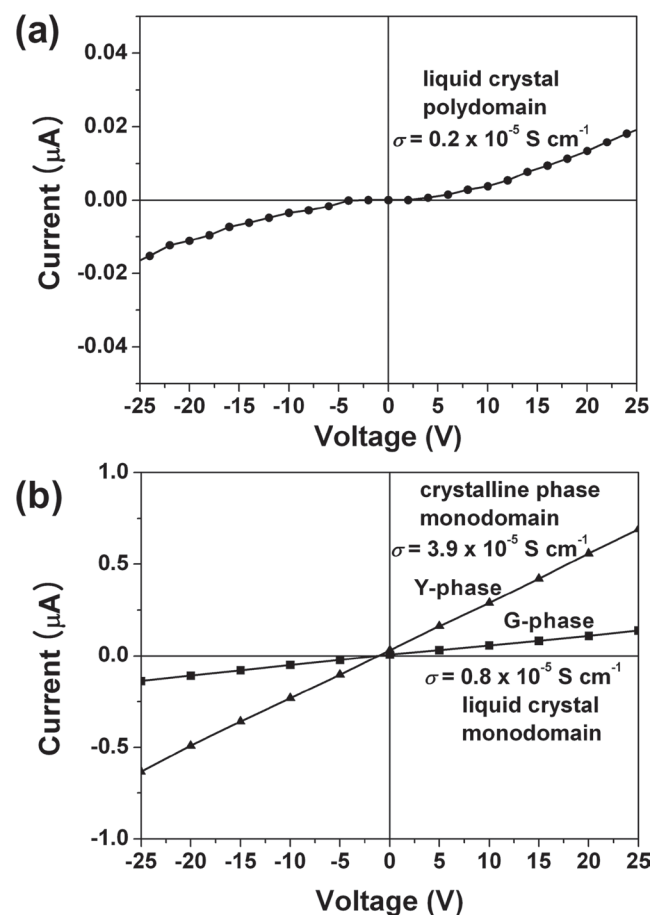
Figure 10. a) *I–V* curve of the GDCS polydomain in the LC state. b) *I–V* curves of the GDCS monodomain in the LC state (squares) and the crystalline state (triangles).

FULL PAPER

G-phase ($\Phi_F = 0.25$) and crystalline Y-phase ($\Phi_F = 0.45$). The hierarchical mesomorphic organizations and their state-dependent PL behavior were thoroughly investigated on the basis of structural, optical, and photophysical analyses. It was found that the GDCS behaved much like a "torsion spring" molecule in the high-temperature liquid state (N- and P-phases), while it formed dimeric "molecular disks" in the liquid-crystalline G-phase to generate a Col$_h$ structure. The crystalline Y-phase was generated from liquid-crystalline G-phase by the formation of intra-column inter-disk dipole coupling to give a highly fluorescent and semiconducting state. Uniaxially aligned GDCS microwires (both G- and Y- phases) showing enhanced fluorescence and semi-conductivity were successfully fabricated by using the MIMIC process. Based on their unique and useful properties of luminescence and electrical conductivity, these materials are expected to have potential applications in novel functional optoelectronic devices.

4. Experimental Section

Material Synthesis: GDCS was synthesized according to the procedure shown in Scheme S1 of the Supporting Information (SI). All chemicals were purchased commercially, and used without further purification.

3,4,5-tris(dodecyloxy)benzaldehyde: K_2CO_3 (2.81 g, 20.33 mmol) and KI (catalytic amount) were added to a solution of 3,4,5-trihydroxybenzaldehyde monohydrate (1.00 g, 5.81 mmol) in dry DMF (20 mL), and the mixture was stirred at 80 °C. 1-Bromododecane (5.62 mL, 23.24 mmol) was slowly dropped into the mixture. The reaction lasted overnight. After cooling to RT, the mixture was poured into brine and extracted with dichloromethane. The organic phase was dried over $MgSO_4$ and the solvent was evaporated in vacuo. The product (3.26 g, 85%) was obtained by column chromatography using ethyl acetate and *n*-hexane (1:10 v/v). ^{1}H NMR (CDCl3) δ [ppm]: 9.83 (s, 1H, -CHO), 7.08 (s, 2H, Ar-H), 4.04 (m, 6H, -OCH$_2$), 1.79 (m, 6H, -CH$_2$), 1.48 (m, 6H, -CH$_2$), 1.26 (m, 48H, -CH$_2$), 0.88 (t, 9H, -CH3).

(2Z,2′Z)-2,2′-(1,4-phenylene)bis(3-(3,4,5-tris(dodecyloxy)phenyl) acrylonitrile) (GDCS): The mixture of 3,4,5-tris(dodecyloxy)benzaldehyde (1.00 g, 1.52 mmol) and (4-cyanomethyl-phenyl)-acetonitrile (0.12 g, 0.76 mmol) in *tert*-butyl alcohol (30 mL) was stirred at 50 °C. Potassium *tert*-butoxide (0.17 g, 1.52 mmol) powder was dropped into the mixture and stirred for 2 h. The resulting precipitate was filtered and purified by column chromatography using dichloromethane. GDCS bulk powder (0.82 g, 75%) was obtained by reprecipitation from chloroform and methanol solution. ^{1}H NMR (CDCl3) δ [ppm]: 7.72 (s, 4H, Ar-H), 7.47 (s, 2H, Vinyl-H) 7.18 (s, 4H, Ar-H), 4.05 (m, 12H, -OCH$_2$), 1.79 (m, 12H, -CH$_2$), 1.49 (m, 12H, -CH$_2$), 1.27 (m, 96H, -CH$_2$), 0.88 (t, 18H, -CH3). *m/z* (FAB MS) Calcd for $C_{96}H_{160}N_2O_6$, 1437.2276; Found, 1437.2274. Anal. Calcd for $C_{96}H_{160}N_2O_6$: C, 80.17; H, 11.21; N, 1.95; O, 6.67. Found: C, 79.95; H, 11.32; N, 1.94; O, 6.68.

X-Ray, Thermal, Morphological Analysis and I–V measurements: The oriented XRD patterns were recorded using a sealed-tube generator (900 W) equipped with a pinhole Cu-Kα ($\lambda = 1.542$ Å) parallel beamline based on a home-mounted Kirkpatrick-Baez optics coupled with a HiStar detector (Bruker AXS). A drop of the crude sample was deposited on a silane-coated glass-slide, and cooled slowly from the isotropic phase. The upper region of the drop was brought to the grazing incidence with the X-ray beam. The sample temperature was controlled to within ±0.03 °C. The detector–sample distance was 109.1 mm. The pattern was analyzed using homemade ImageJ plug-ins (ϕ and 2θ profiles). XRD patterns were also obtained with two different experimental set-ups. In all cases, a linear focalized monochromatic Cu-Kα_1 beam ($\lambda = 1.5405$ Å) was obtained using a sealed-tube generator (900 W) equipped with a bent quartz monochromator. In both cases, the crude powder was filled in Lindemann capillaries of 1 mm diameter and 10 μm

wall-thickness. An initial set of diffraction patterns was recorded on an image plate (scanned by STORM 820 from Molecular Dynamics with 50 μm resolution); periodicities up to 80 Å can be measured, and the sample temperature controlled to within ±0.3 °C from 20 to 350 °C. The second set of diffraction patterns was recorded with a curved Inel CPS 120 counter gas-filled detector linked to a data acquisition computer; periodicities up to 70 Å can be measured, and the sample temperature controlled to within ±0.01 °C from 20 to 200 °C. Alternatively, X-ray patterns were also recorded on image plate; periodicities up to 120 Å can be measured. The thermal properties were investigated using DSC with TA Instruments and DSC-Q2000 instruments operated at various scanning rates. AFM was performed with a PSIA instrument XE-150. AFM image was recorded simultaneously in noncontact mode. The I–V measurements of the devices were performed using an HP-4155A (Hewlett Packard) semiconductor analyzer.

Characterization: ^{1}H NMR spectra were recorded on a Bruker, Avance-300 (300 MHz) in CDCl$_3$ solution. Mass spectra were measured using a JEOL, JMS-600W mass spectrometer. Elemental analyses were carried out using a CE instruments, EA1110 elemental analyzer. UV-visible absorption spectra were recorded on a Shimazu, UV-1650 PC spectrometer. Photoluminescence spectra were obtained using a Varian, Cary Eclipse Fluorescence spectrophotometer. The relative fluorescence quantum yield of the GDCS solution was measured using 9,10-diphenylanthracene (DPA) in benzene as a standard reference (1×10^{-4} mol L^{-1}, $\Phi_F = 0.83$). The absolute photoluminescence quantum efficiency of the GDCS powder was measured using an integrating sphere (Labsphere Co., 600 diameter). A continuous wave Xe-lamp (500 W, Melles Griot Co.) was used as the excitation light source, and a monochromator (Acton Research Co.) attached to a photomultiplier tube (Hamamatsu) was used as the optical detector system. All of the systems were calibrated using a tungsten-halogen standard lamp and deuterium lamp (Ocean Optics LS-1-CAL and DH-2000-CAL, respectively). Φ_{PL} was calculated based on the de Mello method.[21] Time-resolved fluorescence lifetime experiments were performed by the time-correlated single photon counting (TCSPC) and femtosecond fluorescence up-conversion technique. In the TCSPC system, as an excitation light source, we used a mode-locked Ti:sapphire laser (Spectra Physics, MaiTai BB), which provides ultrashort pulses (80 fs at full width half maximum, fwhm) with high repetition rate (80 MHz). This high repetition rate slows down to 1 MHz ~800 kHz by using homemade pulse-picker. The pulse-picked output pulse was frequency-doubled by a 1 mm thickness of a BBO crystal (EKSMA). The fluorescence was collected by a microchannel plate photomultiplier (MCP-PMT, Hamamatsu, R3809U-51) with a thermoelectric cooler (Hamamatsu, C4878) connected to a TCSPC board (Becker&Hickel SPC-130). The overall instrumental response function was about 25 ps (fwhm). A vertically polarized pump pulse by a Glan-laser polarizer was irradiated to samples, and a sheet polarizer, set at an angle complementary to the magic angle (54.7°), was placed in the fluorescence collection path to obtain polarization-independent fluorescence decays. In the case of femtosecond fluorescence up-conversion apparatus the beam sources were a mode-locked Ti:sapphire laser also used in TCSPC system. The second harmonic of the fundamental generated by a 200-μm thick BBO crystal served as pump pulse. A residual fundamental pulse was used as a gate pulse. The pump beam was focused onto a 500-μm-thick quartz cuvette containing sample solution using a 5-cm focal length plano-convex lens with a magic angle (54.7°) in order to prevent polarization-dependent signals. The cuvette was mounted on a motor-driven stage and moved constantly back and forth to minimize photo-degradation. Collection of the fluorescence and focusing into a 1-mm-thick BBO crystal for frequency conversion was achieved by a reflecting microscope objective lens (Coherent). The FWHM of the cross-correlation function between the scattered pump pulse and the gate pulse is measured to be ~310 fs. The average excitation power was kept at a level below 2 mW in order to minimize thermal lens effect. In this excitation intensity regime the fluorescence dynamics was be independent of the excitation intensity for all samples. Deconvolution fitting and global analyses are performed by vfit software (version 2.02).

www.MaterialsViews.com

ADVANCED
FUNCTIONAL
MATERIALS
www.afm-journal.de

FULL PAPER

Supporting Information

Supporting Information is available from the Wiley Online Library or from the author.

Acknowledgements

[1] a) E. Kim, S. B. Park, *Chem. Asian. J.* **2009**, *4*, 1646; b) P. M. Beaujuge, C. M. AMB, J. R. Reynolds, *Acc. Chem. Res.* **2010**, *43*, 1396.

[2] a) R. Davis, N. P. Rath, S. Das, *Chem. Commun.* **2004**, 74; b) T. Mutai, H. Satou, K. Araki, *Nat. Mater.* **2005**, *4*, 685; c) H. Zhang, Z. Zhang, K. Ye, J. Zhang, Y. Wang, *Adv. Mater.* **2006**, *18*, 2369; d) T. Mutai, H. Tomoda, T. Ohkawa, Y. Yabe, K. Araki, *Angew. Chem. Int. Ed.* **2008**, *47*, 9522; e) Y. Zhao, H. Gao, Y. Fan, T. Zhou, Z. Su, Y. Liu, Y. Wang, *Adv. Mater.* **2009**, *21*, 3165; f) S. S. Babu, K. K. Kartha, A. Ajayaghosh, *J. Phys. Chem. Lett.* **2010**, *1*, 3413; g) S. Varghese, S. Das, *J. Phys. Chem. Lett.* **2011**, *2*, 863.

[3] a) M. D. Curtis, J. Cao, J. W. Kampf, *J. Am. Chem. Soc.* **2004**, *126*, 4318; b) H. Moon, R. Zeis, E. J. Borkent, C. Besnard, A. J. Lovinger, T. Siegrist, C. Kloc, Z. Bao, *J. Am. Chem. Soc.* **2004**, *126*, 15322; c) R. Li, W. Hu, Y. Liu, D. Zhu, *Acc. Chem. Res.* **2010**, *43*, 529.

[4] a) F. J. M. Hoeben, P. Jonkheijm, E. W. Meijer, A. P. H. J. Schenning, *Chem. Rev.* **2005**, *105*, 1491; b) B. Moulton, M. J. Zaworotko, *Chem. Rev.* **2001**, *101*, 1629; c) X. Zhang, X. Zhang, K. Zou, C. S. Lee, S. T. Lee, *J. Am. Chem. Soc.* **2007**, *129*, 3527.

[5] S. J. Yoon, J. W. Chung, J. Gierschner, K. S. Kim, M. G. Choi, D. Kim, S. Y. Park, *J. Am. Chem. Soc.* **2010**, *132*, 13675.

[6] S. J. Yoon, S. Y. Park, *J. Mater. Chem.* **2011**, *21*, 8338.

[7] a) F. Camerel, L. Bonardi, G. Ulrich, L. Charbonnière, B. Donnio, C. Bourgogne, D. Guillon, P. Retailleau, R. Ziessel, *Chem. Mater.* **2006**, *18*, 5009; b) F. Camerel, L. Bonardi, M. Schmutz, R. Ziessel, *J. Am. Chem. Soc.* **2006**, *128*, 4548; c) F. Camerel, J. Barberá, J. Otsuki, T. Tokimoto, Y. Shimazaki, L. Y. Chen, S. H. Liu, M. S. Lin, C. C. Wu, R. Ziessel, *Adv. Mater.* **2008**, *20*, 3462;

d) C. Z. Li, Y. Matsuo, E. Nakamura, *J. Am. Chem. Soc.* **2009**, *131*, 17058; e) S. Frein, F. Camerel, R. Ziessel, J. Barberá, R. Deschenaux, *Chem. Mater.* **2009**, *21*, 3950; f) D. Pucci, A. Bellusci, A. Crispini, M. Ghedini, N. Godbert, E. I. Szerb, A. M. Talarico, *J. Mater. Chem.* **2009**, *19*, 7643.

[8] a) Y. Sagara, T. Kato, *Angew. Chem. Int. Ed.* **2008**, *47*, 5175; b) V. N. Kozhevnikov, B. Donnio, D. W. Bruce, *Angew. Chem. Int. Ed.* **2008**, *47*, 6286; c) Y. Sagara, S. Yamane, T. Mutai, K. Araki, T. Kato, *Adv. Funct. Mater.* **2009**, *19*, 1869; d) S. Yamane, Y. Sagara, T. Kato, *Chem. Commun.* **2009**, 3597.

[9] a) C. D. Simpson, J. Wu, M. D. Watson, K. Müllen, *J. Mater. Chem.* **2004**, *14*, 494; b) S. Sergeyev, W. Pisula, Y. H. Geerts, *Chem. Soc. Rev.* **2007**, *36*, 1902; c) B. R. Kaafarani, *Chem. Mater.* **2011**, *23*, 378.

[10] a) M. Yoshio, T. Mukai, H. Ohno, T. Kato, *J. Am. Chem. Soc.* **2004**, *126*, 994; b) T. Sakurai, K. Shi, H. Sato, K. Tashiro, A. Osuka, A. Saeki, S. Seki, S. Tagawa, S. Sasaki, H. Masunaga, K. Osaka, M. Takata, T. Aida, *J. Am. Chem. Soc.* **2008**, *130*, 13812; c) T. Yasuda, H. Ooi, J. Morita, Y. Akama, K. Minoura, M. Funahashi, T. Shimomura, T. Kato, *Adv. Funct. Mater.* **2009**, *19*, 411; d) Z. An, J. Yu, B. Domercq, S. C. Jones, S. Barlow, B. Kippelen, S. R. Marder, *J. Mater. Chem.* **2009**, *19*, 6688.

[11] H. T. Nguyen, C. Destrade, J. Malthete, *Adv. Mater.* **1997**, *9*, 375.

[12] a) B. P. Hoag, D. L. Gin, *Adv. Mater.* **1998**, *10*, 1546; b) K. E. Rowe, D. W. Bruce, *J. Mater. Chem.* **1998**, *8*, 331; c) F. Lincker, P. Bourgun, P. Masson, P. Didier, L. Guidoni, J. Y. Bigot, J. F. Nicoud, B. Donnio, D. Guillon, *Org. Lett.* **2005**, *7*, 1505; d) T. Yasuda, K. Kishimoto, T. Kato, *Chem. Commun.* **2006**, 3399; e) J. Seo, S. Kim, S. H. Gihm, C. R. Park, S. Y. Park, *J. Mater. Chem.* **2007**, *17*, 5052; f) X. Li, A. Liu, S. Xun, W. Qiao, X. Wan, Z. Y. Wang, *Org. Lett.* **2008**, *10*, 3785; g) K. Isoda, T. Yasuda, T. Kato, *J. Mater. Chem.* **2008**, *18*, 4522; h) H. H. G. Tsai, L. C. Chou, S. C. Lin, H. S. Sheu, C. K. Lai, *Tetrahedron Lett.* **2009**, *50*, 1906; i) P. Zhang, B. Bai, H. Wang, S. Qu, Z. Yu, X. Ran, M. Li, *Liq. Cryst.* **2009**, *36*, 7; j) S. Zhang, Y. Guo, L. Wang, Q. Li, K. Zheng, X. Zhan, Y. Liu, R. Liu, L. J. Wan, *J. Phys. Chem. C* **2009**, *113*, 16232.

[13] Gaussian 09, Revision A.02, Gaussian, Inc., Wallingford CT, 2009.

[14] A. Pérez, J. L. Serrano, T. Sierra, A. Ballesteros, D. de Saá, J. Barluenga, *J. Am. Chem. Soc.* **2011**, *133*, 8110.

[15] B. Donnio, B. Heinrich, Th. Gulik-Grzywicki, H. Delacroix, D. Guillon, *Chem. Mater.* **1997**, *9*, 2951.

[16] a) R. O. Loutfy, B. A. Arnold, *J. Phys. Chem.* **1982**, *86*, 4205; b) C. E. Kung, J. K. Reed, *Biochemistry* **1986**, *25*, 6114; c) S. Kim, J. Seo, S. Y. Park, *J. Photochem. Photobiol. A: Chem.* **2007**, *191*, 19.

[17] At the high temperature range from 200 °C to 140 °C, the fluorescence decays are too short to be measured by our lifetime measurement instrument sets ($\tau_F < 80$ ps).

[18] T. Förster, K. Kasper, *Z. Elektrochem.* **1955**, *59*, 976.

[19] E. Kim, Y. Xia, G. M. Whitesides, *Nature* **1995**, *376*, 581.

[20] B. K. Kuila, A. K. Nandi, *Macromolecules* **2004**, *37*, 8577.

[21] J. C. de Mello, H. F. Wittmann, R. H. Friend, *Adv. Mater.* **1997**, *9*, 230.

Effects of Moisture on the Switching Characteristics of Oxide-Based, Gapless-Type Atomic Switches

Tohru Tsuruoka,* Kazuya Terabe, Tsuyoshi Hasegawa, Ilia Valov, Rainer Waser, and Masakazu Aono

Resistive switching memories based on the formation and dissolution of a metal filament in a simple metal/oxide/metal structure are attractive because of their potential high scalability, low-power consumption, and ease of operation. From the standpoint of the operation mechanism, these types of memory devices are referred to as gapless-type atomic switches or electrochemical metallization cells. It is well known that oxide materials can absorb moisture from the ambient air, which causes shifts in the characteristics of metal-oxide-semiconductor devices. However, the role of ambient moisture on the operation of oxide-based atomic switches has not yet been clarified. In this work, current–voltage measurements were performed as a function of ambient water vapor pressure and temperature to reveal the effect of moisture on the switching behavior of Cu/oxide/Pt atomic switches using different oxide materials. The main findings are: i) the ionization of Cu at the anode interface is likely to be attributed to chemical oxidation via residual water in the oxide layer, ii) Cu ions migrate along grain boundaries in the oxide layer, where a hydrogen-bond network might be formed by moisture absorption, and iii) the stability of residual water has an impact on the ionization and migration processes and plays a major role in determining the operation voltages. These findings will be important in the microscopic understanding of the switching behavior of oxide-based atomic switches and electrochemical metallization cells.

1. Introduction

Currently, there is great technological interest in resistive switching devices based on the formation and dissolution of a metal filament in a thin layer for volatile and nonvolatile memory applications.[1,2] The basic structure of the devices consists of a simple metal-ion conductor-metal (MIM) cell, in which a conductive ion layer is sandwiched between an electrochemically active metal electrode (usually Cu or Ag) and an inert metal electrode (for example, Pt). Because its operation mechanism is essentially identical to that of an "atomic switch", whose resistance across a nanometer gap is controlled by the formation and annihilation of a metal bridge under electrical bias,[3] we call this MIM structured cell a "gapless-type atomic switch".[4] On the basis of electrochemical deposition and dissolution of metal on an inert foreign substrate, this type of the cell is also referred to as an electrochemical metallization cell (ECM) or a programmable metallization cell.[5,6] In addition to the simple structures, atomic switches have many unique features, such as low ON resistances, high ON/OFF resistance ratios, excellent scalable potential, low power consumption, and ease of operation.[3,7]

Among the various materials suitable for application in an atomic switches and ECM including sulfides,[8,9] chalcogenide glasses,[10,11] and polymers,[12] metal oxides are one of the most promising materials because of their high compatibility with the fabrication processes of complementary metal-oxide-semiconductor devices. Resistive switching phenomena have been reported for many MIM cells using a thin layer of Ta_2O_5,[13] SiO_2,[14,15] WO_3,[16] ZrO_2,[17] HfO_2,[18] $SrTiO_3$[19], etc. In these reports, an amorphous or polycrystalline oxide layer was deposited by sputtering or pulsed laser deposition. The fabricated cells exhibited bipolar switching behavior such that they were SET from a high-resistance (OFF) state to a low-resistance (ON) state at positive bias relative to the electrochemically active electrode and RESET from the ON state to the OFF state at negative bias. The switching mechanism and device characteristics, such as retention time and cycle endurance, have been investigated for the respective cells. However, in the reported works, different experimental conditions were used for the fabrication processes as well as for the electrical measurements. Therefore, one cannot make an appropriate comparison between the results for different oxide materials from separate papers. To understand the switching mechanism completely and to control the function of atomic switches, it is important to know how

Dr. T. Tsuruoka, Dr. K. Terabe, Prof. T. Hasegawa, Prof. M. Aono
International Center for Materials Nanoarchitectonics (MANA)
National Institute for Materials Science (NIMS)
1-1 Namiki, Tsukuba, 305-0044, Japan
E-mail: TSURUOKA.Tohru@nims.go.jp

Dr. T. Tsuruoka, Prof. T. Hasegawa
Core Research for Evolutional Science and Technology (CREST)
Japan Science and Technology Agency (JST)
5 Sanbancho, Chiyoda-ku, Tokyo 102-0075, Japan

Dr. I. Valov, Prof. R. Waser
Peter Gruenberg Institute (Electric Materials)
Forschungszentrum Jülich, 52425 Jülich, Germany

Dr. I. Valov, Prof. R. Waser
Institut für Werkstoffe der Elektrotecknik 2 (IWE2)
RWTH Aachen, 52074 Aachen, Germany

the operation voltages depend on the structural and chemical properties of each oxide material.

Oxide films deposited by sputtering typically exhibit nanoporous structures with film densities lower than the bulk state.[20] Such porous oxides can absorb moisture during ambient exposure. The presence of moisture has a profound influence on the performance of the device. Zhao et al. reported that the moisture absorption deteriorates the permittivity of La_2O_3 films, which is a promising material to substitute SiO_2 as the gate dielectric film.[21] It was also found that moisture plays a major role in the operation of organic field-effect transistors using ion conducting insulator membranes, and careful control of the moisture is required for stable and consistent device behavior.[22] Thus, it can be expected that the transport properties of metal ions in thin oxide layers would be affected by moisture absorption, giving rise to shifts in the characteristics of the cells. However, despite many observations for oxide-based atomic switches and ECMs, there has been no report of the moisture effect on the switching behavior.

In a previous work, we proposed forming and switching mechanisms in a $Cu/Ta_2O_5/Pt$ atomic switch cell. The forming and SET processes corresponded to the formation of a metal filament by inhomogeneous nucleation, and the RESET process was attributed to the dissolution of a metal filament due to thermochemical reactions assisted by Joule heating.[23] The validity of this switching model was demonstrated by the fact that the temperature variations in the operation voltages and the ON resistance of the cell could be explained in terms of classical nucleation theory.[24] Here, we clarify the role of moisture in the operation of oxide-based atomic switches. To reveal the material dependence on the switching operations, Ta_2O_5 and SiO_2 were selected as the model oxides because they exhibited distinctly different behavior. MIM cells consisting of these oxide layers with different thicknesses were fabricated under nearly identical conditions, and their SET and RESET voltages were measured as a function of ambient H_2O pressure and temperature. By comparing the results of the two cells, we draw a microscopic picture of the migration of metal ions and discuss the influence of moisture on the switching behavior.

2. Electrical Characterizations

Figure 1a and b shows the typical switching characteristics of $Cu/Ta_2O_5/Pt$ and $Cu/SiO_2/Pt$ cells with an oxide layer thickness of 15 and 17 nm, respectively, which were measured under atmospheric conditions (relative humidity > 30%). Both cells were SET at an initial positive bias sweep relative to the Cu anode and RESET at a subsequent negative bias sweep, as shown by the red curves. The first SET operation corresponds to the forming process in which a metal filament is formed between the electrodes by the electrochemical dissolution of Cu at the anode and inhomogeneous nucleation and growth of Cu on the Pt cathode, as illustrated in the inset on the lower right of Figure 1a.[23] The RESET operation is attributed to Joule-heating-assisted electrochemical dissolution of the metal filament, followed by the diffusion of Cu ions due to their own concentration gradient and the applied electric field. The subsequent SET operation results in re-formation of the
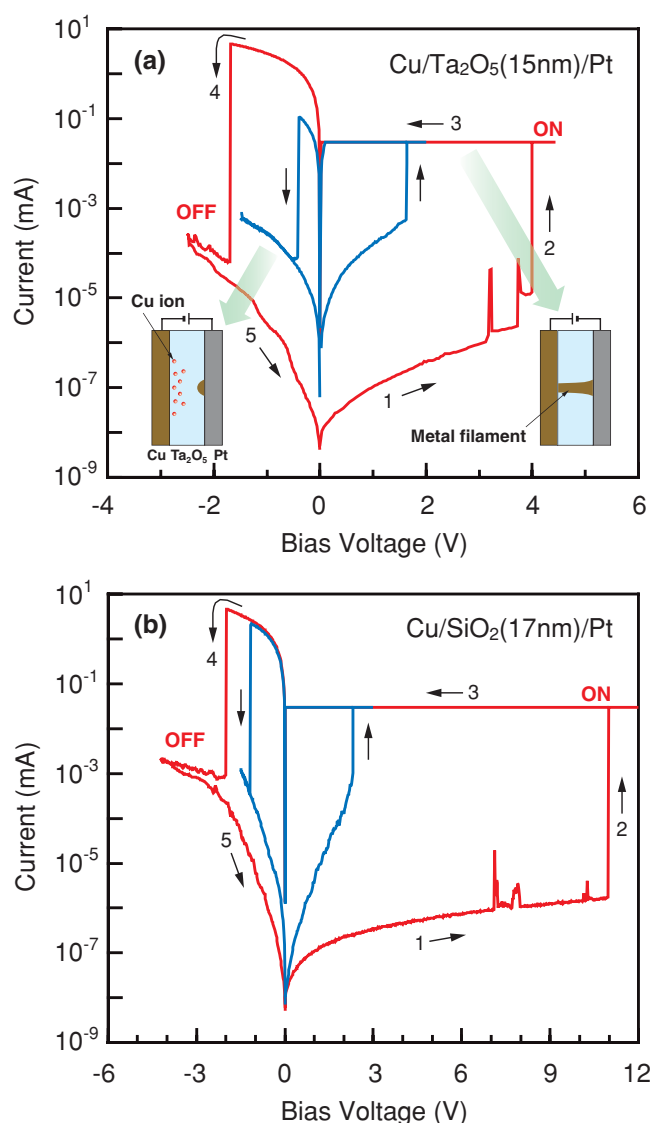
Figure 1. Typical forming (red curves) and subsequent switching (blue curves) characteristics of the $Cu/Ta_2O_5/Pt$ (a) and $Cu/SiO_2/Pt$ (b) cells under atmospheric conditions. The inset of (a) schematically illustrates the ON (right side) and OFF (left side) states of the cell.

metal filament on the remaining Cu precipitate. By repeating the voltage sweep cycles, the SET and RESET voltages gradually decreased in magnitude and became almost constant, as shown by the blue curves. The reduction in the SET voltage can be explained by the fact that Cu ions are already present within the oxide layer, and that the distance between the Cu anode and the remaining Cu precipitate becomes smaller than the oxide-layer thickness in the OFF state, as illustrated in the inset on the lower left of Figure 1a. Another possible explanation for the lowering of the SET voltage could be the formation of a fast ion transport path during the forming process.[14] In either case, the smaller bias voltages are enough to SET the cell after the second sweep cycle. Figure 1 shows that both $Cu/Ta_2O_5/Pt$ and $Cu/SiO_2/Pt$ cells exhibited nonvolatile bipolar switching behavior. However, the forming voltage of the $Cu/SiO_2/Pt$ cell
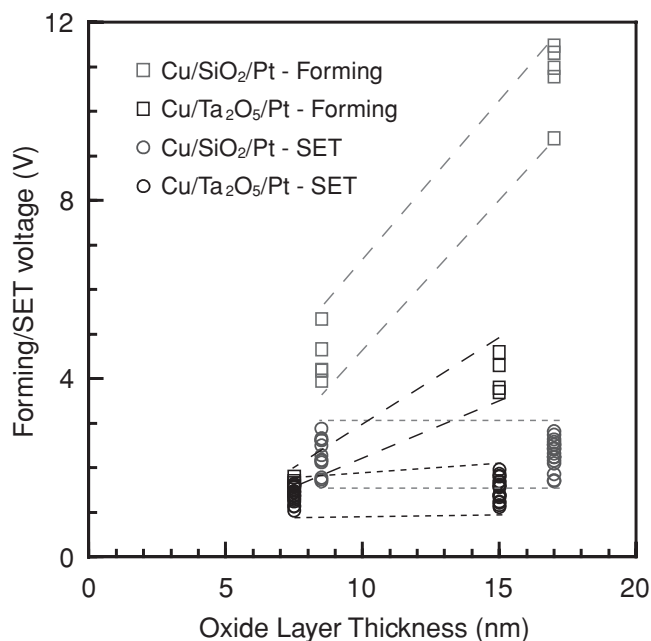
Figure 2. Forming (open squares) and SET (open circles) voltages of Cu/Ta$_2$O$_5$/Pt (black) and Cu/SiO$_2$/Pt (gray) cells plotted as a function of the oxide layer thickness. The dashed and dotted lines are a guide for the eye.

Figure 3. Variation in the SET (open circles) and RESET (open diamonds) voltages of the Cu/Ta$_2$O$_5$/Pt (a) and Cu/SiO$_2$/Pt (b) cells with a reduction in the ambient pressure. The dotted lines are a guide to the eye.

was significantly higher than that of the Cu/Ta$_2$O$_5$/Pt cell, although their oxide layer thicknesses were about the same. The SET and RESET voltages were also larger for the Cu/SiO$_2$/Pt cell than for the Cu/Ta$_2$O$_5$/Pt cell. This result indicates that the operation voltages of the cells depend strongly on the oxide material.

Figure 2 plots the forming (open circles) and SET (open squares) voltages of the Cu/Ta$_2$O$_5$/Pt and Cu/SiO$_2$/Pt cells as a function of the oxide layer thickness. The data were collected from several cells for each layer thickness. The voltage ranges in which the two voltages are distributed represent the statistics in the cell-to-cell data. The forming voltages increased with increasing oxide layer thickness. This might be because higher bias voltages are needed to inject more Cu ions into a thicker oxide layer to reach supersaturation for the first formation of the metal filament under a constant voltage sweep condition. If a constant bias voltage was applied, a longer forming time would be required for a thicker oxide layer.[25] The SET voltages, however, changed little with the oxide layer thickness. This can be attributed to the situation in which the SET and RESET operations are repeated in a nearly constant gap between the Cu anode and the remaining Cu precipitate on the Pt cathode. The electrocrystallization process at the cathode may also determine the thickness-independent SET voltages.[14] Although the SET voltages of the two cells somewhat overlapped, the SET voltage range was higher for the Cu/SiO$_2$/Pt cells than for the Cu/Ta$_2$O$_5$/Pt cells. The forming voltages were more than two times higher for the Cu/SiO$_2$/Pt cells than for the Cu/Ta$_2$O$_5$/Pt cells.

We found that the two cells showed a different switching behavior with the variation of the ambient water-vapor pressure. In **Figure 3** the SET (open circles) and RESET (open diamonds)
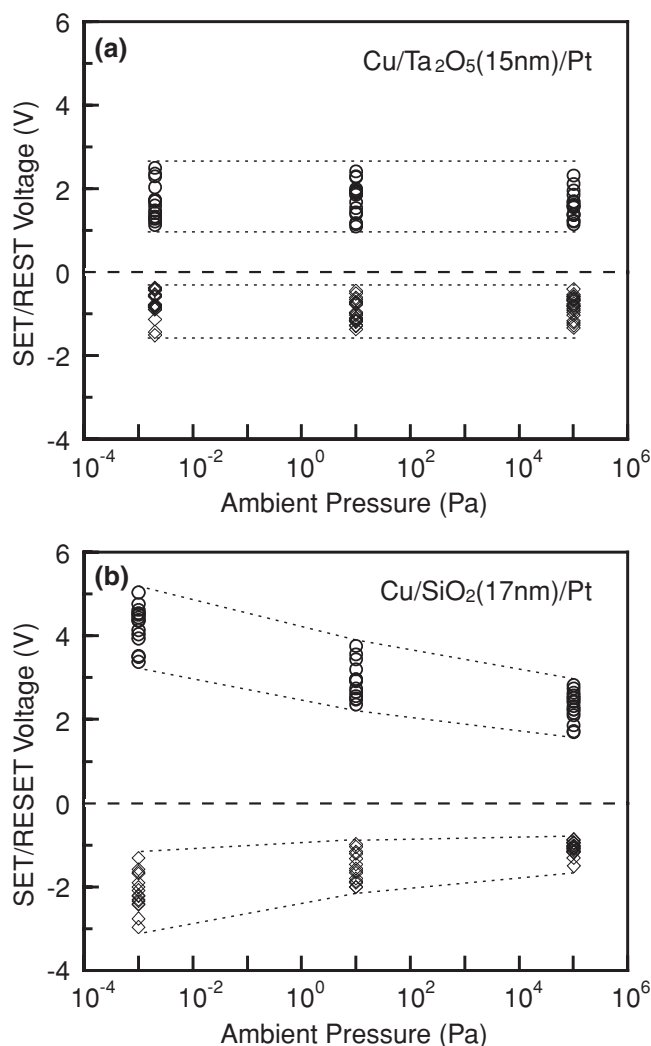
voltages are plotted as a function of ambient pressure ranging from atmosphere down to 10^{-3} Pa. In the Cu/Ta$_2$O$_5$/Pt cell, both the SET and RESET voltages were nearly constant upon varying the ambient H$_2$O pressure, as seen in Figure 3a. However, the Cu/SiO$_2$/Pt cell exhibited a two-fold increase in magnitude of those voltages with a reduction in the ambient pressure (Figure 3b). When the cell was exposed to air again, the SET and RESET voltages gradually returned to the original voltage levels for approximately an hour. The different responses to the pressure between the two cells were also observed in the cells with thinner oxide layers. The data for the Cu/SiO$_2$/Pt cells in Figure 3 were obtained by evacuating the prober in which the cell was set after the forming process was conducted in atmosphere. If the bias voltage was initially applied to the cells in vacuum (after evacuating the prober first), the cell resistance changed from the initial high-resistance state to a low-resistance state at a bias voltage higher than 15 V and then never exhibited any switching behavior. In contrast, the Cu/Ta$_2$O$_5$/Pt cell always showed similar forming and subsequent switching

Materials
Views
www.MaterialsViews.com

ADVANCED
FUNCTIONAL
MATERIALS
www.afm-journal.de

FULL PAPER
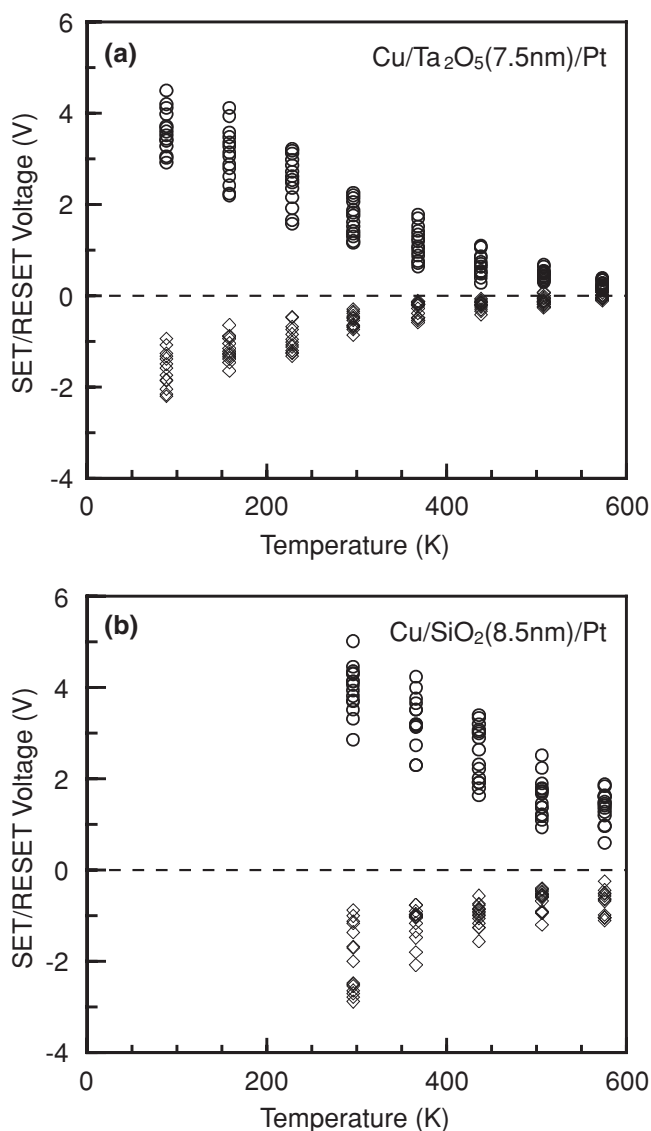
Figure 4. Temperature dependence of the SET (open circles) and RESET (open diamonds) voltages of the Cu/Ta$_2$O$_5$/Pt cells (a) and Cu/SiO$_2$/Pt cells (b), measured under vacuum conditions.

cycles regardless of the ambient H$_2$O pressure (for comparison, the data for the Cu/Ta$_2$O$_5$/Pt cells in Figure 3 were measured upon evacuating after the forming was conducted in atmosphere). The origin of this difference in the initial switching behaviors in vacuum will be discussed later.

After evacuating the prober to below 10^{-3} Pa, the SET and RESET voltages were measured over a temperature range from 88 to 573 K. Typical results for cells with 7.5-nm-thick Ta$_2$O$_5$ and 8.5-nm-thick SiO$_2$ layers are plotted in **Figure 4**a and b, respectively. The data for the Cu/SiO$_2$/Pt cell could not be obtained at low temperatures, due to instability of the switching behavior at bias voltages higher than 7 V. A similar temperature dependence was also obtained for the cells with thicker oxide layers. Both the SET and RESET voltages decreased in magnitude with increasing temperature. In a previous study, we found that the temperature variation in the SET voltage of the Cu/Ta$_2$O$_5$/Pt

cell could be explained by the migration speed of Cu ions in the Ta$_2$O$_5$ layer and the ion concentration required for nucleation (or electrodeposition) of Cu.[24] The hopping conduction model predicts that the migration speed of Cu ions increases for high temperatures. This readily leads to supersaturation for nucleation, resulting in low SET voltages. The ion concentration required for spontaneous growth of Cu decreases with increasing temperature, which also reduces the SET voltage at high temperatures. The RESET voltage is determined by the size of the metal filament formed at a given temperature and its thermal stability against the surrounding temperature. The ON resistance of the Cu/Ta$_2$O$_5$/Pt cell was found to increase with increasing temperature, indicating that a narrower metal filament is formed at higher temperatures.[24] Thus, the RESET voltage also becomes smaller with a rise in temperature. The two cells exhibited a similar tendency in the temperature variations of the SET and RESET voltages, but the amount of those voltages was larger for the Cu/SiO$_2$/Pt cell than for the Cu/Ta$_2$O$_5$/Pt cell at any temperature.

3. Discussion

Based on the switching mechanism that we proposed in previous work,[23,24] the experimental results observed in the present study can be explained by three rate-limiting processes: the ionization of Cu at the anode interface, the migration of Cu ions in the oxide layer, and the ion concentration required for the nucleation of Cu. The results of Figure 3 and 4 were obtained under vacuum conditions after performing the forming and several subsequent switching cycles in atmosphere. Because an adequate amount of Cu ions required for the reformation of the metal filament is already present in the oxide layers, the ionization process at the anode interface would not be the rate-limiting process for the observed variations in the SET voltage. On the other hand, the ON resistance was nearly constant upon pressure reduction both for the Cu/Ta$_2$O$_5$/Pt and Cu/SiO$_2$/Pt cells, as shown in Figure S1 in the Supporting Information. The ON resistance reflects the size of the metal filament formed and is determined by the level of the supersaturation at which spontaneous growth of Cu occurs. Higher supersaturation leads to the formation of a smaller critical nucleus, but this nucleus grows a larger metal filament by incorporating a number of Cu ions from the surroundings with a high ion concentration, giving rise to a lower ON resistance.[24] The almost constant ON resistances (Figure S1) indicate that the supersaturation condition does not change much with the pressure decrease. Under these circumstances, the pressure dependence of the SET voltage could be determined by the migration process of Cu ions in the oxide layer. From Figure 3, it is expected that the migration speed of Cu ions is almost identical in the Ta$_2$O$_5$ layer but decreases in the SiO$_2$ layer with a reduction in the ambient H$_2$O pressure.

The migration of Cu ions is strongly influenced by the structure of the oxide layers. Ta$_2$O$_5$ and SiO$_2$ films sputtered at room temperature generally have a nanoporous structure consisting of piled, small grains, each of which exhibits an amorphous nature.[20,26] These nanoporous oxide materials absorb moisture during ambient exposure. As a result, water molecules adsorb

to the surface of the grains (pores) and thin layers of hydrogen-bonded water molecules might be formed at grain boundaries (pore walls). In such structures, Cu ions are more likely to migrate along the grain boundaries than inside the grains under the action of bias voltages, which is analogous to proton conduction in a hydrogen-bond network of polymer electrolyte membranes, such as Nafion.[27] Hence, the migration of Cu ions in thin oxide layers should be affected by ambient moisture. Recently, Zhao et al. calculated the Gibbs free-energy change for the moisture absorption reaction of SiO_2 and high-permittivity oxides in terms of thermodynamics.[28] They found that most of the rare earth oxides showed larger moisture-absorption-reaction rates compared to SiO_2. The relative attraction of moisture to oxides can be gauged from their polarities. Pauling's electronegativity difference between O and Si is 1.7, whereas the difference between O and Ta is 2.1.[29] Therefore, the metal–oxygen bonds in Ta_2O_5 are more polar (ionic) than those in SiO_2. The larger electronegativity difference for the Ta–O bonds leads to a higher affinity for moisture absorption of Ta_2O_5 than SiO_2.

To examine the chemical states of moisture-related species in Ta_2O_5 and SiO_2 layers, Fourier-transform infrared (FT-IR) absorption measurements were performed on relatively thick (100 nm) films deposited under identical sputtering conditions. **Figure 5**a and b show the FT-IR spectra of Ta_2O_5 and SiO_2 films, respectively, measured in a nitrogen atmosphere. For the Ta_2O_5 film, a very broad band extending from 3700 down to ~2600 cm^{-1} can be assigned to contributions of stretching vibrations of water molecules strongly bound to hydroxyl groups and hydrogen-bonded water molecules.[30] A small peak was also observed at 3740 cm^{-1}, which is probably due to hydroxyl groups. However, the SiO_2 film showed an asymmetric peak at ~3630 cm^{-1} and a shoulder around 3400 cm^{-1} with a tail on the lower wavenumber side. According to Davis and Tomozawa,[31] the former can be attributed to the OH stretching vibration of hydrogen-bonded silanol groups, and the latter corresponds to a combination of stretching vibrations originating from hydrogen-bonded water molecules and free water molecules, respectively. No peak due to isolated surface silanols, which is usually seen at 3747 cm^{-1},[30,32] was observed. The FT-IR results indicate that both the Ta_2O_5 and SiO_2 films contain a certain amount of residual water molecules although their bonding states are slightly different.

The insets of Figure 5 show the spectral change in a wavenumber range from 4000 to 3000 cm^{-1} upon evacuation of the ambient. For the Ta_2O_5 film, the spectral shape was almost identical both in nitrogen (black curves) and vacuum (gray curves) atmospheres (Figure 5a), suggesting that the residual water in the Ta_2O_5 film remains very stable under evacuation at room temperature. This is consistent with the result of Oshio et al., who found that desorption of residual water from sputtered TaO_x films takes place above 623 K in vacuum.[33] In contrast, the SiO_2 film exhibited that the intensity of an absorbance band between 3500 and 3100 cm^{-1} decreases with a reduction in pressure down to ~10^2 Pa, as indicated by the arrow in the inset of Figure 5b. This means that a portion of the residual water, probably hydrogen-bonded and free water molecules, in the SiO_2 film easily desorbs with a pressure decrease. Similar results were reported by Takeuchi et al., who investigated the
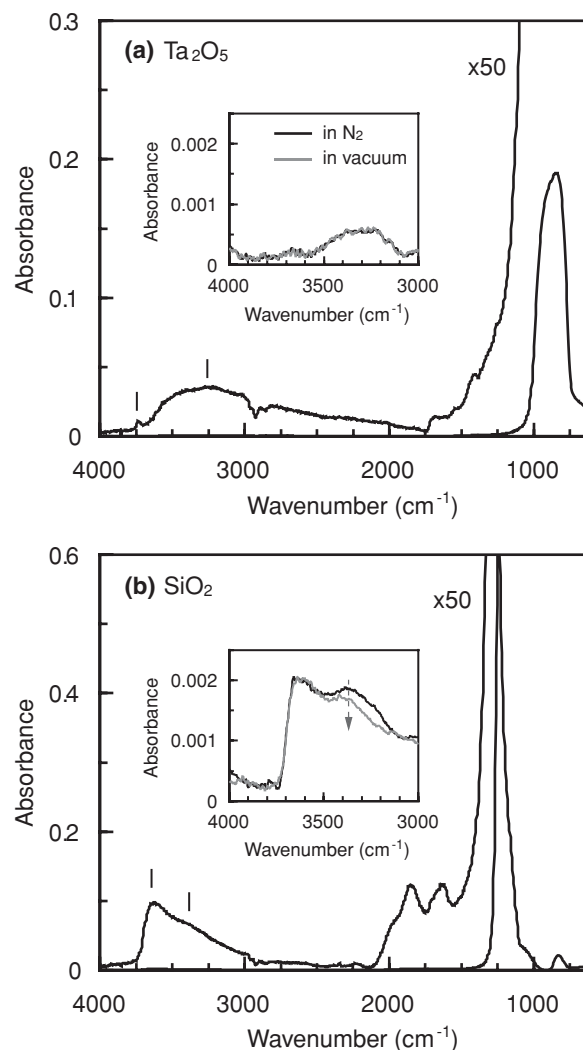
Figure 5. FT-IR spectra of Ta_2O_5 (a) and SiO_2 (b) films sputtered on an Au-covered silicon substrate, measured in a nitrogen atmosphere. Spectral features up to 1200 cm^{-1} correspond to the fundamental vibrational bands of two oxides. Peaks at 1630 and 1850 cm^{-1} and a shoulder at ~1990 cm^{-1} seen in (b) are attributed to combination/overtone bands of the silica matrix. The insets show the spectral change in the absorbance bands due to residual water-related species in nitrogen (black curves) and vacuum (~10^2 Pa, gray curves) atmospheres.

adsorption states of water molecules on several oxide surfaces by means of FT-IR and near-infrared (NIR) spectroscopy.[34] Their FT-IR spectra revealed that water molecules adsorbed on SiO_2 surfaces were easily removed by evacuation compared to TiO_2 and Al_2O_3 surfaces. In combination with the analysis of contributions of hydrogen-bonded water molecules in the NIR region, Takeuchi et al. concluded that water molecules weakly interact with SiO_2 surfaces by hydrogen bonds to silanol groups but strongly interact with TiO_2 and Al_2O_3 surfaces by intermolecular hydrogen bonds. Because water molecules are strongly polarized due to the high electronegativity of oxygen, they bind more strongly with positively charged TiO_2 and Al_2O_3 surfaces with a larger isoelectric point. Stronger interactions with water molecules of Ta_2O_5 surfaces than SiO_2 surfaces is also expected,

www.MaterialsViews.com

ADVANCED
FUNCTIONAL
MATERIALS
www.afm-journal.de

FULL PAPER

because of the larger isoelectric point of Ta_2O_5 compared to SiO_2.[35]

The presence of residual water can also affect the ionization process of Cu at the anode interface. Based on the discussion by Willis and Lang,[36] there are several possible mechanisms for the ionization of Cu at the interface with oxides under the application of positive bias. The first mechanism is an "anodization-like" process in which Cu atoms are injected directly into the oxide layer by the following dissolution reaction $Cu \rightarrow Cu^{z+} + ze^-$. The cation valence z is either 1 or 2. The second mechanism is the oxidation of Cu atoms at the Cu/oxide interface due to reduction of the oxide. As a result, Cu_xO is formed at the anode interface and Cu ions are injected from the oxidized Cu. The third mechanism is the chemical oxidation of Cu atoms via ambient gases such as H_2O and O_2 or via out-gassing of the oxide. Exposure of Cu to moisture might lead to the formation of Cu_2O, CuO, and nonstoichiometric phases (for example, Cu_3O_2) at the interface.[37] In the latter two mechanisms, the oxidized Cu can act as a source of Cu ions, which then are available for subsequent migration under the action of electrical bias.[38] The anodization and the reduction of oxide are independent on the ambient moisture in principle, but the chemical oxidation is strongly influenced by the ambient moisture and the presence of water or oxygen in the oxide layer.

The $Cu/Ta_2O_5/Pt$ cell showed stable switching cycles after forming both under atmospheric and vacuum conditions, whereas the $Cu/SiO_2/Pt$ cell exhibited no switching behavior after the transition to a low-resistance state in vacuum. These different initial switching behaviors in vacuum seem to suggest different ionization processes of Cu between the two cells. Because the switching behavior of the $Cu/Ta_2O_5/Pt$ cell is independent of the ambient H_2O pressure, the ionization at the Cu/Ta_2O_5 interface may be caused by either the anodization or the reduction of oxide. In contrast, the ionization at the Cu/SiO_2 interface can be attributed to chemical oxidation due to the switching failure of the $Cu/SiO_2/Pt$ cell with decreasing pressure. However, given that the residual water remains stable in the Ta_2O_5 layer but easily desorbs from the SiO_2 layer in vacuum, it is reasonable to assume that Cu is ionized at both interfaces by chemical oxidation via the residual water. The $Cu/Ta_2O_5/Pt$ cell always shows forming and subsequent switching behavior, regardless of ambient H_2O pressure, because of the high stability of the residual water in the Ta_2O_5 layer. On the other hand, the $Cu/SiO_2/Pt$ cell exhibits stable switching cycles in atmosphere, just as the $Cu/Ta_2O_5/Pt$ cell (Figure 1b). However, as the cell is subjected to vacuum, the chemical oxidation is significantly inhibited due to a decrease in the amount of the residual water, and the injection rate of Cu ions drastically decreases. As a consequence, the formation of a metal filament becomes difficult even at high bias voltages, and finally an irreversible resistive change occurs, which corresponds to electrical breakdown commonly observed in amorphous oxide layers.[39] Thus, under vacuum conditions, electrical breakdown occurs before the metal filament is formed.

From the above discussions, we infer the moisture effect on the switching kinetics of Ta_2O_5- and SiO_2-based gapless-type atomic switches, as illustrated in **Figure 6**. Sputtered, thin oxide layers have a nanoporous structure in which small amorphous grains with a size of a few nanometers are randomly piled up,
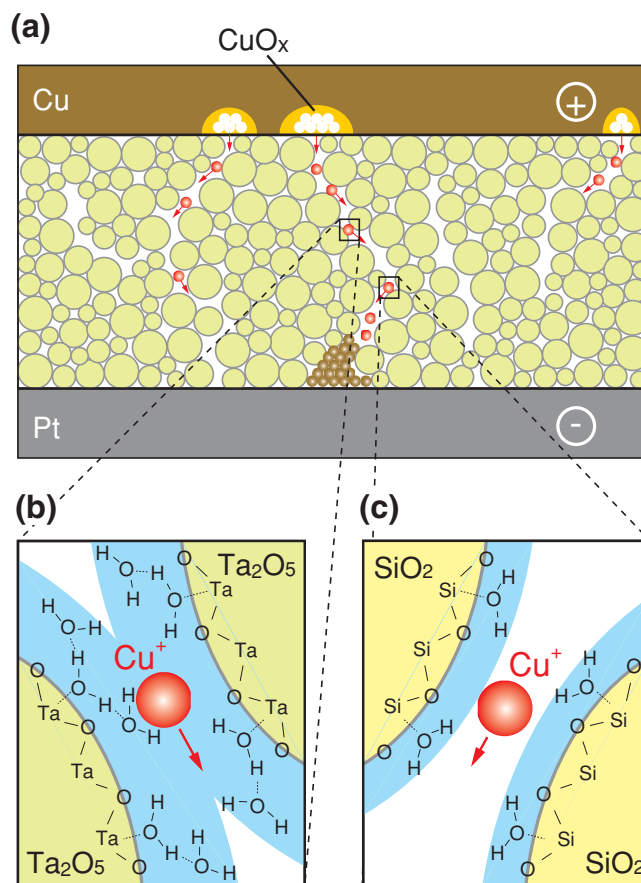
Figure 6. Potential mechanism for the moisture effects on the ionization of Cu and the migration of Cu ions in an oxide-based atomic switch (a). Schematics (b) and (c) illustrate the bonding states of residual water molecules at grain boundaries in Ta_2O_5 and SiO_2 layers, respectively.

as shown in Figure 6a. In the Ta_2O_5 layer, water molecules bound to hydroxyl groups and strongly hydrogen-bonded to one another adsorb on the surface of grains, forming a hydrogen-bond network at grain boundaries, as illustrated in Figure 6b. However, in the SiO_2 layer, water molecules are weakly bound to silanol groups on the grain surface, as illustrated in Figure 6c. When positive bias is applied to the Cu anode, Cu atoms are first oxidized at the anode interface by chemical oxidation via the residual water, and Cu ions are injected from the oxidized Cu into the oxide layer by the dissolution reaction. This dissolution reaction is accompanied by counter charges that are mainly electrons, but it can be influenced by the presence of residual water molecules and mobile protons.[37] Because the first ionization energy of Cu is approximately one-third of its second ionization energy and because the solid solubility of higher ionized states of most metals is much lower than that of the singly ionized state,[40] singly ionized Cu ions, Cu^+, are primarily created. Then, they migrate along the grain boundaries toward the Pt cathode by hopping mechanisms similar to proton conduction in hydrated polymer electrolyte membranes.[41] This migration eventually leads to supersaturation on the Pt cathode (or a remaining Cu precipitate), and the metal filament is formed between the electrodes by nucleation

FULL PAPER

and subsequent growth of Cu. The residual water in the Ta_2O_5 layer is very stable due to strong hydrogen bonds and remains unchanged even in vacuum, which has almost no influence on the migration of Cu ions. Hence, the operation voltages of the $Cu/Ta_2O_5/Pt$ cell are independent of the reduction in ambient H_2O pressure. In the $Cu/SiO_2/Pt$ cell, the chemical oxidation of Cu is inhibited by desorption of residual water, and therefore the injection of Cu ions into the SiO_2 layer is significantly suppressed with decreasing ambient H_2O pressure. Moreover, desorption of the residual water might result in partial defects in the hydrogen-bond network at the grain boundaries and reduces the migration speed of Cu ions. The reduction both in the injection rate and migration speed of Cu ions should retard the formation of the metal filament. Thus, the forming and SET voltages of the $Cu/SiO_2/Pt$ cell increase with decreasing ambient H_2O pressure.

The moisture effect that we proposed here is applicable to other oxide-based atomic switches and ECMs. However, it is emphasized that the effect depends strongly on the fabrication process of the cells as well as the structural and chemical properties of the oxide layers such as composition, density, crystallinity, polarity of the metal-oxygen bonds, and affinity for moisture absorption. In fact, we also measured cells with Al_2O_3 and TiO_2 layers. The former showed no significant influence of the moisture but the ON state was usually unstable, and the latter also exhibited the valence charge mechanism (VCM),[5] so that it was difficult to distinguish between atomic switch (ECM) and VCM behaviors. Careful investigations are required to clarify the effects of moisture on the switching characteristics.

In Figure 4, the decrease in the SET voltage with a rise in temperature is explained by an increase in the migration speed of Cu ions and a lowering of the ion concentration required for the nucleation of Cu, as described above. The SET and RESET voltages of the $Cu/Ta_2O_5/Pt$ cell decreased in magnitude more rapidly than those of the $Cu/SiO_2/Pt$ cell. As a result, the $Cu/Ta_2O_5/Pt$ cell showed a transition from nonvolatile switching to volatile switching, in which the cell is RESET with no negative bias application. In contrast, the $Cu/SiO_2/Pt$ cell retained its nonvolatile switching even at high temperatures. The different switching behaviors with respect to temperature cannot be solely explained by assuming that the migration speed of Cu ions is lower in the SiO_2 layer than in the Ta_2O_5 layer, because a lower migration speed results only in an increase of the SET voltages. This means that the temperature variation of the ion concentration required for nucleation also depends on the oxide material, but we cannot draw further conclusions at this stage. It is necessary through future research to clarify the mechanisms that determine the temperature variations in the switching characteristics of different oxide materials.

4. Conclusions

The operational characteristics of $Cu/Ta_2O_5/Pt$ and $Cu/SiO_2/Pt$ cells were examined as a function of ambient water vapor pressure and temperature, to reveal the effect of moisture on the resistive switching behavior of gapless-type atomic switches using oxide thin layers. After a forming process at higher positive bias to the Cu anode, both cells exhibited bipolar switching behavior in which they were SET at positive bias and RESET at negative bias. The forming and SET voltages were always higher for the $Cu/Ta_2O_5/Pt$ cell than for the $Cu/SiO_2/Pt$ cell under the identical bias sweep condition. The $Cu/Ta_2O_5/Pt$ cell exhibited stable switching behavior regardless of the ambient H_2O pressure. In contrast, if the application of bias voltage to the $Cu/SiO_2/Pt$ cell was started in vacuum, the cell showed no resistive switching and only an electrical breakdown occurred at high bias voltages. When the cells were subjected to vacuum after forming in atmosphere, the SET and RESET voltages of the $Cu/Ta_2O_5/Pt$ cell remained almost constant, while those of the $Cu/SiO_2/Pt$ cell increased in magnitude. The ambient H_2O pressure effect on the $Cu/SiO_2/Pt$ cells was reversible. FT-IR measurements showed the presence of a certain amount of residual water in both the Ta_2O_5 and SiO_2 layers, which is absorbed from the air ambient. It was found that the residual water remained very stable in the Ta_2O_5 layer but easily desorbed from the SiO_2 layer with a reduction in the ambient H_2O pressure. From the results obtained, we concluded that the ionization of Cu at the anode interface is attributed to chemical oxidation via residual water. The moisture absorption also results in the formation of a hydrogen-bond network at grain boundaries in the oxide layers, and Cu ions are likely to migrate along the grain boundaries. Due to strong hydrogen bonds in the Ta_2O_5 layer, the operation voltages of the $Cu/Ta_2O_5/Pt$ cell are independent of the ambient H_2O pressure. On the contrary, the switching behavior of the $Cu/SiO_2/Pt$ cell is significantly influenced by ambient conditions because residual water easily desorbs from the SiO_2 layer. As the temperature was increased up to approximately 600 K, the $Cu/Ta_2O_5/Pt$ cell exhibited a transition from nonvolatile switching to volatile switching, whereas the $Cu/SiO_2/Pt$ cell retained its nonvolatile switching behavior. The origin of the different switching behaviors with temperature is still unclear. Further investigations are necessary to obtain more detailed informations about the correlations between the switching kinetics and the structural and chemical properties of the oxide layer.

5. Experimental Section

The $Cu/Ta_2O_5/Pt$ and $Cu/SiO_2/Pt$ cells were fabricated on quartz or SiO_2-covered silicon substrates. All of the layers were deposited at room temperature by radio-frequency sputtering using metal masks with different patterns. First, 10-nm-thick Ti and 50-nm-thick Pt layers were deposited as the adhesion layer and the bottom electrode, respectively, under an Ar pressure of 0.7 Pa. Then, a Ta_2O_5 or SiO_2 layer was deposited using polycrystalline targets with a 50-% Ar and 50-% O_2 gas mixture. The sputtered oxide layers are amorphous in nature, as confirmed by X-ray diffraction. Two different thicknesses of the oxide layers were used (7.5 and 15 nm for Ta_2O_5, 8.5 and 17 nm for SiO_2). Finally, a 50-nm-thick Cu layer was deposited as the top electrode. Each cell consisted of a cross-point structure with a junction area of 20 μm × 20 μm. Current–voltage (I–V) measurements were performed using a home-made, high-vacuum prober that can operate over a wide temperature range (88 ~ 600 K) and a semiconductor characterization system (Keithley 4200SCS). A bias voltage was applied to the Cu electrode and swept as indicated by the arrows and numbers in Figure 1 at a constant voltage sweep rate of approximately 0.1 V s⁻¹. The Pt electrode was electrically grounded in all of the measurements. The current compliance was set to 30 μA for the positive bias polarity to regulate the ON-state current.

www.MaterialsViews.com

ADVANCED
FUNCTIONAL
MATERIALS
www.afm-journal.de

FULL PAPER

FT-IR measurements were performed on 100-nm-thick films of Ta_2O_5 and SiO_2 that were sputtered on Au-covered silicon substrates under identical conditions. IR absorption spectra were recorded in reflection geometry with a 75° angle of incidence with p-polarized light (RAS mode) using an FT-IR spectrometer (ThermoFisher Scientific Nicolet 6700, equipped with a MCT detector). The spectral resolution was set at 8 cm^{-1}. To minimize the influence of carbon dioxide and water in air, the spectrometer was purged with dry nitrogen gas during the measurements. The background of the obtained spectra was calibrated with an Au-covered silicon substrate. The difference in the spectral shape under nitrogen and vacuum atmospheric conditions were measured in RAS mode using another FT-IR spectrometer (JASCO FT/IR-6300V, equipped with a MCT detector) with a spectral resolution of 8 cm^{-1}. To perform the measurements in vacuum, the sample chamber in the spectrometer was evacuated down to ~10^2 Pa using a rotary pump.

Supporting Information

Supporting Information is available from the Wiley Online Library or from the author.

Acknowledgements

[1] R. Waser, M. Aono, *Nat. Mater.* **2007**, *6*, 833.
[2] T. Hasegawa, Y. Itoh, H. Tanaka, T. Hino, T. Tsuruoka, K. Terabe, H. Miyazaki, K. Tsukagoshi, S. Yamaguchi, M. Aono, *Appl. Phys. Exp.* **2011**, *4*, 015204.
[3] K. Terabe, T. Hasegawa, T. Nakayama, M. Aono, *Nature* **2005**, *433*, 47.
[4] T. Hasegawa, K. Terabe, T. Sakamoto, M Aono, *MRS Bull.* **2009**, *34*, 929.
[5] R. Waser, R. Dittmann, G. Staikov, K. Szot, *Adv. Mater.* **2009**, *21*, 2632.
[6] I. Valov, R. Waser, J. R. Jameson, M. N. Kozicki, *Nanotechnology* **2011**, *22*, 254003.
[7] T. Hino, T. Hasegawa, K. Terabe, T. Tsuruoka, A. Nayak, T. Ohno, M. Aono, *Sci. Technol. Adv. Mater.* **2011**, *12*, 013003.
[8] T. Sakamoto, H. Sunamura, H. Kawaura, K. Terabe, T. Hasegara, T. Nakayama, M. Aono, *Appl. Phys. Lett.* **2003**, *82*, 3032.
[9] M. Morales-Masis, S. J. van der Molen, W. T. Fu, M. B. Haselberth, J. M. Ruithebeek, *Nanotechnology* **2009**, *20*, 095710.
[10] C. Schindler, I. Valov, R. Waser, *Phys. Chem. Chem. Phys.* **2009**, *11*, 5974.
[11] U. Russo, D. Kamalanathan, D. Ielmini, A. L. Lacaita, M. N. Kozicki, *IEEE Trans. Electron Devices* **2009**, *56*, 1040.
[12] S. Wu, T. Tsuruoka, K. Terabe, T. Hasegawa, J. P. Hill, K. Ariga, M. Aono, *Adv. Func. Mater.* **2011**, *21*, 93.
[13] T. Sakamoto, K. Lister, N. Banno, T. Hasegawa, K. Terabe, M. Aono, *Appl. Phys. Lett.* **2007**, *91*, 092110.
[14] a)C. Schindler, G. Staikov, R. Waser, *Appl. Phys. Lett.* **2008**, *92*, 122910; b) C. Schindler, M. Weides, M. N. Kozicki, R. Waser, *Appl. Phys. Lett.* **2009**, *94*, 072109.
[15] Y. Bernard, P. Gonon, V. Jousseaume, *Appl. Phys. Lett.* **2010**, *96*, 193502.
[16] M. N. Kozicki, C. Gopalan, M. Balakrishnan, M. Mitkova, *IEEE Trans. Nanotechnol.* **2006**, *5*, 535.
[17] W. Gua, M. Lui, S. Long, Q. Liu, W. Wang, *Appl. Phys. Lett.* **2008**, *93*, 223506.
[18] M. Haemori, T. Nagata, T. Chikyo, *Appl. Phys. Exp.* **2009**, *2*, 061401.
[19] X. B. Yan, K. Li, J. Yin, Y. D. Xia, H. X. Guo, L. Chen, Z. G. Liu, *Solid State Lett.* **2010**, *13*, H87.
[20] J. M. Ngaruiya, S. Venkataraj, R. Drese, O. Kappertz, T. P. Leedvad Pedersen, M. Wuttig, *Phys. Status Solidi a* **2003**, *198*, 99.
[21] Y. Zhao, M. Toyama, K. Kita, K. Kyuno, A. Toriumi, *Appl. Phys. Lett.* **2006**, *88*, 072904.
[22] N. Kaihovirta, H. Aarnio, C.-J. Wikamn, C.-E. Wilén, R. Österbacka, *Adv. Func. Mater.* **2010**, *20*, 2605.
[23] T. Tsuruoka, K. Terabe, T. Hasegawa, M. Aono, *Nanotechnology* **2010**, *21*, 425205.
[24] T. Tsuruoka, K. Terabe, T. Hasegawa, M. Aono, *Nanotechnology* **2011**, *22*, 254013.
[25] T. Tsuruoka, K. Terabe, T. Hasegawa, M. Aono, unpublished.
[26] Y. Kobayashi, W. Zheng, T. B. Chang, K. Hirata, R. Suzuki, T. Ohdaira, K. Ito, *J. Appl. Phys.* **2002**, *91*, 1704.
[27] K. D. Kreuer, *J. Membr. Sci.* **2001**, *185*, 29.
[28] Y. Zhao, K. Kita, A. Toriumi, *Appl. Phys. Lett.* **2010**, *96*, 242901.
[29] P. Raghu, N. Rana, C. Yim, E. Shero, F. Shadman, *J. Electrochem. Soc.* **2003**, *150*, F186.
[30] M. Takeuchi, L. Bertinetti, G. Martra, S. Coluccia, M. Anpo, *Appl. Catal. A- Gen.* **2006**, *307*, 13.
[31] K. M. Davis, M. Tomozawa, *J. Non-cryst. Solids* **1996**, *201*, 177.
[32] B. A. Morror, I. A. Cody, Lydia S. M. Lee, *J. Phys. Chem.* **1976**, *80*, 2761.
[33] S. Oshio, M. Yamamoto, J. Kuwata, T. Matsuoka, *J. Appl. Phys.* **1992**, *71*, 3471.
[34] M. Takeuchi, G. Martra, S. Coluccia, M. Anpo, *J. Near Infrared Spectrosc.* **2009**, *17*, 373.
[35] *Chemical Properties of Material surfaces*, (Ed: M. Kosmuiski), Chapman & Hall, London **1993**.
[36] B. Willis, D. V. Lang, *Thin Solid Films* **2004**, *467*, 284.
[37] O. R. Rodriguez, W. Cho, R. Saxena, J. L. Plawsky, W. N. Gill. *J. Appl. Phys.* **2005**, *98*, 024108.
[38] L. P. Shepherd, A. Mathew, B. E. McCandless, B. G. Willis, *J. Vac. Sci. Technol. B.* **2006**, *24*, 1297.
[39] G. Dearnaley, A. M. Stoneham, D. V. Morgan, *Rep. Prog. Phys.* **1970**, *33*, 1129.
[40] P. Jain, J. S. Juneja, A. Mallikarjunan, E. J. Rymaszewski, T.-M. Lu, *Appl. Phys. Lett.* **2006**, *88*, 143502.
[41] A. Paciaroni, M. Casciola, E. Cornicchi, M. Marconi, G. Onori, M. Pica, R. Narducci, *J. Phys. Chem. B* **2006**, *110*, 13769.

FULL PAPER

Encapsulation of Perchlorate Salts within Metal Oxides for Application as Nanoenergetic Oxidizers

Chunwei Wu, Kyle Sullivan, Snehaunshu Chowdhury, Guoqiang Jian, Lei Zhou, and Michael R. Zachariah*

In this work, high-oxygen-content strong oxidizer perchlorate salts were successfully incorporated into current nanothermite composite formulations. The perchlorates were encapsulated within mild oxidizer particles through a series of thermal decomposition, melting, phase segregation, and recrystallization processes, which occurred within confined aerosol droplets. This approach enables the use of hygroscopic materials by stabilizing them within a matrix. Several samples, including $Fe_2O_3/KClO_4$, $CuO/KClO_4$ and Fe_2O_3/NH_4ClO_4 composite oxidizer particles, have been created. The results show that these composite systems significantly outperform the single metal oxide system in both pressurization rate and peak pressure. The ignition temperatures for these mixtures are significantly lower than those of the metal oxides alone, and time-resolved mass spectrometry shows that O_2 release from the oxidizer also occurs at a lower temperature and with high flux. The results are consistent with O_2 release being the controlling factor in determining the ignition temperature. High-speed imaging clearly shows a much more violent reaction. The results suggest that a strategy of encapsulating a very strong oxidizer, which may not be environmentally compatible, within a more stable weak oxidizer offers the opportunity to both tune reactivity and employ materials that previously could not be considered.

1. Introduction

Nanothermite, a subset of metastable intermolecular composites (MIC), is a relatively new class of energetic materials (EMs) that is finding applications in propellants and explosives, as well as microscale energetic material applications and micro-electromechanical systems (MEMS).[1,2] These solid-state redox reaction systems have in common very rapid, exothermic and self-propagating behavior. With respect to traditional inorganic solid-state EMs, which are a mixture of fine powders of oxidizer and reducing agent, nanothermite is characterized by

nanoscale constituents that enable intimate mixing of the fuel and oxide, whose nanodimensional homogeneity results in substantial enhancement in heat and mass diffusion, and therefore in reactivity and burn rate.[3–5] It has been experimentally observed that the activation energy for nanoaluminum oxidization and for the oxidizer decomposition is significantly lower than the corresponding values for their macroscopic counterparts,[6] and the higher surface area of nanoaluminum presumably is at least partially responsible for the higher reaction rate and facilitates energy transfer.[7] Aumann et al. were some of the first to see the enhanced performance that nanoenergetic materials could potentially deliver, with a 1000 x increase in reactivity.[8] It has been speculated that this increase in reaction-propagation rate is related to the mode of energy transfer in a composite, which likely shifts from conductive to convective mode.[9,10] These results have been confirmed by further studies by others who have shown that the packing density is inversely correlated with reaction velocity and that intimacy of mixing is a key variable.[11]

This latter point suggests that the manner of assembling the fuel and oxidizer either through physical mixing, or through direct assembly and microstructure manipulation, may yield new and more controllable properties. This approach has lead to, for example, self-assembled Al/Fe_2O_3 nanotubes,[7] self-assembled Al/CuO nanorods,[12,13] nanowired Al/CuO,[2,14] electrostatically assembled Al/Fe_2O_3 nanoparticles,[15] and Al/SnO_2 coating by atomic layer deposition (ALD).[16]

While there is a wide variety of possible metal and oxidizer combinations for thermite mixtures, aluminum (Al) is most often the fuel choice, due to its availability, high reaction enthalpy, low ignition temperature, high thermal conductivity, and the passivation nature of its native oxide. Furthermore, the high negative enthalpy of the oxide of aluminum (Al_2O_3) offers many possible low-cost metal oxides as possible oxidizers, including Fe_2O_3, CuO, MoO_3, Bi_2O_3, WO_3, and SnO_2, etc.[1,17,18]

On the other hand, one can envision many other more powerful oxidizer molecules; many of these are typically composed of salts. For example, ammonium perchlorate (AP) is a very labile species composed of the perchlorate ion ClO_4^-, with

Dr. C. Wu, K. Sullivan, S. Chowdhury, L. Zhou, Prof. M. R. Zachariah
Department of Mechanical Engineering
University of Maryland
College Park, MD 20742, USA
E-mail: mrz@umd.edu
G. Jian, M. R. Zachariah
Department of Chemistry and Biochemistry
University of Maryland
College Park, MD 20742, USA

www.MaterialsViews.com

ADVANCED
FUNCTIONAL
MATERIALS
www.afm-journal.de

FULL PAPER

chlorine in an oxidation state of +7. The high oxygen content and good thermal stability of perchlorates have made them indispensible ingredients for the pyrotechnics industry and as key ingredients in solid rocket propellants. For example, composite solid rocket propellants typically contain 60 wt%–80 wt% ammonium perchlorate (AP), together with a polymer binder [e.g., polybutadiene acrylic acid acrylonitril terpolymer (PBAN), hydroxyl-terminated polybutadiene (HTPB), nitramines, tetrazoles, and nitrourethanes] and metallic fuel like aluminum powder.[19] In microscale MEMS applications, perchlorates such as $Ca(ClO_4)_2$, $KClO_4$ and $NaClO_4$ have been incorporated into nanoporous silicon by impregnation or a vapor deposition technique.[1,20] Among the various perchlorate salts, AP is the most widely used today as it yields high heat and high oxygen content. Potassium perchlorate (PP) is also a good solid propellant additive because of its fast burn rate and high caloric value.

Unfortunately, these oxidizers have not found application in MIC formulations due to their highly hygroscopic nature, which poses long -erm stability constraints on the nanofuel (e.g., aluminum). Perchlorate release, due to its water solubility, has raised many environmental concerns during manufacture, transport, and launch operations.[21]

Ideally one would like to harness the oxidizer properties of perchlorates, with the longevity and stability offered by traditional metal oxides. Herein we focus on developing a generic strategy of encapsulation of the strong oxidizer within a relatively mild and insoluble oxidizer. This strategy was previously tested by us in the fabrication of a core-shell-structured $Fe_2O_3/KMnO_4$ which showed enhanced performance characteristics.[22] In the current work, we describe a generic method to produce composite-structure oxidizer particles, with several powerful oxidizer perchlorates being successfully encapsulated within common inorganic oxides such as Fe_2O_3 and CuO. The synthesis is realized via an aerosol-based spray drying/pyrolysis method, by employing careful control of the precursor-decomposition and melting processes. The aerosol technique enables formation of nanosized perchlorate particles via a process of recrystallization out of solution phase within an aerosol droplet, and simultaneous encapsulation of each perchlorate particle with an oxide shell, which is derived from the thermal decomposition of a metal nitrate precursor. The resulting materials are tested for their combustion behavior and compared with existing formulations.

2. Results and Discussion

2.1. Synthesis of $Fe_2O_3/KClO_4$, $CuO/KClO_4$ and Fe_2O_3/NH_4ClO_4 Composite Oxidizer

Microstructure control of the composite particles was realized by tuning the temperatures of the two furnaces that govern the thermal decomposition of the metal nitrates and the melting of the perchlorate. In a typical synthesis (e.g., $Fe_2O_3/KClO_4$), a precursor aqueous solution of iron (III) nonahydrate and potassium perchlorate was sprayed into aerosol droplets by an atomizer. The molar ratio of the starting components Fe/K was fixed at 1:2, and the total salt precursor concentration was kept constant at 5.0 wt%. The temperature of the first furnace (T_1) was set at 125 °C and the second (T_2) at 550 °C.

Before or just entering the first furnace, water evaporation from the droplet drives the crystallization or precipitation of both iron nitrate and potassium perchlorate. Each aerosol droplet may be considered as a microreactor containing a solid mixture of the two starting component salts. In the first furnace, iron nitrate ($T_{decomp(Fe(NO_3)_3)}$ = 125 °C) decomposes to form iron oxide while potassium perchlorate ($T_{m.p.(KClO_4)}$ = 525 °C) remains a solid. From the TEM image in **Figure 1** one can clearly see the distinct core-shell morphology. This structure

600nm

Figure 1. TEM image (left) and EDS line scan analysis (right) of the composite $Fe_2O_3/KClO_4$ particles, revealing the elemental concentration profile of Fe, O, K and Cl across the line, [Fe/K] = ½ in precursor solution.

was confirmed by use of EDS line-scan analysis (Figure 1) to identify the elemental profile of Fe, O, K, and Cl along the selected line across the particles. Quite clearly we have created a structure of a very strong oxidizer encapsulated within a weak oxidizer shell.

While the mechanism of formation is unknown, we can speculate on likely routes. In one case the drying droplet results in a homogeneously dispersed solid particle containing the two precursors. In the first furnace thermal decomposition of the iron precursor leads to small iron oxide clusters within the solid $KClO_4$ matrix. As the temperature is raised to the melting point of $KClO_4$, i.e., in the second furnace, the solid matrix becomes molten and liquidlike. At this point the iron oxide clusters become mobile, and begin to aggregate and coalesce at the exterior of the aerosol particle due to surface-tension forces. As the particles cool down, the molten $KClO_4$ recrystallizes to form a solid core that is encapsulated by the exterior oxide shell.

A second possibility is that the core-shell structure is created during the drying process and before the chemistry is initiated, which results in a core-shell $KClO_4/Fe(NO_3)_3$ structure. However the perchlorate is about 80 times less soluble than the iron precursor (at room temperature), so one would expect that if this was occurring the perchlorate would be on the outside, where the evaporation of the solvent would cause the local concentration of the solute to be the highest and leading to precipitation of the least soluble component first. In either case it is clear from the figure that the perchlorate is in the interior, that a near perfect phase separation has occurred, and that crystallization of the perchlorate causes the shell to take on a non-spherical shape.

In order to clarify the microstructure formation mechanism, we conducted another similar experiment at lower temperatures, i.e., $T_1/T_2 = 90\ °C/90\ °C$, in which no decomposition of iron nitrate or melting of perchlorate could occur. **Figure 2** exhibits the TEM image along with the EDS analysis of

the derived particles. It is quite clear that a core-shell structure is formed during the drying/precipitation. However, in this case considerably more iron can be found within the core of the particles and less potassium than in the previous case. This result suggests that, despite the lower solubility of the perchlorate, a net phase-separation process occurs during the droplet evaporation process that creates the core-shell structure. Apparently heating the particle to create the oxide and then subsequently melt the perchlorate serves to further drive the phase-separation process.

The copper oxide/potassium perchlorate ($CuO/KClO_4$) composite structure shown in **Figure 3**, was obtained at $T_1/T_2 = 400\ °C/550\ °C$. As in the iron example, the choice of temperatures was governed by the decomposition and melting points. In this example, as before, the nitrate has a much higher solubility than the perchlorate. While the structure is obviously core-shell, crystallization of the perchlorate has clearly been disrupted. Careful examination of the TEM image reveals small CuO crystallites dispersed throughout, which could result from the incomplete coalescence and aggregation of CuO primary particles from the molten $KClO_4$ matrix. Possibly this result is because in this case the reactor temperatures are very close to each other, due to the relatively high decomposition temperature of the copper precursor. So in this case the material can be best described as CuO-rich shell composite.

The influence of phase segregation on morphology is even more prominent for the iron oxide/ammonium perchlorate ($]Fe_2O_3/NH_4ClO_4)]$ system, which was experimentally achieved with $T_1/T_2 = 125\ °C/200\ °C$ and is shown in **Figure 4**. EDS analysis indicates that the two components form a homogeneous hollow shell. In this case both components behave similarly as under conditions seen for spray pyrolysis, in which solvent evaporation from the droplet leads to a hollow structure. In our case the two solutes have solubilities that are similar (ca. sixfold difference at room temperature).
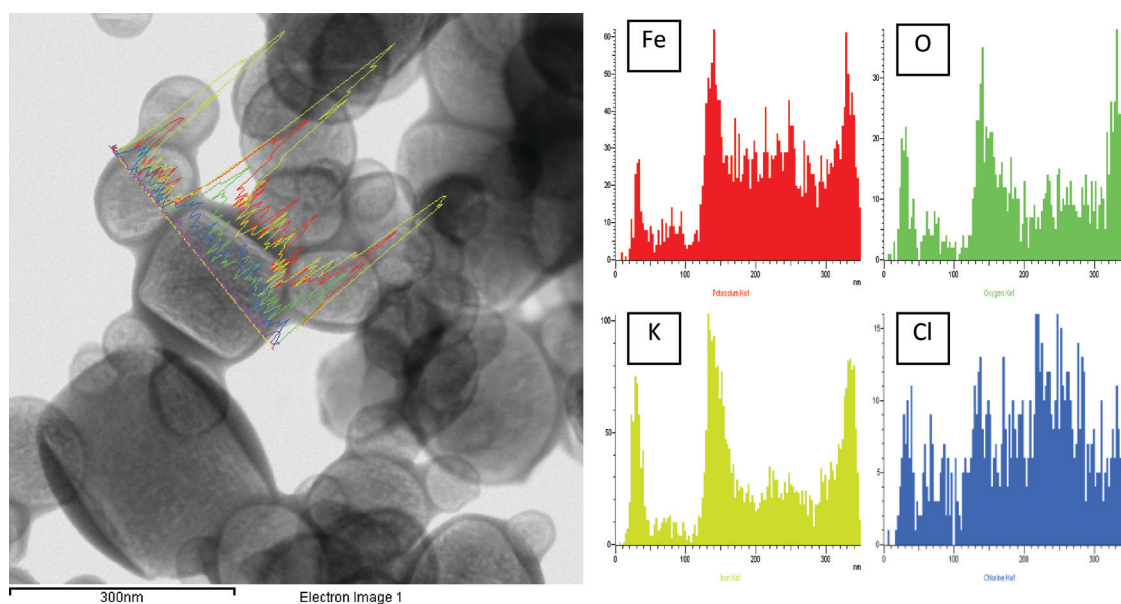
Figure 2. TEM image (left) and EDS line-scan analysis (right) of the composite $Fe_2O_3/KClO_4$ particles obtained at $T_1/T_2 = 90\ °C/90\ °C$.

www.MaterialsViews.com

ADVANCED
FUNCTIONAL
MATERIALS
www.afm-journal.de

FULL PAPER

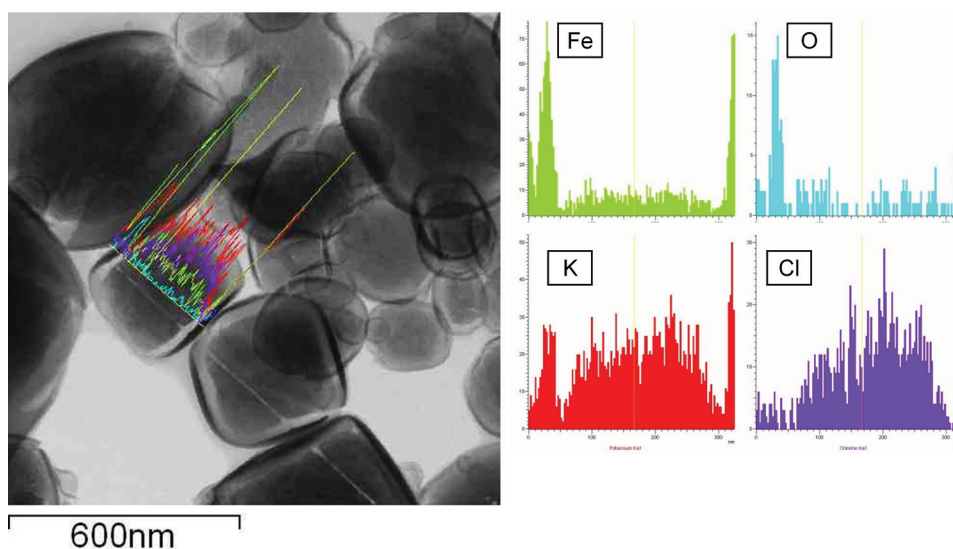**Figure 3.** TEM image (left) and EDS line scan analysis (right) of the composite $CuO/KClO_4$ particles, revealing the elemental concentration profile of Cu, O, K, and Cl across the line, [Cu/K] = ½ in precursor solution.

2.2. Characterizations of Combustion Performance

The relative reactivity for stoichiometric (i.e., equivalence ratio $\varphi = 1$) mixtures of nano-Al with the oxidizers was measured using the combustion cell. The pressure signals are shown for the various synthesized oxidizers in **Figure 5**a along with CuO nanopowder (≈50 nm, Sigma-Aldrich) and Fe_2O_3 nanopowder (<50 nm, Sigma-Aldrich) as reference materials. All systems except Fe_2O_3 show a fast pressure rise which occurs on the order of microseconds. The perchlorate materials, however, exhibit much higher overpressures than the reference CuO (purple curve) and Fe_2O_3 (light blue curve, barely seen on this scale). Another qualitative comparison is with the Al/Bi_2O_3 system. Martirosyan et al.[23] demonstrated the highest pressure pulse for Al/Bi_2O_3 among reported thermite reactions, which suggests that this extraordinary high pressure results from

evaporation of the combustion product Bi, whose boiling point is lower than the maximum reaction temperature. A pressurization rate of up to 650 GPa s^{-1} (≈94.3 psi μs^{-1}) was shown in their study, which is considerably lower than that achieved in our materials, without considering the larger sample mass/cell volume ratio of their testing system (i.e., 500 mg/85 cm^3 vs. 25 mg/13 cm^3). The peak pressure, rise time, and pressurization rate are summarized in **Table 1**.

The corresponding optical emission for the same systems is shown in Figure 5b. In this case, some obvious differences were seen for the various systems. The oxidizers containing CuO exhibited an intense optical rise and decay, whereas the oxidizers with Fe_2O_3 showed a much weaker optical signal with a prolonged "tail". In all cases, the timescale of optical emission was several hundred microseconds, much longer than the rise time of the pressure signal.
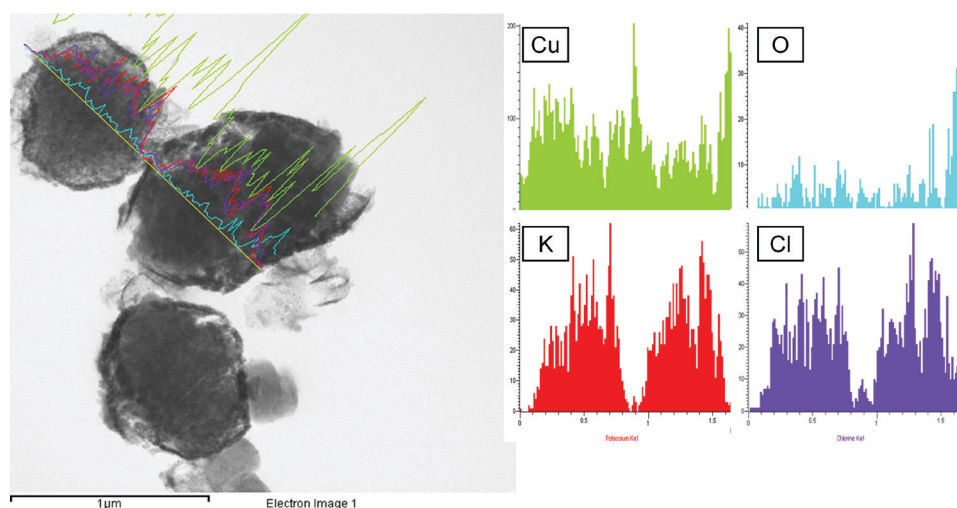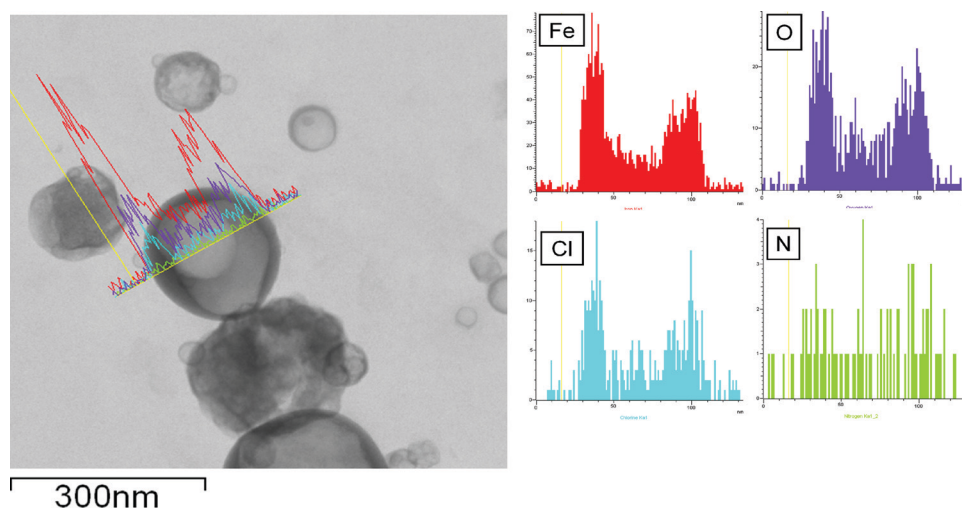

Figure 4. TEM image (left) and EDS line-scan analysis (right) of the composite Fe_2O_3/NH_4ClO_4 particles, revealing the elemental concentration profile of Fe, O, N, and Cl across the line, [Fe/N] = ½ in precursor solution.
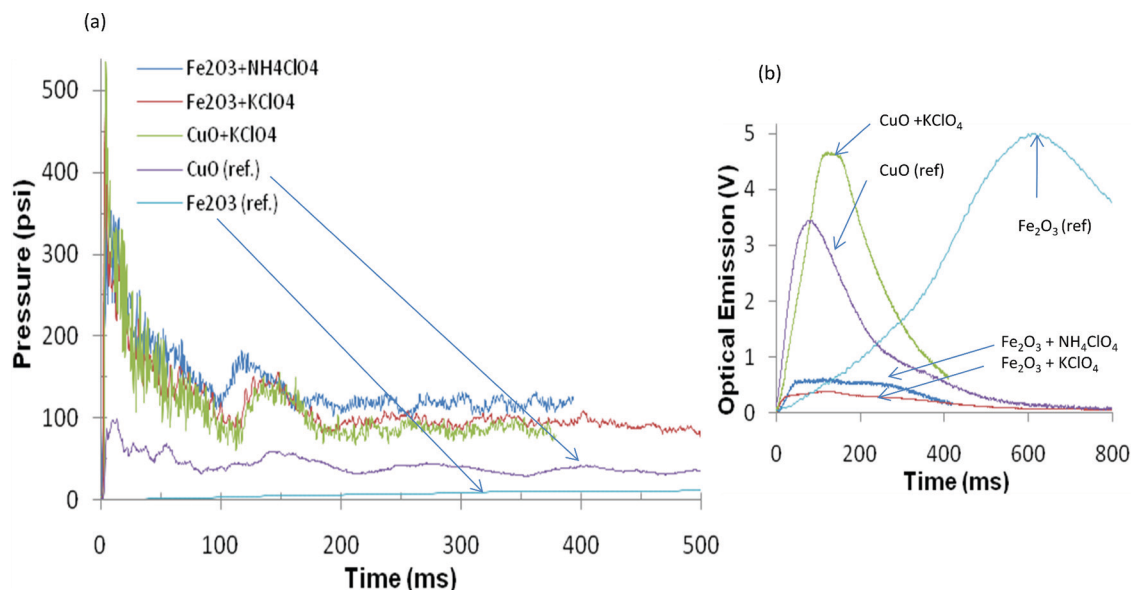
Figure 5. a) Simultaneous pressure and b) optical traces for various thermites as measured during combustion in a constant-volume pressure cell. All pressure traces show a rapid rise, with the synthesized perchlorate-included oxidizers significantly outperforming the reference materials CuO and Fe_2O_3. The optical traces for CuO-containing mixtures show an intense rise to a peak, followed by decay. The Fe_2O_3-containing mixtures, on the other hand, exhibit less-intense optical signals, and a "tail" lasting several hundred microseconds. All thermites were weighed stoichiometrically, assuming complete conversion to Al_2O_3. The elemental molar ratio in the synthesized oxidizers is [Cu/K] = [Fe/K] = [Fe/N] = 1/2.

We have recently argued that the pressurization occurs as a result of rapid oxidizer decomposition to release gaseous species, which can occur well before significant optical emission can be measure.[24] In oxidizers like CuO and Fe_2O_3, the gas is largely O_2, however, the kinetics of the O_2 release differ due to the individual decomposition mechanisms. CuO can rapidly release O_2, whereas Fe_2O_3 cannot, due to the formation of FeO, which essentially traps O_2 in the condensed phase. In the current work, the synthesized oxidizers show the same relative behavior as an Al/CuO thermite; a rapid pressure signal followed by a prolonged optical signal. Therefore, we argue that the perchlorates burn by similar mechanisms. The mixture ignites, and the exothermic reaction rapidly drives the decomposition

Table 1. Measurements of the peak pressure and rise time for thermites prepared with the perchlorate-included systems relative to commercially available CuO. The pressurization rate is an accepted indicator of relative reactivity, and the results show a large enhancement in the reactivity for all synthesized oxidizers. All oxidizers were mixed with Al, and were prepared stoichiometrically assuming complete conversion to Al_2O_3. The elemental molar ratio in the synthesized oxidizers is [Cu/K] = [Fe/K] = [Fe/N] = 1/2. Typically a 25 mg sample was loaded in a 13 mL cell for the measurement.

Oxidizer (w/Al, $\varphi = 1$)	P_{max} [psi]	Rise Time [μs]	Pressurization Rate [psi μs^{-1}]
(CuO+KClO$_4$)	534	1.5	356
(Fe$_2$O$_3$+KClO$_4$)	495	2.4	206
(Fe$_2$O$_3$+NH$_4$ClO$_4$)	389	3.3	117
CuO (ref.)	98	10.4	9.4
Fe$_2$O$_3$ (ref.)	13	800	0.017

of the oxidizer to pressurize the system, then the remainder of the fuel continues to burn in a pressurized, oxygenated environment. In the case of a perchlorate, several other gaseous species (K, Cl, N_2, etc.) can form during the decomposition, and the formation of these gaseous species can greatly enhance the peak pressure, while also aiding in the convective energy transport throughout the thermites.

Direct comparison of the combustion of Al/(CuO+KClO$_4$) and Al/(Fe$_2$O$_3$+KClO$_4$) shows that the CuO system has a higher pressurization rate by about a factor of two, which is consistent with the idea that CuO decomposition contributes to the pressurization more than Fe_2O_3 does.[25] By comparing the optical signals between the two systems, we see qualitative differences in the results. For the CuO system, the optical emission rises and falls, with a burn time (at full-width half-maximum) of $\approx$190 μs. In fact, both Al/CuO and Al/(CuO+KClO$_4$) have similar burn times, which suggests that in both cases the burning is rate-limited by the aluminum fuel. For the Fe_2O_3 system, however, the observed plateau in the optical emission suggests that the combustion occurs in two steps. We speculate that some of the oxidizer in the Fe_2O_3 remains trapped as FeO, and thus the combustion ultimately is rate-limited by the oxidizer. The assignment of a burning time is somewhat ambiguous due to the plateau seen in the optical emission, however, it is characteristically longer than the CuO systems.

The reactivity of the MIC mixture could be tailored by varying the constituent content in the composite oxidizer particles. In particular, the metal oxide was thickened by increasing the ratio of the metal oxide precursor during the process of aerosol synthesis. This was done for both CuO+KClO$_4$ and Fe$_2$O$_3$+KClO$_4$, and the pressure measurements are compared in **Table 2**. Not

Materials Views
www.MaterialsViews.com

ADVANCED
FUNCTIONAL
MATERIALS
www.afm-journal.de

FULL PAPER

Table 2. Effect of changing the relative amount of metal oxide/perchlorate on thermite reactivity. Typically a 25 mg sample was loaded in a 13 mL cell for the measurement.

Oxidizer (w/Al, $\varphi = 1$)	Molar ratio	P_{max} [psi]	Pressurization rate [psi μs^{-1}]
(CuO+KClO$_4$)	[Cu/K] = 1/2	534	356
(CuO+KClO$_4$)	[Cu/K] = 2/1	279	112
(Fe$_2$O$_3$+KClO$_4$)	[Fe/K] = 1/2	495	206
(Fe$_2$O$_3$+KClO$_4$)	[Fe/K] = 2/1	240	97

surprisingly, the pressurization rate decreases as the less reactive metal oxide is thickened, and provides a simple method for tuning the thermite reactivity.

Experiments were conducted at high heating rates ($\approx 5 \times 10^5$ K s^{-1}) on 70-μm diameter platinum wires to measure the ignition temperature of the thermites formulated with nanoaluminum and the synthesized composite oxidizer mixture. Based on the average of three repeated shots, the measured ignition temperatures of Al/(Fe$_2$O$_3$+KClO$_4$) and Al/(CuO+KClO$_4$) thermite are 1105 K and 1087 K, respectively, which are significantly lower than that of their corresponding single metal oxide thermite, i.e., >1500 K of Al/Fe$_2$O$_3$, >1200 K of Al/CuO.

Figure 6 gives sequential snapshots of Al/(Fe$_2$O$_3$+KClO$_4$) and Al/(CuO+KClO$_4$) burning on a wire under fast heating captured by the high-speed digital camera. Both of the perchlorate-containing thermites show much more violent reaction than that of Al/CuO (commercial) as obviously seen from the images; this indicates much faster energy release and pressurization rate for the perchlorate-containing thermites.

Our previous work showed that a clear correlation exists between O$_2$ release from the oxidizer and the overall reactivity of the formulated nano-thermite, i.e., high thermite reactivity can be reasonably attributed to the strong oxygen release of the oxidizer.[25] In this work, time-resolved mass spectrometry was conducted to study the O$_2$ release of the synthesized perchlorate-encapsulated composite oxidizer. O$_2$ peak intensity as a function of time obtained from flash heating along with a comparison of commercial Fe$_2$O$_3$ nanopowder and synthesized (Fe$_2$O$_3$+KClO$_4$) was plotted and shown in **Figure 7**. Not surprisingly, much higher O$_2$ signal intensity was observed from Fe$_2$O$_3$+KClO$_4$ than from commercial Fe$_2$O$_3$ nanopowder. Clearly, quick release of abundant oxygen contributed to the high reactivity in our current thermite. Further, the onset temperature of O$_2$ release from Fe$_2$O$_3$+KClO$_4$ (≈ 1045 K) is much lower than that of commercial Fe$_2$O$_3$ nanopowder (≈ 1524 K), but close to that of KClO$_4$ (≈ 1070 K), which suggests that the dominant source of O$_2$ is the perchlorate. Similar results were also observed from CuO+KClO$_4$ and Fe$_2$O$_3$+NH$_4$ClO$_4$ samples, which further confirmed the origin of the O$_2$.
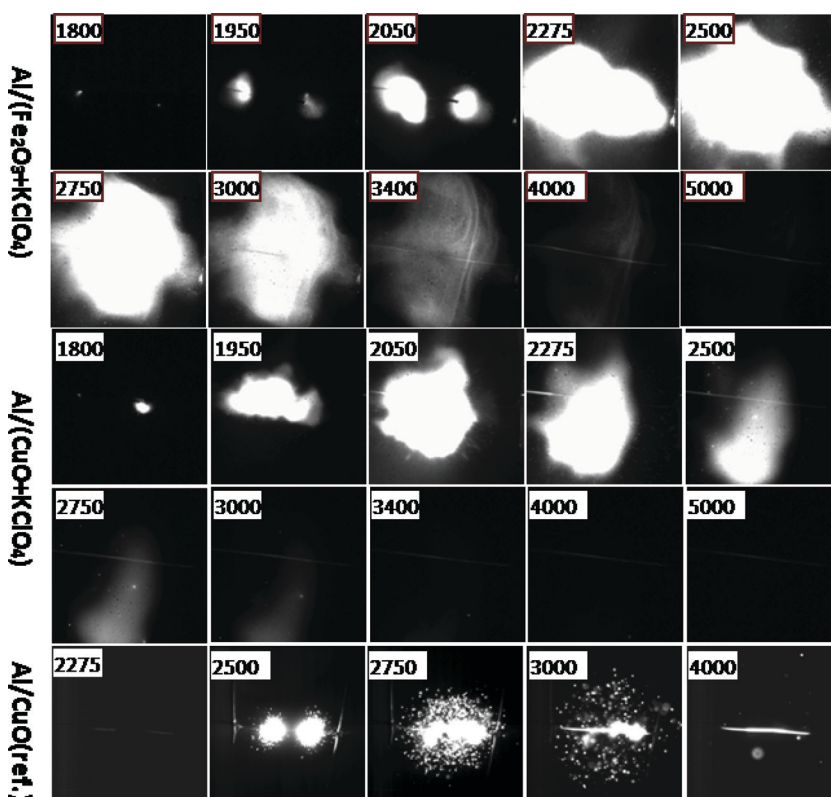
Figure 6. Sequential snapshots of Al/(Fe$_2$O$_3$+KClO$_4$), Al/(CuO+KClO$_4$), and Al/CuO (commercial) burning on fast-heating wire, as captured by high-speed video camera. The labeled numbers are time elapsed (μs) after triggering.

3. Conclusion

Water-soluble and hygroscopic perchlorate salts, including KClO$_4$ and NH$_4$ClO$_4$, were successfully encapsulated by common metal oxides by using an aerosol synthesis approach. The unique microstructures of the composite oxidizer particles were characterized and structure evolution mechanisms discussed. Thermite samples formulated with nanofuel and synthesized oxidizers show a higher pressurization rate and peak pressure, a lower ignition temperature, and a faster and more intense O$_2$ release. High-speed imaging clearly shows a much more violent reaction than for traditional thermites. The results imply that a strategy of incorporating a very strong oxidizer within a milder oxidizer offers many advantages in controlling reactivity and enabling the use of a material that, due to long-term compatibility, would not normally be considered.

4. Experimental Section

Materials: Iron (III) nitrate nonahydrate (Fe(NO$_3$)$_3$·9H$_2$O, > 98%), cupric nitrate trihydrate (Cu(NO$_3$)$_2$·3H$_2$O, > 98%), ammonium perchlorate (NH$_4$ClO$_4$, 99.8%), potassium perchlorate (KClO$_4$, = 99.5%), and reference CuO (≈ 50 nm) and Fe$_2$O$_3$
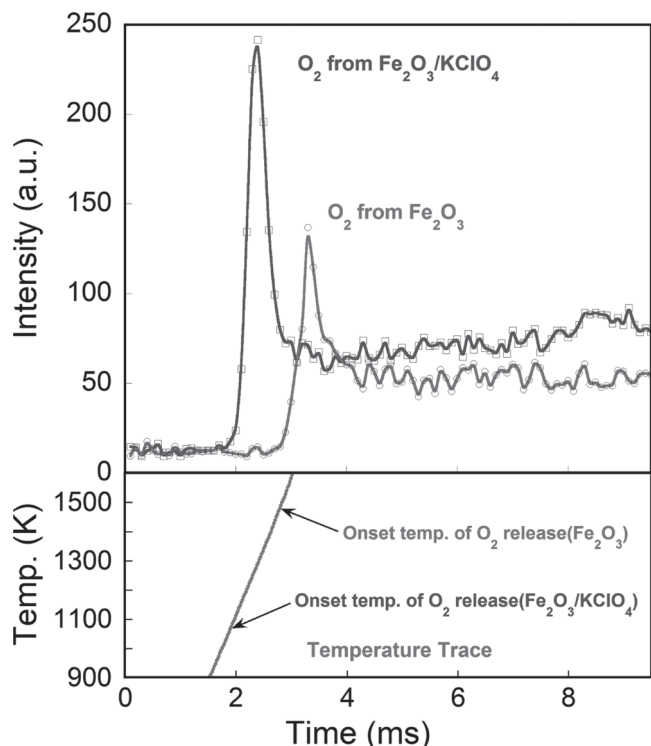
Figure 7. Temporal profile of oxygen release upon heating the synthesized composite oxidizer $Fe_2O_3+KClO_4$ and commercial Fe_2O_3 nanopowder. The heating pulse time was 3.0 ms.

(<50 nm) nanopowders were all purchased from Sigma-Aldrich and were used as received. The aluminum nanopowders used in the combustion test were obtained from the Argonide Corporation, and are designated as 50 nm ALEX by the supplier. The aluminum was found to be 70 wt% active as measured by thermogravimetric analysis (TGA).

Aerosol Spray Drying and Pyrolysis: The composite oxidizer particles were fabricated via a one-step, two-furnace temperature strategy in an aerosol setup, the scheme of which is shown in **Figure 8**. Aerosol droplets containing the dissolved precursors were generated by using a home-built pressure atomizer. The geometric mean diameter of the generated droplet, as measured by a laser aerosol spectrometer, is about 1 μm. Droplets were passed through a diffusion dryer to remove most of the solvent, and then into tube furnaces to thermally decompose the included precursor salts and further densify the particle structure.

Normal residence times were ≈1 second for a total gas flow rate of 3.5 L min^{-1}. Product particles were collected on a 0.4 μm pore Millipore HTTP membrane filter (housed in a stainless-steel holder and covered by a heating tape to prevent recondensation of solvent vapor. Typical product yields exceeded 50%.

Thermite Sample Preparation: The MIC sample powders were prepared by first weighing out the fuel and oxidizer and adding the contents to a ceramic crucible. Approximately 10 mL of hexane was then added, and the mixture was sonicated in an ultrasonicating bath for 20 min to ensure intimate mixing. The hexane was then allowed to evaporate in air and then the samples were placed in a furnace at 100 °C for a few minutes to remove any remaining hexane. The powder was then very gently broken apart with a spatula until the consistency for each sample was that of a loose powder.

Simultaneous Pressure and Optical Characterization of Reactivity: The reactivity of MICs is typically reported as a relative value, due to the current lack of fundamental understanding of the reaction mechanism. Two common methods for measuring the reactivity of MICs are to combust the sample and measure the linear burning rate, and also to combust the material in a constant-volume cell and measure the pressurization rate. The flame velocity and pressurization rate have been shown to correlate with each other, however, the correlation is not quantitative. In this work, the pressurization rate from combustion in a small volume cell has been used to characterize the reactivity of the burning material. Since this is a relative measurement, a reference oxidizer (CuO) is shown with the data as a comparison. In a typical pressurization rate measurement in our experiment, a fixed mass (25 mg) of the sample powder was placed inside a constant-volume (≈13 mL) pressure cell, and a nichrome wire coupled to an external power supply was placed in contact with the top of the powder, which served as an ignition source through resistive heating of the wire. A piezoelectric pressure sensor was employed in series with an in-line charge amplifier and a signal conditioner, and the resultant voltage trace upon ignition was captured by a digital oscilloscope. The pressurization rate (dP/dt) was calculated by converting the voltage rise to pressure (1 mV = 0.237 psi), and dividing by the rise time in microseconds. Three repeated shots were performed for each sample for the average pressurization rate. The optical emission was simultaneously collected using a lens tube assembly, containing a planoconvex lens (f = 50 mm), and a photodetector to collect the broadband emission.

Time-Resolved Mass-Spectrometry Measurement of the Oxygen Release of the Oxidizers: The recently developed temperature-jump/time-of-flight mass spectrometer (T-Jump/TOFMS) was used to characterize the reactivity of the nanocomposites. Typically, the T-Jump filament (Pt wire, length ≈12 mm, diameter ≈76 um) was coated with a thin layer of sample powder (< 0.03 mg) which could be heated up to ca. 1800 K at a heating rate ≈5 × 10^5 K s^{-1}. The filament was replaced after each heating event. From the current and voltage trace, a resistivity measurement can be obtained and related to the instantaneous temperature of the
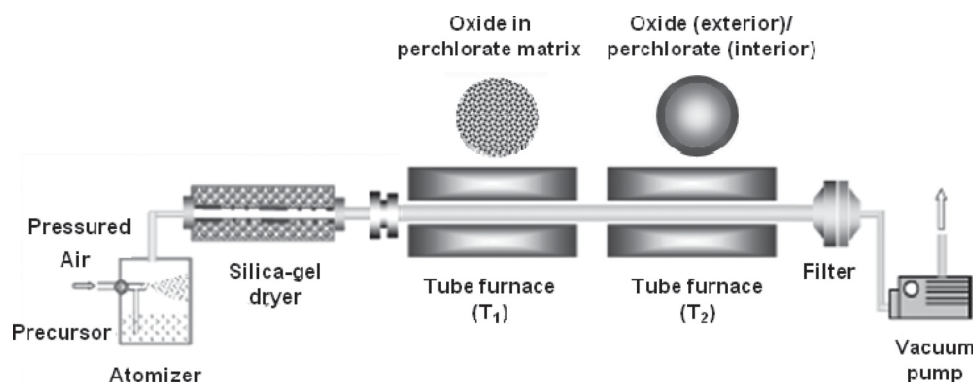
Figure 8. Aerosol spray drying/pyrolysis system for the fabrication of composite oxidizer particles.

filament, which can be mapped against the mass spectra. Time-resolved mass spectra combined with temperature information were then used for characterization of nanocomposite thermite reactions. A detailed experimental description of T-Jump/TOFMS can be found in our previous papers.[25,26]

Simultaneous Fast-Heated Ignition Wire Test and High-Speed Imaging: The T-Jump technique was coupled with a photomultiplier tube (PMT) setup for the measurement of the optical emission. The ignition temperature of the thermite sample reaction was obtained from the correlated emission signal with temperature profile of the T-Jump filament. The experiments used the same T-Jump wire in the T-Jump/TOFMS except for those performed at atmospheric pressure. A detailed experimental description can be found in our previous papers.[25,26] High-speed digital video imaging of sample burning was conducted with a Vision Research Phantom® v9.1 digital camera, which has a maximum resolution of 1632×1200 and maximum frame rate of 153846 fps at 96×8 resolutions.

Acknowledgements

[1] C. Rossi, K. Zhang, D. Estéve, P. Alphonse, P. Thailhades, C. Vahlas, *J. Microelectromech. Syst.* **2007**, *16*, 919.

[2] M. Petrantoni, C. Rossi, V. Conédéra, D. Bourrier, P. Alphonse, C. Tenailleau, *J. Phys. Chem. Solids* **2010**, *71*, 80.

[3] K. B. Plantier, M. L. Pantoya, A. E. Gash, *Combust. Flame* **2005**, *140*, 299.

[4] S. Majumdar, G. B. Kaleb, I. G. Sharma, *J. Alloy Compd.* **2005**, *394*, 168.

[5] M. E. Brown, S. J. Taylor, M. J. Tribelhorn, *Propell. Explos. Pyrotech.* **1998**, *23*, 320.

[6] A. N. Pivkina, Y. V. Frolov, D. A. Ivanov, *Combust. Explos. Shock Waves* **2007**, *43*, 51.

[7] J. L. Cheng, H. H. Hng, H. Y. Ng, P. C. Soon, Y. W. Lee, *J. Phys. Chem. Solids* **2010**, *71*, 90.

[8] C. E. Aumann, G. L. Skofronick, J. A. Martin, *J. Vac. Sci. Technol. B, Microelectron. Process. Phenom.* **1995**, *13*, 1178.

[9] B. W. Asay, S. F. Son, J. R. Busse, D. M. Oschwald, *Propell. Explos. Pyrotech.* **2004**, *29*, 216.

[10] B. S. Bockmon, M. L. Pantoya, S. F. Son, B. W. Asay, J. T. Mang, *J. Appl. Phys.* **2005**, *98*, 064903.

[11] M. L. Pantoya, V. I. Levitas, J. J. Granier, J. B. Henderson, *J. Propul. Power* **2009**, *25*, 465.

[12] S. Apperson, R. V. Shende, S. Subramanian, D. Tappmeyer, S. Gangopadhyay, Z. Chen, K. Gangopadhyay, P. Redner, S. Nicholich, D. Kapoor, *Appl. Phys. Lett.* **2007**, *91*, 243109.

[13] S. Subramaniam, S. Hasan, S. Bhattacharya, Y. Gao, S. Apperson, M. Hossain, R. V. Shende, S. Gangopadhyay, P. Redner, D. Kapoor, S. Nicolich, *Proc. Mater. Res. Soc. Symp.* **2006**, *896*, 0896-H01-05.1.

[14] K. Zhang, C. Rossi, G. A. A. Rodriguez, C. Tenailleau, P. Alphonse, *Appl. Phys. Lett.* **2007**, *91*, 113117.

[15] S. H. Kim, M. R. Zachariah, *Adv. Mater.* **2004**, *16*, 1821.

[16] J. D. Ferguson, K. J. Buechler, A. W. Weimer, S. M. George, *Powder Technol.* **2005**, *156*, 154.

[17] G. M. Dutro, R. A. Yetter, G. A. Risha, S. F. Son, *Proc. Combust. Inst.* **2009**, *32*, 1921.

[18] S. H. Fischer, M. C. Grubelich, Proc. 24th Int. Pyrotechnics Seminar, Monterey, CA, **Jul. 1998**, 1–6.

[19] S. Jain, M. S. Nandagopal, P. P. Singh, K. K. Radhakrishnan, B. Bhattacharya, *Defense Sci. J.* **2009**, *59*, 294.

[20] H. Laucht, H. Bartuch, D. Kovalev, Proc. 7th Int. Symp. Exhib. Sophisticated Car Occupant Safety Syst., **2004**, 12–16.

[21] E. W. Fournier, B. B. Brady, *J. Propul. Power* **2005**, *21*, 937.

[22] A. Prakash, A. V. McCormick, M. R. Zachariah, *Nano Lett.* **2005**, *5*, 1357.

[23] K. S. Martirosyan, L. Wang, A. Vincent, D. Luss, *Nanotechnol.* **2009**, *20*, 405609.

[24] K. Sullivan, M. R. Zachariah, *J. Propul. Power* **2010**, *26*, 467.

[25] L. Zhou, N. Piekiel, S. Chowdhury, M. R. Zachariah, *J. Phys. Chem. C* **2010**, *114*, 14269.

[26] L. Zhou, N. Piekiel, S. Chowdhury, M. R. Zachariah, *Rapid Commun. Mass Spectrom.* **2009**, *23*, 194.

FULL PAPER

Merocyanine/C$_{60}$ Planar Heterojunction Solar Cells: Effect of Dye Orientation on Exciton Dissociation and Solar Cell Performance

Antti Ojala, Andreas Petersen, Andreas Fuchs, Robert Lovrincic, Carl Pölking, Jens Trollmann, Jaehyung Hwang, Christian Lennartz, Helmut Reichelt, Hans Wolfgang Höffken, Annemarie Pucci, Peter Erk, Thomas Kirchartz, and Frank Würthner*

In this study the charge dissociation at the donor/acceptor heterointerface of thermally evaporated planar heterojunction merocyanine/C$_{60}$ organic solar cells is investigated. Deposition of the donor material on a heated substrate as well as post-annealing of the complete devices at temperatures above the glass transition temperature of the donor material results in a twofold increase of the fill factor. An analytical model employing an electric-field-dependent exciton dissociation mechanism reveals that geminate recombination is limiting the performance of as-deposited cells. Fourier-transform infrared ellipsometry shows that, at temperatures above the glass transition temperature of the donor material, the orientation of the dye molecules in the donor films undergoes changes upon annealing. Based on this finding, the influence of the dye molecules' orientations on the charge-transfer state energies is calculated by quantum mechanical/molecular mechanics methods. The results of these detailed studies provide new insight into the exciton dissociation process in organic photovoltaic devices, and thus valuable guidelines for designing new donor materials.

A. Ojala, Prof. F. Würthner
Institut für Organische Chemie and Röntgen
Research Center for Complex Material Systems
Universität Würzburg
Am Hubland, 97074 Würzburg, Germany
E-mail: wuerthner@chemie.uni-wuerzburg.de

A. Ojala, A. Fuchs, Dr. C. Lennartz, Dr. H. Reichelt, Dr. J. Hwang,
Dr. H. W. Höffken, Dr. P. Erk
BASF SE, Carl-Bosch-Straße 38, 67056 Ludwigshafen, Germany

A. Petersen
Robert Bosch GmbH, Robert-Bosch-Platz 1
70839 Gerlingen-Schillerhöhe, Germany

Dr. R. Lovrincic,[+] C. Pölking, J. Trollmann, Prof. A. Pucci
Kirchhoff-Institut für Physik der Universität Heidelberg
Im Neuenheimer Feld 227, 69120 Heidelberg, Germany

Dr. T. Kirchartz
Blackett Laboratory of Physics
Imperial College
South Kensington, London SW7 2AZ, UK

[+] Present address: Department of Materials and Interfaces, Weizmann
Institute of Science, 76100 Rehovot, Israel

1. Introduction

Progress in the field of organic photovoltaics (OPV) has been rapid in recent years and cell efficiencies approaching 8%[1] have been reported. However, to further increase the efficiency beyond 10%, which is generally considered as the watershed for a wider commercialization of the concept, a deeper understanding of the correlation between molecular level processes and the cell performance is needed.[2] One of the key processes in OPV cells and also the major difference compared to inorganic techniques concerns the formation of free charge carriers. In organic solar cells the absorption of a photon leads to the formation of a strongly bound electron–hole pair, known as an exciton. Since the built-in electric field of the device is insufficient to dissociate the excitons, they have to travel to a heterointerface between donor (D) and acceptor (A) components where the local energy level offset supports the dissociation. According to studies with polymer/fullerene blends, the dissociation of an exciton into free electron–hole pair takes place via an intermediate charge transfer (CT) state (D$^+$/A$^-$) in which the electron and hole are located on the lowest unoccupied molecular orbital (LUMO) of an acceptor molecule and on the highest occupied molecular orbital (HOMO) of the adjacent donor molecule, respectively.[3] At this point, the closely bound electron–hole pair is assumed to experience a strong Coulomb binding and can either dissociate into free charges or geminately recombine back to the ground state.[4] Several studies have identified geminate recombination as one of the main loss mechanism in OPV.[3c,5] It is widely accepted that a sufficient energy offset $\Delta E_{LUMO} = E_{LUMO}^D - E_{LUMO}^A$ between the LUMO levels of donor and acceptor materials is needed to provide the driving force for the CT-state dissociation.[3a,3b,6] On the other hand, the open circuit voltage V_{OC} of the organic planar and bulk heterojunction solar cells has been shown to be ultimately limited by the HOMO/LUMO energy level offset at the interface of donor and acceptor molecules.[7] Therefore, ΔE_{LUMO} has

www.MaterialsViews.com

ADVANCED
FUNCTIONAL
MATERIALS
www.afm-journal.de

FULL PAPER

to be optimized in order to maximize V_{OC} and at the same time provide a sufficient driving force for the CT-state dissociation.

In polymer/fullerene[8] bulk heterojunction (BHJ) devices and planar heterojunction (PHJ) phthalocyanine (Pc)/dicyanovinyl-ter-thiophene (DCV)[9] and Pc/fullerene[7d] cells, an efficient CT-state dissociation has been observed for an energy offset of ~0.4 eV. However, very recently, Gong et al.[10] demonstrated modest OPV performance with a poly(3-hexylthiophene) (P3HT)/12-(3,6,-dimethoxy-fluoren-9-ylidene)-12*H*-dibenzo[*b,h*]fluorine blend, which shows a LUMO level offset of only 0.12 eV.

The current–voltage (*J–V*) characteristics of PHJ solar cells often deviate from an ideal diode behavior which results in low fill factor (FF). This behavior has been attributed mainly to the following reasons: i) imbalanced charge carrier mobilities and a high series resistance,[11] ii) low effective electric field at the heterointerface,[12] and iii) accumulation of charges at the electrodes due to interface trapping.[13] The low FF can be significantly improved by inducing crystallization[12] or doping of the semiconductors[14] and thus improve the transport properties of the devices. Molecular orientation at the heterointerface may also play a significant role in the exciton dissociation process as recently discussed in theoretical studies with pentacene/C_{60}[15] and P3HT/C_{60}[16] interfaces.[17] Additionally, depending on the alignment of the molecules' dipole moment at the heterointerface with respect to the applied field, the charge dissociation might be either supported or hindered.[3d,18]

Interestingly, with highly dipolar merocyanine dyes excellent results have recently been obtained in both solution and vacuum deposited bulk heterojunction (BHJ) solar cells.[19] This was achieved, despite the relatively narrow band gap (~2.1 eV), owing to exceptionally high V_{OC} (1.0 V) and J_{SC} values (up to almost 12 mA cm^{-2}), whereas low FF of < 40% for solution-processed and <50% for vacuum-processed devices pinpoint the drawback that needs to be further analyzed.[19b]

In this study, we investigate PHJ and BHJ merocyanine/C_{60} solar cells deposited by thermal evaporation. Current–voltage (*J–V*) characteristics of as-deposited devices show a strong dependence on the applied voltage. The application of thermal treatment steps during the fabrication process significantly diminishes this voltage dependence. We show that the origin of the low FF of the as-deposited cells is the initially low exciton dissociation efficiency at the D/A heterointerface. It dramatically improves during post-annealing above the glass transition temperature of the merocyanine dye. An ellipsometric analysis reveals that the preferred orientation of the donor molecules undergoes a change upon annealing. Based on this result, two heterointerface models are simulated and their charge transfer (CT) exciton energies are calculated. These results support the experimental observation that the orientation of the dye molecules at the heterointerface has a significant influence on the exciton dissociation efficiency.

2. Results and Discussion

2.1. Energy-Level Diagram

The molecular structures of the employed donor and acceptor materials and the energy level diagram of the PHJ cells are
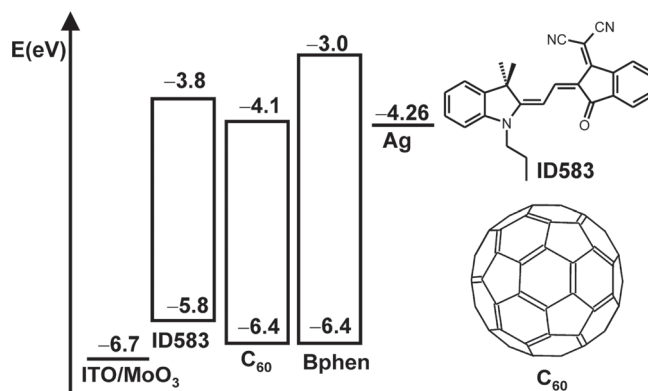
Figure 1. Energy level diagram and molecular structures of the donor (ID583) and acceptor (C_{60}) materials.

depicted in **Figure 1**. The HOMO level of ID583 was obtained from a cyclic voltammetric (CV) measurement and the LUMO position was estimated by adding the optical band gap [λ_{max} (as-deposited thin film) = 605 nm] to the HOMO energy. The HOMO and LUMO values of ID583 are −5.81 and −3.76 eV, respectively. A commonly used HOMO value for C_{60} (obtained by ultraviolet photoelectron spectroscopic (UPS) analysis) is −6.4 eV[7c,20] whilst different values for the LUMO level have been proposed.[20a,21] In this study, a value of −4.1 eV[21b] (obtained by an inverse photoemission spectroscopic method) is assumed as the LUMO level of C_{60}. The energy levels for MoO$_3$, Bphen, and Ag are taken from literature.[22]

2.2. Device Characteristics

The device architecture of planar heterojunction (PHJ) cells comprises: ITO/MoO$_3$ (5 nm)/ID583 (7–28 nm)/C_{60} (35 nm)/Bphen (5 nm)/Ag (100 nm) where the ID583 layer thickness was varied in steps of 7 nm from 7–28 nm. **Figure 2**a depicts the *J–V* characteristics of the illuminated PHJ cells with four different donor layer thicknesses. **Table 1** summarizes their key device parameters. At negative applied voltage (*V* < 0 V), all cells with different thickness of the donor layer show a very similar and well saturated photocurrent indicating an efficient extraction of free charge carriers. The high leakage current of the 7 nm donor film device at the high reverse voltage region (*V* < −0.4 V) is attributed to the low parallel resistance of the cell. When biased in forward direction (*V* > 0 V), the cells with the 14, 21, and 28 nm donor layers show a kink after which the photocurrent starts to decline linearly, until just before the open circuit voltage (V_{OC}) condition a second kink appears due to the exponential increase of the diode current. The formation of the kinks adversely affects the performance of the devices featuring a donor layer thickness of 14, 21, and 28 nm. Their FFs have been measured to be 52, 39, and 28%, respectively. The kinks are not observed, however, in the *J–V* curve of the thinnest cells (7 nm donor layer) which yields the highest fill factor (FF) of 69%. Notably, the exceptionally high V_{OC} (1.04–1.07 V) and the short circuit current (J_{SC}) are not affected by the kinks. The best J_{SC} (5.4 mA cm^{-2}) is observed for the cells with a donor layer

ADVANCED
FUNCTIONAL
MATERIALS
www.afm-journal.de

Materials
Views
www.MaterialsViews.com

FULL PAPER
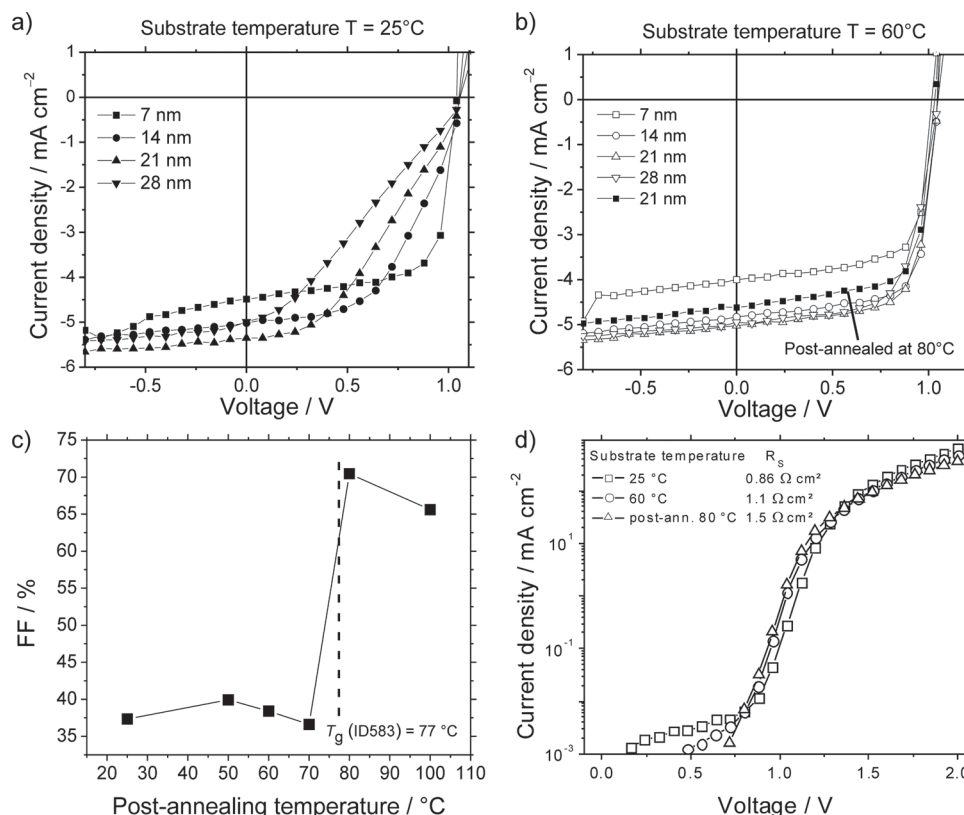
Figure 2. J–V characteristics of the PHJ cells prepared at substrate temperatures of a) 25 °C and b) 60 °C with four different ID583 layer thicknesses. c) Dependence of the FF of PHJ devices with 21 nm thick donor layers on the post-annealing temperature. The glass-transition temperature (T_g) of ID583 is illustrated by the dashed line. The solid lines are to guide the eye. d) Forward dark J–V characteristics of the PHJ cells (21 nm donor film) after different heat treatments. Series resistance (R_S) is estimated by the slope (dV/dJ) at voltage range close to $V = 2$ V.

thicknesses of 21 nm. However, due to the rapidly decreasing FF upon increasing the layer thickness, the cells with the thinnest (7 nm) donor layers give the highest power conversion efficiency (PCE) of 3.2%.

Figure 2b shows the J–V characteristics of PHJ cells deposited on a preheated (60 °C) substrate. Interestingly, these devices do not exhibit similar kinks as the cells prepared at 25 °C. Therefore, the FF of the cells with the 14, 21, and 28 nm donor layers is significantly improved to 72, 70, and 64%, respectively. The enhancement of the FF is especially high for the thickest cell

that showed a 2.2-fold increase compared to a corresponding as-deposited device. Preheating of the substrate does not influence the V_{OC} (1.04 V) but J_{SC} is slightly reduced, which is attributed to the lower absorption strength of the ID583 films evaporated on a preheated substrate (see the Supporting Information). However, due to the significantly improved FF, the optimal donor layer thickness is increased from 7 to 21 nm, which yielded a PCE of 3.9%, which is among the highest values achieved to date for vacuum-deposited PHJ devices.[12b,23]

Additionally, completely manufactured PHJ cells with a 21 nm thick donor layer were tempered on a hot plate at 50, 60, 70, 80, and 100 °C for 5 min. Interestingly, post-annealing of the cells at temperatures of 50, 60 and 70 °C has a negligible or even slightly negative influence on cell performance while annealing the cells at 80 °C almost doubles the FF from 37 to 70% (Figure 2c). The reason for the significantly improved FF is the disappearance of the kinks in the J–V characteristics (Figure 2b). The V_{OC} of the post-annealed (80 °C) devices is 1.04 V but due to a reduced J_{SC} (4.5 mA cm^{-2}), PCE (3.3%) remained below the value obtained on a preheated substrate. Post-annealing of ID583 neat films at 80 °C reduces the absorption strength and

Table 1. Key device characteristics of the PHJ and BHJ devices.

Fabrication temp. [°C]	Cell type	Donor layer thickness [nm]	J_{SC} [mA cm^{-2}]	FF [%]	V_{OC} [V]	PCE [%]
25	PHJ	7	4.5	69	1.04	3.2
25	PHJ	14	5.0	52	1.06	2.8
25	PHJ	21	5.4	39	1.07	2.3
25	PHJ	28	5.0	28	1.07	1.5
80[a]	PHJ	21	4.5	70	1.04	3.3
60[b]	PHJ	21	5.2	70	1.06	3.9
25	BHJ	28[c]	7.5	55	1.00	4.1

[a]Post-annealed; [b]Heated substrate; [c]ID583:C$_{60}$ (40:60 weight ratio) layer.

shifts the maximum to slightly smaller wavelength ($\lambda_{\max} = 595$ nm) compared to the as-deposited film ($\lambda_{\max} = 605$ nm). The decreased J_{SC} of the post-annealed devices is mainly attributed to the reduced absorption strength. However, possible changes in the thermally instable Bphen layer ($T_g = 62$ °C)[24] or the exciton diffusion length of the ID583 layer cannot be excluded. Increasing the temperature to 100 °C does not further improve the device performance; instead a small decline was observed in all cell parameters compared to post-annealing at 80 °C.

2.3. Dye and Film Properties

In order to understand the behavior of the PHJ devices, especially the sudden improvement of the FFs after post-annealing at 80 °C, we applied different analytical methods. First, the thermal properties of a ID583 powder sample were analyzed by differential scanning calorimetric (DSC) method (see the Supporting Information). Heating of an amorphous sample of ID583 (prepared by fast cooling from the melt) reveals an endothermic step in the base line at 77 °C, which is attributed to the glass transition temperature (T_g) of the material. Additionally, an exothermic crystallization peak and endothermic melting characteristics have been observed at 141 and 221 °C, respectively. Hence the T_g is observed at the same temperature region where the post-annealing significantly improves the FF of the PHJ devices (see Figure 2c).

Changes of the film morphology were investigated by atomic force microscopy (AFM). Two samples with 21 nm ID583 neat films were evaporated on ITO/MoO$_3$ (5 nm) covered glass slides at substrate temperatures of 25 and 60 °C. The ID583 films deposited at 25 °C show a root-mean-square (RMS) roughness of 0.84 nm whereas the films deposited at 60 °C have a significantly lower roughness of 0.62 nm (for AFM figures see the Supporting Information). Additionally, X-ray powder diffraction (XRPD) patterns were recorded for ID583 neat films prepared at 25 and 60 °C or post-annealed at 80 °C (see the Supporting Information). No coherent reflections arising from the ID583 layers have been observed. This, together with the AFM results (decreasing roughness at elevated deposition temperatures), suggests that the films are X-ray amorphous.

In a recent study on small molecule PHJ solar cells anomalous J–V characteristics were attributed to imbalanced charge carrier mobilities between the donor and acceptor layers.[11] This possibility in our devices was explored by measuring the hole mobilities of the ID583 hole-only devices prepared under different thermal conditions and by applying a space-charge-limited-current (SCLC) model (see the Supporting Information).[25] The hole mobility of the devices fabricated at 25 °C is 6×10^{-6} cm^2 V^{-1} s^{-1}, whereas the deposition at 60 °C or post-annealing at 80°C yields only 2×10^{-6} and 6×10^{-7} cm^2 V^{-1} s^{-1}, respectively. The previously reported electron mobility of C$_{60}$ is approximately 10^{-2} cm^2 V^{-1} s^{-1}.[26] Obviously, the decrease in hole mobilities with increased deposition temperature or with thermal annealing cannot explain the cause of the improved FFs in our PHJ devices. Consistently with the experimental hole mobilities, also the series resistance (R_S) of the PHJ cells with a 21 nm thick ID583 layer gets worse after the thermal treatments (Figure 2d). Devices prepared at 25 °C show the lowest

R_S of 0.86 Ω cm^2 whilst the highest R_S of 1.5 Ω cm^2 is observed for the post-annealed (80 °C) devices. Depositing the cells at 60 °C results in an intermediate value ($R_S = 1.1$ Ω cm^2). Note, that FFs of the devices prepared at 25 and 60 °C or post-annealed at 80 °C were 39, 70, and 70%, respectively.

2.4. Analytical Electric Field Dependent CT-State Dissociation Model

As discussed above and depicted in Figure 2a, the onset of the kinks in the J–V characteristics of the as-deposited PHJ cells gradually shifts to lower applied voltages with increasing donor layer thickness. By calculating the inverse of the slopes between the kinks and plotting them against the corresponding donor layer thicknesses, a linear correlation is observed (see the Supporting Information). This correlation is directly reflected in the FF of the devices which also linearly declines as the device thickness increases. These findings strongly suggest that the photocurrent at voltages around the maximum power point (mpp) depends on the effective electric field that can be approximated by

$$F_{el} = \frac{(V - V_{bi})}{d} \tag{1}$$

where $d = d_{donor} + d_{acceptor}$ is the total cell thickness. The applied and the built-in voltage are labeled V and V_{bi}, respectively. In previous studies, the strong field dependence has been attributed to a high series resistance[11] or to a low exciton dissociation efficiency at the D/A heterointerface.[12]

Since it was found that the hole mobility and thus the charge transport properties of the donor material did not improve and even slightly decline during thermal treatment, the R_S cannot be the cause of the low FF and high field dependency of the as-deposited (substrate temperature $T = 25$ °C) PHJ cells. Furthermore, the field dependency cannot be attributed to nongeminate recombination since we have a planar heterojunction structure. In order to analyze the charge dissociation efficiency at the heterointerface, a field-dependent CT-state dissociation model has been used to describe the illuminated J–V characteristics of the as-deposited devices. Within the frame of this model the current is given by

$$J(V) = J_{dark,exp}(V) - J_{photo}(V) \tag{2}$$

where $J_{dark,exp}(V)$ is the measured current of the not illuminated cell and the voltage dependent photocurrent is given by

$$J_{photo}(V) = p(V) J_{photo,sat} \tag{3}$$

Here $J_{photo,sat}$ is the saturation value of the photocurrent and $p(V)$ denotes the voltage dependent CT-state dissociation probability which can be calculated from the CT-state dissociation rate $k_{diss}(V)$ and its recombination rate k_f

$$p(V) = \frac{k_{diss}(V)}{k_{diss}(V) + k_f} = \frac{1}{1 + \frac{k_f}{k_{diss}(V)}} \tag{4}$$

This expression assumes a finite lifetime of the CT-state $\tau = k_f^{-1}$ with respect to recombination and was introduced by Braun.[27] The CT-state dissociation rate is expressed as[28]

ADVANCED
FUNCTIONAL
MATERIALS
www.afm-journal.de

FULL PAPER

Materials
Views
www.MaterialsViews.com

$$k_{diss}(V) = k_{diss,0} \frac{\left[1 - \exp\left(\frac{-q\,F_{el}r_s}{k_B T}\right)\right] k_B T}{q\,F_{el}r_s} \quad (5)$$

where $k_{diss,0}$ is the dissociation rate at zero field, k_B and T are the Boltzmann constant and the temperature, respectively, and r_s is the distance over which the electric field is acting on the CT-state. This distance is the difference between the initial electron–hole pair separation in the CT-state and the distance at which the two charge carriers can be considered free. We use r_s as a fitting parameter. A more detailed discussion of the model will be published elsewhere.[28]

Using the loss ratio k_f/k_{diss} and the separation distance r_s as free parameters, the exciton dissociation model is fitted to the J–V characteristics of the illuminated as-deposited PHJ cells. **Figure 3** shows the excellent agreement of the model and the experimental data. The parameters used in the simulation are given in the Supporting Information. The well saturated current densities at the applied voltage region of $V < 0$, imply an efficient CT-state dissociation in all devices. However, when the direction of the applied electric field is reversed ($V > 0$), the CT-state separation probability $p(V)$ decreases notably. For cells with a nominal donor layer thickness of 14 nm and at $V = 0.5$ V, the model predicts a separation probability of $p = 89\%$ while the cells with a 21 nm donor layer only reach about 76%, at the same value of the applied voltage V. Furthermore, when the nominal donor layer thickness increases to 28 nm, the predicted probability for the CT-state dissociation at $V = 0.5$ V is only 62%. Since the internal field decreases with increasing cell thickness, the concurrent decrease of the field-assisted separation probability is a strong indication of the photocurrent being controlled by a geminate recombination process. Thus, the formation of kinks around the mpp of the as-deposited solar cells may be attributed to the high recombination rates of the geminately bound electron–hole pairs (CT-states).
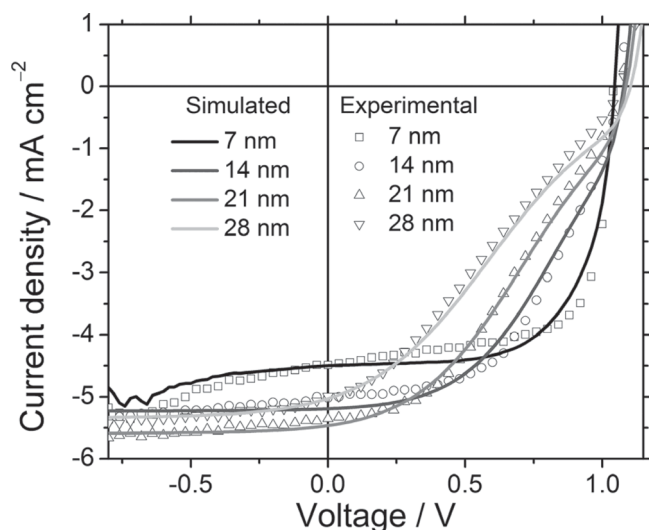
Figure 3. Experimental (symbols) and simulated (solid lines) J–V characteristics of PHJ cells with different donor layer thicknesses. The simulated curves are calculated according to Equation 3 using the parameters shown in the Supporting Information.
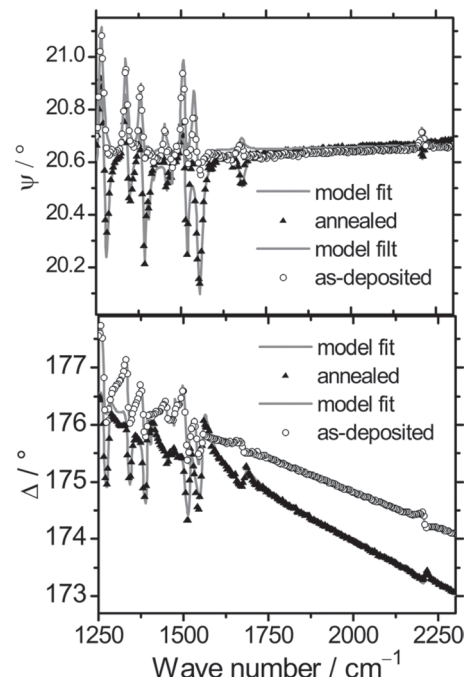
Figure 4. Measured ellipsometric parameters (symbols) Ψ and Δ for an as-deposited and annealed film on $MoO_3/SiO_2/Si$ substrates, and the corresponding modeled spectra (continuous lines). The ID583 films (thicknesses around 30 nm) were modeled as optically uniaxial (see the Supporting Information for details).

2.5. Molecular Orientations as Deduced from Infrared Spectroscopic Ellipsometry

The XRPD measurements indicate that the amorphous ID583 neat films did not crystallize upon evaporation at elevated substrate temperatures or at post-annealing above the T_g of the dye. However, it is well known that organic films may possess different degrees of order, although the size of the ordered regions is too small to give coherent reflections in XRPD (X-ray amorphous). Therefore, we have performed infrared spectroscopic ellipsometry (IRSE) analysis for two types of samples: thin films of ID583 (28 nm) evaporated on $Si/SiO_2/MoO_3$ with and without post-annealing at 80 °C for 5 min. In all cases the thicknesses of the MoO_3 and the natural Si oxide have been found to be around 3 nm. **Figure 4** shows the ellipsometric parameters obtained from both sample types at an angle of incidence of $\theta = 60°$ (see the Supporting Information for results at $\theta = 75°$) and the corresponding modeled spectra (see the Supporting Information for details on the IRSE modeling). Already the raw data reveal clear indications for a change of molecular orientation upon annealing. Thus, the peak at 2209 cm^{-1} ($\nu_{C–N}$) is a dip-down in Ψ for the annealed film and a dip-up for the as-deposited film, corresponding to out-of-plane and in-plane vibrations, respectively.[29] For a precise determination of the structural change in the film upon annealing, the accordance between the modeled dielectric function and the DFT (BP86/SV(P) level of theory) predicted absorption intensities was optimized by rotating a basis molecule set (and thereby the dipole moments) relative to the substrate. For each

www.MaterialsViews.com

ADVANCED
FUNCTIONAL
MATERIALS
www.afm-journal.de

FULL PAPER
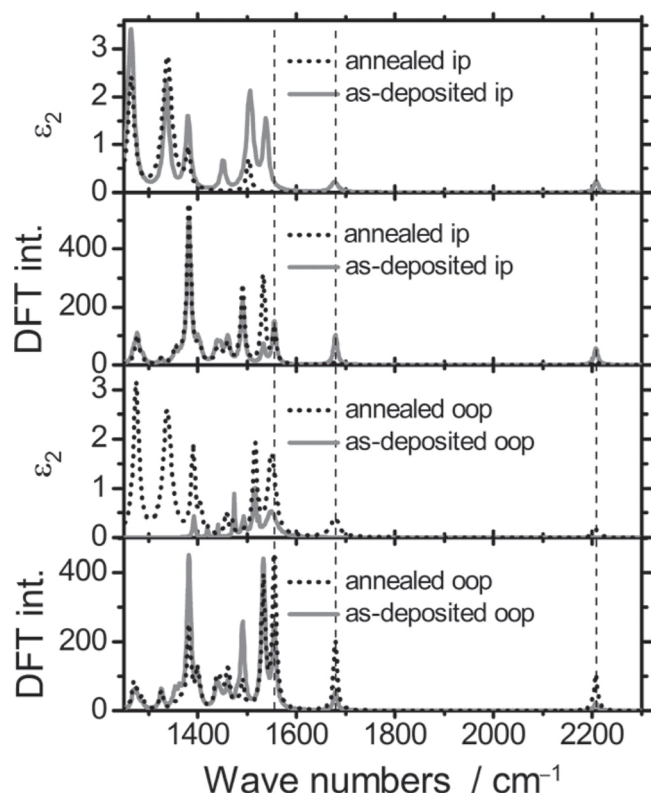
Figure 5. In-plane (ip) and out-of-plane (oop) contributions of ε_2 and the absorption peaks calculated by DFT. Fitting of DFT (BP86/SV(P) level of theory) based intensities to the experimental results was performed by using the three peaks marked with broken lines.

orientation a figure of merit (rating) was computed, and the orientation with best rating is then regarded as the preferred orientation of the molecules (see the Supporting Information for details). The optimization process was performed on three pronounced peaks at 1555 (δ_{C-H}), 1678 (ν_{C-O}), and 2209 cm^{-1} (ν_{C-N}). **Figure 5** shows the experimentally derived imaginary parts ε_2 of the dielectric functions for the two direction components of each sample in comparison to DFT intensity predictions for the optimized orientations of the molecule. As can be seen in **Figure 6**, the result indicates that in the as-deposited film the molecules are preferably standing with their long axis perpendicular to the substrate surface, and undergo a tilt of 45° upon annealing at 80 °C. This change is certainly driven by a higher packing density for the tilted orientation. As no peaks were observed in X-ray diffraction measurements for both annealed and non-annealed films, it can be concluded that the films are X-ray amorphous but the molecules tend to align their long molecular axes along certain directions, namely along the surface normal in as-deposited films and along 45° relative to the surface normal after annealing.

2.6. Computations of the CT-State Energies at the ID583/C$_{60}$ Interface

The kinks disappear and the fill factors significantly improve when substrate heating is applied or the devices are post-annealed at 80 °C which is just above the T_g (77 °C) of the dye. The fact that the post-annealing below the T_g has negligible influence on the device performance strongly suggests that the reorientation of the dyes, as shown by the IRSE spectroscopic analysis, is the key for the improved device performance. In a recent theoretical[15] study with pentacene/C$_{60}$ PHJ cells, it was observed that changes on the relative orientation of the quadrupolar donor molecule at the D/A interface have a significant influence on the charge dissociation energetics. Exposing the negatively charged π-plane of the pentacene to the C$_{60}$ interface was found to give an additional driving force for the exciton dissociation. Unlike pentacene, ID583 contains a donor-acceptor π-conjugated molecular scaffold with a permanent ground state dipole moment (7.1 D along the long and 5.5 D along the short axis of the molecule on BP86/TZVP level of theory).[30] Upon optical excitation of such push-pull chromophores the electron density is even further displaced toward the acceptor part of the dye leading to even larger dipole moments in the excited state.[31] Therefore, the relative orientation of molecules close to or at the D/A interface can have a significant impact on stabilization of the electron–hole pair and its dissociation at the interface.[15]

To assess the influence of the dyes' orientation on the stabilization of the electron–hole pair in the ID583/C$_{60}$ cells, two model interfaces were built using the crystal structures of C$_{60}$ and ID583. In order to create meaningful interface structures, the preferred orientations from the IRSE study were compared with the single crystal structure of ID583 (Figure 6c). It is obvious that the perpendicular orientation of the long molecular axis of ID583 in the as-deposited films and the tilted (45°) arrangement after annealing match very well with the lattice

Figure 6. Schematics of the dye molecules' orientations before (a) and after (b) annealing at 80 °C deduced from the ellipsometric analysis. c) A brick wall packing motif in the single crystal structure of ID583. The shortest atom-to-π-plane distances are also shown. Schematics of the interfaces ID583[01-1]:C$_{60}$[001] (d) and ID583[-110]:C$_{60}$[001] (e).

Table 2. Energy of the CT-state for different bimolecular ID583/C_{60} interface configurations.

Interface	Exposed side of the dye	E(CT) [eV]	$\Delta G_{S1 \rightarrow CT}$ [eV][a]	Configuration
[−110]:[001]	Acceptor	1.54	−0.51	2A
[−110]:[001]	Donor	1.95	−0.10	2D
[01−1]:[001]	Acceptor	1.35	−0.70	1A
[01−1]:[001]	Donor	1.61	−0.45	1D

[a]The driving force between the measured optical gap (S1) of ID583 (2.05 eV) and the calculated energy of the CT-state.

planes [01–1] and [–110], respectively. Therefore, the interface models ([01–1]:[001] and [–110]:[001]) were constructed by positioning the C_{60} plane [001] over the dye layers. The distances between the layers were optimized using the Dreiding-force field[32] (Figure 6). All other degrees of freedom (intramolecular relaxation, translation and rotation of the molecules) were kept fixed. Note, that the space group of the crystal structure of ID583 is centrosymmetric P-1 having two molecules with antiparallel orientation of the long molecular axis in the unit cell. We expect the antiparallel orientation of ID583 also to be found at the interface of the planar heterojunction. Therefore, two different types of interfaces with clearly distinct contacts between the merocyanine and fullerene components must be considered: One where the acceptor part (indane) of the ID583 dye molecule is exposed to the C_{60} surface (in the following called A configurations) and one where the dyes' donor part (indoline) is exposed (in the following called D configurations). A detailed description of the simulations can be found in the Supporting Information.
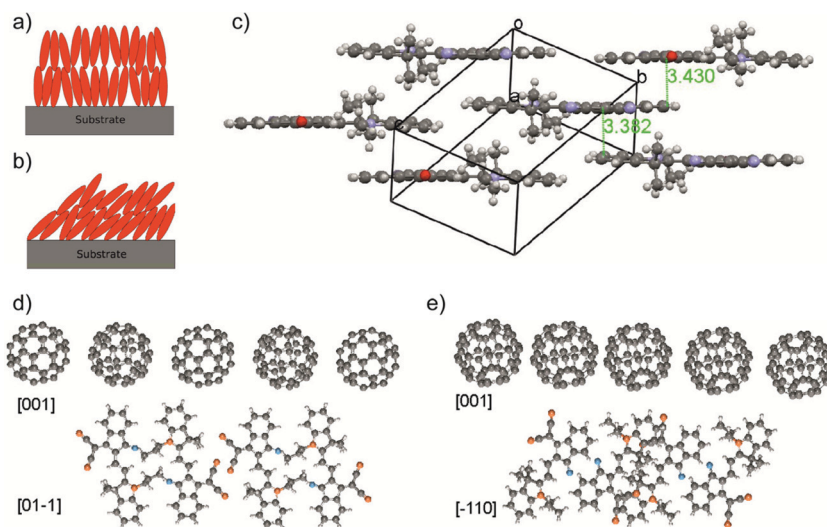
The energy of the charge transfer exciton for the different bimolecular (ID583/C_{60}) interface configurations is shown in **Table 2**. **Figure 7** demonstrates the energy-level diagram of the ID583/C_{60} interface with energy levels of the different electron–hole pairs at the perpendicular and tilted interfaces. The energy levels of the electron–hole pairs are given relative to the HOMO energy of ID583. As expected, the energy of the CT-state critically depends on the interface geometry as well as on the orientation of ID583 towards the C_{60} surface. It is interesting to note that, irrespective of the interface geometry, the CT-state is lower in energy when the (partially negatively charged) indane acceptor group of the dye is exposed to the C_{60} surface (configurations 1A and 2A). Due to the antiparallel orientation, the neighboring ID583 molecules of the bimolecular complexes 1A and 2A (which define the local polarization field) are oriented such that the indoline group is exposed to the C_{60} surface. Therefore, the CT-state is stabilized by the positive partial charge of the indoline group of the neighboring ID583 molecules. Furthermore, due to the fact that the CT-state is generated by an electron transfer from the S_1-state of ID583 to the LUMO of C_{60}, the electron density distribution of the ID583 S_1-state crucially influences the energy of the CT-state. Therefore, when the vectors of the transition dipole moment of the $S_0 \rightarrow S_1$ transition in ID583 and the transition dipole moment of the S_1(ID583) $\rightarrow$ CT excitation are oriented parallel, the electron density distribution is closer to the interface and the CT-state is
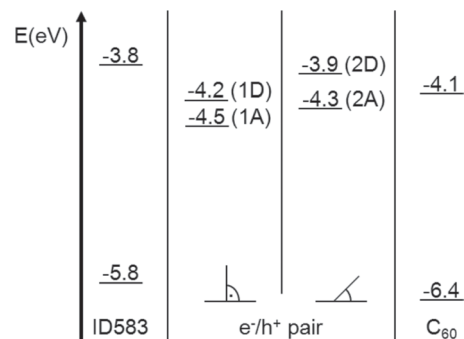
Figure 7. Energy level diagram of the ID583/C_{60} interface with energy levels of the different electron–hole pairs at the perpendicular (second column) and tilted (third column) interfaces. D configurations refer to orientations where the dyes' donor subunit is in contact to C_{60}, A configurations refer to orientations where the dyes' acceptor subunit is in contact to C_{60}. The energy levels of the electron–hole pairs are obtained by adding the energy of the CT-state E(CT) (see Table 2) to the HOMO of ID583.

already preformed in the S_1-state of ID583. Hence, the CT-state at the interface can be formed more easily due to the kinetic reasons.

As can be seen in Table 2, the driving force for the formation of the CT-state, which is defined as the energy difference between the optical gap and the energy of the CT-state ($\Delta G_{S1 \rightarrow CT} = E_{CT} - E_{opt}$), is negative for all interface configurations and relative orientations. Therefore, in principle the generation of a CT-state is possible for all four molecular orientations.

It is known from Marcus theory that the rate of charge transfer depends on the driving force.[33] The highest rates are realized when $\Delta G_{S1 \rightarrow CT}$ is equal to the negative reorganization energy λ of the system. The estimated λ is 0.3–0.5 eV so that the highest charge transfer rates occur at configurations 2A and 1D.[34] Note that 2A corresponds to the low energy CT-state at the tilted interface whereas 1D is the high energy CT-state at the perpendicular interface (see Figure 7). Therefore, the electron–hole pair is expected to stay on the bimolecular ID583/C_{60} complex 2A in the tilted case whereas the hole hops to the bimolecular complex 1A in the perpendicular case. The energy difference of 0.26 eV between the bimolecular complex 1D and 1A prevents the hole from hopping back to the other ID583 so that 1A acts as a trap state at the perpendicular interface. The rate of an electron leaving the interface can be approximated from the energy distance between the CT-state and the transport level (LUMO) of C_{60} ($\Delta E_{CT\text{-}LUMO}^A$). Using the Marcus formula and assuming a reorganization energy λ of 0.4 eV and a transfer integral of 0.050 eV, the rate for the electron hopping from the C_{60} molecule in configuration 2A to the bulk C_{60} is 400 times higher (3×10^{10} Hz vs. 8×10^7 Hz) than the respective rate for the configuration 1A, which is due to the high $\Delta E_{CT\text{-}LUMO}^A$ of 0.4 eV. Note that it can be assumed that the LUMO level of the C_{60} molecules close to the interface is different from the respective bulk level so that the electron does not need to perform the energetic jump of 0.4 eV in one step but could reach the bulk LUMO level in several smaller steps.[15] Since this effect is expected to be similar for both interfaces, the dissociation rate of the CT-state at the tilted interface remains higher than the respective rate at the perpendicular interface. This shows that

www.MaterialsViews.com

ADVANCED
FUNCTIONAL
MATERIALS
www.afm-journal.de

FULL PAPER

the high energetic stabilization of the CT-state 1A (which is the global minimum of all calculated interface excitons) makes its dissociation at the perpendicular interface very unlikely. Due to the absence of an energetic trap and the lower stabilization of the exciton at the tilted interface, it is expected to show a higher exciton dissociation rate compared to the perpendicular orientation, as indicated by the CT-state dissociation simulations. Summarizing the theoretical discussion, we have demonstrated that the CT-state is stabilized when the neighboring molecules are oriented such that the positive end of ID583 is exposed to the interface. Furthermore, the exciton dissociation rate is higher when the energy difference between the interface and bulk energy level is smaller. The calculated changes of the CT-state energies, caused by the change of the molecular orientation, also agree with our CT-state dissociation model. It predicts that the driving force for the CT-state dissociation has to be increased by at least 0.1 eV in order to account for the observed device behavior.[28] Our results are also in accordance with previous findings on merocyanine dye sensitized solar cells (DSC) which suggest that the electron injection efficiency improves if the electron accepting part of the push-pull chromophores, e.g. cyano groups, are closely located at the titanium dioxide (TiO_2) surface.[35] Likewise, in our ID583/C_{60} devices, the tilted orientation, in which the two cyano groups of the ID583 are closest to the C_{60} surface, yields the highest CT-state dissociation efficiency.

2.7. Bulk Heterojunction Cells

As a comparison, we also fabricated bulk heterojunction (BHJ) cells featuring following layer structure: ITO/MoO_3 (5 nm)/ID583:C_{60} (7-28 nm)/C_{60} (35 nm)/BPhen (5 nm)/Ag (100 nm). The active layer thickness (ID583:C_{60} 40:60 weight ratio) was varied from 7–28 nm in steps of 7 nm. **Figure 8** shows that the *J–V* characteristics of these devices do not show similar kinks as has been observed for the PHJ cells. Instead, even with the

Figure 8. Illuminated *J–V* characteristics of BHJ devices with different ID583:C_{60} layer thicknesses.

active layer thicknesses of 28 nm, the devices exhibit high FFs of 55%. Although the open circuit voltage V_{OC} = 1.00 V is lower than for the PHJ cells, the PCE (4.1%) is slightly increased due to a significantly increased J_{SC} (7.5 mA cm^{-2}) (for more results of devices, see the Supporting Information).

It is intriguing that the *J–V* characteristics of the BHJ cells resemble that of the heat-treated PHJ devices. This is explained by the different heterointerface structures of PHJ and BHJ devices. It can be assumed that the interface structure of BHJ blends is random, which leads to broad distribution of energetically different pathways for excitons to dissociate. Due to the energetically heterogeneous landscape a significant number of excitons are able to dissociate into free charges even at low effective electric field strength. In contrast, in the PHJ devices, the interface structure is expected to be more ordered leading to energetically homogenous surrounding which, depending of the dyes' relative orientation, either supports or hinders the exciton dissociation.

3. Conclusion

We have shown that by evaporating the dye film on a heated substrate or by post-annealing the complete devices above the glass transition temperature (T_g) of the donor material, we can significantly improve the FF of merocyanine/C_{60} PHJ solar cells. By employing a field dependent charge transfer (CT) state dissociation model, we show that the low FF of the as-deposited cells is a result of the poor exciton dissociation efficiency at the D/A heterointerface which is significantly improved after the heat treatments. Although, we observe no coherent reflections in the XRPD study, the utilization of an IRSE spectroscopic analysis demonstrated that the preferred orientation of the dye molecules in the donor film changes upon post-annealing at 80 °C. Based on this finding, we simulated two D/A heterointerface models and estimated their CT-state energies via QM/MM calculations. The computations suggest that the exciton dissociation rate is higher in post-annealed devices compared to as-deposited cells. Hereby, we argue that the low exciton dissociation efficiency of as-deposited devices is a result of the unfavorable molecular orientation at the heterointerface together with an insufficient driving force (LUMO(D)-LUMO(A) offset is ~0.3 eV). However, post-annealing the devices above the T_g of the donor material changes the interface structure, facilitates the CT-state dissociation, and thus leads to a two-fold increase of the FF. Furthermore, the kinks cannot be observed in the *J–V* characteristics of the BHJ devices deposited at 25 °C; instead the curves resemble heat treated PHJ cells. This is due to the random orientation of the dyes at the heterointerface in BHJ devices which is expected to result in energetically favorable pathways for a significant number of excitons to dissociate.

Our comprehensive study suggests that push–pull chromophores can be beneficial for exciton dissociation at the planar and bulk heterojunction interface if they are oriented in a proper way with respect to the acceptor manifold. This finding hints that by carefully tailoring the molecular structure and/or the film morphology, the energy level alignment at the heterojunction can be further optimized. This is important, especially since dyes with pronounced charge redistributions upon
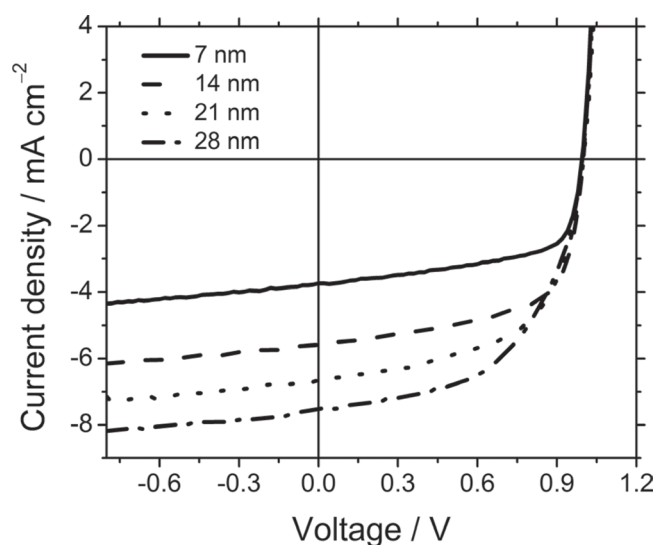
ADVANCED
FUNCTIONAL
MATERIALS
www.afm-journal.de

Materials
Views
www.MaterialsViews.com

electronic excitation, e.g., in particular dipolar merocyanines (D-A),[19] but also quadrupolar squaraines and diketopyrrolopyr-roles (D-A-D),[36,37] or dicyanovinyloligothiophenes (A-D-A)[38] are increasingly utilized in organic small-molecule planar and bulk heterojunction solar cells.

4. Experimental Section

Synthesis: Merocyanine dye ID583 (1-propyl-2-[2-(3,3-trimethyl-1,3-dihydro-indol-2-ylidene)-ethylidene]-3-dicyanovinyl-indan-1-one) was synthesized by refluxing a mixture of methylene base (8.05 g, 0.04 mol), 3-dicyanovinylindan-1-one (7.76 g, 0.04 mol) and orthoformic ethyl ester (8.88 g, 0.06 mol) for 2 h in ethanol. After cooling, the crystallized product was filtered and washed with ethanol. Finally, the product was purified by recrystallizing it from dimethylformamide. Yield: 14.0 g (0.034 mol, 85%), green solid. Mp. 219–221°C. ^{1}H NMR (CDCl$_3$, 360 MHz, δ): 9.05 (d, J = 13.6 Hz, 1H), 8.57 (m, 1H), 8.08 (d, J = 14.0 Hz, 1H), 7.72 (m, 1H), 7.59 (m, 2H), 7.36 (m, 2H), 7.25 (m, 1H), 7.07 (m, 1H), 4.04 (t, J = 7.2 Hz, 2H), 1.96 (m, 2H), 1.81 (s, 6H), 1.09 (t, J = 7.2 Hz, 3H). UV–vis (CH$_2$Cl$_2$): λ_{max} (ε) = 575 nm (66500 M^{-1} cm^{-1}). Elemental analysis (%) calcd. for C$_{27}$H$_{23}$N$_3$O: C, 80.0; H, 5.7; N, 10.4; O, 4.0. Found: C, 80.1; H, 5.8; N, 10.4; O, 4.1.

Cyclic Voltammetry (CV): The CV measurement of ID583 was performed on a commercial electrochemical analyzer (EC epsilon; BAS Instrument, UK) in a three electrode single-compartment cell under argon. Dichloromethane (HPLC grade; J. T. Baker) was dried over calcium hydride and degassed prior to use. The supporting electrolyte tetrabutylammonium hexafluorophosphate (TBAHFP) was synthesized according to a published method.[39] The measurements were carried out under exclusion of air and moisture at a concentration of 10^{-4} M with ferrocene (–5.15 eV) as internal standard for the calibration of the potential; working electrode: Pt disc; reference electrode: Ag/AgCl; auxiliary electrode: Pt wire.

Atomic Force Microscopy (AFM): The AFM experiments (Dimension 5000 Microscope, Veeco Instruments) were performed on two different 21-nm-thick ID583 films evaporated on ITO substrates at substrate temperatures of 25 and 60 °C. The measurements were carried out in the tapping mode using silicon cantilevers with a nominal force constant of 42 N/m and a tip radius of ~7 nm from Olympus, type OMCL-AC160TS (Tokyo, Japan) at a resonance frequency of about 320 kHz. The scan rate was kept at 0.7 Hz, while the tip-sample forces were carefully minimized to avoid artifacts.

Differential Scanning Calorimetry (DSC): The glass transition temperature of ID583 was measured using Q2000 (TA-instruments) differential scanning calorimeter. ID583 powder (5.4 mg) was heated/cooled at rate 20 K min^{-1} in aluminum pan under nitrogen atmosphere.

Single-Crystal Analysis: Red block crystals of ID583 were grown by slow evaporation of a dichloromethane solution of this dye at room temperature. The diffraction data were collected at 103 K with a Bruker AXS CCD detector, using graphite-monochromated Cu Kα (λ = 1.51478 Å) radiation. The structure was solved by a direct method and refined on F^2 using the full matrix least square method in SHELXTL program package.[40] All non-hydrogen atoms were anisotropically refined and hydrogen atoms were placed on idealized positions. The unit cell of the analyzed crystal is a = 9.2930(10) Å, b = 9.6240(11) Å, c = 12.6184(13) Å, α = 104.859(5)°, β = 97.120(4)°, and γ = 90.374(5)°. The space group is P-1 with Z = 2. A total amount of 2067 reflections was collected with 1651 unique reflections in the range from 3.65–57.29° (2θ). The R1 and wR1 of the refinement are 0.0354 and 0.0832, respectively. The goodness of the fit (GooF) for the solution is 1.065. Crystallographic data (excluding structure factors) for the structure reported in this paper are available at the Cambridge Crystallographic Data Centre as supplementary publication no. CCDC-834686. Copies of the data can be obtained free of charge from www.ccdc.cam.ac.uk/conts/retrieving.html or on application to the Director.

Device Fabrication: The same materials were used in all planar heterojunction (PHJ) and bulk heterojunction (BHJ) cells throughout this work. The commercial MoO$_3$ (Merck), C$_{60}$ (CreaPhys, 2 × sublimed), 4,7-diphenyl-1,10-phenanthroline (Bphen; Fluka) and the synthesized ID583 dye were used as received. The solar cells were manufactured in a high vacuum (typically 2 × 10^{-6} mbar) chamber (Lesker Ltd) on prestructured indium tin oxide (ITO) substrates with an active cell area of 4 mm^2. Prior to transferring the ITO substrates into the chamber they were cleaned in UV/O$_3$ oven for 15 min. All PHJ devices were fabricated according to following steps: first a MoO$_3$ film (5 nm ±10%) was evaporated on the ITO substrate, followed by a 7, 14, 21, or 28 nm (±10%) thick ID583 donor layer. After the ID583 film, a C$_{60}$ acceptor layer (35 nm ±10%) and a Bphen buffer film (5 nm ±10%) were deposited before preparation of the silver cathode (100 nm ±10%). The evaporation rate of all organic materials was 1.0 Å s^{-1} whereas the MoO$_3$ and Ag layers were deposited at rates of 0.8 and 4 Å s^{-1}, respectively. Compared to the PHJ cells, the following changes were made in fabrication of the BHJ devices: the ID583 layers were replaced with ID583:C$_{60}$ (40:60 wt ratio) mixed layers with thicknesses of 7, 14, 21, and 28 nm (±10%), followed by a 25 nm (±10%) thick C$_{60}$ layer. Some of the PHJ devices were prepared on a heated substrate or post-annealed after fabrication. When substrate heating was applied, the substrate was first heated with a copper block heater to 60 °C before evaporation of the ID583 layer after which the substrate was cooled below 30 °C until the successive layers were deposited. Post-annealing of the cells was carried out such that the complete devices were heated directly after fabrication on a hot plate at 50, 60, 70, 80, and 100 °C for 5 min in nitrogen atmosphere. The current–voltage (J–V) characteristics of the cells were measured under AM 1.5G simulated illumination (Xe lamp) in ambient air and controlled by a Keithley 2425 source measurement unit. The light intensity (100 mW cm^{-2}) was adjusted by a calibrated Si reference cell.

Infrared Spectroscopic Ellipsometry (IRSE): Ellipsometry measures the complex reflectance ratio $\rho = r_p/r_s = \tan(\Psi)\exp(i\Delta)$, where r_p and r_s are the reflection coefficients for light polarized parallel and perpendicular to the plane of incidence and Ψ and Δ are the standard ellipsometric parameters.[41] By modeling the obtained values for Ψ and Δ, a best-fit parameterized description of the dielectric function can be achieved, including optical anisotropy.[42] IRSE measurements at different angles of incidence were performed with a Woollam IR-VASE ellipsometer. The modeling was done using the WVASE-32 software package, which appropriately considers the layered structure of the samples. The anisotropic dielectric function can then provide information on crystal orientation and structural disorder of the film.[43] For polycrystalline thin films and amorphous films with a substrate-induced preferred orientation of the molecules, an effective uniaxial anisotropy can be expected with vibrations parallel (in-plane) and perpendicular (out-of-plane) to the substrate surface,[44] even if the single molecules are orientated with an angle off the surface normal.

To obtain the orientation of the molecules with regard to the substrate, the experimentally observed vibrational modes were compared to density functional theory (DFT) calculations (SV(P)/BP86 level of theory)[45] of vibrational eigenvalues and eigenvectors for a single molecule; DFT yields peak positions of vibrational modes and the directions of dipole moments relative to the molecule for each normal mode. Further information on the calculation of vibrational frequencies can be found in the Supporting Information. We developed a software tool that optimizes the accordance between DFT based vibration spectra and the experimental anisotropic dielectric function by varying the orientation of a molecule relative to the substrate.[46] In that way, by combining DFT results, which give us the orientation of the dipole moments with respect to the molecule, and ellipsometry results, which give us the orientation of the dipole moments with respect to the substrate surface, we can reliably determine the orientation of the molecules with respect to the substrate surface.

Supporting Information

Supporting Information is available from the Wiley Online Library or from the author.

www.MaterialsViews.com

ADVANCED
FUNCTIONAL
MATERIALS
www.afm-journal.de

FULL PAPER

Acknowledgements

[1] a) C. J. Brabec, S. Gowrisanker, J. J. M. Halls, D. Laird, S. Jia, S. P. Williams, *Adv. Mater.* **2010**, *22*, 3839; b) M. A. Green, K. Emery, Y. Hishikawa, W. Warta, *Prog. Photovolt: Res. Appl.* **2010**, *18*, 144; c) P.-L. T. Boudreault, A. Najari, M. Leclerc, *Chem. Mater.* **2011**, *23*, 456.

[2] P. K. Nayak, J. Bisquert, D. Cahen, *Adv. Mater.* **2011**, *23*, 2870.

[3] a) D. Veldman, S. C. J. Meskers, R. A. J. Janssen, *Adv. Funct. Mater.* **2009**, *19*, 1; b) H. Ohkita, S. Cook, Y. Astuti, W. Duffy, S. Tierney, W. Zhang, M. Heeney, I. McCulloch, J. Nelson, D. D. C. Brandley, J. R. Durrant, *J. Am. Chem. Soc.* **2008**, *130*, 3030; c) R. A. Marsh, J. M. Hodgkiss, R. H. Friend, *Adv. Mater.* **2010**, *22*, 3672; d) P. Peumans, S. R. Forrest, *Chem. Phys. Lett.* **2004**, *398*, 27.

[4] I. G. Hill, A. Kahn, Z. G. Soos, R. A. Paskal, *Chem. Phys. Lett.* **2000**, *327*, 181.

[5] a) D. Veldman, O. Ipek, S. C. J. Meskers, J. Sweelssen, M. M. Koetse, S. C. Veenstra, J. M. Kroon, S. S. van Bavel, J. Loos, R. A. J. Janssen, *J. Am. Chem. Soc.* **2008**, *130*, 7721; b) V. D. Mihailetchi, L. J. A. Koster, J. C. Hummelen, P. W. M. Blom, *Phys. Rev. Lett.* **2004**, *93*, 216601.

[6] a) S. Kalyan, T. Kesti, M. Maiti, F. Zhang, O. Inganäs, S. Hellström, M. R. Andersson, F. Oswald, F. Langa, T. Österman, T. Pascher, A. Yartsev, V. Sundström, *J. Am. Chem. Soc.* **2010**, *132*, 12440; b) J.-L. Bredas, D. Beljonne, V. Coropceanu, J. Cornil, *Chem. Rev.* **2004**, *104*, 4971.

[7] a) M. C. Scharber, D. Mühlbacher, M. Koppe, P. Denk, C. Waldauf, A. J. Heeger, C. J. Brabec, *Adv. Mater.* **2006**, *18*, 789; b) B. P. Rand, D. P. Burk, S. R. Forrest, *Phys. Rev. B* **2007**, *75*, 115327; c) C. J. Brabec, A. C. Cravino, D. Meissner, N. S. Sariciftci, T. Fromherz, M. T. Rispens, L. Sanchez, J. C. Hummelen, *Adv. Funct. Mater.* **2001**, *11*, 374; d) C. Uhrich, D. Wynands, S. Olthof, M. K. Riede, K. Leo, S. Sonntag, B. Maenning, M. Pfeiffer, *J. Appl. Phys.* **2008**, *104*, 043107.

[8] B. C. Thompson, J. M. J. Fréchet, *Angew. Chem. Int. Ed.* **2008**, *47*, 58.

[9] C. Uhrich, R. Schüppel, A. Petrich, M. Pfeiffer, K. Leo, E. Brier, P. Kilickiran, P. Bäuerle, *Adv. Funct. Mater.* **2007**, *17*, 2991.

[10] X. Gong, M. Tong, F. G. Brunetti, J. Seo, Y. Sun, D. Moses, F. Wudl, A. J. Heeger, *Adv. Mater.* **2011**, *23*, 2272.

[11] a) W. Tress, A. Petrich, M. Hummert, M. Hein, K. Leo, M. Riede, *Appl. Phys. Lett.* **2011**, *98*, 063301; b) D. Kekuda, J.-H. Huang, K.-C. Ho, C.-W. Chu, *J. Phys. Chem. C* **2010**, *14*, 2764.

[12] a) A. Liu, S. Zhao, S.-B. Rim, J. Wu, M. Könemann, P. Erk, P. Peumans, *Adv. Mater.* **2008**, *20*, 1065; b) J. Wagner, M. Gruber, A. Hinderhofer, A. Wilke, B. Bröker, J. Frisch, P. Amsalem, A. Vollmer, A. Opitz, N. Koch, F. Schreiber, W. Brütting, *Adv. Funct. Mater.* **2010**, *20*, 4295.

[13] J. C. Wang, X. C. Ren, S. Q. Shi, C. W. Leung, P. K. L. Chan, *Org. Electron.* **2011**, *12*, 880.

[14] M. Chikamatsu, T. Taima, Y. Yoshida, K. Saito, K. Yase, *Appl. Phys. Lett.* **2004**, *84*, 127.

[15] S. Verlaak, D. Beljonne, D. Cheyns, C. Rolin, M. Linares, F. Castet, J. Cornil, P. Heremans, *Adv. Funct. Mater.* **2009**, *19*, 3809.

[16] C. F. N. Marchiori, M. Koehler, *Synth. Met.* **2010**, *160*, 643.

[17] R. D. Pensack, K. M. Banyas, L. W. Barbour, M. Hegadorn, J. B. Asbury, *Phys. Chem. Chem. Phys.* **2009**, *11*, 2575.

[18] a) V. I. Arkhipov, P. Heremans, H. Bässler, *Appl. Phys. Lett.* **2003**, *82*, 4605; b) N. Koch, *ChemPhysChem* **2007**, *8*, 1438; c) G. Heimel, I. Salzmann, S. Duhm, N. Koch, *Chem. Mater.* **2011**, *23*, 359.

[19] a) F. Würthner, K. Meerholz, *Chem. Eur. J.* **2010**, *16*, 9366; b) N. M. Kronenberg, V. Steinmann, H. Bürckstümmer, J. Hwang, D. Hertel, F. Würthner, K. Meerholz, *Adv. Mater.* **2010**, *22*, 4193; c) N. Kronenberg, M. Deppisch, F. Würthner, H. W. A. Lademann, K. Deing, K. Meerholz, *Chem. Commun.* **2008**, 6489; d) V. Steinmann, N. M. Kronenberg, M. R. Lenze, S. M. Graf, D. Hertel, K. Meerholz, H. Bürckstümmer, E. V. Tulyakova, F. Würthner, *Adv. Energy Mater.* **2011**, *1*, 888.

[20] a) M. Brumbach, D. Placencia, N. R. Armstrong, *J. Phys. Chem. C* **2008**, *112*, 3142; b) Y. Tanaka, K. Kanai, Y. Ouchi, K. Seki, *Chem. Phys. Lett.* **2007**, *441*, 63.

[21] a) R. W. Lof, M. A. Vanveenendaal, B. Koopmans, H. T. Jonkman, G. A. Sawatzky, *Phys. Rev. Lett.* **1992**, *68*, 3924; b) Z.-L. Guan, J. B. Kim, H. Wang, C. Jaye, D. A. Fischer, Y.-L. Loo, A. Kahn, *Org. Electron.* **2010**, *11*, 1779; c) K. Kanai, K. Akaike, K. Koyasu, K. Sakai, T. Nishi, Y. Kamizuru, T. Nishi, Y. Ouchi, K. Seki, *Appl. Phys. A* **2009**, *95*, 309.

[22] a) M. Kröger, S. Hamwi, J. Meyer, T. Riedl, W. Kowalsky, A. Kahn, *Org. Electron.* **2009**, *10*, 932; b) M. Y. Chan, S. L. Lai, K. M. Lau, C. S. Lee, S. T. Lee, *Appl. Phys. Lett.* **2006**, *89*, 163515; c) D. R. Lide, *Handbook of Chemistry and Physics*, 75th ed. (Ed.: D. R. Lide), CRC Press, Boca Raton, USA **1995**.

[23] a) K. Schulze, C. Uhrich, R. Schüppel, K. Leo, M. Pfeiffer, E. Brier, E. Reinold, P. Bäuerle, *Adv. Mater.* **2006**, *18*, 2872; b) H.-W. Lin, L.-Y. Lin, Y.-H. Chen, C.-W. Chen, Y.-T. Lin, S.-W. Chiu, K.-T. Wong, *Chem. Commun.* **2011**, *47*, 7872.

[24] B. W. D'Andrade, S. R. Forrest, A. B. Chwang, *Appl. Phys. Lett.* **2003**, *19*, 3858.

[25] V. D. Mihailetchi, J. Wildeman, P. W. M. Blom, *Phys. Rev. Lett.* **2005**, *94*, 1.

[26] B. P. Rand, J. Xue, S. Uchida, S. R. Forrest, *J. Appl. Phys.* **2005**, *98*, 124902.

[27] C. L. Braun, *J. Chem. Phys.* **1984**, *80*, 4157.

[28] A. Petersen, A. Ojala, T. Kirchartz, T. A. Wagner, F. Würthner, U. Rau, unpublished.

[29] K. Hinrichs, S. D. Silaghi, C. Cobet, N. Esser, D. R. T. Zahn, *Phys. Status Solidi B* **2005**, *242*, 2681.

[30] F. Weigend, R. Ahlrichs, *Phys. Chem. Chem. Phys.* **2007**, *7*, 3297.

[31] S. Beckmann, K.-H. Etzbach, P. Krämer, K. Lukaszuk, R. Matschiner, A. J. Schmidt, P. Schuhmacher, R. Sens, G. Seybold, R. Wortmann, F. Würthner, *Adv. Mater.* **1999**, *11*, 536.

[32] S. L. Mayo, B. D. Olafson, W. A. Goddard, *J. Phys. Chem.* **1990**, *94*, 8897.

[33] a) R. A. Marcus, *J. Chem. Phys.* **1956**, *24*, 966; b) R. A. Marcus, *J. Chem. Phys.* **1957**, *26*, 872.

[34] Y. Yi, V. Coropceanu, J.-L. Brédas, *J. Mater. Chem.* **2011**, *21*, 1479.

[35] a) Y. Ooyama, Y. Shimada, S. Inoue, T. Nagano, T. Fujikawa, K. Komaguchi, I. Imae, Y. Harima, *New. J. Chem.* **2011**, *35*, 111; b) Y. Ooyama, Y. Shimada, Y. Kawaga, Y. Yamada, I. Imae, K. Komaguchi, Y. Harima, *J. Photochem. Phtobiol. A* **2009**, *203*, 177;

c) Y. Hao, X. Yang, J. Cong, H. Tian, A. Hagfeldt, L. Sun, *Chem. Commun.* **2009**, 4031.

[36] B. Walker, C. Kim, T.-Q. Nguyen, *Chem. Mater.* **2011**, *23*, 470.

[37] G. Wei, S. Wang, K. Sun, M. E. Thompson, S. R. Forrest, *Adv. Energy Mater.* **2011**, *2*, 184.

[38] R. Fitzner, E. Reinold, A. Mishra, E. Mena-Osteritz, H. Ziehlke, M. Pfeiffer, P. Bäuerle, *Adv. Funct. Mater.* **2011**, *21*, 897.

[39] A. J. Fry, in *Laboratory Techniques in Electroanalytical Chemistry*, (Eds.: P. Kissinger, W. R. Heineman), Marcel Dekker Ltd, New York, USA **1996**, p. 481.

[40] a) SHELXTL program package, V. 6.14, Bruker-AXS, **2000**; b) G. M. Sheldrick, *Acta Cryst.* **2008**, *A64*, 112.

[41] R. M. A. Azzam, N. M. Bashara, *Ellipsometry and Polarized Light*, North-Holland, Amsterdam, The Netherlands **1987**.

[42] M. Schubert, *Infrared Ellipsometry on Semiconductor Layer Structures; Springer Tracts in Modern Physics*, (Ed.: G. Höhler), Springer-Verlag, Berlin, Germany **2005**.

[43] M. Schubert, T. E. Tiwald, C. M. Herzinger, *Phys. Rev. B* **2000**, *61*, 8187.

[44] M. Schubert, C. Bundesmann, G. Jacopic, H. Maresch, H. Arwin, *Appl. Phys. Lett.* **2004**, *84*, 200.

[45] a) J. P. Perdew, *Phys. Rev. B* **1986**, *33*, 8822; b) A. D. Becke, *Phys. Rev. A* **1988**, *38*, 3098.

[46] R. Lovrincic, J. Trollmann, C. Pölking, A. Pucci, unpublished.

www.MaterialsViews.com

ADVANCED
FUNCTIONAL
MATERIALS
www.afm-journal.de

FULL PAPER

Solution-Processed Ambipolar Field-Effect Transistor Based on Diketopyrrolopyrrole Functionalized with Benzothiadiazole

Yuan Zhang, Chunki Kim, Jason Lin, and Thuc-Quyen Nguyen*

Ambipolar charge transport in a solution-processed small molecule 4,7-bis{2-[2,5-bis(2-ethylhexyl)-3-(5-hexyl-2,2′:5′,2′′-terthiophene-5′′-yl)-pyrrolo[3,4-c]pyrrolo-1,4-dione-6-yl]-thiophene-5-yl}-2,1,3-benzothiadiazole (BTDPP2) transistor has been investigated and shows a balanced field-effect mobility of electrons and holes of up to ~10^{-2} cm^2 V^{-1} s^{-1}. Using low-work-function top electrodes such as Ba, the electron injection barrier is largely reduced. The observed ambipolar transport can be enhanced over one order of magnitude compared to devices using Al or Au electrodes. The field-effect mobility increases upon thermal annealing at 150 °C due to the formation of large crystalline domains, as shown by atomic force microscopy and X-ray diffraction. Organic inverter circuits based on BTDPP2 ambipolar transistors display a gain of over 25.

1. Introduction

Organic field-effect transistors (OFETs) have potential applications in large-area displays, sensors, radiofrequency identification tags, and logic circuits with low-cost processability, and high flexibility.[1–6] OFETs using a bottom gate structure generally display hole transport only. This can be attributable to the trapping of the electrons by the hydroxyl group from the SiO$_2$ gate dielectrics.[7] Treatment of SiO$_2$ gate dielectric surfaces with organic self-assembled monolayers leads to improved performance in *n*-type OFETs fabricated from thermally evaporated small molecules or solution-processed polymer semiconducting layers.[7,8] Using a trap-free polymer gate dielectric layer, electron transport in conducting polymers has been observed, revealing a comparable field-effect mobility as holes.[9] However, for certain types of applications, ambipolar transport is required. For example, complimentary metal-oxide-semiconductor (CMOS) ambipolar transistors are preferable to increase the noise margin for logic circuits.[10] Furthermore for light-emitting transistors,[11–13] ambipolar transport is required so that the

electric potential and the light emission zone can be controlled by the applied gate voltage.[14]

Recently, several solution-processed polymer-based OFETs using a regular bottom-gate structure with hole mobilities of ~10^{-1} cm^{-2} V^{-1} s^{-1} have been reported.[15–19] The charge-carrier mobility can be improved by tuning the intermolecular interactions between the nearest neighboring molecules,[20] which can be achieved using fused aromatic rings such as thienothiophene, cyclopentanedithiophene, and naphthodithiophene.[21–23] It is believed that the fused aromatic structures enhance π–π stacking and hence induce higher molecular ordering, which drastically improves charge transport.[16] However, conjugated polymers suffer batch-to-batch variation in terms of molecular weight and polydispersity that affect solar cell performance and field-effect mobility.[24,25]

Recently a family of soluble small organic molecules containing a diketopyrrolopyrrole (DPP) core have been synthesized.[26–33] DPP-based materials have been used in solution-processable organic solar cells showing a power conversion efficiency (PCE) up to 5.2%.[29] OFETs fabricated from soluble DPP materials show hole mobility of ~10^{-2} cm^2 V^{-1} s^{-1}.[34] Incorporating fused aromatic ring moieties, the crystallinity of this type of materials can be well controlled by choosing appropriate solvents or thermal annealing, leading to desired film morphologies.[35] To the best of our knowledge, ambipolar transport based on this class of materials has not been observed previously.

Here, we report a newly synthesized bis-DPP compound, 4,7-bis{2-[2,5-bis(2-ethylhexyl)-3-(5-hexyl-2,2′:5′,2′′-terthiophene-5′′-yl)-pyrrolo[3,4-c]pyrrolo-1,4-dione-6-yl]-thiophene-5-yl}-2,1,3-benzothiadiazole (BTDPP2), with two electron-accepting units (DPP and benzothiadiazole, BT). The chemical structure of BTDPP2 is shown in **Figure 1**a. Detailed synthetic procedures can be found in the Experimental Section. The benzothiadiazole group strongly increases the electron affinity, leading to *n*-channel transport characteristics. We observe balanced carrier mobilities up to 10^{-3} cm^2 V^{-1} s^{-1} using a bottom-gate, top electrode device architecture (Figure 1b) with appropriate top contacts. Various top electrodes with work function (Φ_m) from 5.1 eV (Au) to 2.7 eV (Ba) were compared to examine the effect of the injection barrier on the ambipolar transport. Using a

Dr. Y. Zhang, Dr. C. Kim, J. Lin, Prof. T.-Q. Nguyen
Center for Polymers and Organic Solids
Department of Chemistry and Biochemistry
University of California
Santa Barbara, Santa Barbara, CA 93106, USA
E-mail: quyen@chem.ucsb.edu

ADVANCED
FUNCTIONAL
MATERIALS
www.afm-journal.de

Materials
Views
www.MaterialsViews.com

FULL PAPER
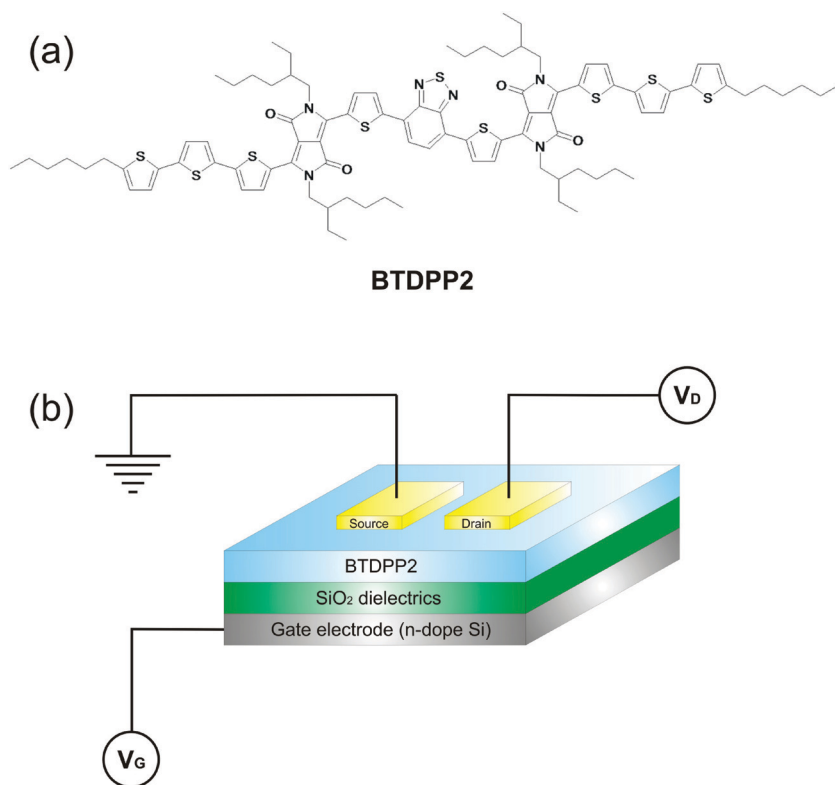
Figure 1. a) Chemical structure of BTDPP2. b) FET device structure.

low-work-function Ba contact ($\Phi_m \sim 2.7$ eV), the drain–source currents of holes and electrons are both enhanced by more than one order of magnitude compared to OFETs with Al and Au contacts. Both the hole and electron mobilities increase from 10^{-4} to 10^{-3} cm^2 V^{-1} s^{-1} with increased the annealing temperature up to 150 °C. Atomic force microscopy (AFM) shows a transition of the BTDPP2 film morphology from a fiber-like (as-cast) to crystalline-like features (above 200 °C). X-ray diffraction (XRD) measurements on BTDPP2 films prove the formation of crystalline and close intermolecular packing upon thermal annealing. Organic complementary inverters using BTDPP ambipolar OFETs show effective inversion of the input signals operating in both the first and third quadrants. Gains exceeding 25 have been achieved as a result of balanced transport properties.

2. Results and Discussion

We first study the effect of thermal annealing on BTDPP2 film morphology and on the charge transport in OFET devices utilizing gold top contact. BTDPP2 films were annealed for 30 min at different temperatures inside a nitrogen glovebox. **Figure 2**a shows the saturation drain current with $V_d = \pm 60$ V as a function of gate bias upon various annealing temperatures (T). We observe the lowest drain current (I_d) from the as-cast BTDPP2 films. The current increases with increasing annealing temperature up to 150 °C. This enhancement holds both for the hole and electron currents, while the leakage currents are

nearly unchanged. With further increase in annealing temperature to 200 °C, I_d dramatically drops below that of the device annealed at 120 °C. V_g(min), defined by the gate voltage for the crossover point of the minimal drain current under electron accumulation, slightly shifts towards a lower voltage when annealed due to the change of the fixed charges at the interface. In contrast, the OFET operated in the hole-accumulation regime shows a random variation of V_g(min). Mobilities were calculated using the standard FET equation under saturation regime (Equation 1),

$$\mu_{sat} = \frac{2L}{WC_i}\left(\frac{d\sqrt{I_d}}{dV_g}\right)^2 \tag{1}$$

where μ_{sat} stands for the field-effect mobility at saturation regime, C_i for the area capacitance of the gate dielectrics, and L/W for channel width to length ratio, the saturation mobility μ_{sat} of BTDPP2 is calculated and plotted as a function of annealing T (Figure 2b).

The μ_{sat} of the hole and electron are both in the range of ~10^{-4} to 10^{-3} cm^2 V^{-1} s^{-1}. Except for the devices annealed at 150 °C, the hole FET mobility of 4×10^{-4} cm^2 V^{-1} s^{-1} is almost the same for the as-cast and annealed films and it is lower than that of the electron mobility by a factor of two. The FET mobility is almost constant when $T \leq 120$ °C, suggesting that the film morphology does not change when annealed at such temperatures. The sharp increase of μ_{sat} up to 2.1×10^{-3} cm^2 V^{-1} s^{-1} when annealing temperature increases from 120 °C to 150 °C may indicate an improved film morphology and/or molecular packing. Under different annealing temperatures, all BTDPP2 transistors demonstrate balanced hole and electron carrier mobilities.

To further understand the transport results observed above, AFM was employed to probe change in surface morphology as a functional of thermal annealing temperature. Topographic images of the as-cast and annealed films are shown in **Figure 3** with a scan size of 2 μm × 2 μm. The as-cast film exhibits continuous fiber-like features, similar to what has been observed on other DPP derivatives.[34] Upon thermal annealing, the fiber-like structures gradually evolve into a particle-like structures showing sharper boundaries. Compared to the recently reported morphology of 2,5-di-*n*-hexyl-3,6-bis(5''-*n*-hexyl[2,2';5',2'']terthiophen-5-yl)pyrrolo[3,-4-*c*]pyrrole-1,4-dione (DHT6DPPC6) films,[34] which displays large crystalline domains upon annealing at 150 °C, large crystalline domains of BTDPP2 films were only observed at higher annealing temperatures (240 °C). The average size of these domains is around 0.2 μm × 1 μm. Figure 3f shows the surface roughness as a function of annealing temperature. The roughness of the as-cast film decreases from 3.3 nm to 0.5 nm when annealed at 150 °C and inversely increases to 2.5 nm when $T = 240$ °C where large crystalline domains are formed. The highest mobility value is observed from films with small

Figure 2. a) Saturation transfer characteristics of BTDPP2 FETs upon different annealing temperature using Au top contact. b) BTDPP2 carrier mobility as a function of annealing temperature.
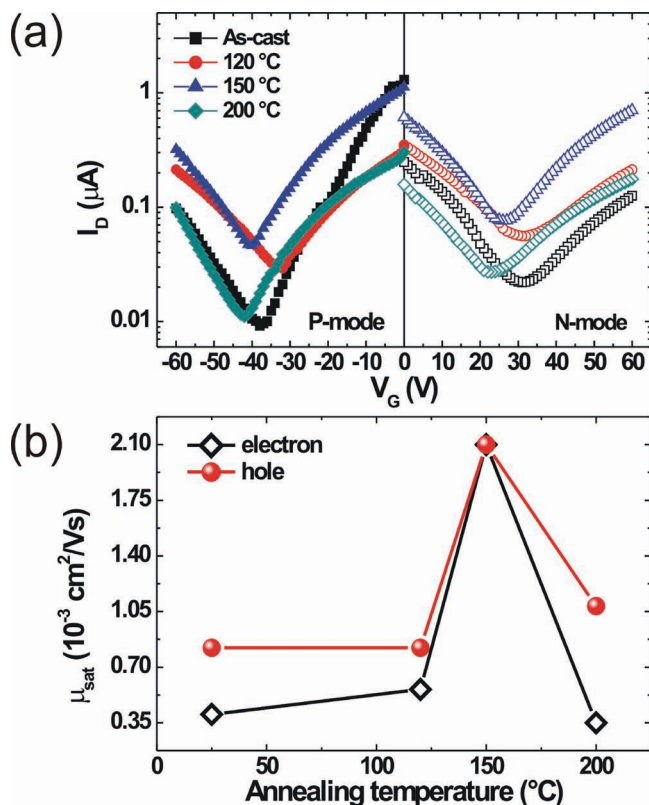
domains and low surface roughness (150 °C). Large domain formation at 240 °C lead to discontinuous grain boundaries, which are detrimental to charge transport, and hence the carrier mobility decreases from 2.1×10^{-3} to 1.0×10^{-4} cm^2 V^{-1} s^{-1} for holes and from 2.1×10^{-3} to 3.5×10^{-4} cm^2 V^{-1} s^{-1} for electrons.

From AFM images, one can only probe the surface morphology. To probe change in the internal morphology as a function of annealing temperature, we performed XRD with the normal-to-surface mode and extracted the intermolecular spacing (d-spacing) of BTDPP2 films. **Figure 4**a shows the XRD spectra of as-cast and thermal annealed BTDPP2 films. There is no XRD peak observed for the as-cast film. The 2θ XRD peak appears at 6.2 degrees for the BTDPP2 film annealed at 120 °C, which shifts to 6.33 degrees for films annealed at 150 °C and further to 4.63 degrees when annealed at 200 °C, and 240 °C, respectively, implying that the intermolecular spacing becomes closer. The intensity of the XRD signals increases with increasing annealing temperature, indicative of the enhanced film crystallinity. For the films annealed at 120 °C and 150 °C, the XRD peak intensities are quite weak, indicating a disorder structure consistent with AFM images shown in Figure 3a–c. The d-spacing was calculated using Bragg's law, $\lambda = 2d \sin\theta$, where λ is the X-ray wavelength, and plotted in Figure 4b for various annealing conditions. When annealed at 150 °C, the d-spacing abruptly decreases from 16.5 Å to 13.95 Å and remains nearly unchanged at

higher annealing temperatures. This result helps explain why thermal annealing at 150 °C leads to highest hole and electron mobilities.

Next, we explore the use of low-work-function metal electrodes on the OFET performance. One of the advantages of applying bottom-gate, top-electrode device geometry is the great flexibility to utilize different metal contacts by which the injection barriers can be tuned. The OFET transfer curves using Au ($\Phi_m = 5.0$ eV), Al ($\Phi_m = 4.3$ eV), Ca ($\Phi_m = 3.0$ eV), and Ba ($\Phi_m = 2.7$ eV) contacts are compared in **Figure 5**. Figure 5a shows the electron current I_d at low drain bias V_d. Clearly I_d increases when the work function is lowered. This is attributed to the reduced electron injection barrier of Ba and Ca, leading to an Ohmic contact with the LUMO of BTDPP2 (3.7 eV from cyclic voltammetry). Surprisingly, the transfer characteristics of Ba OFETs display a more ambipolar feature compared to those with Au and Al contacts. To further understand this observation, the electron and hole currents in the saturation regime are compared in Figures 5b and 5c with, $V_d = \pm60$ V. Under the same carrier concentration induced by the gate dielectrics, the lowered electron injection barrier with Ba or Ca contacts results in higher drain currents in the first quadrant. Interestingly, the hole current in the third quadrant using Ba electrode is also much higher, leading to symmetric transfer characteristics. Under a large drain bias, the strong electric field leads to a pronounced Schottky barrier lowering and hence facilitates the carrier injection both for the electrons and holes. In contrast to unipolar OFETs, the electric potential in ambipolar OFETs reaches a minimum at some point far from either the drain or source electrodes as the gate bias approaches that applied to the drain. Thus, the drain current at saturation regime actually comprised of both types of charge carriers, similar to a p–n junction. Using low-work-function contacts, the enhancement of the electron injection upon high drain bias helps attract more holes injected from the counterpart electrode. This is the main reason that the drain current of the Ba devices under both the hole and electron accumulations is large compared to the devices using Al or Au electrodes. The carrier mobility with different top electrodes is summarized in **Table 1**. BTDPP2 demonstrates balanced saturation FET mobilities ranging from 10^{-4} to roughly 1×10^{-2} cm^2 V^{-1} s^{-1}. The difference between the hole and electron mobility is low and insensitive to the electrode used. Utilizing a low-work-function Ba contact facilitates electron injection into BTDPP2 increasing not only the electron, but hole mobility when operating the OFETs in the saturation regime. The hole and electron mobilities are enhanced by one order of magnitude compared to those using Au or Al electrodes.

In inorganic FETs, the threshold voltage V_{th} refers to the onset of strong inversion. Below V_{th}, since the conduction channel is totally depleted, there should ideally be no current flowing from the drain to the source.[36] In contrast, organic FETs work in accumulation and the current in an inversion regime is hardly attainable.[37] Thus, defining the V_{th} in organic FETs is difficult as already addressed by Horowitz.[38] Although classical MOSFET equations are good approximations for describing the V_{th} in OFETs, these equations neglect the dependence of the carrier mobility by the carrier concentration and electric fields.[39] To examine the V_{th} of BTDPP2

Figure 3. 2 µm × 2 µm AFM topographic images of BTDPP2 films prepared at different conditions: a) as-cast, annealed at b) 120 °C, c) 150 °C, d) 200 °C, and e) 240 °C. f) RMS film roughness versus annealing temperature.

by impedance analysis agrees well with the results extracted directly from the transfer characteristics (Figure 5) under saturation regime using the following equation:

$$\frac{V_d}{2} = V_g(\min) - V_{th} \qquad (2)$$

where $V_g(\min)$ is the gate voltage for inflection point of I_d. The relatively low V_{th} and equivalent mobility both demonstrate well-balanced, ambipolar transport in BTDPP2 transistors.

Lower electron injection barriers observed using Ba electrodes should result in low contact resistance (R_C). R_C in an OFET describes the potential drop across the contacts, which causes a voltage loss for an effective voltage on transport channel from the fully applied drain–source bias.[40] In a staggered, bottom-gate configuration, the charge accumulation regime is formed opposite to the top drain–source contacts and it is found that R_C shows a weaker dependence on the injection barrier than in the coplanar geometry.[41] Next, we study the contact resistance and channel length dependence of the BTDPP2 charge transport at a low drain-source bias of $V_d = 11$ V (linear regime). The OFET transfer curves using a Ba/Al top contact are shown in **Figure 6**a using various channel lengths. The applied drain bias of 11 V is much lower than the gate bias to ensure that the majority of carriers in the conduction channel are electrons and the OFETs operate in a unipolar mode. At high R_C, one can observe a strong suppression and even sign reversal of the drain current at the linear regime. From Figure 6a, with $V_d = 11$ V, the drain current clearly increases as the gate bias exceeds 40 V. It also scales with the channel length ranging from 40 to 100 µm. This is a the signature of an Ohmic contact for electron injection and thus the R_C for the electron injection is small. Linear electron current using Al or Au top electrode is hardly attained with large channel lengths. When applying a large enough drain voltage (60 V), the devices using Al contacts show electron transport with a large channel length (100 µm) while the overall magnitude is much lower than the Ba devices, by roughly one order of magnitude ($I_d = 10^{-7}$ A when $V_g = 60$ V, see Figure 1S, Supporting Information). From Figure 6a, the hole current under linear regime using Ba contacts is not measurable for different channel lengths. This is because the hole injection barrier under linear regime is still quite high due to the low horizontal electric field. Hence, the holes can not be easily injected over a relatively large energetic barrier considering the difference between the Ba work function (2.7 eV) and the highest occupied molecular orbital (HOMO) of BTDPP2 (~5.0 eV from cyclic voltammetry). Figures 6b and 6c show the

OFETs, impedance measurements were performed on the metal-insulator-semiconductor (MIS) diode prepared by the same active layers. For this measurement, charge carriers in BTDPP2 films were accumulated or depleted by sweeping the gate voltage (V_g) leading to a different bulk capacitance, C. Under a certain V_g, C is minimized when the charge carriers are entirely depleted. This given V_g is a fingerprint of flat-band condition and can be considered the V_{th}. Figure 5d shows the C of the BTDPP2 MIS diode as a function of gate bias. Using Ba and Ca top contact, C strongly decreases with the gate bias from 10 V to 6 V, giving rise to a minimal value of 0.73 nF for C when $V_g = V_{th} = 5$ V. Conversely, using Au contact the capacitance exhibits less pronounced changes and the value of C at large positive bias lags behind that of devices using Ba and Ca contacts. This can be explained by the difficulty of electron injection from Au, as compared to that from low-work-function metals. As a result the charge accumulation is weaker. Importantly, the V_{th} of ~5 V determined

www.MaterialsViews.com

ADVANCED
FUNCTIONAL
MATERIALS
www.afm-journal.de

FULL PAPER

Figure 4. a) XRD patterns of as-spun and annealed BTDPP2 films. b) d-spacing of the molecular packing for the RMS film roughness as a function of annealing temperature.

ambipolar transfer curves with $V_d = \pm 60$ V for the electron and hole accumulation, respectively. The drain bias is high enough to overcome the hole injection barrier and the transfer curves exhibit a transition at ±30 V, a signal of the ambipolar behavior. Using Equation 1 and the OFET formula in the linear regime expressed by Equation 3,

$$\mu_{lin} = \frac{L}{WC_i V_d} \frac{d I_d}{d V_g} \tag{3}$$

where μ_{lin} is the FET mobility at linear regime, the electron and hole mobility are calculated and plotted as a function of channel length L (Figure 6d). Generally, if the R_C is the cause of the voltage drop in an OFET, the linear mobility exhibits an asymptotic dependence on L. The mobility should greatly increase with larger L and gradually saturate at certain channel length, where the bulk resistance dominates the total channel resistance. The higher FET mobility with a larger L is ascribed to the larger bulk resistance as proportional to L and the R_C becomes less dominant. From Figure 6d, this trend is invisible and the carrier mobility increases only from 8×10^{-3} cm^2 V^{-1} s^{-1} to 1.6×10^{-2} cm^2 V^{-1} s^{-1}, when L is increases from 40 to 100 μm. This further confirms that R_C in the Ba electrode devices is negligible.

Lastly, due to the balanced carrier mobilities observed in BTDPP2, we attempt to fabricate organic inverters based on two identical BTDPP2 OFETs. The equivalent circuit diagram is shown in the inset of **Figure 7**a. A highly n-doped Si gate electrode serves for the input voltage V_{in} and one of two OFET drain electrodes is grounded while the other is constantly biased at the control voltage, denoted as V_{dd}. The
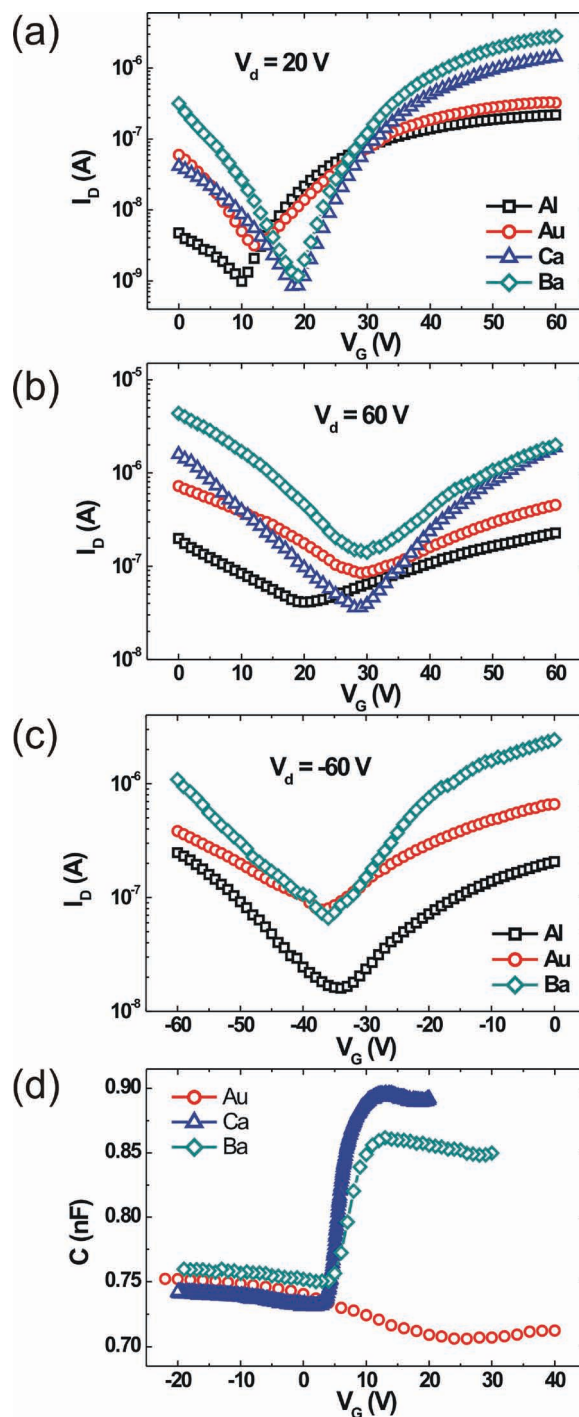
Figure 5. Transfer curves of BTDPP2 FETs using various top electrodes at a) linear regime, b) ambipolar regime under electron accumulation, and c) ambipolar regime under hole accumulation. d) Capacitance of BTDPP2 MIS as a function of the gate bias.

two source electrodes are shorted for the output voltage V_{out}. Owing to the tunable channel conductivity of both the electrons and holes, one of the merits of ambipolar over unipolar inverters is that the device can be effectively operated in the first and the third quadrants,[42] greatly simplifying practical

Table 1. Comparison of BTDPP2 FET mobility with different top contacts (e = elecron, h = hole).

Electrode	$\mu_{lin}(e)$ (cm^2 V^{-1} s^{-1})	$\mu_{sat}(e)$ (cm^2 V^{-1} s^{-1})	$\mu_{sat}(h)$ (cm^2 V^{-1} s^{-1})
Al	4×10^{-4}	3×10^{-4}	1.3×10^{-3}
Au	5.6×10^{-4}	1×10^{-3}	1.4×10^{-3}
Ca	3.3×10^{-3}	4.7×10^{-3}	N/A
Ba	7×10^{-3}	8.1×10^{-3}	9.5×10^{-3}

CMOS circuits. From Figure 7a we find that V_{out} can be efficiently inverted from a low voltage of ±10 V to high voltage of ±80 V as a function of V_{in} with both positive and negative signs. The inversion of the input voltage is found to be ±50 V, half of the control V_{dd} (±100 V), nearly ideal for ambipolar inverters. With different V_{dd}, which equals the maximum of V_{in}, the voltage inversion always occurs at $V_{dd}/2$. These results strongly suggest that the carrier mobility and turn-on voltages in BTDPP2 OFETs are equivalent. The AC response of the BTDPP2 inverters is also characterized by different wave functions with an AC magnitude of 10 V (peak to valley) (Figure S2, Supporting Information). The output signals display a 90 degree phase shift compared to the input sine or triangle signals at low frequencies (50 Hz). Using dV_{out}/dV_{in}, the inverter gain, defined as how fast an input voltage can be inverted are shown in Figure 7b. Noticeably, the gains exceed 25 at both the first and third quadrants, facilitated from the balanced charge transport in BTDPP2 OFETs. These values are competitive to organic inverters based on high-mobility polymers and thermally evaporated crystalline small molecules.[43,44]

3. Conclusion

In summary, solution-processable ambipolar transistors fabricated from DPP-based small molecules show field-effect hole and electron mobilities of up to 1.6×10^{-2} cm^2 V^{-1} s^{-1} and 1.5×10^{-2} cm^2 V^{-1} s^{-1}, respectively. Balanced transport behavior in this DPP material is confirmed by equivalent electron and hole mobilities, which is independent of the work function of the top electrodes. Thermal annealing enhances the charge transport by improving film morphology and smoothness, with an optimal OFET performance obtained after annealing at 150 °C. Large crystalline domains are observed for annealing temperatures above 200 °C, hindering the charge transport due to the formation of discontinuous grain boundaries. Closer intermolecular packing of BTDPP2 films occurs when $T = 150$ °C, which further explains the enhanced carrier mobility. Using low work function Ba contacts, the electron injection is greatly enhanced, leading to an improvement of both the electron and hole currents at saturation regime. Organic inverters based on BTDPP2 OFETs exhibit competitive gains in excess of 25 at both the first and third quadrants, facilitated by the balanced transport properties of BTDPP2. Thus, it is possible to design solution-processed molecules with balanced electron and hole mobilities using the donor–acceptor building-block approach.
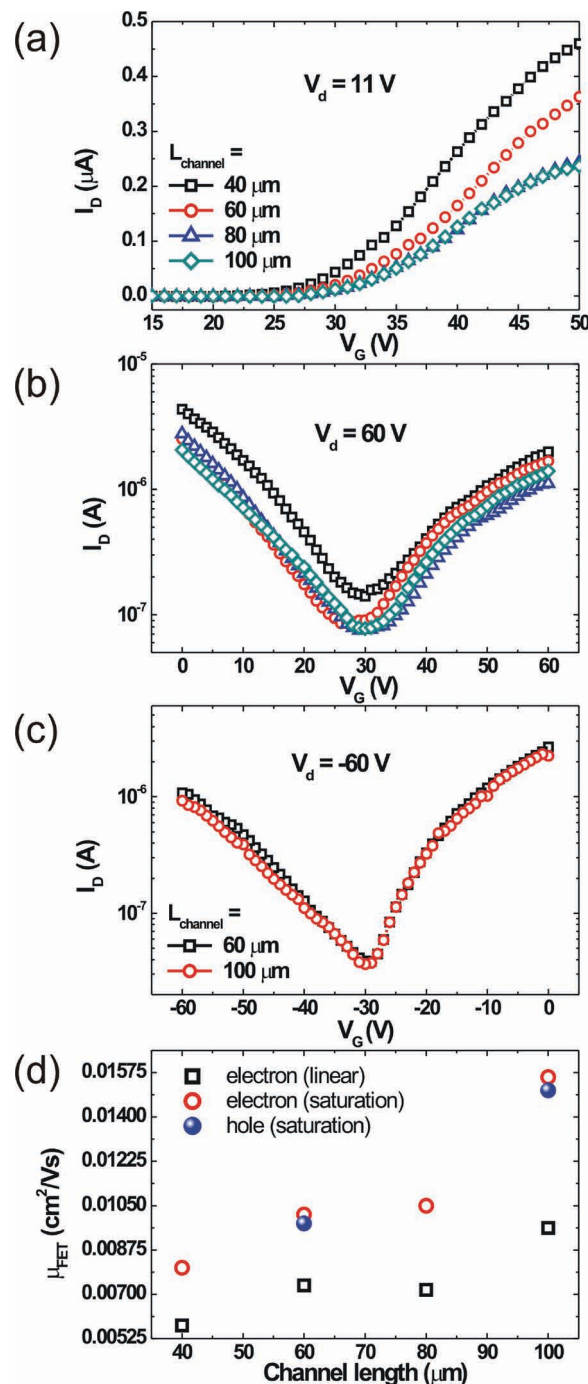
Figure 6. Transfer characteristics of BTDPP2 FETs using a Ba top electrode operated at a) linear regime, b) ambipolar regime under electron accumulation, and c) ambipolar regime under hole accumulation. d) FET mobility of electrons and holes as function of channel length.

4. Experimental Section

Material Synthesis: 5-hexyl-2,2′-bithiophene-5′-boronic acid pinacol ester and 2,1,3-benzothiadiazole-4,7-bis(boronic acid pinacol ester) were purchased from Sigma–Aldrich Chemical Co. and used as received. Other chemicals and solvents were used as received from commercial sources if there was no description. The synthesis of BTDPP2 is shown in **Scheme 1**.

www.MaterialsViews.com

ADVANCED
FUNCTIONAL
MATERIALS
www.afm-journal.de

FULL PAPER
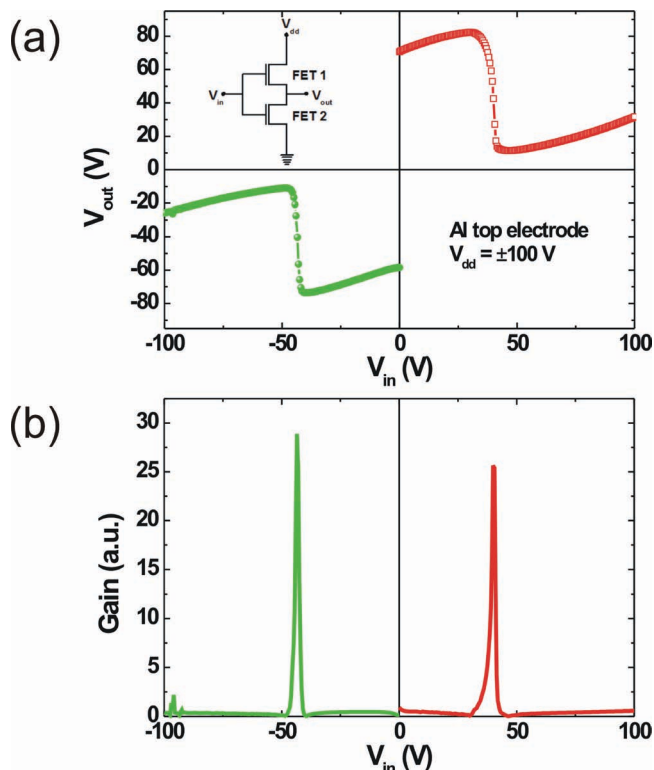
Figure 7. a) Transfer characteristics of BTDPP2 inverter. Inset: equivalent circuit as used. b) Gains of the BTDPP2 inverter under the hole and electron accumulation, respectively.

Conditions: i) 2,1,3-Bnezothiadiazole-4,7-bis(boronic acid piancol ester), Pd$_2$(dba)$_3$, HP(tBu)$_3$BF$_4$, K$_3$PO$_4$, THF; ii) NBS, Chloroform; iii) 5′-Hexyl-2,2′-bithiophene-5-boronic acid pinacol ester, Pd$_2$(dba)$_3$, HP(tBu)$_3$BF$_4$, K$_3$PO$_4$, THF.

2,5-Bis(ethylhexyl)-3-(5-bromo-thiophen-2-yl)-6-(thiophen-2-yl)-pyrrolo[3,4-c]pyrrol-1,4-dione, 1: To a solution of 2,5-bis(2-ethylhexyl)-3,6-di(thiophen-2-yl)-pyrrolo[3,4-c]pyrrole-1,4-dione (2.3 g, 7.8 mmol)[1]

in 55 mL of chloroform, *N*-bromosuccinimde (NBS) (0.92 g, 5.2 mmol) was added. The reaction solution was stirred for 5 hours at room temperature in the dark. After adding more chloroform, solution was washed with waster and dried over magnesium sulfate. After solvent was removed under reduced pressure, the crude product was purified by column chromatography on a silica gell with chloroform/hexane from 1/1 to 2/1 (ν/ν) to afford **1** (1.5 g, 50%). ^{1}H NMR (400 MHz, CDCl$_3$, δ): 8.89 (d, 1H, *J* = 2.8 Hz), 8.62 (d, 1H, *J* = 3.6 Hz), 7.63 (d, 1H, *J* = 4.8 hz), 7.26 (d, 1H, *J* = 4.0 Hz), 7.21 (d, 1H, *J* = 3.6 Hz), 3.88–4.05 (m, 4H), 1.84 (bs, 2H), 1.20 –1.36 (m, 16H), 0.82–0.89 (m, 12 H).

4,7-Bis{5-[2,5-bis(2-ethylhexyl)-6-(thiophen-2-yl)-pyrrolo[3,4-c]pyrrole-1,4-dione-3-yl]thiophen-2-yl}-2,1,3-benzothiadiazole, 2: To a mixture of 2,1,3-benzothiadiazole-4,7-bis(boronic acid pinacol ester) (0.23 g, 0.60 mmol), 1 (0.90g, 1.5 mmol), tri(dibenzylidene-acetone)palladium(0) (Pd$_2$(dba)$_3$) (0.027 g, 0.030 mmol), tri-tert-butylphosphonium tetrafluoroborate (0.052 g, 0.18 mmol), and potassium phosphate (1.0 g, 4.8 mmol), a degassed THF/water (20 mL/2 mL) was added. After stirring under argon at 50 °C overnight, the reaction mixture was poured into water. The crude product was extracted by chloroform and dried over magnesium sulfate. After evaporate solvent, the crude product was purified by column chromatography on a silica gel with from pure chloroform to 1% acetone in chloroform to afford 2 (0.5 g, 71%). ^{1}H NMR (400 MHz, CDCl$_3$, δ): 9.13 (d, 2H, *J* = 4 Hz), 8.96 (d, 2H, *J* = 4Hz), 8.17 (d, 2H, *J* = 3.6 Hz), 8.01 (s, 2H), 7.63 (d, 2H, *J* = 5.2 Hz), 7.29 (d, 2H, *J* = 4Hz), 4.04–4.16 (m, 8H), 2.00 (bs, 2H), 1.90 (bs, 2H), 1.25–1.46 (m, 32H), 0.86–0.98 (m, 24H).

4,7-Bis{5-[2,5-bis(2-ethylhexyl)-6-(5-bromo-thiophen-2-yl)-pyrrolo[3,4-c]pyrrole-1,4-dione-3-yl]thiophen-2-yl}-2,1,3-benzothiadiazole, 3: NBS (0.16 g, 0.88 mmol) was added to a solution of 2 (0.50 g, 0.42 mmol) in 40 mL of chloroform. The solution was stirred overnight in the dark. The solution was diluted with additional chloroform and washed with water. After evaporate solvent under reduced pressure, the crude product was purified by column chromatography on a silica gel with chloroform/hexane from 5/1 to 20/1 (ν/ν) to yield 3 (0.35 g, 62%). ^{1}H NMR (400 MHz, CDCl$_3$, δ): 9.11 (d, 2H, *J* = 2.8 Hz), 8.70 (d, 2H, *J* = 4.0 Hz), 8.07 (d, 2H, *J* = 4.0 Hz), 7.89 (d, 2H), 7.17 (d, 2H, *J* = 4.0 Hz), 3.85–4.14 (m, 8H), 1.97 (bs, 2H), 1.86 (bs, 2H), 1.28–1.44 (m, 32H), 0.87–0.97 (m, 24H).

4,7-Bis{2-[2,5-bis(2-ethylhexyl)-6-(5-hexyl-2,2′:5′,2″-terthiophen-5″-yl)-pyrrolo[3,4-c]pyrrole-1,4-dione-3-yl]-thiophen-5-yl}-2,1,3-benzothiadiazole, 4: Degassed THF/water (10 mL/1 mL) was added to a mixture of 3 (0.35 g, 0.26 mmol), 5-hexyl-2,2′-bithiophene-5′-boronic acid pinacol ester (0.24 g, 0.64 mmol), Pd$_2$(dba)$_3$ (0.012 g, 0.013 mmol), tri-tert-butylphosphonium tetrafluoroborate (0.023 g, 0.79 mmol), and potassium phosphate (0.44 g,
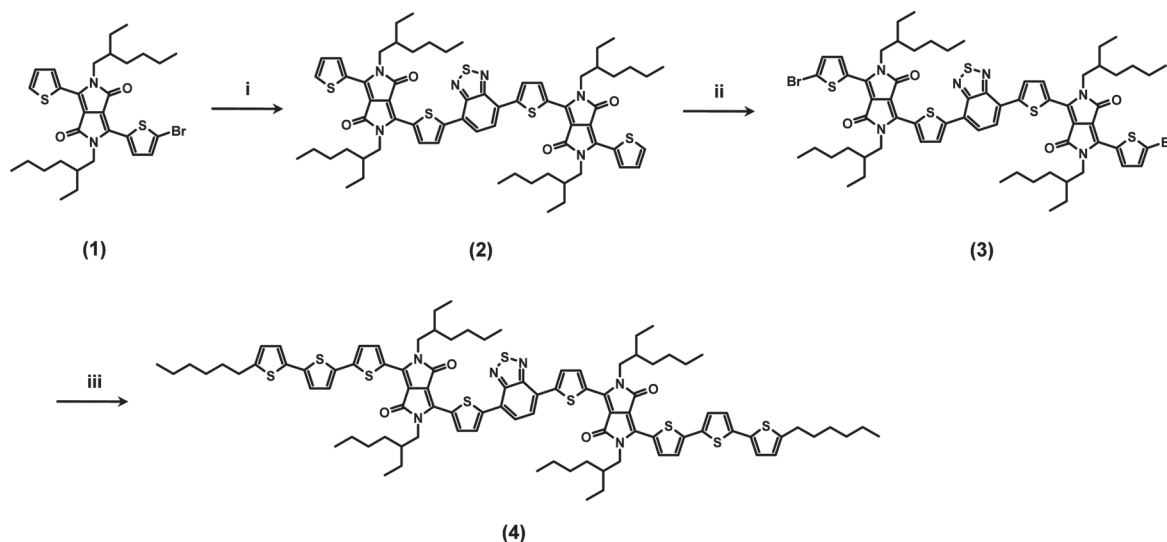
Scheme 1. Synthetic Route for 4 (BTDPP2).

FULL PAPER

2.1 mmol). After stirring overnight under argon at 60 °C, the reaction mixture was poured into water. The crude product was extracted with chloroform and purified by column chromatography on a silica gel with from chloroform/hexane 5/1 (v/v) to pure chloroform to obtain 4 (0.22 g, 50%). ^{1}H NMR (400 MHz, CDCl$_3$, δ): 9.03 (s, 2H), 8.97 (s, 2H), 7.90 (s, 2H), 7.71 (s, 2H), 7.06 (d, 2H, $J = 4.0$ Hz), 6.98 (d, 2H, $J = 4.0$ Hz), 6.88 (d, 2H, $J = 3.2$ Hz), 6.84 (d, 2H, $J = 3.6$ Hz), 6.58 (d, 2H, $J = 3.2$ Hz), 3.78–4.05 (m, 8H), 2.68 (t, 4H, J = 7.2 Hz), 1.82–1.98 (m, 4H), 1.61 (m, 4H), 1.21–1.50 (m, 44H), 0.86–1.02 (m, 30H). Anal. Calcd. for C$_{94}$H$_{112}$N$_6$O$_4$S$_9$ (%): C, 67.26; H, 6.73; N, 5.01 Found: C, 66.78; H, 6.69; N, 5.11.

Device Fabrication and Characterization: N^{++} Si wafers from Silicon Quest International were used for the bottom gate electrode with 150 nm of SiO$_2$ layer as the gate dielectric, leading to a capacitance of ~2.3 × 10^{-4} F m^{-2}. Prior to casting the BTDPP2 active layer, the substrates were sonicated sequently with acetone, and propan-2-ol, 2-propanol and then baked on a hotplate at 140 °C for 1 hour. Following with 30 min of UV-ozone treatment, the substrates were then transferred into a nitrogen purged glove box and passivated with diluted octadecyltrichlorosilane solution in hexane (0.1% vol). BTDPP2 was dissolved in chloroform at a concentration of 6 mg mL and stirred on a hotplate at 60 °C. Filtered through a PTFE filter with 0.45 μm pore size, the films were deposited from BTDPP2 solution at a spin-speed of 2000 RPM resulting in ~50 nm film thickness. Finally 90 nm Au, or Al top contacts were thermally evaporated under a vacuum lower than 5 × 10^{-7} torr through a shadow mask (2 mm channel width and 40~100 μm channel length). For low work function metals, 5 nm Ba or Ca was evaporated and immediately capped with 100 nm of Al. The samples were tested in a LakeShore probe station under 10^{-6} mBa. A Keithley 4200 semiconductor parametric analyzer was used for the OFET and inverter characterizations. Impedance of the metal–insulator–semiconductor diodes was recorded using a Solartron SI 1260 impedance/gain-phase analyzer. The capacitance was obtained by sweeping the gate voltage while keeping the top electrode grounded.

For morphological studies the same BTDPP2 films were used to the OFET active layers. The tapping mode AFM images were captured by a Veeco MultiMode® 8 scanning probe microscope under nitrogen atmosphere. Thin-film XRD spectra were measured on device architectures of Si/SiO$_2$/BTDPP2 using an X'Pert Phillips Material Research diffractometer. Samples were scanned at 45 kV and 40 mA with a scanning rate of 0.004 degree per second, and Cu Kα radiation (wavelength $\lambda = 1.5405$ Å). In the 2θ–ω scan configurations each film was scanned from 4 to 30 2θ.

Supporting Information

Supporting Information is available from the Wiley Online Library or from the author.

Acknowledgements

[1] H. Sirringhaus, N. Tessler, R. H. Friend, *Science* **1998**, *280*, 1741.

[2] R. Kagan, D. B. Mitzi, C. D. Dimitrakopoulos, *Science* **1999**, *286*, 945.

[3] B. Crone, A. Dodabalapur, A. Gelperin, L. Torsi, L. H. E. Katz, J. Lovinger, Z. Bao, *Appl. Phys. Lett.* **2001**, *78*, 2229.

[4] F. Cicoira, C. Santato, *Adv. Funct. Mater.* **2007**, *17*, 3421.

[5] C. F. Sung, D. Kekuda, L. F. Chu, Y. Z. Lee, F. C. Chen, M. C. Wu, C. W. Chu, *Adv. Mater.* **2009**, *21*, 4845.

[6] H. Sirringhaus, *Adv. Mater.* **2005**, *17*, 2411.

[7] L. L. Chua, J. Zaumseil, J. F. Chang, E. C. W. Ou, P. K. H. Ho, H. Sirringhaus, R. H. Richard, *Nature* **2005**, *434*, 194.

[8] R. P. Oritz, H. Herrera, R. Blanco, H. Huang, A. Facchetti, T. J. Marks, Y. Zheng, J. Segura, *J. Am. Chem. Soc.* **2010**, *132*, 8440.

[9] R. C. G. Naber, M. Bird, H. Sirringhaus, *Appl. Phys. Lett.* **2008**, *93*, 023301.

[10] M. Spijkman, E. C. P. Smits, P. W. M. Blom, D. M. de Leeuw, Y. Bon Saint Come, S. Setayesh, E. Cantatore, *Appl. Phys. Lett.* **2008**, *92*, 143304.

[11] J. Zaumseil, H. Sirringhaus, *Chem Rev.* **2007**, *107*, 1296.

[12] J. Zaumseil, C. L. Donley, J. S. Kim, R. H. Friend, H. Sirringhaus, *Adv. Mater.* **2006**, *18*, 2708.

[13] L. Bürgi, M. Turbiez, R. Pfeiffer, F. Bienewald, H.-J. Kirner, C. Winnewisser, *Adv. Mater.* **2008**, *20*, 2217.

[14] J. Zaumseil, R. H. Friend, H. Sirringhaus, *Nat. Mater.* **2006**, *5*, 69.

[15] C. Kima, M. C. Chen, Y. J. Chiang, Y. J. Guo, J. Youn, H. Huang, Y. J. Liang, Y. J. Lin, Y. W. Huang, T. S. Hu, G. H. Lee, A. Facchetti, T. J. Marks, *Org. Electron.* **2010**, *11*, 801.

[16] Y. Li, S. P. Singh, P. Sonar, *Adv. Mater.* **2010**, *22*, 4862.

[17] J. C. Bijleveld, A. P. Zoombelt, S. G. J. Mathijssen, M. M. Wienk, M. Turbiez, D. M. de Leeuw, R. A. J. Janssen, *J. Am. Chem. Soc.* **2009**, *131*, 16616.

[18] H. Bronstein, Z. Chen, R. S. Ashraf, W. Zhang, J. Du, J. R. Durrant, P. S. Tuladhar, K. K. Song, S. E. Watkins, Y. Geerts, M. M. Wienk, R. A. J. Janssen, T. Anthopoulos, H. Sirringhaus, M. Heeney, I. McCulloch, *J. Am. Chem. Soc.* **2011**, *133*, 3272.

[19] M. Zhang, H. N. Tsao, W. Pisula, C. Yang, A. K. Mishra, K. Müllen, *J. Am. Chem. Soc.* **2007**, *127*, 3472.

[20] D. Dimitrakopoulos, P. R. L. Malenfant, *Adv. Mater.* **2002**, *14*, 99.

[21] I. Osaka, T. Abe, S. Shinamura, E. Miyazaki, K. Takimiya, *J. Am. Chem. Soc.* **2010**, *132*, 5000.

[22] H. N. Tsao, D. Cho, J. W. Andreasen, A. Rouhanipour, D. W. Breiby, W. Pisula, K. Müllen, *Adv. Mater.* **2009**, *21*, 209.

[23] I. McCulloch, M. Heeney, C. Bailey, K. Genevicius, I. Macdonald, M. Shkunov, D. Sparrowe, S. Tierney, R. Wagner, W. M. Zhang, M. L. Chabinyc, R. J. Kline, M. D. McGehee, M. F. Toney, *Nat. Mater.* **2006**, *5*, 328.

[24] M. Morana, P. Koers, C. Waldauf, M. Koppe, D. Muehlbacher, P. Denk, M. Scharber, D. Waller, C. Brabec, *Adv. Funct. Mater.* **2007**, *17*, 3274.

[25] C. Goh, R. J. Kline, M. D. McGehee, E. N. Kadnikova, J. M. J. Frechet, *Appl. Phys. Lett.* **2005**, *86*, 122110.

[26] B. Tamayo, M. Tantiwiwat, B. Walker, T.-Q. Nguyen, *J. Phys. Chem. C* **2008**, *112*, 15543.

[27] A. B. Tamayo, X. D. Dang, B. Walker, J. Seo, T. Kent, T.-Q. Nguyen, *Appl. Phys. Lett.* **2009**, *94*, 103301.

[28] A. B. Tamayo, B. Walker, T.-Q. Nguyen, *J. Phys. Chem. C* **2008**, *112*, 15545.

[29] Y. Zhang, X.-D. Dang, C. Kim, T.-Q. Nguyen, *Adv. Energ. Mater.* **2011**, *1*, 610.

[30] B. Walker, A. B. Tomayo, X. D. Dang, P. Zalar, J. H. Seo, A. Garcia, M. Tantiwiwat, T.-Q. Nguyen, *Adv. Funct. Mater.* **2009**, *19*, 3063.

[31] B. S. Jeong, H. Choi, N. Cho, H. M. Ko, W. Lim, K. Song, J. K. Lee, J. Ko, *Sol. Energy Mater. Sol. Cells* **2011**, *95*, 1731.

[32] K. A. Mazzio, M. J. Yuan, K. Okamoto, C. K. Luscombe, *ACS Appl. Mater. Interface* **2011**, *3*, 271.

[33] P. Sonar, G. M. Ng, T. T. Lin, A. Dodabalapur, Z. K. Chen, *J. Mater. Chem.* **2010**, *20*, 3626.

[34] M. Tantiwiwat, A. Tamayo, N. Luu, X. D. Dang, T.-Q. Nguyen, *J. Phys. Chem. C* **2008**, *112*, 17402.

[35] P. Sonar, S. P. Singh, Y. Li, M. S. Soh, A. Dodabalapur, *Adv. Mater.* **2010**, *22*, 5409.

[36] S. M. Sze, *Physics of Semiconductor Devices*, Wiley, New York **1981**.

[37] E. J. Meijer, C. Tanase, P. W. M. Blom, E. van Veenendaal, B.-H. Huisman, D. M. de Leeuw, *Appl. Phys. Lett.* **2002**, *80*, 3838.

[38] G. Horowitz, R. Hajlaoui, H. Bouchriha, R. Bourguiga, M. Hajlaoui, *Adv. Mater.* **1998**, *10*, 923.

[39] M. Shur, M. Hack, J. G. Shaw, *J. Appl. Phys.* **1989**, *66*, 3371.

[40] T. J. Richards, H. Sirringhaus, *J. Appl. Phys.* **2007**, *102*, 094510.

[41] D. J. Gundlach, L. Zhou, J. A. Nichols, T. N. Jackson, P. V. Necliudov, M. S. Shur, *J. Appl. Phys.* **2006**, *100*, 024509.

[42] A. Dzwilewski, P. Matyba, L. Edman, *J. Phys. Chem. B* **2010**, *114*, 135.

[43] F. S. Kim, X. Guo, M. D. Watson, S. A. Jenekhe, *Adv. Mater.* **2010**, *22*, 478.

[44] Th. B. Singh, P. Senkarabacak, N. S. Sariciftci, A. Tanda, C. Lackner, R. Hagelauer, G. Horowitz, *Appl. Phys. Lett.* **2006**, *89*, 033512.

FULL PAPER

Controlling The Mobility Of Oligonucleotides In The Nanochannels Of Mesoporous Silica

Timo Lebold, Axel Schlossbauer, Katrin Schneider, Lothar Schermelleh, Heinrich Leonhardt, Thomas Bein,* and Christoph Bräuchle*

Oligonucleotides used in gene therapy and silencing are fragile compounds that degrade easily in biological environments. Porous biocompatible carrier particles may provide a useful strategy to deliver these therapeutics to their target sites. Development of appropriate delivery vehicles, however, requires a better understanding of the oligonucleotide-host interactions and the oligonucleotide dynamics inside carrier particles. We investigated template-free SBA-15 type mesoporous silica particles and report their loading characteristics with siRNA depending on the surface functionalization of their porous network. We show that the siRNA uptake capability of the particles can be controlled by the composition of the functional groups. Fluorescence recovery after photobleaching measurements revealed size-dependent mobility of siRNA and double-stranded DNA oligonucleotides within the functionalized silica particles and provided evidence for the stability of the oligonucleotides inside the pores. Hence, our study demonstrates the potential of mesoporous silica particles as a means for alternative gene delivery in nanomedicine.

1. Introduction

Within the last decade gene therapy, gene silencing and RNA interference (RNAi) methods have attracted increasing interest. However, the fragile oligonucleotides utilized in gene therapy and RNA interference are easily degraded and therefore require robust delivery strategies in order to reach their target

site within the cell. In gene therapy, for example, the DNA needs to be transported into the cell nucleus, either actively or indirectly due to the disassembly of the nuclear envelope during mitosis, whereas siRNAs used in post-transcriptional gene-silencing only need to be delivered to the cytosol.[1–3] Consequently, very different target sites need to be addressed to achieve a safe and efficient delivery of the fragile oligonucleotides.[4–6]

Mesoporous silica, including the M41S materials introduced by the Mobil company[7,8] or Santa Barbara Amorphous (SBA) type materials,[9,10] represents a versatile class of porous nanomaterials. These materials break the long-standing pore size constraint of zeolites by offering pore sizes ranging from about 2–30 nm. Moreover, their specifications such as pore diameter, surface properties, and topologies can be tailor-made according to individual requirements. Various applications for mesoporous silica materials have been suggested, such as molecular sieves,[11] catalysis,[12] chromatography,[13] stabilization of conducting nanoscale wires[14–16] and novel drug-delivery systems.[17–25]

Recently, the potential of mesoporous silica nanoparticles with a diameter of about 100 nm for the delivery of siRNA into mammalian cells was highlighted.[26] In the present study we utilized SBA-15 type mesoporous silica particles with nanometer-sized template-free pores to carry potential gene therapeutics inside their porous network. By varying the chemical nature of the organic pore functionalizations, the loading behavior of the particles with siRNA can be tuned. We used fluorescence recovery after photobleaching (FRAP)[27–29] to investigate the dynamics of siRNA and short double-stranded DNA sequences inside the particles. Moreover, we show that the observed double-stranded oligonucleotides remain intact inside the carrier particles.

Dr. T. Lebold, Dr. A. Schlossbauer, Prof. T. Bein, Prof. C. Bräuchle
Center for Nanoscience (CeNS) and Center for
Integrated Protein Science Munich (CIPSM)
Ludwig-Maximilians-Universität München
Department of Chemistry
Butenandtstraße 11, 81377 Munich, Germany
E-mail: christoph.braeuchle@cup.uni-muenchen.de; bein@lmu.de
K. Schneider, Dr. L. Schermelleh[+]
Ludwig-Maximilians-Universität München
Department of Biology
Großhaderner Straße 2, 82152 Planegg-Martinsried, Germany
Prof. H. Leonhardt
Center for Nanoscience (CeNS) and Center for Integrated Protein
Science Munich (CIPSM)
Ludwig-Maximilians-Universität München
Department of Biology
Großhaderner Straße 2, 82152
Planegg-Martinsried, Germany
[+] Present Address: University of Oxford, Department
of Biochemistry, Oxford OX1 3QU, United Kingdom

2. Results and Discussion

Four different modifications of SBA-15 materials were synthesized: (i) unfunctionalized (UN), functionalized with (ii) 10 mol% cyanopropyl (CP), (iii) 8 mol% aminopropyl + 2 mol% cyanopropyl (APCP), and (iv) 5 mol% aminopropyl + 5 mol% phenyl (APPh). Prior to the loading experiments, the

www.MaterialsViews.com

ADVANCED
FUNCTIONAL
MATERIALS
www.afm-journal.de

FULL PAPER

organic template was extracted from the SBA-15 materials (i–iv) and the template free materials resulted as white solid powders (for details see Materials and Methods).

Scanning electron microscopy (SEM) microscopy images of the SBA-15 materials revealed spherically shaped micrometer-sized particles that show a clear tendency to aggregate independent of their functionality. Moreover, in all samples fused aggregates can be observed that consist of two or more individual spherical particles (**Figure 1**a).

Figure 1b displays a schematic of an SBA-15 particle and cross-sections through a pore for the differently functionalized particles.

Nitrogen sorption isotherms of the different samples confirmed the porosity of the materials (Figure 1c). Accordingly, all synthesized SBA-15 materials contain a porous network that is accessible from the outside. Furthermore, the introduction of organic functionalizations leads to a reduction of the mean pore size by 0.7–1.7 nm compared to an unfunctionalized sample as seen by the resulting pore size distributions (Figure 1d, see also below).

One-dimensional X-ray diffractograms of the different synthesized SBA-15 materials indicate the mesoporous nature of the particles (Figure 1e). The XRD data further show that the introduction of functional groups leads to an increase in the 2θ value and thus to a reduction of the pore-to-pore distance compared to unfunctionalized SBA-15 (see Supporting Information (SI)).

The utilized oligonucleotides (siRNA and dsDNA) were labeled with a green (ATTO532) and a red excitable (ATTO647N) fluorescent dye at the 3′ and 5′ ends of the opposite strands, respectively (Figure 1f). With the dye pair being located on the same side of the double-strand, its stability can be tested through Förster Resonance Energy Transfer (FRET): upon excitation with green light, energy transfer will take place from the red emitting ATTO532 (donor) to the ATTO647N (acceptor) dye and its far-red fluorescence can be monitored. Since FRET is only effective within a distance of both dyes of about 2–10 nm, a denatured oligonucleotide does not yield a FRET signal (see SI).

Table 1 summarizes the data extracted from nitrogen sorption and XRD measurements. The term "pore-to-pore distance" used in combination with XRD data is not identical to the term "pore size" used for discussing nitrogen sorption data, since with X-ray diffractometry only the distance between the different layers (one center of a pore to the center of the adjacent pore) can be calculated and no direct conclusion about the wall thickness can be drawn (see SI). In contrast, nitrogen sorption methods directly yield the pore sizes. Both techniques clearly show that the introduction of functional groups leads to a reduction of the pore dimensions. With a reduction of the mean pore size from 8.9 nm (UN) to 7.8 nm (APPh), the pore-to-pore distance also shrinks from 13.5 nm (UN) to 10.7 nm (APPh). The differences in the BET surface areas result from the co-condensation of TEOS with the different functionalized organo-silanes, all having a specific influence on the condensation of the silica backbone and on the remaining pore volume. This behavior has already been reported in other articles, especially for aminopropyltriethoxysilane.[30–32]

Figure 2 shows images obtained with confocal laser scanning microscopy of the four differently functionalized SBA-15 materials suspended inside the buffered labeled-siRNA solution.
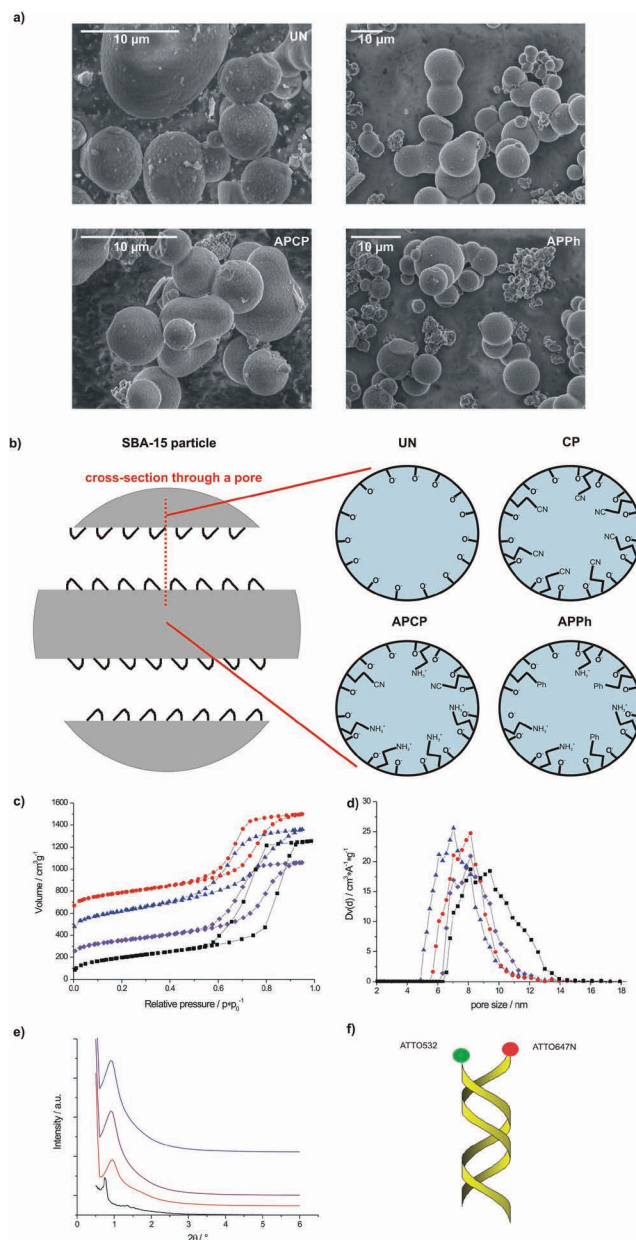
Figure 1. Characterization of the SBA-15 particles and utilized oligonucleotides. a) Scanning electron microscopy images of unfunctionalized (UN), cyanopropyl-functionalized (CP), aminopropyl/cyanopropyl-functionalized (APCP) and aminopropyl/phenyl-functionalized (APPh) SBA-15 particles. The synthesized particles are micrometer-sized, spherically shaped and tend to aggregate. b) Schematic of an SBA-15 particle and cross-sections through a pore for the differently functionalized particles. c) Nitrogen sorption isotherms of UN (black rectangles), CP (purple diamonds, 200 cm³/g offset), APCP (blue triangles, 400 cm³/g offset) and APPh (red dots, 600 cm³/g offset). d) Pore size distribution for UN (black rectangles), CP (purple diamonds), APCP (blue triangles) and APPh (red dots). e) 1D XRD diffractograms for UN (black), APPh (red), CP (purple), and APCP (blue) SBA-15 particles. The introduction of functional groups results in a higher 2θ value and thus a smaller pore-to-pore distance. f) Schematic of an ATTO532 and ATTO647N labeled oligonucleotide double-strand. 20 bp siRNA as well as 20, 60, and 90 bp dsDNA sequences were loaded into the SBA-15 particles. The dye labels are situated on the same side of the opposite strands and thus allow for testing oligonucleotide stability by Förster resonance energy transfer (FRET).

ADVANCED
FUNCTIONAL
MATERIALS
www.afm-journal.de

Materials
Views
www.MaterialsViews.com

Table 1. Nitrogen sorption and 1D-X-ray diffractometry (XRD) data. The mean pore size, the BET surface[47] and the mean pore volume were calculated from nitrogen sorption data. Additionally, the pore-to-pore distances obtained from X-ray diffractograms are listed (see SI).

	Nitrogen sorption			XRD
	Mean pore size [nm]	BET surface [m²g⁻¹]	Mean pore volume [cm³g⁻¹]	Pore-to-pore distance [nm]
UN	8.9	700	1.80	13.5
CP	8.2	580	1.27	11.0
APCP	7.2	815	1.33	11.1
APPh	7.8	680	1.33	10.7

The several micrometer-large mesoporous particles are seen as spherically shaped objects that occasionally aggregate. In confocal mid-sections of APPh particles the siRNA fluorescence can be clearly detected inside the particle indicating that the particles were successfully loaded with siRNA (Figure 2a). Since the confinement of the pore and the specific interaction with different functional groups can influence the extinction coefficient of the dye label significantly, only the relative amounts of siRNA incorporated inside the particles are evaluated here. For example, in APCP particles only about 75% of the amount of siRNA detected inside the APPh particles is observed indicated by a lower signal-to-noise ratio (Figure 2b). The observed variations in the fluorescence intensities cannot be simply due to a

Figure 2. Loading characteristics of functionalized mesoporous SBA-15 particles. Confocal mid-sections of SBA-15 particles dissolved in a buffered solution containing fluorescently labeled siRNA and particles functionalized with a) aminopropyl and phenyl (APPh), b) aminopropyl and cyanopropyl (APCP), c) cyanopropyl (CP), or d) unfunctionalized particles (UN). The images were acquired by exciting the ATTO532 label and detecting the ATTO647N FRET fluorescence signal, thus only stable siRNA can be seen. While fluorescence of the labeled siRNA can be detected inside the APPh and APCP particles, CP and UN particles remain unloaded. Only weak fluorescence in the surrounding solution can be detected. The length and intensity scale bars apply to all panels (a–d).

different quenching or enhancement of the fluorophore brightness through the different functional groups in the samples, since the free label dyes do not show significant fluorescence intensity fluctuations inside the four different samples (data not shown). Consequently, the observed variations must result from a different amount of incorporated siRNA. In contrast, CP and UN particles do not take up detectable amounts of siRNA (Figure 2c and d), even though the nitrogen sorption data of Table 1 clearly show that all four particle types are accessible and open to an exchange with the surrounding environment. With the utilized confocal microscopy setup concentrations of siRNA down to about 10^{-8} molL^{-1} in solution can be detected.

The pore sizes calculated from nitrogen sorption of the different samples range from 7.2 nm (APCP), 7.8 nm (APPh), 8.2 nm (CP) to 8.9 nm (UN) (see Table 1). However, the overall loading behavior cannot be explained by a simple pore-size effect. The pore sizes of the CP and UN SBA-15 materials are even slightly larger than those with functionalizations that do allow siRNA incorporation. We thus attribute the observed behavior to an unfavorable interaction of the particle surfaces with the negatively charged siRNA. All investigated SBA-15 materials possess hydroxyl groups on their surface that may be partially deprotonated. These (deprotonated) hydroxyl groups and the cyanopropyl groups seem to repel the siRNA because of their negative charge density. In contrast, the aminopropyl-functionality attached to the pore walls of the APCP and APPh particles seems to favor siRNA uptake, which may result from hydrogen bonding between the negatively charged siRNA and the (protonated) amino groups. Taking these considerations into account, the increased loading capacity of APPh silica particles compared to the APCP particles could also result from the electrostatic repulsion between the negatively charged siRNA and the cyanopropyl-groups. Additionally, recent work from Mellaerts et al.[33] demonstrates that variations in the electrostatic interactions between a guest molecule, such as the drug itraconazole, and the pore walls, e.g., by adapting the water content inside the pores, lead to a different drug release rate and thus also different drug dynamics inside the SBA-15 network. A comparison with purely aminopropyl-functionalized SBA-15 particles was not possible, as the corresponding synthesis solution did not yield a mesoporous powder but an undefined gelated structure.

Notably, the successful loading of APPh and APCP particles was detected by the FRET signal of closely positioned ATTO532 and ATTO647N fluorophores. This clearly indicates that the siRNAs were present as double-stranded hybrid molecules, which is essential within the therapeutic context of gene silencing by RNA interference. Control measurements under denaturing conditions show a complete loss of FRET signal (see SI). No significant loss of siRNA fluorescence inside the APPh and APCP particles was observed within 48 h, demonstrating long-term stability of siRNAs inside the particles as well as inside the surrounding buffered solution.

The above results provide evidence that aminopropyl-containing functionalities favor siRNA uptake into the mesoporous materials. We next aimed to characterize the mobility of oligonucleotides inside functionalized SBA-15 particles. We therefore applied fluorescence recovery after photobleaching (FRAP) and kinetic modeling to determine the diffusion constants of
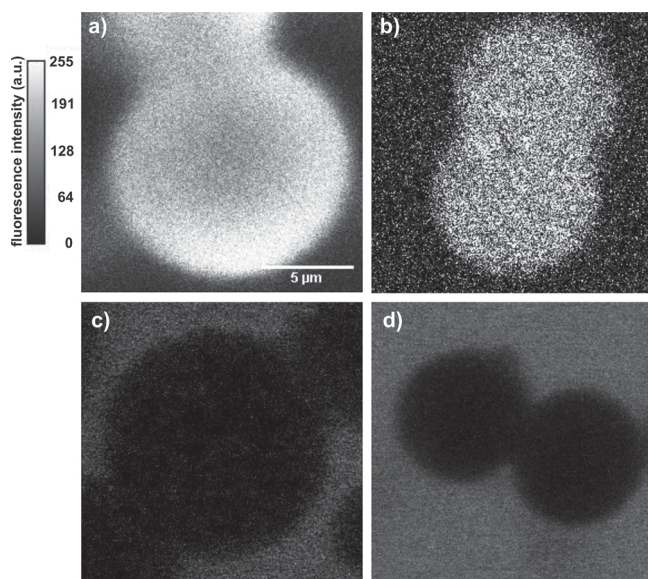
www.MaterialsViews.com

ADVANCED
FUNCTIONAL
MATERIALS
www.afm-journal.de

FULL PAPER

Figure 3. FRAP recovery curves and mean diffusion coefficients for the different oligonucleotides inside the functionalized SBA-15 particles. a) Recovery kinetics of the 20 bp siRNA molecules inside APCP functionalized particles (green) and inside APPh functionalized particles (black). b) APPh functionalized particles loaded with 20 bp DNA (red), 60 bp DNA (blue) and 90 bp DNA (black). c, d) Results of the kinetic modeling with diffusion coefficients $\langle D_{fast} \rangle$ and $\langle D_{slow} \rangle$ determined for the two mobile populations in each sample. c) siRNA inside APCP particles (green) and inside APPh particles (black). d) APPh particles loaded with 20 bp DNA (red), 60 bp DNA (blue) and 90 bp DNA (black). The error bars indicate standard deviation (a, b) and standard error (c, d).

(i) the 20 bp siRNA oligonucleotides inside APPh and APCP particles and (ii) DNA double-strands of different length (20, 60 and 90 bp) inside APPh particles. The utilized double-stranded labeled oligonucleotides have an estimated length of about 7 nm (20 bp), 21 nm (60 bp) and 31 nm (90 bp). All sequences were randomly chosen, however, it was ascertained that they do not form large hairpins or bubbles that might additionally affect diffusion. The measurements started 3 h after incubation of the particles with the oligonucleotide solution and DNA stability was again confirmed through FRET.

For FRAP experiments small circular regions of interest (ROIs) were bleached by a high intensity laser beam to result in a bleach spot with a diameter of about 2 μm. The bleaching sites were randomly chosen inside the particle, either centrally or closer to the edges. Fluorescence recovery was observed for 10–15 min. Mean curves were calculated for the siRNA and the DNA sequences in the differently functionalized particles by averaging the recovery kinetics of at least 10 bleach spots each (**Figure 3**a, b).

We first measured the mobility of siRNA inside APCP and APPh particles (Figure 3a) and found significantly faster recovery kinetics of siRNAs inside the cyanopropyl-containing particles despite of their smaller pore size (see Table 1). As discussed for Figure 2 this may be due to an increased repulsive interaction between the siRNA and the cyanopropyl groups compared to the phenyl groups. A similar slowdown of the diffusing species upon insertion of phenyl groups was observed

in a recent study.[34] It is important to note that the apparent standard deviations displayed in Figure 3a and b do not reflect the error in determining the mean fluorescence intensity, but originate from the inherent heterogeneity of the different mesoporous particles. Such heterogeneities are typical for these mesoporous silica materials due to the existence of adsorption sites, dead ends and structural defects.[35–39] The effective diameter of the circular bleaching ROI in the FRAP experiments was about 2 μm. Heterogeneities occurring within this length-scale might account for some of the variability of recovery kinetics observed for different bleaching sites. Detailed diffusion studies of molecules in mesoporous hosts have demonstrated that heterogeneities due to structural variations indeed occur on such a length-scale.[35]

Figure 3b displays mean recovery curves for the 20 bp (red), 60 bp (blue) and 90 bp (black) dsDNA sequences diffusing inside APPh SBA-15 particles. The results clearly demonstrate a size-dependent decrease of dsDNA mobility. In neither case full recovery was observed, indicating a distinct immobile fraction of molecules present inside the particles.[40] It is important to note that bleaching only implies that the fluorescent label attached to the DNA gets irreversibly inactivated and thus the DNA becomes invisible. However, the dsDNA is still present and, due to its immobility, may block the adsorption sites inside the particle, preventing new fluorescent oligonucleotides from diffusing to these sites. In contrast, bleached mobile DNA molecules should be able to diffuse out of the particle. The data

ADVANCED
FUNCTIONAL
MATERIALS
www.afm-journal.de

Materials
Views
www.MaterialsViews.com

shown in Figure 3b clearly indicate that the fraction of immobile molecules increases significantly with increasing length of the DNA double-strand. This could be explained by stronger adsorption of longer dsDNA inside the porous network due to an increased negative charge.

Next, the mean fluorescence recovery curves were fitted to a diffusion model in order to extract diffusion coefficients and thereby quantify the mobility of the oligonucleotides inside the mesoporous particles. In order to describe the data adequately a model assuming two different diffusion coefficients was necessary (see exemplary data in the Supporting Information). The utilized model for the fluorescence recovery curve $f(t)$ is given in Equation 1.

$$
\begin{aligned}
f(t) = {} & 1 - \phi + \phi \exp\left(\frac{-2t_{D_{fast}}}{t}\right)\left[I_0\left(\frac{2t_{D_{fast}}}{t}\right) + I_1\left(\frac{2t_{D_{fast}}}{t}\right)\right] \\
& + \theta\left(\phi \exp\left(\frac{-2t_{D_{slow}}}{t}\right)\left[I_0\left(\frac{-2t_{D_{slow}}}{t}\right) + I_1\left(\frac{-2t_{D_{slow}}}{t}\right)\right]\right. \\
& \left.\left(-\phi \exp\left(\frac{-2t_{D_{fast}}}{t}\right)\left[I_0\left(\frac{2t_{D_{fast}}}{t}\right) + I_1\left(\frac{2t_{D_{fast}}}{t}\right)\right]\right)\right) \\
= {} & f_{D_{fast}}(t) + \theta\left[f_{D_{slow}}(t) - f_{D_{fast}}(t)\right]
\end{aligned}
$$

(1)

with $t_D = \omega^2/4D$ and thus the two diffusion coefficients $\langle D_{fast}\rangle$ and $\langle D_{slow}\rangle$. The superposition parameter θ indicates the relative contributions of the two populations. The values of ϕ (bleached fraction) and ω (full width at half maximum of the bleach spot) were extracted from the experimental data (for details of the modeling see Supporting Information). Modeling the mean fluorescence recovery curves of Figure 3a and b according to Eq. 1 yielded the two mean diffusion coefficients $\langle D_{fast}\rangle$ and $\langle D_{slow}\rangle$ for the mobile populations in each sample (see Figure 3c and d). The mean diffusion coefficients obtained from siRNA inside APCP particles (green) and inside APPh particles (black) are displayed in Figure 3c, whereas the data for 20 bp DNA (red), 60 bp DNA (blue) and 90 bp DNA (black) diffusing inside APPh particles are displayed in Figure 3d. The calculated values of $\langle D_{fast}\rangle$ and $\langle D_{slow}\rangle$ are listed in **Table 2**. The recovery kinetics of the 90 bp double-stranded DNA are too slow to be fitted accurately by the utilized model. Thus, only an upper limit for the mean diffusion coefficients could be determined. The mean diffusion coefficient of the faster diffusing population $\langle D_{fast}\rangle$ can be attributed to oligonucleotide molecules diffusing inside the mesoporous channels of the SBA-15 particles. The determined diffusion coefficients (see Table 2) lie within the range of those known for diffusion dynamics of organic molecules such as dyes or drugs inside mesoporous materials, which is in the range of hundreds to thousands nm²/s,[34,36,41] and slightly above those found for intraparticle diffusion in zeolites.[42] The siRNA is significantly slower in the phenyl-containing particles and the DNA diffusion slows down with increasing double-strand length. A quantitative model for the relationship between the mean diffusion coefficients $\langle D_{fast}\rangle$ and the length of the dsDNA is beyond the scope of this publication. The real situation could only be approximated by the Stokes–Einstein equation[1] for an ellipsoid moving lengthwise inside the pore.[2] However, effects such as the interaction of

the highly charged oligonucleotides with the channel walls that could influence the diffusion coefficients would not be included in this case.

Regarding the second slow diffusing population, it was previously shown that the presence of binding sites can be detected as an "effective diffusion coefficient".[44] This effective diffusion thus refers to a slowing down of the initially unhindered diffusion due to binding events. However, this would not necessarily explain a distinct second population, but a general decrease in the observed mean diffusion coefficient. Interestingly, $\langle D_{slow}\rangle$ does not show a clear trend for the different samples in contrast to $\langle D_{fast}\rangle$. If the oligonucleotides degraded, resulting in the presence of shorter labeled fragments, one would expect to find fragments with higher dynamics compared to the intact double-strands. We thus attribute the observation of a slow diffusion coefficient not to the existence of a distinct second slow diffusing population, but rather to a manifestation of the inherent heterogeneity of the samples resulting in a variation of the diffusion coefficients.[36]

3. Conclusion

In conclusion, this study shows that the loading behavior of oligonucleotides into SBA-15 particles critically depends on the surface functionalization. Unfunctionalized and cyanopropyl-functionalized SBA-15 could not be loaded with siRNA. We attribute this behavior to an unfavorable repulsive interaction of the negatively charged siRNA with the negative charge density of these functional groups. However, when adjusting the surface polarity of the particles by coating the channels with aminopropyl groups, the repulsive interactions get reduced, further hydrogen bonding sites and favorable Coulombic interactions are introduced and thus the particles become accessible for siRNA and can be loaded. Moreover, the SBA-15 particles could be loaded with DNA double-strands, ranging from 20 up to a double-strand sequence of 90 bp in length. The stretched-out 90 bp oligonucleotide double-strands have a length of about 31 nm including the labels. This is a striking observation, since the pore sizes of the mesoporous silica samples only range from about 7–9 nm. The fact that fairly long DNA sequences can be loaded into mesoporous silica

Table 2. Calculated mean diffusion coefficients for the fast and slow diffusing populations (±standard error of the mean).

	APPh [nm²/s]	APCP [nm²/s]
siRNA	$\langle D_{fast}\rangle = 5.7 * 10^2 + 1.7 * 10^2$	$\langle D_{fast}\rangle = 3.4 * 10^3 + 5.9 * 10^2$
	$\langle D_{slow}\rangle = 3.7 * 10^2 + 1.2 * 10^2$	$\langle D_{slow}\rangle = 1.8 * 10^2 + 4.9 * 10^1$
20 bp DNA	$\langle D_{fast}\rangle = 6.9 * 10^2 + 1.3 * 10^2$	—
	$\langle D_{slow}\rangle = 1.1 * 10^2 + 1.7 * 10^1$	—
60 bp DNA	$\langle D_{fast}\rangle = 4.6 * 10^2 + 1.6 * 10^2$	—
	$\langle D_{slow}\rangle = 1.3 * 10^2 + 2.6 * 10^1$	—
90 bp DNA	$\langle D_{fast}\rangle < 1.9 * 10^2 + 9.1 * 10^1$	—
	$\langle D_{slow}\rangle < 8.9 * 10^1 + 1.4 * 10^1$	—

www.MaterialsViews.com

ADVANCED
FUNCTIONAL
MATERIALS
www.afm-journal.de

FULL PAPER

opens up numerous potential applications in drug-delivery. Importantly, for all oligonucleotide sequences studied here, their stability inside the mesoporous materials could be proven by FRET. Our study also demonstrates that the diffusion dynamics of siRNA inside the template-extracted particles could be tuned through adding functional groups. The experiments show that the diffusion dynamics of the DNA critically depend on their length and that long DNA sequences show a higher tendency to get immobilized at adsorption sites inside the porous network.

Understanding the principles that govern oligonucleotide dynamics inside the channels of mesoporous silica is of great importance for the design of successful drug carriers with controlled retarded release of a drug over a prolonged period of time. Thus, our study shows that mesoporous silica materials are a versatile platform for siRNA delivery and that they enable alternative strategies for gene therapy.

4. Experimental Section

Preparation of Template-Free SBA-15 Particles: The large-pore SBA-15 spherical particles were synthesized following a procedure generally introduced by Katiyar et al.[45] and later used by Schlossbauer et al.[46] for producing mesoporous silica spheres as a matrix for biofunctionalization. The surfactant Pluronic P123 (3.0 g, poly(ethylene oxide)$_{20}$-poly(propylene oxide)$_{70}$-poly(ethylene oxide)$_{20}$) was dissolved in hydrochloric acid (60 mL, 1.5 molL^{-1}). Cetyltrimethyl ammonium bromide (CTAB, 0.6 g) was used as a co-surfactant in combination with 1,3,5-trimethylbenzene (TMB, 0.3 g) as a swelling agent to increase the pore diameter. CTAB and TMB were mixed with 25 mL of distilled water. After combining the aqueous solution with the acidic solution, ethanol (pure, 20 mL) was added under stirring. Subsequently, tetraethyl orthosilicate (TEOS, 10 mL) was added dropwise. The resulting mixture was stirred vigorously (500 rpm) at 35 °C for 45 min before being transferred into an autoclave (Parr Instrument Company) for hydrothermal treatment at 75 °C for 12 hours under static conditions. Subsequently, the mixture was treated at 125 °C for 12 h. The resulting white powder was filtered out, washed with distilled water (100 mL) and ethanol (pure, 100 mL) and dried at 60 °C for another 12 h. For the synthesis of functionalized silica particles, a certain molar fraction (up to 10 mol%) of the silica source (TEOS) was replaced with a functionalized silica source. The functionalized silica precursors were: $H_2NC_3H_6Si(OC_2H_5)_3$ for aminopropyl-, $C_6H_5Si(OC_2H_5)_3$ for phenyl- and $CNC_3H_6Si(OC_2H_5)_3$ for cyanopropyl-functionalization. Four different modifications of SBA-15 materials were synthesized: (i) unfunctionalized (UN), functionalized with (ii) 10 mol% cyanopropyl (CP), (iii) 8 mol% aminopropyl + 2 mol% cyanopropyl (APCP), and (iv) 5 mol% aminopropyl + 5 mol% phenyl (APPh).

Extraction of the organic template from the SBA-15 materials was performed by heating 1 g of the white powder twice under reflux at 90 °C for 30 min in 100 mL of a solution containing concentrated hydrochloric acid (10 mL) and ethanol (90 mL). The SBA-15 material was separated by filtration and washed with ethanol (100 mL) after each extraction step. The template-extracted samples were obtained as white solid powders.

Particle Characterization: The four different SBA-15 samples were characterized with scanning electron microscopy (SEM), nitrogen sorption and 1D X-ray diffractometry. SEM micrographs were recorded on a JEOL JSM-6500F scanning electron microscope. Nitrogen sorption measurements were performed on a Quantachrome Nova 4000e instrument. The structure of the SBA-15 powders was determined by using a Scintag XDS 2000 powder diffractometer in θ/θ Bragg-Brentano scattering geometry. From the obtained X-ray diffractograms the pore-to-pore distances were calculated (for details see Supporting Information).

Particle Loading with siRNA: First, the loading behavior of the particles with siRNA was examined. For this purpose, the differently functionalized SBA-15 powders obtained after surfactant removal were dissolved in PBS buffer (pH = 7.4) and labeled siRNA (20 bp) was added at a concentration of 10^{-5} molL^{-1} to each of the different SBA-15 samples. Then the samples were incubated for 3 h at room temperature in order to give the siRNA sufficient time to access the particles (control experiments showed that no increase of siRNA-dye-fluorescence could be observed inside the SBA-15 particles after that time). The particles were then microscopically investigated in a sample chamber immersed in the buffered siRNA solution. The following double-labelled siRNA double-strand was used: 5' GGA CUC CAG UGG UAA UCU AC ATTO647N 3'; 3' CCU GAG GUC ACC AUU AGA UG ATTO532 5' (IBA GmbH, Göttingen, Germany). The double-strand sequence was randomly chosen.

Microscopy Setup: The different oligonucleotide SBA-15 samples were measured on a LSM510 confocal laser scanning microscope (Carl Zeiss AG) as follows: only the green fluorescent dye label was excited with a He-Ne-laser emitting at 543 nm through a 40x/1.3 NA oil-immersion objective (Zeiss Plan Neofluar) The fluorescence was filtered by a beamsplitter (HFT, UV/488/543/633) in combination with a long-pass filter (LP 650) in order to detect the FRET fluorescence signal from the red fluorescent dye label. The FRET signal was detected with a photomultiplier.

Fluorescence Recovery after Photobleaching (FRAP) Measurements: The utilized confocal setup is identical to the setup introduced above with the following additional settings for the FRAP measurements: integration time per frame: 983 ms/frame; a new frame was recorded every 4 s; 10 scans before bleaching; circular bleaching region of 10 pixels in diameter. The bleaching sites were chosen randomly amongst different particles and also within the particle (either centrally or closer to the edges). For each sample at least 10 bleaching spots were analyzed. Individual recovery curves were extracted for each bleaching event and then averaged. The method of data evaluation in order to obtain fluorescence recovery curves is explained in detail in the Supporting Information.

DNA Sequences for FRAP Measurements: The following DNA double-strand sequences were used: 5' GGA CGC CAG GGG GAA GCG AC ATTO647N 3'; 3' CCT GCG GTC CCC CTT CGC TG ATTO532 5' for the 20bp DNA, 5' GGA CGC CAG GGG GAA GCG ACG GAC GCC AGG ATTO532 3'; 3' CCT GCG GTC CCC CTT CGC TGC CTG CGG TCC ATTO647N 5' for the 30 bp DNA, 5' GGA CGC CAG GGG GAA GCG ACG GAC GCC AGG CTG ATT TGA AGC TTA TGA CTT ATT GGA CCT ATTO532 3'; 3' CCT GCG GTC CCC CTT CGC CTC CTG CGG TCC GAC TAA ACT TCG AAT ACT GAA TAA CCT GGA ATTO647N 5' for the 60 bp DNA and 5' GGA CGC CAG GGG GAA GCG ACG GAC GCC AGG CTG ATT TGA AGC TTA TGA CTT ATT GGA CCT ATC TCT GAC ATA TTA TAC TAG GCT GTG TTT ATTO532 3'; 3' CCT GCG GTC CCC CTT CGC TGC CTG CGG TCC GAC TAA ACT TCG AAT ACT GAA TAA CCT GGA TAG AGA CTG TAT AAT ATG ATC CGA CAC AAA ATTO647N 5' for the 90 bp DNA (IBA GmbH, Göttingen, Germany). The procedures for loading the SBA-15 particles were identical to those for siRNA.

Supporting Information

Supporting Information is available from the Wiley Online Library or from the author.

Acknowledgements

FULL PAPER

[1] A. R. Vanderkrol, L. A. Mur, M. Beld, J. N. M. Mol, A. R. Stuitje, *Plant. Cell.* **1990**, *2*, 291.

[2] J. M. Kooter, R. Vanblokland, P. Delange, M. Stam, J. N. M. Mol, *J. Cell. Biochem.* **1994**, 115.

[3] D. A. Dean, D. D. Strong, W. E. Zimmer, *Gene Ther.* **2005**, *12*, 881.

[4] H. Mok, S. H. Lee, J. W. Park, T. G. Park, *Nat. Mater.* **2010**, *9*, 272.

[5] K. A. Whitehead, R. Langer, D. G. Anderson, *Nat. Rev. Drug Discov.* **2010**, *9*, 412.

[6] S. C. Semple, A. Akinc, J. X. Chen, A. P. Sandhu, B. L. Mui, C. K. Cho, D. W. Y. Sah, D. Stebbing, E. J. Crosley, E. Yaworski, I. M. Hafez, J. R. Dorkin, J. Qin, K. Lam, K. G. Rajeev, K. F. Wong, L. B. Jeffs, L. Nechev, M. L. Eisenhardt, M. Jayaraman, M. Kazem, M. A. Maier, M. Srinivasulu, M. J. Weinstein, Q. M. Chen, R. Alvarez, S. A. Barros, S. De, S. K. Klimuk, T. Borland, V. Kosovrasti, W. L. Cantley, Y. K. Tam, M. Manoharan, M. A. Ciufolini, M. A. Tracy, A. de Fougerolles, I. MacLachlan, P. R. Cullis, T. D. Madden, M. J. Hope, *Nat. Biotechnol.* **2010**, *28*, 172.

[7] J. S. Beck, J. C. Vartuli, W. J. Roth, M. E. Leonowicz, C. T. Kresge, K. D. Schmitt, C. T. W. Chu, D. H. Olson, E. W. Sheppard, S. B. McCullen, J. B. Higgins, J. L. Schlenker, *J. Am. Chem. Soc.* **1992**, *114*, 10834.

[8] C. T. Kresge, M. E. Leonowicz, W. J. Roth, C. E. Vartuli, J. S. Beck, *Nature* **1992**, *359*, 710.

[9] D. Y. Zhao, J. L. Feng, Q. S. Huo, N. Melosh, G. H. Fredrickson, B. F. Chmelka, G. D. Stucky, *Science* **1998**, *279*, 548.

[10] D. Y. Zhao, Q. S. Huo, J. L. Feng, B. F. Chmelka, G. D. Stucky, *J. Am. Chem. Soc.* **1998**, *120*, 6024.

[11] S. J. L. Billinge, E. J. McKimmy, M. Shatnawi, H. Kim, V. Petkov, D. Wermeille, T. J. Pinnavaia, *J. Am. Chem. Soc.* **2005**, *127*, 8492.

[12] D. E. De Vos, M. Dams, B. F. Sels, P. A. Jacobs, *Chem. Rev.* **2002**, *102*, 3615.

[13] V. Rebbin, R. Schmidt, M. Fröba, *Angew. Chemie Int. Ed.* **2006**, *45*, 5210.

[14] N. Petkov, N. Stock, T. Bein, *J. Phys. Chem. B* **2005**, *109*, 10737.

[15] B. Ye, M. L. Trudeau, D. M. Antonelli, *Adv. Mat.* **2001**, *13*, 561.

[16] D. J. Cott, N. Petkov, M. A. Morris, B. Platschek, T. Bein, J. D. Holmes, *J. Am. Chem. Soc.* **2006**, *128*, 3920.

[17] H. A. Meng, M. Xue, T. A. Xia, Y. L. Zhao, F. Tamanoi, J. F. Stoddart, J. I. Zink, A. E. Nel, *J. Am. Chem. Soc.* **2010**, *132*, 12690.

[18] V. Cauda, H. Engelke, A. Sauer, D. Arcizet, C. Brauchle, J. Radler, T. Bein, *Nano Lett.* **2010**, *10*, 2484.

[19] A. Sauer, A. Schlossbauer, N. Ruthardt, V. Cauda, T. Bein, C. Bräuchle, *Nano Lett.* **2010**, *10*, 3684.

[20] T. Lebold, C. Jung, J. Michaelis, C. Brauchle, *Nano Lett.* **2009**, *9*, 2877.

[21] D. P. Ferris, Y. L. Zhao, N. M. Khashab, H. A. Khatib, J. F. Stoddart, J. I. Zink, *J. Am. Chem. Soc.* **2009**, *131*, 1686.

[22] I. Roy, T. Y. Ohulchanskyy, D. J. Bharali, H. E. Pudavar, R. A. Mistretta, N. Kaur, P. N. Prasad, *Proc. Natl. Acad. Sci. USA* **2005**, *102*, 279.

[23] S. Giri, B. G. Trewyn, V. S. Y. Lin, *Nanomed.* **2007**, *2*, 99.

[24] S. Giri, B. G. Trewyn, M. P. Stellmaker, V. S. Y. Lin, *Angew. Chemie Int. Ed.* **2005**, *44*, 5038.

[25] F. Torney, B. G. Trewyn, V. S. Y. Lin, K. Wang, *Nature Nanotech.* **2007**, *2*, 295.

[26] C. Hom, J. Lu, M. Liong, H. Luo, Z. Li, J. I. Zink, F. Tamanoi, *Small* **2010**, *6*, 1185.

[27] D. Axelrod, D. E. Koppel, J. Schlessinger, E. Elson, W. W. Webb, *Biophys. J.* **1976**, *16*, 1055.

[28] D. E. Koppel, D. Axelrod, J. Schlessinger, E. L. Elson, W. W. Webb, *Biophys. J.* **1976**, *16*, 1315.

[29] T. K. L. Meyvis, S. C. De Smedt, P. Van Oostveldt, J. Demeester, *Pharm. Res.* **1999**, *16*, 1153.

[30] A. Sayari, E. Da'na, *Chem. Eng. J.* **2011**, *166*, 445.

[31] J. H. Yim, J. A. Bae, S. H. Hwang, K. C. Song, J. K. Jeon, Y. S. Ko, *J. Nanosci. Nanotechnol.* **2010**, *10*, 290.

[32] S. R. Zheng, Q. Tao, Z. Y. Xu, J. H. Wang, F. L. Liu, H. Q. Wan, *Microp. Mesop. Mat.* **2010**, *131*, 177.

[33] R. Mellaerts, M. B. J. Roeffaers, K. Houthoofd, M. Van Speybroeck, G. De Cremer, J. A. G. Jammaer, G. Van den Mooter, P. Augustijns, J. Hofkens, J. A. Martens, *Phys. Chem. Chem. Phys.* **2011**, *13*, 2706.

[34] T. Lebold, L. A. Mühlstein, J. Blechinger, M. Riederer, H. Amenitsch, R. Köhn, K. Peneva, K. Müllen, J. Michaelis, C. Bräuchle, T. Bein, *Chem. Europ. J.* **2009**, *15*, 1661.

[35] A. Zürner, J. Kirstein, M. Doblinger, C. Bräuchle, T. Bein, *Nature* **2007**, *450*, 705.

[36] J. Kirstein, B. Platschek, C. Jung, R. Brown, T. Bein, C. Bräuchle, *Nat. Mater.* **2007**, *6*, 303.

[37] C. Jung, J. Kirstein, B. Platschek, T. Bein, M. Budde, I. Frank, K. Müllen, J. Michaelis, C. Bräuchle, *J. Am. Chem. Soc.* **2008**, *130*, 1638.

[38] M. B. J. Roeffaers, G. De Cremer, H. Uji-i, B. Muls, B. F. Sels, P. A. Jacobs, F. C. De Schryver, D. E. De Vos, J. Hofkens, *Proc. Natl. Acad. Sci. USA* **2007**, *104*, 12603.

[39] G. De Cremer, B. F. Sels, D. E. De Vos, J. Hofkens, M. B. J. Roeffaers, *Chem. Soc. Rev.* **2010**, *39*, 4703.

[40] E. A. J. Reits, J. J. Neefjes, *Nat. Cell. Biol.* **2001**, *3*, E145.

[41] G. De Cremer, M. B. J. Roeffaers, E. Bartholomeeusen, K. F. Lin, P. Dedecker, P. P. Pescarmona, P. A. Jacobs, D. E. De Vos, J. Hofkens, B. F. Sels, *Angew. Chemie Int. Ed.* **2010**, *49*, 908.

[42] M. Pfenniger, G. Calzaferri, *ChemPhysChem* **2000**, *1*, 211.

[43] A. Einstein, *Ann. Phys. Berlin* **1905**, *17*, 549.

[44] B. L. Sprague, R. L. Pego, D. A. Stavreva, J. G. McNally, *Biophys. J.* **2004**, *86*, 3473.

[45] A. Katiyar, S. Yadav, P. G. Smirniotis, N. G. Pinto, *J. Chromatogr. A* **2006**, *1122*, 13.

[46] A. Schlossbauer, D. Schaffert, J. Kecht, E. Wagner, T. Bein, *J. Am. Chem. Soc.* **2008**, *130*, 12558.

[47] S. Brunauer, P. H. Emmett, E. Teller, *J. Am. Chem. Soc.* **1938**, *60*, 309.

FULL PAPER

CO$_2$-Laser-Induced Growth of Epitaxial Graphene on 6H-SiC(0001)

Spyros N. Yannopoulos,* Angeliki Siokou,* Nektarios K. Nasikas, Vassilios Dracopoulos, Fotini Ravani, and George N. Papatheodorou

The thermal decomposition of SiC surface provides, perhaps, the most promising method for the epitaxial growth of graphene on a material useful in the electronics platform. Currently, efforts are focused on a reliable method for the growth of large-area, low-strain epitaxial graphene that is still lacking. Here, a novel method for the fast, single-step epitaxial growth of large-area homogeneous graphene film on the surface of SiC(0001) using an infrared CO$_2$ laser (10.6 μm) as the heating source is reported. Apart from enabling extreme heating and cooling rates, which can control the stacking order of epitaxial graphene, this method is cost-effective in that it does not necessitate SiC pre-treatment and/or high vacuum, it operates at low temperature and proceeds in the second time scale, thus providing a green solution to EG fabrication and a means to engineering graphene patterns on SiC by focused laser beams. Uniform, low–strain graphene film is demonstrated by scanning electron microscopy, X-ray photoelectron spectroscopy, secondary ion-mass spectroscopy, and Raman spectroscopy. Scalability to industrial level of the method described here appears to be realistic, in view of the high rate of CO$_2$-laser-induced graphene growth and the lack of strict sample–environment conditions.

1. Introduction

Although graphene has been known for long time,[1,2] the isolation of free-standing monolayers[3] triggered extensive investigations over the last few years exploring its outstanding electronic, mechanical and thermal properties.[3,4] Three basic methods have been employed for graphene production, as reviewed recently.[2] Chemical vapor deposition (CVD) of hydrocarbons and epitaxial growth on transition metals' surfaces such as Ni or Cu has been successfully used for large area graphene growth.[5] Mechanical cleavage of graphene (MCG) from highly oriented pyrolitic graphite (HOPG) produces high-quality, small-size, graphene monolayers (MLs),[3] whose potential for electronics applications is still unclear, although being useful for studying fundamental properties of two-dimensional crystals. Perhaps

the most promising method for large-area, high-quality graphene production is the thermal decomposition of SiC due to Si sublimation, which leads to the growth of or epitaxial graphene (EG);[6] a method known since the seventies.[7] The main advantage of this method is that graphene grows directly on a material useful in the electronics platform. The epitaxial growth method has itself several variants, it can proceed under ultrahigh vacuum (UHV) at ~1200 °C,[1] in the presence of inert gasses at ambient pressure or low vacuum and high temperature (~1550 °C),[8] and under other confinement controlled sublimation conditions of SiC.[1] Recently, EG was grown on SiC by molecular beam epitaxy.[9] Graphene grows on both the Si-terminated (0001) and the C-terminated (000$\bar{1}$) face (faster growth rate) of the SiC wafer, albeit with different electronic properties. Finally, other methods employ exfoliation of graphite oxide to form graphene oxide, which can be reduced to become electrically active.[10]

The above methods for EG growth employ high-temperature induction furnaces where the whole SiC wafer area is exposed to heat. Although EG produced in this way can be patterned using nanolithography methods[4,11,12] in order to be compatible with semiconductors technology, more convenient methods that make use of in situ patterning of graphene would be more valuable for the scale-up of the EG growth on an industrial scale. Along this direction, few studies have pointed out the possibility for simultaneous synthesis and patterning of graphene using laser beams.[13,14] In a recent investigation, EG was grown on the Si-face of SiC by the UV laser line (248 nm) of an KF excimer pulsed laser.[13] The surface-induced laser decomposition of the Si surface led to spatially controlled and scalable EG synthesis. The substrate was held at room temperature and the operation was carried in a vacuum chamber (10^{-6} Torr). Using the visible (532 nm) line of a solid-state laser to increase local heating, rapid printing of graphene patterns on nickel foil were achieved by means of CVD in a CH$_4$/H$_2$ environment.[14] The substrate was held at room temperature and the graphene growth rate was estimated to be orders of magnitude faster than that of conventional CVD. Finally, in the pre-graphene era, it was observed that irradiation of polycrystalline SiC with a pulsed near-infrared Nd:YAG laser (1064 nm) yields

Dr. S. N. Yannopoulos, Dr. A. Siokou, N. K. Nasikas,
Dr. V. Dracopoulos, F. Ravani, Prof. G. N. Papatheodorou
Foundation for Research and Technology–Hellas
Institute of Chemical Engineering and High-Temperature
Chemical Processes (FORTH/ICE–HT), P.O. Box 1414,
GR-26504, Rio-Patras, Greece
E-mail: sny@iceht.forth.gr; siokou@iceht.forth.gr

"crystallized" graphite on the SiC surface.[15] The graphitic structure of the irradiated area (~500 μm²) was confirmed by Raman scattering. Unfortunately, the spectra obtained at that time were not extended above 1800 cm⁻¹ and the typical graphene spectral features were not examined. From the above brief survey, it becomes clear that the use of focused laser beams, apart from enabling patterning, offer viable solutions to lower the graphene growth temperature down to ambient as well as to speed-up the growth process.

In the present article we demonstrate a novel facile method for the single-step, fast production of large-area, homogeneous EG on the SiC(0001) using a continuous-wave infrared CO_2 laser (10.6 μm) as a heating source. The process does not require high-vacuum or strict sample-chamber conditions; it takes place under Ar gas flow at atmospheric pressure and temperature. The present method offers a number of advantages in relation not only to conventional EG growth methods but also compared with the UV-laser-assisted EG growth.[13] i) Ambient growth of EG; UHV or high vacuum is not necessary. ii) The CO_2 laser beam can induce EG growth within the second time scale, depending on laser power, over a large area (~3–4 mm²). iii) Irradiation takes place at one SiC face (000$\bar{1}$ in the present case), while graphene grows epitaxially at the opposite side (polished Si-face). As a result, the Si-face smoothness is preserved. This geometry (**Scheme 1**) enables the feasibility of writing graphene patterns on a SiC(0001) surface in contact with a substrate. iv) The cooling rate, which is essential for the uniformity of the stresses that develop on EG, can be as high as ~600 K s⁻¹ The fast cooling rate might also affect the stacking order or stacking faults of Si-face EG, which is the dominant factor affecting carrier mobility.[8,11] v) No pre-treatment (e.g., H_2 etching, and so on) of SiC surface is needed to obtain high-quality graphene, in contrast to the vast majority of the previous studies.
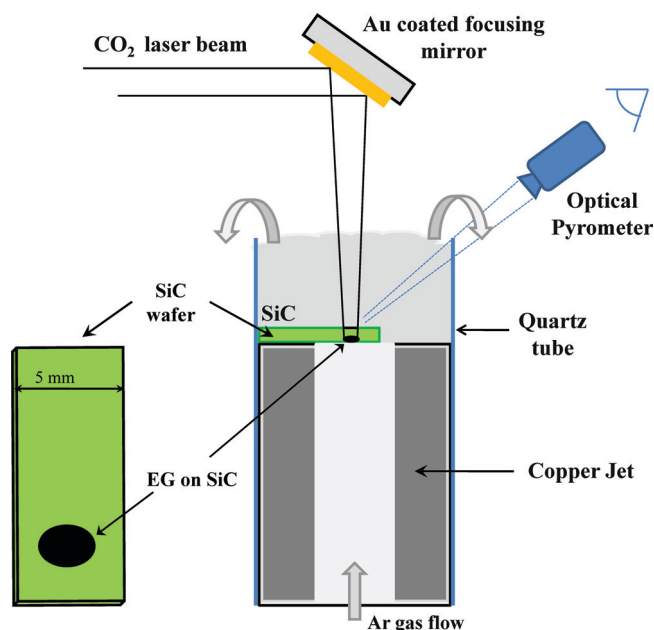
Scheme 1. Schematic diagram of the CO_2-laser induced epitaxial growth of graphene on SiC wafers.

The formation of few layer EG on SiC and its features were investigated by scanning electron microscopy (SEM), X-ray photoelectron spectroscopy (XPS), secondary ion-mass spectroscopy (SIMS), and Raman scattering.

2. Results and Discussion

Graphene was grown on SiC (0001) using the set-up shown in Scheme 1. The set-up is a modification of an experimental arrangement developed previously for melting refractive ceramics in controlled gas atmosphere at temperatures above 2000 K.[16] **Figure 1**a shows a representative microscopy image of EG on 6H- SiC(0001). The image covers partly the surface of non-irradiated SiC (grey area), the irradiated area (1) and the border between the two regions (2). Actually, both the grey area (SiC) and the border region (2) correspond to the 6H-SiC(0001) surface, which was not directly illuminated and was thus exposed to lower temperature due to the power density distribution of the heating CO_2 laser beam. At the non-irradiated area SiC undergoes milder annealing during the heating procedure, which causes purification from surface contamination and limited silicon desorption. As a result, wide, highly uniform, atomically flat terraces emerge.

The first stages of graphene layer formation on these flat terraces are quite clear in Figure 1d, which is an enlargement of the border area. Graphene grows initially at the terrace step edges where the large continuous terraces are found, extending parallel to the step edges. Graphene nucleation and growth is highly dependent on the SiC surface morphology. This type of growth has been previously observed for films grown under 900 mbar of argon on 6H-SiC(0001).[10]

Enlargement of the irradiated area is shown at low and high magnification in Figure 1b and c, respectively. Similar characteristics to that observed on graphene films on SiC[17] and Ni[18] substrates are evident from these images. The terraces are not observable any longer, while the whole area is covered by the EG layers. The change of the image contrast from light to dark grey (or black) is directly correlated with the number of graphene layers on the substrate.[18] The lighter grey areas indicate thinner graphene film where the secondary electrons can more efficiently escape from the SiC substrate as compared with the darker ones.

Typical XPS C1s and Si2s spectra collected from the homogeneous large area of EG are shown in **Figure 2**. The Si2s photopeak from the SiC substrate appears at binding energy 151.4 eV in agreement with literature values.[19] The spectrum does not contain components attributable to silica (SiO_2) or silicon oxycarbide (SiC_xO_y) which could be located at the interface between the SiC substrate and the EG overlayer. The C1s spectrum is analyzed into four components, at binding energies 283.5, 284.5, 285.5 and 287.2 eV originating from C atoms in the bulk SiC substrate, in the aromatic rings (sp² bonding) of the EG layer, in configurations with sp³ bonding hybridization and in surface C=O species, respectively.[20] The peak at 285.5 eV has also been attributed to the first carbon layer grown on top of the SiC(0001) substrate forming strong covalent bonds with the latter and thus lacking the graphene electronic properties.

www.MaterialsViews.com

ADVANCED
FUNCTIONAL
MATERIALS
www.afm-journal.de

FULL PAPER
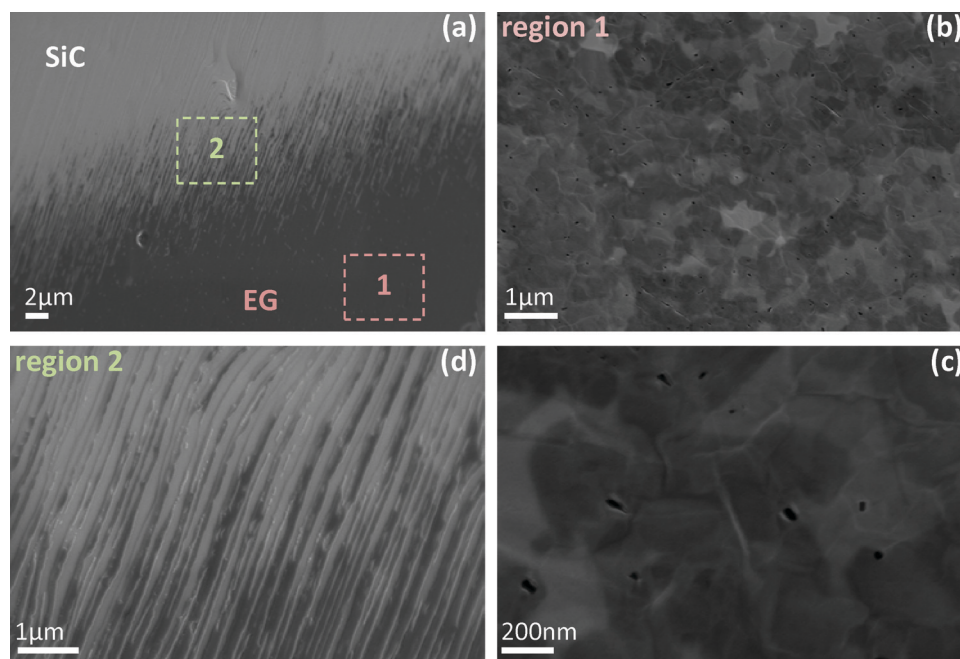
Figure 1. a) SEM image showing the formation of epitaxial graphene (dark area, 1) on 6H-SiC(0001) (grey area); b,c) detail from the irradiated area at high magnification; d) close view of the borders (2) between the EG and SiC.
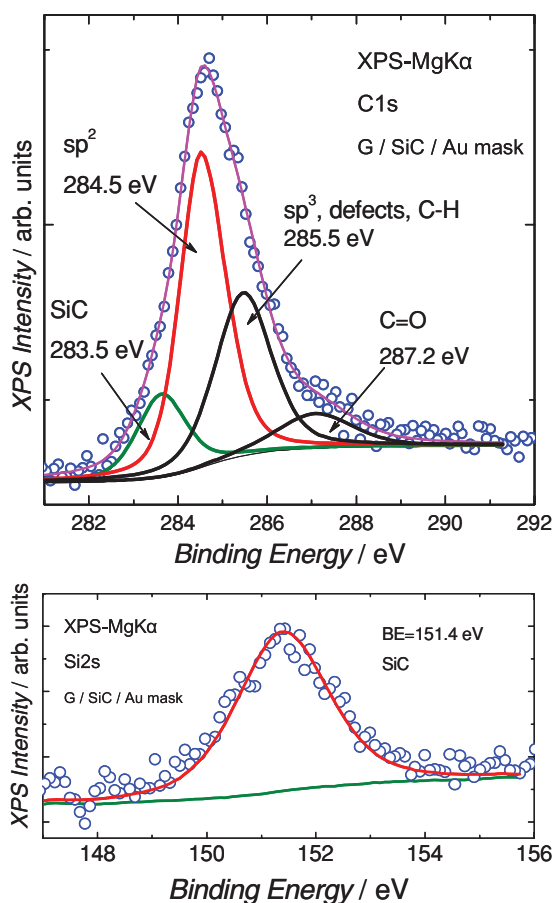
Figure 2. XPS core level spectra of Si2s (bottom) and C1s (top) of the EG/SiC sample (the non-irradiated area of SiC is covered with a gold mask).

This acts as a buffer layer, enabling the first graphene layer, to behave electronically like an isolated graphene sheet.[21]

Assuming that the graphene–SiC sample can be described as a semiinfinite SiC substrate with a uniform graphene overlayer of thickness d, the latter can be calculated from the total C1s peak intensities using the equation: $d = \lambda \ln[(I_{EG}C_{SiC}/I_{SiC}C_{EG})+1]$. λ is the C1s electrons inelastic mean free path, assumed to be the same in SiC and in graphene; its values are reported elsewhere.[22] I_{EG} and I_{SiC} are the intensities (areas) of the C1s signal from the EG overlayer and the SiC substrate, respectively, while C_{SiC} and C_{EG} are the corresponding carbon atomic densities in each material.[23] The intensity ratio between the EG C1s and the SiC C1s lines was found to be $I_{EG}/I_{SiC} = 3.4$. For this ratio, the EG thickness is ~2.5 ± 0.5 nm, which, considering the thickness of a graphene layer to be equal to the interlayer distance in the graphitic structure (0.34 nm), corresponds to 5.5–8.5 monolayers. The relatively large error margin in this calculation emerges due to the uncertainty in the inelastic mean free path values and also because the estimate is based on a simple model of a bulk-terminated substrate. It is worth mentioning that the XPS signal is averaged over an area of ~2 mm^2 on which, the EG layer is considered to be homogenous.

Dynamic SIMS was used for depth profile measurements of the irradiated samples. **Figure 3** shows the depth distribution of amu 12, 41, and 28 recorded in the positive mode and representing $^{12}C^{+}$, $^{29}Si^{12}C^{+}$, and $^{28}Si^{+}$ or $^{12}C^{16}O^{+}$ species, respectively. The inset in Figure 3, is a chemical image of the sample. It shows five craters in the dark area (crater size ~158 μm). These are the spots where repeated depth profile measurements took place. All spots produced similar profiles ascertaining the homogeneity of the irradiated area in depth. An additional depth profile figure from a different area of the sample is provided in the Supporting Information.
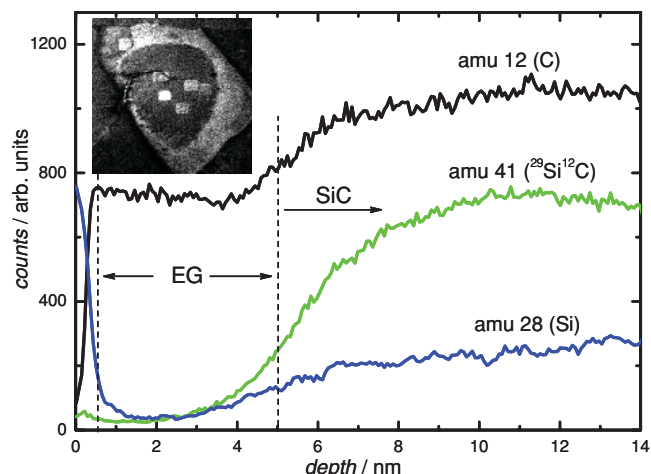
Figure 3. Dynamic SIMS depth profile analysis of the irradiated area of the SiC sample. Inset: Chemical image of the irradiated SiC sample. The grey colored area represents amu 16 ($^{16}O^{-}$) and the black domain shows amu $^{12}C^{-}$. The square craters are the sputtered spots on the sample.

The large signal of amu 28 in the initial steps of the procedure is attributed to surface species of oxidized carbon ($^{12}C^{16}O^{+}$) due to surface contamination.[24] It is observed that up to a depth of about 3 nm the signals of Si and SiC are close to the detection limit while that of carbon is considerably high and homogenous in depth. After the first 3 nm (i.e., ~9 ML of EG) the intensity of the Si-containing species starts to increase, indicating that the EG/SiC interface is reached. A certain plateau (bulk SiC) is attained after a depth of about 5.5–6 nm. When approaching the SiC substrate, the intensity of amu 12 increases as well, due to the higher sputter yield of carbon in the SiC matrix as compared to that in graphite.[25] From this profile the thickness of the EG layer appears to be in good agreement with the value estimated by XPS for the same sample. Details about SIMS measurements and depth calibration are given in the Supporting Information.

Raman spectra were recorded from several EG samples prepared in this work. Representative Raman spectra from various points of the SiC irradiated area are shown in **Figure 4**. For one of the samples the irradiated area of ~3 mm^2 was scanned systematically and Raman spectra measurements for over 100 different points were obtained (see Supporting Information). Data collected from the borders of the irradiated spot exhibit strong peaks arising from the second order Raman spectrum of SiC, on which the G-band of EG is superimposed (see Figure 4a). Comparing the relative intensities of the G peak and the SiC bands with corresponding spectra in previous studies our spectra could be interpreted as indicating the presence of 1 or 2 ML of EG at the borders of the illuminated area. For Raman spectra recorded from points located well within the spot, the SiC bands are much weaker than the graphene bands and hence are practically invisible; see lower spectrum in Figure 4b. A line scan performed at the periphery of the irradiated area revealed rather sharp limits between these two types of Raman spectra. Practically, spectra as that shown in Figure 4a are recorded from a thin belt of about 10 μm in thickness around the irradiated area. This finding demonstrates homogeneous heating of the irradiated area with negligible lateral heat flow to the surrounding area.
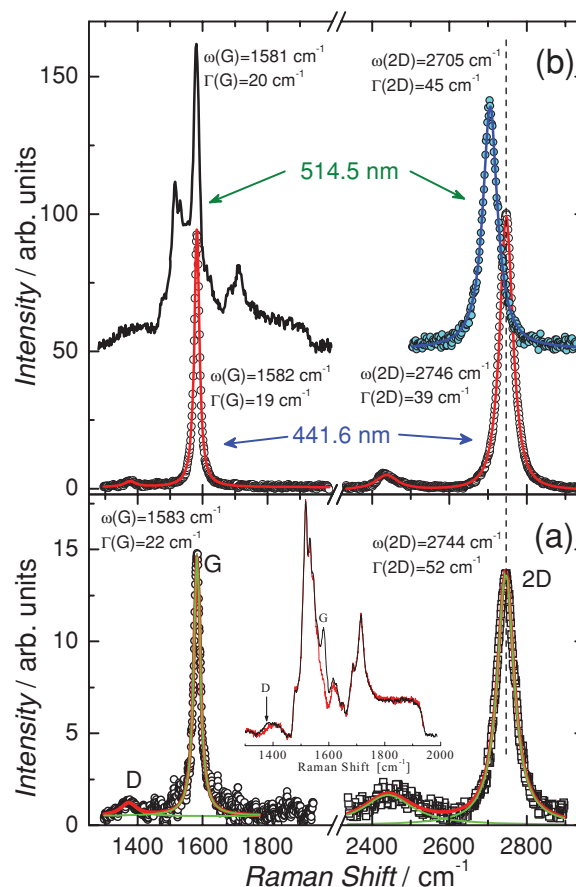
Figure 4. Representative Raman spectra of EG on SiC(0001) recorded (a) from the borders of the irradiated area and (b) from the irradiated spot. The upper spectrum in (b) was recorded with a macro-Raman set-up from a macroscopic sample area ~10^5 μm^2.

Extensive reviews on Raman scattering in MCG and EG have appeared over the last few years providing the means of characterizing the properties of graphene though the energy and width of certain Raman bands.[26–29] In brief, three main bands dominate Raman spectra of graphene: The G-band (~1582 cm^{-1}), present to all sp^2 carbon networks corresponds to the in-plane, doubly degenerate E_{2g} phonon at the center of the Brillouin zone. The defect-induced D-band (dispersive mode in the range 1300–1370 cm^{-1}) arises from the breathing mode of the sp^2 rings and becomes Raman active in the presence of defects. The 2D band (the second order of D-band, sometimes referred to as the G′ band) originates from a double resonance process, being also dispersive; its presence in the Raman spectrum does not require the presence of the D band. A number of Raman studies have concentrated on EG,[30–36] which in combination with other techniques have provided information on graphene quality and phenomenological correlations between spectral Raman features and graphene properties. Combinations of the D, G, and 2D peak parameters have led to five main criteria which provide information on (a) disorder and crystallite size (D/G intensity ratio), (b) number of graphene ML (2D band shape and 2D/G ratio), (c) layer stacking order (2D band shape, i.e. single or multiple lines), (d) stresses (G band shift;

www.MaterialsViews.com

ADVANCED
FUNCTIONAL
MATERIALS
www.afm-journal.de

FULL PAPER

shape and Raman shift of 2D band), and (e) carrier mobility (2D band width).[26–29] The analysis of our Raman spectra will proceed alongside the aforementioned phenomenological correlations/observations.

a) In the vast majority of our Raman spectra, recorded well inside the irradiated area, (see Supporting Information) a very low D/G area ratio (~0.05) was found indicating rather large crystallite size L_a and thus high-quality graphene. Using the expression given by Cancado et al.[37] which relates crystallite size with D/G area ratio we obtain L_a ~ 182 nm for the 441.6 nm excitation energy. This value indicates EG quality comparable with that reported elsewhere.[33,36] At the borders of the illuminated spot the D/G area ratio is of about 0.1, which is, however, much smaller than that reported in studies of furnace grown EG.[31] Furthermore, CO_2-laser-induced grown EG exhibits much lower disorder than UV-laser-synthesized EG, where the D/G area is of about unity.[13]

b) For monolayer MCG there is consensus that the 2D/G intensity ratio assumes values near 4 (the ratio decreases with the number of MLs) and the 2D band shape is a single Lorentzian with full width at half maximum $\Gamma(2D) < 30$ cm^{-1}, which broadens appreciably so as four Lorentzians are needed for a correct fitting for bilayer MCG.[38] In general, the 2D/G ratio in EG is much lower than that in MCG; values around 0.5 or 2 are frequently reported.[33] However, this ratio is not considered as a valuable indicator of the number of MLs in EG. Our Raman spectra spanning the whole illuminated area show consistently 2D/G>1.5.

Controversial findings have been reported concerning the use of the 2D band-shape for estimating the number of MLs in EG. Faugeras et al.[32] studied EG grown on 4H-SiC(000$\bar{1}$) reporting that the 2D peak is single Lorentzian, irrespective of the number of layers; the number of layers affects only its width. They reported $\Gamma(2D)$ ~60 cm^{-1} and ~80 cm^{-1} for few-layer (up to 10) and multi-layer (90 layers) EG, respectively. Röhrl et al.[30] studied EG grown on 6H-SiC(0001) reporting that the 2D band is single Lorentzian for graphene ML, while it turns to a broader and asymmetric band composed of four Lorentzians for the bilayer and to even broader line for few (6) layer graphene. Single Lorentzian 2D band with $\Gamma(2D)$ ~60 cm^{-1} and 95 cm^{-1} for ML and bilayer graphene grown on 6H-SiC(0001) was reported by Ni et al.[31] A more detailed investigation of monolayer and bilayer EG grown 6H-SiC(0001) and a tri-layer grown on 4H-SiC(0001) was undertaken by Lee et al.[33] They found that $\Gamma(2D)$ ~46, 64, and 74 cm^{-1} for the monolayer, bilayer and trilayer, respectively. The authors noted that up to 14 ML of EG, the 2D band does not develop any shoulder or asymmetry but it is poorly fitted by a single Lorentzian even for the bilayer which needs four Lorentzians for a satisfactory fitting. Lee et al.[33] found a correlation between the inverse number, N, of MLs and the width of the 2D band, i.e., $\Gamma(2D) = (-45 N^{-1} + 88)$ cm^{-1}. The relation was derived for (Si-face) SiC(0001) EG while the data for SiC(000$\bar{1}$) do not follow any systematic trend with N. A large number of Raman spectra recorded with the 441.6 nm excitation energy in this study showed that $\Gamma(2D)$ ~50 cm^{-1}, although at few points $\Gamma(2D)$ was found narrower, i.e., of about 40 cm^{-1}. According to the above relation between $\Gamma(2D)$ and N the EG grown by the method of the current work would nominally consist of N ~ 2 or lower, which is certainly lower than

the XPS and SIMS result. This finding shows that Raman scattering does not still provide an accurate determination of EG graphene MLs.

c) Attempts to study the number of ML in graphene have up to now focused on samples with AB Bernal stacking, and this is mainly the case of MCG. When graphene layers are randomly rotated (turbostratic graphene) a single Lorentzian line can adequately fit the 2D band due to the decreasing inter-layer interactions. Similarities between EG on SiC(000$\bar{1}$) and turbostratic graphite were noticed in view of the single Lorentzian, wide 2D band.[25] It has also been stated that EG is characterized by disordered stacking only when grown on C-face and not on the Si-face SiC(0001).[1,8] UV-laser-grown EG was found to exhibit large $\Gamma(2D)$, i.e. ~60 cm^{-1} for the ML and ~75 cm^{-1} for 2–3 ML.[13] Our results, i.e., the fact that the 2D band for all Raman spectra is a single Lorentzian line, demonstrate that few-layer EG with disordered stacking or stacking faults can also be produced on SiC(0001). The origin of this effect is still speculative; however, we suggest that the extremely faster heating and cooling rates offered by the method employed here, in comparison with the furnace treated graphenes, might provide a rational explanation for the emergence of non-Bernal stacking. This stems as an important result given that the existence of rotational stacking faults has been shown to provide EG grown on SiC electronic properties similar to those of the isolated single graphene layer.[39,40]

d) A great deal of controversy can be found also in the literature regarding the use of the frequency of the G- and 2D-band and its shift in relation to that of MCG monolayers, in the determination of stresses in EG grown on SiC. While Faugeras et al.[32] reported that the G-band energy (1582 cm^{-1}) is the same for MCG, graphite and EG grown on SiC(000$\bar{1}$), other works for EG on 6H-SiC(0001) showed that $\omega(G)$ can be higher, i.e., $\omega(G)$ ~1608,[30] 1597,[31] and 1591[33] cm^{-1}. According to Rohrl et al.[30] $\omega(G)$ red-shifts with increasing number of graphene layers tending to the graphite value. As regards the 2D band, contradictory results appear also: $\omega(2D)$ was found to be almost fixed in the interval 2655–2665 cm^{-1} (for 632.8 nm excitation);[32] $\omega(2D)$ decreases with increasing the number of EG layers;[30] $\omega(2D)$ increases by ~40 cm^{-1} from the monolayer to the tri-layer;[33] and $\omega(2D)$ increases by ~21 cm^{-1} from the monolayer to the bilayer, both being lower than the $\omega(2D)$ of MCG.[31] Compressive strain and in few cases electron/hole doping have been considered in most of the above studies to account for the differences of $\omega(G)$ and $\omega(2D)$ between EG and MCG.

In our measurements we find that $\omega(G) \approx 1582 \pm 1$ cm^{-1} and $\omega(2D) \approx 2745 \pm 3$ cm^{-1} (for 441.6 nm laser energy) for all Raman spectra recorded from a large area of EG. This finding points to a very uniform distribution of strain along the whole area where EG has grown. To confirm this we present in Figure 4b the Raman spectrum recorded with the aid of a macro-Raman set-up using the excitation line 514.5 nm. This is to our knowledge the first Raman spectrum from a really macroscopic EG scattering area (10^5 μm^2). The sample was scanned at few various, not overlapping, points exhibiting indistinguishable Raman spectra. The 2D band is red-shifted, relative to the value obtained with the 441.6 nm laser line, owing to its dispersive nature to $\omega(2D) \approx 2705$ cm^{-1}, while its width is similar, $\Gamma(2D)$ ~45 cm^{-1}, to the other values recorded from a limited spatial

region. The most striking result is that its band-shape can be excellently fitted by a single Lorentzian. These findings demonstrate that the present EG preparation method yields very homogeneous EG as regards the developed strain. Finally, it is instructive to note that a large shift of $\omega(2D)$ of about 30 cm^{-1} for 1 ML and 2–3 ML EG is reported for UV-laser-synthesized EG.[13]

In a detailed spatially resolved Raman study[34] of EG grown on 6H-SiC(0001) it was found that EG strain varies substantially between various points few μm apart, i.e., the 2D frequency can vary by ~65 cm^{-1}. The strain was significant to cause shifts of the 2D band by ~25 cm^{-1} even for points located 600 nm apart. This shows that furnace produced EG can be highly non-uniform at the μm scale. Robinson et al.[34] categorized EG as high strain or low strain when the 2D band energy is higher or lower, respectively, than the corresponding band in bulk graphite; while EG would be strain free when $\omega(2D)$ approaches that of MCG. Their study showed that high and low strain areas coexist at comparable fractions. Considering that (at 514.5 nm excitation) $\omega(2D) \sim 2687$ cm^{-1} for free standing monolayers of MCG,[28] and $\omega(2D) \sim 2726$ cm^{-1} for bulk graphite,[28] it can be concluded that our $\omega(2D) \sim 2705$ cm^{-1} supports that the CO_2-grown EG on SiC(0001), apart from being uniform at the macro-scale, experiences also very low-strain. Finally, compressive strain, which is usually adopted to account for EG Raman band shifts, would affect (shift) simultaneously the G and 2D bands with a shift ratio of about 1/2.5.[41] The absence of shift for the G-band renders the hypothesis of strain in the CO_2-laser synthesized EG questionable. Apart from compressive strain, charge doping from the substrate, and/or doping emerging from oxygen/water in the atmosphere, can account for the blue-shift of the 2D band. The finding by Lee et al.[33] that $\omega(2D)$ does not red-shift substantially after transferring EG from SiC to SiO_2 substrates led to the conclusion that SiC does not exert any appreciable strain on EG. Therefore, in the present case we cannot exclude the possibility that the small shift (18 cm^{-1}) of the 2D band, between EG and MCG (for 514.5 nm) could originate from doping (carriers provided by SiC).

e) A remarkable correlation was proposed between the carrier mobility and $\Gamma(2D)$ in EG grown on SiC(000$\bar{1}$).[35] $\Gamma(2D)$ was considered to be affected by the stacking order of graphene layers. Narrow single Lorentzian 2D bands ($\Gamma(2D) < 40$ cm^{-1}) originate from rotationally faulted multilayer EG. Broad, asymmetric 2D-band shapes were interpreted as originating from the simultaneous contribution of both rotationally faulted and Bernal stacked. Comparing $\Gamma(2D)$ and carrier mobility data, it was found that sample regions with narrow $\Gamma(2D)$ exhibit high carrier mobilities, while in samples areas where Bernal stacking also contributes to $\Gamma(2D)$ the mobility is severely lower.[35] The correlation holds only for uniform sample areas exhibiting less than 10% variation in $\Gamma(2D)$. Our findings show that EG grown on SiC(0001) by CO_2 laser heating can be considered as uniform based on the negligible (much less than 10%) spatial variation of $\Gamma(2D)$ over large areas. However, although our 2D bands can be satisfactorily fitted by a single Lorentzian, the width is higher than the corresponding bandsreported previously[35] in the regime where rotational faults dominate. It would thus be unsafe to draw any conclusion of carrier mobility in the EG grown by the current method simply based on $\Gamma(2D)$, especially

considering that areas in the scattering volume, which contain EG grown on the edges of the terraces (with different curvature) can also contribute to the 2D-band broadening.[33]

3. Conclusions

In summary, we presented a novel method for the fast, one-step epitaxial growth of large-area homogeneous graphene on SiC(0001). The use of a CO_2 laser as the heating source provides flexibility in growing uniform, low–strain graphene film composed of few monolayers. The method is quite simple and cost-effective in that it does not necessitate SiC pretreatment and/or high vacuum, it operates at low temperature and proceeds in the second time scale, thus providing a green solution to EG fabrication and a means to engineering graphene patterns on SiC by focused laser beams. The very high heating rate achieved by CO_2-laser heating seems to have beneficial results in avoiding the different Si desorption rates from adjacent SiC steps,[42] while the corresponding ultrafast cooling rate influences the stacking order of EG on SiC(0001). Work underway is focused on controlling EG thickness by changing illumination time and/or laser power density.

4. Experimental Section

Epitaxial Graphene Synthesis on 6H-SiC(0001): Graphene was grown on 260 μm thick *n*-doped 6H-SiC wafers, Si-face polished with orientation 0°, 20′ with respect to the ideal (0001) plane. Rectangular strips (~5 × 10 mm²) cut from the wafer, were washed with HF solution and rinsed with ethanol. The SiC strip was placed on top of an opening of a small copper metal support where Ar gas was flowing through, thus creating an inert gas blanket around the sample at atmospheric pressure. The laser beam was focused with a gold coated concave mirror on the C-terminated (000$\bar{1}$) face (unpolished wafer side) of the SiC strip producing a visible elliptical trace with short and long axes of ~1.5 and ~2.5 mm, respectively (Figure S1 in the Supporting Information). The temperature of the spot was monitored with a two-color optical pyrometer (model OS 3722, Omega Engineering Inc.). In a series of experiments different percentages of the CO_2 laser power were utilized and the sample was irradiated at different time intervals reaching temperatures up to ~2400 K. The modification of the SiC surfaces became (visually) detectable at temperature above ~2000 K and at exposure times of few seconds. However, it was found by various experiments that a rather uniform modification of the SiC surfaces occurs when about 40% of the maximum CO_2 laser power was utilized and the irradiation lasted for ~10 s. The laser power was preset at this level with the beam blocked and the illumination of the C-face of the SiC wafer was sudden. Under these conditions, the illuminated volume reaches the maximum temperature of ~2400 K with a heating rate of ~600 K s^{-1}. At the end of the heating procedure the illuminated SiC surface became slightly blackish as shown in Figure S1. The spot on the reverse surface (Si-face) of the SiC strip was rather uniform and smooth and was the subject of our studies. Raman scattering and XPS showed no evidence of graphitic material on the C-face of the SiC wafer. This can be attributed to the fact that the atmospheric O_2 partial pressure is significantly higher on the C-face of SiC–which is directly exposed to the CO_2 laser beam–in comparison to that of the Si-face.

EG Characterization by SEM, XPS and SIMS: Scanning electron microscopy was carried out with a high-resolution field-emission SEM instrument (Zeiss SUPRA 35VP) operated at 15 kV. XPS measurements were carried out in an ultrahigh vacuum chamber equipped with a SPECS LHS-10 hemi-spherical electron analyzer and a dual X-ray anode, using

Materials
Views
www.MaterialsViews.com

ADVANCED
FUNCTIONAL
MATERIALS
www.afm-journal.de

FULL PAPER

the unmonchromatized Mg K_α (1253.6 eV) line. The analyzer operated at the constant pass energy mode, $E_p = 36$ eV giving a full width at half maximum of 1.1 eV for the main C1s XPS peak. The XPS core level spectra were analyzed using a fitting routine, which can decompose each spectrum into individual mixed Gaussian-Lorentzian peaks after a Shirley background subtraction. Regarding the measurement errors, for the XPS core level peaks we estimate that errors in peak positions are of about ±0.05 eV for a good signal to noise ratio. For the photoemission measurements the sample was wrapped by a gold foil mask covering all the untreated SiC substrate and having an opening with diameter ~1.5 mm to expose about 60% of the treated sample area. A drawing of the sample is shown in Scheme S1. Dynamic SIMS were performed at the Millbrook MiniSIMS spectrometer using a liquid gallium ion gun ($E = 6$ keV). The mass analyzer was a quadruple filter with mass range of 2–300 Da.

Raman Spectroscopy: The overall area where the EG growth took place was monitored by micro-Raman spectroscopy. The sample was mounted on the calibrated *XY* stage of the microscope and consecutive measurements were performed at selected points of the square grid superimposed on the image shown in Figure S1. Over a hundred of Raman spectra of EG were systematically measured from different points from the sample shown. Raman measurements were repeated in few other samples prepared in a similar way. The majority of the spectra were collected with the Labram HR800 (Jobin–Yvon) micro-Raman system equipped with a He-Cd laser operating at 441.6 nm. Circumstantially, Raman spectra were recorded with the 514.5 nm laser line using the T64000 (Jobin-Yvon) Raman spectrometer in the micro- and macro-configurations. Microscope objectives with magnifications 100× and 50× were used to focus the light onto a ~1 and ~3 μm spots, respectively. In the macro-Raman measurements, the light was incident on the EG surface at an angle of ~60° in relation to the normal of the SiC wafer and the scattered light was collected at right angle. The thus formed laser spot area on the EG surface was of about 10^5 μm² covering a large fraction of the sample area. The large penetration depth of the laser line at this configuration is responsible for the SiC modes appearing around the G-band spectral range. Furthermore, in selected areas 5 to 10 consecutive spectra were recorded every ~5–10 μm on a line. The uniformity (homomorphism) – as regards the energy and the shape of the G and 2D bands – of the measured spectra for selected points on the grid is evident from Figure S3. The figure contains representative spectra – out of the over 100 spectra measured – along four lines, A, B, C, and D as marked in Figure S1. For each line, the three spectra shown were recorded from areas near the borders and around middle of the illuminated spot. The second order Raman bands of SiC is evident in all spectra recorded from the edges of the EG spot. Representative Raman spectra recorded with the 514.5 nm laser are shown in Figure S4, where the first order Raman spectrum of SiC is shown at wavenumbers below 1000 cm^{-1}.

Supporting Information

Supporting Information is available from the Wiley Online Library or from the author.

[1] For a historical survey on EG growth see for example: W. A. de Heer, C. Berger, M. Ruan, M. Sprinkle, X. Li, Y. Hu, B. Zhang, J. Hankinson, E. H. Conrad, *Proc. Nat. Acad. Sci.* **2011**, *108*, 16900.

[2] S. Park, R. S. Ruoff, *Nature Nanotechnol.* **2009**, *4*, 217.

[3] K. S. Novoselov, A. K. Geim, S. V. Morozov, D. Jiang, M. I. Katsnelson, I. V. Grigorieva, S. V. Dubonos, A. A. Firsov, *Nature* **2005**, *438*, 197.

[4] C. Berger, Z. Song, T. Li, X. Li, A. Y. Ogbazghi, R. Feng, Z. Dai, A. N. Marchenkov, E. H. Conrad, P. N. First, W. A. de Heer, *J. Phys. Chem. B* **2004**, *108*, 19912.

[5] K. S. Kim, Y. Zhao, H. Jang, S. Y. Lee, J. M. Kim, K. S. Kim, J.-H. Ahn, P. Kim, J.-Y. Choi, B. H. Hong, *Nature* **2009**, *457*, 706.

[6] J. Hass, W. A. de Heer, E. H. Conrad, *J. Phys.: Condens. Matter* **2008**, *20*, 323202.

[7] A. J. Van Bommel, J. E. Crombeen, A. Van Tooren, *Surf. Sci.* **1975**, *48*, 463.

[8] K. V. Emstev, A. Bostwick, K. Horn, J. Jobst, G. L. Kellogg, L. Ley, J. L. McChesney, T. Ohta, S. A. Reshanov, J. Röhrl, E. Rotenberg, A. K. Schmid, D. Waldmann, H. B. Weber, T. Seyller, *Nat. Mater.* **2009**, *8*, 203.

[9] J. Park, W. C. Mitchel, L. Grazulis, H. E. Smith, K. G. Eyink, J. J. Boeckl, D. H. Tomich, S. D. Pacley, J. E. Hoelscher, *Adv. Mater.* **2010**, *22*, 4140.

[10] C. Mattevi, G. Eda, S. Agnoli, S. Miller, K. A. Mkhoyan, O. Celik, D. Mastrogiovanni, G. Granozzi, E. Garfunkel, M. Chhowalla, *Adv. Funct. Mater.* **2009**, *19*, 2577.

[11] C. Berger, Z. M. Song, X. B. Li, X. S. Wu, N. Brown, C. Naud, D. Mayou, T. B. Li, J. Hass, A. N. Marchenkov, E. H. Conrad, P. N. First, W. A. de Heer, *Science* **2006**, *312*, 1191.

[12] N. Camara, G. Rius, J.-R. Huntzinger, A. Tiberj, N. Mestres, P. Godignon, J. Camassel, *Appl. Phys. Lett.* **2008**, *93*, 123503.

[13] S. Lee, M. F. Toney, W. Ko, J. C. Randel, H. J. Jung, K. Munakata, J. Lu, T. H. Geballe, M. R. Beasley, R. Sinclair, H. C. Manoharan, A. Salleo, *ACS Nano* **2010**, *12*, 7524.

[14] J. B. Park, W. Xiong, Y. Gao, M. Qian, Z. Q. Xie, M. Mitchell, Y. S. Zhou, G. H. Han, L. Jiang, Y. F. Lu, *Appl. Phys. Lett.* **2011**, *98*, 123109.

[15] Y. Ohkawara, T. Shinada, Y. Fukada, S. Ohshio, H. Saitoh, H. Hiraga, *J. Mater. Sci.* **2003**, *30*, 2447.

[16] A. G. Kalampounias, G. N. Papatheodoroy, in *Proceedings of the 13th International Symposium on Molten Salts*, PV 2004-19, The Electrochemical Society, Inc., Pennington **2002**, p.485.

[17] N. Camara, A. Tiberj, B. Jouault, A. Caboni, B. Jabakhanji, N. Mestres, P. Godignon, J. Camassel, *J. Phys. D: Appl. Phys.* **2010**, *43*, 374011.

[18] H. J. Park, J. Meyer, S. Roth, V. Shakalova, *Carbon* **2010**, *48*, 1088.

[19] K. Shimoda, J.-S. Park, T. Hinoki, A. Kohyama, *Appl. Surf. Sci.* **2007**, *24*, 9450.

[20] J. Penuelas, A. Ouerghi, D. Lucot, C. David, J. Gierak, H. Estrade-Szwarckopf, C. Andreazza-Vignolle, *Phys. Rev. B* **2009**, *79*, 033408.

[21] C. Virojanadara, R. Yakimova, A. A. Zakharov, L. I. Johansson, *J. Phys. D: Appl. Phys.* **2010**, *43*, 374010.

[22] S. Tougaard, QUASES-IMFP-TPP2M program, http://www.quases.com (accessed October, 2011).

[23] L. B. Biedermann, M. L. Bolen, M. A. Capano, D. Zemlyanov, R. G. Reifenberger, *Phys. Rev. B* **2009**, *79*, 125411.

[24] D. S. McPhail, *J. Mater. Sci.* **2006**, *41*, 873.

[25] K. D. Krantzman, R. P. Webb, B. J. Garrison, *Appl. Surf. Sci.* **2008**, *255*, 837.

[26] A. C. Ferrari, *Solid State Comm.* **2007**, *143*, 47.

[27] Z. Ni, Y. Wang, T. Yu, Z. Shen, *Nano Res.* **2008**, *1*, 273.

[28] L. M. Malard, M. A. Pimenta, G. Dresselhaus, M. S. Dresselhaus, *Phys. Rep.* **2009**, *473*, 51.

[29] B. Tang, H. Guoxin, H.-Y. Gao, *Appl. Spectrosc. Rev.* **2010**, *45*, 369.

[30] J. Röhrl, M. Hundhausen, K. V. Emtsev, Th. Seyller, R. Graupner, L. Ley, *Appl. Phys. Lett.* **2008**, *92*, 201918.

[31] Z. H. Ni, W. Chen, X. F. Fan, J. L. Kuo, T. Yu, A. T. S. Wee, Z. X. Shen, *Phys. Rev. B* **2008**, *77*, 115416.

[32] C. Faugeras, A. Nerriere, M. Potemski, A. Mahmoud, E. Dujardin, C. Berger, W. A. de Heer, *Appl. Phys. Lett.* **2008**, *92*, 011914.

[33] D. S. Lee, C. Riedl, B. Krauss, K. von Klitzing, U. Starkle, J. H. Smet, *Nano Lett.* **2008**, *8*, 4320.

[34] J. A. Robinson, C. P. Puls, N. E. Staley, J. P. Stitt, M. A. Fanton, K. V. Emtsev, T. Seyller, Y. Liu, *Nano Lett.* **2009**, *9*, 964.

[35] J. A. Robinson, M. Wetherington, J. L. Tedesco, P. M. Campbell, X. Weng, J. Stitt, M. A. Fanton, E. Frantz, D. Snyder, B. L. VanMil, G. G. Jernigan, R. L. Myers-Ward, C. R. Eddy, D. K. Gaskill, *Nano Lett.* **2009**, *9*, 2873.

[36] J. Robinson, X. Weng, K. Trumbull, R. Cavalero, M. Wetheringhton, E. Frantz, M. LaBella, Z. Hughes, M. Fanton, D. Snyder, *ACS Nano* **2010**, *4*, 153.

[37] L. G. Cancado, K. Takai, T. Enoki, M. Endo, Y. A. Kim, H. Mizusaki, A. Jorio, L. N. Coelho, R. Magalhaes – Paniago, M. A. Pimenta, *Appl. Phys. Lett.* **2006**, *88*, 163106.

[38] A. C. Ferrari, J. C. Meyer, V. Scardaci, C. Casiraghi, M. Lazzeri, F. Mauri, S. Piscanec, D. Jiang, K. S. Novoselov, S. Roth, A. K. Geim, *Phys. Rev. Lett.* **2006**, *97*, 187401.

[39] J. Hass, F. Varchon, J. E. Millan – Otoya, M. Sprinkle, N. Sharma, W. A. de Heer, C. Berger, P. N. First, L. Magaud, E. H. Conrad, *Phys. Rev. Lett.* **2008**, *100*, 125504.

[40] O. Pankratov, S. Hensel, M. Bochstedte, *Phys. Rev. B* **2010**, *82*, 121416.

[41] N. Ferralis, R. Maboudian, C. Carraro, *Phys. Rev. Lett.* **2008**, *101*, 156801.

[42] M. Hupalo, E. H. Conrad, M. C. Tringides, *Phys. Rev. B* **2009**, *80*, 041401.

FULL PAPER

www.MaterialsViews.com

ADVANCED
FUNCTIONAL
MATERIALS
www.afm-journal.de

FULL PAPER

Formation of Embryoid Bodies with Controlled Sizes and Maintained Pluripotency in Three-Dimensional Inverse Opal Scaffolds

*Yu Zhang and Younan Xia**

Embryoid bodies (EBs) are aggregates of cells derived from embryonic stem (ES) cells, which can serve as a good model system to investigate molecular and cellular interactions in the earliest stages of embryo development. Current methods for producing EBs mainly rely on the use of hanging drops or suspensions in non-tissue culture treated plates, microwells, and spinner flasks. The capability of these methods is limited in terms of size uniformity and distribution as well as scalability. Here, a new platform based on three-dimensional alginate inverse opal scaffolds with uniform pores is presented, where uniform EBs with controllable sizes could be produced in the pores and then recovered after disintegration of the scaffolds. The size of the EBs could be readily controlled by varying the culture time and/or by using scaffolds with different pore sizes. The EBs maintained their viability and undifferentiated state, and they were able to differentiate into specific lineages upon stimulation.

1. Introduction

Embryonic stem (ES) cells hold great potential for therapeutic applications because of their unique capability in terms of unlimited self-renewal and differentiation into a rich variety of cell lineages including osteoblasts,[1,2] neural cells,[3,4] endothelial cells,[5] cardiomyocytes,[6,7] and pancreatic islet cells,[8] among others. The differentiation of ES cells in vivo is regulated by a number of parameters, such as direct interactions with the surrounding cells, extracellular matrices (ECMs), and soluble growth factors.[9] During early embryo development, ES cells aggregate into a cluster, in which the cells then gradually migrate and differentiate into different germ layers.[10] Significantly, this feature could be partially conserved and recapitulated in vitro by assembling ES cells into embryoid bodies (EBs) prior to the actual fate direction.[11,12] A commonly used method for the formation of EBs involves plating a suspension of the ES cells on a non-tissue culture treated substrate in the absence of self-renewing factors.[12,13] The ES cells and their small clusters would clump together to produce larger aggregates with increasing sizes over time. Although this culture technique is simple and scalable, the resulting EBs are often polydispersed in terms of size and shape.

It has been shown that differentiation of ES cells is sensitive to a number of parameters; one of them is the size of the EBs.[14] The size of the EBs influences cell–cell interactions, ECM deposition, as well as diffusion of soluble growth factors.[15] For example, cardiogenesis was enhanced in large EBs (~450 μm in size) while small EBs (~150 μm) favored endothelial cell differentiation.[16] In this regard, it is highly desired to work with EBs with uniform and precisely controlled sizes in an effort to better direct them to differentiate into specific lineages. To solve the problems associated with the traditional suspension culture technique, a variety of new methods has been developed for generating EBs. Among them, the hanging-drop method allows one to control the EB size[17,18] but the culture is labor intensive and thus not scalable. The approach based on microwell arrays shows advantages in controlling the size and shape of EBs.[15,19] However, the number of EBs that could be obtained from an array of microwells is rather limited due to the involvement of a two-dimensional setting.

Recently, inverse opal scaffolds have been developed for tissue-engineering applications.[20–23] Inverse opal scaffolds have three major unique features: the three-dimensional (3D) setting, the involvement of pores with remarkably uniform and yet controllable sizes, and the presence of small windows connecting adjacent pores. Thanks to the high uniformity and interconnectivity, the diffusion of oxygen/nutrients and the distribution of cells after seeding could be significantly enhanced, as compared to other types of 3D scaffolds with non-uniform pore sizes and structures.[24] Inverse opal scaffolds based on hydrogels have been explored for the culture of hepatocytes and the formation of uniform 3D liver tissue spheroids has also been demonstrated.[25] On the other hand, Zhang et al. recently proposed an intriguing idea to grow human ES cells in crosslinked alginate–chitosan scaffolds, where the cells could be recovered by physical disintegration of the scaffolds using a Ca^{2+} chelatin solution.[26] Combining these ideas, here, we demonstrate that EBs with controlled sizes could be obtained by seeding and growing ES cells in crosslinked alginate inverse opal scaffolds with uniform pore sizes (**Figure 1**). The size distribution of the EBs is narrow because (i) the inverse opal scaffold enabled uniform cell

Y. Zhang, Prof. Y. Xia
Department of Biomedical Engineering
Washington University
St. Louis, MO 63130, USA
E-mail: xia@biomed.wustl.edu

**ADVANCED
FUNCTIONAL
MATERIALS**
www.afm-journal.de
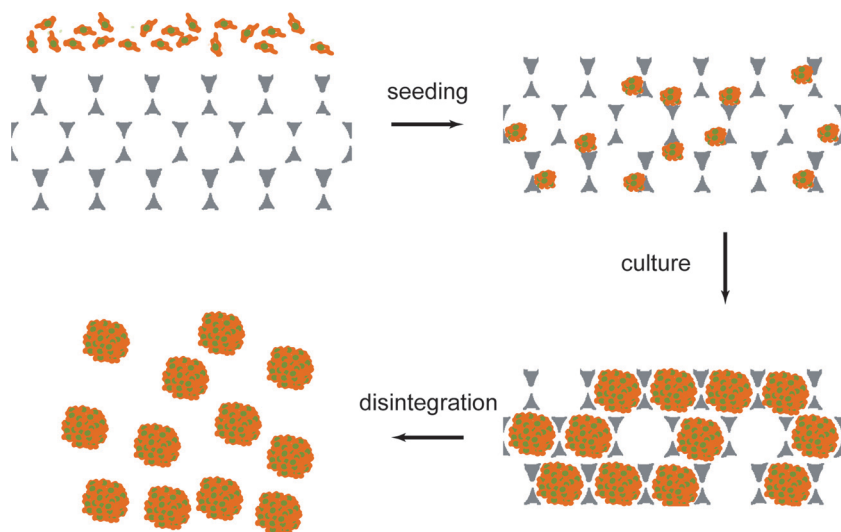
Materials Views
www.MaterialsViews.com

Figure 1. A schematic illustrating all major steps involved in the fabrication of EBs with a 3D inverse opal scaffold made of alginate: i) seeding of ES cells into the pores of a scaffold; ii) proliferation of the cells under the confinement of the pores; iii) disintegration of the scaffold with a PBS solution containing 100 mM ethylenediaminetetraacetic acid (EDTA) and 100 mM K$_2$HPO$_4$ for 10 min; and iv) separation of EBs from the debris of the disintegrated scaffold.

seeding at the initial stage, and (ii) the uniform pore structure created a homogeneous microenvironment among different pores, facilitating homogeneous growth for the EBs. The size of resultant EBs could be readily controlled by varying the pore size and/or the culture time; and the EBs could be efficiently recovered by disintegration of the alginate scaffold. We also demonstrated that, the EBs produced using this technique maintained their undifferentiated state and could readily differentiate into bone and neural lineages.

2. Results and Discussion

The alginate inverse opal scaffolds were fabricated by templating against cubic-close packed (ccp) lattices of polystyrene microspheres.[20,22,24] **Figure 2**A shows the scanning electron microscopy (SEM) image of such a lattice infiltrated with alginate. Figure 2B shows a magnified view, revealing the microstructure associated with the freeze-dried alginate. Figure 2C shows the typical SEM image of a freeze-dried alginate inverse opal scaffold after the polystyrene microspheres had been selectively removed. It is clear that the scaffold had a uniform pore structure, and there were more than one small windows connecting adjacent pores. The latter feature is of great importance for a 3D scaffold, as it ensures the formation of open channels through the entire volume of a scaffold, facilitating cell migration and/or nutrient transport.[24] Figure 2D shows a transmission optical microscopy image of

a single pore in a hydrated scaffold. When the scaffold is immersed in water, the microstructures of freeze-dried alginate would rehydrate to become a hydrogel. This feature is also important as the alginate hydrogel system could potentially prevent the seeded cells from adhering to the walls of a scaffold. As a result, most of the cells would form EBs rather than attaching to and spreading on the walls of a scaffold.[30]

The CE3 mouse ES cells we chose to work with are well-suited for monitoring the formation of EBs in the alginate inverse opal scaffolds because they express green fluorescent protein (GFP) under the β-actin promoter and thus enable easy visualization of the cells under a fluorescence microscope. In a typical procedure, CE3 ES cells were seeded into the alginate inverse opal scaffold using a spinner flask to ensure a uniform distribution for the cells at the initial time point. Right after seeding, the scaffold with cells was subjected to optical imaging (Figure S1 in the Supporting Information). EBs with various sizes had formed and distributed uniformly throughout the scaffold. It is interesting to note that each pore could contain one large EB or multiple small EBs that would fuse together later during culture (Figure S1, C). The good uniformity for seeding ensured the eventual development of uniform EBs in the scaffold.
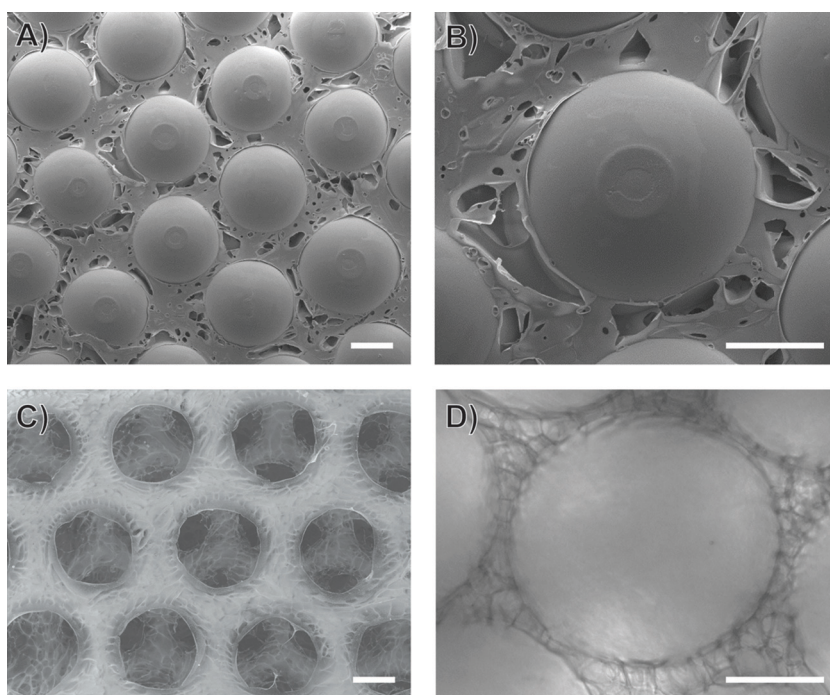

Figure 2. A,B) SEM images of an opaline lattice of polystyrene microspheres (250 μm in diameter) filled with alginate and then freeze-dried. C) SEM image of an alginate inverse opal scaffold after the polystyrene microspheres had been selectively removed. D) Optical microscopy image of the alginate inverse opal scaffold after hydration. Scale bars: 100 μm.
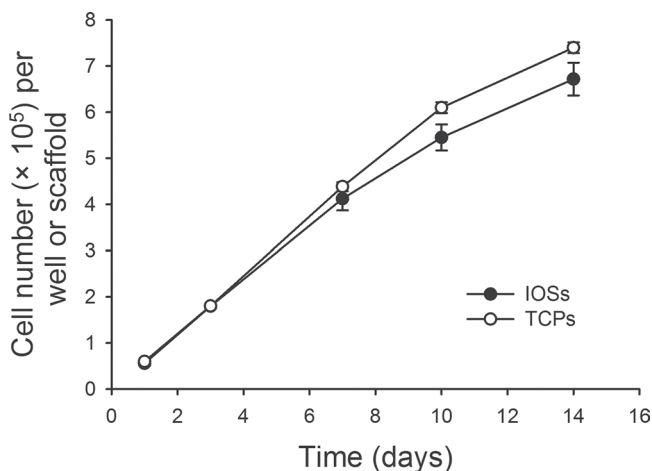
www.MaterialsViews.com

ADVANCED
FUNCTIONAL
MATERIALS
www.afm-journal.de

FULL PAPER

Figure 3. Proliferation profiles of ES cells seeded in alginate inverse opal scaffolds (IOSs) and suspended in culture medium in the wells of tissue culture plates (TCPs), as determined by DNA quantification.

After seeding, the cell/scaffold constructs were transferred into the wells of a nontreated tissue culture plate and kept in a stationary culture condition. We assessed the proliferation of ES cells by quantifying the DNA contents. For the total number of ES cells actually seeded into the alginate inverse opal scaffold, it was determined to be 6×10^4 cells per scaffold on average. As a control, ES cells of the same number were used for suspension culture in the agar-coated tissue culture plates (TCPs). As shown in **Figure 3**, the ES cells continued to proliferate with a nearly linear relationship in both cases during the entire culture period up to 14 days, with the only difference being the slightly higher growth rate for the cells in the suspension culture. Such high proliferation rate for the cells grown in the scaffolds throughout the culture period could be attributed to the high connectivity of the inverse opal scaffold system, as well as the nonadhesive properties of the hydrogel material. Since the formation of cell spheroids did not block surface pores or the windows connecting the adjacent pores, the oxygen/nutrients transport could be kept at a high level throughout the scaffold. In contrast, for inverse opal scaffolds fabricated from a cell-adhesive material such as poly(lactic-co-glycolic) acid (PLGA), the stretching of cells might completely block the surface pores or windows, thus limiting the transport of oxygen/nutrients to the central region of the scaffold.[22]

Figure 4A–D, shows superimposed images containing fluorescence microscopy images of EBs derived from CE3 cells (in green) and transmission optical microscopy images of the alginate scaffolds, during the course of EB formation. At day 1 post seeding, some

ES cells already began to form small aggregates with a size of ~50 μm (Figure 4A). These small aggregates could be a result of the proliferation of an anchored cluster of cells during the seeding process or the aggregation of several anchored single cells (or clusters of cells) in the same pore, which is common in the presence of a surface (e.g., alginate hydrogel) nonadhesive to cells.[31] The EBs gradually grew in size over time. After 14 days of culturing, the size (~220 μm) of the EBs had almost reached the size of the pores (~250 μm). The physical confinement imposed by the pores limited the EBs from further growth, making it possible to control the maximum size of EBs derived from a scaffold.

The alginate scaffolds were disintegrated in a solution containing 100 mM EDTA and 100 mM K_2HPO_4 to harvest the EBs. The same solution was also used for effective disintegration of crosslinked alginate-chitosan scaffolds with minimal toxicity towards the cells.[26] Although no chitosan was involved in the current system, we could still disintegrate the $CaCl_2$-crosslinked alginate scaffolds in the presence of a chelator for Ca^{2+} ions. Upon the addition of the solution, the scaffolds began to fall apart in a few minutes and could reach nearly complete disintegration in less than 10 min. As a result, we were able to obtain EBs with uniform and controllable sizes from the scaffolds after the cells have been seeded and cultured for different periods
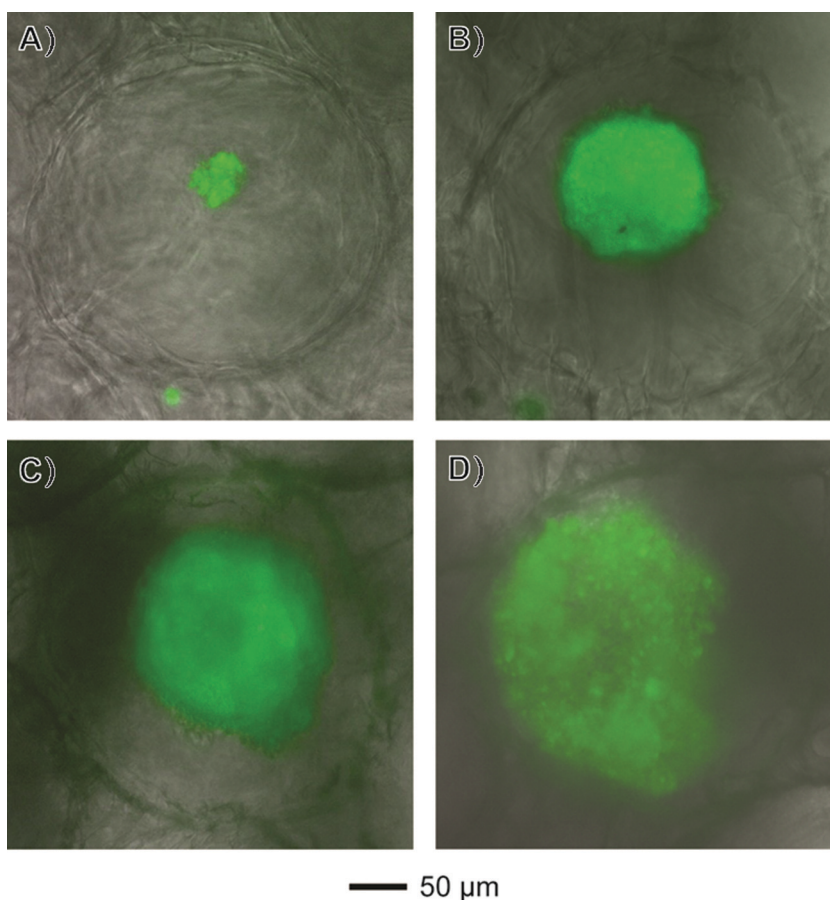

— 50 μm

Figure 4. Fluorescence optical microscopy images of CE3 cells cultured in an inverse opal scaffold of alginate with a pore size of 250 μm at day 1, 3, 7, and 14 post-seeding, clearly showing the growth in size for the EB.
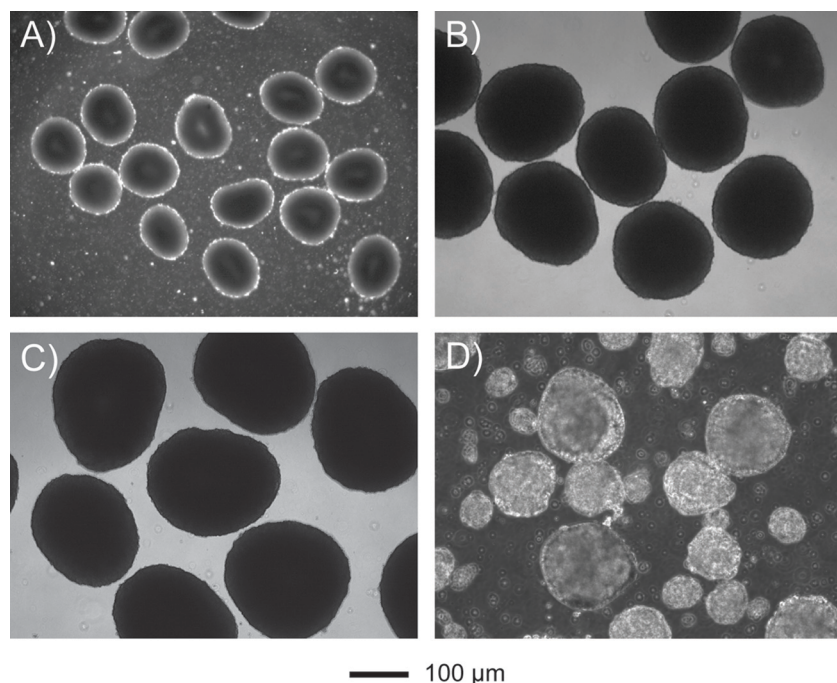
——— 100 μm

Figure 5. A–C) Optical microscopy images of EBs formed in the alginate inverse opal scaffolds for 3, 7, and 14 days, respectively, and then harvested by disintegrating the scaffolds. D) EBs formed on a traditional agar-coated Petri dish, showing a nonuniform distribution in size.

percentages of EBs formed under both conditions were similar at the initial time point (day 1). However, starting at day 3 through to day 14, the number of EBs did not vary much when grown in the scaffolds. By contrast, the number of EBs kept decreasing during a 14-day culture period in suspension culture because of the continuous fusion of EBs over time. This process did not happen in the case of an inverse opal scaffold because only those EBs in the same pore could fuse together during the first few days. Starting from day 3, most EBs only grew individually in size because the wall of a scaffold could effectively prevent the EBs in adjacent pores from aggregating. This is confirmed by the constant EB formation efficacy during day 3 to14 (Table 1 and Figure S2).

Not all the pores were involved in the formation of EBs. Typically, this method based on inverse opal scaffolds could reach a maximum occupancy of ~70% (Table 1). The occupancy percentage could not be calculated at day 1 post seeding since there were multiple small EBs coexisting in a single pore, and the number of released EBs did not represent the number of pores occupied. By day 3, the small EBs in a pore had merged into a single, larger EB, thus enabling more accurate calculation of the occupancy percentage (67.3%, 63.8%, and 62.2% at day 3, 7, and 14, respectively). To compare the occupancy percentages of EBs in different locations of a scaffold, we obtained a fluorescence microscopy image (**Figure 6**A) from EBs residing in a vertical cross-section of the scaffold after 14 days of culture. The occupancy percentage of the EBs in each layer was counted from multiple sections, and no obvious difference was found.

of time. For example, **Figure 5**A–C, shows transmission optical microscopy images of the EBs recovered from the scaffolds at 3, 7, and 14 days post-seeding, respectively. The EBs obtained at these time points were roughly 100, 180, and 220 μm, respectively, in size, and all of them showed a uniform size distribution. By contrast, when the EBs were formed using a traditional method by culturing dissociated ES cells on nonadhesive, agar-coated Petri dishes, there was a huge variation in size for the EBs (Figure 5D).

The efficiency of EB formation (i.e., the number of formed EBs divided by the initial number of seeded ES cells) in the alginate inverse opal scaffolds and in the suspension culture were calculated and compared in **Table 1** and Figure S2. The

It should be pointed out that all the EBs formed in the alginate scaffold did not conform to a perfectly spherical shape, with a portion of them taking an ellipsoidal shape. Most EBs residing close to the edge of the scaffold conformed to a

Table 1. The formation efficacy of EBs in the alginate inverse opal scaffolds (IOSs) and in suspension culture in agar-coated tissue culture plates (TCPs). Initial numbers of actual seeded ES cells were 6×10^4 per scaffold or per well in TCPs. In the table, EB# indicates the number of EBs formed, N% indicates the formation efficacy of EBs (the ratio between the number of EBs formed at each time point and the initial number of ES cells), and Ocp% indicates the occupancy percentage of the EBs in the scaffolds (the ratio between the number of EBs formed at each time point and the number of pores in a scaffold, which was estimated to be ~2800).

|	Sample	Day 1		Day 3			Day 7			Day 14		
		EB#	N%	EB#	N%	Ocp%	EB#	N%	Ocp%	EB#	N%	Ocp%
IOSs	1	2220	3.70	1878	3.13	67.1	1820	3.03	65.0	1610	2.68	57.5
	2	2412	4.02	1934	3.22	69.1	1748	2.91	62.4	1838	3.06	65.5
	3	2479	4.13	1844	3.07	65.9	1789	2.98	63.9	1778	2.96	63.5
	Mean	2370	3.95	1885	3.14	67.3	1786	2.98	63.8	1742	2.90	62.2
TCPs	1	2348	3.91	1787	2.98	N/A	1520	2.53	N/A	1214	2.02	N/A
	2	2635	4.39	1977	3.30	N/A	1448	2.41	N/A	1289	2.15	N/A
	3	2705	4.51	1731	2.89	N/A	1372	2.29	N/A	1147	1.91	N/A
	Mean	2563	3.99	1832	3.05	N/A	1447	2.56	N/A	1217	2.03	N/A
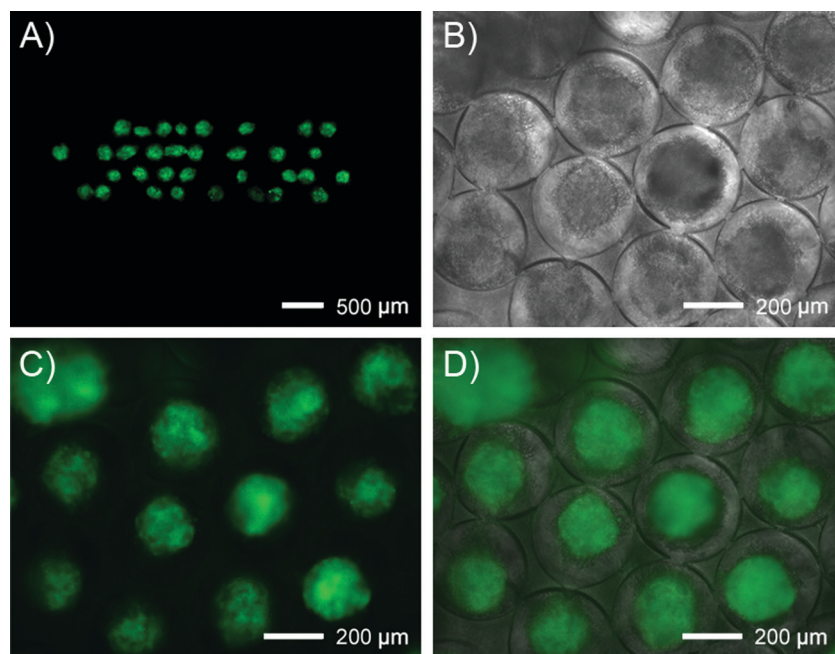
Figure 6. A) Fluorescence microscopy image showing the distribution of EBs in a vertical cross-section of the scaffold. B) Transmission optical microscopy image showing an alginate inverse opal scaffold. C) Fluorescence microscopy image showing the distribution of EBs in the surface layer of the scaffold. D) Superimposed image of (B) and (C). The images were taken after the CE3 ES cells had been cultured in the scaffold for 14 days.

spherical shape (Figure 6), while more EBs with an ellipsoidal shape were found in the center of a scaffold (Figure 6A). Still, some ellipsoidal EBs could reside by the edge, and spherical EBs could exist in the center, as shown in the magnified views of EBs residing in the surface layer of the scaffold (Figure 6B–D). Therefore, we conclude that, although the inverse opal scaffolds have high interconnectivity and provide a higher degree of nutrients/wastes diffusion, the residing EBs can sometimes block the windows connecting to the adjacent pores, depending on the exact positions of the residing EBs relative to the pores and the windows. As a result, the deviation from a spherical shape could be attributed to the differential cell growth rates in EBs mainly caused by local rather than the overall nutrient gradient in the entire scaffold construct.

The alginate scaffolds could not be dissolved completely although they could be readily disintegrated into small pieces. In general, there were some tiny pieces of debris left in the sample. Therefore, a purification step is required to sort out the EBs. Usually a simple sedimentation step was sufficient to separate the slow-settling debris since the heavier EBs settled more quickly to the bottom of the collection tube. For EBs with sizes smaller than 50 μm, however, repeated purification was required to obtain pure samples.

In addition to varying culture time, the size of the EBs could be controlled by varying the pore size of the scaffold. For example, when alginate scaffolds with a pore size of 130 μm were used, EBs with an average diameter of roughly 110 μm were obtained after 14 days of culture (Figure S3).

We further characterized the EBs by various staining methods. To avoid possible interference with fluorescence

staining, we chose RW4, a ES cell line same as CE3 except for the absence of GFP expression, for all these studies. We firstly performed live/dead staining. **Figure 7**A shows a typical confocal fluorescence image of a sample, where live and dead cells are shown in green and red, respectively. Nucleus staining of the same sample is shown in Figure 7B. Most (98.6%) of the cells in the EB were determined to be viable by quantifying cell viability in multiple, randomly chosen samples. We also performed the same stainings for EBs obtained from a control group where they were obtained from suspension culture (Figure 7C and D) and the viability was 97.7%. We believe that the high viability for the cells in the EBs grown in the alginate scaffolds (comparable to suspension culture) could be attributed to the high openness and interconnectivity intrinsic to an inverse opal scaffold, which could ensure a sufficient transport of both oxygen and nutrients.[24]

To test the cell spreading from the EBs, the EBs recovered from scaffold disintegration were seeded individually into the wells of a 6-well plate (Figure S4). The EB settled down and adhered to the culture plate shortly after seeding. Subsequently, cells migrated out from the EB and proliferated on the substrate. By 60 h post seeding, the spreading area reached ~16 times of the original EB, indicating fast and robust spreading of the cells.

The undifferentiated state of the EBs is desired, so that they can be further induced to differentiate into designated lineages. We performed immunostaining of SSEA-4, which is a widely used surface marker of pluripotent stem cells.[32] As shown in Figure 7E, the EBs maintained high expression of SSEA-4 in nearly all the cells (96.4% positive), in comparison with the EBs obtained from suspension culture (Figure 7F, 97.2% positive). A SEM image (Figure S5) also reveals the spherical cell shape which is the characteristic morphology of undifferentiated ES cells.[26]

ES cells are pluripotent and thus can be induced to differentiate into specific lineages. The pluripotency of the EBs formed using alginate scaffolds were then assessed by inducing osteogenic (mesoderm) and neurogenic (ectoderm) differentiation for the EBs. Osteoblasts were differentiated by culture EBs in an osteogenic medium for 20 days.[22] We performed Alizarin Red staining, which stains minerals, and immunostaining of osteocalcin, which is a common marker for bone-forming cells.[33] It was found that the cells were stained intensively with Alizarin Red (**Figure 8**A, red color), and clusters of minerals could be observed in a magnified view (Figure 8B). Osteocalcin staining also confirmed the osteogenesis (Figure 8C and D). We have demonstrated that EBs from CE3/RW4 ES cells have the potential to differentiate into mature neural lineage cells such as neurons and oligodendrocytes.[28] To confirm this, we induced the differentiation of the EBs into neural precursor cells by applying a 4–/4+ retinoic acid treatment during the last 8 days
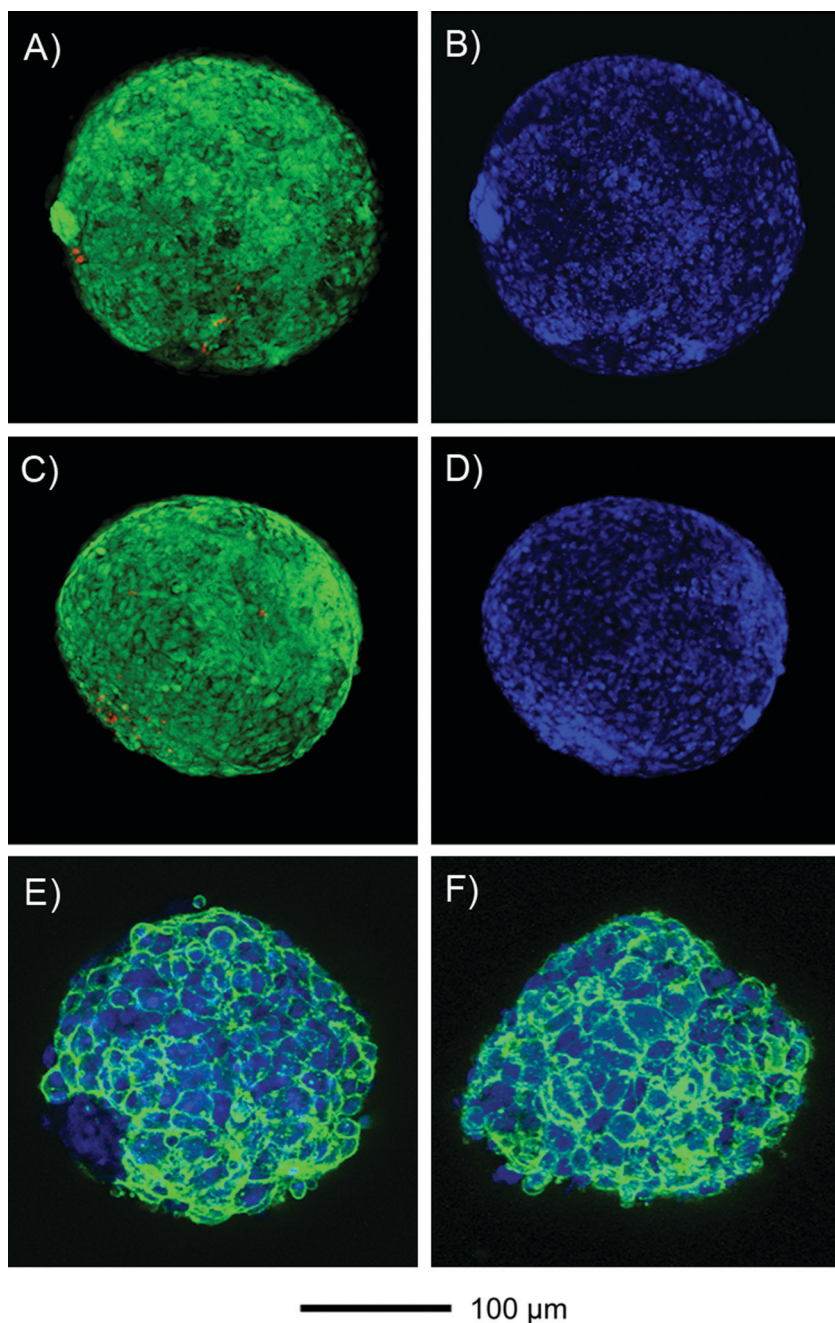
ADVANCED
FUNCTIONAL
MATERIALS

www.afm-journal.de

Materials Views

www.MaterialsViews.com

FULL PAPER

Figure 7. Confocal fluorescence microscopy images of EBs after different stainings: A,C) live/dead (green/red); B,D) nuclei (Hoechst 33342, blue); E,F) SSEA-4/nuclei (green/blue). The EBs in (A,B,E) were obtained from cultures in the alginate inverse opal scaffolds, while those in (C,D,F) were obtained from suspension culture.

in culture in alginate scaffolds.[28,29] This treatment did not change the formation kinetics of the EBs in alginate scaffolds, as compared to normal culture conditions. Further neural differentiation was conducted by culturing recovered EBs in neural basal media containing a B27 supplement for two weeks.[28] Figure 8E and F shows fluorescence microscopy images of the Tuj1 (β-III tubulin) staining. β-III tubulin is a structural protein expressed in neurons, and it contributes to microtubule

stability in neuronal cell bodies and axon.[34] From the images, it is clear that the cells differentiated and displayed a neuronal phenotype, as indicated by strong staining of Tuj1 in both cell bodies and the extending axons. Figure 8G and H show fluorescence microscopy images of the O4 staining, which recognizes oligodendrocyte-specific glycolipid.[35] The cells stained positive for O4 exhibited a multipolar morphology, which was characteristic of oligodendrocytes.

3. Conclusions

In summary, we have successfully developed an effective method for producing uniform, spherical EBs using 3D alginate inverse opal scaffolds. The sizes of the EBs could be readily controlled by varying the culture time and/or by using scaffolds with different pore sizes. The EBs formed inside the scaffolds could be recovered after disintegrating the scaffolds. Our in vitro studies demonstrated that the EBs produced using this method conserved high cell viability and, more importantly, the undifferentiated state. Differentiation assays confirmed that the EBs maintained their pluripotency, and they were able to differentiate into bone and neural lineages depending on the chemical stimuli. We expect this technique for generating EBs to be highly useful for tissue engineering and stem-cell research.

4. Experimental Section

Materials: Polystyrene ($M_w \sim 350\,000$, Sigma–Aldrich, St. Louis, MO) and poly(vinyl alcohol) (PVA, $M_w \sim 13\,000$–$23\,000$, 98% hydrolyzed, Sigma–Aldrich) were used to generate uniform polystyrene microspheres using a fluidic device. Alginate (Sigma–Aldrich) was used for fabrication of the inverse opal scaffolds. Dichloromethane (DCM, 99.0% by vol.), ethanol (99.5%) and CaCl$_2$ were purchased from Sigma–Aldrich. The water used in all experiments was obtained by filtering through a set of Millipore cartridges (Epure, Dubuque, IA).

Preparation of Alginate Inverse Opal Scaffolds: Uniform polystyrene microspheres were produced using a fluidic device according to our previous work,[27] and then assembled into cubic-close packed (ccp) lattices. Briefly, an aqueous suspension of the polystyrene microspheres (~1.5 wt%) was placed in a 50 mL centrifuge tube and sonicated for 10 s. The tube was placed on an orbital shaker set to 80 rpm overnight at room temperature, allowing the water to evaporate. The resultant ccp lattice was placed in an oven heated at 110 °C for 2 h to generate necks between adjacent polystyrene microspheres. After cooling down to room temperature, the pellet of ccp lattice was carefully harvested with a spatula, placed on a filter paper, wetted with a mixture of ethanol and water (1:1 by vol.), and then infiltrated with a 4%
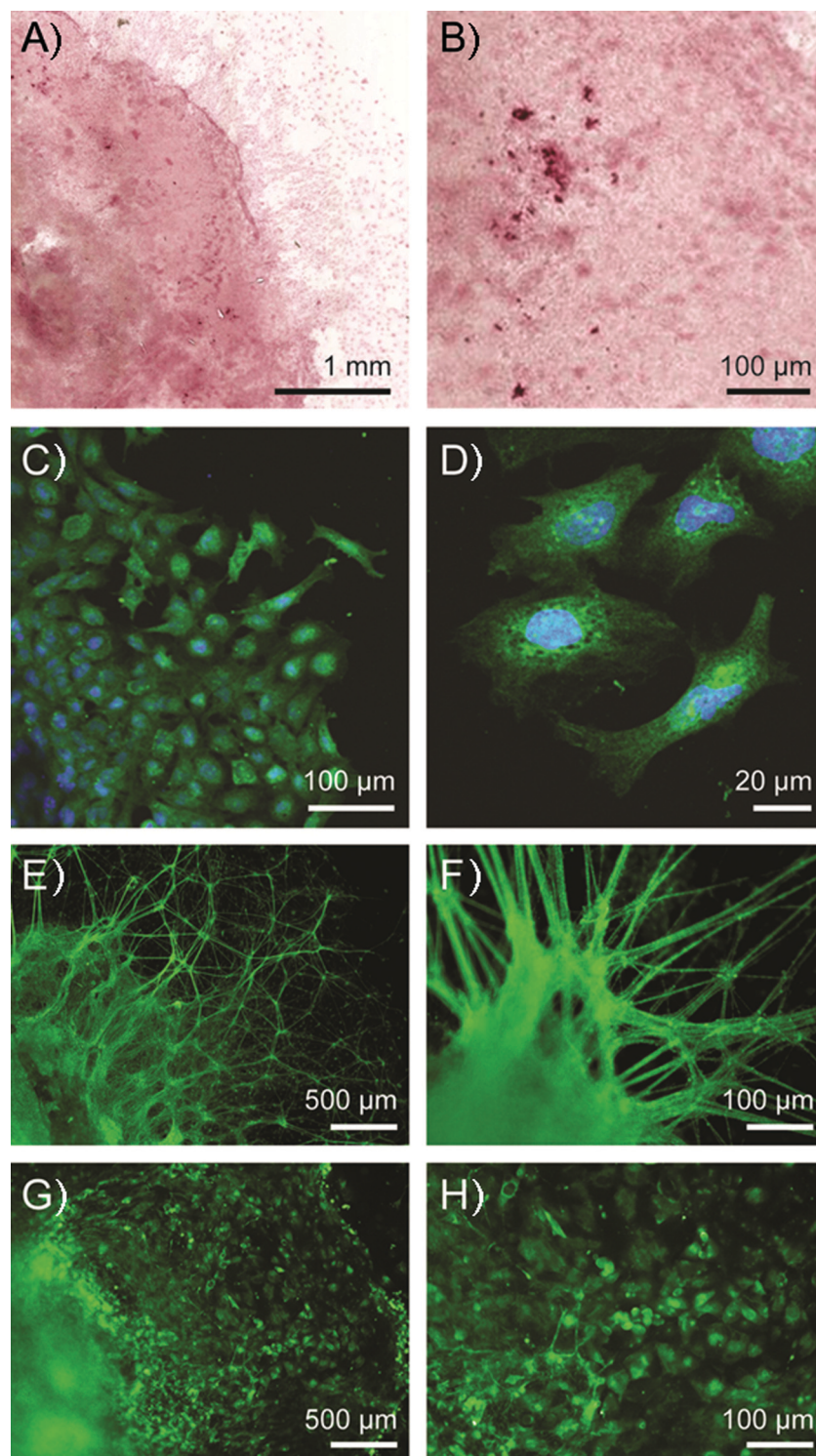
www.MaterialsViews.com

ADVANCED
FUNCTIONAL
MATERIALS
www.afm-journal.de

FULL PAPER

Figure 8. Osteogenesis and neurogenesis of EBs isolated from the alginate scaffolds. A,B) Alizarin red and C,D) osteocalcin staining indicating the differentiation of EBs into osteoblasts. E,F) Tuj1 and G,H) O4 staining showing the differentiation of EBs into neurons and oligodendrocytes.

aqueous solution of alginate. After removing the excess alginate solution with filter paper, the ccp lattice filled with alginate solution was frozen in a refrigerator (−20 °C) for 5 h, and then lyophilized in a freeze-dryer

(Labconco, Kansas City, MO) overnight. The pellet containing freeze-dried alginate was placed in ethanol for 3 h and then immersed in DCM for 5 h to remove all the polystyrene microspheres. The alginate inverse opal scaffold was washed with ethanol three times and equilibrated in a mixture of DCM and ethanol (1:1 by vol.) for 30 min. The alginate was crosslinked by immersing the sample in the following two solutions: 2 wt% $CaCl_2$ in ethanol for 30 min and 1 wt% $CaCl_2$ in water for 30 min. The alginate scaffold was finally washed twice with DI water.

Culture of Embryonic Stem Cells within the Scaffolds: We cultured the mouse ES cells using a protocol similar to what was described previously.[28] RW4 and CE3 mouse ES cells were obtained from Dr. Gottlieb at Washington University School of Medicine and cultured in flasks coated with a 0.1% gelatin solution. 1000 U mL^{-1} leukemia inhibitory factor (LIF, Millipore, Billerica, MA) and 10^{-4} M β-mercaptoethanol (BME, Invitrogen, Carlsbad, CA) were added to maintain their undifferentiated state. Cells were cultured in complete media consisting of Dulbecco's Modified Eagle Medium (DMEM) supplemented with 10% new-born calf serum, 10% fetal bovine serum (Invitrogen), and 0.3 mM of each of the nucleosides (adenosine, guanosine, cytosine, thymidine, and uridine, all from Sigma–Aldrich), and passaged twice a week. Prior to seeding, the scaffolds were sterilized with 70% ethanol overnight on an orbital shaker, and washed with PBS three times. A total of 2×10^5 cells were used to seed each scaffold using a spinner flask at 60 rpm for 24 h in an incubator. The scaffolds were then transferred into the wells (one scaffold per well) of a 12-well plate (not treated for tissue culture, BD, San Jose, CA), rinsed once with phosphate buffered saline (PBS), and then filled with 1 mL of the culture medium in each well. The actual number of ES cells seeded into a scaffold was determined to be ∼6 × 10^4 by DNA analysis (see below).

Recovery of Embryoid Bodies from the Scaffolds: EBs formed inside the alginate scaffold were recovered by disintegrating the scaffold with a solution containing 100 mM EDTA and 100 mM K_2HPO_4 (Sigma–Aldrich) for 5–10 min, and then washed with the culture medium to remove small pieces of scaffold fragments when necessary.

Formation of Embryoid Bodies on a Two-Dimensional Substrate: Undifferentiated mouse ES cells were cultured in 100 mm Petri dishes coated with a 0.1% agar solution (Sigma–Aldrich) with a complete medium in the absence of LIF and BME. The medium was changed every other day until the EBs reached desired sizes.

Cell Proliferation Assay: Cell proliferations in scaffolds and in suspension culture were measured by quantifying the DNA contents. The DNAs were extracted using the Wizard Genomic DNA Purification Kit (Promega, Madison, WI), and were quantified using the PicoGreen dsDNA reagent (Invitrogen), according to the manufacturers' instructions. The fluorescence intensity at 530 nm was measured using a spectrophotometer (Infinite 200, TECAN, Durham, NC).

Calculation of EB Formation Efficacy and Occupation Percentage: At days 1, 3, 7, and 14 post-seeding, EBs formed from CE3 ES cells in the alginate inverse opal scaffolds were freed by disintegrating the scaffolds,

FULL PAPER

and counted under a fluorescence microscope. At the same time points, the numbers of EBs formed in the wells (agar-coated) of a tissue culture plate were also counted. The formation efficacy of EBs is calculated as the number of EBs formed at each time point divided by the initial number of seeded ES cells (6×10^4 in both cases). To calculate the occupation percentage of EBs in the scaffolds, the number of EBs were divided by the number of pores in a scaffold. For a typical inverse opal scaffold (250 μm in pore size) with a dimension of 4 mm (diameter, top surface) × 5 mm (diameter, bottom surface) × 1 mm (height), the number of pores is estimated to be ~2800.

Osteogenic and Neurogenic Differentiations of the Embryoid Bodies: EBs recovered from the disintegrated scaffold were placed in the wells of a 6-well plate (2–3 EBs per well). For osteogenic differentiation, the EBs were cultured in a medium supplemented with 300 μM L-ascorbic acid and 10 mM β-glycerol phosphate (Sigma–Aldrich),[24] and the medium was changed every other day during a three-week period. For neurogenic differentiation, the medium was changed during the last 8 days prior to scaffold disintegration, according to the 4–/4+ retinoic acid treatment protocol.[29] Briefly, the cells were cultured in the absence of LIF and BME for 4 days. Retinoic acid (Sigma–Aldrich) was then added at a concentration of 500 nM during the last 4 days of culture. After harvesting EBs containing neuron precursor cells from disintegrated scaffolds and plating them in the wells of a 6-well plate, they were further differentiated by culturing with a neurobasal medium containing B27 supplement for two weeks.[28]

Fluorescence Staining, Immunohistochemistry and Characterization: Live/Dead assay (Invitrogen) was performed according to the manufacturer's instructions. Hoechst 33342 (Sigma–Aldrich) was used to counter-stain the nuclei, as it can work for both live and dead cells. Undifferentiated or differentiated EBs were fixed with a 3.7% formaldehyde solution and washed three times with PBS. SSEA-4 (Millipore) was used as the marker for undifferentiated ES cells, and the nuclei were stained with 4′,6-diamidino-2-phenylindole (DAPI, Invitrogen). Alizarin Red (Sigma–Aldrich) was used to stain the mineral content after osteogenic differentiation. A solution of 1% Alizarin Red in a mixture of ethanol and water (1:50 by vol.) was prepared, and the pH was adjusted to 4.1–4.3 using 10% ammonium hydroxide. The cells were stained with Alizarin Red for 5 min, and rinsed thoroughly with water. Osteocalcin was used as a maker of osteoblasts for EBs cultured in an osteogenic medium, while Tuj1 and O4 were used as markers of neurons and oligodendrocytes for EBs differentiated in a neurogenic medium. Cells were blocked in 1% bovine serum albumin solution for 1 h, and permeabilized (when necessary) in 0.1% Triton X-100 solution for 1 h. Primary antibodies (Millipore) were used at a dilution of 1:100–500, and incubated at 4 °C overnight. After washing with PBS, the cells were incubated with secondary antibodies (Invitrogen, 1:200 dilution) at room temperature for 1 h, and rinsed with PBS.

When necessary, the cells were fixed in 3.7% formaldehyde, and cell/scaffold constructs were embedded in O.C.T. compound (Tissue-Tek, Ted Pella, Redding, CA) and frozen at –80 °C. Vertical sections with a thickness of ~1 mm were obtained by manually cutting the frozen samples, which were then subjected to fluorescence imaging.

Fluorescence was detected with an Olympus microscope with Capture 2.90.1 (Olympus, Center Valley, PA), or a confocal laser scanning microscope (CLSM, Carl Zeiss, Thornwood, NY). Images of Alizarin Red staining were taken using a Nanozoomer virtual microscope (Hamamatsu, Bridgewater, NJ).

Cell death was determined by quantifying the ratio between the number of ethidium homo-dimer 1 positive nuclei and the total number of cells as obtained from nucleus staining. The number of SSEA-4 positive cells was determined by quantifying the ratio between the number of SSEA-4 positive cells and the total number of cells as obtained from nucleus staining.

Scanning Electron Microscopy: A scanning electron microscope (Nova NanoSEM 2300, FEI, Hillsboro, OR) was used to characterize the lattices of polystyrene microspheres, the alginate inverse opal scaffolds, and the EBs. Prior to imaging, the EBs were fixed and dehydrated through a graded ethanol series. The samples were sputter-coated

with gold for 60–120 s. Images were taken at an accelerating voltage of 5–10 kV.

Statistics: All the data were presented as mean ± standard deviation. For assays on cell proliferation and EB formation efficacy, three individual samples in each group at each time point were counted. For quantification of cell viability and SSEA-4 expression, at least ten EBs randomly chosen from each group were examined. All the experiments were performed in at least three independent replicates.

Supporting Information

Supporting Information is available from the Wiley Online Library or from the author.

Acknowledgements

[1] J. M. Karp, L. S. Ferreira, A. Khademhosseini, A. N. Kwon, J. Yeh, R. S. Langer, *Stem Cells* **2006**, *24*, 835.

[2] R. C. Bielby, A. R. Boccaccini, J. M. Polak, L. D. Buttery, *Tissue Eng.* **2004**, *10*, 1518.

[3] J. H. Kim, J. M. Auerbach, J. A. Rodriguez-Gomez, *Nature* **2002**, *418*, 50.

[4] S. C. Zhang, M. Wernig, I. D. Duncan, O. Brustleand, J. A. Thomson, *Nat. Biotechnol.* **2001**, *19*, 1129.

[5] S. Levenberg, J. S. Golub, M. Amit, J. Itskovitz-Eldor, R. S. Langer, *Proc. Natl. Acad. Sci.* **2002**, *99*, 4391.

[6] A. M. Wobus, G. Kaomei, J. Shan, M.-C. Wellner, J. Rohwedel, J. Guanju, B. Fleischmann, H. A. Katus, J. Hescheler, W. M. Franz, *J. Mol. Cell. Cardiol.* **1997**, *29*, 1525.

[7] T. Takahashi, B. Lord, C. Schulze, R. M. Fryer, S. S. Sarang, S. R. Gullans, R. T. Lee, *Circulation* **2003**, *107*, 1912.

[8] Y. Moritoh, E. Yamato, Y. Yasui, S. Miyazaki, J. Miyazaki, *Diabetes* **2003**, *52*, 1163.

[9] F. M. Watt, B. L. M. Hogan, *Science* **2000**, *287*, 1427.

[10] T. A. Pelton, M. D. Bettess, J. Lake, J. Rathjen, P. D. Rathjen, *Reprod. Fertil. Dev.* **1998**, *10*, 535.

[11] G. Hopfl, M. Gassmann, I. Desbaillets, *Methods Mol. Biol.* **2004**, *254*, 79.

[12] J. Itskovitz-Eldor, M. Schuldiner, D. Karsenti, A. Eden, O. Yanuka, M. Amit, H. Soreq, N. Benvenisty, *Mol. Med.* **2000**, *6*, 88.

[13] S. M. Dang, M. Kyba, R. Perlingeiro, G. Q. Daley, P. W. Zandstra, *Biotechnol. Bioeng.* **2002**, *78*, 442.

[14] B. Valamehr, S. J. Jonas, J. Polleux, R. Qiao, S. Guo, E. H. Gschweng, B. Stiles, K. Kam, T.-J. M. Luo, O. N. Witte, X. Liu, B. Dunn, H. Wu, *Proc. Natl. Acad. Sci.* **2008**, *105*, 14459.

[15] H.-C. Moeller, M. K. Mian, S. Shrivastava, B. G. Chung, A. Khademhosseini, *Biomaterials* **2008**, *29*, 752.

[16] Y.-S. Hwang, B. G. Chung, D. Ortmann, N. Hattori, H.-C. Moeller, A. Khademhosseini, *Proc. Natl. Acad. Sci.* **2009**, *106*, 16978.

[17] J. S. Boo, Y. Yamada, Y. Okazaki, *J. Craniofacial. Surg.* **2002**, *13*, 231.

[18] T. Yamada, M. Yoshikawa, S. Kanda, Y. Kato, Y. Nakajima, S. Ishizaka, Y. Tsunoda, *Stem Cells* **2002**, *20*, 146.

[19] J. C. Mohr, J. J. de Pablo, S. P. Palecek, *Biomaterials* **2006**, *27*, 6032.

[20] S.-W. Choi, J. Xie, Y. Xia, *Adv. Mater.* **2009**, *21*, 2997.

[21] N. A. Kotov, Y. Liu, S. Wang, C. Cumming, M. Eghtedari, G. Vargas, M. Motamedi, J. Nichlos, J. Cortiella, *Langmuir* **2004**, *20*, 7887.

[22] S.-W. Choi, Y. Zhang, S. Thomopoulos, Y. Xia, *Langmuir* **2010**, *26*, 12126.

[23] A. N. Stachowiak, D. J. Irvine, *J. Biomed. Mater. Res.* **2008**, *85A*, 815.

[24] S.-W. Choi, Y. Zhang, Y. Xia, *Langmuir* **2010**, *26*, 19001.

[25] J. Lee, M. J. Cuddihy, G. M. Cater, N. A. Kotov, *Biomaterials* **2009**, *30*, 4687.

[26] Z. Li, M. Leung, R. Hopper, R. Ellenbogen, M. Zhang, *Biomaterials* **2010**, *31*, 404.

[27] S.-W. Choi, I. W. Cheong, J.-H. Kim, Y. Xia, *Small* **2009**, *5*, 454.

[28] J. Xie, S. M. Willerth, X. Li, M. R. Macewan, A. Rader, S. E. Sakiyama-Elbert, Y. Xia, *Biomaterials* **2009**, *30*, 354.

[29] G. Bain, D. Kitchens, M. Yao, J. E. Huettner, D. I. Gottlieb, *Dev. Biol.* **1995**, *168*, 342.

[30] A. D. Augst, H. J. Kong, D. J. Moone, *Macromol. Biosci.* **2006**, *6*, 623.

[31] G. H. Underhill, A. A. Chen, D. R. Albrecht, S. N. Bhatia, *Biomaterials* **2007**, *28*, 256.

[32] C. L. Kerr, C. M. Hill, P. D. Blumenthal, J. D. Gearhart, *Hum. Reprod.* **2008**, *23*, 589.

[33] H. Vilmann, *J. Anat.* **1969**, *105*, 533.

[34] P. F. Moskowitz, R. Smith, J. Pickett, A. Frankfurter, M. M. Oblinger, *J. Neurosci. Res.* **1993**, *34*, 129.

[35] R. Bansal, A. E. Warrington, A. L. Gard, B. Ranscht, S. E. Pfeiffer, *J. Neurosci. Res.* **1989**, *24*, 548.

FULL PAPER

ADVANCED FUNCTIONAL MATERIALS

DRUG DELIVERY

The generation of near-infrared-sensitive microcapsules with programmable release properties is reported by Daeyeon Lee and co-workers on page 131. Poly(DL-lactic-co-glycolic) acid (PLGA) microcapsules are generated using monodisperse water-in-oil-inwater double emulsions as templates. The composition of the oil phase of double emulsions and that of PLGA determine the morphology and, in turn, the release properties of microcapsules. These microcapsules enable the release of hydrophobic and hydrophilic agents in a programmed sequence.

FULL PAPER

Harnessing Interfacial Phenomena to Program the Release Properties of Hollow Microcapsules

Myung Han Lee, Kolin C. Hribar, Teresa Brugarolas, Neha P. Kamat, Jason A. Burdick, and Daeyeon Lee*

The generation of near-infrared (NIR)-sensitive microcapsules is presented and it is demonstrated that the release properties of these microcapsules can be tailored by controlling their morphology. A biocompatible polymer, poly(DL-lactic-co-glycolic)acid (PLGA) is used to form hollow microcapsules from monodisperse water-in-oil-in-water (W/O/W) double emulsions. Both the composition of PLGA and the oil phase of W/O/W double emulsions significantly affect the morphology of the subsequently formed microcapsules. PLGA microcapsules with vastly different morphologies, from spherical to "snowman-like" capsules, are obtained due to changes in the solvent quality of the oil phase during solvent removal. The adhesiveness of the PLGA-laden interface plays a critical role in the formation of snowman-like microcapsules. NIR-sensitive PLGA microcapsules are designed to have responsive properties by incorporating Au nanorods into the microcapsule shell, which enables the triggered release of encapsulated materials. The effect of capsule morphology on the NIR responsiveness and release properties of PLGA microcapsules is demonstrated.

1. Introduction

Hollow microcapsules containing an aqueous core covered by a thin shell are useful for encapsulating, protecting and delivering active ingredients such as drugs, nutrients, fragrances and living cells.[1] Microcapsules can be further engineered to actively release encapsulated materials in response to external stimuli such as pH,[2] temperature,[3] ultrasound,[4] and light,[5–7] providing an effective way to locally release their payloads on demand. Various methods of microcapsule generation, including self-assembly of amphiphiles (e.g., diblock copolymers and phospholipids) and layer-by-layer assembly of polymers, have been used to prepare stimuli-responsive microcapsules.[8–13]

Generally, these fabrication techniques lead to the formation of microcapsules that release one type of encapsulated material upon the application of a stimulus. For a number of applications, however, it is highly desirable to design and fabricate carriers that can deliver multiple encapsulants, especially both hydrophilic and hydrophobic species, in a programmed fashion.[14] For example, in the area of drug delivery, there is a clear demand for drug delivery systems that can deliver multiple drugs of drastically different solubility in a pre-determined sequence.[15,16] Conventional methods of microcapsule fabrication also suffer from low encapsulation of active ingredients, which can be a critical problem since a number of pharmaceutical actives such as enzymes and antibodies are prohibitively expensive.[17]

In this study, we demonstrate the generation of near-infrared (NIR)-sensitive PLGA microcapsules with release properties that can be programmed by controlling the morphology of the microcapsules. More specifically, we fabricate PLGA microcapsules that can release hydrophobic and hydrophilic agents in a sequential fashion. PLGA microcapsules are fabricated by using a water-in-oil-in-water (W/O/W) double emulsion as a template. The use of a microfluidic device ensures high encapsulation efficiency (≈100%) and also the generation of highly monodisperse emulsions.[18–21] We use a commonly available, bioresorbable polymer, poly(DL-lactic-co-glycolic)acid (PLGA), to stabilize double emulsions and form microcapsules. This polymer has been widely used in various biomedical applications and is also approved for use in therapeutic devices by the US Food and Drug Administration (FDA), making it an ideal material to form microcapsules for future in vivo studies. Although a previous study has shown that PLGA microparticles with a hollow core can be generated from double emulsions, the effect of the PLGA composition and effect of the oil phase composition on the microcapsule morphology has not been presented in detail.[22,23] Here, we show that varying the composition of PLGA and that of the organic phase of W/O/W double emulsions leads to the formation of PLGA microcapsules with vastly different morphologies. The physical mechanism contributing to the observed morphological differences of PLGA microcapsules is elucidated. By studying this

Dr. M. H. Lee, T. Brugarolas, Prof. D. Lee
Department of Chemical and Biomolecular Engineering
University of Pennsylvania
Philadelphia, PA 19104, USA
E-mail: daeyeon@seas.upenn.edu
K. C. Hribar, N. P. Kamat, Prof. J. A. Burdick
Department of Bioengineering
University of Pennsylvania
Philadelphia, PA 19104, USA

composition-morphology relationship, we demonstrate that it is possible to program the release properties of these PLGA microcapsules by incorporating gold nanorods (AuNRs) and controlling the capsule morphology.

2. Results and Discussion

2.1. Effect of PLGA and Oil-phase Compositions on the Morphology of Microcapsules

Water-in-oil-in-water (W/O/W) double emulsions, used to prepare PLGA microcapsules, are prepared using a glass-capillary microfluidic device, as shown in **Figure 1**a. The inner phase (W) is a phosphate buffered saline (PBS) solution and the outer phase (W) is a 2 wt% poly(vinyl alcohol) (PVA) aqueous solution. The middle phase (O), which is immiscible with the inner and outer aqueous phases, is a mixture of volatile organic solvents, toluene and chloroform, containing PLGA. It is important to note that no additional surface active agents are added to the middle phase. The outer fluid hydrodynamically focuses the inner and middle fluid streams into the collection channel, leading to the formation of double emulsions with core-shell structures. The generated double emulsions are collected into a PBS solution in a glass Petri dish to match the osmolarity of inner and outer aqueous phases. In the absence of PVA, double emulsions generated using PBS as the outer phase

undergo coalescence, illustrating the importance of PVA as a stabilizer of the outer oil/water interface (see Figure S1 in Supporting Information). Removal of the solvents from the oil layer of W/O/W double emulsions leads to the formation of PLGA microcapsules.

The composition of PLGA and that of the oil phase of W/O/W double emulsions are found to have a significant influence on the morphology of double emulsions during solvent removal. PLGAs with a molar ratio of lactide to glycolide ranging from 50:50 to 100:0 (i.e., 50:50, 65:35, 75:25, 85:15, and 100:0) are used to form microcapsules. PLGA 100:0 corresponds to the homopolymer, poly(DL-lactic acid) (PLA). We also vary the composition of the oil phase by mixing chloroform and toluene at different volumetric ratios. During solvent removal, we observe that some double emulsions undergo a dewetting transition, as seen in Figure 1b.[20] Initially, the oil layer of W/O/W double emulsions completely encapsulates a water droplet. As the solvent mixture is removed, the inner water droplet partially separates out of the oil droplet without coalescing with the outer aqueous phase; this morphological change leads to the formation of an acorn-like configuration (partial engulfing). In contrast, double emulsions generated using a PLGA polymer with a different lactide to glycolide composition and in a different toluene to chloroform solvent mixture show a core-shell configuration (complete engulfing) throughout the solvent removal process as shown in Figure 1c. These trends are independent of the polymer concentration (C_p) above 0.6 wt% and the thickness of the oil phase (h) in the range of 50 and 90 μm. When $C_p < 0.6$ wt%, less than 90% of double emulsions are stable; thus, all of our subsequent experiments are performed by generating double emulsions with oil shell thickness of 60–80 μm and with a polymer concentration in the range of 0.7 and 1.0 wt%.

We characterize the effect of PLGA composition ($x_{lactide}$) and that of the oil phase composition (i.e., volume fraction of chloroform, $\varphi_{chloroform}$) on the morphology of double emulsions during solvent removal, as shown in **Figure 2** (movies showing the morphological transitions are provided in the Supporting Information). For double emulsions containing PLGA with compositions of 50:50 and 65:35, a decrease in the volume fraction of chloroform in the solvent mixture leads to the dewetting of the oil phase from the inner droplet (partial engulfing) during solvent removal. Similar observations have been made in the formation of polymersomes from amphiphilic diblock copolymer containing double emulsions.[20] In contrast, double emulsions generated with increased lactide content in the PLGA (PLGA with 75:25, 85:15, and 100:0 composition) maintain the core–shell structure (complete engulfing) regardless of the composition of solvent mixtures.

The difference in the density of the oil phase and the inner aqueous phase does
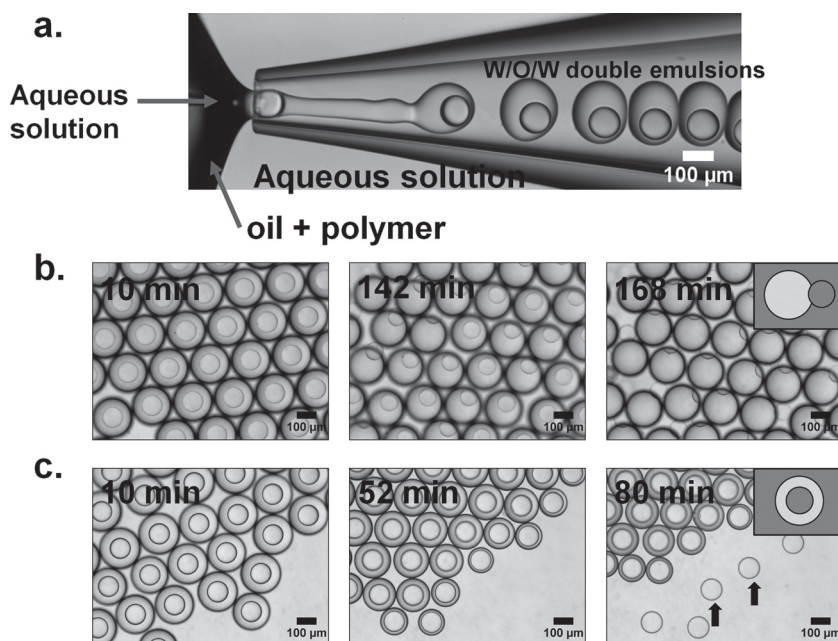
Figure 1. a) Optical microscopy image of W/O/W double emulsions generated in a microfluidic device. b,c) The structural evolution of double emulsions generated with (b) PLGA 50:50 dissolved in a mixture of chloroform and toluene in a volume ratio of 2:3 and (c) PLGA 85:15 dissolved in pure chloroform during solvent evaporation. b) Double emulsions adopt partial engulfing morphology during solvent removal. In contrast, the morphology of double emulsions in (c) does not change (i.e., complete engulfing). Some double emulsions (arrows) in the rightmost image in (c) have become PLGA microcapsules due to solvent removal. The insets show the schematic illustration of the morphology of double emulsion; light gray and dark gray indicate oil containing PLGA and aqueous solution, respectively.

Materials
Views
www.MaterialsViews.com

ADVANCED
FUNCTIONAL
MATERIALS
www.afm-journal.de

FULL PAPER

Figure 2. State diagram showing the morphology of double emulsions during solvent evaporation as functions of the volume fraction of chloroform ($\varphi_{chloroform}$) and the composition of PLGA ($x_{lactide}$): (■) complete engulfing and (△) partial engulfing. The shaded area indicates the insoluble region of PLGA in solvent mixtures. In regime I, double emulsions sediment upon collection into a vessel. In regime II, double emulsions initially sediment because of the dense oil phase. After partial removal of the solvents, these double emulsions float to the free water surface and subsequently sediment. In Regime III, double emulsions float to the air/water interface upon collection.

not strongly correlate with the observed morphological transformation. The state diagram in Figure 2 can be divided into three regimes depending on the density of the oil phase. In regime I, the solvent mixture is denser than water; thus, double emulsions sediment upon collection into a vessel, and the organic solvents are removed through dissolution into the aqueous phase and subsequent evaporation. In regime II, double emulsions initially sediment because of the dense oil phase. After a short while (≈60 min), these double emulsions float to the free water surface and subsequently sediment. This phenomenon is likely due to the fact that the removal rate of chloroform is faster than that of toluene (the solubility of chloroform in water (≈8 g/L at 20 °C) is higher than that of toluene (≈0.5 g/L at 20 °C)). The preferential removal of chloroform while the double emulsions are completely submerged leads to the reduction of the density of the oil phase, making the overall double emulsions less dense and resulting in floating emulsions. Subsequently, as the oil phase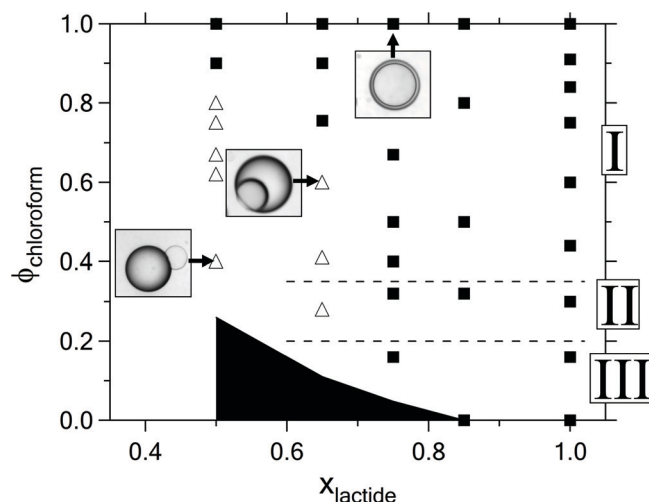 becomes a solid polymer shell, double emulsions sediment due to the increased density. In regime III, double emulsions float to the air/water interface upon collection because of the low density of the oil phase. The double emulsions then sediment during solvent evaporation because of the gradual increase in the density of the oil phase. From these observations we determine that the morphology of the double emulsions during solvent removal does not depend on the density of the oil phase.

The three possible configurations of double emulsions that we observe (such as complete engulfing, partial engulfing and non-engulfing) have previously been theoretically described using spreading coefficients, defined as

$$S_1 = \gamma_{jk} - \gamma_{ij} - \gamma_{ik} \ (i \neq j \neq k = \text{o, i, m}) \tag{1}$$

where γ_{jk}, γ_{ij}, and γ_{ik} are the interfacial tensions between j–k, i–j, and i–k fluids of the three fluid phases.[24–26] In our case, however, the morphology of double emulsions containing PLGA cannot be rationalized by the spreading coefficients of the three fluid phases. Interfacial tension between the two aqueous phases is close to 0 ($\gamma_{io} \sim 0$). The presence of PVA in the outer phase ensures that the interfacial tension between the inner aqueous phase and the middle oil phase is always greater than that between the middle oil phase and the outer aqueous phase (i.e., $\gamma_{im} > \gamma_{om}$). The spreading coefficients, determined using pendant drop tensiometry (**Figure 3**), thus lead to $S_i < 0$, $S_o > 0$,
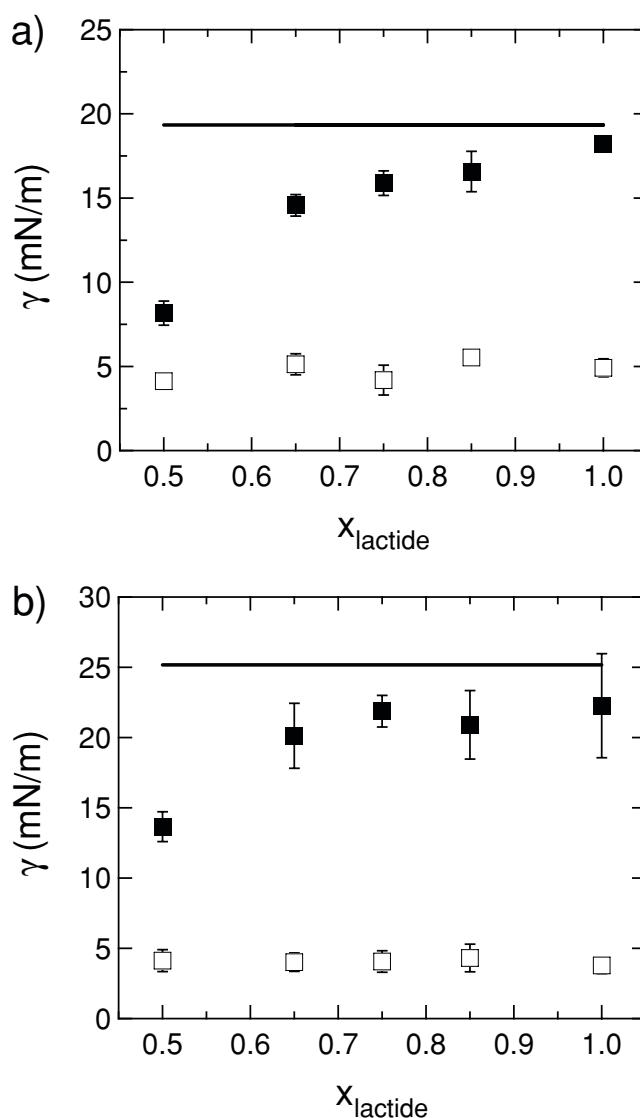
Figure 3. Interfacial tension between an aqueous phase and an oil phase containing PLGA (■). The oil phase in (a) is a chloroform/toluene (2v/3v) mixture containing PLGA with the different compositions and in (b) is pure chloroform containing PLGA with the different compositions. The solid lines indicate the interfacial tension between PBS solution and oil without PLGA. Open squares represent surface tension between a 2 wt% PVA solution and PLGA containing oil phases.

and $S_m < 0$ (subscripts i, o, and m indicate the inner, outer, and middle phases, respectively), regardless of the composition of PLGA in the oil phase as shown in **Figure 4**. These spreading coefficients correspond to the formation of two separated droplets (non-engulfing). When the fraction of lactide content in the PLGA increases from PLGA 50:50 to PLGA 100:0, the spreading coefficients of double emulsions move further away from the origin into the lower-right corner of the non-engulfing quadrant (Figure 4). This trend does not agree with the experimental results, which show that double emulsions containing PLGA with greater lactide content have complete engulfing morphology (see Figure 2). It is important to note that all double emulsions generated in the absence of PLGA polymer are converted into oil-in-water single emulsions immediately after collection. In this case, the spreading coefficients are $S_i < 0$, $S_o > 0$, and $S_m < 0$, corresponding to the non-engulfing condition. These results indicate that the spreading coefficients do not satisfactorily predict the morphology of double emulsions and that the PLGA polymer in the middle phase is a critical component in stabilizing the double emulsions.

Our hypothesis that PLGA plays a critical role in the stabilization of double emulsions can also be verified by the fact that PLGA lowers the surface tension between the oil and water phases. Figure 3 shows the reduction of surface tension between oil and water as a function of the composition of PLGA in two different solvent mixtures. In both cases, it is clearly seen that the increase in the fraction of glycolide content leads to a larger reduction in surface tension. These results strongly indicate that PLGA, which is a random copolymer of glycolide and lactide, is surface active and that the surface activity of PLGA strongly depends on its composition. Although the surface activity of various diblock copolymers has been reported, to the best of our knowledge, our study is the first to report the surface activity of PLGA. Based on these observations, we believe that W/O/W double emulsions containing PLGA are in
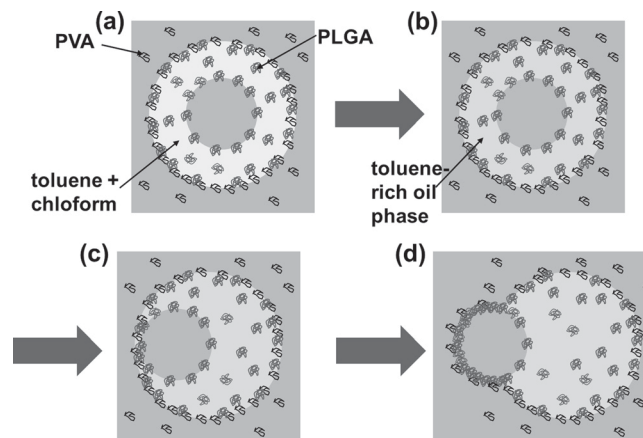
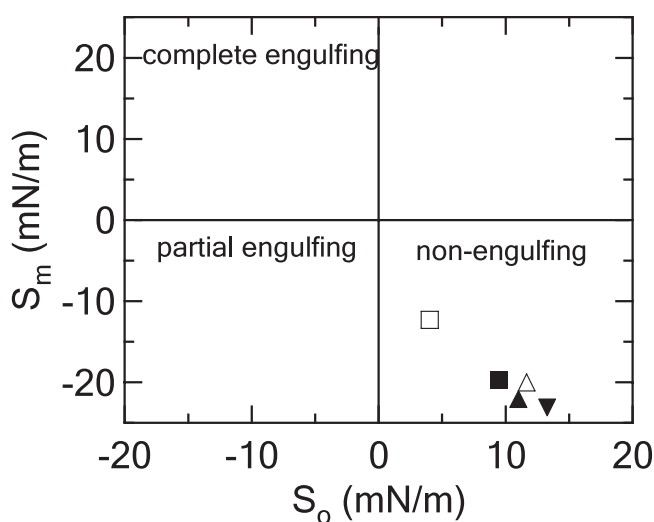**Figure 5.** Schematic illustration showing the formation of a snowman-like capsule induced by the change in the solubility of polymer in the oil phase and the subsequent formation of the adhesive polymer layer at the two interfaces. a) Upon the formation of a W/O/W double emulsion, PVA stabilizes the outer oil/water interface, and PLGA stabilizes both the inner and outer water/oil interfaces, b) the solvent quality of the oil phase reduces to fully solubilize PLGA due to the faster removal of chloroform, c) the two oil/water interface covered with PLGA becomes adhesive initiating the dewetting process, and d) the inner drop, covered with a solid film of PLGA, protrudes out of the oil drop.

a kinetically stable state because of the adsorption of PLGA to the inner water/oil interface.

The morphological evolution of double emulsions that leads to the acorn-like structure (Figure 1b) is believed to be induced by the change in the solvent quality of the oil phase and the subsequent formation of adhesive interfaces as schematically illustrated in **Figure 5**. For instance, in the case of a double emulsion with PLGA 50:50 dissolved in a mixture of chloroform (a good solvent for both the lactide and glycolide) and toluene (a poor solvent for glycolide and a good solvent for lactide)[27] (Figure 1b), PLGA adheres to the inner and outer water/oil interface upon the emulsion formation (Figure 5a). The quality of the solvent in the oil phase becomes poor due to the preferential removal of chloroform (Figure 5b). As this occurs, the PLGA chains at the inner water/oil and outer oil/water interfaces become adhesive and form a solid film (Figure 5c). This adhesion process between the two interfaces protects the inner drop from coalescing with the outer aqueous phase as it protrudes out of the oil phase (Figure 5d). We note that the formation of adhesive interfaces has been reported in high melting point surfactant-stabilized single emulsions and, more recently, in diblock copolymer-stabilized double emulsions.[28,29] The absence of the acorn-like structure in double emulsions containing PLGA with the lactide fraction above 0.75 supports this mechanism since the oil phase remains a good solvent for the polymer throughout the solvent removal process.

2.2. Controlling the Release Properties of PLGA Microcapsules

Upon the removal of the solvents from the oil phase, double emulsions are converted into stable polymer-shelled microcapsules with aqueous cores. To clearly observe the structure of

Figure 4. Spreading coefficients (S_m and S_o) calculated for double emulsions generated using a chloroform/toluene (2v/3v) solution containing random copolymer PLGA with the different compositions: (□) 50:50, (■) 65:35, (△) 75:25, (▲) 85:15, and (▼) 100:0.

www.MaterialsViews.com

ADVANCED
FUNCTIONAL
MATERIALS
www.afm-journal.de

FULL PAPER

the shell and the encapsulation capability of the microcapsules, hydrophobic (red) and hydrophilic (green) fluorescent dyes are added to the oil and inner water phases of W/O/W double emulsions, respectively. The final structure of microcapsules is strongly dependent on the morphology of double emulsions during solvent removal, as shown in **Figure 6**. Double emulsions exhibiting complete engulfing morphology are converted into microcapsules with a uniform polymer shell (Figure 6a), as evidenced by the uniform distribution of the hydrophobic dye in the PLGA shell (Figure 6b). This result also indicates that a hydrophobic dye can be uniformly incorporated into the PLGA shell. In contrast, double emulsions that have undergone the dewetting transition form microcapsules with a thick patch in one region (Figure 6c and d). This effect is more evident when gold nanorods (AuNR) are added to the oil phase of W/O/W double emulsions. Snowman-like microcapsules with a round solid aggregate are formed after solvent removal (Figure 6e and f). The scanning electron microscopy (SEM) image of dried samples (inset of Figure 6e) clearly shows that these aggregates are solid (i.e., it does not undergo severe crumpling upon drying). As will be discussed below, the incorporation of AuNRs enables the generation of NIR-sensitive microcapsules

for triggered release of encapsulated materials through heating of the polymer shells.

We investigate the possibility of triggering the release of encapsulated materials from PLGA microcapsules in response to an external stimulus. Among many external stimuli, near-infrared (NIR) light is an attractive means to trigger the release because NIR is minimally absorbed by the body's water and hemoglobin, thus readily penetrates skin. It is also relatively straightforward to localize the application of NIR light *in vivo* compared to other stimuli such as heat and pH.[5,30] We use AuNRs, which have been used as an NIR-absorbing material for light-triggered release of encapsulated materials.[31–35] We add AuNRs to the oil phase of W/O/W double emulsions and upon solvent evaporation, generate AuNR/PLGA nanocomposite microcapsules. FITC-dextran is encapsulated in the inner aqueous phase to monitor the encapsulation and triggered release.

The morphology of AuNR/PLGA microcapsules has a significant influence on the NIR sensitivity of these capsules. The application of NIR light to neat PLGA microcapsules formed using PLGA 50:50 in pure chloroform does not induce any changes in the shape and the fluorescence intensity of the aqueous core (**Figure 7**a), demonstrating the insensitivity of PLGA capsules to NIR light. In contrast, AuNR/PLGA nanocomposite microcapsules with a homogeneous shell significantly deform and release encapsulated FITC-dextran after NIR light exposure as shown in Figure 7b. The fluorescence intensity profiles of NIR light irradiated samples also clearly show that NIR induces essentially the complete release of the encapsulated FITC-dextran, whereas little release is detected from PLGA microcapsules without AuNR (Figure 7c and d). Since AuNRs are known to generate heat upon NIR light absorption, the mechanism of the triggered release is likely the heating of PLGA shell above its glass transition temperature (40–60 °C), which disrupts the integrity of the microcapsule as seen by the drastic change in the shape and size of the irradiated samples. Neat PLGA microcapsules also undergo similar deformation when they are heated above 48 °C (see the Supporting Information, Figure S2), indicating that NIR irradiation of AuNR/PLGA microcapsules increases the local temperature in the shell to at least 48 °C.

Snowman-like microcapsules formed using a chloroform/toluene (2v/3v) mixture and containing PLGA 50:50 and AuNRs show a completely different release behavior. After 20 min of NIR exposure, the size of the solid aggregate decreases significantly, as shown in **Figure 8**. On a close inspection, small particles (less than 5 μm in size) are found in solution (arrows in Figure 8), indicating that the solid aggregate on the capsule surface transitioned into these particles due to the elevated temperature during NIR light exposure. Microcapsules, however, remain intact and retain the encapsulated molecules in the aqueous core (Figure 8). We attribute this selective dissolution of the solid aggregate to the non-uniform distribution of AuNRs in the shell of the snowman-like capsules; that is, the majority of AuNRs are believed to have segregated into the polymer aggregates, which is evident from the dark appearance of the aggregate due to strong absorption of AuNRs. The fact that toluene is a good solvent for PEG on the AuNR surface also supports the hypothesis that AuNRs segregate into the toluene rich domain during solvent removal and, eventually, are trapped in the solid aggregates. These AuNRs cause local heating in the
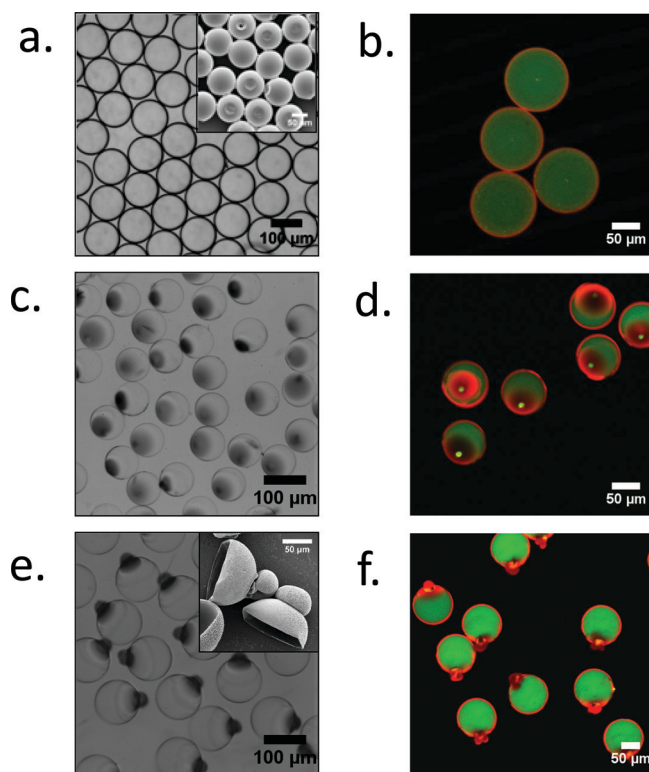
Figure 6. Optical (a,c,e) and confocal (b,d,f) microscope images of polymer microcapsules generated using (a,b) a PLGA 75:25 dissolved in pure chloroform and (c–f) a PLGA 50:50 dissolved in a mixture of chloroform and toluene (2:3 by volume) phase. e,f) The middle phase used for the double emulsion generation contains the AuNRs. For confocal microscopy, FITC-dextran (green) and Nile Red (red) are added to the inner aqueous phase and middle oil phase, respectively. The insets show the SEM images of polymer microcapsules after being completely air-dried at room temperature.
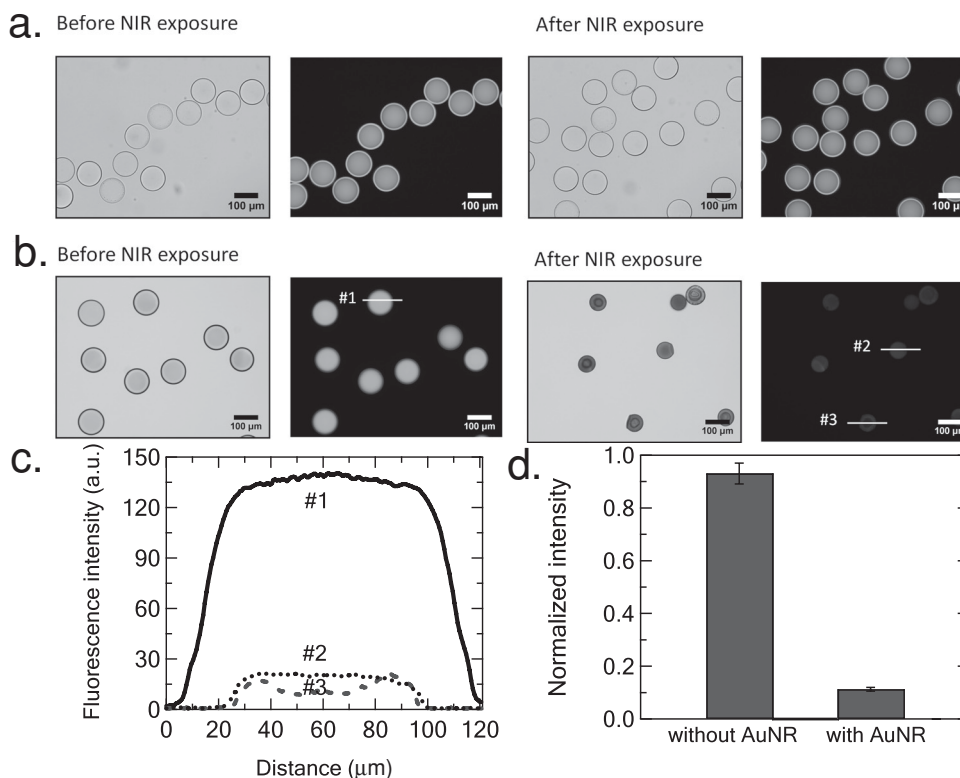
Figure 7. Optical (left) and fluorescent (right) images of FITC-dextran loaded capsules (a) without AuNRs and (b) with AuNRs before and after 20 min NIR exposure. The nanocomposite capsules are generated using a chloroform solution containing PLGA 50:50 and AuNRs. c) Fluorescence intensity profiles along the lines through the capsules in (b) and (d) average fluorescence intensity from over 20 microcapsules (error bars represent the standard error of the mean). The release experiments are carried out within the three days of capsule preparation.

solid aggregates inducing its dissolution. The lack of AuNRs in the thin shell of these snowman-like microcapsules prevents the release of the encapsulated material, indicating that heating must be local to cause changes in the membrane. Eventually, the spontaneous degradation of these microcapsules due to the hydrolysis of PLGA will release the encapsulated material.[36] The degradation kinetics of PLGA shells is known to depend on the PLGA composition, shell thickness and molecular weight as well as the solution temperature and pH.[37]

These results clearly demonstrate that it is possible to control the release sequence of hydrophobic and hydrophilic species from these PLGA microcapsules, depending on their preparation method and subsequent morphology. By creating uniform spherical capsules, for example, a hydrophilic encapsulant can be released using NIR light. Subsequently, a hydrophobic molecule encapsulated in the shell can be slowly released via the hydrolysis of PLGA. In contrast, the release of a hydrophobic species can be triggered first from snowman-like microcapsules via NIR light irradiation. Due to their size, small particles (less than 5 μm) released from the polymer/AuNR aggregates are likely to be more susceptible to cellular uptake compared to the original microcapsules.[38] Subsequently, a hydrophilic species from the core can be released via the spontaneous hydrolytic degradation of PLGA shell or by uniformly heating the local environment above the glass transition temperature of PLGA (Figure S2 in the Supporting Information).

3. Conclusions

We have demonstrated that the composition of PLGA and that of the solvent mixture have a significant influence on the final structure of PLGA microcapsules generated from W/O/W double emulsions. More importantly, we have shown that it is possible to program the release properties of NIR-sensitive PLGA microcapsules by incorporating Au nanorods into the PLGA shell and controlling the capsule morphology. This tunable morphology is due to the surface activity of PLGA, which depends on the composition of the copolymer, and the change in the solvent quality of the oil phase during solvent removal. The ability of biocompatible PLGA microcapsules to load both hydrophobic and hydrophilic materials in the shell and core, respectively, and subsequently release these materials in a controlled sequence, provides a unique opportunity to employ these novel structures in biomedical and pharmaceutical applications.

4. Experimental Section

Polymer Microcapsule Generation: Water-in-oil-in-water (W/O/W) double emulsions are generated using a glass-capillary microfluidic device, as described previously.[17,39] Briefly, two circular capillary tubes with inner and outer diameters of 0.58 mm and 1.0 mm (World Precision Instrument Inc.) are tapered to desired diameters of 15–25 μm for the injection of an inner phase and 120–200 μm for the collection of double

FULL PAPER

Before NIR exposure
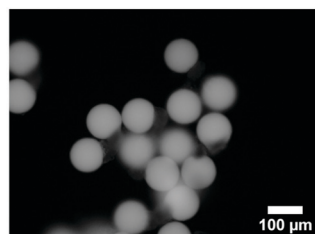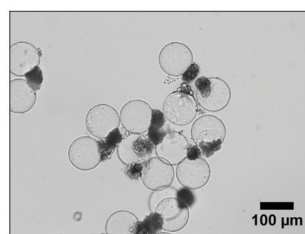
After NIR exposure
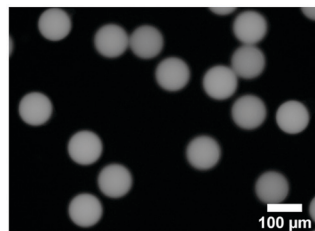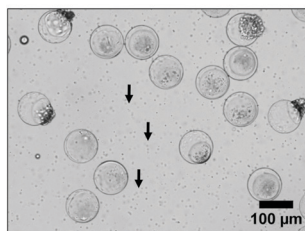
Figure 8. Optical (left) and fluorescent (right) images of FITC-dextran loaded capsules with AuNRs before and after 20 min NIR exposure. The capsules are generated using a chloroform/toluene (2:3 v/v) solution containing PLGA 50:50 and AuNRs. The release experiments are carried out with capsules 3 days after generation of double emulsions. The arrows indicate small particles dissolved from solid aggregate on the capsule surface after NIR exposure.

emulsions using a micropipette puller (P-1000, Sutter Instrument Inc.) and a microforge (Narishige MF-830). The circular capillary tube used for the inner fluid is hydrophobically functionalized with octadecyltrichlorosilane (OTS), enhancing the wettability of oil outside the capillary tube, and facilitating the formation of double emulsions. The two tapered capillaries are inserted into a square capillary with an inner dimension of 1.0 mm, and sealed with epoxy.

To fabricate double emulsions, three liquid phases are introduced into a microfluidic device at independently controlled flow rates by three syringe pumps (PHD, Harvard Apparatus). The inner water phase is a pH 7.4 phosphate buffered saline solution (PBS, sigma P4417), which is composed of 0.01 M phosphate buffer, 0.0027 M potassium chloride, and 0.137 M sodium chloride. The middle oil phase consists of 0.7–1.0 wt% polymer dissolved in a mixture of chloroform and toluene. We use a random copolymer of lactide and glycolide with different molar ratios ranging from 50:50 (Inherent Viscosity (η_i) = 0.41 dL g^{-1} in hexafluoroisopropanol (HFIP)), 65:35 (η_i = 0.55–0.75 dL g^{-1} in HFIP), 75:25 (η_i = 0.55–0.75 dL g^{-1} in CHCl$_3$), to 85:15 (η_i = 0.66 dL g^{-1} in CHCl$_3$) (PLGA, (poly(DL-lactic-co-glycolic)acid, Durect Corp.) as well as a homopolymer (100:0; PLA, (poly(DL-lactic acid), η_i = 0.55–0.75 dL g^{-1} in CHCl$_3$, Durect Corp). The outer water phase is a 2 wt% PVA aqueous solution (PVA, 87–89% hydrolyzed, average M_w = 13 000–23 000, Aldrich). Generated double emulsions flow into the collection tube, and then 20–30 drops containing double emulsions are collected into a large pool of PBS ($\approx$15 mL) in a glass Petri dish. This effectively lowers the concentration of PVA in the continuous phase, leading to a decrease in the osmotic pressure difference between the inner and outer aqueous phases. The polymer microcapsules are generated from the double emulsions by evaporation of the volatile solvent. For the generation of fluorescent microcapsules, two florescent dyes, 0.02 wt% fluorescein isothiocyanate-dextran (FITC-dextran, M_w = 2000 K, sigma) and 0.02 wt% Nile Red (sigma) are added into the inner and middle phases, respectively.

Microcapsule Characterization: All double emulsion generation is monitored with a 10× objective using an inverted light microscope (Nikon Diaphot 300) equipped with a high-speed camera (Phantom V7.1)

capable of recording 13,000 frames per second at the frame resolution of 800 × 200 pixels. The evolution from double emulsions to microcapsules by evaporation of the solvent are observed using an upright microscope (Carl Zeiss Axio Plan II) with a CCD camera (Qimaging Retiga 2000R Fast 1394). Fluorescently labeled microcapsules containing FITC-dextran and Nile Red are imaged using a confocal laser scanning microscope (Olympus FluoView FV1000, Center Valley, PA). The scanning electron microscope (SEM) images of air-dried microcapsules are taken using a Quanta 600 FEG Mark II at an acceleration voltage of 5 kV.

Nanorod Synthesis, Incorporation, and Characterization: Gold nanorods (AuNRs) are synthesized using a seed-mediated technique, as described previously.[40] Briefly, a seed solution is prepared through a mixture of hexadecyltrimethylammonium bromide (CTAB), sodium borohydride, and gold chloride. Small gold seeds then grow into nanorods by adding CTAB, silver nitrate, ascorbic acid, and gold chloride to a seed solution. The prepared AuNRs are PEGylated using poly(ethylene glycol)-thiol, then re-dispersed in chloroform. The PEGylation enhances the stabilization of AuNRs against aggregation in chloroform. The resulting AuNRs have an average length of 32.5 ± 3.0 nm and an average width of 8.2 ± 1.0 nm (see Figure S3 in the Supporting Information). The absorption spectra of the AuNR are taken using a Cary 5000 (Varian Inc.) UV-Vis-NIR spectrophotometer to determine its plasmon resonance band. The synthesized nanorod shows an absorption peak of 770–800 nm, while PLGA polymer does not absorb the NIR light (see Figure S3 in Supporting Information). The concentration of AuNRs in chloroform is determined using a molar extinction coefficient of 4.4 × 10^9 M^{-1} cm^{-1}. The PEGylated AuNRs are incorporated in the polymer shell by suspending AuNRs ($\approx$10^{-9} molar) into the oil layer of double emulsions. The prepared PLGA microcapsules with/without AuNRs in an Eppendorf microtube are exposed to NIR laser with 1 W output power at 808 nm, and, subsequently, a small aliquot is transferred onto a microscope slide for optical/fluorescence microscopy. NIR-triggered release experiments are performed within three days of capsule preparation. We have confirmed that there is essentially no release of the encapsulated species from PLGA microcapsules in three days (Figure S4 in the Supporting Information). Thus, the effect of PLGA degradation on the NIR-triggered release is negligible within the timeframe of these studies.

Interfacial Tension Measurements: Interfacial tension between two liquid phases is measured using the pendant drop method,[41] using a Ramé–Hart model 200 goniometer with DROPimage Advanced software. Interfacial tensions are measured from the shape of a liquid droplet created at the flat tipped stainless steel needle in the other liquid using a micrometer syringe (GS-1200, Gilmont Instruments). The reproducibility of interfacial tension measurements is within ±1.0 mN m^{-1}.

Supporting Information

Supporting Information is available from the Wiley Online Library or from the author.

Acknowledgements

ADVANCED
FUNCTIONAL
MATERIALS
www.afm-journal.de

www.MaterialsViews.com

FULL PAPER

[1] M. Motornov, Y. Roiter, I. Tokarev, S. Minko, *Prog. Polym. Sci.* **2010**, *35*, 174.

[2] K. Bala, P. Vasudevan, *J. Pharm. Sci.* **1982**, *71*, 960.

[3] M. Prevot, C. Dejugnat, H. Mohwald, G. B. Sukhorukov, *ChemPhysChem* **2006**, *7*, 2497.

[4] B. G. De Geest, A. G. Skirtach, A. A. Mamedov, A. A. Antipov, N. A. Kotov, S. C. De Smedt, G. B. Sukhorukov, *Small* **2007**, *3*, 804.

[5] B. Radt, T. A. Smith, F. Caruso, *Adv. Mater.* **2004**, *16*, 2184.

[6] A. G. Skirtach, P. Karageorgiev, M. F. Bedard, G. B. Sukhorukov, H. Mohwald, *J. Am. Chem. Soc.* **2008**, *130*, 11572.

[7] A. G. Skirtach, A. A. Antipov, D. G. Shchukin, G. B. Sukhorukov, *Langmuir* **2004**, *20*, 6988.

[8] D. E. Discher, F. Ahmed, *Ann. Rev. Biomed. Eng.* **2006**, *8*, 323.

[9] F. Caruso, R. A. Caruso, H. Mohwald, *Science* **1998**, *282*, 1111.

[10] F. Caruso, H. Lichtenfeld, M. Giersig, H. Mohwald, *J. Am. Chem. Soc.* **1998**, *120*, 8523.

[11] G. Decher, *Science* **1997**, *277*, 1232.

[12] E. Donath, G. B. Sukhorukov, F. Caruso, S. A. Davis, H. Mohwald, *Angew. Chem. Int. Ed.* **1998**, *37*, 2202.

[13] Y. J. Zhang, S. G. Yang, Y. Guan, W. X. Cao, J. Xu, *Macromolecules* **2003**, *36*, 4238.

[14] J. Yoon, K. J. Lee, J. Lahann, *J. Mater. Chem.* **2011**, *21*, 8502.

[15] K. C. Wood, H. F. Chuang, R. D. Batten, D. M. Lynn, P. T. Hammond, *Proc. Natl. Acad. Sci. USA* **2006**, *103*, 10207.

[16] E. Vazquez, D. M. Dewitt, P. T. Hammond, D. M. Lynn, *J. Am. Chem. Soc.* **2002**, *124*, 13992.

[17] R. K. Shah, H. C. Shum, A. C. Rowat, D. Lee, J. J. Agresti, A. S. Utada, L. Y. Chu, J. W. Kim, A. Fernandez-Nieves, C. J. Martinez, D. A. Weitz, *Mater. Today* **2008**, *11*, 18.

[18] H. C. Shum, D. Lee, I. Yoon, T. Kodger, D. A. Weitz, *Langmuir* **2008**, *24*, 7651.

[19] H. C. Shum, J. W. Kim, D. A. Weitz, *J. Am. Chem. Soc.* **2008**, *130*, 9543.

[20] R. C. Hayward, A. S. Utada, N. Dan, D. A. Weitz, *Langmuir* **2006**, *22*, 4457.

[21] J. Thiele, A. R. Abate, H. C. Shum, S. Bachtler, S. Forster, D. A. Weitz, *Small* **2010**, *6*, 1723.

[22] S. W. Choi, Y. Zhang, Y. N. Xia, *Adv. Funct. Mater.* **2009**, *19*, 2943.

[23] E. Pisani, C. Ringard, V. Nicolas, E. Raphael, V. Rosilio, L. Moine, E. Fattal, N. Tsapis, *Soft Matter* **2009**, *5*, 3054.

[24] S. Torza, S. G. Mason, *J. Colloid Interface Sci.* **1970**, *33*, 67.

[25] N. Pannacci, H. Bruus, D. Bartolo, I. Etchart, T. Lockhart, Y. Hennequin, H. Willaime, P. Tabeling, *Phys. Rev. Lett.* **2008**, *101*, 4.

[26] T. Nisisako, T. Hatsuzawa, *Microfluid. Nanofluid.* **2010**, *9*, 427.

[27] S. Schenderlein, M. Luck, B. W. Muller, *Int. J. Pharm.* **2004**, *286*, 19.

[28] H. C. Shum, Y. J. Zhao, S. H. Kim, D. A. Weitz, *Angew. Chem. Int. Ed.* **2011**, *50*, 1648.

[29] P. Poulin, J. Bibette, *Langmuir* **1999**, *15*, 4731.

[30] R. Weissleder, *Nat. Biotechnol.* **2001**, *19*, 316.

[31] K. C. Hribar, R. B. Metter, J. L. Ifkovits, T. Troxler, J. A. Burdick, *Small* **2009**, *5*, 1830.

[32] K. Mitamura, T. Imae, *Plasmonics* **2009**, *4*, 23.

[33] A. G. Skirtach, P. Karageorgiev, B. G. De Geest, N. Pazos-Perez, D. Braun, G. B. Sukhorukov, *Adv. Mater.* **2008**, *20*, 506.

[34] M. B. Charati, I. Lee, K. C. Hribar, J. A. Burdick, *Small* **2010**, *6*, 1608.

[35] C. Loo, A. Lowery, N. J. Halas, J. West, R. Drezek, *Nano Lett.* **2005**, *5*, 709.

[36] S.-H. Kim, J. W. Kim, J.-C. Cho, D. A. Weitz, *Lab Chip* **2011**.

[37] A. C. R. Grayson, M. J. Cima, R. Langer, *Biomaterials* **2005**, *26*, 2137.

[38] J. A. Champion, A. Walker, S. Mitragotri, *Pharm. Res.* **2008**, *25*, 1815.

[39] D. Lee, D. A. Weitz, *Adv. Mater.* **2008**, *20*, 3498.

[40] H. W. Liao, J. H. Hafner, *Chem. Mater.* **2005**, *17*, 4636.

[41] S. Fordham, *Proc. Royal Soc. London, Ser. A* **1948**, *194*, 1.

FULL PAPER

Low-Power-Photon Up-Conversion in Dual-Dye-Loaded Polymer Nanoparticles

Angelo Monguzzi,* Michel Frigoli, Chantal Larpent, Riccardo Tubino, and Francesco Meinardi

Sensitized triplet–triplet annihilation in multicomponent organic systems is already demonstrated to be suitable for obtaining efficient up-conversion in solution with excitation power densities comparable to solar irradiance, but loses efficiency in the solid state. Here, it is demonstrated that it is possible to reduce this limitation by incorporating a standard bicomponent system in polymer nanoparticles. The confinement of all of the involved photophysical processes in a nanometer-scale volume makes each nanoparticle a single and isolated high-efficiency up-converting unit. As a consequence, these dual-dye-loaded nanoparticles can be used to produce drop-cast films, as well as dopants for polymeric matrices, preserving the performances of the starting moieties in solution.

1. Introduction

People working on renewable energy sources have been trying to up-convert the solar spectrum to recover the large number of low-energy photons that are not exploited by photovoltaic devices and in photocatalytic electrochemical cells for hydrogen production.[1–5] Indeed, this goal cannot be achieved by traditional approaches, as second-harmonic generation or two-photon absorption requires power densities several orders of magnitude larger than solar irradiance.[6] In the last few years, a new strategy to obtain up-conversion at low power and with non-coherent radiation has been pursued.[7–10] It is based on bicomponent organic systems operating through the following sequence of photophysical steps: i) absorption of light by a donor molecule, producing singlet excited states; ii) intersystem crossing (ISC) switching the excitation from singlet to triplet states; iii) energy transfer (ET) towards the metastable triplet states of an acceptor molecule; and iv) triplet-triplet annihilation (TTA) giving rise to high-energy singlet excited states of the acceptor moiety, leading to up-converted emission (see Figure S1E, Supporting

Information).[11–21] In such a way, efficient up-conversion has been demonstrated in liquid systems at excitation power densities as low as 0.1 mW cm^{-2}.[14] Despite these results, the fabrication of devices suitable for practical applications appears still far away, since it is quite difficult to obtain high-efficiency solid-state systems. Indeed, the largest up-conversion efficiency reported up to now for a rigid polymeric matrix is as low as 0.02%.[22] Moreover, a direct comparison between the performance of the same bicomponent system in solution versus the solid state shows that, in the latter, the up-conversion efficiency drops by a factor of 100–1000.[23] The origin of this difference is the large molecular mobility in solution, which strongly enhances the interaction probability and, as a consequence, enhances both the ET and TTA processes. On the contrary, in rigid, polymeric co-doped films, the lack of any relevant molecular mobility is only partially counter-balanced by the ability of the excited states to migrate, because of the rather-short exciton diffusion lengths. When considering crystalline systems, despite the fact that they are not very appealing for the realization of low-cost devices, the situation is not much better. Here, the typical exciton diffusion lengths may be comparable with those of small molecules in low-viscosity solvents, but the donor and acceptor moieties (usually metallo-porphyrins and oligoacenes, respectively) tend to segregate into two independent frameworks.

In this communication, we report an original approach to incorporate bicomponent organic systems for high-efficiency sensitized up-conversion in the solid state. We embedded a proper combination of two donor-acceptor dyes within polymeric nanoparticles (NPs) that acted as a container. Since each NP behaves as a high-efficiency single and isolated up-converting unit, they can be dispersed in a liquid solvent, used as a dopant in polymeric matrices or employed to produce drop-cast films, preserving their intrinsic efficiency and allowing the tuning of the doped-material optical density. We want to underline that the proposed approach is not peculiar of a specific colorant or plastic host.[24–32] Indeed, the idea of including interacting species in nanometer-scale shells is, on the contrary, quite general and easily adaptable for a large number of small molecules exploited in sensitized up-conversion and other photonic applications. Moreover, as an additional but fundamental benefit, the NPs were prepared to completely shield the dyes from the external environment, and especially from oxygen,

Dr. A. Monguzzi, Prof. R. Tubino, Prof. F. Meinardi
Dipartimento di Scienza dei Materiali
Università Milano Bicocca
via R. Cozzi 53, 20125 Milano, Italy
E-mail: angelo.monguzzi@mater.unimib.it
Dr. M. Frigoli, Prof. C. Larpent
Institut Lavoisier UMR-CNRS 8180
Université de Versailles Versailles-Saint Quentin en Yvelines 45
Avenue des Etats-Unis, 78035 Versailles Cedex, France

**ADVANCED
FUNCTIONAL
MATERIALS**
www.afm-journal.de

*Materials
Views*
www.MaterialsViews.com

which is a quencher of all of the metastable triplets involved in the up-conversion process.[33,34]

2. Results and Discussion

In order to demonstrate the validity of the proposed strategy, we selected two among the best and most-investigated dyes for sensitized up-conversion: Pt(II)octaethylprophyrin (PtOEP), which acts as the light harvester and donor, and 9,10-diphenylanthracene (DPA), which acts as the energy acceptor and final emitter (**Figure 1**a). These two dyes have been embedded within cross-linked polystyrene-based nanoparticles (NPs) of 16 nm diameter, obtained as a stable aqueous suspension by polymerization in an oil-water microemulsion stabilized with a cationic surfactant (dodecyltrimethylammonium bromide (DTAB)) (Figure 1b).[35,36] The embedding process within the NP core was obtained by swelling with a dichloromethane (DCM) solution of DPA and PtOEP (50:1 molar ratio), followed by evaporation of the solvent.[37–41] The average loading of each NP was one PtOEP molecule and 50 DPA molecules (see "NP Preparation and Doping" in the Experimental Section).
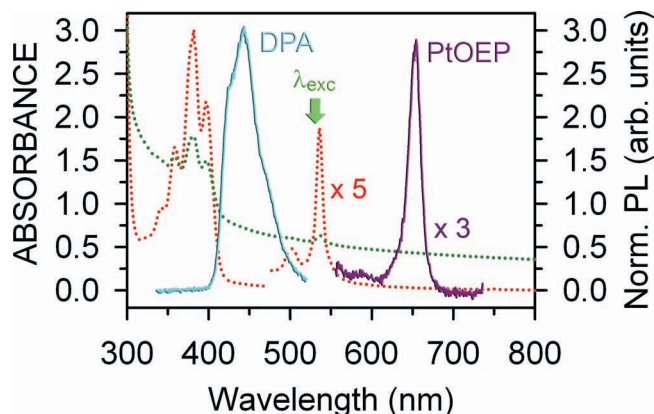
Figure 2. UV–vis absorption spectrum of NP$_{Susp}$, 25 μmol of NP L^{-1} (red dotted line) and NP$_{Film}$ (green dotted line) with an optical path of 0.1 cm. The solid lines are the normalized photoluminescence (PL) spectra for the NP$_{Susp}$ sample under excitation at 532 nm with a power density of 0.03 W cm^{-2}. Laser stray-light has been removed for clarity.

The up-conversion effect was studied, as described in the Experimental Section, by continuous-wave (CW) and time-resolved photoluminescence measurements on dye-loaded NPs in a colloidal aqueous suspension (NP$_{Susp}$, 25 μmol of NPs per litre) and drop-cast films (NP$_{Film}$).

Figure 2 shows the absorption spectra for NP$_{Susp}$ and NP$_{Film}$ (data regarding suspensions with different NP concentrations are shown in Figure S2E, S3E and S4E, Supporting Information). The absorption of the DPA and PtOEP in the NPs was very similar to that in solution. This indicates that the chromophores behave as monomeric species, suggesting that the distances between the chromophores were large enough to prevent the formation of dimeric species or π–π interactions between the neighbouring chromophoric groups, in agreement with a homogeneous dispersion of the dyes. The vibronic band centered on 375 nm is due to the DPA S_0-S_1 allowed transition, while the narrow peak at 536 nm is the Q-band of the porphyrin. The large background detectable in the absorption spectrum of NP$_{Film}$ was produced by the light scattering of the NPs in the cast film. NPs of both samples, when excited at 532 nm in the PtOEP Q-band, gave rise to a bright, up-converted emission at CW excitation intensities of less than 10 mW cm^{-2}. The same behavior was preserved in the cast film.

Time-resolved photoluminescence (PL) measurements provided a description of the donor-acceptor ET process inside the NPs. The decay of the residual PtOEP phosphorescence at 645 nm was clearly biexponential (**Figure 3**) with characteristic lifetimes of $\tau_1 = 72.1$ μs and $\tau_2 = 8.9$ μs for NP$_{Susp}$ and $\tau_1 = 63.7$ μs and $\tau_2 = 8.3$ μs for NP$_{Film}$. This biexponential decay suggests that the PtOEP molecules were in two different local environments within the NP. The slow PL component τ_1 of about 70 μs is comparable to the natural lifetime ($\tau_0 = 65.0$ μs) of the PtOEP phosphorescence measured in oxygen-free THF solution (see Figure S5E, Supporting Information). Therefore, a fraction of the PtOEP molecules does not seem to be able to transfer its excitation to the DPA, probably because of the statistical distribution of the dyes inside each NP. Consequently, the red emission of the PtOEP was still observed. Optimizing the
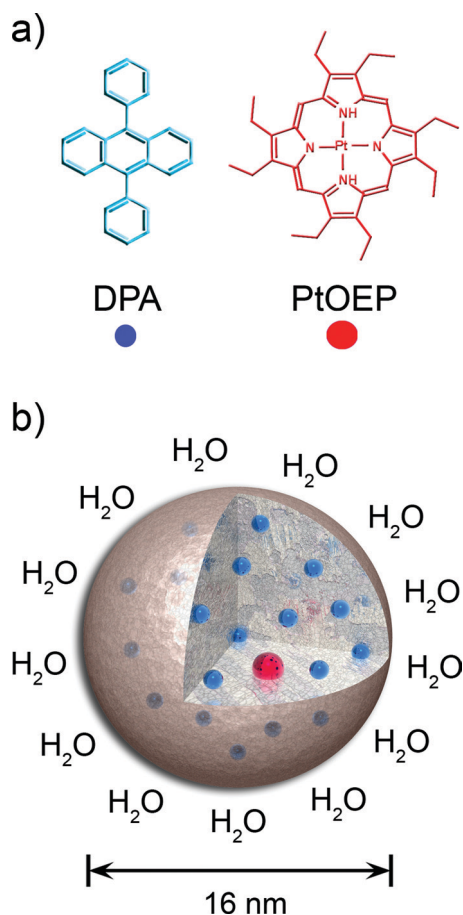

Figure 1. a) Molecular structure of the compounds in the study. b) Schematic representation of a dual-doped nanoparticle with PtOEP (red sphere) and DPA (blue spheres), showing the shielding from the external environment exerted by the NPs.
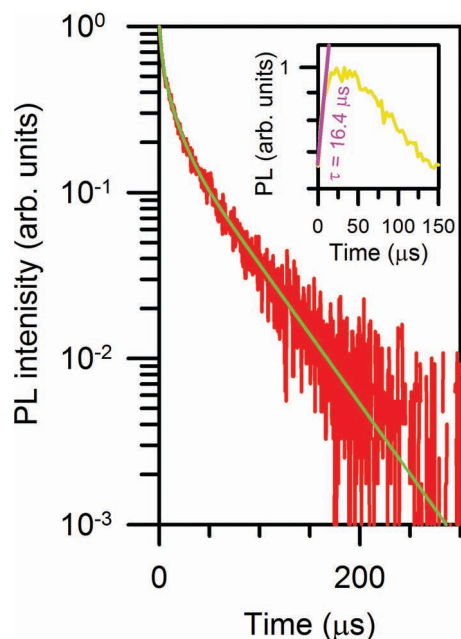
Figure 3. PL decay of the NP_{Susp} luminescence at 645 nm (PtOEP emission) under an average excitation power density of 3 mW cm^{-2} at 200 Hz. The decay follows a biexponential behavior, with characteristic lifetimes of $\tau_1 = 71.2$ μs and $\tau_2 = 8.9$ μs. The inset shows the DPA PL during the first 150 μs, where it is possible to appreciate the rise of the blue emission in NP_{Susp}.

concentration ratio of the DPA and PtOEP molecules per NP and the NP dimensions could allow the fraction of PtOEP molecules that were not involved in the ET to be eliminated, or at least to be strongly reduced.

The presence of PtOEP molecules decaying with their natural lifetime underlines another relevant benefit of the dye embedding in the NPs, namely the shielding from the external surroundings, and, in particular, from molecular O_2. It is known that O_2 is a quencher of all of the phosphorescent emissions in organic molecules, representing a major drawback for standard organic bicomponent systems for up-conversion, which only work efficiently in oxygen-free solutions (O_2 concentration below 1 ppm), thus requiring sample preparation and manipulation in a glove-box.[33] As a consequence, their use is expensive, time consuming, and, in summary, not very appealing. In contrast, the shield offered by the NPs doesn't require any special care for sample preparation, allowing efficient up-conversion in such adverse conditions as the aqueous solutions used in the present work, or in air. It should be noted that the protection from oxygen is not only provided by the NP shell but also by the combination of the NPs and DTAB. Indeed, DTAB could be removed by several dialyses and the removal of surfactant could be easily followed by conductometry. No fluorescence was detected from the dialysates, indicating that the dyes remained in the cores of the NPs after dialysis. Once the DTAB was removed, the suspension was still highly fluorescent. However, once this suspension was drop-cast onto a glass slip, the up-converted PL quickly disappeared.

Regarding the fast, red PL-decay component ($\tau_2 = 8.9$), this arose from PtOEP molecules that were able to transfer their

excitation to the DPA. Indeed, the up-converted PL was not prompt, showing a rise time of $\tau_{rise} = 16.4$ μs (inset of Figure 3), which suggests that the DPA molecules were indirectly excited via ET from the PtOEP. In such a case, since the up-conversion arises from a bimolecular process, the DPA rise time is expected to be twice the decay time of the sensitizer emission. The experimental value of the DPA rise time was in good agreement with the expected value. The transfer efficiency (φ_{ET}) can be evaluated from $\varphi_{ET} = 1 - (\tau_{exp}/\tau_0)$.[38] By considering $\tau_{exp} = \tau_2$ and $\tau_0 = \tau_1$, a φ_{ET} value as high as 88% is obtained both for NPs in solution and in the cast films. The relative concentrations of PtOEP able (D) and unable (D') to transfer their excitation to the DPA can be determined directly from the ratio between the fast- and slow-component PL intensities at time $t = 0$.[38] In NP_{Susp}, $D/(D' + D) = 0.85$, which means that only few donors do not participate in the ET. Even considering this effect, the overall ET efficiency is still rather large: $\varphi_{ET} = 0.85 \times 0.88 \approx 75\%$. Similar findings were also obtained for suspensions with different NP concentrations (see Supporting Information), showing that, since the ET process was confined within each individual NP, its efficiency did not depend on the NPs' average separation distance. It should be noted that, since we performed time-resolved experiments with pulsed excitation at low repetition rates, the observed up-converted emission in these measurements arose from NPs containing more than one donor, where it was possible to excite more than one DPA with the same laser pulse via ET. Of course, this implies that the up-conversion efficiency was lower in the pulsed regime than under CW conditions (see Figure S7E, Supporting Information).

The performances of the PtOEP/DPA-doped NP_{Susp} and NP_{Film} were compared with those of the same dyes in a liquid polystyrene solution (2 g, 5% in tetrahydrofuran (THF), 1×10^{-3} M DPA and 1×10^{-4} M PtOEP). **Figure 4** shows the absolute DPA PL intensity upon CW excitation of PtOEP as a function of the absorbed photons per cm^2 in unit time (I_{exc}). Two parameters were evaluated: the excitation-power threshold (I_{th}) and the up-conversion quantum yield (QY). For the NPs, the absorbed flux was calculated by considering only the fraction of PtOEP
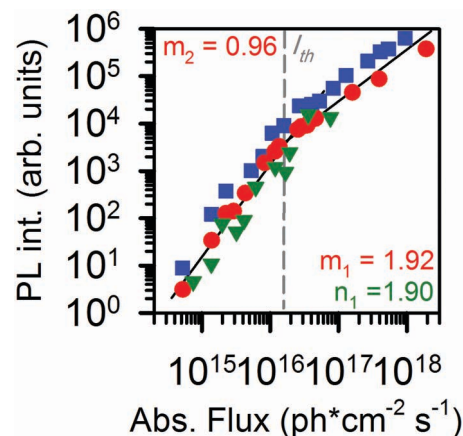

Figure 4. PL intensity at 435 nm under CW excitation at 532 nm as a function of the absorbed photon density of NP_{Film} (green triangles), NP_{Susp} (red circles) and a DPA (1×10^{-3} M)/PtOEP (1×10^{-4} M) polystyrene:THF solution (blue squares). For the NPs, the absorbed flux was calculated by considering only the fraction of PtOEP involved in ET to DPA.

**ADVANCED
FUNCTIONAL
MATERIALS**

www.afm-journal.de

Materials Views

www.MaterialsViews.com

involved in the ET to the DPA. The corresponding QY traces are shown in Figure S6E, Supporting Information. I_{th} corresponds to the power at which the spontaneous decay rate of the excited acceptor triplets equals the TTA rate. Above I_{th}, the overall efficiency of the systems becomes constant, reaching its maximum value.[14] Therefore, I_{th} determines if a system is suitable for solar applications or not.

It is easy to demonstrate that below I_{th} the up-converted PL increases as the square of the exciting power, while above this value the increase is only linear.[14] From an experimental point of view, I_{th} can be evaluated by plotting the up-converted PL as a function of the excitation power in a log–log plot (as in Figure 4) and looking at the excitation power at which the curves change their slope from two to one. For the NP_{Susp} sample (Figure 4, red circles), the calculated slopes are very close to the expected ones, being $m_1 = 1.92$ (quadratic versus I_{exc}) and $m_2 = 0.96$ (linear versus I_{exc}) for the low- and high-excitation-power-density regimes, respectively (for the NP_{Film} sample, because of the strong light scattering, the only regime carefully analyzable is the first one, where the calculated slope is $n_1 = 1.90$).[14] The corresponding I_{th} is 1.5×10^{16} ph cm^{-2} s^{-1} (5.6 mW cm^{-2}), not far from solar irradiance, considering that the width of the PtOEP absorption peak around 530 nm is about 15 nm. The measured value is almost equal to that of the prepared viscous solution (Figure 4, blue squares). These findings confirm the effectiveness of sensitized up-conversion within the NPs. As I_{th} did not change by tuning the NP concentration in the suspension (Figure S4E, Supporting Information), this demonstrates that each NP worked as a single up-converting unit. NP_{Susp} and NP_{Film} show the same QY (3.7% and 3.0% respectively) within experimental accuracy, the highest reported so far for up-converting systems in a solid environment.[42] Moreover, this value is not far from that obtained for the dyes in the THF:polystyrene solution (7.7%), without any dramatic efficiency drop moving from the solution to the solid state.[43,44]

The origin of the up-conversion QY difference in bulky rigid polymeric matrices and in NPs is not completely clear. Besides the oxygen shielding effect, we can draw some hypotheses: i) the local environment in the NP affects the DPA electronic structure and thus its intrinsic properties; ii) the interaction with the host matrix is too small to strongly reduce non-radiative mechanisms, determining the DPA triplet lifetime; iii) a latter possibility under investigation is the formation of coherent states delocalized on the whole DPA framework inside the NP.

3. Conclusions

In summary, sensitized photon up-conversion from 532 nm to 435 nm was successfully obtained in PtOEP/DPA-doped polymer NPs in both an aqueous suspension and drop-cast films. The I_{th} was as low as a few mW cm^{-2}, approaching solar irradiance, and the up-conversion efficiency of our solid samples was comparable to that of the corresponding dye solution. The dyes embedded within the NPs provided the crucial benefit of shielding both the chromophores from the external environment, preventing quenching by oxygen and suggesting a more-general employment of this material as a dye-protective shell. Finally, contrary to solution standard samples, in which the relative dye concentration is a crucial parameter, the observed kinetics were exactly

the same for both NP_{Susp} and NP_{Film} (see Figure S2E, S3E, and S4E, Supporting Information). Each NP worked as single up-converting unit; thus, the obtained results offer the possibility of tuning the average dye concentrations in every solid system by varying the amount of embedded NPs, preventing typical concentration quenching effects such as self-absorption and allowing the manipulation of the material's optical density.

4. Experimental Section

NP Preparation and Doping: An aqueous suspension of nanoparticles (NPs) of 16 nm diameter was prepared by copolymerization in a microemulsion stabilized with the cationic surfactant DTAB (15 wt%) using a procedure described previously.[36,37] A microemulsion was prepared by progressive addition of a mixture of monomers (styrene/divinylbenzene/vinylbenzylchloride: 3.6/34.6/11.9 mmol) and 2,2-dimethoxy-2-phenylacetophenone (radical photoinitiator, 1.3 mmol) to 220 g of a 15 wt% solution of DTAB in demineralized water, under gentle magnetic stirring. The resulting microemulsion was degassed with nitrogen for 30 min and the polymerization was then carried out under white-light irradiation using two 60 W lamps, at room temperature under nitrogen, for 24 h. Chromatographic analysis indicated complete polymerization of all of the monomers. A stable, translucent, aqueous suspension of halobenzyl-functionalized nanoparticles was obtained. Cyclam-functionalized nanoparticles (NPs) were obtained by adding 1.30 g of cyclam (6.48 mmol) to 60 g of a crude suspension of the NPs. The mixture was stirred at room temperature for one week. The excess of cyclam was then removed by dialysis through a porous cellulose membrane (molecular-weight cut-off (MWCO) = 12 000 g mol^{-1}) towards an aqueous solution of DTAB (15 wt%). A stable, translucent aqueous suspension of cyclam-functionalized nanoparticles (NPs) was obtained.

Cyclam-functionalized nanoparticles were used in order to provide proper colloidal stability. The average particle diameter, deduced from dynamic light scattering (DLS), was 16 nm (polydispersity index (PDI) = 0.06); the particle content in the suspension was 4 wt%. 80 µL of a DCM solution containing DPA ([DPA] = 38.58 mmol L^{-1}) and PtOEP ([PtOEP] = 0.79 mmol L^{-1}) were added to 2 mL of an aqueous suspension of the nanoparticles. The resulting mixture was stirred at room temperature for 3 h in a capped sample tube. The tube was then uncapped and the solution was stirred for an additional 12 h to allow evaporation of the DCM. The suspension was filtered through a 0.2 µm MF-Millipore^{TM} filter before use. The average numbers of molecules of DPA (50) and PtOEP (1) encapsulated per particle were deduced from the values of the absorbance of DPA at 374 nm ($\varepsilon = 15\,500$ mol^{-1} L cm^{-1} in DCM)[36,38] and of PtOEP at 380 nm ($\varepsilon = 290\,000$ mol^{-1} L cm^{-1} in toluene) and 535 nm ($\varepsilon = 174\,000$ mol^{-1} L cm^{-1} in toluene).[41]

In the mother solution, the concentration of NP was 31 µmol L^{-1} and the concentrations of DPA and PtOEP were: [DPA] = 1.55 mmol L^{-1} in solution, [PtOEP] = 0.031 mmol L^{-1} in solution; [DPA] = 38.75 µmol g^{-1} of polymer, [PtOEP] = 0.775 µmol g^{-1} of polymer; [DPA] = 38.75 mmol L^{-1} of polymer, [PtOEP] = 0.775 mmol L^{-1} of polymer; [DPA] = 0.117 µg g^{-1} of polymer, [PtOEP] = 1.065 ng g^{-1} of polymer.

Photophysical Studies: The optical-absorption measurements were carried out using a Cary Varian 50 Spectrometer with a bandwidth of 1 nm and using quartz cuvettes with an optical path of 0.1 cm (for the suspensions). For the steady-state PL measurements, a Coherent Verdi TEM00 CW laser at 532 nm (2.33 eV) was used as the excitation source, and a nitrogen-cooled charge coupled device (CCD) (Spex~2000) coupled to a polychromator (Triax 190 from J-Horiba) with a bandwidth of 0.5 nm was used for the signal detection. The time-resolved PL measurements involved excitation at 532 nm (2.33 eV) using the II harmonic of a Nd:YAG laser (Laser-Export Co. LCS-DTL-374QT), and detection in photon-counting mode using a Hamamatsu R943-02 photomultiplier connected to an Ortec 9353 multichannel scaler. Overall, the time resolution was better than 50 ns. Laser stray-light was reduced using a 532 nm notch filter. All of the measurements were performed at room

temperature (RT), and were corrected for the instrumental spectral response. None of the investigated samples showed any photoinduced degradation at the excitation power investigated. The up-conversion QY for the NP_{Susp} aqueous dispersion was measured using Rhodamine B as a fluorescence standard (see Figure S6E, Supporting Information), while for NP_{Film}, the yield was measured using an integrating sphere and the method reported by de Mello et al.[45]

Supporting Information

Supporting Information is available from the Wiley Online Library or from the author.

Acknowledgements

[1] A. Shalav, B. S. Richards, T. Trupke, K. W. Kramer, H. U. Gudel, *Appl. Phys. Lett.* **2005**, 86.
[2] T. Trupke, A. Shalav, B. S. Richards, P. Würfel, M. A. Green, *Sol. Energy Mater. Sol. Cells* **2006**, *90*, 3327.
[3] A. Shalav, B. S. Richards, M. A. Green, *Sol. Energy Mater. Sol. Cells* **2007**, *91*, 829.
[4] X. F. Liang, X. Y. Huang, Q. Y. Zhang, *J. Fluoresc.* **2009**, *19*, 285.
[5] J. A. O'Brien, S. Rallabandi, U. Tripathy, M. F. Paige, R. P. Steer, *Chem. Phys. Lett.* **2009**, *475*, 220.
[6] Y. R. Shen *The Principles of Nonlinear Optics*, John Wiley & Sons, Hoboken, NJ, USA **2002**.
[7] S. Baluschev, T. Miteva, V. Yakutkin, G. Nelles, A. Yasuda, G. Wegner, *Phys. Rev. Lett.* **2006**, 97.
[8] R. R. Islangulov, F. N. Castellano, *Angew. Chem. Int. Ed.* **2006**, *45*, 5957.
[9] S. Balusachev, V. Yakutkin, T. Miteva, Y. Avlasevich, S. Chernov, S. Aleshchenkov, G. Nelles, A. Cheprakov, A. Yasuda, K. Mullen, G. Wegner, *Angew. Chem. Int. Ed.* **2007**, *46*, 7693.
[10] R. R. Islangulov, J. Lott, C. Weder, F. N. Castellano,. *J. Am. Chem. Soc.* **2007**, *129*, 12652.
[11] S. Baluschev, V. Yakutkin, G. Wegner, T. Miteva, G. Nelles, A. Yasuda, S. Chernov, S. Aleshchenkov, A. Cheprakov, *Appl. Phys. Lett.* **2007**, 90.
[12] S. Baluschev, V. Yakutkin, G. Wegner, B. Minch, T. Miteva, G. Nelles, A. Yasuda, *J. Appl. Phys.* **2007**, 101.
[13] A. Monguzzi, R. Tubino, F. Meinardi, *Phys. Rev. B: Condens. Matter* **2008**, 77.
[14] A. Monguzzi, J. Mezyk, F. Scotognella, R. Tubino, F. Meinardi, *Phys. Rev. B: Condens. Matter* **2008**, 78.
[15] R. E. Keivanidis, S. Baluschev, G. Lieser, G. Wegner, *ChemPhysChem* **2009**, *10*, 2316.
[16] J. Mezyk, R. Tubino, A. Monguzzi, A. Mech, F. Meinardi, *Phys. Rev. Lett.* **2009**, *102*, 4.
[17] F. Laquai, Y. S. Park, J. J. Kim, T. Basche, *Macromol. Rapid Commun.* **2009**, *30*, 1203.
[18] T. N. Singh-Rachford, J. Lott, C. Weder, F. N Castellano, *J. Am. Chem. Soc.* **2009**, *131*, 12007.
[19] A. A. Rachford, S. Goeb, F. N. Castellano, *J. Am. Chem. Soc.* **2008**, *130*, 2766.
[20] A. Kohler, H. Bassler, *Mater. Sci. Eng. R: Rep.* **2009**, *66*, 71.
[21] F. Laquai, G. Wegner, C. Im, A. Busing, S. Heun, *J. Chem. Phys.* **2005**, 123.
[22] P. B. Merkel, J. P. Dinnocenzo, *J. Lumin.* **2009**, *129*, 303.
[23] A. Monguzzi, R. Tubino, F. Meinardi, *J. Phys. Chem. A* **2009**, *113*, 1171.
[24] S. Ji, Dr. H. Guo, W. Wu, W. Wu, J. Zhao, *Angew. Chem. Int. Ed.* **2011**, *50*, 8283.
[25] S. Ji, W. Wu, W. Wu, Dr. H. Guo, J. Zhao, *Angew. Chem. Int. Ed.* **2011**, *50*, 1626.
[26] H. Sun, H. Guo, W. Wu, X. Liu, J. Zhao, *J. Chem. Soc. Dalton Trans.* **2011**, *40*, 7834.
[27] W. Wu, W. Wu, S. Ji, H. Guo, J. Zhao, *J. Chem. Soc. Dalton Trans.* **2011**, *40*, 9085.
[28] W. Wu, W. Wu, S. Ji, H. Guo, J. Zhao, *J. Chem. Soc. Dalton Trans.* **2011**, *40*, 5953
[29] W. Wu, H. Guo, W. Wu, S. Ji, J. Zhao, *J. Org. Chem.* **2011**, *76*, 7056.
[30] J. Sun, W. Wu, H. Guo, J. Zhao, *Eur. J. Inorg. Chem.* **2011**, 3165.
[31] L. Huang, L. Zeng, H. Guo, W. Wu, W. Wu, S. Ji, J. Zhao, *Eur. J. Inorg. Chem.* **2011**, DOI: 10.1002/ejic.201100777.
[32] L. F. M. L. Ciscato, D. Weiss, R. Beckert, E. L. Bastos, F. H. Bartoloni, W. J. Baader, *New J. Chem.* **2011**, *35*, 773.
[33] A. K. Bansal, W. Holzer, A. Penzkofer, T. Tsuboi, *Chem. Phys.* **2006**, *330*, 118.
[34] A. Monguzzi, R. Tubino, M. M. Salamone, F. Meinardi, *Phys. Rev. B: Condens. Matter* **2010**, 82.
[35] M. Frigoli, K. Ouadahi, C. Larpent, *Chem. Eur. J.* **2009**, *15*, 8319.
[36] F. Gouanve, T. Schuster, E. Allard, R. Meallet-Renault, C. Larpent, *Adv. Funct. Mater.* **2007**, *17*, 2746.
[37] R. Meallet-Renault, R. Pansu, S. Amigoni-Gerbier, C. Larpent, *Chem. Commun.* **2004**, 2344.
[38] J. R. Lakowicz, *Principles of Fluorescence Spectroscopy*, Springer, Berlin,Germany **2008**.
[39] B. P. Lyons, A. P. Monkman, *Phys. Rev. B: Condens. Matter* **2005**, 71.
[40] R. C. Evans, P. Douglas, *Appl. Mater. Interfaces* **2009**, *1*, 1023.
[41] S. L. Pan, L. J. Rothberg, *J. Am. Chem. Soc.* **2005**, *127*, 6087.
[42] T. N. Singh-Rachford, F. N. Castellano, *Coord. Chem. Rev.* **2010**, *254*, 2560.
[43] Y. Y. Cheng, B. Fückel, T. Khoury, R. Clady, M. J. Y. Tayebjee, N. J. Ekins-Daukes, M. J. Crossley, T. W. Schmidt, *J. Phys. Chem. Lett.* **2010**, *1*, 1795.
[44] Y. Y. Cheng, T. Khoury, R. Clady, M. J. Y. Tayebjee, N. J. Ekins-Daukes, M. J. Crossley, T. W Schmidt, *Phys. Chem. Chem. Phys.* **2010**, *12*, 66.
[45] J. C. de Mello, H. F. Wittmann, R. H. Friend, *Adv. Mater.* **1997**, *9*, 230.

ADVANCED
FUNCTIONAL
MATERIALS
www.afm-journal.de

Materials
Views
www.MaterialsViews.com

FULL PAPER

Charge-Carrier Balance and Color Purity in Polyfluorene Polymer Blends for Blue Light-Emitting Diodes

Li-Ping Lu, Dinesh Kabra,* Kerr Johnson, and Richard H. Friend*

A study of an efficient blue light-emitting diode based on a fluorescent aryl polyfluorene (aryl-F8) homopolymer in an inverted device architecture is presented, with ZnO and MoO_3 as electron- and hole-injecting electrodes, respectively. Charge-carrier balance and color purity in these structures are achieved by incorporating poly(9,9-dioctylfluorene-co-N-(4-butylphenyl)-diphenylamine (TFB) into aryl-F8. TFB is known to be a hole-transporting material but it is found to act as a hole trap on mixing with aryl-F8. Luminance efficiency of ≈ 6 cd A^{-1} and external quantum efficiency (EQE) of 3.1% are obtained by adding a small amount (0.5% by weight) of TFB into aryl-F8. Study of charge injection and transport in the single-carrier devices shows that the addition of a small fraction of hole traps is necessary for charge-carrier balance. Optical studies using UV–vis and fluorescence spectroscopic measurements, photoluminescence quantum yield, and fluorescence decay time measurements indicate that TFB does not affect the optical properties of the aryl-F8, which is the emitting material in these devices. Luminance efficiency of up to ≈ 11 cd A^{-1} and EQE values of 5.7% are achieved in these structures with the aid of improved out-coupling using index-matched hemispheres.

1. Introduction

Since the discovery of electroluminescence from conjugated-polymer-based diodes in the late 1980s,[1] polymer light-emitting diodes (PLEDs) have been a research field of great interest due to their potential use in display and lighting applications. Amongst the three primary colors, blue is the most critical for these applications as color purity, efficiency, and device stability are still significant issues. Polyfluorenes (F8) are promising and very well-studied blue light-emitting polymers due to their wide band-gap and high photoluminescence quantum efficiency.[2]–[4] In previous studies, polyfluorene PLEDs have been reported to show high injection barriers for holes due to their deep highest occupied molecular orbital (HOMO) level.[5] Also, electron transport is very often limited by traps which are caused by defects or impurities during synthesis. During device operation, ketone defects have been observed and these result in color impurity

as ketones are an electron-withdrawing group and have a low-lying lowest unoccupied molecular orbital (LUMO).[6] Overall, it is difficult to obtain pure blue color in polyfluorene-based diodes due to defects as well as excimer formation[2] and recently the role of triplet states in green emission has also been reported.[7] A poly-spirobifluorene (spiro-F8) polymer was developed to address this problem. In the spiro-F8 molecule, a sp^3-hybridized carbon atom, C-9, connects the two fluorene units and results in a spiro-bridge. The two fluorene planes are orthogonal to each other which prohibits close-packing and therefore prevents excimer formation, as the twisted molecular structure makes π–π stacking virtually impossible. Spiro-F8 leads to increased stability and stack-reduction in comparison to F8, hence bathochromic shifts caused by aggregation and ketone formation due to oxidation of the C-9 atom are thus suppressed.[8] The spiro-F8 homopolymer can reduce green emission significantly as compared to pure F8but device efficiency is still poor due to the high injection barrier for holes since spiro-F8 also has a similarly deep HOMO level of 5.9 ± 0.2 eV.

Recently, Blom and co-workers showed that device efficiency can be increased significantly by using modified spiro-F8 with attached hole-transporting molecules.[9] Similar approaches were used previously in the case of F8-based PLEDs.[10–12] This approach reduces the hole-injection barrier and improves charge-carrier balance. However, such modification in chemical structure needs careful design so that it does not obstruct charge transport, nor produce any charge-transfer states which can affect photoluminescence (PL) quantum yield. Herein we use a new aryl-F8 polymer for our PLED studies (see the chemical structure in **Figure 1**c); it showed high PL quantum efficiency (PLQE) of 70%, which is greater than those of F8 ($55 \pm 5\%$) and spiro-F8,[13] a wide band-gap, and a deep HOMO level at 5.9 eV (see Figure 1b and **Figure 2**). Aryl units attached to polyfluorene prevent stacking of polymer chains and reduce the chance of oxidation of the C-9 atom, as is the case with polyfluorene with different functional groups[14] and spiro-F8. Also, with the introduction of the alkyl chains at carbon atoms on the aryl units, the solubility of the polymer can be tuned without changing the electronic structure of the polymer, as seen for other polyfluorene polymers.[2,15] Our previous studies

L.-P. Lu, Dr. D. Kabra, K. Johnson, Prof. R. H. Friend
Cavendish Laboratory
JJ Thomson Avenue
Cambridge, CB3 0HE, UK
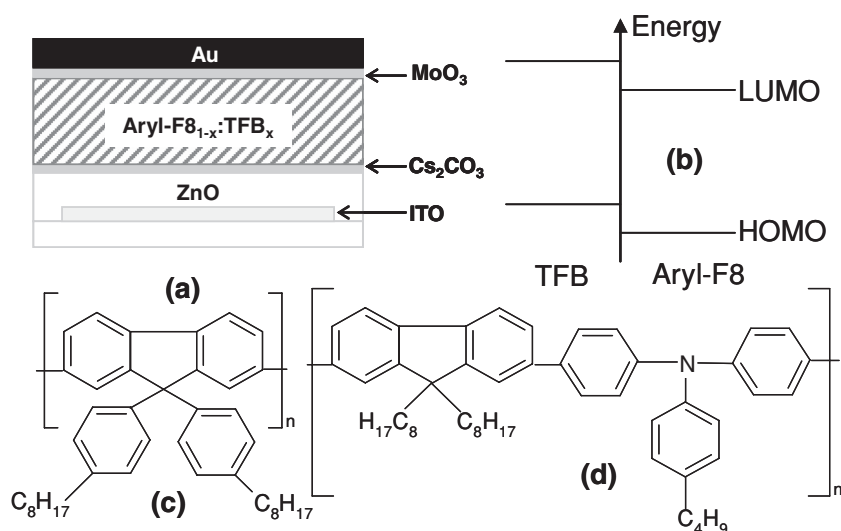E-mail: dk366@cam.ac.uk; rhf10@cam.ac.uk

Figure 1. a) Inverted hybrid light-emitting diode structure, b) visualization of band offsets at the aryl-F8:TFB heterojunction. HOMO and LUMO correspond to the ionization potential and the electron affinity, respectively. HOMO energies, with respect to vacuum level, were estimated from cyclic voltammetry to be 5.3 eV (TFB) and 5.9 eV (aryl-F8). Chemical structures of c) aryl-F8 and d) TFB.

on inverted structure devices (see Figure 1a) demonstrated that MoO_3 provides ohmic hole injection in deep HOMO level systems due to formation of a p-doped surface layer.[16,17] For the cathode, n-type metal oxide (ZnO) modified with Cs_2CO_3 can provide promising electron-injecting properties similar to a Ca/Al contact due to possible interfacial doping into the polymer, as seen in other organic semiconductor systems.[18] Aryl-F8 is therefore a promising blue light-emitting polymer for PLEDs in an inverted structure. However, electron injection is expected to be more difficult then hole injection, so these devices are likely to be dominated by hole currents. By introducing a small fraction of poly(9,9-dioctylfluorene-co-N-(4-butylphenyl)-diphenylamine (TFB; see chemical structure in Figure 1d), to aryl-F8 we can achieve better charge balance and also reduced red-shifted emission on electrical excitation. This molecular additive is known to be a good hole-transporting material in PLEDs,[19] however we find it acts as a hole trap on mixing with aryl-F8.

2. Results and Discussion

2.1. Aryl-F8 Polymer

The aryl-F8 polymer was procured from Cambridge Display Technology, UK, with a molecular weight (M_n) of 380k and a polydispersity index (PDI) of 2.7. Electrochemistry measurements ascertained the HOMO level to be at 5.9 eV with respect to vacuum level. Atomic force microscope imaging of the homopolymer film and blend showed very similar morphology and there were no evident separate phases of Aryl-F8 and TFB with r.m.s. roughness below 5 nm (see Supporting Information, Figure S1).

2.2. Optical Studies

We characterized the aryl-F8 polymer and blends of aryl-F8$_{1-X}$:TFB$_X$ films (thickness ≈ 30 nm, different weight fractions of TFB additive in aryl-F8 from 0.1% to 1%) using UV-Vis absorption, PL emission and fluorescence decay-time studies. The absorption and fluorescence spectra for the homopolymer and TFB are shown in Figure 2a. We note that emission from TFB is red-shifted by comparison to the aryl-F8 so we should expect to see emission from TFB upon exciton migration towards heterojunctions. Therefore, we carried out these studies to understand the influence of TFB addition on the optical properties of aryl-F8.

The UV-Vis absorption of the blend films illustrates that the absorption intensity decreases with increased TFB ratio; however the position of the absorption peak is not shifted and no new spectral feature was observed as compared to the homopolymer film prepared on quartz substrate. The fluorescence spectra
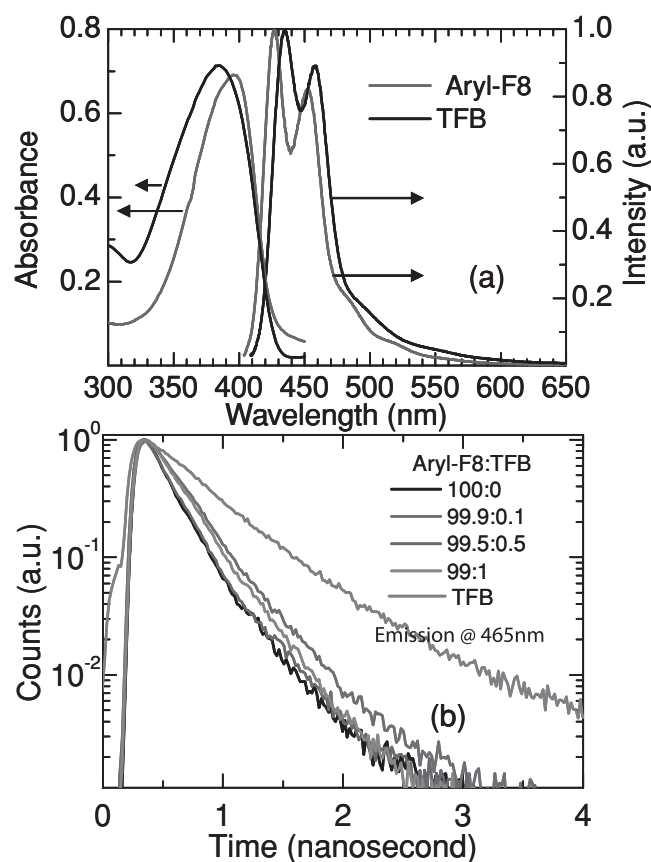

Figure 2. a) Absorption and fluorescence spectrum for aryl-F8 (blue line) and TFB (black line) polymer films and b) fluorescence decay time of TFB, aryl-F8, and aryl-F8:TFB blends on quartz substrate at an emission wavelength of 465 nm. Excitation laser wavelength was 407 nm.

also showed no changes between the aryl-F8 and aryl-F8$_{1-X}$:TFB$_X$ blends (see Figure S2a). Fluorescence spectra showed clear vibronic peaks of electronic transitions with almost constant energy separation of ≈150 meV, which is associated with a C=C bond-stretching mode. These spectral studies reveal that there are no new states being populated due to the addition of small fractions of TFB to the homopolymer. We also found that there is no difference in fluorescence spectra between annealed and nonannealed aryl-F8$_{1-x}$:TFB$_x$ film blends measured under high vacuum (10^{-6} mbar), which confirms the lack of β-phase formation that is seen in F8.[20] The PL quantum yield of blend films also did not alter from the pure aryl-F8 film and remained similar at 70 ± 3%. Furthermore, the study of the fluorescence decay time confirmed that the decay time is not significantly influenced by the TFB additive in the aryl-F8 polymer, with similar decay times as shown in Figure 2b for the aryl-F8 and aryl-F8:TFB blends at an emission wavelength of 465 nm. TFB is found to have a much longer decay time than aryl-F8 and aryl-F8:TFB blends (see Figure 2b). Similar decay times were also observed for the other vibronic peaks (see Figure S2b–d) arising from the homopolymer and blends. It is important to note that on mixing TFB with aryl-F8 we do not see long-lived red-shifted exciplex emission, in agreement with the absence of exciplex formation in F8:TFB blends with very similar energy levels.[21] This observation further confirms that emission is coming from bulk aryl-F8 in polymer blends and excitons are not trapped at heterojunctions. These studies indicate that the addition of a small fraction of TFB does not change the optical properties of the aryl-F8 homopolymer.

2.3. Single-Carrier Devices

Single-carrier devices of aryl-F8 and aryl-F8$_{1-X}$:TFB$_X$ films were prepared using similar work-function electrodes in a sandwich configuration. The purpose of this study was to understand charge transport along with the selection of the optimum charge-injecting contacts to achieve the best charge-carrier balance in bipolar devices. Optimum charge-carrier balance results in high efficiency and prevents efficiency roll-off in PLEDs.

2.3.1. Hole-Only Devices

To understand the influence of the TFB additive in aryl-F8 on hole injection and transport, hole-only devices with aryl-F8 and aryl-F8$_{1-x}$:TFB$_x$ blends were fabricated by replacing the ZnO/Cs$_2$CO$_3$ layer with poly(3,4-ethylenedioxythiophene):poly(styrenesulfonate) (PEDOT:PSS; see Figure 1a). Structures of ITO/PEDOT:PSS/aryl-F8$_{1-X}$:TFB$_X$/MoO$_3$/Au support only hole injection from either of the contacts, so this set-up provides bulk hole-conduction properties for aryl-F8$_{1-x}$:TFB$_x$ films. J–V characteristics of the homopolymer hole-only devices are shown in **Figure 3** (for blend see Figure S3)

We observed that MoO$_3$ provides ohmic hole injection in aryl-F8 as the hole current from the MoO$_3$/Au contact is five orders of magnitude higher than the current injected from the PEDOT:PSS side, as found in our previous work with a similar HOMO-level polymer system.[16] We found that the hole current decreases significantly with increasing amount of TFB additive
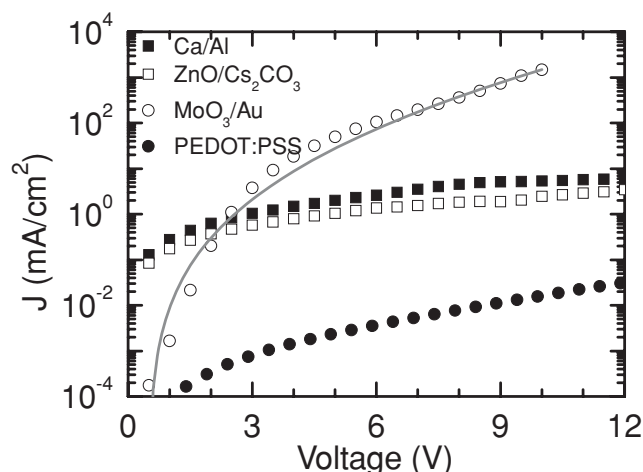
Figure 3. J–V characteristics for hole-only (ITO/PEDOT:PSS/aryl-F8/MoO$_3$/Au) (●, ○) and electron-only (ITO/ZnO/Cs$_2$CO$_3$/aryl-F8/Ca/Al) (■, □) devices with a polymer layer thickness of 500 nm. Hole-only current injected from the MoO$_3$/Au (○) side was fitted using the Pool–Frenkel enhanced SCLC model for V$_0$ = 0.5 V.

in aryl-F8 (see Figure S3). To model these J–V characteristics, we adopted the Mott–Gurney space-charge-limited current (SCLC)[22] combined with field-dependent mobility[23] and used a simplified form of SCLC enhanced by the Pool–Frenkel model[24] which takes care of shallow traps, as illustrated by Equation (1):

$$J = \frac{9}{8}\varepsilon_0\varepsilon_r\mu_0\frac{(V - V_0)^2}{d^3}\exp\left(\beta\sqrt{(V - V_0)}\right) \tag{1}$$

where J is the current density, $\varepsilon_0\varepsilon_r$ the dielectric constant, μ_0 the zero-field mobility, V the applied voltage, V_0 the built-in voltage, d the thickness of the active layer, and β is a parameter which describes the field-dependence effect.

The hole mobility and β values were obtained by fitting J–V curves (see in Figure S3) using Equation 1 and are summarized in **Table 1**. V_0 was 0.5 V, as extracted from the J–V curves as the voltage at which the current starts to deviate from the exponential diffusion current.[25] From the J–V measurements, we observed that the current reduced by almost three orders of magnitude when a small amount of TFB (0.1%) was added to aryl-F8, but this tendency becomes less pronounced upon TFB addition of up to 1%, with only a small further decrease. A plausible interpretation might be that TFB has a HOMO level of 5.3 eV,[26] which is higher than that of aryl-F8 (5.9 eV) (see Figure 1b) and so it introduces hole traps. We also note that

Table 1. Hole-transport parameters extracted by fitting hole-only current injected from MoO$_3$/Au side in ITO/PEDOT:PSS/Aryl-F8$_{1-X}$:TFB$_X$/MoO$_3$/Au hole-only device using Equation 1 for constant V_0 = 0.5 V.

TFB doping in aryl-F8 [wt.%]	Hole mobility (μ_0) [cm^2 V^{-1} s^{-1}]	β [cm$^{1/2}$ V$^{-1/2}$]
0	2.0×10^{-6}	2.59
0.1	7.46×10^{-7}	0.97
0.5	3.31×10^{-7}	0.62
1	1.32×10^{-7}	0.64

Materials Views
www.MaterialsViews.com

ADVANCED
FUNCTIONAL
MATERIALS
www.afm-journal.de

FULL PAPER

the β value decreases rapidly upon addition of TFB, which is difficult to interpret as we would expect it to increase on introduction of traps considering the J–V curves are well fitted by Equation 1 for a constant V_0. However, we were mainly interested in getting a parameter to control hole currents in aryl-F8 to achieve charge-carrier balance, which we demonstrate in Table 1 (also in Supporting Information Figure S3). We note the similar hole mobility for aryl-F8 as compared to previous reports on analogous spiro-F8 molecules.[27]

2.3.2. Electron-Only Devices

Electron transport in conjugated polymers is hard to measure due to intrinsic traps[9] and thin insulating oxide layer formation at low work-function injecting contacts. Electron-only devices are usually fabricated by sandwiching the semiconducting layer between two thermally evaporated low work-function metals. In this case the bottom layer makes a thin oxide layer which can reduce the true electron current extraction. However, we recently reported a new electron-only device structure, in which the bottom electron-injecting contact is prepared in air by solution processing. These devices were fabricated by replacing the top contact MoO_3/Au with Ca/Al from the bipolar devices shown in Figure 1a. We show J–V characteristics of the homopolymer in Figure 3 for electrons injected from either contact in a ITO/ZnO/Cs_2CO_3/aryl-F8$_{1-X}$:TFB$_X$/Ca/Al structure. The J–V curves of these devices show some scatter from device to device, but a very similar current injection from either contact electrode for aryl-F8$_{1-X}$:TFB$_X$ blend films of ≈500 nm thickness.

Electron-only J–V curves did not fit with the Pool–Frenkel enhanced SCLC model and seemed to be limited by deep traps and/or injection barriers. We note that at the device operational voltage (>4 V) the hole current is almost three orders higher than electron current for the homopolymer, hence adding hole traps is necessary to achieve charge-carrier balance. However, we found that the electron current also dropped four- to five-fold on introduction of TFB, which may be due to the low electron mobility of TFB and reduced pathways in aryl-F8 for electron transport. Thus, in the case of blends we get better charge-carrier balance due to greater influence of TFB on hole current.

2.4. Bipolar Devices

Bipolar devices were made in conventional (ITO/PEDOT:PSS/aryl-F8$_{1-X}$:TFB$_X$/Ca/Al) and HyLED (ITO/ZnO/Cs_2CO_3/aryl-F8$_{1-X}$:TFB$_X$/MoO_3/Au) structures. We found that conventional structures give almost five times lower efficiency than HyLED structures, so we focused our studies on HyLED structures (conventional structure J–V–L and efficiency data is in Figure S4). We varied the thickness of the emissive layer from 300 –600 nm and found that devices thinner than 500 nm show lower luminance efficiency and stability and also break down more quickly than thicker devices. Devices thinner than 300 nm are highly unstable in the HyLED structure, possibly due to high current density arising from the doped emissive polymer region at either end of the emissive layer and inherent ITO/ZnO/Cs_2CO_3 substrate roughness. Further increase in thickness of device
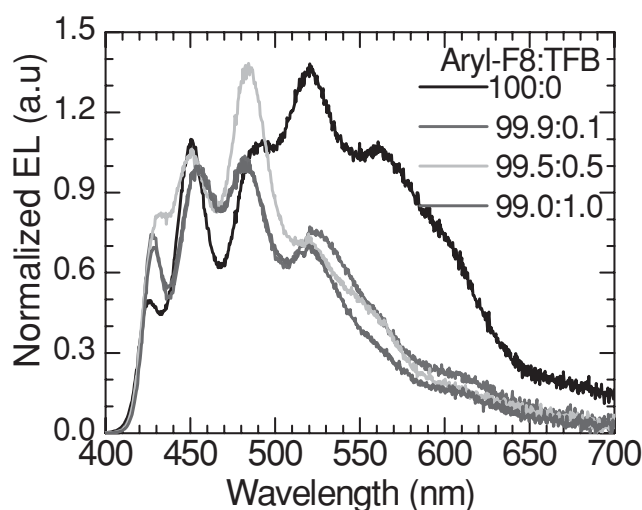
Figure 4. EL spectra of aryl-F8$_{1-X}$: TFB$_X$ blends in inverted HyLED structures with an emissive layer thickness of 500 nm.

from 500 nm resulted in higher operating voltages, hence we used emissive layer thicknesses of 500 nm for our studies.

2.4.1. Electroluminescence Spectrum

Electroluminescence (EL) spectral studies on aryl-F8$_{1-X}$:TFB$_X$ blends were performed using the HyLED structure, and the results are shown in **Figure 4**. We observed that for homopolymer HyLEDs the dominating contribution comes from emission peaks at 530 and 570 nm. We note that these peaks were not observed in PL measurements on the same device before and after LED operation (see Figure S5). This undesirable green emission is also the source of overall decrease of the luminescence efficiency, as shown in a previous report for other polyfluorene blue emitters.[28] The origin of the green emission is still a source of debate within the conjugated polymer community;[29] whether it is due to interchain interactions such as aggregates and excimers[30] or oxidative (keto) defects formed along the polymer backbone.[2] However, this green emission is suppressed strongly by mixing just 0.1% TFB into the aryl-F8 and it is further improved towards blue emission by increasing theTFB content in the homopolymer. This result can be mainly attributed to reduced charge-carrier density in aryl-F8$_{1-X}$:TFB$_X$ blend bipolar devices, as shown in **Figure 5**. Reduced current densities in blend devices are consistent with hole-only devices. The EL spectra show two emission peaks at 430 and 450 nm which resemble the fluorescence of the aryl-F8 polymer and are assigned to the π–π^* transition. The peak at 480 nm in EL spectra is also one of the vibronic features observed in the PL spectra of aryl-F8. A detailed investigation on the reduction of green emission by addition of TFB to aryl-F8 needs a careful spectroscopic study to track exciton dynamics, which is being pursued in our laboratory. However, a qualitative explanation may be that there is a high probability of trapping of charge carriers on defect sites as compared to excitons generated by optical excitation due to limited diffusion length of excitons in aryl-F8, and TFB addition clearly controls trapping of charge carriers to those defect sites, as shown in Figure 4.

ADVANCED
FUNCTIONAL
MATERIALS
www.afm-journal.de

Materials
Views
www.MaterialsViews.com

Figure 5. a) J–V–L characteristics and b) luminance efficiency and external quantum efficiency of the HyLED for different additive concentration of TFB in aryl-F8 with a layer thickness of 500 nm. Solid symbols correspond to left and open symbols correspond to right y axis in both panels.
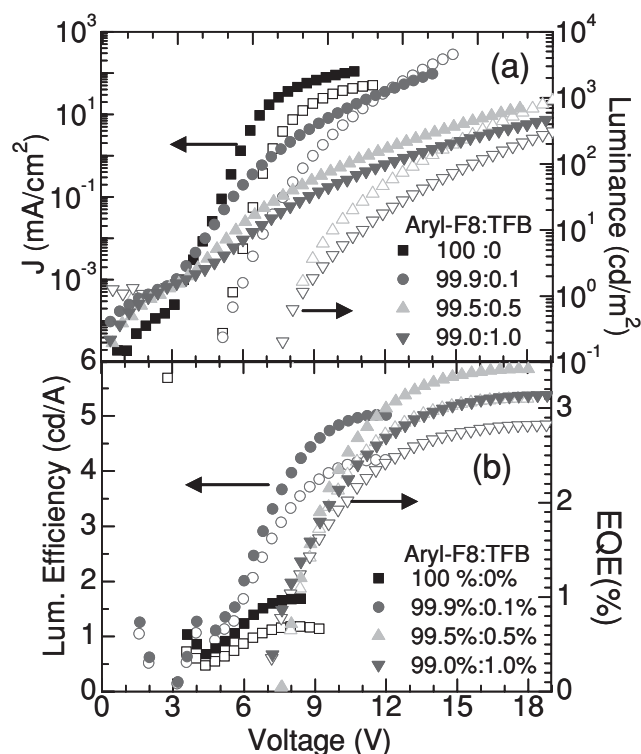
2.4.2. J–V–L Characteristics

We made HyLED structures, as shown in Figure 1a, for different weight fractions of TFB in aryl-F8. The J–V–L characteristics and efficiency data of these devices are shown in Figure 5a and **Table 2**. We observed the operating voltages gradually increase with increasing TFB additive in aryl-F8 and bipolar current for the homopolymer reduced as compared to the hole-only device. Reduction in bipolar current for the homopolymer will be explained later in this section, while discussing the role of Cs_2CO_3 interlayer. From our single-carrier device measurements we know that this polymer has injection- and/or trap-limited electron current and MoO_3 provides ohmic injection with hole mobility that is a factor of two to three higher in the homopolymer. Due to this, hole current builds-up near the Cs_2CO_3/polymer interface and redistributes the electric field to facilitate electron injection into

Table 2. Summary of HyLED characteristic parameters obtained from Figure 5.

TFB doping in aryl-F8 [wt.%]	Bias @ 10 mA cm⁻²	Brightness [cd m⁻²]	Luminance Efficiency [cd A⁻¹]	EQE [%]
0	7.2 V	1000 @10 V	1.0 @11 V	0.5
0.1	9.8 V	1000 @11 V	5.0 @12 V	2.5
0.5	16.9 V	100 @12.6 V	5.9 @18 V	3.1
1	7.8 V @19 V	100 @14.8 V	5.4 @19 V	2.8
0.5 (with hemisphere)	16.9 V	1000 @16.5 V	11 @18 V	5.7

the polymer layer.[31,32] Since Cs_2CO_3 blocks holes, the higher the hole-current density the lower the diode turn-on voltage. We note that addition of 0.1% TFB significantly reduces bipolar current density, which is consistent with hole-only device measurements, without affecting turn-on voltages, as shown in Figure 5. However, increasing the amount of TFB additive further improves device efficiency, although at the expense of reduced brightness and higher operating voltages, as summarized in Table 2 and shown in Figure 5. A maximum luminance efficiency was achieved when 0.5% TFB was added to aryl-F8, i.e., 5.9 cd A⁻¹, corresponding to an external quantum efficiency (EQE) of 3.1% and CIE coordinates of (x = 0.186, y = 0.242).

Luminance efficiency and EQE values gradually increase with operating voltage and saturate at higher operating bias. We do not observe the commonly seen efficiency roll-off for thin devices in our HyLEDs before they break down. We can interpret the increase in efficiency with applied voltage as being due to a balancing of charge carriers and/or movement of the recombination zone in the bulk of the polymer, i.e., away from the Cs_2CO_3/polymer interface. It has been proposed previously for the F8/Cs interface that Cs forms two new bipolaron states at the interface in photoemission spectroscopy studies, which is detrimental to radiative recombination in PLEDs.[33] We have also seen previously that a Cs_2CO_3 interlayer introduces optical losses as compared to a ZnO/polymer interface.[16] At higher operating voltages shallow traps are also screened by application of an electric field, which can reduce trap-assisted recombination losses observed in PLEDs.[34]

To understand the role of the Cs_2CO_3 interlayer we studied bipolar devices with and without this interlayer to identify the influence of trapped and interfacial charges on device performance.[35] By comparing the hole-only current density with bipolar currents in diodes with and without Cs_2CO_3 based on homopolymer and blend, we obtained further insight into how TFB and Cs_2CO_3 affect charge injection and transport in the inverted structure. Aryl-F8 has a high hole mobility ($\approx10^{-6}$ cm² V⁻¹ s⁻¹), as indicated in Table 1; its hole-only current density is more than one order of magnitude higher than that in the diodes (see **Figure 6**), while usually bipolar current is the sum of single-carrier currents. However, in this case, Cs_2CO_3 blocks the hole-leakage current. Also Cs^{1+} belongs to the alkali metal group, so tends to diffuse into the polymer,[36] and that introduces interfacial traps for holes which may also lower the mobility of holes. The current density of diodes without Cs_2CO_3 is comparable to that of the hole-only, but no luminescence was observed as holes travel to the cathode and leak through subgap states of the ZnO layer; this confirms the importance of a hole-blocking layer. However, by introducing hole traps we reduce hole current significantly in both single-carrier devices and in diodes so the bipolar current is similar to the hole-only current at higher operating voltages, shown for the case of 1% TFB additive in Figure 6. At lower operating voltages, reduced bipolar current can be explained by interfacial trapping by the Cs_2CO_3 interlayer. To verify the trapping effect of Cs_2CO_3, we also ran these bipolar devices based on pure homopolymer in different sweep directions with successive operating voltage steps of 0.1 V, as illustrated in **Figure 7**. The current density curves overlap when the device is run upwards and downwards in an inverted diode without Cs_2CO_3 interlayer, whereas they form a hysteresis loop
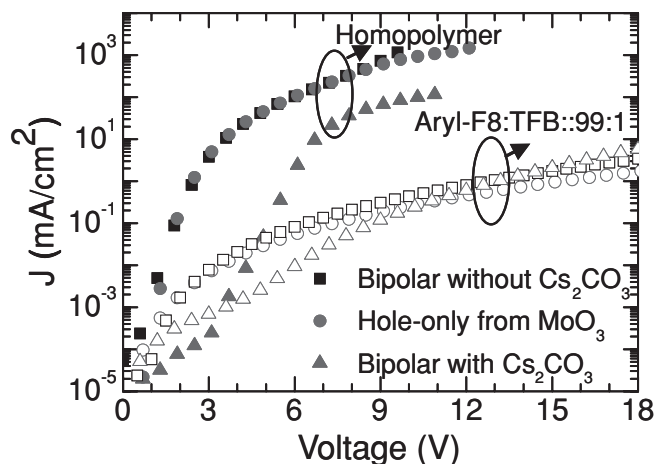
www.MaterialsViews.com

ADVANCED
FUNCTIONAL
MATERIALS
www.afm-journal.de

FULL PAPER

Figure 6. *J–V* characteristics of homopolymer aryl-F8 (solid) and aryl-F8$_{99\%}$:TFB$_{1\%}$ blend (empty) in hole-only device injected from MoO$_3$/Au side (circle), bipolar current in inverted diodes without Cs$_2$CO$_3$ (square) and with Cs$_2$CO$_3$ (triangle). Thickness of polymer layer was 500 nm for all measurements.

in the inverted structure using a Cs$_2$CO$_3$ interlayer. This result indicates that Cs$_2$CO$_3$ does introduce interfacial traps and/or charges in the polymer film and causes a barrier for electron injection, which is consistent with the lower turn-on of the device observed while running the device downwards. With increased operating voltage, we observe that the *J–V* curves completely overlap again since all the traps are already filled and conduction is more bulk-limited. We note that without a Cs$_2$CO$_3$ interlayer, current magnitudes are always higher.

One of the major issues that needs addressing in organic LEDs is the out-coupling of the emitted light, which holds back optimal device performance.[37] By mounting an index-matched glass half-sphere with an index-matching oil onto the glass substrate, we can reduce total internal reflection at the substrate/air interface (see Figure S6)[38] and achieve even higher efficiency values of 5.7% EQE and luminance efficiency of 11 cd A^{-1}. This further improvement is, however, still significantly less than predicted due to considerable nonidealities like size and position of the HyLED in the optical setup as well as residual light scattering at the substrate/oil/hemisphere interfaces due to imperfect index-matching and interfacial unevenness. Thus, there is further room for optimization if a perfectly coupled hemisphere were used.

3. Conclusions

The device performance of aryl-F8 blue emissive polymer-based light-emitting diodes in an inverted structure has been studied and optimized to achieve charge-carrier balance and color purity by use of a polymer additive. By adding small amounts of TFB into the aryl-F8, the device performance is greatly improved from 1 cd A^{-1} in a pure aryl-F8 to 5.9 cd A^{-1} in the blend of aryl-F8$_{99.5\%}$:TFB$_{0.5\%}$. Further, for this blend ratio, luminance efficiency up to 11 cd A^{-1} was achieved by improved out-coupling using an index-matched hemisphere lens. Aryl-F8:TFB blends show significantly higher performance than aryl-F8 only, without compromising the optical properties, which could be a
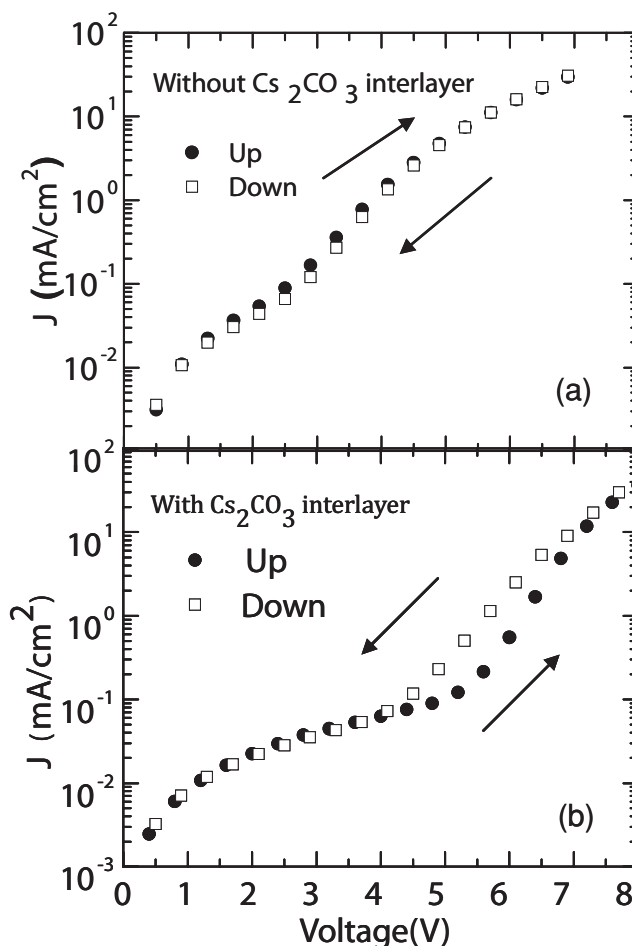
Figure 7. *J–V* characteristic of 500-nm-thick aryl-F8 layer based HyLEDs a) without Cs$_2$CO$_3$ and b) with Cs$_2$CO$_3$ interlayer, measured in different sweep directions with delays of 100 ms in consecutive steps of 0.1 V.

future route to electrically pumped organic laser diodes, as suggested by Song et al.[3]

4. Experimental Section

Fabrication: Indium–tin oxide (ITO) substrates were cleaned separately in acetone and isopropanol in an ultrasonic bath for 10 minutes each, sequentially. For hole-only devices, substrates were treated with oxygen plasma and spin-coated with PEDOT-PSS followed by annealing at 230 °C under nitrogen for 30 minutes. For inverted diodes, substrates then were heated to 400 °C to deposit zinc oxide by spray pyrolysis from the organic precursor zinc acetate dihydrate dissolved in methanol (80 g L^{-1}). Cs$_2$CO$_3$ was dissolved in 2-methoxyethanol (7 g L^{-1}; Fluka) at 80 °C and spin-coated onto the ZnO layer at 3000 rpm. Aryl-F8 (procured from Cambridge Display Technology, M$_n$ = 386k, PDI = 2.7) and TFB (procured from Cambridge Display Technology, M$_n$ = 130k) were dissolved in mixed xylene isomers at 80 °C with the concentration of 30 g L^{-1} for aryl-F8 and 3 g L^{-1} for TFB and then mixed to form aryl-F8$_{1-x}$:TFB$_x$ blends by mixing in different weight fractions. The polymer blends were spin-coated directly upon Cs$_2$CO$_3$ films. All samples were annealed at 120 °C under nitrogen for one hour. Film thicknesses for these films were measured using a Dektak profilometer and found to be around 500 ± 30 nm. We also prepared similar films of different concentration (film thickness 30 ± 5 nm) on quartz substrates for optical studies.

FULL PAPER

Finally, all the samples were transferred to a thermal evaporation chamber for MoO_3 (10 nm; powder, 99.999% from Testbourne) and Au (70 nm) deposition under high vacuum of 1×10^{-6} mbar. The devices were then encapsulated under inert conditions.

Optical and Electrical Measurements: The absorption spectra in this work were measured using a Hewlett Packard 8453 UV-Vis spectrometer, with an operating spectral range of 280–1100 nm on quartz substrates for film thicknesses of about 30 nm. PL decay kinetics were measured by time-correlated single photon counting (TCSPC). The excitation source was a pulsed 407 nm, 80 ps full width at half maximum, 10 MHz diode laser (PicoQuant LDH400) and the luminescence was detected using a microchannel-plate photomultiplier (Hamamatsu Photonics) coupled to a monochromator and TCSPC electronics (Lifespec-ps and VTC900 PC card, Edinburgh Instruments). With the same 407 nm laser excitation source, PL spectra were taken using a 500 mm spectrograph (SpectraPro2500i, Princeton Instruments) combined with a charge-coupled device (CCD) camera (PIXIS 100-F, Princeton Instruments). Current density (Keithley 2400 source measurement unit) and brightness (Keithley 2000 multimeter) versus applied voltage (Keithley 2400 sourcemeter) characteristics for the LEDs were measured in air using a calibrated reference Si photodetector located in the forward direction, typically at a distance of 42 mm from the substrate. EL spectra were recorded with a multimode optical fiber (diameter = 600 μm) attached to an intensity calibrated Ocean Optics USB2000 spectrometer

Angular Emission Profile and Optical Out-Coupling Measurements: An angular stage was used to collect EL spectra at various angles from 0° to 85° while keeping the device stationary and moving the optical fiber attached to the Ocean Optics USB 2000 spectrometer while maintaining a distance of 24 mm from substrate, with and without a hemisphere mounted on the device. These profiles were used to estimate the absolute efficiency of the HyLEDs.

Supporting Information

Supporting Information is available from the Wiley Online Library or from the author.

Acknowledgements

[1] J. H. Burroughes, D. D. C. Bradley, A. R. Brown, R. N. Marks, K. Mackey, R. H. Friend, P. L. Burn, A. B. Holmes, *Nature* **1990**, *347*, 539.

[2] E. J. W. List, R. Guentner, P. S. de Freitas, U. Scherf, *Adv. Mater.* **2002**, *14*, 374.

[3] M. H. Song, D. Kabra, B. Wenger, R. H. Friend, H. J. Snaith, *Adv. Funct. Mater.* **2009**, *19*, 2130.

[4] A. W. Grice, D. D. C. Bradley, M. T. Bernius, M. Inbasekaran, W. W. Wu, E. P. Woo, *Appl. Phys. Lett.* **1998**, *73*, 629.

[5] M. Gross, D. C. Müller, H. G. Nothofer, U. Scherf, D. Neher, C. Bräuchle, K. Meerholz *Nature*, **2000**, *405*, 661.

[6] E. Zojer, A. Pogantsch, E. Hennebicq, D. Beljonne, J. L. Bredas, P. S. de Freitas, U. Scherf, E. J. W. List, *J. Chem. Phys.* **2002**, *117*, 6794.

[7] M. Arif, S. Mukhopadhyay, S. Ramasesha, S. Guha, *Eur. Phys. Lett.* **2009**, *87*, 57008.

[8] Conjugated polymers having spiro centers and their use as electro-luminescence materials, U.S. Patent 5,621,131 (**1997**)

[9] H. T. Nicolai, A. Hof, J. L. M. Oosthoek, P. W. M. Blom, *Adv. Funct. Mater.* **2011**, *21*, 1505.

[10] T. Miteva, A. Meisel, W. Knoll, H. G. Nothofer, U. Scherf, D. C. Muller, K. Meerholz, A. Yasuda, D. Neher, *Adv. Mater.* **2001**, *13*, 565.

[11] J. Li, Y. Hirayama, T. Sano, T. Tomita, H. Fujii, K. Wakisaka, *Thin Solid Films* **2006**, *515*, 2686.

[12] S.-R. Tseng, S.-Y. Li, H.-F. Meng, Y.-H. Yu, C.-M. Yang, H.-H. Liao, S.-F. Horng, C.-S. Hsu, *Org. Elec.* **2008**, *9*, 279.

[13] Md. A. Karim, Y.-R. Cho, J. S. Park, k.-J. Yoon, S. J. Lee, S.-H. Jin, G.-D. Lee, Y.-S. Gal, *Macromol. Res.* **2008**, *16*, 337.

[14] S.-F. Lim, R. H. Friend, I. D. Rees, J. Li, Y. Ma, K. Robinson, A. B. Holmes, E. Hennebicq, D. Beljonne, F. Cacialli *Adv. Funct. Mater.* **2005**, *15*, 981.

[15] S. Setayesh, A. C. Grimsdale, T. Weil, V. Enkelmann, K. Mullen, F. Meghdadi, E. J. W. List, G. Leising, *J. Am. Chem. Soc.* **2001**, *123*, 946.

[16] a) D. Kabra, L.-P. Lu, M. H. Song, H. J. Snaith, R. H. Friend, *Adv. Mater.* **2010**, *22*, 3194; b) M. C. Gwinner, R. D. Pietro, Y. Vaynzof, K. J. Greenberg, P. K. H. Ho, R. H. Friend, H. Sirringhaus, *Adv. Func. Mater.* **2011**, *21*, 1432; c) D. Kabra, M. H. Song, B. Wenger, R. H. Friend, H. J. Snaith, *Adv. Mater.* **2008**, *20*, 3447.

[17] M. Kroeger, S. Hamwi, J. Meyer, T. Riedl, W. Kowalsky, A. Kahn, *Org. Elec.* **2009**, *10*, 932.

[18] Y. Vaynzof, D. Kabra, L. L. Chua, R. H. Friend, *Appl. Phys. Lett.* **2011**, *98*, 113306.

[19] a) M. Redecker, D. D. C. Bradley, M. Inbasekaran, W. W. Wu, E. P. Woo, *Adv. Mater.* **1999**, *11*, 241; b) J.-S. Kim, P. K. H. Ho, C. E. Murphy, R. H. Friend, *Macromolecules* **2004**, *37*, 2861.

[20] M. Grell, D. D. C. Bradley, G. Ungar, J. Hill, K. S. Whitehead, *Macromolecules* **1999**, *32*, 5810.

[21] a) A. C. Morteani, R. H. Friend, C. Silva, Electronic processes at semiconductor polymer heterojunctions (Eds. K. Müllen, U. Scherf), *Organic Light Emitting Devices: Synthesis, Properties and Applications*, Wiley-VCH, Weinheim **2006**; b) A. C. Morteani, R. H. Friend, C. Silva, *Chem. Phys. Lett.* **2004**, *391*, 81.

[22] M. A. Lambert, P. Mark, *Current injection in solids*, Academic Press, New York, **1970**.

[23] W. F. Pasveer, J. Cottaar, C. Tanase, R. Coehoorn, P. A. Bobbert, P. W. M. Blom, D. M. de Leeuw, M. A. Michels, *Phys. Rev. Lett.* **2005**, *94*, 206601.

[24] R. I. Fran, J. G. Simmons, *J. Appl. Phys.* **1967**, *38*, 832.

[25] V. D. Mihailetchi, P. W. M. Blom, J. C. Hummelen, M. T. Rispens, *J. Appl. Phys.* **2003**, *94*, 6849.

[26] J. Hwang, E.-G. Kim, J. Liu, J.-L. Brédas, A. Duggal, A. Kahn, *J. Phys. Chem. C* **2007**, *111*, 1378.

[27] F. Laquai, G. Wegner, C. Im, H. Bassler, S. Heun, *J. Appl. Phys.* **2006**, *99*, 023712.

[28] F. Montilla, R. Mallavia, *Adv. Funct. Mater.* **2007**, *17*, 71.

[29] F. B. Dias, S. Maiti, S. I. Hintschich, A. P. Monkman, *J. Chem. Phys.* **2005**, *122*, 054904.

[30] V. N. Bliznyuk, S. A. Carter, J. C. Scott, G. Klarner, R. D. Miller, D. C. Miller, *Macromolecules* **1999**, *32*, 361.

[31] K. Murata, S. Cina, N. C. Greenham, *Appl. Phys. Lett.* **2001**, *79*, 1193.

[32] H. J. Bolink, E. Coronado, D. Repetto, M. Sessolo, E. M. Barea, J. Bisquert, G. Garcia-Belmonte, J. Prochazka, L. Kavan, *Adv. Funct. Mater.* **2008**, *18*, 145.

[33] M. K. Fung, S. L. Lai, S. N. Bao, C. S. Lee, S. T. Lee, W. W. Wu, M. Inbasekaran, J. J. O'Brien, *J. Vac. Sci. Technol. A* **2002**, *20*, 911.

[34] Y. Zhang, P. W. M. Blom, *Appl. Phys. Lett.* **2011**, *98*, 143504.

[35] W. Brutting, H. Riel, T. Beierlein, W. Riess, *J. Appl. Phys.* **2001**, *89*, 1704.

[36] F. Scheiba, N. Benker, U. Kunz, C. Roth, H. Fuess, *J. Power Sources* **2008**, *177*, 273.

[37] Y. Sun, S. R. Forrest, *Nat. Photon.* **2008**, *2*, 483.

[38] S. Reineke, F. Lindner, G. Schwartz, N. Seidler, K. Walzer, B. Luessem, K. Leo, *Nature* **2009**, *439*, 234.

FULL PAPER

Stoichiometry Controlled, Single-Crystalline Bi$_2$Te$_3$ Nanowires for Transport in the Basal Plane

Nicola Peranio,* Eva Leister, William Töllner, Oliver Eibl, and Kornelius Nielsch

Thermoelectric Bi$_2$Te$_3$ based bulk materials are widely used for solid-state refrigeration and power-generation at room temperature. For low-dimensional and nanostructured thermoelectric materials an increase of the thermoelectric figure of merit *ZT* is predicted due to quantum confinement and phonon scattering at interfaces. Therefore, the fabrication of Bi$_2$Te$_3$ nanowires, thin films, and nanostructured bulk materials has become an important and active field of research. Stoichiometric Bi$_2$Te$_3$ nanowires with diameters of 50–80 nm and a length of 56 µm are grown by a potential-pulsed electrochemical deposition in a nanostructured Al$_2$O$_3$ matrix. By transmission electron microscopy (TEM), dark-field images together with electron diffraction reveal single-crystalline wires, no grain boundaries can be detected. The stoichiometry control of the wires by high-accuracy, quantitative enegy-dispersive X-ray spectroscopy (EDX) in the TEM instrument is of paramount importance for successfully implementing the growth technology. Combined electron diffraction and EDX spectroscopy in the TEM unambiguously prove the correct crystal structure and stoichiometry of the Bi$_2$Te$_3$ nanowires. X-ray and electron diffraction reveal growth along the [110] and [210] directions and the *c* axis of the Bi$_2$Te$_3$ structure lies perpendicular to the wire axis. For the first time single crystalline, stoichiometric Bi$_2$Te$_3$ nanowires are grown that allow transport in the basal plane without being affected by grain boundaries.

1. Introduction

Since Hicks and Dresselhaus predicted in 1993 a higher thermoelectric figure of merit *ZT* due to quantum confinement effects in low-dimensional systems,[1–3] fabrication of nanowires have become a main topic of research on thermoelectric materials. For room temperature applications, Bi$_2$Te$_3$-based bulk materials are usually the best choice, since they are known for their large thermopower (S = 200 µV K^{-1}), large electrical conductivity (σ = 1000 Ω^{-1} cm^{-1}), and low thermal conductivity (λ = 1.5 W m^{-1} K^{-1}) and thereby a high thermoelectric figure of merit $ZT = (S^2\sigma/\lambda)T = 1$ at T = 300 K.[4]

Dr. N. Peranio, Prof. O. Eibl
Institut für Angewandte Physik
Eberhard Karls Universität Tübingen
Auf der Morgenstelle 10, Tübingen 72076, Germany
E-mail: nicola.peranio@uni-tuebingen.de
E. Leister, W. Töllner, Prof. K. Nielsch
Institut für Angewandte Physik
Universität Hamburg
Jungiusstrasse 11, Hamburg, 20355, Germany

Binary and ternary Bi–Te, Bi–Sb–Te, and Bi–Te–Se nanowires and multilayer nanowires were grown by various techniques.[5–19] To achieve a maximum *ZT*, a precise control of stoichiometry better than 1% is one key requirement in Bi$_2$Te$_3$ based materials, since the thermopower and the electrical conductivity strongly depend on charge carrier density, e.g., Bi–Te bulk materials with a Te content of 60 at.% revealed *p*-type character and a thermopower of 227 µV K^{-1}, whereas *n*-type conduction and a thermopower of –224 µV K^{-1} was observed for 63.5 at.% Te.[4] Particularly for Bi$_2$Te$_3$ nanomaterials an accurate control of the chemical composition is required, since in Bi$_2$Te$_3$-based nanostructured bulk materials non-stoichiometric precipitates were found and identified as a limiting factor for high *ZT* values.[20] A second key requirement is to control the texture of these materials, since Bi$_2$Te$_3$ is known for its anisotropy, i.e., transport along the basal plane yields an electrical conductivity three times larger than transport along the *c* axis.[21]

Growth by potential-pulsed electrodeposition was found to be a promising growth technique.[5–7] Basic requirements were achieved,[5–12] but the results were still unsatisfactory: i) Nanowires were fabricated which showed the optimum texture but were polycrystalline[10] or which were single-crystalline but showed an unfavorable crystal orientation with respect to the wire axis.[7] ii) The chemical composition was usually qualitatively analyzed by energy dispersive X-ray spectrometry (EDX) in a scanning electron microscopy (SEM) instrument and/or transmission electron microscopy (TEM) instrument, resulting in vague statements such as Bi/Te ratio close to 2:3.[5–12] iii) The size of the crystallites was rarely determined although transmission electron microscopy was used.

Our previous investigation[22] revealed that deviations in the order of 6–7% from optimum stoichiometry of the nanowires lead to a thermopower reduced to one third of the bulk value. On the other hand, the power factor $S^2\sigma$ could be enhanced using the pulsed deposition technique. This was mainly due to the higher degree of crystallinty of the nanowires, which strongly increased the electrical conductivity. Therefore it is anticipated that the nanowires presented in this work will exhibit high power factors. Measurement of thermoelectric properties results will be presented elsewhere.

FULL PAPER

In this work, a thorough analysis of the microstructure, texture, and chemical composition of Bi–Te nanowires grown by potential-pulsed electrodeposition is presented. A different solution was used as compared to a previous report[5] (i.e., ion concentrations of Bi and Te, less-acidic solution), thus reduction- and relaxation potentials had to be adjusted to reach optimum composition. The texture was measured by X-ray diffraction (XRD) and selected-area electron diffraction (SAED) in a TEM instrument. Crystallite sizes were determined by TEM dark-field images of nanowires in two-beam diffraction conditions. The stoichiometry was analyzed by a high-accuracy EDX chemical analysis in the TEM instrument, including a reduction of hole-count artifacts and using Cliff–Lorimer k-factors calibrated on $Bi_2(Te,Se)_3$ and $(Bi,Sb)_2Te_3$ bulk materials.[23,24]

2. Results and Discussion

A cross-section of the Bi_2Te_3 nanowire array is shown in the SEM image in **Figure 1**. Nanowires (2) grew from the bottom gold layer (1) upwards within the template. A uniform growth of the nanowires was obtained, the nanowires showed a length of 56 μm at variations smaller than 10%. Potential-pulsed electrodeposition is known to be more effective in uniform growth than potentiostatic or galvanostatic electrodeposition.[5,17,18] It is assumed that during the relaxation time (t_{off}) a recovery and redistribution of the metal ion concentration at the deposition interface occurs that inhibits a decrease of the concentration of metal ions at the cathode interfaces during the entire reaction time.[5] Although the growth front is fairly uniform, beginning overgrowth could be observed as hemispherical deposits on the top side of the PAA membrane (4). This is very likely due to slight pore-diameter deviations in the PAA membrane (3). A certain fraction of pores might provide a better ion supply, being slightly wider than average, thus leading to an enhanced growth speed.

Figure 2 shows the XRD pattern obtained at the plan-view bottom section of the Bi_2Te_3 nanowire array with the gold layer
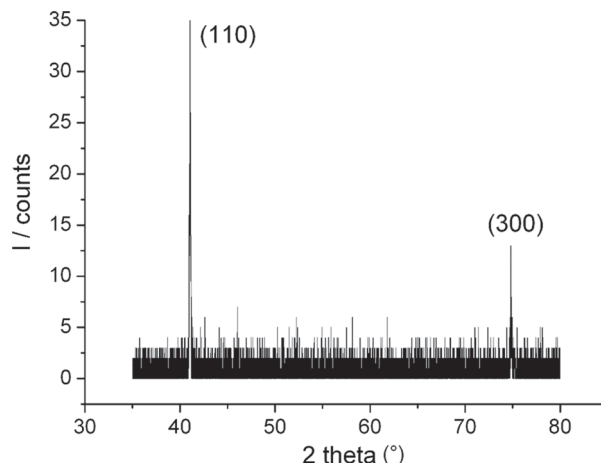
Figure 2. XRD diffraction pattern obtained on a Bi_2Te_3 nanowire array.

removed. A scan over a larger range (10–90°) of diffraction angles was carried out (not shown here). In Figure 2 only (110) and (300) reflections were found, which proves the strong texture of the Bi_2Te_3 nanowire array with [110] and [210] axes of the crystallites being parallel to the wire axis, respectively. Diffraction peaks of elemental Bi and Te were not observed, indicating that a complete Bi_2Te_3 phase formation occurred. These results confirm previous observations[5–7] that potential-pulsed electrodeposition is an effective method to grow crystalline, highly textured Bi_2Te_3 nanowires, preferable to other electrodeposition techniques.

The diameter of the nanowires and the size of the crystallites within the nanowires were determined by dark-field images of nanowires under two-beam diffraction conditions using the (015) reflections (**Figures 3**a and b). Two parallel nanowires, labeled (1) and (2), with a length of about 1.7 μm can be seen in the images. Over this length a single orientation was observed for both nanowires, the contrast is due to thickness fringes, as it is well known in electron diffraction. Two-beam dark-field images are most sensitive to identify the crystallite size, however, are rarely shown in publications. The diameter of the nanowires labeled (1) and (2) were found to vary over the length from 69 to 73 nm. The right-most nanowire, labeled (3), is thinner, with a diameter of 56 nm. Over larger areas nanowire diameters varied between 50 nm and 80 nm.

The texture of the nanowires was analyzed in more detail: i) Diffraction patterns observed at various points of one nanowire revealed the same reflections over a length of 18 μm (not shown here). ii) High-resolution images of a wire in a pole orientation were acquired (Figures 3c and d), the corresponding diffraction pattern is shown in Figure 3e. The (00l) Bragg reflections can clearly be seen, thereby, an angle of 85° between c axis of the crystallite and the wire axis was determined. From this diffraction pattern it can also be concluded that the (300) planes are almost perpendicular to the wire axis. Hence, electron diffraction confirmed the X-ray diffraction results. In summary, electron diffraction revealed nanowires with (i) the c axis and the (300) planes being almost perpendicular to the wire axis and (ii) the ⟨210⟩ direction and the basal plane being parallel to the wire axis. Single-crystallinity could be proved by electron diffraction over a length between 1.7 μm (Figure 3a) and 18 μm.
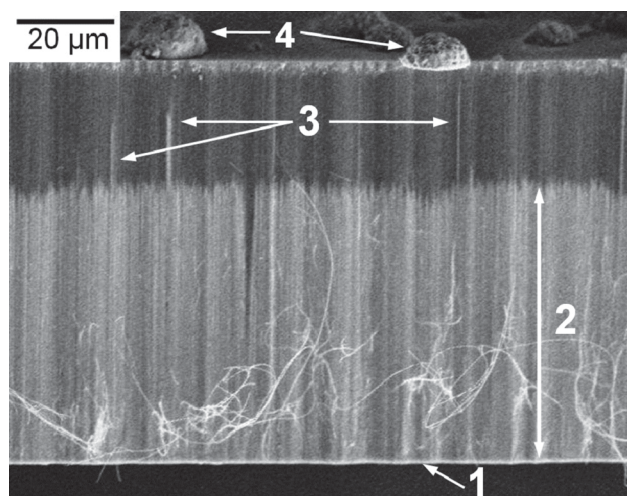

Figure 1. SEM image of Bi_2Te_3 nanowire array in cross-section. 1) bottom gold layer, 2) nanowires, 3) nanowires with outstanding length, 4) hemispherical overgrowth on top of the membrane.

Materials
Views
www.MaterialsViews.com

ADVANCED
FUNCTIONAL
MATERIALS
www.afm-journal.de

FULL PAPER
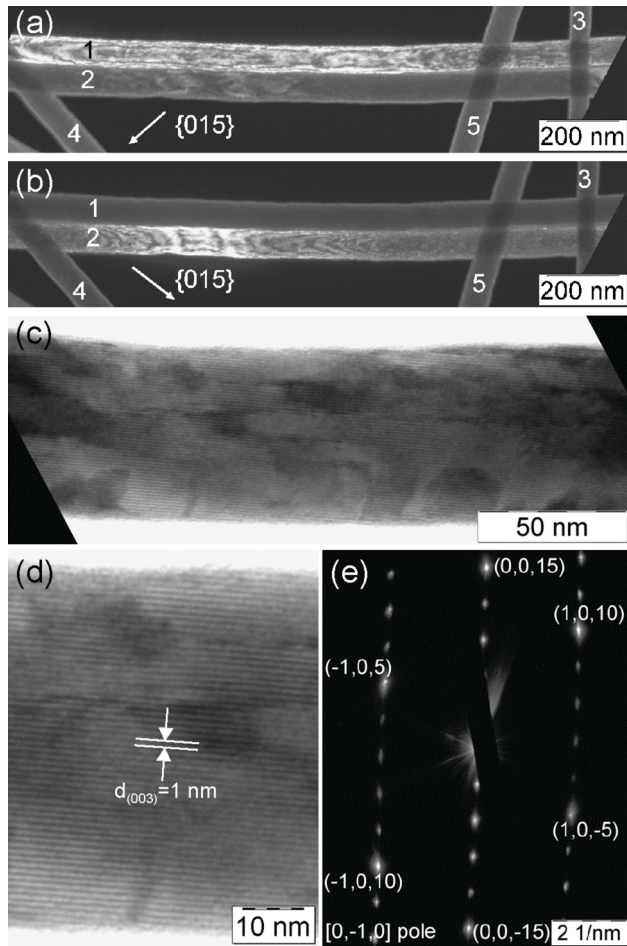
Figure 3. TEM images and electron diffraction pattern obtained in Bi_2Te_3 nanowires: a,b) Dark-field images obtained with two different {015} reflections at a sample region with five nanowires labeled 1 to 5. c–e) HRTEM images and diffraction pattern of a nanowire tilted in [0,–1,0] pole.

Figure 4. a,b) EDX spectrum acquired in the TEM instrument on a Bi_2Te_3 nanowire with a Te mole fraction of 60.9 at.% shown in linear and logarithmic scale. c) Low-loss EEL spectrum acquired in the TEM instrument on a Bi_2Te_3 nanowire.

The chemical composition and variations in stoichiometry were precisely measured by EDX in the TEM instrument (**Table 1**, **Figures 4**a and b). First, spectra were acquired on arbitrarily chosen nanowires, and an average Te mole fraction of 62.2 at.% was determined (Table 1, line 1). A fairly large Te variation of 1.7 at.% was obtained which was analyzed in more detail. The chemical composition was analyzed for nanowires with different wire diameters (Table 1, lines 2 and 3) and along the axis of a nanowire (Table 1, lines 4 and 5). Over the length of one nanowire, small Te variations of 0.8 at.% were found. However, a slightly larger Te content of 63.1 at.% was found in

Table 1. Mole fractions obtained in Bi_2Te_3 nanowires by bulk calibrated EDX the TEM instrument.

Specimen	Number of measurements	Bi [at.%]	Te [at.%]
arbitrarily selected nanowires	6	37.8 ± 1.7	62.2 ± 1.7
thick nanowires	6	37.6 ± 0.4	62.4 ± 0.4
thin nanowires	6	36.9 ± 0.6	63.1 ± 0.1
along one thick nanowire	6	37.7 ± 0.7	62.3 ± 0.7
along one thin nanowire	6	36.2 ± 0.8	63.8 ± 0.8

FULL PAPER

thin nanowires (diameter 50 nm) compared to 62.4 at.% in thick nanowires (diameter 80 nm). Note, the compositional variations observed here occurred for wires deposited in the same membrane, different diameters were caused by pore diameter variations. In preliminary experiments we have found, that the pore diameter affects the composition of the deposited nanowires. Thus, adjustments of the electrochemical parameters have to be performed when the diameter is to be varied. Details of this investigation will be reported elsewhere.

EDX spectra revealed Bi and Te X-ray lines, as expected, but also Cu, Fe, Al, and Cr lines (Figures 4a and 4b). The Cu and Fe X-ray lines are well-known artifacts, generated by stray radiation hitting the TEM grid, the sample holder, and the pole piece of the objective lens. The Al and Cr X-ray lines are due to residual Cr on the surface of the nanowires after dissolving the Al_2O_3 membrane. An oxygen peak could not be observed, and therefore, no significant oxidation of the surface occurred.

Finally, a low-loss electron energy loss spectrum (EELS) is shown in Figure 4c. A plasmon energy of 16.6 eV was determined, close to the value found in bulk materials. The low-energy Bi $O_{4,5}$ and Te $N_{4,5}$ core loss ionization edges are indicated.

The potential-pulsed electrodeposition method was used to grow single-crystalline, stoichiometric Bi_2Te_3 nanowires. Reduction potentials of −200 and −250 mV were found to be the most suitable for nanowires growing in the [110] and [210] direction and being single-crystalline and close to stoichiometry.

In Bi_2Te_3 materials, (00l) reflections with lattice spacing $d_{(003)} = 1.016$ nm unambiguously prove the presence of the highly anisotropic rhombohedral phase and allow to determine the orientation of the c axis with respect to the wire axis. Therefore, the nanowires were tilted to the [0,−1,0] pole and showed the characteristic small spaced (00l) reflections, which were not presented elsewhere.[5–7,9,10] Dark-field imaging in two-beam diffraction conditions was found to be the most reliable method of determining the crystallite size of the nanowires. Combined with electron-diffraction patterns acquired along the entire length of the nanowires it proved their single-crystalline character over a length of several micrometers. In the literature single-cystallinity was frequently claimed over the full length of nanowires (**Table 2**) without an adequate proof as shown here.

Control of the chemical composition of the nanowires is of utmost importance, however, precise published measurements are still rare. Quantitative EDX spectroscopy in the TEM including reduced hole-counts as described here offers unique possibilities for controlling the chemical composition precisely.[23,24] In the literature the chemical composition of the nanowires is unprecisely described, e.g., Bi/Te mole fraction ratios "close to" 2:3 are reported (Table 2). For stoichiometric Bi_2Te_3 the Bi-$M_{\alpha 1}$ peak should be markedly higher than the Te $L_{\alpha 1}$ peak, and the ratio of integrated counts was obtained as 0.97 for Bi-L/Te-L. In contrast, EDX spectra of Bi_2Te_3 nanowires published elsewhere, for which stoichiometry was claimed, revealed the Te-$L_{\alpha 1}$ peak being markedly higher than the Bi-$L_{\alpha 1}$ peak.[9] In summary, the calibrated EDX measurements allow preparation of stoichiometry-controlled Bi_2Te_3 based nanomaterials. The chemical homogeneity over the length of the wire was shown and the chemical composition of the nanowires varied slightly with the wire diameter.

3. Conclusions

In this work stoichiometric and single-crystalline Bi_2Te_3 nanowires with diameters of 50–80 nm for transport along the basal plane were presented, which were prepared by potential-pulsed electrochemical deposition in a nanostructured Al_2O_3 matrix. Single-crystallinity was adequately proven by dark-field imaging in the TEM under two-beam conditions and by electron diffraction. The orientation of the nanowires is established by the growth process, there was no additional control besides the electrochemical process parameters. The chemical composition was precisely measured by high accuracy, calibrated energy-dispersive X-ray spectrometry in the TEM instrument. The nanowires presented here were markedly different to nanowires described elsewhere (Table 2).[5–12] The nanowires presented by Zhang et al. were single-crystalline but do not allow basal plane transport since they have (015) reciprocal direction parallel to the wire axis.[7] The wires reported by Stacy et al. yielded (110) orientation along the wire axis; however, they were polycrystalline.[6,10–12] These wires would also allow basal

Table 2. Overview of publications about microstructure analyses on electrodeposited binary Bi-Te nanowires using (1) potential-pulsed or (2) potentiostatic and galvanostatic growth methods.

Ref.	Growth method	Wire diameter [nm]	Wire length [μm]	Character	Chemical composition	Wire axis paralell to	Orientation of c axis
This work	(1)	50–80	56	single-crystalline	62 at.% Te[a,c]	⟨110⟩, ⟨210⟩	⊥ to wire axis
[5]	(1)	40	25	single-crystalline	close to 2:3[b]	⟨110⟩, ⟨210⟩	⊥ to wire axis
[6]	(1)	35	65		65 at.% Te[c]	⟨110⟩, ⟨210⟩	⊥ to wire axis
[7]	(1)	40–60	50	single-crystalline	close to 2:3[b]	(015)	
[8]	(2)	40–120		single-crystalline	54 at.% Te[a]	⟨110⟩	⊥ to wire axis
[9]	(2)	50	25	single-crystalline	close to 2:3[a]	⟨110⟩	⊥ to wire axis
[10]	(2)	25–75		highly textured	close to 2:3[a,b]	⟨110⟩, ⟨210⟩	⊥ to wire axis
[11]	(2)	45	45		close to 2:3[b]	⟨110⟩, ⟨210⟩	⊥ to wire axis
[12]	(2)	40	30–80		60 at.% Te[b]	⟨110⟩, ⟨210⟩	⊥ to wire axis

[a]Determined by EDX in a TEM instrument; [b]Determined by EDX in a SEM instrument; [c]Determined with an electron probe microanalyzer (EPMA).

www.MaterialsViews.com

ADVANCED
FUNCTIONAL
MATERIALS
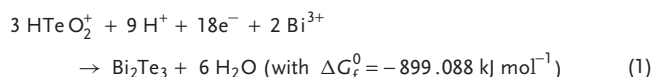www.afm-journal.de

FULL PAPER

plane transport; however, grain boundaries occured on a length scale of several 100 nm.

4. Experimental Section

Ordered porous anodic alumina (PAA) membranes provide a well-established template system for nanowire growth. For sufficient mechanical stability, membranes with thicknesses between 60 μm and 80 μm were produced. Self-organized PAA membranes with nominal pore diameters between 40 nm and 60 nm were prepared by a two-step anodization process in oxalic acid as described elsewhere.[25–27] Pores were opened using a 5 wt.% phosphoric acid solution at 45 °C. To ensure a complete barrier layer removal, this process was prolonged to 55 min. This also yielded a short chemical etching process within the pores, enhancing porosity above 10% of as-prepared membranes.[28] The slightly widened pores exhibited diameters between 50 nm and 80 nm.

A thin layer of gold was sputtered onto the pore-opened back side of the membranes, acting as seed layer for a subsequent electrodeposition of a gold film from a commercial gold plating solution (Umicore Auruna 5000). This gold layer served as the working electrode for the electrodeposition of the Bi_2Te_3 nanowires. An aqueous solution containing 10 mM Bi^{3+} and 15 mM $HTeO_2^+$ ions in 1 M HNO_3 was prepared by dissolution of bismuth(III)-nitrate pentahydrate $Bi(NO_3)_3 \cdot 5H_2O$ (Sigma–Aldrich) and pure Te powder (99.999% Fluka) in concentrated nitric acid (69%) and consequent dilution with deionized water (Millipore) to the appropriate volume. Prior to electrodeposition, cyclic voltammetry was performed in order to determine suitable ranges for reduction and relaxation potentials. A reduction potential between −150 and −250 mV was found suitable, i.e., slightly more negative than the main reduction peak of −80 mV, see below. The relaxation potential was set to +80 mV. Based on previous results,[5] fixed pulses of 10 ms for reduction (t_{on}) and 50 ms for relaxation (t_{off}) were selected.

The total chemical reaction for the formation of Bi_2Te_3 from acidic solutions was reported as

$$3\,HTeO_2^+ + 9\,H^+ + 18\,e^- + 2\,Bi^{3+}$$
$$\rightarrow Bi_2Te_3 + 6\,H_2O \quad (\text{with } \Delta G_f^0 = -899.088 \text{ kJ mol}^{-1}) \quad (1)$$

for the main reduction peak at −80 mV.[29] Thus, a series of five samples was deposited with reduction potentials between −150 and −250 mV, i.e., −150, −175, −200, −225, −250 mV. A conventional three-electrode setup was used, consisting of a Gamry Series G 300 PC card potentiostat, an Ag/AgCl/KCl (saturated) reference electrode (U_{ref}) and a Pt wire mesh counter electrode. Voltammetry and depositions were conducted at room temperature in unstirred solution. Platinum wire served as working electrode for voltammetry with a scanning rate of 20 mV s^{-1} between 0.5 V and −0.5 V vs. U_{ref}. Bi_2Te_3 nanowires were grown in an electrochemical cell with stirred solution to provide better ion supply to the pores. Consequently, the filled membranes were broken and cross-sections were examined by scanning electron microscopy (Zeiss Evo50) to determine growth rate and uniformity. A growth rate of 13 μm h^{-1} was determined for a reduction potential of −200 mV.

For TEM and XRD investigations, the gold electrode was removed by KI–I$_2$ solution and overgrowth on the top side of the membrane was dissolved by a short dip in concentrated nitric acid. XRD measurements were conducted on a PANalytical X'Pert Pro system with Cu K$_\alpha$ radiation. Subsequent, nanowires were isolated by dissolving the PAA membrane in a mixture of 6 wt.% H_3PO_4 and 1.8 wt.% H_2CrO_4 for several days at 45 °C. Droplets of the suspension, that had been centrifuged and rinsed with deionized water several times, were deposited on holey TEM grids and dried at room temperature. Electron diffraction in the TEM was used to select the nanowires with the best crystallinity, i.e., with a reduction potential of −200 and −250 mV. These samples were analyzed by analytical TEM, however, only results obtained on the sample with a reduction potential of -200 mV are shown here.

Bi_2Te_3 has a rhombohedral crystal symmetry with space group $R\bar{3}m$. The lattice parameters of the pseudo-hexagonal unit cell are $a = 0.4386$ nm and $c = 3.0497$ nm.[30] For XRD and electron diffraction in the TEM the hexagonal crystal symmetry was taken as basis. For understanding texture three relations between diffracting planes {hkl} and crystal directions uvw are important: i) {00l} planes and thereby the basal plane are perpendicular to the c axis, ii) {110} planes are perpendicular to the ⟨110⟩ directions, and (iii) {300} planes are perpendicular to the ⟨210⟩ directions.

A Zeiss 912Ω TEM instrument was operated at 120 kV yielding a point resolution of 0.37 nm and an energy resolution of 1 eV. High-resolution images were acquired to prove the quality of the crystal lattice. The size of the crystallites was determined by bright- and dark-field images of nanowires in two-beam diffraction conditions with strongly excited {015} Bragg reflections. Diffraction patterns were acquired using a selected area electron diffraction (SAED) aperture selecting regions with a diameter of 750 nm.

The TEM instrument is equipped with an EDX detector and a low-background specimen holder for chemical analysis with an energy resolution of 136 eV at the Mn K$_\alpha$ line and with an OMEGA® energy filter for acquisition of electron energy loss spectra (EELS). A high-accuracy quantitative chemical analysis was established for Bi_2Te_3 materials by EDX in the TEM instrument, including the following points: i) A stray aperture was additionally mounted to reduce hole-count artifacts by a factor of five. ii) The Cliff–Lorimer k-factors were calibrated such that the mean values of the mole fractions in Bi_2Te_3 bulk materials measured by EDX in the TEM instrument corresponded to those of electron probe microanalyses (EPMA).[23,24] The acquisition conditions for the EDX spectra were a spot size of 32 nm and an acquisition time of 300 s. For quantitative chemical analysis, the integrated counts under the Bi L and Te L X-ray lines were used. The integrated counts N were larger than 15 000 yielding a minimum statistical error of $\sigma_N/N = 0.8\%$ (Poisson statistics) for the determination of the local mole fractions. For EELS acquisition a spot size of 10 nm was used.

Supporting Information

Supporting Information is available from the Wiley Online Library or from the author.

[1] L. D. Hicks, M. S. Dresselhaus, *Phys. Rev. B* **1993**, *47*, 12727–12731.
[2] L. D. Hicks, M. S. Dresselhaus, *Phys. Rev. B* **1993**, *47*, 16631–16634.
[3] L. D. Hicks, T. C. Harman, X. Sun, M. S. Dresselhaus, *Phys. Rev. B* **1996**, *53*, R10493–R10496.
[4] D. M. Rowe, *CRC Handbook of Thermoelectrics*, CRC Press, Boca Raton, FL, **1995**, ch. 19.
[5] J. Lee, S. Farhangfar, J. Lee, L. Cagnon, R. Scholz, U. Gösele, K. Nielsch, *Nanotechnology* **2008**, *19*, 365701.
[6] L. Trahey, C. R. Becker, A. M. Stacy, *Nano Letters* **2007**, *7*, 2535–2539.
[7] L. Li, Y. W. Yang, X. H. Huang, G. H. Li, L. D. Zhang, *Nanotechnology* **2006**, *17*, 1706–1712.

[8] J. H. Zhou, C. G. Jin, J. H. Seol, X. G. Li, L. Shi, *Appl. Phys. Lett.* **2005**, *87*, 133109.

[9] C. G. Jin, X. Q. Xiang, C. Jia, W. F. Liu, W. L.Cai, L. Z. Yao, X. G. Li, *J. Phys. Chem. B* **2004**, *108*, 1844–1847.

[10] M. S. Sander, R. Gronsky, T. Sands, A. M. Stacy, *Chem. Mater.* **2003**, *15*, 335–339.

[11] M. S. Sander, A. L. Prieto, R. Gronsky, T. Sands, A. M. Stacy, *Adv. Mater.* **2002**, *14*, 665–667.

[12] A. L. Prieto, M. S. Sander, M. S. Martín-González, R. Gronsky, T. Sands, A. M. Stacy, *J. Am. Chem. Soc.* **2001**, *123*, 7160–7161.

[13] W. Wang, G. Q. Zhang, X. G. Li, *J. Phys. Chem. C* **2008**, *112*, 15190–15194.

[14] W. Wang, X. L. Lu, T. Zhang, G. Q. Zhang, W. J. Jiang, X. G. Li, *J. Am. Chem. Soc.* **2007**, *129*, 6702–6703.

[15] M. Martín-Gonzáles, G. J. Snyder, A. L. Prieto, R. Gronsky, T. Sands, A. M. Stacy, *Nano Letters* **2003**, *3*, 973–977.

[16] M. Martín-Gonzáles, A. L. Prieto, R. Gronsky, T. Sands, A. M. Stacy, *Adv. Mater.* **2003**, *15*, 1003–1006.

[17] C. Jin, X. Xiang, C. Jia, W. Liu, W.Cai, L. Yao, X. Li, *J. Phys. Chem. B* **2004**, *108*, 1844–1847.

[18] S. H. Li, M. S. Toprak, H. M. A. Soliman, J. Zhou, M. Muhammed, D. Platzek, E. Müller, *Chem. Mater.* **2006**, *18*, 3627–3633.

[19] C. Frantz, N. Stein, L. Gravier, S. Granville, C. Boulanger, *J. Electron. Mater.* **2010**, *39*, 2043–2048.

[20] Y. Lan, A. J. Minnich, G. Chen, Z. Ren, *Adv. Funct. Mater.* **2010**, *20*, 357–376.

[21] H. Süssmann, W. Heiliger, *Phys. Status Solidi A* **1979**, *51*, K201–K206.

[22] J. Lee, Y. Kim, L. Cagnon, U. Gösele, J. Lee, K. Nielsch, *Phys. Status Solidi RRL* **2010**, *4*, 43–45.

[23] D. Eyidi, D. Maier, O. Eibl, M. Westphal, *Phys. Status Solidi A* **2001**, *187*, 585–600.

[24] N. Peranio, O. Eibl, *Phys. Status Solidi A* **2007**, *204*, 3243–3255.

[25] H. Masuda, K. Fukuda, *Science* **1995**, *268*, 1466–1468.

[26] O. Jessensky, F. Müller, U. Gösele, *Appl. Phys. Lett.* **1998**, *72*, 1173–1175.

[27] A. P. Li, F. Müller, A. Birner, K. Nielsch, U. Gösele, *J. Appl. Phys.* **1998**, *84*, 6023–6026.

[28] K. Nielsch, J. Choi, K. Schwirn, R. B. Wehrspohn, U. Gösele, *Nano Letters* **2002**, *2*, 677–680.

[29] M. S. Martín-González, A. L. Prieto, R. Gronsky, T. Sands, A. M. Stacy, *J. Electrochem. Soc.* **2002**, *149*, C546–C554.

[30] S. Nakajima, *J. Phys. Chem. Solids* **1963**, *24*, 479–485.

FULL PAPER

Charge Transport in a Highly Phosphorescent Iridium(III) Complex-Cored Dendrimer with Double Dendrons

Salvatore Gambino, Shih-Chun Lo, Zehua Liu, Paul L. Burn,* and Ifor D. W. Samuel*

The charge transporting properties of a phosphorescent iridium(III) complex-cored dendrimer, with two dendrons attached to each ligand of the core are reported. The results show that the high photoluminescence quantum yield of this material is obtained without compromising charge transport. The hole mobility values are reported over a wide range of temperatures and electric fields using the charge-generation layer time-of-flight technique. The results are analysed using the Gaussian disorder model (GDM), the correlated disorder model, the polaronic correlated disorder model, and the short-range correlated Gaussian disorder model. It is found that the GDM model gives the most comprehensive description of hole transport in this material. In spite of its larger size, the hole mobility of the doubly dendronised material compares favourably with that of a smaller singly dendronised material, and its spherical shape leads to low energetic disorder and clearly non-dispersive charge transport. This shows how molecular shape can be used to combine favourable photoluminescence and charge-transporting properties.

1. Introduction

The development of light-emitting materials for organic light-emitting diodes has led to a range of strategies for controlling intermolecular interactions. For organic light-emitting diodes (OLEDs) it is important that the materials have a high photo-luminescence quantum yield (PLQY) but still have sufficient charge mobility to avoid high driving voltages. There is often a trade-off between efficiency of light emission and charge transport; namely it is advantageous to space the luminescent chromophores apart to reduce intermolecular interactions

that can quench the luminescence,[1–5] but as the luminescent chromophore is normally also responsible for charge transport, a large separation would be detrimental to charge mobility.[6] Hence the challenge for materials development is to have good photophysical properties without sacrificing charge transporting properties.[7–10]

We explore this issue of solid-state inter-chromophore interactions using light-emitting conjugated dendrimers, which are well-defined soluble organic semiconductors.[11–13] Light-emitting dendrimers generally comprise a light-emitting core, to which one or more dendrons (branched structures) are attached. Surface groups are often used at the distal ends of the dendrons to provide solubility and processability. Light-emitting dendrimers allow good control over intermolecular interactions, giving a powerful way of exploring their role in the charge transport and photophysics of organic semiconductors. We have shown that the degree of interaction between chromophores can also be manipulated by dendrimer generation and have investigated the effect this has on the material properties.[14,15] We have also demonstrated that the dendron type can have a dramatic effect on the optoelectronic properties of the materials.[5,8,13,16]

Another strategy for controlling the intermolecular interactions is increasing the number of dendrons attached to the core. In our work on phosphorescent *fac*-tris(2-phenylpyridyl) iridium(III) complex-cored dendrimers we have prepared three generations of materials that contain a single biphenyl dendron with 2-ethylhexyloxy surface groups attached to each of the ligands.[17,18] However, with these mono-dendronised (one dendron per ligand) materials, the dendrons fan out from the core in one direction giving the shape of a shuttlecock with the complex at its base due to the octahedral geometry. This means that for these mono-dendronised materials one face of the opto-electronic core chromophore is open to intermolecular interactions. This can be overcome by making the so-called "double-dendron" materials, which have two dendrons attached to each ligand of the core. **Figure 1** shows the space filling models for a first generation mono- (IrG1) and doubly dendronised (DDIrG1) iridium(III) complex-cored dendrimer. The use of the doubly dendronised material has enabled very efficient film photoluminescence (PLQY 81%)[19] and electroluminescence (13.6% external quantum efficiency at 110 cd/m²) to be

Dr. S. Gambino, Prof. I. D. W. Samuel
Organic Semiconductor Centre
SUPA, School of Physics and Astronomy
University of St Andrews, North Haugh
St Andrews KY16 9SS, UK
E-mail: idws@st-andrews.ac.uk

Dr. S.-C. Lo, Prof. P. L. Burn
Centre for Organic Photonics and Electronics
The University of Queensland, Chemistry Building
Queensland 4072, Australia
E-mail: paul.burn@uq.edu.au

Dr. Z. Liu
Department of Chemistry
Chemistry Research Laboratory
University of Oxford
Mansfield Road, Oxford, OX1 3TA, UK

ADVANCED
FUNCTIONAL
MATERIALS
www.afm-journal.de

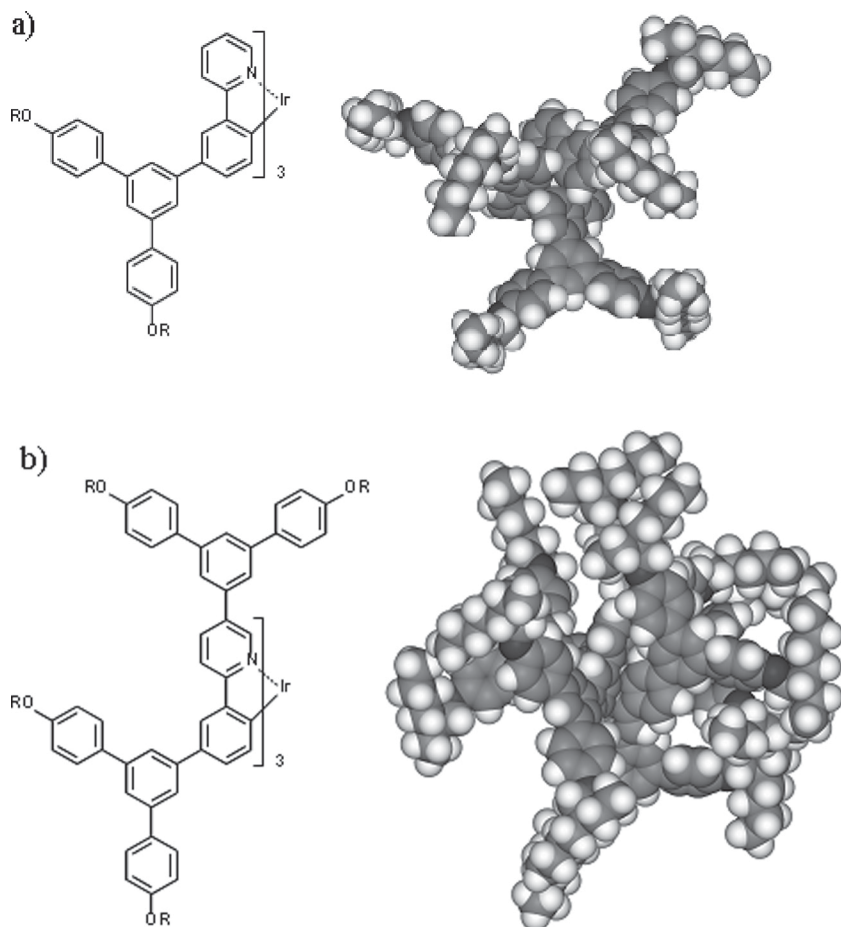Materials
Views
www.MaterialsViews.com

Figure 1. a) Mono-dendronised (IrG1) and b) doubly dendronised (DDIrG1) *fac*-tris(2-phenylpyridyl)iridium(III) complex cored-dendrimers with first generation biphenyl dendrons and 2-ethylhexyloxy surface groups. R = 2-ethylhexyl.

obtained from neat films of a first-generation material.[19,20] In contrast the mono-dendronised IrG1 has a solid state PLQY of 65%,[19] showing that a double-dendron structure is more effective in controlling the intermolecular interactions that affect the luminescence efficiency. However, the question arises as to how this protection of the luminescent core affects the charge transport in neat films of the doubly dendronised material and whether adequate charge transport properties can be combined with highly efficient luminescence.

In this paper we explore the effect that the double dendron structure has on the charge transport properties in order to show how good luminescence quantum yield and sufficient charge transport can be achieved in the same material. We explore this by measuring the temperature and field dependence of the hole mobility, using the charge-generation layer time-of-flight (TOF) technique (**Figure 2** inset), for the doubly dendronised iridium(III) complex. Furthermore we analyze the experimental results within the Gaussian disorder model (GDM),[21] correlated disorder model (CDM),[22] polaronic correlated disorder model (polaronic CDM),[23] and short range correlated Gaussian disorder model (short CDM).[24]

2. Results

Figure 3 shows the hole photocurrent transient on linear and log-log scales for a DDIrG1 film, at room temperature for an applied electric field, $E = 2.5 \times 10^5$ Vcm^{-1}. The plot shows an initial spike followed by a clear constant-current plateau. This corresponds to non-dispersive hole transport with a time-independent drift velocity. The subsequent drop in the current is caused by the holes reaching the ITO electrode, where they are discharged. The carrier transit time (t_{tr}) was evaluated from the intersection point of the asymptotes to the plateau and to the long tail, $t_{tr} = 0.07$ ms. The transit time of 0.07 ms corresponds to a mobility of 2.2×10^{-6} cm^2 V^{-1} s^{-1}. The TOF measurements give the hole mobility in the direction perpendicular to the substrate, and we have studied its field dependence, as shown in **Figure 4**. As the electric field is increased from 1.2×10^5 to 5×10^5 V cm^{-1}, the hole mobility increases from 1.1×10^{-6} to 8.3×10^{-6} cm^2 V^{-1} s^{-1} at room temperature. In order to compare the effect of having two dendrons attached to each ligand on the charge mobility the room temperature hole mobility of the singly dendronised dendrimer (IrG1) was also measured, with the results plotted in Figure 4 for a direct comparison. It is clear that both materials have the same field dependence and similar mobility values, which is surprising given that the core, which is responsible for the hole transport, of the DDIrG1 is encapsulated by the dendrons and so might be expected to have lower charge mobility.
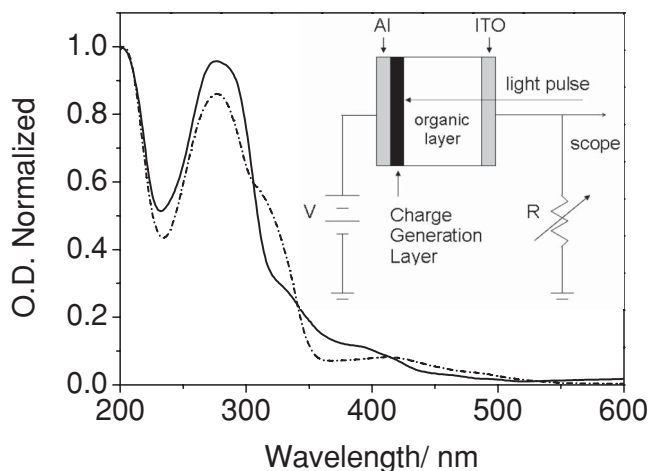

Figure 2. Absorption spectra of the first generation mono- (solid line) and doubly (dotted line) dendronised iridium(III) complex-cored dendrimer (i.e., IrG1 and DDIrG1, respectively) thin films. Charge-generation layer TOF set-up schematic (inset).
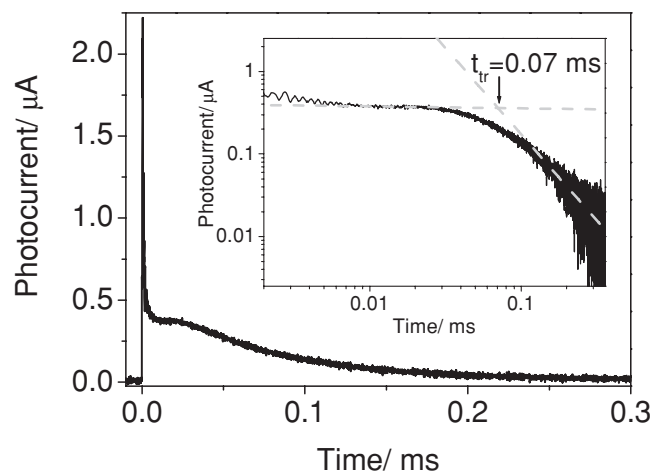
www.MaterialsViews.com

ADVANCED
FUNCTIONAL
MATERIALS
www.afm-journal.de

FULL PAPER

Figure 3. Hole photocurrent transient on linear and log-log scales (inset) for a DDIrG1 film, at room temperature for an applied electric field $E = 2.5 \times 10^5$ Vcm^{-1}.

To learn more about the charge-transport mechanism, temperature-dependent measurements were performed on DDIrG1. **Figure 5** shows the hole photocurrent transients on a linear scale from 295 K down to 235 K for an applied electric field $E = 2.5 \times 10^5$ V cm^{-1}. As the temperature is decreased, the photocurrent plateau becomes less distinct and starts to disappear below 275 K. **Figure 6** shows DDIrG1 hole mobility as a function of field for temperatures from 215 K to 335 K in intervals of 20 K.

2.1. Gaussian Disorder Model

We first analysed the field and temperature dependent mobility data on the basis of Equation 1 to determine σ, μ_0, Σ and C:[21]

$$\mu(T, E) = \mu_0 \exp\left[-\left(\tfrac{2}{3}\hat{\sigma}\right)^2\right] \exp\left[C\left(\hat{\sigma}^2 - \Sigma^2\right) E^{1/2}\right] \quad \Sigma \geq 1.5$$
$$\mu(T, E) = \mu_0 \exp\left[-\left(\tfrac{2}{3}\hat{\sigma}\right)^2\right] \exp\left[C\left(\hat{\sigma}^2 - 2.25\right) E^{1/2}\right] \quad \Sigma < 1.5$$

$$(1)$$
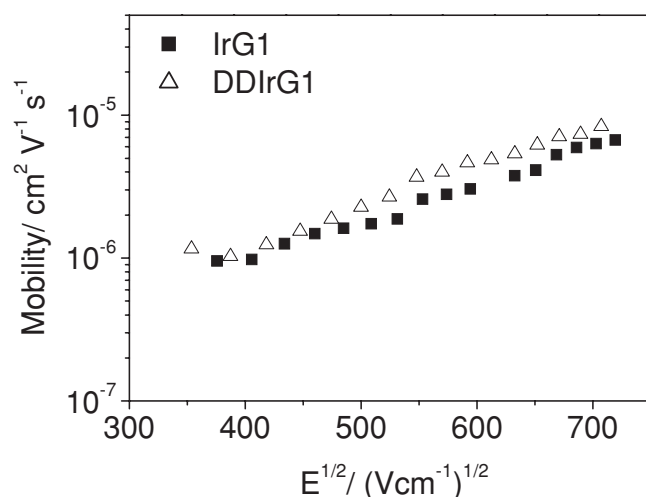
Figure 4. Room temperature IrG1 and DDIrG1 hole mobility as a function of the square root of the electric field.
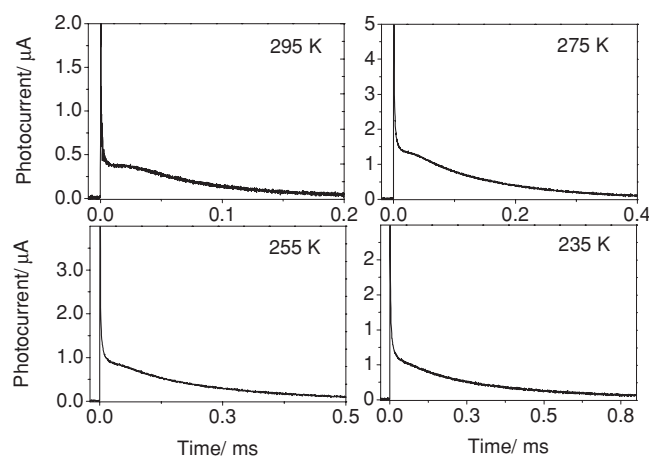
Figure 5. Hole photocurrent transients at an electric field of $E = 2.5 \times 10^5$ Vcm^{-1}. Measurements were performed in vacuum and in a temperature range of 235–295 K.

where σ and Σ are the two central parameters of the disorder formalism; σ is the energy width of the hopping site manifold, and Σ is the positional disorder due to a distribution of intersite distances; C is a constant and $\hat{\sigma} = \sigma / kT$. Equation 1 predicts a Poole–Frenkel (PF) like electric field dependence for a given temperature. Therefore, we plotted mobility against $E^{1/2}$ at each temperature, as shown in Figure 6. The experimental data of Figure 6 are well described by Equation 1 for external electric field $E \geq 1 \times 10^5$ V cm^{-1} ($E^{1/2} > 300$ (V cm^{-1})$^{1/2}$).

The energetic disorder parameter (σ) has been derived from the temperature dependence of the minimum of the mobility, as representative of the asymptotic $\mu(E = 0)$ values:[25–27]

$$\mu_{(E=0)} = \mu_0 \exp\left(-\left(T_0/T\right)^2\right) \tag{2}$$

where μ_0 is the mobility at infinite temperature and T_0 is the characteristic temperature of the material investigated. By
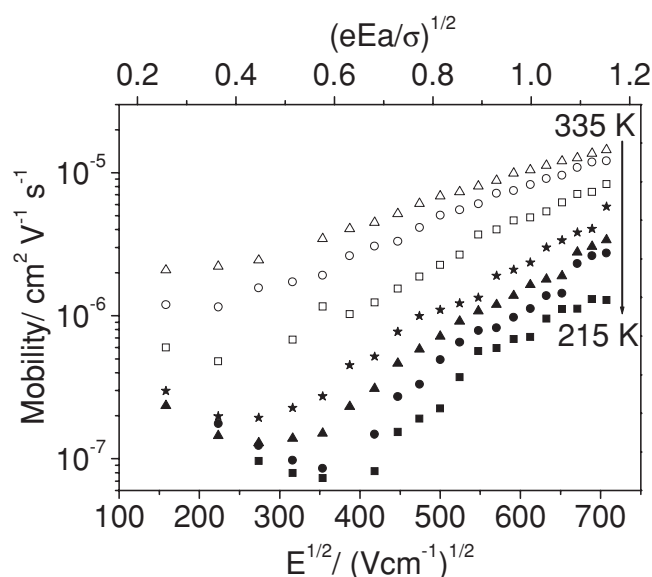
Figure 6. Electric field dependence of mobility of DDIrG1 at temperatures from 215 K to 335 K at intervals of 20 K.
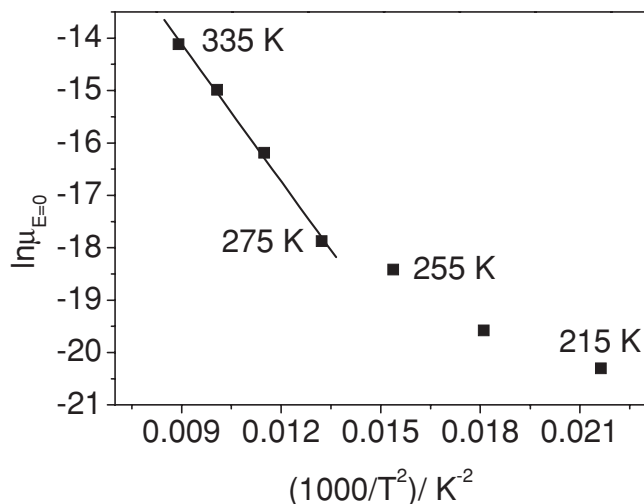
Figure 7. DDIrG1 zero-field mobilities obtained for the various temperatures against $1/T^2$.

Figure 8. The slope, S, of the data in Figure 6 at different temperatures is plotted against $\hat{\sigma}^2$ to obtain the positional disorder parameter, Σ. The solid line is a fit to the Gaussian disorder model in the region of non-dispersive transport.

plotting $\ln\mu(E = 0)$ against $1/T^2$, as shown in **Figure 7**, and fitting in the range 335 K to 275 K, we can deduce T_0 from the slope to be 750 K for DDIrG1, and μ_0 from the intercept with the y-axis to be 3.4×10^{-4} cm^2 V^{-1} s^{-1}. The width of the Gaussian density of states (DOS) is related to T_0 through the relation, $T_0 = 2\sigma/3k$, where k is the Boltzmann constant. Hence, given a value of $T_0 = 750$ K, the width of the density of states σ was found to be 96 meV.

The change in slope for the data in Figure 7 below 275 K is attributed to the onset of the non-dispersive to dispersive transition (ND–D).[21] This can be clearly seen in the shape of the photocurrent transients as a function of temperature (see Figure 5). As the temperature is decreased, the photocurrent plateau becomes less distinct and disappears below 275 K. The temperature dependence of the mobility is expected to change at the non-dispersive to dispersive transition temperature T_c according to Equation 3

$$(\sigma/kT_c)^2 = 44.8 + 6.7 \log L \qquad (3)$$

where L is the thickness of the sample in centimetres.[21,28] For a film of thickness 400 nm and $\sigma = 96$ meV, the onset of the ND–D transition should occur at 285 K according to Equation 3, which is similar to that observed experimentally.

The value of Σ was determined by plotting the slope S of the field dependence of the mobility for various temperatures against $\hat{\sigma}^2$. The slopes (S) for each temperature range are determined by fitting the experimental data of Figure 6 for an electric field range $E^{1/2} > 300$ (V cm^{-1})$^{1/2}$, that is in the region where mobility shows a Poole–Frenkel-like electric field dependence. The result is shown in **Figure 8**, and by fitting the data points for the non-dispersive regime of charge transport[21] (275–335 K), we extract Σ from the intercept with the x-axis and C from the slope. This analysis yielded a positional disorder parameter Σ of 2.3 and a value for C of 6.8×10^{-4} (cm V^{-1})$^{1/2}$.

2.2. Correlated Disorder Model

It has been reported that long-range correlations due to charge-dipole interactions exist in disordered organic
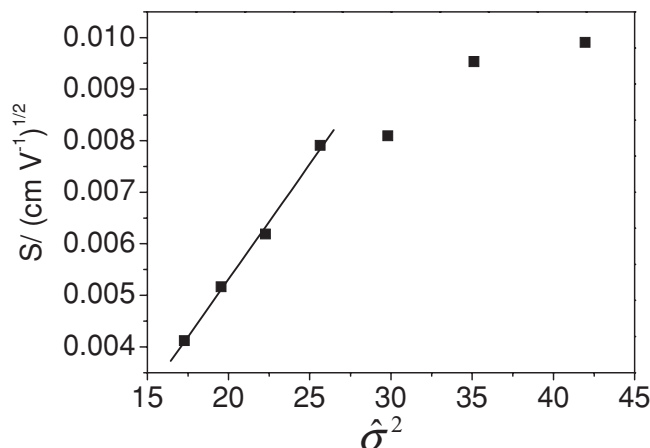
semiconductors.[22,29] In the GDM, the correlation is not taken into account and thus in order to consider the effects of charge-dipole interactions on charge transport, Novikov et al.[22] have developed a 3D CDM and proposed the following empirical relation to describe charge transport in a correlated disordered material:

$$\mu = \mu_0 \exp\left[-\left(\frac{3\hat{\sigma}_{CDM}}{5}\right)^2 + C_0\left(\hat{\sigma}_d^{3/2} - \Gamma\right)\sqrt{\frac{eaE}{\sigma_d}} \right] \qquad (4)$$

In Equation 4 σ_{CDM} denotes the total energetic disorder such as $\sigma_{CDM}^2 = \sigma_d^2 + \sigma_{vdw}^2$, where σ_d is the dipolar component of the disorder and σ_{vdw} is the contribution due to non dipolar disorder (van der Waals). μ_0 has the same meaning as before, C_0 and Γ are constants, and a is the average hopping distance between two adjacent sites. The major difference between the GDM and the CDM is that the latter does not include any spatial disorder.

σ_{CDM} and μ_0 have been deduced by using the same fitting parameters obtained from Figure 7 for the GDM and then using Equation 2, with the only difference that in this case $T_0 = 3\sigma/5k$. Hence, μ_0 has the same value as in the GDM and the value of σ_{CDM} was found to be 107 meV.

We have recently reported neutron reflectivity measurements for a family of iridium(III) complex-cored dendrimers[30] that have allowed us to measure the effective volume and hence diameter of DDIrG1. The effective diameter in the solid state was determined to be 22.6 Å. For conjugated dendrimers such as those studied here, in which the dendron has a wider energy gap than the core, charge resides on the core and charge transport is by hopping between the cores.[14,31,32] Thus we can assume that the average inter-site separation for DDIrG1 is $a =$ 22.6 Å. Hence, C_0 and Γ can be easily determined by plotting the slope (S) of mobility at the different temperatures obtained from Figure 6 against $(\sigma/kT)^{3/2}$. The result is shown in **Figure 9** for the temperature range 215–335 K. We fit the data points in the temperature range 275–335 K, because this is the non-dispersive regime of charge transport, and extract C_0 from the slope and Γ from the intercept with the x-axis. This analysis yielded a value of 1 for C_0 and of 4.45 for Γ.

Materials
Views

www.MaterialsViews.com

ADVANCED
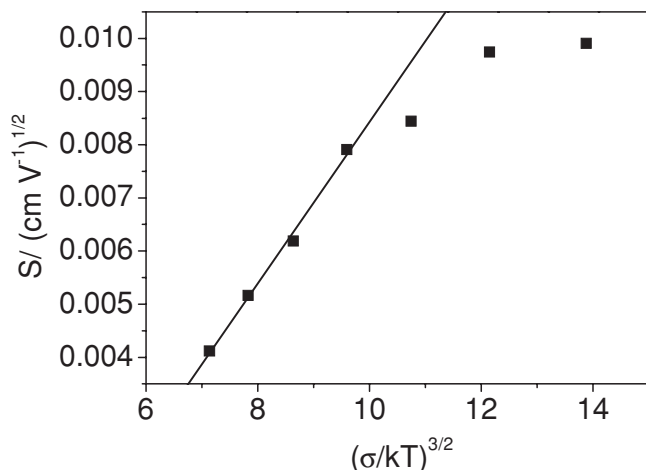FUNCTIONAL
MATERIALS
www.afm-journal.de

FULL PAPER

Figure 9. The slope, S, of the data in Figure 6 at different temperatures is plotted against $(\sigma/kT)^{3/2}$ to obtain C_0 and Γ. The solid line is a fit over the non-dispersive region to the CDM.
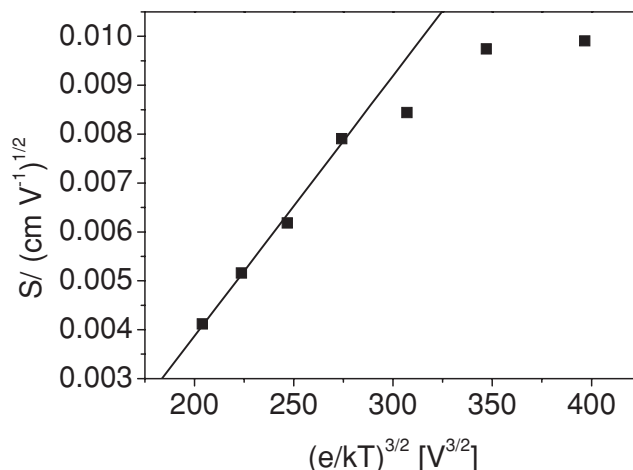

Figure 10. The slope, S, of the data in Figure 6 at different temperatures is plotted against $(e/kT)^{3/2}$ to obtain the energetic disorder parameter (σ_{pCDM}) and the constant Γ. The solid line is a fit over the non-dispersive region to the polaronic CDM.

2.3. Correlated Disorder Model with Polaron Effects

Although Equations 1 and 4 can be used to analyze TOF data, recent theoretical work[23] has cast doubt on whether the σ extracted from the experiment using Equations 1 and 4 represents the actual width of the full DOS. Here, we report the first application of incorporating the inter-site correlation and polaron effects to explain the charge transport mechanism in dendrimer films. We analyze the field and temperature dependent mobility data using the model proposed by Parris and co-workers[23] based on the small polaron motion in a correlated disorder landscape. Mobility values from Figure 6 were fitted to Equation 5 to determine the width of the DOS in the polaronic CDM model, σ_{pCDM}, μ_0, E_a, Γ:

$$\mu(T, E) = \mu_0 \exp\left(-\frac{E_a}{kT}\right) \exp-\left(\frac{3\hat{\sigma}_{pCDM}}{5}\right)^2$$

$$\exp\left[C_0\left(\hat{\sigma}_{pCDM}^{3/2} - \Gamma\right)\sqrt{\frac{eaE}{\sigma_{pCDM}}}\right] \quad (5)$$

In a similar way to the GDM and CDM, Equation 5 predicts a PF-like behavior, where σ_{pCDM}, μ_0 and a have the same meanings as before and C_0 and Γ are constants.

The values of σ_{pCDM} and Γ have been determined by plotting the slope (S) of the mobility field dependence at the different temperatures obtained from Figure 6 against $(e/kT)^{3/2}$. The result is shown in **Figure 10** for the temperature range 215–335 K, and by fitting the data points for the temperature range 275–335 K, σ_{pCDM} and Γ are extracted. Assuming the same value of C_0 determined by the CDM, this analysis yielded an energetic disorder of 112 meV and a Γ value of 4.76.

In order to determine the last unknown parameters (E_a and μ_0), we consider mobility at zero field. Equation 5 simplifies to the following:

$$\mu(T, E = 0) = \mu_0 \exp\left(-\frac{E_a}{kT}\right) \exp-\left(\frac{3\hat{\sigma}_{pCDM}}{5}\right)^2 \quad (6)$$

By plotting the zero field mobility against T^{-1} we find E_a to be -20 ± 30 meV (graph not shown). Clearly a negative value of the activation energy would be unphysical, and even the positive value at the upper end of the error range is unreasonable as it is much smaller than the energetic disorder (σ_{pCDM}).

2.4. Short-Range Correlated Gaussian Disorder Model

Although the GDM explains the field and temperature dependence of a wide range of organic materials,[33–36] its PF-like mobility dependence is only valid over a short range of electric fields, and for relatively high electric fields ($E \geq 3 \times 10^5$ V cm^{-1}).[22] In the last decade starting from the original GDM many authors[22,29,37,38] have reported that introducing a long-range correlation between hopping sites (CDM and polaronic CDM) produces the expected PF-like dependence over a wider range of electric fields. In these models the correlation arises from interactions between charges and randomly oriented permanent dipoles.[29]

Here we apply the model of Tonezer and Freire[24] to our TOF mobility measurements. The model is based on Gaussian distribution of DOS, where the only source of the hopping site energies is given by the interaction of the charge in the site with the surrounding induced dipoles (short-range correlation). This model predicts a PF-like mobility dependence over a significant range of fields and give the following expression for the mobility:[24]

$$\mu = \mu_0(T) \exp\left[\left(1.6\frac{\alpha e^e}{2kTa^4} - 2.9\right)\sqrt{\frac{eEa}{kT}}\right] \quad (7)$$

where α is the isotropic polarizability of all sites and the other parameters have the same meaning as before.

Figure 6 shows the logarithm of the mobility as function of the square root of dimensionless field ($\sqrt{eEa/\sigma}$) for different temperature values. Our experimental data show a PF mobility
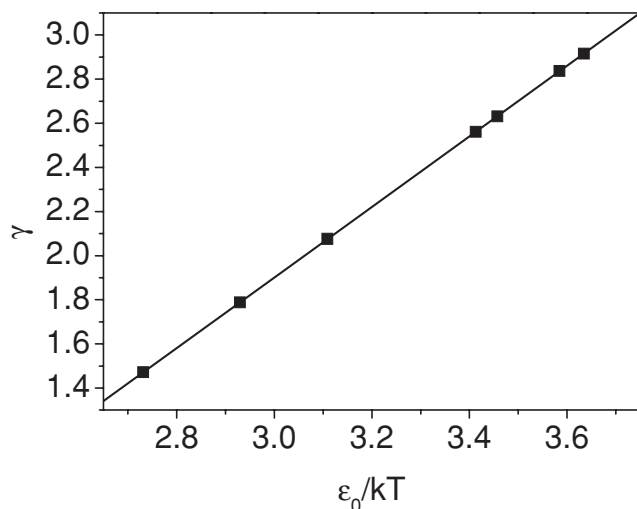
ADVANCED
FUNCTIONAL
MATERIALS
www.afm-journal.de

Materials
Views
www.MaterialsViews.com

FULL PAPER

Figure 11. The dimensionless parameter γ against ε_0/kT.

dependence in the range of $0.5 < \sqrt{eEa/\sigma} < 1.15$. The energetic disorder parameter has been defined as $\sigma = \sqrt{1.16}\varepsilon_0$, where ε_0 is the energy scale of the polarization energy and is given by $\varepsilon_0 = e^2\alpha/2a^4$. ε_0 has been determined measuring the field dependence (slope) of the mobility from Figure 6. In fact from Equation 7, the slope (γ) is related to ε_0 by the following equation:

$$\gamma = 1.6\frac{\alpha e^2}{2kTa^4} - 2.9 = 1.6\frac{\varepsilon_0}{kT} - 2.9 \qquad (8)$$

Figure 11 shows a plot of γ against ε_0/kT, and the solid line is the linear fit to the experimental data using Equation 8. This fit gives a value of 85 meV for the energetic disorder parameter σ.

3. Discussion

We first consider the nature of charge transport in DDIrG1. The shape of the current transient for DDIrG1 signifies that hole transport is highly non-dispersive in this dendrimer at room temperature, in contrast to the previously reported room temperature measurements for the singly dendronised IrG1 and its second generation analogue (IrG2).[32] That is, the current transient indicates that films of DDIrG1 are less disordered than those of the first- and second-generation singly dendronised materials IrG1 and IrG2.[8] Non-dispersive transients in more ordered films have also been observed in conjugated polymers. Inigo and co-workers[39] reported a non-dispersive photocurrent transient in a low defect density MEH-PPV sample with an energetic and positional disorder parameters of $\sigma = 76$ meV and $\Gamma = 1.48$; meanwhile for a higher defect density sample a dispersive photocurrent transient was observed together with higher values of σ (82 meV) and of Γ (4.5) for the same material. A similar result but on a different conjugated polymer (PFO) has been reported by Kreouzis and co-workers.[40] They found a reduction in the energetic disorder from 95 meV down to 73 meV upon annealing the sample that indicates that the film becomes more ordered after annealing. This transition is

clearly manifested from a highly dispersive photocurrent transient for the non annealed PFO sample to a clearly non-dispersive behaviour for the annealed one. Laquai and co-workers[41] report for a polyspirobifluorene polymers that increasing the disorder in their materials leads to a higher dispersion of TOF transients.

We have investigated whether the GDM can explain the variation of photocurrent transients with temperature and field for DDIrG1. Our value of σ of 96 meV, yields an energetic disorder of $\hat{\sigma} = 3.7$ at room temperature. This value is within the estimated values from Monte Carlo simulation for a non-dispersive photocurrent transient, where $\hat{\sigma} \leq 3.5 - 4$ is expected for non-dispersive charge transport behaviour.[21]

The temperature transition from non-dispersive to dispersive charge transport behaviour means that below this temperature (see Figure 5), the carriers will cross the sample without relaxing to their mean energy. DDIrG1 exhibits non-dispersive transport at temperatures down to 275 K, which is lower than the transition temperature of 293 K for IrG1. The theoretical transition temperature determined from Equation 3 of 285 K is very close to that determined from experiment (275 K).

We have discussed so far the good agreement of our experimental data with PF-like behaviour for electric fields higher than 1×10^5 V cm^{-1} ($E^{1/2} > 300$ (Vcm^{-1})$^{1/2}$); another important feature of the data in Figure 6 is the negative field dependence of the mobility at low fields. This negative field dependence has been observed in a wide range of organic materials.[42–44] This is due to the positional disorder, because faster routes made up of more favourable charge-transporting site, with part of their path going against the field are forbidden as the field increases. These results are in very good agreement with the GDM.[21,28]

Different theoretical models have been used to explain charge transport in molecularly doped polymers (MDP),[29,45] polymers,[46–48] and organic glasses.[22] For instance, recently Kreouzis and co-workers[40] have reported a detailed study regarding the consistency of their PFO TOF experimental data to the polaronic CDM. Another recent development is the possibility of modelling the mobility of an organic material starting from the consideration of the atomic structure of the material as recently reported by Nelson et al.[49] and Vukmirovic et al.[50,51]

To characterize the CDM we measured the energetic disorder parameter in a similar way to the GDM and we found $\sigma_{CDM} = 107$ meV. The σ_{CDM} is slightly higher than σ_{GDM} but this is consistent with the results reported by others on a range of materials,[52,53] suggesting that the charge–dipole interaction is a stronger source of energetic disorder. For a direct comparison with the GDM, we calculated $\hat{\sigma}_{CDM}$ and the transition temperature using Equation 3. This yielded $\hat{\sigma}_{CDM} = 4.2$ and $T_c = 317$ K. This is substantially higher than the experimental value of 275 K, and the energetic disorder parameter fails to satisfy the relation $\hat{\sigma}_{CDM} \leq 3.5$.

The coefficient Γ is analogous to the positional disorder parameter Σ^2 of Equation 1, but in the CDM it is supposed to be a constant value. Our estimated value of Γ of 4.45 is more than double the value of 2 calculated by Novikov et al.[22] This discrepancy between experimental and simulation value of Γ is consistent with previous reported results on an organic glass material[22] and polymers,[54] and it has been ascribed to the

Materials
Views
www.MaterialsViews.com

ADVANCED
FUNCTIONAL
MATERIALS
www.afm-journal.de

FULL PAPER

fact that the CDM does not take into account any positional disorder.

Hence the introduction of inter-site correlations does not improve the agreement between experimental and theoretical data, at least for films of DDIrG1. The next step in the analysis was to use the polaronic CDM. A critical test for a polaron activated contribution to temperature-dependent transport is provided by the comparison between the temperature-dependence of the carrier mobility and the onset of dispersion of TOF signals at lower temperature.[21] If both sets of data are consistent, the polaronic contribution must be negligible compared with disorder effects. If, on the other hand, the onset of dispersion starts at a lower temperature, that is, smaller $\hat{\sigma}$, this provides a handle for separating disorder from polaronic effects. We have already seen from the experimental data that the transition temperature T_c is lower than that predicted by theory, showing that for DDIrG1 the activation energy of transport could then be the sum of disorder and polaron contributions.[21]

The polaronic CDM analysis yielded an energetic disorder parameter $\sigma_{pCDM} = 112$ meV and a Γ value of 4.76. The value of the energetic disorder is even higher than in the CDM, which leads to a $\hat{\sigma}_{pCDM}$ value of 4.4 and once again the expected relation $\hat{\sigma} \leq 3.5$ for non-dispersive charge transport behaviour[21] is not satisfied. This value of the energetic disorder parameter leads to (via equation 6) a negative value of the polaron activation energy (E_a). This is unphysical and clear evidence that the polaronic CDM does not fit our experimental data.

Our results suggest that the analysis of the experimental data carried out within the polaronic CDM does not work well for dendrimers even though it did work for poly(9,9-di-*n*-octylfluorene).[40] However, it is important to remember that polymers are pseudo one-dimensional whereas the dendrimers in this study are three-dimensional.

The last model to be discussed is the one based on short range correlation. This model has been developed quite recently and to the best of our knowledge so far no TOF experimental data have been analyzed using it. It predicts a PF-like dependence of the mobility in the range $0.5 < \sqrt{eEa/\sigma} < 1.1$, that is in very good agreement with our experimental data. The value of the energetic disorder parameter of 85 meV, gives a room temperature value of $\hat{\sigma}$ of 3.3, thus satisfying the relation $\hat{\sigma} \leq 3.5$, which is expected for non dispersive charge transport behaviour.

The good fit of this model to our TOF experimental results could be due to the fact that this model is based on site locations that are supposed to be the center of hard spheres randomly distributed. That is a scenario similar to our system, i.e. spherical shape molecules[30] whose hopping site is at the center of the molecule itself (chromophore).

We finally consider how the field dependent mobility of the first generation doubly dendronised dendrimer (DDIrG1) compares with the first generation mono-dendronised material (IrG1). Both dendrimers show similar mobility, which is double that of the second-generation mono-dendronised dendrimer (IrG2).[32]

We have recently reported[30] that the average volumes occupied by IrG1 and IrG2 in a film are 3100 and 6000 Å³, respectively. These volumes correspond to diameters of 18.1 and 22.5 Å for IrG1 and IrG2. Hence it is clear that increasing the distance

between the electroactive chromophore in moving from IrG1 to IrG2 gives rise to a decreased mobility. Given that the diameter for DDIrG1 is similar to IrG2 and larger than IrG1 it is very interesting that the mobility of DDIrG1 is almost double that of IrG2. For the doubly dendronised dendrimer dendrons on both (hetero)aromatic units of the ligands of the complex will give rise to a more spherical shape[30] and hence a narrower distribution of chromophore spacing. This would mean that the DDIrG1 is less disordered in the solid state than IrG1. This is consistent with the clearly non-dispersive photocurrent transient of DDIrG1 mentioned above and its lower energetic disorder ($\sigma = 96$ meV) compared to the reported value for IrG1 ($\sigma = 103$ meV).[32] In a previous dendrimer family having the same iridium based chromophore, but carbazole containing dendrons and 9,9-di-*n*-propylfluorenyl surface groups, we also found that a less disordered material has higher mobility and a clearly non-dispersive photocurrent transient when compared to a more disordered one.[8] Similar effects have been seen in polymers. For example, regioregular poly(3-*n*-hexylthiophene) shows a higher mobility than that of regiorandom material.[55]

4. Conclusions

TOF mobility measurements have been used to study the influence of dendrimer structure on charge transport. The data were analysed using four models: the Gaussian disorder model (GDM), the correlated disorder model (CDM), the polaronic correlated disorder model (polaronic CDM), and the short range correlated Gaussian disorder model (short CDM).

The experimental results analyzed within the GDM show a very good agreement between the calculated main parameters such as the energetic disorder $\hat{\sigma}$, the transition temperature (T_c) and the expected simulation values. Furthermore, the non-dispersive charge transport nature of DDIrG1 has allowed investigating its charge transport behaviour in a wide range of temperature and electric fields showing a very good match in the description of the non-dispersive to dispersive transition within the Gaussian disorder model.

The introduction of spatial correlation in site energies has led to the so-called CDM, which has been applied to our experimental data. The calculated parameters differ in value to the ones reported by simulation,[22] which arises because the CDM does not take into account any positional disorder. This is consistent with previous reported results where the presence of the positional disorder due to the amorphous nature of the organic material plays an important role and clearly must be taken into account in a theoretical model describing charge transport.

We apply for the first time the polaronic CDM into the analysis of the experimental TOF measurements in conjugated dendrimers. Despite the introduction of both energy correlation and the polaronic hopping effect, the experimental results analyzed within the polaronic CDM leads to an unphysical value of the activation energy. This means that there is no contribution to the activation energy of charge transport from polaronic effects. This is consistent with our results because of the good agreement between the simulated (in the GDM) and the experimental value of the non-dispersive to dispersive transition temperature.

Finally we report, to the best of our knowledge, also the first attempt of fitting TOF experimental data to a recently developed model based on a spatially disordered system where the site energies are given by the interaction of a charge with the induced dipoles in the surrounding sites. This short CDM model describes, better than the previous two correlated models (CDM and polaronic CDM), our experimental TOF results. Its good description of the dendrimer studied here suggests it would be worthwhile to investigate its application to TOF measurements of other organic semiconductors.

Furthermore we found that the first generation doubly dendronised (DDIrG1) and mono-dendronised dendrimer (IrG1) have the same mobility, which is double that of the second generation singly dendronised dendrimer (IrG2).[32] The improvement in charge transport is directly related to the reduced disorder in the DDIrG1 film. Hence, the enhanced film PLQY of DDIrG1 is not gained at the expense of charge transport, showing that we were able to improve the PL properties of the core without inhibiting its charge transport properties. Our results show that it is not only the size, but also the shape of the macromolecule which determines the mobility. We show that a doubly dendronised configuration is an efficient way of reducing molecular interactions that cause the quenching of the luminescence, whilst maintaining good mobility values.

5. Experimental Section

Charge transport was measured by the charge-generation layer TOF technique. Solutions of IrG1 and DDIrG1 were made with concentrations of 45–50 mg mL^{-1} in chloroform. Films were made by spin-coating onto an indium tin oxide (ITO) substrate at speeds of 800–1000 rpm to obtain films of about 400 nm thickness. The samples were then transferred to an evaporator where under high vacuum a 10 nm layer of a perylene dye (Lumogen Red) followed by 100 nm of aluminum were deposited through a shadow mask to define the active area of approximately 6 mm^2.

The sample was mounted in a vacuum cryostat allowing control of the sample temperature both above and below room temperature. Device testing was undertaken by exciting the charge generation layer through the ITO and dendrimer layer. Charge carriers were generated within the perylene layer by excitation from a 500 ps pulse of a dye laser at a wavelength of 580 nm. At this excitation wavelength the dendrimers are completely transparent (see Figure 2) and Lumogen Red has its peak of absorption.[56] The total photogenerated charge was kept small enough to avoid space charge effects, usually around 2–3% CV, where C is the capacitance of the device and V the applied voltage. The electronic time response of the measurement circuit ($\tau = RC$) was always selected to be much smaller than the transit time, $\tau \ll t_{tr}$.

The aluminium electrode was biased positively and the photocurrent signal detected from the ITO (see Figure 2, inset). Hole mobilities, μ, were deduced from the transit times, t_{tr}, via the relation $\mu = d^2/Vt_{tr}$, where d is the film thickness.

[1] T. Swager, *Nat. Mater.* **2002**, *1*, 151.
[2] I. F. Perepichka, D. F. Perepichka, H. Meng, F. Wudl, *Adv. Mater.* **2005**, *17*, 2281.
[3] E. B. Namdas, A. Ruseckas, I. D. W. Samuel, S.-C. Lo, P. L. Burn, *Appl. Phys. Lett.* **2005**, *86*, 091104.
[4] J.-C. Ribierre, A. Ruseckas, I. D. W. Samuel, H. S. Barcena, P. L. Burn, *J. Chem. Phys.* **2008**, *28*, 204703.
[5] S.-C. Lo, R. E. Harding, E. Brightman, P. L. Burn, I. D. W. Samuel, *J. Mater. Chem.* **2009**, *19*, 3213.
[6] M. Pope, C. E. Swenberg, *Electronic Processes in Organic Crystals*, Oxford University Press, Oxford, UK **1982**.
[7] B. K. Yap, R. Xia, M. Campoy-Quiles, P. N. Stavrinou, D. D. C. Bradley, *Nat. Mater.* **2008**, *7*, 376.
[8] S. Gambino, S. G. Stevenson, K. A. Knights, P. L. Burn, I. D. W. Samuel, *Adv. Funct. Mater.* **2009**, *19*, 317.
[9] H. Kim, N. Schulte, G. Zhou, K. Müllen, F. Laquai, *Adv. Mater.* **2011**, *23*, 894.
[10] S. Z. Bisri, T. Takenobu, Y. Yomogida, H. Shimotani, T. Yamao, S. Hotta, Y. Iwasa, *Adv. Funct. Mater.* **2009**, *19*, 1728.
[11] S.-C. Lo, P. L. Burn, *Chem. Rev.* **2007**, *107*, 1097.
[12] P. L. Burn, S.-C. Lo, I. D. W. Samuel, *Adv. Mater.* **2007**, *19*, 1675.
[13] N. C. Cumpstey, R. N. Bera, P. L. Burn, I. D. W. Samuel, *Macromolecules* **2005**, *38*, 9564.
[14] M. Halim, J. N. G. Pillow, I. D. W. Samuel, P. L. Burn, *Adv. Mater.* **1999**, *11*, 371.
[15] J. M. Lupton, I. D. W. Samuel, R. Beavington, P. L. Burn, H. Bässler, *Adv. Mater.* **2001**, *13*, 258.
[16] S.-C. Lo, R. E. Harding, C. P. Shipley, S. G. Stevenson, P. L. Burn, I. D. W. Samuel, *J. Am. Chem. Soc.* **2009**, *131*, 16681.
[17] S.-C. Lo, N. A. H. Male, J. P. J. Markham, S. W. Magennis, P. L. Burn, O. V. Salata, I. D. W. Samuel, *Adv. Mater.* **2002**, *14*, 975.
[18] E. J. Wren, X. Wang, A. Farlow, S.-C. Lo, P. L. Burn, P. Meredith, *Org. Lett.* **2010**, *12*, 4338.
[19] J.-C. Ribierre, S. Stevenson, I. D. W. Samuel, S. V. Staton, P. L. Burn, *J. Display Technol.* **2007**, *3*, 233.
[20] S.-C. Lo, T. D. Anthopoulos, E. B. Namdas, P. L. Burn, I. D. W. Samuel, *Adv. Mater.* **2005**, *17*, 1945.
[21] H. Bässler, *Phys. Status Solidi B* **1993**, *175*, 15.
[22] S. V. Novikov, D. H. Dunlap, V. M. Kenkre, P. E. Parris, A. V. Vannikov, *Phys. Rev. Lett.* **1998**, *81*, 4472.
[23] P. E. Parris, V. M. Kenkre, D. H. Dunlap, *Phys. Rev. Lett.* **2001**, *87*, 126601.
[24] C. Tonezer, J. A. Freire, *J. Chem. Phys.* **2010**, *133*, 214101.
[25] P. M. Borsenberger, R. Richert, H. Bässler, *J. Chem. Phys.* **1991**, *94*, 5447.
[26] P. M. Borsenberger, L. T. Pautmeier, H. Bässler, *Phys. Rev. B* **1992**, *46*, 12145.
[27] P. M. Borsenberger, R. Richert, H. Bässler, *Phys. Rev. B* **1993**, *47*, 4289.
[28] P. M. Borsenberger, D. S. Weiss, *Organic Photoreceptors for Xerography*, M. Dekker, New York **1998**.
[29] D. H. Dunlap, P. E. Parris, V. M. Kenkre, *Phys. Rev. Lett.* **1996**, *77*, 542.
[30] S. V. Vickers, H. Barcena, K. A. Knights, R. K. Thomas, J.-C. Ribierre, S. Gambino, I. D. W. Samuel, P. L. Burn, G. Fragneto, *Appl. Phys. Lett.* **2010**, *96*, 263302.
[31] J. M. Lupton, I. D.W. Samuel, R. Beavington, M. J. Frampton, P. L. Burn, H. Bässler, *Phys. Rev. B* **2001**, *63*, 155206.
[32] J. P. J. Markham, I. D. W. Samuel, S.-C. Lo, P. L. Burn, M. Weiter, H. Bässler, *J. Appl. Phys.* **2004**, *95*, 438.
[33] H. H. Fong, K. C. Lun, S. K. So, *Chem. Phys. Lett.* **2002**, *353*, 407.
[34] A. R. Inigo, H. C. Chiu, W. Fann, Y. S. Huang, U. S. Jeng, T. L. Lin, C. H. Hsu, K. Y. Peng, S. A. Chen, *Phys. Rev. B* **2004**, *69*, 075201.
[35] M. Redecker, D. D. C. Bradley, M. Inbasekaran, W. W. Wu, E. P. Woo, *Adv. Mater.* **1999**, *11*, 241.

[36] F. Laquai, G. Wegner, C. Im, H. Bässler, S. Heun, *J. Appl. Phys.* **2006**, *99*, 033710.

[37] A. Dieckmann, H. Bässler, P.M. Borsenberger, *J. Chem. Phys.* **1993**, *99*, 8136.

[38] Y. N. Garstein, E. M. Conwell, *Chem. Phys. Lett.* **1995**, *245*, 351.

[39] A. R. Inigo, H.-C. Chiu, W. Fann, Y.-S. Huang, U. S. Jeng, C. H. Hsu, K.-Y. Peng, S.-A. Chen, *Synth. Metal.* **2003**, *139*, 581.

[40] T. Kreouzis, D. Poplavskyy, S. M. Tuladhar, M. Campoy-Quiles, J. Nelson, A. J. Campbell, D. D. C. Bradley, *Phys. Rev. B* **2006**, *73*, 235201.

[41] F. Laquai, G. Wegner, C. Im, H. Bässler, S. Heun, *J. Appl. Phys.* **2006**, *99*, 023712.

[42] A. Peled, L. B. Schein, *Chem. Phys. Lett.* **1988**, *153*, 422.

[43] H. Kageyama, K. Ohnishi, S. Nomura, Y. Shirota, *Chem. Phys. Lett.* **1997**, *277*, 137.

[44] P. M. Borsenberger, L. Pautmeier, H. Bässler, *J. Chem. Phys.* **1991**, *94*, 5447.

[45] L. B. Schein, D. Glatz, J. C. Scott, *Phys. Rev. Lett.* **1990**, *65*, 472.

[46] S. V. Rakhmanova, E. M. Conwell, *Synth. Met.* **2001**, *116*, 389.

[47] C. Tanase, E. J. Meijer, P. W. M. Blom, D. M. de Leeuw, *Phys. Rev. Lett.* **2003**, *91*, 216601.

[48] C. Tanase, P. W. M. Blom, D. M. de Leeuw, E. J. Meijer, *Phys. Staus. Solidi A* **2004**, *201*, 1236.

[49] J. Nelson, J. J. Kwiatkowski, J. Kirkpatrick, J. M. Frost, *Acc. Chem. Res.* **2009**, *42*, 1768.

[50] N. Vukmirović, L.-W. Wang, *Phys. Rev. B* **2010**, *81*, 035210.

[51] N. Vukmirović, L.-W. Wang, *Nano Lett.* **2009**, *9*, 3996.

[52] C. Vijila, A. Pivrikas, H. Chun, C. Zhikuan, R. Osterbacka, C. S. Jin, *Org. Electron.* **2007**, *8*, 8.

[53] M. Parameswaran, G. Balaji, T. M. Jin, C. Vijila, S. Vadukumpully, Z. Furong, S. Valiyaveettil, *Org. Electron.* **2009**, *10*, 1534.

[54] R. U. A. Khan, D. Poplavskyy, T. Kreouzis, D. D. C. Bradley, *Phys. Rev. B* **2007**, *75*, 035215.

[55] H. Sirringhaus, P. J. Brown, R. H. Friend, M. M. Nielsen, K. Bechgaard, B. M. W. Langeveld-Voss, A. J. H. Spiering, R. A. J. Janssen, E. W. Meijer, P. Herwig, D. M. De Leeuw, *Nature* **1999**, *401*, 685.

[56] S. Gambino, I. D. W. Samuel, H. Barcena, P. L. Burn, *Org. Electron.* **2008**, *9*, 220.

ADVANCED
FUNCTIONAL
MATERIALS
www.afm-journal.de

Materials
Views
www.MaterialsViews.com

FULL PAPER

Mesoporous Anatase Titania Hollow Nanostructures though Silica-Protected Calcination

Ji Bong Joo, Qiao Zhang, Ilkeun Lee, Michael Dahl, Francisco Zaera, and Yadong Yin*

The crystallization of nanometer-scale materials during high-temperature calcination can be controlled by a thin layer of surface coating. Here, a novel silica-protected calcination process for preparing mesoporous hollow TiO_2 nanostructures with a high surface area and a controllable crystallinity is presented. This method involves the preparation of uniform silica colloidal templates, sequential deposition of TiO_2 and then SiO_2 layers through sol–gel processes, calcination to transform amorphous TiO_2 to crystalline anatase, and finally etching of the inner and outer silica to produce mesoporous anatase TiO_2 shells. The silica-protected calcination step allows crystallization of the amorphous TiO_2 layer into anatase nanocrystals, while simultaneously limiting the growth of anatase grains to within several nanometers, eventually producing mesoporous anatase shells with a high surface area (~311 m^2 g^{-1}) and good water dispersibility upon chemical etching of the silica. When used as photocatalysts for the degradation of Rhodamine B under UV irradiation, the as-synthesized mesoporous anatase shells show significantly enhanced photocatalytic activity with greater enhancement for samples calcined at higher temperatures thanks to their improved crystallinity.

1. Introduction

Titania (TiO_2) is considered to be one of the most useful semiconducting metal oxides for applications ranging from sensors to photonic crystals, energy storage, and photocatalysis.[1] Its wide band gap energy (E_g, 3.0–3.2 eV) allows absorption of UV light, generating electrons (e^-) and holes (h^+), which can subsequently induce red-ox reactions. Since Honda and Fujishima first achieved hydrogen production from water by photocatalysis with TiO_2 under UV irradiation,[2] this material has been widely used as a photocatalyst for water splitting and environmental remediation. TiO_2 offers a number of advantageous features, including its low cost, relatively high photocatalytic activity, low toxicity, and high chemical stability.[3] Photocatalysis on TiO_2 (and other semiconductors) is usually considered to occur in three sequential steps: 1) TiO_2 absorbs photon energy greater than the band gap energy and generates photoexcited electron–hole pairs; 2) the photoexcited electrons

and holes separate and then migrate to the surface of the catalyst; and 3) redox reactions occur on the surface. It has been determined that a highly crystalline structure for the TiO_2 material is essential to enhance the generation and migration of photogenerated electrons/holes (steps (1) and (2)).[4] A high surface area is also critically important to increase the number density of redox reaction sites on the catalyst surface (step (3)).[4]

TiO_2 has three main polymorphs of crystalline phases, brookite, anatase, and rutile, from which the latter two are photocatalytically active. Although rutile has a lower band-gap energy than anatase, from a photocatalytic point of view anatase is undoubtedly considered to be the more active phase due to its higher reduction potential and lower re-combination rate of electron-hole pairs.[5] A well-crystallized anatase phase material with a small grain size and large surface area is therefore considered the preferred form for TiO_2 based photocatalysts. Ideally, in order to maximize the catalytically active surface area, one can directly use dispersed anatase nanocrystals for photocatalysis. The challenge in this case, however, is the difficulty in maintaining the stability of the nanocrystals while concurrently keeping the catalyst surface clean, because colloidal nanocrystals are typically stabilized by capping ligands, which greatly limit the access of reactants to the catalytically active sites.[6]

An alternative approach to producing high-surface-area anatase materials is the creation of mesoscale porosity in such materials.[7] The synthesis of mesoporous structures has been most extensively reported for amorphous TiO_2 structures, which are created by combining sol–gel processes and popular surfactant templating methods. However, the porosity is significantly diminished when the materials are converted from the amorphous to anatase phase at high temperatures.[8] It is highly desirable to develop an effective method for producing mesoporous anatase structures with both good crystallinity and high surface areas. As diffusion is often a problem that limits the overall performance of bulk catalysts, making catalysts in the form of mesoporous colloidal particles instead of a conventional bulk powder is expected to greatly increase the number of accessible active sites and ultimately enhance the catalytic efficiency. One approach to achieve this goal is by removing the core portion of a colloidal sphere produces a hollow shell,

Dr. J. B. Joo, Q. Zhang, Dr. I. Lee, M. Dahl, Prof. F. Zaera, Prof. Y. Yin
Department of Chemistry
University of California
Riverside, CA 92521, USA
E-mail: yadong.yin@ucr.edu

www.MaterialsViews.com

ADVANCED
FUNCTIONAL
MATERIALS
www.afm-journal.de

FULL PAPER

a procedure that is expected to further reduce the diffusion length and improve the accessibility of active sites by the reactants. As shown in both previous literature and our later discussions,[9] the conventional templating method for hollow TiO$_2$ structures cannot concurrently guarantee the anatase phase, high crystallinity, and high porosity, which are all important features required for optimal photocatalytic performance. Crystalline TiO$_2$ hollow nanostructures have also been prepared through hydrothermal or solvothermal processes, but, again, only with considerably low porosity.[7b,10]

Calcination at high temperatures is a simple method to induce crystallization of amorphous TiO$_2$ produced using sol-gel processes.[11] Typically, amorphous TiO$_2$ first transforms into small crystals of metastable anatase, which grow upon continuous heating, and then changes to rutile phase at higher temperatures when the crystal grains reach a certain size (~14 nm).[12] The crystallization from amorphous to anatase and from anatase to rutile usually occurs in the temperature ranges of 450~550 °C and 600~700 °C, respectively. Since crystallization and grain coalescence occur simultaneously under normal calcination conditions, it is very difficult to induce crystallization while at the same time avoiding a significant increase in the grain size of the resulting anatase nanocrystals. This also explains why mesoporous amorphous TiO$_2$ can easily lose its porosity when converted to the anatase phase during high temperature calcination.

Herein, we report a robust process for preparing mesoporous hollow TiO$_2$ nanostructures consisting of small anatase grains, and demonstrate their greatly enhanced photocatalytic activity by systematically tuning the grain sizes. We have termed this process "silica-protected calcination" because the key step is the conversion of amorphous TiO$_2$ to the anatase phase under the protection of a silica layer.[13] Briefly, this method involves the sequential coating of uniform silica colloidal particles with an amorphous TiO$_2$ layer with a thickness of 20~60 nm and another SiO$_2$ layer through sol–gel processes, calcination at high temperature to induce phase transformation from the amorphous TiO$_2$ to anatase with small grain sizes, and removing silica by chemical etching with NaOH solution to finally produce hollow TiO$_2$ spheres with mesoporous anatase shells. Silica protection plays a central role in this process: it limits the growth of TiO$_2$ during calcination, leading to small anatase grains (<5 nm) and mesoscale porosity with a high surface area up to 311 m^2 g^{-1} while preserving the hollow sphere morphology, preventing interparticle coalescence so that discrete hollow spheres can be obtained after removing the silica, and ensuring a hydrophilic surface and therefore excellent water dispersibility after chemical etching by NaOH. The mesoporous anatase shells, which feature well-controlled crystallinity, high surface areas, and good water dispersibility, show significantly enhanced photocatalytic activity. By controlling the calcination temperature, we have been able to fine tune the grain size of the anatase nanocrystals on the shell and optimize the catalyst structure for further enhanced photocatalytic activity.
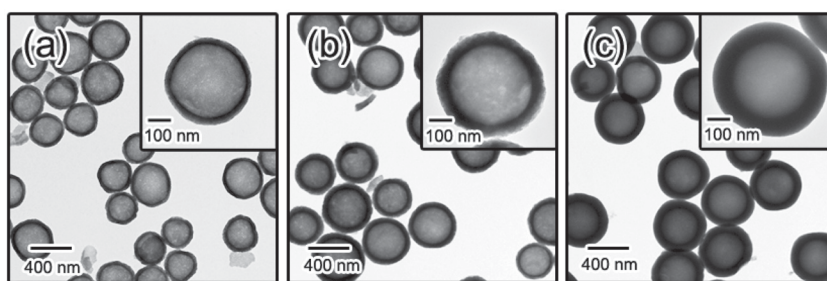

Figure 1. Transmission electron microscopy (TEM) images of amorphous TiO$_2$ hollow spheres (TiO$_2$-E) with different thicknesses prepared by multiple sol-gel coating processes: a) once, b) 3 times, and c) 5 times.

2. Results and Discussion

Amorphous TiO$_2$ hollow spheres can be synthesized by following the archetype of conventional templating methods. Specifically, a typical synthesis involves three main steps: 1) preparation of uniform silica templates using the Stöber method;[14] 2) deposition of a TiO$_2$ layer on the silica surface to form SiO$_2$@TiO$_2$ nanocomposites through the sol-gel reaction of titanium tert-butoxide (TBOT) with hydroxypropyl cellulose (HPC) as the surfactant;[11,15] and 3) etching to remove the silica template using an aqueous solution of NaOH. The thickness of the TiO$_2$ shells can be conveniently tuned by carrying out multiple coating steps (**Figure 1**). Under the typical reaction conditions described in the Experimental Section, a single run of the TiO$_2$ coating procedure produces a ~25 nm thick TiO$_2$ shell (Figure 1a). Raising the number of TiO$_2$ coating steps to 3 and 5 increases the thickness to ~50 and ~ 70nm, respectively (Figure 1b and c). **Table 1** summarizes the notations, preparation conditions and crystalline phases of the hollow TiO$_2$ samples synthesized in this work. The hollow spheres produced by etching with NaOH, labeled as "TiO$_2$-E," are found to be amorphous as expected (**Figure 2**a and e).[9a–d]

Direct calcination of the amorphous hollow TiO$_2$ spheres cannot produce the targeted anatase phase while at the same time retaining the hollow sphere morphology. When the amorphous sample TiO$_2$-E was calcined at 500 °C for 2 h, the hollow morphology remained but there was no significant improvement in crystallinity. Upon increasing the calcination temperature to 800 °C, the hollow structure was completely destroyed, producing large aggregates of irregular shapes (Figure 2c, TiO$_2$-E-C-800). An additional problem is phase purity: while crystallinity was improved by high temperature calcination, the product obtained that way contained a mixture of sodium titanate, anatase and rutile phases (Figure 2e). It is possible that some oligomeric species of sodium titanate may be produced during NaOH etching and subsequently crystallized during calcination.[16] Although sodium titanate has a number of applications, its photocatalytic activity is considerably lower than that of anatase phase titania, and therefore it is not a desirable phase in our synthesis. Also, the anatase domains grow quickly at high calcination temperatures and then lead to a partial transformation to the rutile phase.[12a,12b] In a reversed process where SiO$_2$@TiO$_2$ was firstly calcined at 500 °C before etching of the silica, the final product (TiO$_2$-C-E-500) exhibited a well-crystallized anatase structure in XRD analysis (Figure 2e) but did

ADVANCED
FUNCTIONAL
MATERIALS
www.afm-journal.de

www.MaterialsViews.com

FULL PAPER

Table 1. Notations, preparation conditions, and crystalline phases of TiO$_2$ samples synthesized in this work.

Sample notation	Preparation conditions	Calcination temperature	Crystalline Phase
TiO$_2$-E	Etching of SiO$_2$ from SiO$_2$@TiO$_2$	-	Amorphous
TiO$_2$-E-C-500	Etching of SiO$_2$ from SiO$_2$@TiO$_2$, then calcination	500 °C	Amorphous
TiO$_2$-E-C-800	Etching of SiO$_2$ from SiO$_2$@TiO$_2$, then calcination	800 °C	Mixture of sodium titnate, rutile and anatase
TiO$_2$-C-E-500	Calcination using SiO$_2$@TiO$_2$, then etching of SiO$_2$	500 °C	Anatase
TiO$_2$-SPC-500	Silica protected calcination of SiO$_2$@TiO$_2$@SiO$_2$, then etching of silica	500 °C	Amorphous
TiO$_2$-SPC-650	Silica protected calcination of SiO$_2$@TiO$_2$@SiO$_2$, then etching of silica	650 °C	Anatase
TiO$_2$-SPC-800	Silica protected calcination of SiO$_2$@TiO$_2$@SiO$_2$, then etching of silica	800 °C	Anatase
TiO$_2$-SPC-900	Silica protected calcination of SiO$_2$@TiO$_2$@SiO$_2$, then etching of silica	900 °C	Anatase

not maintain the hollow sphere morphology after calcination and etching. As shown in the TEM image in Figure 2d, more than half of the particles were broken into smaller pieces. This morphology loss is most likely due to the significant structural rearrangement in the TiO$_2$ shells associated with the extensive crystallization and grain growth during calcination.

The "silica-protected calcination" process proposed here not only addresses the above challenges but also brings additional benefits towards photocatalytic applications. **Figure 3** shows the schematic outline of the procedure and the corresponding TEM images of the particles at each step. The major change we introduced into this process is the deposition of an additional silica layer on the titania surface. Calcination of the SiO$_2$@TiO$_2$@SiO$_2$ composites followed by chemical etching produces well-defined hollow spheres containing mesoscale pores in shells which can be easily observed by TEM imaging (Figure 3d). Apparently, the outer silica layer protects the TiO$_2$ shell from breakage even during calcination at high temperatures (e.g., 800 and 900 °C).

In order to investigate the crystallization process, we carried out an XRD study on SiO$_2$@TiO$_2$@SiO$_2$ core-shell composites calcined at different temperatures. Because silica remains amorphous at the calcination temperatures used in this work, the change in the diffraction peaks closely relates to the crystalline phase transition of the TiO$_2$. As shown in **Figure 4**, SiO$_2$@TiO$_2$@SiO$_2$ particles calcined at 400 °C and 500 °C show a broad peak between 20° and 35°, indicating amorphous phases for both silica and titania. XRD peaks corresponding to anatase TiO$_2$ start to emerge when the samples are calcined at 650 °C, and are further enhanced at 800 °C. For the sample calcined at 900 °C, a number of characteristic peaks for anatase TiO$_2$, especially those at $2\theta = 25$ and 48°, which correspond to the (101) and (200) crystal planes, respectively, can be clearly identified. On the other hand, the diffraction peaks still remain broad compared to those prepared by conventional calcination methods (for example, TiO$_2$-C-E-500), suggesting that the anatase grains remain relatively small when the silica protecting layer is used even after high-temperature treatment.[1c,6a,17]

In a simple calcination scheme (without additional silica protection), TiO$_2$ crystallization and subsequent grain growth can readily occur at ~500 °C, as can be seen in Figure 2d. However, with the protection of an outer silica layer, the crystallization of amorphous TiO$_2$ becomes difficult at the same calcination temperature; higher temperatures, up to ~900 °C, were required for

this transformation. On the other hand, it is generally agreed that bulk anatase TiO$_2$ transforms to the rutile phase in the temperature range of 600~700 °C, but even though in this work the silica-protected samples were treated at high temperatures, e.g., 900 °C, the anatase crystalline structure was still retained, and no obvious rutile structure was observed. This result suggests that the outer silica layer on the TiO$_2$ surface inhibits both phase transformations of TiO$_2$ from amorphous to anatase and from anatase to rutile. Zhu et al. have reported a similar phenomenon in which a commercial titania photocatalyst P25 coated with graphitic-like carbon requires a higher calcination temperature than bare P25 to convert to the rutile phase.[18] It was suggested there that the outer carbon shells may act as barriers and inhibit the phase transformation of anatase to rutile, thus leading to the higher thermal stability of the anatase phase. Although the exact mechanism for the inhibiting effect of the silica protection needs to be explored more carefully in future studies, we would like to advance the following hypothesis. Similar to colloidal silica, the sol–gel derived TiO$_2$ layer contains micropores typically below two nanometers in diameter. It may therefore be possible for silicate species to penetrate into these pores and condense there during the addition of the outer protective silica coating. The resulting silica nanostructures may then act as barriers, preventing the extensive structural reorganization and growth of the amorphous titania into large crystals during calcination. This behavior may result in smaller anatase grains than those produced at the same temperature but without silica protection. This same hindrance may also interfere with the phase transformation from anatase to rutile, during which structural reorganization is also needed. In addition, it is known that the anatase-to-rutile transformation occurs rapidly only when the anatase grains are above a critical size of ~14 nm.[1d,12a,b] As the growth of anatase crystals during calcination is limited by silica protection, they may not reach this critical size, so that the transformation to rutile phase is kinetically forbidden even at a significantly high calcination temperature, e.g., 900 °C.

After calcination, the outer and inner silica are removed by treatment in a concentrated NaOH solution to produce hollow TiO$_2$ structures. Compared to untreated SiO$_2$@TiO$_2$ core–shell particles, which can be easily etched using 1 mL of 2.5 M NaOH solution for ~6 h (Figure 2a), the calcined silica has a significantly enhanced degree of condensation of the Si–O–Si bonds so that a much longer time is needed to remove
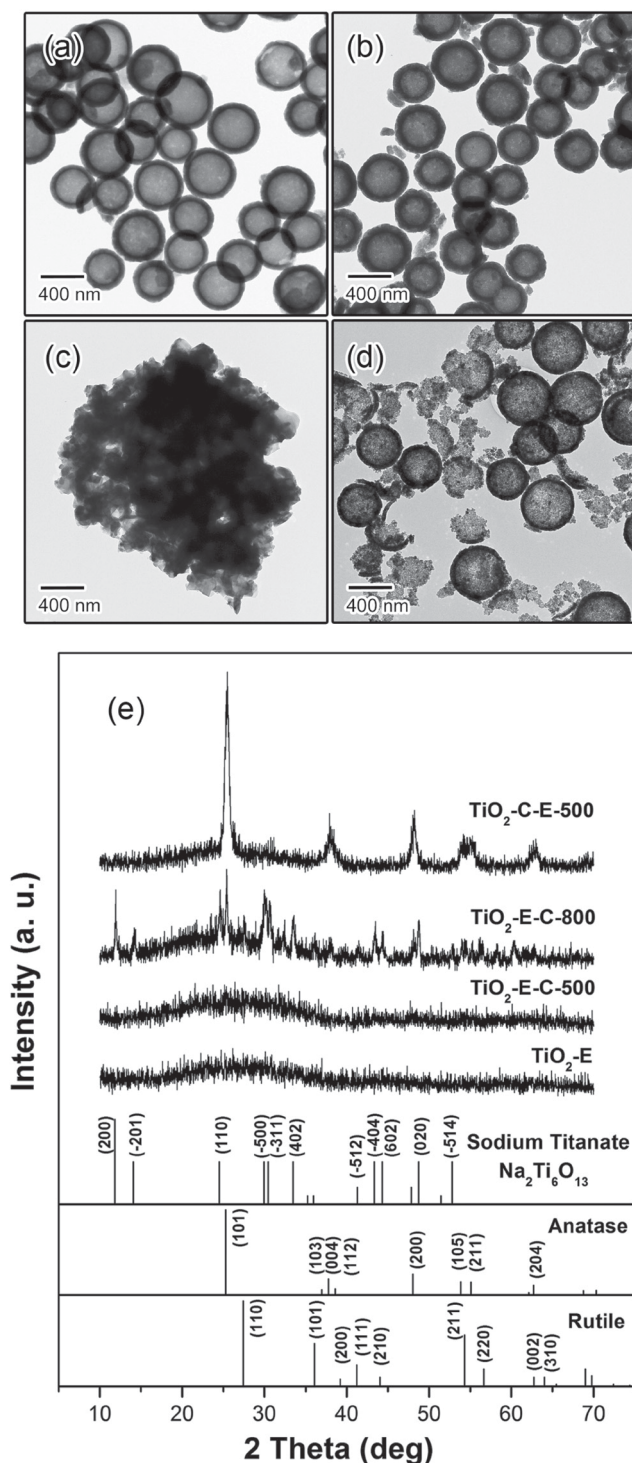
www.MaterialsViews.com

**ADVANCED
FUNCTIONAL
MATERIALS**
www.afm-journal.de

FULL PAPER

Figure 2. TEM images (a–d) and X-ray diffraction (XRD) patterns (e) showing that the TiO$_2$ samples prepared under various simple etching and calcination conditions cannot be converted to the anatase phase while still retaining a well-defined shell structure. All the samples were started from SiO$_2$@TiO$_2$ core–shell structures. Sample TiO$_2$-E (a) was produced by selective etching of SiO$_2$ by NaOH. Samples TiO$_2$-E-C-500 (b) and TiO$_2$-E-C-800 (c) were prepared by selective etching of SiO$_2$ followed by calcination at 500 °C and 800 °C, respectively. Sample TiO$_2$-C-E-500 (d) was synthesized by first calcining at 500 °C and then etching in NaOH solution.
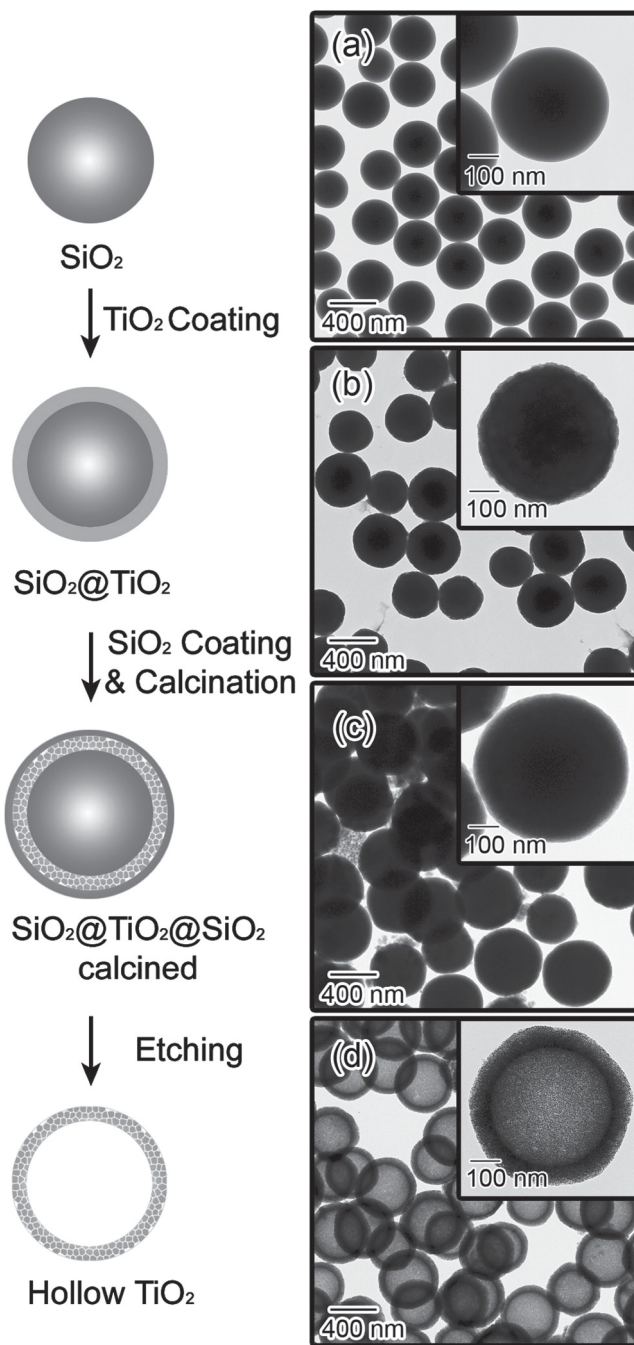
Figure 3. Left: Schematic illustration of our silica-protected calcination procedure developed for the fabrication of mesoporous anatase TiO$_2$ hollow spheres. Right: corresponding TEM images of the products at each step: a) SiO$_2$, b) SiO$_2$@TiO$_2$, c) SiO$_2$@TiO$_2$@SiO$_2$ after calcination and d) final hollow TiO$_2$ after the removal of the SiO$_2$. In this case, the TiO$_2$ coating was repeated three times to achieve a shell thickness of ~50 nm.

the inner and outer silica completely. As shown in **Figure 5**, it takes ~72 h to completely remove the silica from the SiO$_2$@TiO$_2$@SiO$_2$ composites calcined at 400 °C using 1 mL of 2.5 M NaOH at ambient temperature. For samples calcined at higher temperatures (500–900 °C), etching becomes even slower. As

Figure 4. XRD patterns of SiO$_2$@TiO$_2$@SiO$_2$ samples after calcination at different temperatures for 2 hours: a) 400 °C, b) 500 °C, c) 650 °C, d) 800 °C, and e) 900 °C.

Figure 5. TEM images of SiO$_2$@TiO$_2$@SiO$_2$ samples after calcination at different temperatures for 2 h and then base etching at ambient conditions for 72 h: a) 400 °C, b) 500 °C, c) 650 °C, d) 800 °C, and e) 900 °C.

a result, a larger portion of the silica core remaines after treatment in NaOH solution for the same amount of time (~72 h), producing yolk–shell morphologies. The sample calcined at 900 °C is so stable that no apparent etching is seen in the silica core after etching.
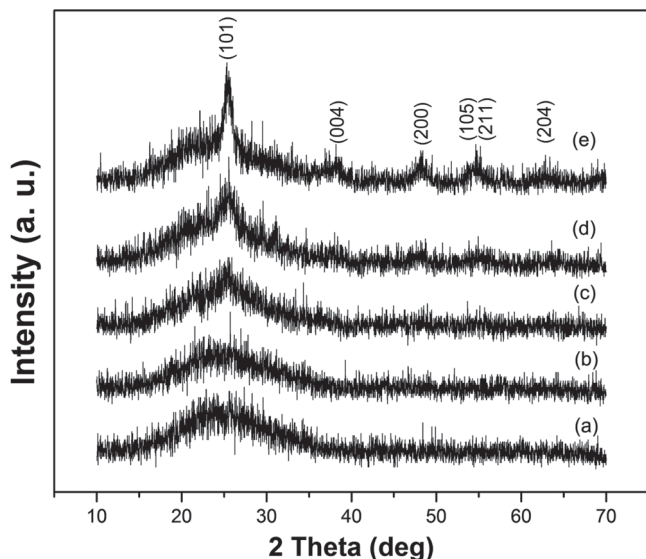
The etching rate can be increased by raising the temperature of the etching solution. In **Figure 6**, the etching time required for complete removal of the silica from a SiO$_2$@TiO$_2$@SiO$_2$ sample calcined at 800 °C is plotted as a function of etching temperature. When etching was carried out at room temperature, it took more than 72 h to obtain hollow TiO$_2$ samples. When the temperature of the solution was increased to 40, 55, 70, 85 and 100 °C, the etching time was dramatically reduced, to ~42, 10, 6, 1 and 0.5 h, respectively. The improved etching rates make this silica-protected etching process practical for large-scale production.

Etching at elevated temperatures does not destruct the morphology of the final products. **Figure 7** shows the morphology evolution of the SiO$_2$@TiO$_2$@SiO$_2$ sample calcined at 800 °C during the etching of silica at 70 °C for 6 h. After the initial 30 min of etching, the outer silica layer was completely removed, and the inner silica was partially etched as evidenced by a small gap between inner silica core and the TiO$_2$ shell (Figure 7a). Continued etching led to gradual dissolution of the inner silica core, producing yolk-shell, and eventually hollow structures (Figure 7b–d). With a titania shell thickness of ~45–55 nm, the TiO$_2$ hollow spheres clearly show mesoscale disordered pores (inset in Figure 7d).

XRD was used to monitor the crystal structure of the TiO$_2$-SPC-800 samples before and after chemical etching. As shown in Figure 7e, upon removal of the silica, the anatase (101) and (200) peaks at 2θ = 25 and 48° become more discernable while the intensity of the broad peak of amorphous silica in the 2θ range of 20 to 30° is reduced. The average crystal sizes of the

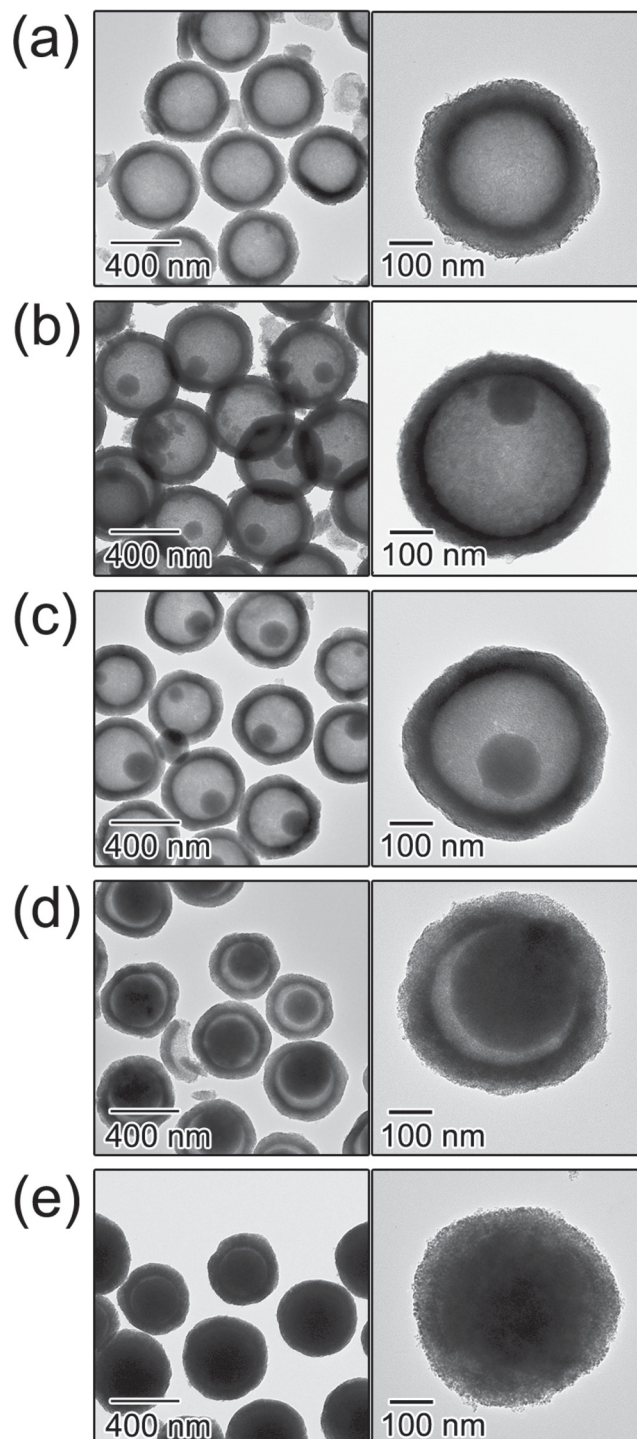TiO$_2$ were estimated using Scherrer's formula to be around 4.1 and 4.9 nm for the samples prepared at 800 and 900 °C, respectively.[19]

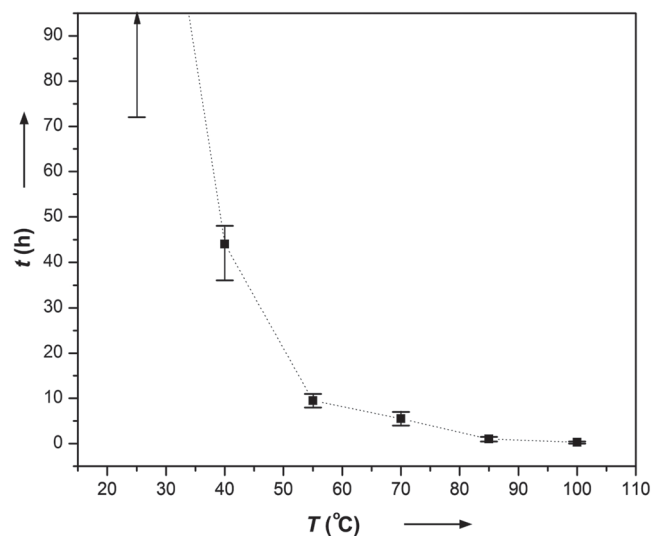Figure 7f shows the nitrogen adsorption–desorption isotherm and the corresponding pore size distribution for

www.MaterialsViews.com

ADVANCED
FUNCTIONAL
MATERIALS
www.afm-journal.de

FULL PAPER

Figure 6. Temperature (*T*) dependence of etching time (*t*) needed for complete removal of SiO_2 from $SiO_2@TiO_2@SiO_2$ particles calcined at 800 °C.

TiO$_2$-SPC-800. The hollow TiO$_2$-SPC-800 displays a Type IV isotherm with a well-defined hysteresis loop indicating well-developed mesoporous characteristics. The sharp peak at ~2.6 nm

in the Barrett-Joyner-Halenda (BJH) pore size distribution analysis suggests a relatively narrow pore size distribution (inset in Figure 7f). The Brunauer–Emmett–Teller (BET) surface area of TiO$_2$-SPC-800 was found to be ~311 m^2 g^{-1}, a considerably high value for crystalline titania.[7c,7d] The TiO$_2$-SPC-500 sample shows a comparable high surface area, ~295 m^2 g^{-1}, consistent with the fact that calcination at higher temperatures causes minimal grain growth in this "silica-protected calcination" scheme. These surface area values are much higher than those of anatase phase catalysts prepared by conventional synthesis methods or P25 (ca. 50~60 m^2 g^{-1}), a commercially used TiO$_2$ photocatalyst.[1d]

The photocatalytic properties of the mesoporous anatase hollow microspheres were studied and contrasted to those of control samples by carrying out chronoamperometry (CA) measurements under an inducing potential of 0.8 V (vs. Ag/AgCl) and a periodic irradiation of UV light. As shown in **Figure 8**, the photogenerated current, which is closely related to the degree of charge separation during the photocatalysis and correlated to the photocatalytic activity,[1c,3b] were recorded in these experiments. Without light exposure, all samples showed only a small electrochemical current. When they were irradiated by UV light, however, the current density increased due to the contribution from photogenerated electrons. For a series of samples tested, we found the following relative order of photogenerated
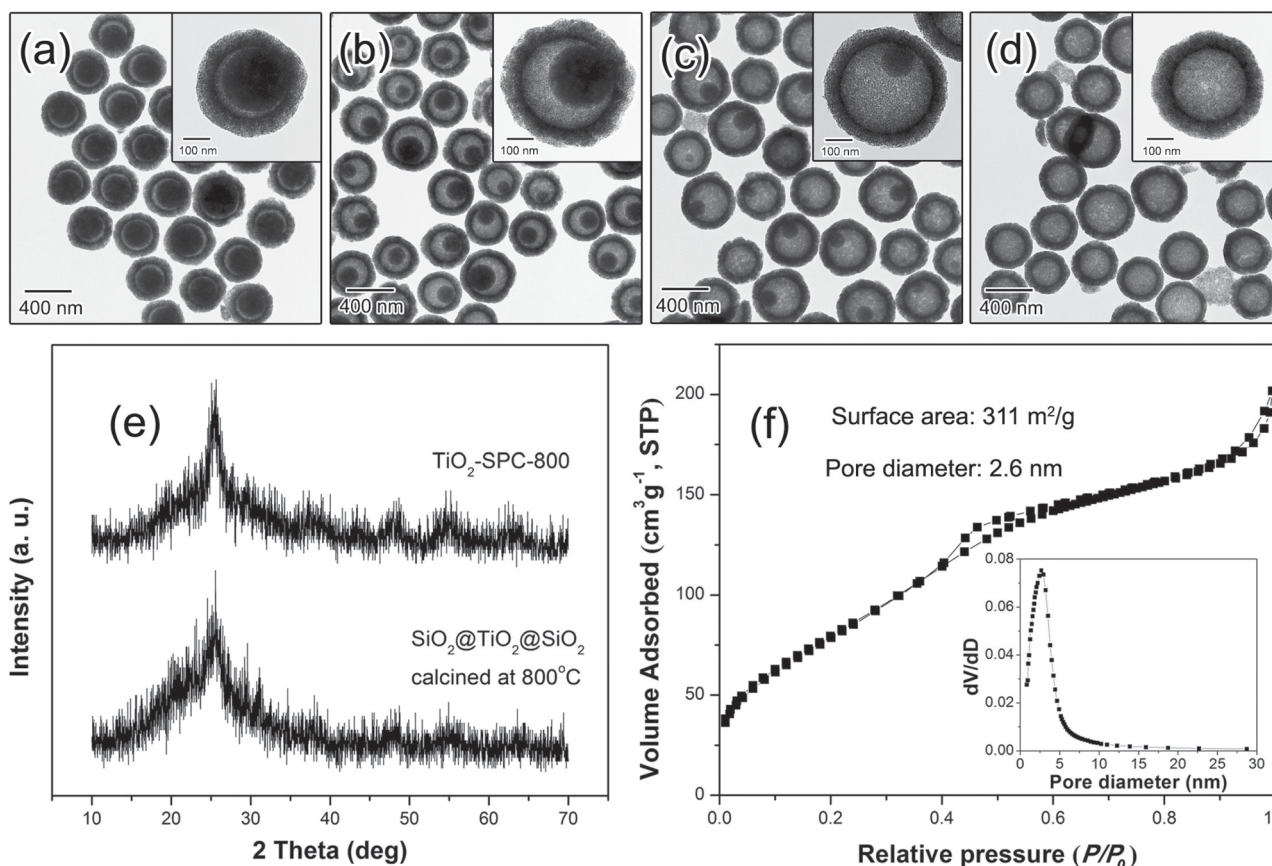
Figure 7. a–d) TEM images showing the morphology evolution of $SiO_2@TiO_2@SiO_2$ samples calcined at 800 °C after base etching at 70 °C for different time periods: a) 30 min, b) 2 h, c) 4 h, and d) 6 h. e) XRD patterns showing the crystallinity of the products before and after the removal of the SiO_2. f) Nitrogen adsorption isotherm from the final mesoporous TiO$_2$-SPC-800 hollow shells, showing a considerably higher surface area compared to that for TiO$_2$ shells produced without silica protected calcination (several m^2 g^{-1} in average).

ADVANCED
FUNCTIONAL
MATERIALS
www.afm-journal.de

FULL PAPER

Materials
Views
www.MaterialsViews.com

Figure 8. Photoelectrochemical chronoamperometry results from experiments using the TiO₂ samples employed in this work; a) TiO$_2$-E-C-500, b) TiO$_2$-E-C-800, c) TiO$_2$-SPC-500, d) TiO$_2$-SPC-650, e) TiO$_2$-SPC-800, and f) TiO$_2$-SPC-900.

current density: TiO$_2$-SPC-900 > TiO$_2$-SPC-800 > TiO$_2$-SPC-650 > TiO$_2$-E-C-800 ≈ TiO$_2$-SPC-500 > TiO$_2$-E-C-500. As expected, the amorphous TiO$_2$ shells obtained after low temperature calcination, including both TiO$_2$-E-C-500 and TiO$_2$-SPC-500, showed very low photogenerated current. The TiO$_2$-E-C-800 sample, prepared by selective etching of SiO$_2$ and then calcination at 800 °C, also exhibited low photocatalytic activity, mainly due to the presence of mixed phases, collapse of the shell structure, and the formation of large aggregates. On the other hand, the mesoporous hollow microspheres prepared by silica-protected calcination and subsequent etching showed significantly higher photogenerated current under UV irradiation. The shapes and current densities of TiO$_2$-SPC-x samples could be maintained after many cycles of light irradiation, implying excellent stability of photocatalytic activity. As pointed out earlier, TiO$_2$ materials with high crystallinity are advantageous for the genera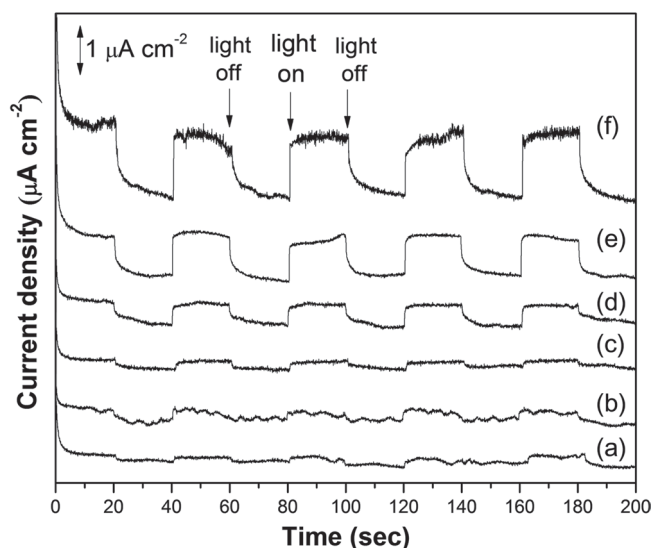tion and migration of photogenerated electrons/holes. This conclusion has been directly confirmed by the results in Figure 8, which shows a great enhancement in photogenerated current for samples calcined at higher temperatures: as the TiO$_2$-SPC-900 sample has the highest degree of crystallinity among all the mesoporous hollow spheres (Figure 4), it generates the highest photocurrent density under UV irradiation.

The photocatalytic activity of our crystalline titania shell samples was further evaluated by monitoring the degradation of Rhodamine B (RhB) under UV light. **Figure 9**a shows typical adsorption spectra for an aqueous RhB solution after UV irradiation for various time periods using TiO$_2$-SPC-800 as the catalyst. The strong adsorption peak at ~553 nm gradually decreased and finally completely disappeared after 70 min, indicating the complete photodegradation of RhB molecules. The performance of the relevant photocatalysts toward RhB degradation, measured by following the intensity of the 553 nm peak versus time, is summarized in Figure 9b. Before UV illumination,
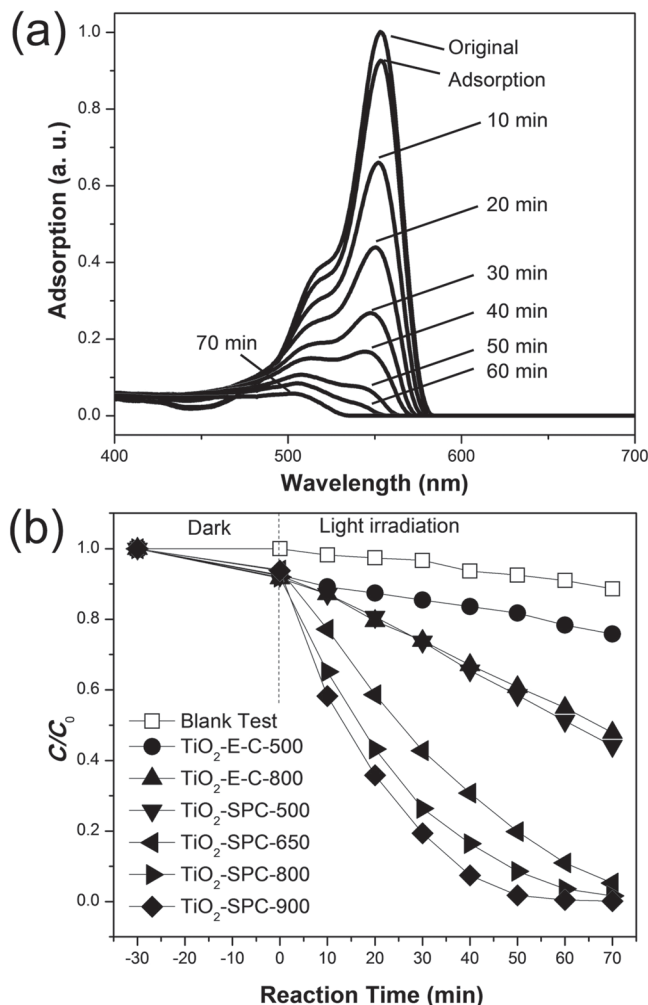
Figure 9. a) UV–vis adsorption spectra showing UV-degradation of RhB using the TiO$_2$-SPC-800 catalyst. b) Evolution of RhB concentration versus UV irradiation time (t) in the presence of different TiO$_2$ catalysts.

the mixtures containing the catalysts and RhB were stirred in the dark for 30 min to ensure that RhB was adsorbed to saturation on the surface of catalysts; all the catalysts have similar adsorption capacity in the range of 7~8% of C/C$_0$ of RhB. In the blank experiment (without catalyst) only ~12% of C/C$_0$ of RhB molecules were decomposed after UV irradiation for 70 min, but the degradation rates were significantly enhanced in the presence of the photocatalysts. In particular, the RhB molecules can be completely decomposed in the presence of the TiO$_2$-SPC-900 catalyst after only 60 min of irradiation with UV light. The relative photocatalytic activity of the catalysts for RhB degradation follows the order: TiO$_2$-SPC-900 > TiO$_2$-SPC-800 > TiO$_2$-SPC-650 > TiO$_2$-SPC-500 ≈ TiO$_2$-E-C-800 > TiO$_2$-E-C-500. Consistent with the chronoamperometry studies, the mesoporous hollow anatase microspheres prepared by calcination at higher temperatures display enhanced activity because of their improved crystallinity. In addition, TiO$_2$-SPC-800 shows a higher catalytic activity than TiO$_2$-E-C-800, supporting the conclusion that the silica-protected etching process can allow crystallization into the anatase phase and create high porosity while

www.MaterialsViews.com

ADVANCED
FUNCTIONAL
MATERIALS
www.afm-journal.de

FULL PAPER

suppressing further grain growth. The fact that TiO$_2$-SPC-500 performed better than TiO$_2$-E-C-500 is also consistent with the higher surface area associated with samples produced by silica-protected calcination.

It has been well understood that higher activity can be achieved by improving many aspects of TiO$_2$-based photocatalysts, including surface area, crystallinity, adsorption ability, nonmetal doping, and water dispersity.[1d,11] Besides the advantage of creating well-crystallized anatase mesoporous structures with a high surface area, the silica-protected calcination strategy also brings the additional benefit of excellent water dispersibility. In our prior work, silica protection followed by calcination and chemical etching was shown to enhance the water dispersity of the calcined materials.[20] First, the silica coating protects the particles from aggregation during calcination. Even though slight interparticle aggregation may occur due to silica fusion at high temperatures (~700–900 °C), the subsequent etching by NaOH removes the silica layer and releases the TiO$_2$ shells. Second, the etching process introduces a relatively high density of hydroxyl groups so that the TiO$_2$ surface becomes negatively charged, rendering the shells highly dispersible in water. The mesoporous anatase shells prepared by silica protected calcination and subsequent etching show better dispersibility than other TiO$_2$ samples, such as TiO$_2$-E-C-500 or TiO$_2$-E-C-800, whose surface hydroxyl groups are partially removed during direct calcination of the TiO$_2$ surface in air. It is believed that the high water dispersibility also contributes considerably to the enhanced photocatalytic performance of the mesoporous anatase shells.

3. Conclusions

We have developed a new silica-protected calcination process for the synthesis of mesoporous hollow TiO$_2$ nanostructures containing small crystalline anatase grains, and further explored their improved performance in photocatalysis. The synthesis involves the sol-gel coating of colloidal silica with a TiO$_2$ layer, an additional coating with an outer silica layer, thermal treatment at high temperature to transform the amorphous TiO$_2$ to the anatase phase, and a final etching step of the inner and outer silica to yield hollow TiO$_2$ shells consisting of small anatase grains. The outer silica layer allows the amorphous-anatase transformation to occur but at the same time inhibits the growth of the anatase into large grains, therefore limiting the phase transformation from anatase to rutile during calcination at high temperatures (up to 900 °C). Subsequent etching generates mesoporous hollow TiO$_2$ shells with small anatase grains of controllable crystallinity, a high surface area, and excellent dispersity in water. Combining these features, the as synthesized mesoporous TiO$_2$ shells show significantly enhanced photocatalytic activity towards the degradation of organic molecules such as RhB, with greater enhancement for samples calcined at higher temperatures due to their improved crystallinity. We believe the silica-protected calcination strategy represents a very powerful method for controlling the crystallinity and porosity of TiO$_2$ photocatalysts and for improving photocatalytic activity.

4. Experimental Section

SiO$_2$ Particle Synthesis: Tetraethyl orthosilicate (TEOS, 99%, 0.86 mL) was mixed with de-ionized water (4.3 mL), ethanol (23 mL) and an aqueous solution of ammonia (26%, 0.62 mL). After stirring for 6 h at room temperature, the precipitated silica particles were separated by centrifugation and washed 3 times with ethanol, then re-dispersed in 5 mL of ethanol under sonication.

TiO$_2$ Coating: The SiO$_2$ particles were dispersed in a mixture of hydroxypropyl cellulose (HPC, 0.1 g), ethanol (20 mL), and de-ionized water (0.1 mL). After stirring for 30 min, titanium tert-butoxide (TBOT, 1 mL) in 5 mL ethanol was injected into the mixture using a syringe pump at a rate of 0.5 mL min^{-1}. After injection, the temperature was increased to 85 °C at 900 rpm stirring under refluxing conditions for 100 min. The precipitate was isolated using centrifugation, washed with ethanol, and re-dispersed in 5 mL of ethanol to give SiO$_2$@TiO$_2$ composites. In order to increase the thickness of the TiO$_2$ layer, the above coating procedure was repeated multiple times.

SiO$_2$ Coating: Above SiO$_2$@TiO$_2$ particles were separated from their ethanol solution, dispersed in 20 mL of water, treated with polyvinylpyrrolidone (PVP, Mw ~ 40000, 0.2 g) overnight to allow for the adsorption of PVP onto the TiO$_2$ surface, separated from solution by centrifugation, and then re-dispersed in 10 mL ethanol. The solution of SiO$_2$@TiO$_2$ was sequentially mixed with ethanol (13 mL), water (4.3 mL), TEOS (0.86 mL) and aqueous ammonia (28%, 0.62 mL). After stirring for 4 h, the resulting SiO$_2$@TiO$_2$@SiO$_2$ particles were centrifuged, washed 3 times with ethanol and dried under vacuum.

Calcination and SiO$_2$ Etching: The SiO$_2$@TiO$_2$@SiO$_2$ was calcined in air at the desired temperature for 2 h to remove all organic compounds and crystallize the amorphous TiO$_2$. Then the calcined samples were dispersed in 20 mL water under sonication and heated to the desired temperature (≤100 °C). An aqueous NaOH solution (2.5 M, 1 mL) was added to the above solution. After etching for various periods, the hollow TiO$_2$ particles (TiO$_2$-SPC-x, where x is calcination temperature) were finally isolated by centrifugation and washed 5 times with de-ionized water.

Control Experiments: After TiO$_2$ coating, SiO$_2$@TiO$_2$ particles were etched with an aqueous NaOH solution for 6 h to produce amorphous hollow TiO$_2$ (TiO$_2$-E), and then calcined at 500 °C and 800 °C for 2 h to yield samples of TiO$_2$-E-C-500 and TiO$_2$-E-C-800, respectively. In addition, SiO$_2$@TiO$_2$ particles were calcined first at 500 °C for 2h and then etched with NaOH solution at 70 °C to remove SiO$_2$ and produce sample TiO$_2$-C-E-500.

Characterization: The morphology of the samples was assessed using transmission electron microscopy (TEM, Tecnai T12). The crystalline structures were evaluated by X-ray diffraction (XRD) analysis using a Bruker D8 Advance Diffractometer with Cu Kα radiation ($\lambda = 1.5406$ Å). Nitrogen adsorption isotherms were obtained at 77 K using a nitrogen sorption instrument (Micromeritics ASAP 2010). Pore size distributions were calculated by the BJH method using the adsorption branches of the isotherm.

Photoelectrochemical and Photocatalytic Activity Tests: Photoelectrochemical analyses were carried out using a standard three-electrode cell with Ag/AgCl as the reference electrode and Pt wire as the counter electrode. The working electrode was prepared by deposition of a TiO$_2$ slurry (0.4 mg) on ITO glass (1 cm × 1 cm). An aqueous Na$_2$SO$_4$ (0.1 mol L^{-1}) solution containing RhB (1 × 10^{-5} mol L^{-1}) was used as the electrolyte. Chronoamperometry tests were conducted using a potentiostat (VersaSTAT 4, Princeton Applied Research). Photocatalytic activity testing on the degradation of RhB was carried out in a 100 mL beaker containing 50 mL of 2 × 10^{-5} mol L^{-1} RhB and 10 mg of catalyst under 400 rpm stirring at room temperature. Before the photocatalytic reaction was initiated, as-synthesized catalysts were firstly irradiated with UV light for 30 min to remove any residual organic compounds. A 15 W UV lamp (254 nm, XX-15G, USA) was used as the UV light source. The concentration of RhB was measured by UV-Vis spectrophotometry (HR2000CG-UV-NIR, Ocean Optics) at 10 min intervals during reaction.

FULL PAPER

Supporting Information

Supporting Information is available from the Wiley Online Library or from the author.

Acknowledgements

[1] a) H. G. Moon, Y.-S. Shim, H. W. Jang, J.-S. Kim, K. J. Choi, C.-Y. Kang, J.-W. Choi, H.-H. Park, S.-J. Yoon, *Sens. Actuators B* **2010**, *149*, 116–121; b) J. E. G. J. Wijnhoven, W. L. Vos, *Science* **1998**, *281*, 802–804; c) H. J. Yun, H. Lee, J. B. Joo, W. Kim, J. Yi, *J. Phys. Chem. C* **2009**, *113*, 3050–3055; d) Q. Zhang, J.-B. Joo, Z. Lu, M. Dahl, D. Oliveira, M. Ye, Y. Yin, *Nano Res.* **2011**, *4*, 103–114; e) B. O'Regan, M. Gratzel, *Nature* **1991**, *353*, 737–740.

[2] A. Fujishima, K. Honda, *Nature* **1972**, *238*, 37–38.

[3] a) X. W. Lou, C. M. Li, L. A. Archer, *Adv. Mater.* **2009**, *21*, 2536–2539; b) H. J. Yun, H. Lee, J. B. Joo, N. D. Kim, J. Yi, *Electrochem. Commun.* **2010**, *12*, 769–772; c) H. J. Yun, H. Lee, J. B. Joo, N. D. Kim, M. Y. Kang, J. Yi, *Appl. Catal. B: Environmental* **2010**, *94*, 241–247; d) A. Kudo, Y. Miseki, *Chem. Soc. Rev.* **2009**, *38*, 253–278.

[4] K. Maeda, K. Domen, *J. Phys. Chem. C* **2007**, *111*, 7851–7861.

[5] a) J. Augustynski, *Electrochim. Acta* **1993**, *38*, 43–46; b) A. L. Linsebigler, G. Lu, J. T. Yates, *Chem. Rev.* **1995**, *95*, 735–758; c) M. A. Fox, M. T. Dulay, *Chem. Rev.* **1993**, *93*, 341–357; d) A. Fujishima, X. Zhang, D. A. Tryk, *Surf. Sci. Rep.* **2008**, *63*, 515–582.

[6] a) B. Wu, C. Guo, N. Zheng, Z. Xie, G. D. Stucky, *J. Am. Chem. Soc.* **2008**, *130*, 17563–17567; b) H. G. Yang, C. H. Sun, S. Z. Qiao, J. Zou, G. Liu, S. C. Smith, H. M. Cheng, G. Q. Lu, *Nature* **2008**, *453*, 638–641; c) T. J. Trentler, T. E. Denler, J. F. Bertone, A. Agrawal, V. L. Colvin, *J. Am. Chem. Soc.* **1999**, *121*, 1613–1614.

[7] a) J. Ye, W. Liu, J. Cai, S. Chen, X. Zhao, H. Zhou, L. Qi, *J. Am. Chem. Soc.* **2010**, *133*, 933–940; b) H. Li, Z. Bian, J. Zhu, D. Zhang, G. Li, Y. Huo, H. Li, Y. Lu, *J. Am. Chem. Soc.* **2007**, *129*, 8406–8407;

c) X. Liu, Y. Gao, C. Cao, H. Luo, W. Wang, *Langmuir* **2010**, *26*, 7671–7674; d) D. Chen, L. Cao, F. Huang, P. Imperia, Y.-B. Cheng, R. A. Caruso, *J. Am. Chem. Soc.* **2010**, *132*, 4438–4444.

[8] a) J. Lee, M. Christopher Orilall, S. C. Warren, M. Kamperman, F. J. DiSalvo, U. Wiesner, *Nat. Mater.* **2008**, *7*, 222–228; b) Y. Tanaka, M. Suganuma, *J. Sol–Gel Sci. Technol.* **2001**, *22*, 83–89; c) M. Bockmeyer, P. Löbmann, *Chem. Mater.* **2006**, *18*, 4478–4485.

[9] a) K. Kamata, Y. Lu, Y. Xia, *J. Am. Chem. Soc.* **2003**, *125*, 2384–2385; b) H. Sakai, T. Kanda, H. Shibata, T. Ohkubo, M. Abe, *J. Am. Chem. Soc.* **2006**, *128*, 4944–4945; c) Z. Yang, Z. Niu, Y. Lu, Z. Hu, C. C. Han, *Angew. Chem. Int. Ed.* **2003**, *42*, 1943–1945; d) P. Wang, D. Chen, F.-Q. Tang, *Langmuir* **2006**, *22*, 4832–4835; e) W. Li, M.-O. Coppens, *Chem. Mater.* **2005**, *17*, 2241–2246; f) T. H. Kim, K. H. Lee, Y. K. Kwon, *J. Colloid Interface Sci.* **2006**, *304*, 370–377.

[10] a) X. Li, Y. Xiong, Z. Li, Y. Xie, *Inorg. Chem.* **2006**, *45*, 3493–3495; b) S. Ding, J. S. Chen, Z. Wang, Y. L. Cheah, S. Madhavi, X. Hu, X. W. Lou, *J. Mater. Chem.* **2011**, *21*, 1677–1680; c) S. Liu, J. Yu, S. Mann, *Nanotechnology* **2009**, *20*, 325606; d) X. W. Lou, L. A. Archer, *Adv. Mater.* **2008**, *20*, 1853–1858; e) X. W. Lou, L. A. Archer, Z. Yang, *Adv. Mater.* **2008**, *20*, 3987–4019; f) J. S. Chen, D. Luan, C. M. Li, F. Y. C. Boey, S. Qiao, X. W. Lou, *Chem. Commun.* **2010**, *46*, 8252–8254.

[11] M. Ye, Q. Zhang, Y. Hu, J. Ge, Z. Lu, L. He, Z. Chen, Y. Yin, *Chem.–Eur. J.* **2010**, *16*, 6243–6250.

[12] a) Y. Hu, H. L. Tsai, C. L. Huang, *Mater. Sci. Eng. A* **2003**, *344*, 209–214; b) H. Zhang, J. F. Banfield, *J. Mater. Chem.* **1998**, *8*, 2073–2076; c) A. R. Phani, S. Santucci, *J. Phys.: Condens. Matter* **2006**, *18*, 6965–6978.

[13] Y. Piao, J. Kim, H. B. Na, D. Kim, J. S. Baek, M. K. Ko, J. H. Lee, M. Shokouhimehr, T. Hyeon, *Nat. Mater.* **2008**, *7*, 242–247.

[14] W. Stöber, A. Fink, E. Bohn, *J. Colloid Interface Sci.* **1968**, *26*, 62-69.

[15] a) Q. Zhang, D. Q. Lima, I. Lee, F. Zaera, M. Chi, Y. Yin, *Angew. Chem. Int. Ed.* **2011**, *123*, 7226–7230; b) I. Lee, J. B. Joo, Y. Yin, F. Zaera, *Angew. Chem., Int. Ed.* **2011**, DOI: 10.1002/anie.201007660; c) M. Ye, S. Zorba, L. He, Y. Hu, R. T. Maxwell, C. Farah, Q. Zhang, Y. Yin, *J. Mater. Chem.* **2010**, *20*, 7965–7969.

[16] a) D. Wei, Y. Zhou, Y. Wang, D. Jia, *Thin Solid Films* **2008**, *516*, 1818–1825; b) E. Conforto, D. Caillard, L. Müller, F. A. Müller, *Acta Biomaterialia* **2008**, *4*, 1934–1943; c) J. Ramírez-Salgado, E. Djurado, P. Fabry, *J. Eur. Ceram. Soc.* **2004**, *24*, 2477–2483.

[17] F. Zuo, L. Wang, T. Wu, Z. Zhang, D. Borchardt, P. Feng, *J. Am. Chem. Soc.* **2010**, *132*, 11856–11857.

[18] L.-W. Zhang, H.-B. Fu, Y.-F. Zhu, *Adv. Funct. Mater.* **2008**, *18*, 2180–2189.

[19] J. Zhong, F. Chen, J. Zhang, *J. Phys. Chem. C* **2009**, *114*, 933–939.

[20] a) Z. Lu, M. Ye, N. Li, W. Zhong, Y. Yin, *Angew. Chem. Int. Ed.* **2010**, *49*, 1862–1866; b) Z. Lu, J. Duan, L. He, Y. Hu, Y. Yin, *Anal. Chem.* **2010**, *82*, 7249–7258.

Mechanistic Considerations of Bending-Strain Effects within Organic Semiconductors on Polymer Dielectrics

Anatoliy N. Sokolov, Yadong Cao, Olasupo B. Johnson, and Zhenan Bao*

The development of organic transistors for flexible electronics requires the understanding of device behavior upon the application of strain. Here, a comprehensive study of the effect of polymer-dielectric and semiconductor chemical structure on the device performance under applied strain is reported. The systematic change of the polymer dielectric results in the modulation of the effects of strain on the mobility of organic field-effect transistor devices. A general method is demonstrated to lower the effects of strain in devices by covalent substitution of the dielectric surface. Additionally, the introduction of a hexyl chain at the peripheries of the organic semiconductor structure results in an inversion of the effects of strain on device mobility. This novel behavior may be explained by the capacitive coupling of the surface energy variations during applied strain.

1. Introduction

The development of flexible electronics based on organic materials is an important goal in the context of radio frequency identification tags (RFID),[1,2] photovoltaics (PV),[3,4] memory,[5] and sensors.[6–12] The utilization of organic materials takes advantage of low-temperature, solution-based techniques allowing for integration of electronic materials onto flexible substrates.[13–15] This integration is expected to enable both novel applications, as well as facile, and cheap manufacturing techniques (i.e., printing).[16–18] Much research, thus far, has focused on the development of flexible materials to enable the light-emitting component of flexible displays, or organic light-emitting diodes (OLEDs).[19,20] To achieve fully flexible electronic displays, the circuit driving elements of OLED pixels,[21] consisting of organic field effect transistors (OFETs), must also be engineered to withstand the effects of local stress or strain.[22] However, the effects of strain on the operation of OFETs have only recently begun to be explored. The placement of strain-sensitive components within a "neutral plane" can eliminate the effects of longitudinal strain, and thus lead to drastically improved performance under flexing conditions.[23,24] While this presents an attractive alternative, the precise placement of all strain-sensitive components within a neutral plane may not always

be feasible in a real application, making it critical to understand the influence of strain on device performance. Additionally, mechanistic insight into the operation of organic transistors under strain may provide new pathways to eliminate or enhance the coupling of strain into the electronic signal, enabling flexible display operation or a new generation of cheap mechanical strain sensors.

The effect of compressive or tensile strain on the performance of OFETs was initially reported by Sekitani et al.[25–27] The authors demonstrated that compressive strain led to an increase, while tensile strain led to a decrease, in the mobility of pentacene-based field-effect transistors beyond that expected solely from variation in the capacitance of the dielectric layer. Grazing incidence x-ray diffraction studies later attributed the effect to strain induced reorganization of the pentacene film between the thin-film and bulk phases within the device.[28] A more recent study set out to explore the relationship between the semiconductor molecular structure and the behavior of OFETs under strain.[29] However, the authors found that the devices degraded under strain, and showed irreversible strain dependant behavior. Additionally, the study concluded that the dielectric layer of the transistor does not play a significant role in flexible device performance.[29] During our comprehensive study to gain mechanistic insight into the effects of strain on device performance, we discovered that both the dielectric and the semiconductor play a major role in device performance under compressive and tensile strain. Moreover, we applied our mechanistic understanding to demonstrate a general approach to reduce the effects of strain on mobility demonstrating a pathway towards strain-insensitive flexible displays.

2. Results and Discussion

2.1. Device Fabrication and Characterization

Our study involved two commonly used organic semiconductor active materials; namely, pentacene and 5,5′-bis-(7-hexyl-9H-fluoren-2-yl)-2,2′-bithiophene (DHFTTF).[9,30] The materials were chosen owing to their relatively high hole mobility along with a difference in the substitution of the aromatic core (non-substituted vs hexyl groups). The dielectric materials included

Dr. A. N. Sokolov, Y. Cao, O. B. Johnson, Prof. Z. Bao
Department of Chemical Engineering
Stanford University
381 North-South Mall, Stanford, CA 94305, USA
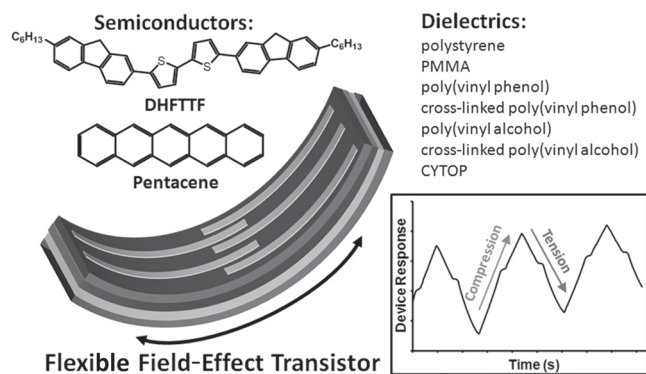E-mail: zbao@stanford.edu

Figure 1. A schematic representation of a field-effect transistor under strain showing the semiconductor and dielectric materials evaluated in this study. The plot shown is a time vs device response plot from a real device highlighting the change in I_{DS} current as a response to tensile and compressive strain.

poly(4-vinylphenol) and thermally crosslinked poly(4-vinylphenol) (PVP, x-PVP), polyvinyl alcohol and photocrosslinked polyvinyl alcohol (PVA, x-PVA), poly(methyl methacrylate) (PMMA), polystyrene (PS), and CYTOP (an amorphous perfluorinated polymer) (**Figure 1**). These materials were chosen owing to previous reports on their use as polymer dielectric films.[9,31–33] The devices were fabricated and tested as described in the Experimental Section.

The device characteristics (drain-source current (I_{DS}) vs. gate voltage (V_{GS}), at a constant drain-source voltage (V_{DS}) (transfer plot)) were recorded in an ambient atmosphere in a light-protected chamber. To ensure the reproducibility of the flexing results, each device was operated under a constant bias in saturation mode while applying at least ten complete flexing cycles of (+/−) strain. It should be noted that the application of a compressive strain greater than ~1.3% resulted in the buckling/cracking of gold source–drain contacts and an apparent decrease in the device mobility.[29,34] Previous results have also suggested that the delamination of the semiconductor material from the substrate can be expected to occur at ~1.5% strain based on a nanoindentation analysis.[35] In our experiments, delamination was not observed; however, the cracking/buckling of the gold electrodes did lead to a small, permanent negative shift of threshold voltage (~15%). We anticipate that the cracking leads to an increase in the resistance of the electrode; thus, requiring a higher bias for transistor operation. The use of higher voltages restored the original material performance (mobility) in all cases within our testing range. Additional bending cycles did not result in further device degradation, and the devices exhibited stable performances. This de-coupled the effects of the electrodes from strain within the active material. Mobility

(μ) and threshold voltage (V_T) values were extracted from each transfer plot and utilized as comparative device metrics during flexing stress application. For each device, an average mobility is reported to ensure an accurate portrayal of the effects of strain application. The calculation of mobility is described in the note below.[36] Prior to the application of strain, the devices were characterized to establish the optimal operating conditions for each dielectric. The summary of the device performance in the absence of strain is shown in **Table 1**. Additionally, the surface morphology of each OFET device was evaluated by atomic force microscopy (AFM). Representative AFM images of each device are shown in **Figure 2**. For all polymer dielectric layers DHFTTF films exhibit highly two-dimensional growth, similar to previously reported morphologies.[37] A larger morphological variation is observed for pentacene active layers; however, in all cases the films consist of micrometer-sized, three-dimensional pentacene grains.[13] The variations in the morphologies as well as the grain sizes explain the difference in the device performance *prior* to strain application. A wide distribution of grain sizes was observed for pentacene and DHFTTF, yet device behavior under strain did not depend on grain size. Additionally, both molecules are known to pack in a herringbone structure within the thin films.[37,38] Therefore, neither a difference in structure, nor the morphological differences observed for the varying polymer dielectrics could be correlated to device performance in the presence of strain.

2.2. Effect of Strain on Device Performance

Upon establishing the viability of each polymer dielectric layer to produce acceptable performance in OTFT devices, the dependence of the OTFT performance on applied strain was

Table 1. A summary of the device performances and conditions of testing in the absence of strain.

	Dielectric	μ [cm^2 V^{-1} s^{-1}]	V_T [V]	On/Off	V_G [V]	C_i [nF cm^{-2}]	Carrier Density [cm^{-2}]
Pentacene	PVP	1.01	−0.88	3.6×10^3	−2.25	77.90	6.66×10^{11}
	x-PVP	0.52	−1.09	5.7×10^3	−1.50	70.10	1.79×10^{11}
	PVA	0.92	−1.25	1.6×10^4	−2.50	99.90	7.79×10^{11}
	x-PVA	0.53	−1.36	1.5×10^4	−2.15	51.90	2.56×10^{11}
	PS	0.59	−127.3	4.1×10^5	−145.0	1.60	1.77×10^{11}
	PMMA	0.025	−2.59	1.6×10^3	−6.75	24.90	6.47×10^{11}
	CYTOP	0.041	−2.56	3.7×10^3	−3.90	48.20	4.03×10^{11}
	x-PVP-OTS	2.99	−1.29	2.7×10^3	−1.95	73.20	3.02×10^{11}
DHFTTF	PVP	0.077	−1.41	1.8×10^4	−2.10	77.90	3.36×10^{11}
	x-PVP	0.26	−1.34	6.5×10^3	−1.93	70.10	2.58×10^{11}
	PVA	0.019	−2.34	1.6×10^4	−2.90	99.90	3.49×10^{11}
	x-PVA	0.075	−2.05	4.5×10^3	−2.65	51.90	1.94×10^{11}
	PS	0.32	−141.5	3.4×10^5	−127.0	1.60	1.45×10^{11}
	PMMA	0.0039	−3.36	1.0×10^3	−7.80	24.90	6.90×10^{11}
	CYTOP	0.027	−2.23	4.3×10^3	−4.40	48.20	6.53×10^{11}
	x-PVP-OTS	0.17	−1.36	3.5×10^3	−1.90	73.20	2.47×10^{11}

www.MaterialsViews.com

ADVANCED
FUNCTIONAL
MATERIALS
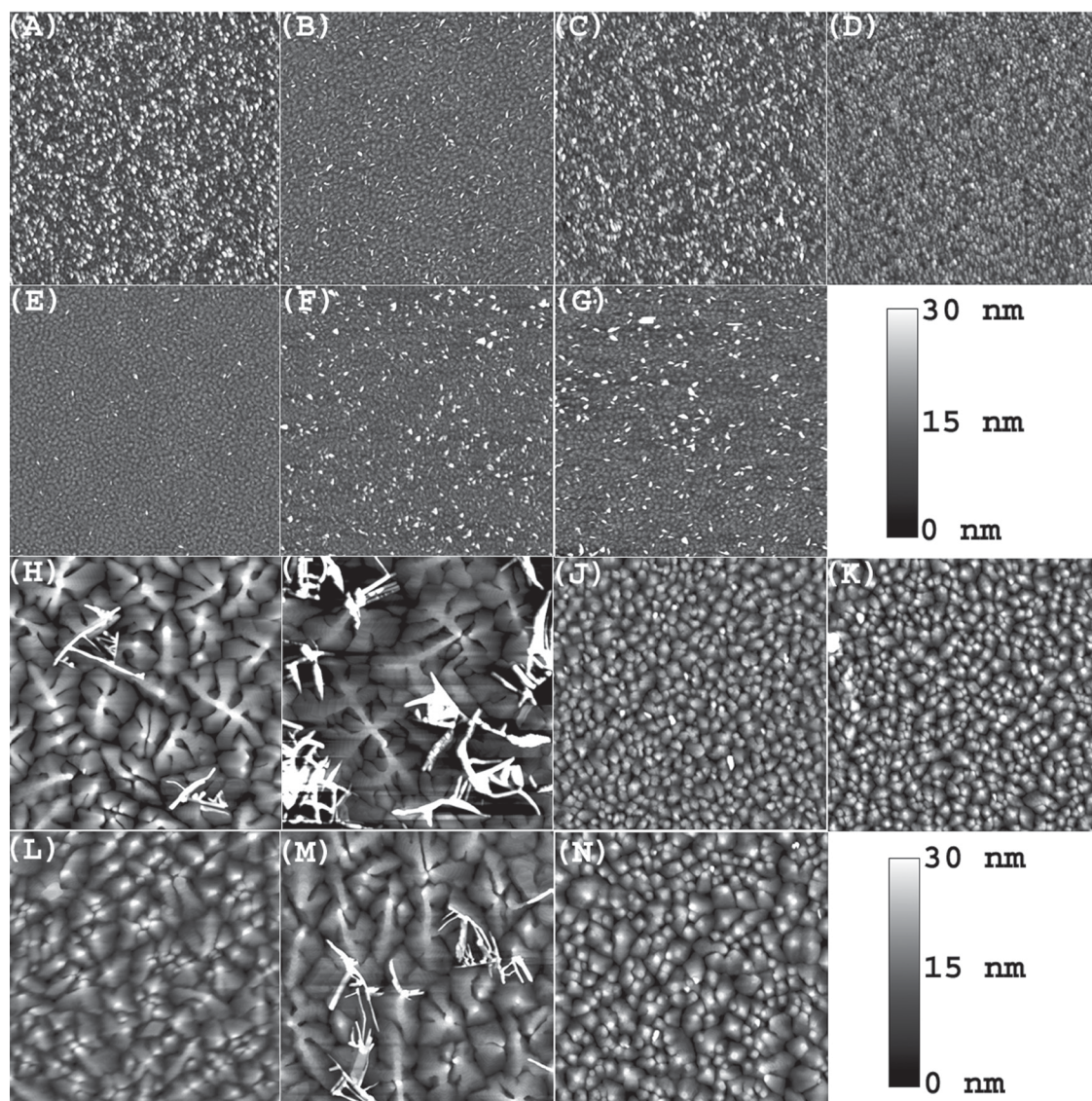www.afm-journal.de

FULL PAPER

Figure 2. The AFM images of flexible OFET device with DHFTTF (top rows) and Pentacene (bottom rows) active materials on varying polymer dielectrics. A,H) x-PVP; B,I) PVP; C,J) x-PVA; D,K) PVA; E,L) PS; F,M) PMMA; and G,N) CYTOP. All presented AFM images are a 5 μm × 5 μm scans.

evaluated. Bending radii of several millimeters were tested to mimic the predicted strain necessary to enable display applications.[22] The maximum compressive (positive) and the maximum tensile (negative) strains applied were 2.4% (2.5 mm concave or convex bending radii, respectively) (Figure S1). The maximum strain values were dictated by the geometrical constraints of the mechanical setup shown in Figure S1. The strain in the device was evaluated from the bending radius by quantitative analysis.[25,39] In all cases, the thickness of the polymer dielectric does not play a role in strain determination. The strain is determined by the total device thickness, dominated by the 120 μm polycarbonate film and the bending radius.[39] Thus, for each compressive and tensile cycle the device was systematically taken from 0% strain to +2.4%, back to 0%, then to −2.4% and back to 0% strain again. In total, the device was evaluated during four complete, consecutive strain cycles. For each summary plot, at least two separate devices, manufactured

in two separate batches were tested to ensure reproducibility of the device characteristics. To make certain that any changes in device performance are not caused by a strain-induced change in the dielectric capacitance, capacitor structures of similar active area were evaluated at identical compressive and tensile strain forces as the OFET devices. In all cases, a small change in capacitance was observed upon the application of strain to the dielectric layers. This change has been previously reported, and was explained by the change in dielectric layer thicknesses induced by the Poisson effect.[25]

The electrical behavior of the flexible devices was characterized during the systematic application of compressive or tensile strain. Representative examples of the change in observed electrical characteristics for pentacene and DHFTTF-based devices on PMMA are shown in **Figure 3** and **Figure 4**A,B. In agreement with previous reports, pentacene-based devices on polymer dielectrics exhibited an increase in saturation I_{DS} upon the
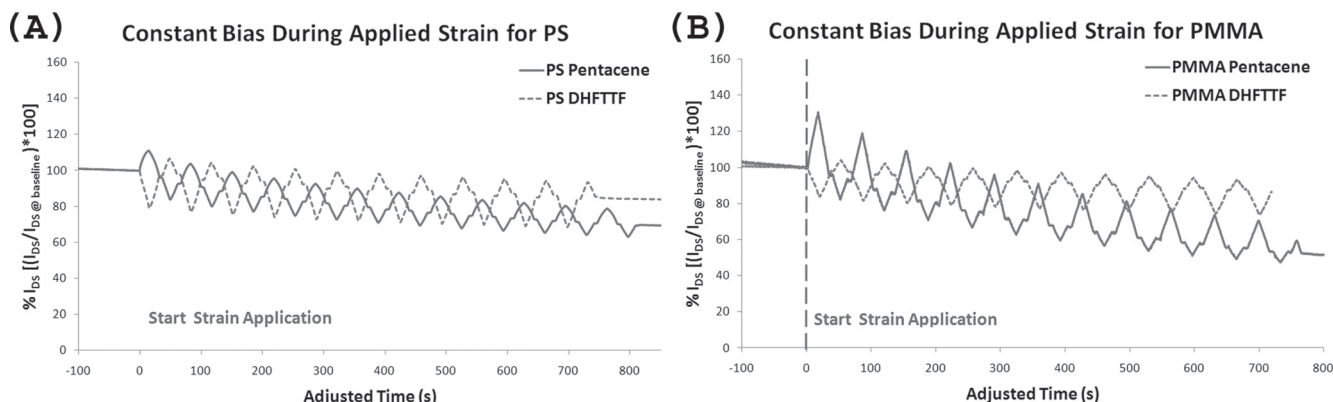
FULL PAPER

Figure 3. The effect of applied strain on the normalized I_{DS} current of an OFET held at constant bias for (A) PS or (B) PMMA as the dielectric. The application of cycles of strain from positive (+2.4%) to negative (–2.4%) is shown. The effect of strain is inverted based on the hexyl substitution of the DHFTTF semiconductor.

application of compressive (+) strain and a decrease in saturation I_{DS} upon the application of tensile (–) strain.[25,27] However, the use of a hexyl-substituted semiconductor DHFTTF results in the observation of the opposite trend; namely, decrease in I_{DS} upon the application of compressive (+) and an increase in I_{DS} upon the application of tensile (–) strain. While there is a single, previous report characterizing the use of alkyl substituted semiconductor molecules in strained OFET devices,[29] this reversal of device behavior has not previously been described. However, this observation is important to advance the mechanism of OFET behavior under strain and to enable both strain insensitive devices as well as potential strain sensors.

To compare the effect of strain across varying semiconductor and dielectric layer combinations, the percent response of mobility (%μ) and percent response of the threshold voltage (%V_T) were plotted vs the applied strain. The relationship between the strain and the semiconductor performances, termed mobility factor (F_M) (Δ%μ/%strain) and V_T factor (F_{VT}) (Δ%V_T/%strain), were used as metrics to compare the varying OFET devices (Figure 4E). The effect of strain on the average mobility is shown in Figure 4C and D.

The variation of the underlying dielectric layer proved to have a significant effect on mobility in response to the applied strain. Interestingly, devices based on pentacene generally exhibited positive mobility factors (F_M), while devices based on DHFTTF exhibited a negative F_M. The only exception to this was observed for x-PVA with pentacene, which demonstrated a negative F_M. However, this may be cause by the presence of the cross-linking agent, ammonium dichromate, on the surface of the polymer leading to an unpredictable surface energy landscape. The use of polystyrene (PS) as the gate dielectric resulted in the largest impact for pentacene, while the use of x-PVA resulted in the largest impact for DHFTTF, with mobility factors of 7.3 and –7.92, respectively (Figure 4). This means that the application of 1% strain to a pentacene device on PS results in a 7.3% change in the mobility. For pentacene-based devices the use of CYTOP resulted in the smallest shift in effective mobility (F_M = 1.6). Thus, the average mobility of this device during strain application remained nearly constant. The smallest F_M for DHFTTF-based devices was observed for either CYTOP or PVP dielectrics (F_M = –4.4 and –4.3, respectively), (Figure 4). Interestingly,

the threshold voltage shift factors (F_{VT}) for all devices were between –0.1 and +1.5, with no obvious correlation to applied strain (Figure S2).

2.3. Understanding the Effect of Strain on Device Mobility

Strain-induced rearrangement of the polymer chains may be the key to understanding the effect of the dielectric on the performance of the semiconductor active layer. It is well understood that the surface energy of the dielectric as well as the surface dipole plays a large role in controlling charge-carrier density within organic semiconductors.[40–44] A recent report has demonstrated that the device mobility is critically dependent on polymer surface heterogeneity.[45] In that report, the presence of additional chain ends on the surface of a PS film, owing to low PS molecular weight (MW), resulted in increased surface heterogeneity, and drastically lower mobilities. Therefore, upon induction of strain into polymer systems, a rearrangement of the polymer structure can be expected, leading to a change in surface heterogeneity and a change in surface energy. The change of polarization in response to strain, or piezoelectricity, has been observed for crystalline polymers such as PVDF, and is typically not observed in the amorphous or poorly crystalline polymers described in this work.[46,47] However, as previously mentioned, the behavior of OTFTs depends strongly on the surface dipoles and the surface energy at the interface. Thus, bulk polarization is not necessary to induce a change in device performance upon the application of strain; a change in polymer orientation at the surface will suffice. The field-effect mobility will change in response to polymer rearrangement at the surface, manifested as a change in the surface energy or surface dipole reorientation.[48] As an example, polystyrene is comprised of alkyl and phenyl groups, and does not contain moieties capable of hydrogen bonding. The local rearrangement of polymer chains upon strain application can involve in-plane reorientation of the phenyl group or the promotion of additional alkyl chain ends to the surface.[45,49] The rearrangement of this polymer upon strain may be expected due to higher polymer mobility (weak intrachain interaction), and thus, the devices exhibit a higher than average response to strain (F_M = 4.8 for

Materials
Views
www.MaterialsViews.com

ADVANCED
FUNCTIONAL
MATERIALS
www.afm-journal.de

FULL PAPER
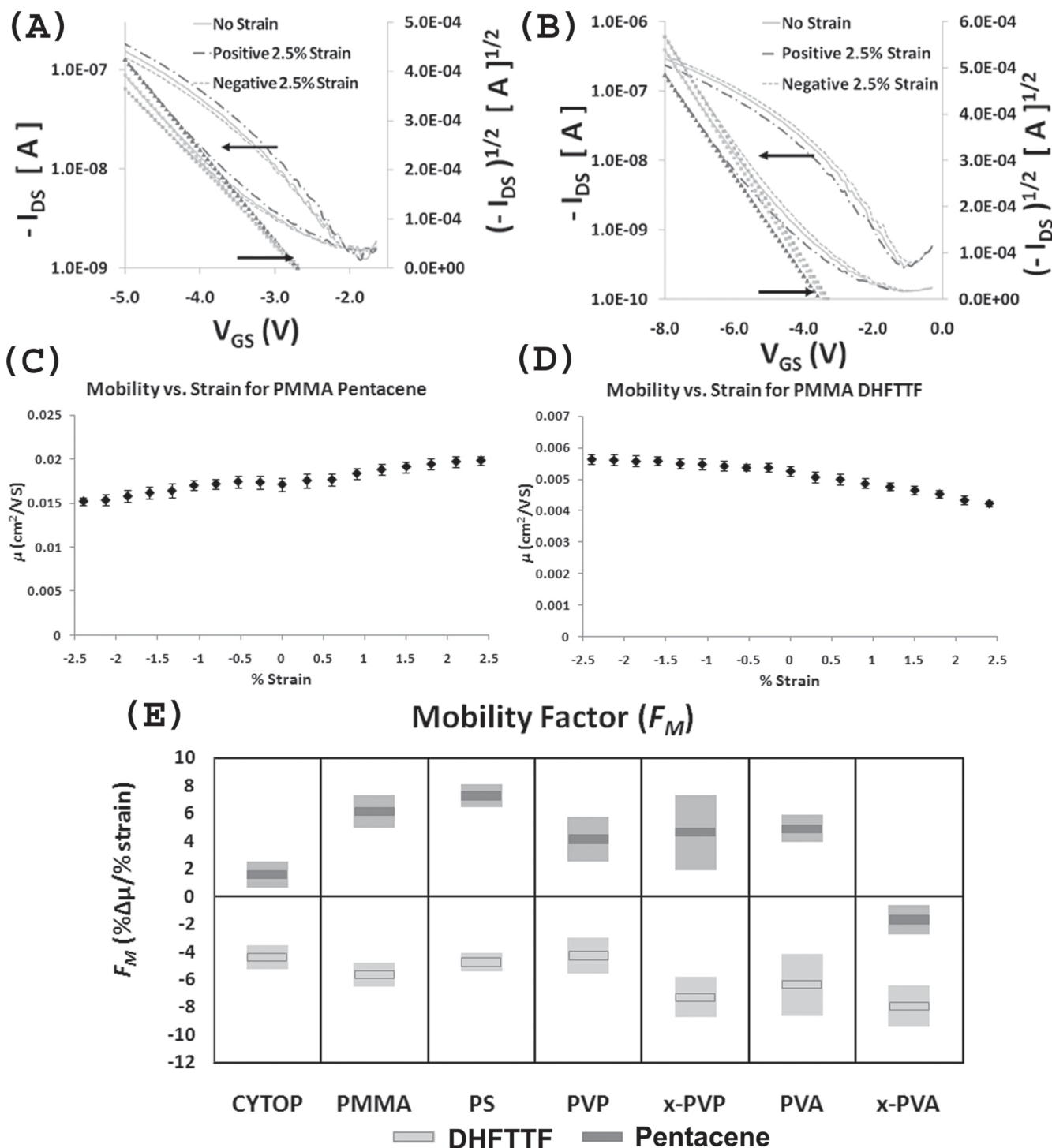
Figure 4. A representative figure of device performance on PMMA for both DHFTTF and pentacene during strain. Plots (A) and (B) show I_{DS} vs. V_{GS} performance for (a) pentacene and (b) DHFTTF before and during the application of maximum (2.4%) strain. Plots (C) and (D) show the average mobility change for (C) pentacene and (D) DHFTTF during the application of strain. E) A graphical comparison of the mobility factors (F_M) for each of the seven polymer dielectrics utilizing pentacene (filled marker) and DHFTTF (open marker) within OFET devices.

DHFTTF and 7.3 for pentacene). The dielectric that shows the lowest F_M to strain is CYTOP. This material contains a fluorine substitution on every carbon, thus, the rearrangement of the polymer in response to strain will result in a low surface

heterogeneity, and a low *change* in surface energy upon applied strain. It should be mentioned that while a small change in F_M would be expected for the two crosslinked dielectrics (*x*-PVA and *x*-PVP), the introduction of crosslinking materials into

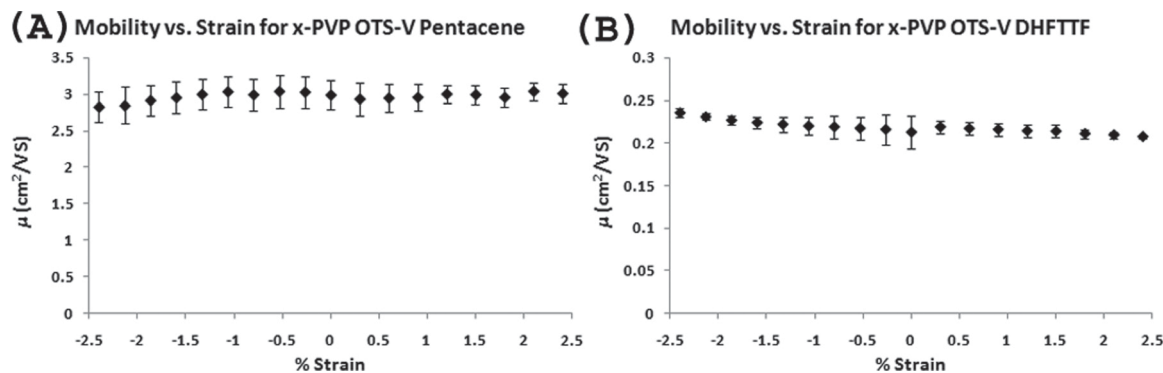**Figure 5.** A representative plot of device performance on OTS-V treated *x*-PVP for both pentacene and DHFTTF. A) Mobility change in pentacene; B) mobility change in DHFTTF vs applied compressive (+) and tensile (–) flexing strain.

the polymer matrices, i.e., HDA or ammonium dichromate, may lead to unexpected results. Regardless, in these cases, the rearrangement of polymer chains is expected to be difficult or induce a small degree of change in the surface energy, and thus, lead to a small F_M. This is consistent with the results of Sekitani et al., who report that pentacene exhibited an F_M of ~5 on a polyimide dielectric.[24]

Taking into account that surface energy variation can lead to a change in F_M, the covalent modification of a surface with a self-assembled monolayer (SAM) of tightly packed alkyl chains (e.g., octadecylsilane (OTS)) should provide a surface that consists of a crystalline layer of methyl groups. This, new, dielectric surface consists of tightly packed chains composed of poorly polarizable carbon–hydrogen bonds, lowering the heterogeneity in surface energy during applied strain on the F_M. In this case, the low heterogeneity is expected to lead to a small variation in surface energy, and thus, a small variation in device performance upon polymer chain reorganization. Our group has previously reported the functionalization of the *x*-PVP dielectric with a vapor-based octadecylsilane (OTS-V) treatment.[50] The introduction of the OTS groups on the surface is confirmed with a contact angle measurement (contact angle is increased from 69.4° for *x*-PVP, to 88.9° for OTS-V treated *x*-PVP). Both pentacene and DHFTTF devices were fabricated on the OTS-V treated *x*-PVP surface, and the F_M for both devices was calculated.[51,52] As predicted, the F_M for OTS-V treated surfaces was significantly lowered in both cases. The F_M of pentacene was calculated to be 0.15 and the F_M of DHFTTF was calculated to be –2.06 (**Figure 5**). These findings explain the result of Jedaa et al., who demonstrated that a hybrid inorganic/organic dielectric, that consists of alkyl chains, displayed a low overall response to strain application.[29] This implies that the introduction of a dense alkane layer on a polymer surface is a general methodology to decrease the effect of strain on device mobility.

The introduction of a covalently bound alkyl SAM onto the polymer dielectric served to minimize the effect of strain on the device performance. However, the inclusion of the hexyl group on the semiconductor, DHFTTF, led to an inversion in the sign of F_M, when compared with pentacene. This finding comes as a surprise, because in all previous work the devices under strain exhibited behavior similar to pentacene, that is to say positive F_M. The negative F_M of *x*-PVA with pentacene is

an exception, and may be rationalized based on the presence of the cross-linking agent, ammonium dichromate. To understand the nature of the negative F_M in alkyl substituted DHFTTF we reasoned that the variation in the surface energy of the dielectric under applied strain is responsible for the change in F_M.[48] Thus, the critical interface must be between the noncovalnetly bound semiconductor molecules on the surface of the dielectric. At the neutral strain position, the performance of the device is partially dependent on the equilibrium surface energy of the dielectric. However, once strain is applied to the system, the extent of surface energy variation will be the driving influence on device performance. Thus, greater surface heterogeneity will result in a larger F_M. For the case of pentacene, the net change in the nanoscopic surface energy of the dielectric is intimately linked to the carriers present in the semiconductor material. This is attributed to the direct interaction of the highest occupied molecular orbital (HOMO) frontier molecular orbitals of pentacene with the surface of the polymer dielectric. The direct coupling leads to a change in the energetic disorder at the interface, and a change in mobility. Thus, chemical modification of the dielectric surface with a crystalline alkyl-chain SAM results in decreased energetic variation upon strain application, and can only influence the magnitude of the F_M. However, the introduction of an alkyl substituent on the semiconductor core (e.g., DHFTTF) prevents the direct interaction between the surface energy of the dielectric and the carriers within the semiconductor molecular cores. In this fashion, the changing surface potential during applied strain cannot directly influence the charge carriers in the DHFTTF. Owing to the insulating nature of the substituent, a nanometer-scale parallel plate capacitor structure can form, as defined by the dielectric surface and the semiconductor layer. The application of charge to one of the plates (surface potential variation during applied strain) will induce a mirror charge onto the other plate (**Figure 6**, right). This leads to the observation of the inverted F_M, as shown in Figure 5. It has been previously shown in work involving molecular junctions that an 8-carbon alkyl chain is sufficient to create a monolayer capacitor structure.[53] Modeling of the frontier orbitals of DHFTTF demonstrates that the outer phenyl ring of the fluorine is not involved in charge transport (the HOMO electrons are localized on the two thiophenes and the adjacent phenyl ring). Thus, chemically, a 1-hexylbenzene group acts as
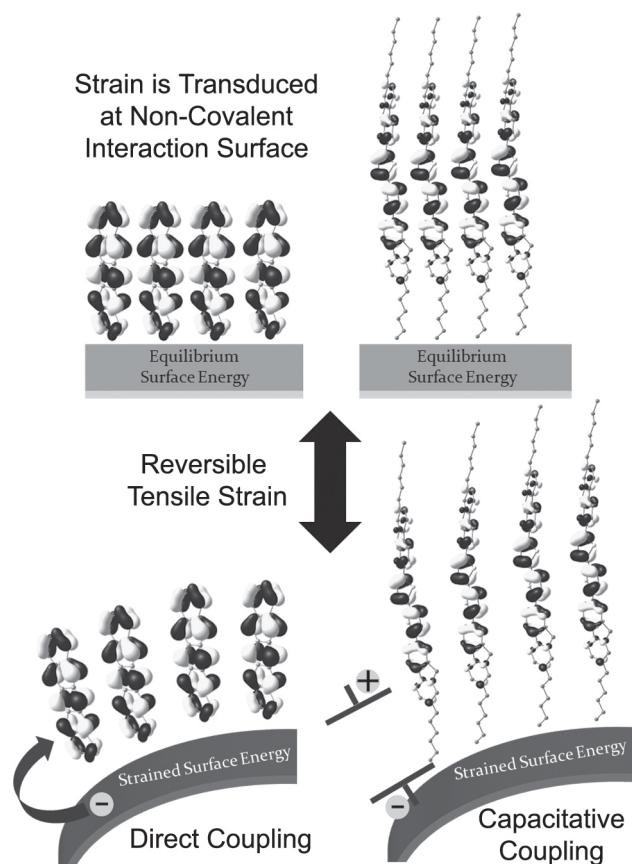
www.MaterialsViews.com

ADVANCED
FUNCTIONAL
MATERIALS
www.afm-journal.de

FULL PAPER

Figure 6. A cartoon of energetic variation of the polymer dielectric surface during strain with pentacene and DHFTTF devices. The influence of strain on device performance occurs at the non-covalent, semiconductor/dielectric interface. For pentacene (left) the changing surface energy is directly coupled into the HOMO orbitals of the semiconductor. For DHFTTF (right), the alkyl substituent serves to prevent the direct coupling of the surface energy into the semiconductor core. Instead, a parallel plate capacitor structure is formed, resulting in a mirror charge being induced into the semiconductor HOMO orbitals.

the molecular dielectric ($\varepsilon \approx 2.1$).[53] It is clear that this chemical group provides sufficient resistance to charge leakage from the applied strain induced surface charge. For that reason, we attribute the change in the sign of the F_M to capacitive coupling of the changing surface energy across the 1-hexylbenzene substituent. It is important to note, that the substitution of the polymer cannot lead to this effect, as only the surface of the dielectric influences the magnitude of the F_M, while the semiconductor substituents influences the sign of the F_M. In order to establish the validity of the proposed model, additional studies exploring the dependence of the effect on substituent length and composition are underway.

3. Conclusions

In conclusion, a study describing the effect of strain on flexible organic field-effect transistors fabricated on polymer dielectrics is described. By using two types of semiconductors,[29] we

demonstrated that both the organic semiconductor material, as well as the polymer dielectric play a significant role in determining the effect of applied strain on the OFET characteristics. The dependence of strain effects on dielectric material composition is governed by the relative change in the surface energy of the dielectric material. The magnitude of polymer surface reorganization depends on the intermolecular interactions and polymer substitution, and can thus impact F_M. The introduction of a SAM of a linear alkyl chain onto the surface of the dielectric material served as a general method to drastically decrease the effects of strain on semiconductor mobility for both pentacene and DHFTTF active materials. The understanding of the mechanism of strain-induced mobility effects in organic semiconductors can potentially lead to the realization of new applications for OFET-based strain sensors. Interestingly, the introduction of short alkyl chains on the semiconductor core resulted in an inversion of the influence of strain onto the device mobility. This novel discovery was attributed to the formation of a capacitor structure by the hexyl chain between the charges present in the organic semiconductor and the surface of the polymer dielectric. Future studies will elucidate the mechanistic effect of alkyl chain length on the effect of strain in OFETs.

4. Experimental Section

The devices were fabricated on flexible polycarbonate substrates (120 μm thick) utilizing thermally deposited (70 nm) aluminum (Al) gate electrode. Al was chosen as the gate electrode material both for known resistance to cracking/delamination, as well as for solution wetting properties imparted by the native Al_2O_3 layer. The polymer dielectric layers were deposited via spin coating on the Al layer. The polymer dielectrics were separately spin coated onto highly doped n++ Si substrates to obtain film thickness measurements via ellipsometry or profilometry (for PS). Additionally, Au pads were thermally evaporated on both flexible and rigid substrates to form capacitor structures. Transistors were prepared via thermal evaporation of a 40 nm layer of the organic semiconductor onto the flexible substrates held at room temperature. The substrates were held at room temperature to prevent the decrease in semiconductor performance observed when active materials are evaporated onto polymers at temperatures approaching the glass-transition temperature, g.[54] The evaporation of 40-nm-thick Au electrodes as top source/drain contacts completed the transistor architecture. Au instead of Al was utilized as the source–drain electrode material to prevent charge injection problems into the p-channel semiconductors. The device geometry was defined via a shadow mask to provide a W/L (width/length) ratio of 240 (W = 12 mm, L = 50 μm). The device geometry relative to the substrate positions the electrodes such that strain is applied perpendicular to the direction of the drain–source current (Figure S1). Previous reports have suggested that the direction of the strain is arbitrary, owing to isotropic charge transport within polycrystalline thin-films.[25] The bending experiments were performed on a computer-controlled, home-built, semiconductor parameter analyzer station (Keithley 2635 (Drain-Source), Keithley 2400 (Gate)) capable of achieving a concave or a convex bending radius of 2.5 mm (Figure S1). During the flexing cycle, the device is held securely in place via two electrode-containing clips. To prevent device failure from the electrode clips, the drain-source electrode contact with the flexible device is created via a minute amount of a Gallium Indium eutectic laminated on the clip electrode. The gate electrode is a sharp needle that pierces the soft polymer dielectric to ensure a reliable gate contact. The application of strain is done via the rotation of a stepper motor capable of 0.12° revolution per step. The electrical contacts to the drain and source electrodes are made through clips. A photo of the set-up is included in the supporting material.

DFT Calculations: Density functional theory was used to calculate HOMO (highest occupied molecular orbital) and LUMO (lowest unoccupied molecular orbital) levels of the geometry optimized structures (B3LYP/6-31G∗) of DHFTTF and Pentacene using Gaussian 03. The models were visualized using Chemcraft V1.6 software.

Materials: All materials were purchased from Aldrich and used as received unless otherwise noted. The organic semiconductor DHFTTF was synthesized according to previously reported methods.[30] DHFTTF was purified by gradient sublimation under high vacuum twice before use. Pentacene (Aldrich, triple-sublimed grade CAS:135-48-8, >99.995%, trace metals basis) was used as received. Galium Indium Eutectic 99.99% was purchased from Alfa Aesar.

Dielectric Layers: Prior to spin coating, the blank polycarbonate, or silicon substrates were exposed to gentle UV-ozone treatment (Jelight Model 42) for a period of three minutes to promote polymer adhesion. To form the thin dielectric film, a filtered (0.2 um PTFE filter, unless otherwise specified) dielectric solution (~200 ul) was deposited onto the desired substrate, and allowed to settle for a period of 30 s. The substrate was subsequently spun coated at the required speed for a period of 1 min.

Octadecylsilane Modification: The x-PVP dielectric surfaces were treated with gentle UV-ozone treatment for a period of 3 minutes. The devices were immediately transferred into a glass dessicator that contained a vial of 200 μl of octadecyltrimethoxysilane. The dessicator was placed under a static vacuum (~100 mtorr) and was subsequently heated up on a hot plate to a temperature of 150 °C for a period of 48 h. The devices were removed and rinsed copiously with toluene and water prior to semiconductor deposition.

Poly(4-vinylphenol) (PVP): Poly(4-vinylphenol) (Aldrich, MW 25,000) was dissolved in propylene glycol monomethyl ether acetate (PGMEA, Aldrich) with ratio of 40 mg mL^{-1}. It should be noted that a PGMEA solution without an industrial inhibitor was used. The solution was deposited via the described spin-coating procedure at 4000 rpm for one minute and then cured on a hot plate at 100 °C for a period of one hour. The resulting device capacitance was measured to be 77.9 nF cm^{-2} on the polycarbonate substrate, and 38.6 nF cm^{-2} on the silicon substrate. The device thickness on the silicon substrate was measured to be 146.4 nm by ellipsometry.

Crosslinked Poly(4-vinylphenol) (x-PVP): Poly(4-vinylphenol) (Aldrich, MW 25,000) was dissolved in propylene glycol monomethyl ether acetate (PGMEA) with ratio of 40 mg mL^{-1}. Separately, the cross-linker with 4,4′-(hexafluoroisopropylidene) diphthalic anhydride (HDA, Aldrich) was dissolved in PGMEA at a ratio of four mg mL^{-1}. Into a two ml solution of PVP, two microliters of triethylamine was added, and the solution was shaken for a period of 30 s to ensure complete mixture. To this mixture, 2 mL of HDA solution was added, and the solution was shaken to ensure complete mixture. The solution was deposited via the described spin-coating procedure at 4000 rpm for 1 min and then cured on a hot plate at 100 °C for a period of 1 h. A second UV ozone treatment of the x-PVP layer (3 min) was followed by the spin-coated deposition of an additional x-PVP layer following the above procedure. The device was subsequently cured on a 100 °C hot plate for a period of 4 h. The resulting device capacitance was measured to be 70.1 nF cm^{-2} on the polycarbonate substrate, and 76.0 nF cm^{-2} on the silicon substrate. The device thickness on the silicon substrate was measured to be 72.9 nm by ellipsometry.

Polyvinyl alcohol (PVA): Polyvinylalcohol (Fluka, MW 205,000) was dissolved in distilled H$_2$O at a concentration of three wt%/vol. The solution was vigorously stirred for a period of 3 h at 100 °C to achieve complete dissolution. The solution was subsequently filtered through a 0.45 μm PVDF filter into a clean vial. The solution was deposited via the described spin-coating procedure at 3000 rpm for 1 min and cured at 100 °C for a period of 1 h. The resulting device capacitance was measured to be 99.9 nF cm^{-2} on the polycarbonate substrate, and 68.5 nF cm^{-2} on the silicon substrate. The device thickness on the silicon substrate was measured to be 86.3 nm by ellipsometry.

Cross-linked Polyvinyl alcohol (x-PVA): Polyvinylalcohol (Aldrich, MW 205,000) was dissolved in distilled H$_2$O at a concentration of three wt%/vol. The solution was vigorously stirred for a period of 3 h at 100 °C to achieve complete dissolution. The solution was subsequently filtered through a 0.45 μm PVDF filter into a clean vial. To this solution, a 1:6 mass ratio of ammonium dichromate (Aldrich):PVA was added. The solution was stirred at RT for one hour and again filtered through a 0.45 μm PVDF filter into a clean vial. The solution was deposited via the described spin-coating procedure at 3000 rpm for 1 min. The film was crosslinked with 254 nanometer UV radiation for a period of 10 min. The film was rinsed with distilled H$_2$O. A second UV ozone treatment of the x-PVA layer (3 min) was followed by the spin-coated deposition of an additional x-PVA layer following the above procedure. A second 254 nm UV exposure, followed by a distilled H$_2$O rinse completed the film process. The device was subsequently cured on a 100 °C hot plate for a period of 1 h to remove any trace H$_2$O. The resulting device capacitance was measured to be 51.9 nF cm^{-2} on the polycarbonate substrate, and 85.7 nF cm^{-2} on the silicon substrate. The device thickness on the silicon substrate was measured to be 78.2 nm by ellipsometry.

CYTOP: CYTOP films were made from a commercially available CYTOP solution. The solution for deposition was made by combining the two provided solutions CTL-809M and CT-Solv.180 in a ratio of 1:2, respectively. The solution was deposited via the described spin-coating procedure at 7000 rpm for 1 min and cured at 100 °C for a period of 1 h. The resulting device capacitance was measured to be 48.2 nF cm^{-2} on the polycarbonate substrate, and 36.3 nF cm^{-2} on the silicon substrate. The device thickness on the silicon substrate was measured to be 48.4 nm by ellipsometry.

Poly(methyl methacrylate) (PMMA): Poly(methyl methacrylate) (Aldrich, MW 15,000) was dissolved in toluene at a concentration of five wt%/vol. The solution was deposited via the described spin-coating procedure at 4000 rpm for 1 min and cured at 120 °C for a period of 1 h. The resulting device capacitance was measured to be 24.9 nF cm^{-2} on the polycarbonate substrate, and 22.4 nF cm^{-2} on the silicon substrate. The device thickness on the silicon substrate was measured to be 117.6 nm by ellipsometry.

Polystyrene (PS): Polystyrene (Aldrich, MW 97,000) was dissolved in toluene at a concentration of ten wt%/vol. The solution was deposited via the described spin-coating procedure at 1000 rpm for 1 min and cured at 85 °C for a period of 1 h. The resulting device capacitance was measured to be 1.63 nF cm^{-2} on the polycarbonate substrate, and 1.38 nF cm^{-2} on the silicon substrate. The device thickness on the silicon substrate was measured to be 1300 nm by profilometry.

Device Fabrication: Heavily doped silicon wafers (no thermally grown oxide) were cleaned by rinsing with acetone, H$_2$O, and isopropanol prior to use. Polycarbonate films (Teijin Chemical Ltd., SS-120) were rinsed with H$_2$O and isopropanol before use. 70 nm aluminum films were deposited by thermal evaporation (Angstrom Engineering, Inc.) at a rate of 3–5 Å s^{-1} under a pressure of 5.0×10^{-7} Torr. Polymer dielectric deposition was carried out as described above. The DHFTTF and pentacene films were deposited by thermal evaporation (Angstrom Engineering, Inc.) at a rate of 0.1–0.2 Å s^{-1} under a pressure of 5.0×10^{-7} Torr. The substrate temperature for the organic semiconductor deposition was kept at RT.

Characterization: Atomic force microscopy (AFM) was performed using a Digital Instruments Nanoscope IV operated in tapping mode (~320 kHz frequency, Si tip). Ellipsometry measurements were taken using a Gaertner Ellipsometer L116C at a 70 degree angle of incidence with a 632.8 nm 1 mW laser from a Helium Neon laser and a beam size of 1 mm × 2.92 mm. The polystyrene film thickness was determined using profilometry, Veeco Dektak 150 Surface Profiler. The capacitance values of the polymer dielectrics on both rigid and flexible substrates were evaluated using an Agilent E4980 precision LCR meter operating at 1 V and 1 kHz frequency.

Supporting Information

Supporting Information is available from the Wiley Online Library or from the author.

www.MaterialsViews.com

ADVANCED
FUNCTIONAL
MATERIALS
www.afm-journal.de

FULL PAPER

Acknowledgements

[1] P. F. Baude, D. A. Ender, M. A. Haase, T. W. Kelley, D. V. Muyres, S. D. Theiss, *App. Phys. Lett.* **2003**, *82*, 3964.

[2] R. Rotzoll, S. Mohapatra, V. Olariu, R. Wenz, M. Grigas, K. Dimmler, O. Shchekin, A. Dodabalapur, *Appl. Phys. Lett.* **2006**, *88*, 123502.

[3] L. J. A. Koster, V. D. Mihailetchi, P. W. M. Blom, *Appl. Phys. Lett.* **2006**, *88*, 0935111.

[4] P. Peumans, S. Uchida, S. R. Forrest, *Nature* **2003**, *425*, 158.

[5] T. Sekitani, T. Yokota, U. Zschieschang, H. Klauk, S. Bauer, K. Takeuchi, M. Takamiya, T. Sakurai, T. Someya, *Science* **2009**, *326*, 1516.

[6] B. Crone, A. Dodabalapur, A. Gelperin, L. Torsi, H. E. Katz, A. J. Lovinger, Z. Bao, *App. Phys. Lett.* **2001**, *78*, 2229.

[7] L. Torsi, A. Dodabalapur, *Anal. Chem.* **2005**, 381.

[8] M. E. Roberts, S. C. B. Mannsfeld, R. M. Stoltenberg, Z. Bao, *Org. Electron.* **2008**, *10*, 377.

[9] M. E. Roberts, S. C. B. Mannsfeld, N. Queralto, C. Reese, J. Locklin, W. Knoll, Z. Bao, *Proc. Natl. Acad. Sci. USA* **2008**, *105*, 12134.

[10] E. Zampetti, S. Pantalei, A. Pecora, A. Valletta, L. Maiolo, A. Minotti, A. Macagnano, G. Fortunato, A. Brarzotti, *Sens. Actuators. B* **2009**, *143*, 302.

[11] T. Someya, A. Dodabalapur, J. Huang, K. C. See, H. E. Katz, *Adv. Mater.* **2010**, *22*, 3799.

[12] J. T. Mabeck, G. G. Malliaras, *Anal. Bioanal. Chem.* **2006**, *384*, 343.

[13] Z. Bao, J. Locklin, *Organic Field-Effect Transistors*, Taylor & Francis Group, Boca Raton, FL, USA **2007**.

[14] A. L. Briseno, S. C. B. Mannsfeld, M. M. Ling, S. Liu, R. J. Tseng, C. Reese, M. E. Roberts, Y. Yang, F. Wudl, Z. Bao, *Nature* **2006**, *444*, 913.

[15] A. L. Briseno, R. J. Tseng, M. M. Ling, E. H. L. Falcao, Y. Yang, F. Wudl, Z. Bao, *Adv. Mater.* **2006**, *18*, 2320.

[16] J. A. Rogers, *Science* **2001**, *291*, 1502.

[17] T. Sekitani, Y. Noguchi, U. Zschieschang, H. Klauk, T. Someya, *Proc. Natl. Acad. Sci. USA* **2008**, *105*, 4976.

[18] H. E. Katz, *Chem. Mater.* **2004**, *16*, 4748.

[19] A. C. Grimsdale, K. L. Chan, R. E. Martin, P. G. Jokisz, A. G. Holmes, *Chem. Rev.* **2009**, *109*, 897.

[20] K. Walzer, B. Maennig, M. Pfeiffer, K. Leo, *Chem. Rev.* **2007**, *107*, 1233.

[21] X.-H. Zhang, W. J. Potscavage, S. Choi, B. Kippelen, *Appl. Phys. Lett.* **2009**, *94*, 0433121.

[22] J. Jang, *Mater. Today* **2006**, *9*, 46.

[23] Z. Suo, Y. E. Ma, H. Gleskova, S. Wagner, *App. Phys. Lett.* **1999**, *74*, 1177.

[24] T. Sekitani, S. Iba, Y. Kato, Y. Noguchi, T. Someya, T. Sakurai, *App. Phys. Lett.* **2005**, *87*, 173502.

[25] T. Sekitani, Y. Kato, S. Iba, H. Shinaoka, T. Someya, T. Sakurai, S. Takagi, *App. Phys. Lett.* **2005**, *86*, 0735111.

[26] T. Sekitani, S. Iba, Y. Kato, Y. Noguchi, T. Sakurai, T. Someya, *J. Non-Cryst. Solids* **2006**, *352*, 1769.

[27] T. Sekitani, S. Iba, Y. Kato, T. Someya, *Jpn. J. Appl. Phys.* **2005**, *44*, 2841.

[28] C. Yang, J. Yoon, S. H. Kim, K. Hong, D. S. Chung, K. Heo, C. E. Park, M. Ree, *App. Phys. Lett.* **2008**, *92*, 243305.

[29] A. Jedaa, M. Halik, *App. Phys. Lett.* **2009**, *95*, 103309.

[30] H. Meng, J. Zheng, A. J. Lovinger, B. C. Wang, P. G. Van Patten, Z. Bao, *Chem. Mater.* **2003**, *15*, 1778.

[31] C. J. Bettinger, Z. Bao, *Adv. Mater.* **2010**, *22*, 651.

[32] A. Facchetti, M.-H. Yoon, T. J. Marks, *Adv. Mater.* **2005**, *17*, 1705.

[33] J. Veres, S. Ogier, G. Lloyd, D. de Leeuw, *Chem. Mater.* **2004**, *16*, 4543.

[34] S. P. Lacour, S. Wagner, Z. Huang, Z. Suo, *Appl. Phys. Lett.* **2003**, 2404.

[35] M. Kanari, M. Kunimoto, T. Wakamatsu, I. Ihara, *Thin Solid Films* **2010**, *518*.

[36] For each measurement between 120–300 V_{GS} data points were collected. The slope of the $I_{DS}^{1/2}$ line was taken over the a 20 point average around maximum derivative point to establish a consistant average maximum mobility, which would be independent of the shifting threshold voltage.

[37] T. J. Shin, H. Yang, M.-m. Ling, J. Locklin, L. Yang, B. Lee, M. E. Roberts, A. B. Mallik, Z. Bao, *Chem. Mater.* **2007**, *19*, 5882.

[38] S. C. B. Mannsfeld, A. Virkar, C. Reese, M. F. Toney, Z. Bao, *Adv. Mater.* **2009**, *20*, 2294.

[39] The strain (S) can be approximated by the equation $S = d_s/2R$, where d_s is the thickness of the substrate (120 μm) and R is the bending radius.

[40] J. Takeya, T. Nishikawa, T. Takenobu, S. Kobayashi, Y. Iwasa, T. Mitani, C. Goldmann, C. Krellner, B. Batlogg, *Appl. Phys. Lett.* **2004**, *85*, 5078.

[41] S. Kobayashi, T. Nishikawa, T. Takenobu, S. Mori, T. Shimoda, T. Mitani, H. Shimotani, N. Yoshimoto, S. Ogawa, Y. Iwasa, *Nat. Mater.* **2004**, *3*, 317.

[42] A. A. Virkar, S. C. B. Mannsfeld, Z. Bao, *J. Mater. Chem.* **2010**, *20*, 2664.

[43] J. Veres, S. D. Ogier, S. W. Leeming, D. C. Cupertino, S. M. Khaffaf, *Adv. Funct. Mater.* **2003**, *13*, 199.

[44] M. F. Calhoun, J. Sanchez, D. Olaya, M. E. Gershenson, V. Podzorov, *Nat. Mater.* **2008**, *7*, 84.

[45] X. Sun, Y. Liu, C.-a. Di, Y. Wen, Y. Guo, L. Zhang, Y. Zhao, G. Yu, *Adv. Mater.* **2011**, *23*, 1009.

[46] R. Hayakawa, Y. Wada, in *Fortschritte der Hochpolymeren-Forschung*, vol. *11*, Springer, Berlin/Heidelberg, Germany **1973**, 1.

[47] T. Furukawa, *Phase Transitions* **1989**, *18*, 143.

[48] R. C. G. Naber, C. Tanese, P. W. M. Blom, G. H. Gelinck, A. W. Marsman, F. J. Touwslager, S. Setayesh, D. M. De Leeuw, *Nat. Mater.* **2005**, *4*, 243.

[49] Y. Liu, T. P. Russell, M. G. Samant, J. Stöhr, H. R. Brown, A. Cossy-Favre, J. Diaz, *Macromolecules* **1997**, *30*, 7768.

[50] M. E. Roberts, N. Queralto, S. C. B. Mannsfeld, B. N. Reinecke, W. Knoll, Z. Bao, *Chem. Mater.* **2009**, *21*, 2292.

[51] A previous report on the effects of strain on liquid crystalline OFET performance has demonstrated the use of an OTS-functionalization PVA dielectric; however, in the report, the effects of stress on the OTS-modified devices were not discussed. See the following reference.

[52] F. Zhang, M. Funahashi, N. Tamaoki, *Org. Electron.* **2010**, *11*, 363.

[53] H. B. Akkerman, R. C. G. Naber, B. Jongbloed, P. A. van Hal, P. W. M. Blom, D. M. de Leeuw, B. de Boer, *Proc. Natl. Acad. Sci. USA* **2007**, *104*, 11161.

[54] C. Kim, A. Facchetti, T. J. Marks, *Science* **2007**, *318*, 76.

FULL PAPER

Magnetic Memory Effect of Nanocomposites

M. Y. Razzaq, M. Behl, and A. Lendlein*

The magnetic memory effect (MME) is the ability of magneto-sensitive materials to remember the magnetic field strength (H_{def}), at which they were deformed recently. They respond close to H_{def} either by recovering their initial shape at a switching magnetic field strength H_{sw} under stress-free conditions or by building up stress with a peak maximum at $H_{\sigma max}$ under constant strain conditions. This paper explores whether such a MME can be created for polymer-based nanocomposites. The concept is based on temperature-memory polymers (TMP) as matrix, in which silica coated iron(III)oxide nanoparticles (mNP) are dispersed. The MME was explored in a cyclic magneto-mechanical test, in which the nanocomposite sample was elongated to ε_m while being exposed to an alternating magnetic field at H_{def}. The magnetic memory was read out by determining $H_{\sigma max}$ or H_{sw}. A linear correlation between $H_{\sigma max}$ (or H_{sw}) and H_{def} in a range from 15 to 23 kA m^{-1} at a fixed frequency of $f = 258$ kHz is observed and demonstrates the excellent magnetic memory properties of the investigated nanocomposites containing either crystallizable or amorphous, vitrifiable domains as controlling units. The deformation ε_m at H_{def} can be fixed with an accuracy of more than 72% and the initial shape can be recovered almost completely by more than 86%. The MME allows the design of magnetically programmable devices such as switches or mechanical manipulators.

List of symbols/abbreviations

CMME, cyclic, magneto-mechanical experiment; cPEVA, crosslinked poly[ethylene-*ran*-(vinyl acetate)]; cPEVA(XX), crosslinked poly[ethylene-*ran*-(vinyl acetate)] composite with XX indicating mNP content in wt%; DCP, dicumyl peroxide; ΔH_{rec}, range of H applied during recovery of the sample; ΔT_g, glass transition temperature range; ΔT_m, melting temperature range; mNP, magnetic nanoparticles; mNPCs, mNP-polymer composites; H, magnetic field strength; H_{def}, magnetic field strength at deformation; $H_{\sigma\ max}$, magnetic field strength at stress maximum; H_{sw}, switching magnetic field strength at which shape recovery under stress-free conditions occurs; MME, magnetic memory effect; PEVA, poly[ethylene-*ran*-(vinyl acetate)]; R_f,

shape-fixity ratio; R_r, shape-recovery ratio; SME, shape-memory effect; TMP, temperature-memory polymer; TMPU, temperature-memory polyurethane; TMPU(XX), temperature-memory polyurethane composite with XX indicating mNP content in wt%; T_{prog}, programming temperature; T_{sw}, switching temperature; T_{trans}, transition temperature; X_c, degree of crystallinity

1. Introduction

The ambitious aim to create a memory in plastics has attracted tremendous attention in polymer science and motivated numerous fundamental studies on stimuli-sensitive polymers. The capability of a polymer to remember an initial shape, which had been deformed and fixed in a second, temporary shape, is called a shape-memory effect (SME) and was described first for thermo-sensitive polymer networks and their composites.[1–8] The netpoints, which can be of chemical or physical nature, determine the initial, permanent shape while the switching domains, which are associated to a thermal transition such as a melting or a glass transition, can fix a temporary shape by crystallization or vitrification.[9–11] Even two or three different shapes could be successfully memorized in polymers in terms of thermally-induced triple-shape[9,12–15] and multiple-shape effects.[16–18] Varying the programming temperature T_{prog}, at which the permanent shape is deformed for creating a shape-memory, influenced the recovery kinetics[19] or the switching temperature T_{sw},[19–22] at which the SME occurred in polymers having a broad glass transition ΔT_g associated to the switching domains. The latter effect was initially reported for polyvinyl alcohol-carbon nanotube nanocomposites, in which a linear correlation between T_{sw} and T_{prog} was found in the range of ΔT_g.[20] This ability to remember the temperature T_{prog}, where the polymer was deformed recently is named the temperature memory effect (TME). Recently, temperature-memory polymers (TMP) with crystallizable controlling units could be successfully created as well.[23] Here, the temperature-memory effect results from the fact that a mechanical deformation ε_m is predominantly fixed by the volume fraction of the domains associated with a thermal transition (T_m or T_g) close to T_{prog}.[20,23]

Here, we explored whether a magnetic memory effect (MME) can be created by introducing magneto-sensitivity in a TMP by incorporation of magnetic silica coated iron(III)oxide nanoparticles (mNP).[24] The mNP shall enable an indirect heating of

M. Y. Razzaq, Dr. M. Behl, Prof. A. Lendlein
Centre for Biomaterial Development
Institute of Polymer Research
Helmholtz-Zentrum Geesthacht
Kantstr. 55, 14513 Teltow, Germany
Berlin-Brandenburg Center for Regenerative Therapies
13353 Berlin, Germany
E-mail: andreas.lendlein@hzg.de

Materials
Views

www.MaterialsViews.com

ADVANCED
FUNCTIONAL
MATERIALS

www.afm-journal.de

FULL PAPER

the mNP-polymer composites (mNPCs) in an alternating magnetic field.[24] The temperature increase in an alternating magnetic field of a fixed frequency caused by hysteresis or eddy current loss mechanisms depends on the square of H.[25,26] In this way, the MME will rely on a controlled melting of the crystalline respectively softening of the glassy controlling units at T_{prog} achieved by an alternating magnetic field strength H applied during deformation (H_{def}). The magnetic memory can be read-out as H_{sw} at stress-free recovery conditions or as $H_{\sigma max}$ at strain-controlled recovery conditions. The desirable broad range ΔH, in which H_{def} can be potentially varied for creating a MME, requires a TMP nanocomposite with a broad ΔT_{trans}.

A high accuracy of the magnetically-induced response demands the magnetic field strength range ΔH_{rec} of the mechanical recovery process to be narrow. Finally, the shape fixity (R_f) and shape recovery (R_r) ratio should be consistently good over the broad range of ΔH.

Two different TMP matrices were selected to examine the generality of the concept. The first TMP contains crystallizable control units. It is a crosslinked binary mixture of two different poly[ethylene-*ran*-(vinyl acetate)]s (PEVA) differing in the their comonomer ratio. PEVA contains crystallizable polyethylene (PE) segments and generally exhibits a broad melting temperature range (ΔT_m). PEVA9 (PE content = 91 wt%, T_m = 94 °C, $\Delta T_m \approx 80$ °C) and PEVA40 (PE content = 60 wt%, T_m = 47 °C, $\Delta T_m = 60$ °C) were mixed in a weight ratio 1:1 to further increase ΔT_m to 100 °C. Crosslinking was carried out after incorporation of mNP using dicumyl peroxide (DCP) as thermally-induced initiator. The second TMP matrix material is a thermoplastic temperature-memory polyether urethane (TMPU) containing amorphous, vitrifiable controlling units. TMPU is synthesized from methylene bis(*p*-cyclohexyl isocyanate) (H12MDI), 1,4-butanediol (1,4-BD), and poly(tetramethylene glycol) (PTMG). It consists of H12MDI/1,4-BD hard segments, and H12MDI/PTMG soft segments.[24] In addition, TMPU exhibits a mixed phase with a broad T_g ($\Delta T_{g,mix} = 70$ °C), which is acting as vitrifiable switching domain. Besides a broad ΔT_{trans} both TMP exhibit small ΔT_{rec}. The selection of these two TMP matrices allows to explore the influence of the type of permanent netpoint (covalent or physical) and of the controlling unit (vitrifiable or crystallizable) on MME. Silica coated mNP having a mean aggregate size of 90 nm and a mean Fe_2O_3 domain size of 20–26 nm were chosen.[24] The silica coating mNP reduces the formation of agglomerates and supports a homogenous distribution of the mNP within the polymer matrix.[27] A frequency of 258 kHz was selected for the alternating magnetic field as it is compatible with tissue.[28]

In the following the preparation of the two series of mNPCs as well as their thermal, mechanical and magneto-mechanical properties are described. Finally, the MME of the mNPCs is explored in specifically designed cyclic, magneto-mechanical experiments (CMME).

2. Results and Discussion

2.1. Composition and Morphology of the Composites

cPEVA(xx) (xx denotes the amount of mNP in wt% determined by thermogravimetric analysis) were prepared by incorporating between 2.4 and 13.6 wt% mNP in a 1:1 mixture of PEVA9 and PEVA40 containing 1 wt% dicumylperoxide (DCP) via extrusion and subsequent crosslinking by press molding at increased temperature. The efficiency of crosslinking was confirmed by high values obtained for the gel content (G), (Supporting Information, Method S1). In pure cPEVA(00), the value of G was higher compared to the cPEVA containing mNP samples indicating a diminishing effect of mNP on crosslinking of the PEVAs (**Table 1**). The TMPU-based nanocomposites (TMPU(xx)) were prepared according to the method described previously.[24]

The distribution of mNP within the mNPCs was investigated by microscopic analysis. **Figure 1**a-1/a-2 and Figure 1d display representative SEM images of cPEVA(2.4) and cPEVA(13.6) as well as the TMPU(15.1). mNPs showed individual, small clusters in the sub micrometer length-scale, which were distributed uniformly throughout the polymer matrix. However, in cPEVA(13.6) a pattern of areas having increased mNP concentrations became apparent in the matrix, which might be attributed to the morphology of the PEVA9/PEVA40 blend. With the exception of this one sample, an excellently homogenous dispersion of the mNP in both matrix polymers was achieved.

The shape-fixity ratio of TMPs with crystallizable switching domains is substantially determined by the degree of crystallinity. The overall degree of crystallinity (X_c) of the cPEVA samples was determined by wide angle X-ray scattering (WAXS) measurements. The diffraction patterns for all samples with varying amount of mNP look qualitatively similar (Supporting Information Figure S1). cPEVA(00) exhibits two characteristic

Table 1. Thermal and morphological properties of cPEVA and its nanocomposites.

Sample ID	$G^{a)}$ [%]	Filler content[b)] [wt%]	$T_{m(2nd)}{}^{c)}$ [°C]	$\Delta H_m{}^{d)}$ [J·g⁻¹]	$T_{c1}{}^{e)}$ [°C]	$T_{c2}{}^{f)}$ [°C]	$\Delta H_c{}^{g)}$ [J·g⁻¹]	$X_c{}^{h)}$ [%]
cPEVA(00)	92 ± 1	0	92 ± 1	38 ± 1	28 ± 1	81 ± 1	59 ± 1	12 ± 2.2
cPEVA(2.4)	90 ± 1	2.4	94 ± 1	44 ± 1	29 ± 1	82 ± 1	59 ± 1	13 ± 1.9
cPEVA(7.6)	88 ± 1	7.6	96 ± 1	45 ± 1	30 ± 1	85 ± 1	61 ± 1	24 ± 3.2
cPEVA(13.6)	86 ± 1	13.6	94 ± 1	37 ± 1	29 ± 1	82 ± 1	52 ± 1	11 ± 3.7

[a)]Gel content determined by swelling experiment in CH_2Cl_2; [b)]Particle content in wt% determined by TGA; [c)]Melting temperature determined by the second heating run of DSC; [d)]Overall melting enthalpy (corrected by particle loading) determined by DSC; [e)]The crystallization temperature of PEVA40 in the blend determined by the second cooling scan of DSC; [f)]The crystallization temperature of PEVA9 in the crosslinked blend determined by the second cooling scan of DSC; [g)]Overall crystallization enthalpy of the crosslinked blend; [h)]degree of crystallinity X_c determined by WAXS analysis.
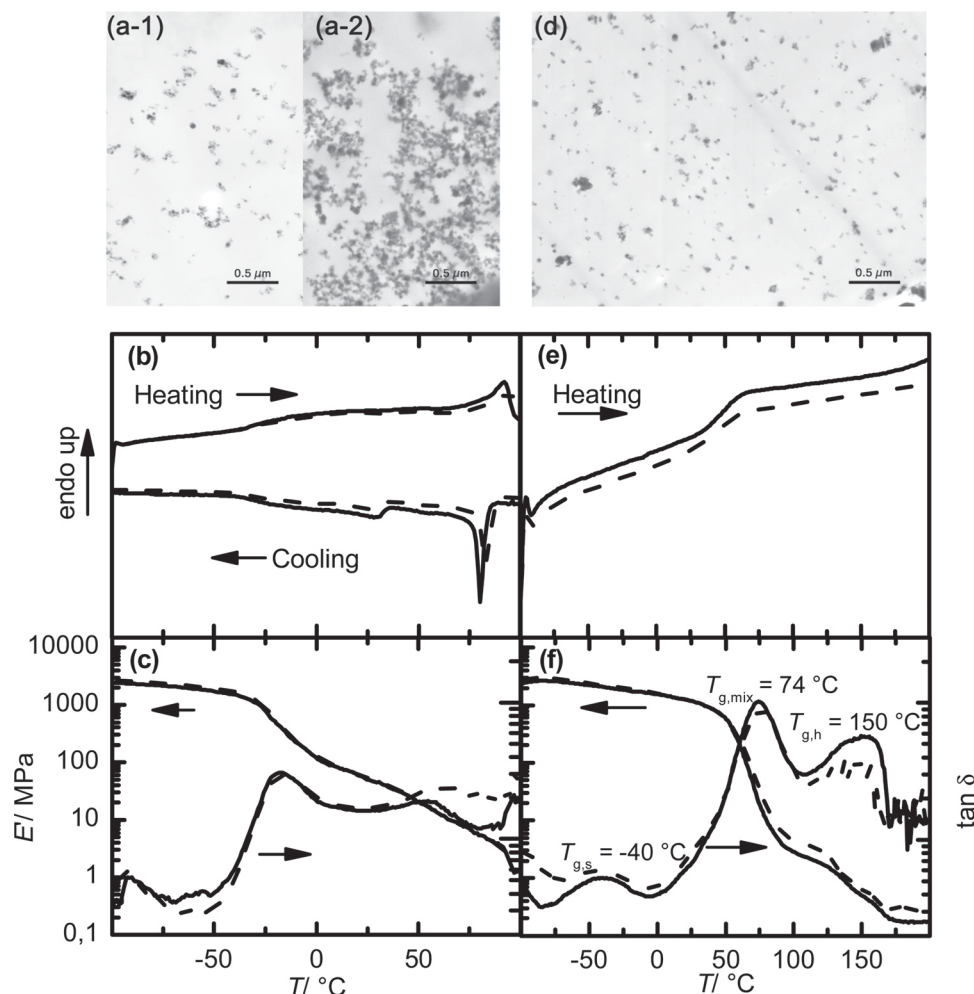
FULL PAPER

Figure 1. Characterization of mNPCs. a) SEM image taken from the cross-section of a-1) cPEVA(2.4), a-2) cPEVA(13.6). b) Melting and non-isothermal crystallization behavior of cPEVA samples determined by DSC; solid lines for pure cPEVA(00) and dashed lines for cPEVA(13.6). c) DMTA curves for cPEVA samples; solid line for cPEVA(00), dashed line for cPEVA(13.6). d) SEM image taken from the cross-section of TMPU(15.1), e) DSC thermograms of the TMPU containing samples; solid line for TMPU(00) and dashed line for TMPU(15.1). f) DMTA curves of the TMPU containing samples; solid line for TMPU(00), dashed line for TMPU(15.1)

peaks at 21.18° and 23.32°, which are assigned to the 110 and 200 reflections of the orthorhombic subcells.[23] X_c of cPEVA(00) was ~12%. The intensity of the characteristic peaks of the cPEVA-based mNPCs decreased systematically with increasing mNP content (Table 1).

2.2. Thermal and Mechanical Properties of mNPCs

The existence of a broad ΔT_{trans}, and the effect of mNPs on the thermal properties of the TMP matrices was explored by DSC and DMTA measurements. cPEVA(xx) was investigated with regard to the particle influence of mNP on the melting and crystallization behavior (Figure 1b/c, Table 1). In DSC measurements, the first heating of plain cPEVA(00) and its mNPCs exhibited two distinct melting peaks indicating the presence of two populations of crystalline lamella in the blend originating from PEVA9 and PEVA40. However, in the second heating run,

a broad $\Delta T_m = 100$ °C with only one peak maximum $T_{m(2nd)}$ was determined, which can be attributed to a crystal structure modification caused by the melting/crystallization procedure.[23] $T_{m(2nd)}$ was slightly increased from 92 °C to 96 °C by the addition of the mNP. Two crystallization peaks were detected, which were ($T_{c1} = 28$ °C, $T_{c2} = 81$ °C) attributed to PE crystallization as observed similarly in DSC of the two starting materials PEVA40 and PEVA9. A shift of both T_c to higher temperatures with increased particle content was observed for all cPEVA mNPCs, resulting in a ΔT_{trans} from 28 to 96 °C.

DSC thermograms of the TMPU-based mNPCs revealed only one T_g at 55 °C attributed to the mixed phase ($T_{g,mix}$) (Figure 1e), while in the tan δ curve two additional peaks were observed for the plain TMPU and its mNPCs (Figure 1f), corresponding to the T_g of the soft domains (–40 °C) and of the hard domains (140 °C). The broad peak with the maximum at around 74 °C reflects the $\Delta T_{g,mix}$, which ranges from 20 to 90 °C, and which was only slightly decreased when mNP were added.[19,24,25,29]
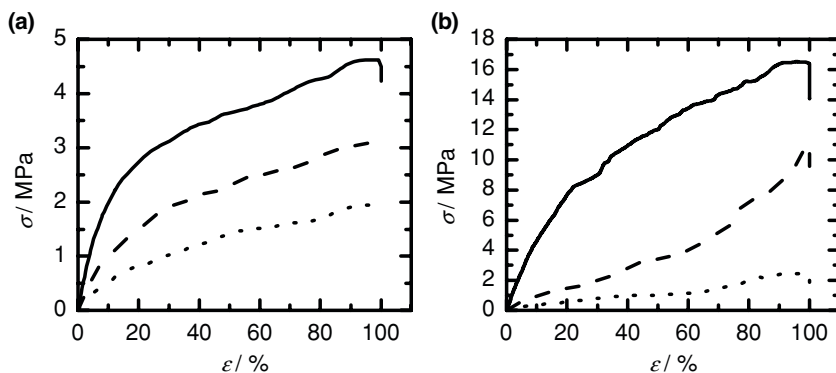
www.MaterialsViews.com

ADVANCED
FUNCTIONAL
MATERIALS

www.afm-journal.de

FULL PAPER

Figure 2. Stress versus strain curves of nanocomposite samples stretched to $\varepsilon_m = 100\%$ at three different field strengths. a) cPEVA(13.6), solid lines for $H = 15$ kA m^{-1}, dashed lines for $H = 19$ kA m^{-1}, dotted lines for $H = 23$ kA m^{-1}, b) TMPU (15.1), solid lines for $H = 15$ kA m^{-1}, dashed lines for $H = 19$ kA m^{-1}, dotted lines for $H = 23$ kA m^{-1}.

The storage modulus (E') indicated an inflection point at $T_{g,mix}$ with an onset temperature of 35 °C. The corresponding ΔT_{trans} covered the range from 35 to 90 °C.

2.3. Considerations for Material Selection and Experimental Setup for Investigating the MME

In a magneto-mechanical analysis, the extent of deformation is geometrically limited in the experimental setup by the height of the induction coil, determining the geometrical dimensions of the magnetic field. A deformation by bending[27] is not applicable for the exploration of the MME as the sample would be exposed to different magnetic field strengths during unbending in the inductor coil, as the magnetic field is most densely and homogenously in its center.

The elastic properties of the mNPCs were explored in tensile tests conducted up to a maximum elongation $\varepsilon_m = 100\%$ so that it remained within the geometric boundaries of the inductor coil, while the sample was exposed to H between 15 and 23 kA m^{-1}. This is the same H-range, which was used for the variation of H_{def} and in this way for varying T_{prog} of the mNPC matrix. In all investigated mNPC compositions the elongation at break ε_R was higher than ε_m. **Figure 2**a shows the stress needed to stretch cPEVA(13.6) to $\varepsilon_m = 100\%$ at H between 15 and 23 kA m^{-1}. A higher σ is needed to deform the composites at $H = 15$ kA m^{-1}. At higher H the samples soften due to the increased temperature. However, the σ required for deformation of TMPU(15.1) was much higher when compared to the cPEVA(13.6) mNPC (Figure 2b). This can be attributed to the high elastic modulus of the TMPU matrix as compared to the cPEVA (see **Table 3**, below).

T_{max} of the sample decreased during stretching as it depends on the sample's surface to volume ratio. The influence of stretching on T_{max} was investigated by a simultaneous recording of the strain and the temperature under magnetic field influence by using an *IR* camera. When the mNPC TMPU(15.1) was exposed to a field strength of $H = 23$ kA m^{-1} an initial $T_{max,\varepsilon=0}$ of 108 °C was achieved. Deformation to $\varepsilon_m = 50\%$ resulted in a decrease of T_{max,ε_m} to 86 °C. The lower the $T_{max,\varepsilon=0}$, the lower was the decrease and the resulting temperature difference $T_{max,\varepsilon=0} - T_{max,\varepsilon_m}$: this temperature difference was

14 °C for $H = 19$ kA m^{-1} and 7 °C for $H = 15$ kA m^{-1}. However, it should be noted that in all cases an uniform heat distribution could be achieved over the whole sample length as shown exemplarily for TMPU(15.1) at $H = 15$ kA m^{-1} for $\varepsilon_m = 0$ and $\varepsilon_m = 50\%$ (Supporting Information Figure S2). In general, the decrease of the sample's temperature occurred relatively slowly, so that only slow fixation processes are influenced by this effect, which occur especially at high H_{def}. For keeping the influence of the changing geometry small, a low value should be selected for ε_m.

The selection of a suitable mNPC for the exploration of the MME was based on the thermal and magnetic properties of the mNPCs as the temperature increase from the ambient temperature to T_{max} depends on the square of H multiplied by a constant k, which is influenced by the mNP content. k was found to be 0.06 for TMPU(04.5), 0.10 for TMPU(11), and 0.15 for TMPU(15.1); 0.02 for cPEVA(2.4), 0.08 for cPEVA(7.6) and 0.14 for cPEVA(13.6). In TMPU-based mNPCs ΔT_{trans} for the TME was between 35 and 90 °C, which correlates according to this relationship to the following ΔH ranges: from 14 to 33 kA m^{-1} for TMPU(04.5), from 11 to 25 kA m^{-1} for TMPU(11), and from 9 to 21 kA m^{-1} for TMPU(15.1). In cPEVA-based mNPCs the ΔT_{trans} for the TME was between 28 and 96 °C, correlated to a ΔH range from 15 to 60 kA m^{-1} for cPEVA(2.4), from 8 to 30 kA m^{-1} for cPEVA(7.6), and from 6 to 23 kA m^{-1} for cPEVA(13.6). Here, it can be concluded that the ΔH ranges of TMPU(04.5), cPEVA(2.4), and cPEVA(7.6) exceed the experimentally achievable range of H. A broader H range can be obtained for TMPU(15.1) when compared to TMPU(11). Therefore, cPEVA(13.6) and TMPU(15.1) were selected as suitable mNPCs to explore MME, as they show a maximum ΔT_{trans} ($\Delta T_{g,mix}$ or ΔT_m) and the best fit of the experimentally adjustable range for H between 15 kA m^{-1} and 23 kA m^{-1} (**Table 2**).

Table 2. T_{max} obtained in nanocomposites at different applied H.

Sample ID	H[a] [kA m^{-1}]	T_{max}[b] [°C]
cPEVA(13.6)	15	50 ± 1
	17	64 ± 1
	19	78 ± 2
	21	86 ± 1
	23	100 ± 2
TMPU(15.1)	15	53 ± 1
	17	66 ± 1
	19	81 ± 1
	21	91 ± 2
	23	108 ± 2

[a]Applied magnetic field strength; [b]Maximum temperature obtained in the samples.

Table 3. Magnetic memory properties of the nanocomposites.

Sample ID	H_{def}[a] [kA m^{-1}]	R_f[b] [%]	R_r[c] [%]	$E_{H(prog)}$[d] [MPa]	$H_{\sigma max}$[e] [kA m^{-1}]	σ_{max}[f] [MPa]	H_{sw}[g] [kA m^{-1}]
	15	72 ± 2	89 ± 8	3.9 ± 2	17.0 ± 0.4	2.2 ± 0.3	14.7 ± 0.5
	17	76 ± 1	88 ± 2	2.8 ± 2	18.4 ± 0.3	2.0 ± 0.1	15.3 ± 0.4
cPEVA(13.6)	19	79 ± 3	90 ± 7	1.7 ± 1	19.4 ± 0.1	1.7 ± 0.1	18.8 ± 0.5
	21	83 ± 1	92 ± 3	1.0 ± 1	20.6 ± 0.2	0.9 ± 0.2	21.0 ± 0.3
	23	90 ± 1	86 ± 3	0.8 ± 2	23.0 ± 0.6	0.4 ± 0.1	22.6 ± 0.6
	15	83 ± 4	95 ± 6	61.7 ± 5	17.0 ± 0.6	6.0 ± 0.5	16.0 ± 0.4
	17	90 ± 2	90 ± 2	33.0 ± 5	18.4 ± 0.3	5.3 ± 0.3	17.5 ± 0.3
TMPU(15.1)	19	95 ± 1	96 ± 5	16.0 ± 2	19.0 ± 0.5	4.4 ± 0.2	19.0 ± 0.2
	21	94 ± 2	92 ± 2	8.0 ± 3	21.4 ± 0.2	3.9 ± 0.2	19.3 ± 0.1
	23	97 ± 1	87 ± 5	4.6 ± 2	22.5 ± 0.6	1.7 ± 0.2	19.5 ± 0.3

[a]Values of H used for programming the mNPCs; [b]Shape fixity rate; [c]Shape recovery rate; [d]Youngs modulus at H_{def} determined during the tensile tests; [e]Maximum stress at the corresponding $H_{\sigma max}$; [f]Switching magnetic field strength during stress-free recovery.

2.4. Cyclic, Magneto-Mechanical Experiment (CMME)

The MME is quantified in cyclic magneto-mechanical experiments (CMME), whereby each cycle consists of an elongation of the sample to $\varepsilon_m = 50\%$, which is significantly smaller as the geometric boundaries given by the height of the inductor coil. Subsequently, the recovery was investigated by gradually changing H from $H_{low} = 0$ kA m^{-1} to $H_{high} = 27$ kA m^{-1} with a rate of 0.2 kA m^{-1} min^{-1} under stress-free or strain-controlled recovery conditions. This specific rate dH/dt was selected as it enables a differentiation of two different H_{sw} by the eye. However, also higher rates for dH/dt such as 0.4 kA m^{-1} min^{-1} could be used successfully. H_{def} was varied between 15 and 23 kA m^{-1}. The MME is characterized in the strain-controlled experiment by $H_{\sigma max}$ determined as H at the peak maximum stress σ_{max} during recovery and in the stress-free recovery experiment by H_{sw}, which is determined as the inflection point in the recovery curve. The magnetic field strength interval ΔH_{rec}, in which the MME occurs, describes the precision of the MME. In **Figure 3**a a scheme of the strain-magnetic field strength plot of TMPU(15.1) deformed at $H_{def} = 19$ kA m^{-1} with stress-free recovery is illustrated. The recovery curve clearly displays the correlation of the inflection point of the recovery curve H_{sw} with H_{def}. Figure 3b displays a schematic representation of the stress-magnetic field strength plot of TMPU(15.1) deformed at $H_{def} = 19$ kA m^{-1} with strain-controlled recovery. The occurrence of a peak recovery stress at fixed strain conditions has already been observed for other shape-memory nanocomposites.[19,20]

2.5. Magnetic Memory Properties

The CMME for cPEVA-based mNPC is designed in such a way that the mechanical deformation to ε_m is fixed by the fraction of crystalline domains with $T_m < T_{max}$ achieved at H_{def}. In addition, strain-induced crystallization might contribute to the fixation of the deformation of the cPEVA-based mNPC. Figure 3c displays the resulting strain recovery for cPEVA(13.6) under stress-free recovery conditions. R_rs > 85% were achieved for samples programmed at all investigated H_{def} (Table 3). R_f increased with increasing H_{def} from 72% at $H_{def} = 15$ kA m^{-1} to 90% at $H_{def} = 23$ kA m^{-1}. This increase in R_f is apparent in Figure 3c, were ε at H = 0 kA· m^{-1} is increased for high H_{def}. Excellent magnetic–memory properties with $H_{sw} = 14.7$ kA m^{-1} ($H_{def} = 15$ kA m^{-1}), $H_{sw} = 18.9$ kA m^{-1} ($H_{def} = 19$ kA m^{-1}) and $H_{sw} = 22.6$ kA m^{-1} ($H_{def} = 23$ kA m^{-1}) were obtained for cPEVA(13.6).

The strain-controlled recovery of cPEVA(13.6) samples is shown in Figure 3d. An increase of H_{def} resulted in a significant decrease of σ_{max} from 2.2 MPa for the sample deformed at $H_{def} = 15$ kA m^{-1} to around 0.4 MPa for sample programmed at $H_{def} = 23$ kA m^{-1} (Table 3), which can be explained by a decrease of the crystalline domains with increasing H_{def}. The decrease of stress after σ_{max} was most rapid in the case of the sample programmed at $H_{def} = 15$ kA m^{-1} due to the highest content of crystalline domains deformed by cold-drawing.

Furthermore, the MME of TMPU(15.1) was investigated by CMME. In the amorphous mNPCs, the mechanical deformation is predominantly fixed by the fraction of the amorphous domains associated to $T_{g,mix}$, which is in the viscoelastic state at H_{def}, whereas the amorphous domains of the mixed phase, which remain in the vitrified state at H_{def}, should support the stability of the permanent shape and in this way contribute to an almost complete recovery.[19,29] Figure 3e shows the stress-free recovery of TMPU(15.1). R_r > 85% were achieved at all investigated H_{def} (Table 3). R_f of the TMPU(15.1) mNPCs was higher compared to the cPEVA mNPCs; e.g. $R_f = 97\%$ at $H_{def} = 23$ kA m^{-1} (Table 1). An increase of R_f was also observed for TMPU(15.1) in case of higher H_{def}. Excellent magnetic–memory properties with $H_{sw} = 17$ kA m^{-1} ($H_{def} = 15$ kA m^{-1}), $H_{sw} = 19$ kA m^{-1} ($H_{def} = 19$ kA m^{-1}) and $H_{sw} = 19.5$ kA m^{-1} for $H_{def} = 23$ kA m^{-1} were obtained for the TMPU(15.1) mNPCs.

In Figure 3f the strain-controlled recovery of the amorphous TMPU(15.1) is displayed. The stress generated in this system was much higher compared to the cPEVA mNPCs. σ_{max} for TMPU(15.1) at $H_{def} = 15$ kA m^{-1} was 6 MPa, while for the cPEVA(13.6) at $H_{def} = 15$ kA m^{-1} a σ_{max} of only 2.2 MPa

www.MaterialsViews.com

ADVANCED
FUNCTIONAL
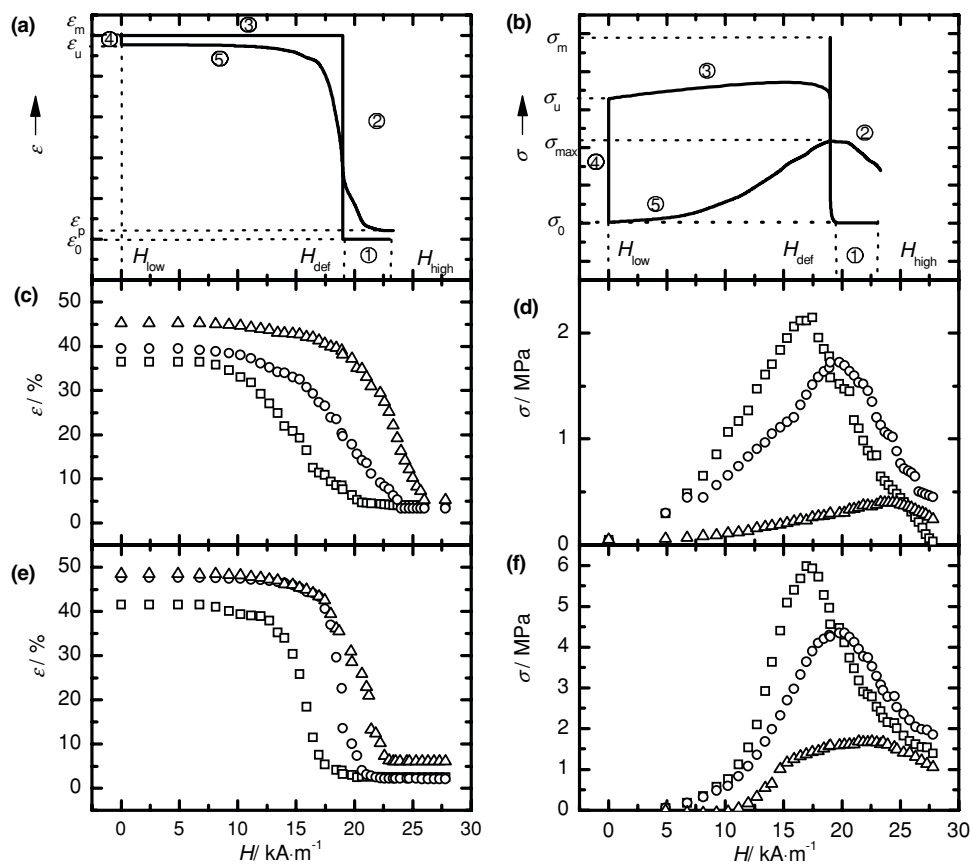MATERIALS
www.afm-journal.de

FULL PAPER

Figure 3. a) Strain-magnetic field plot for TMPU(15.1) during the stress-free rexcovery. b) Stress-magnetic field plot for TMPU(15.1) during the strain-controlled recovery. c) Strain recovery curves for cPEVA(13.6) under stress free recovery conditions. □ for H_{def} = 15 kA m^{-1}, ○ H_{def} = 19 kA m^{-1}, and Δ for H_{def} = 23 kA m^{-1} d) Stress generated for cPEVA(13.6) programmed at three different H_{def} under strain control recovery. e) Strain recovery curves for TMPU(15.1) under stress free recovery conditions. f) Stress generated for TMPU(15.1) programmed at three different H_{def} under strain control recovery conditions.

was determined. This high value of the generated stress can be attributed to the high elastic modulus of the TMPU-based mNPC. When H_{def} was increased, σ_{max} decreased due to the reduced potential of mechanical energy storage.

The MME of the stress-free recovery for both mNPCs is visualized in **Figure 4**a showing an almost linear correlation between H_{def} and H_{sw}. For the TMPU-based mNPC a better correlation between H_{def} and H_{sw} is obtained at lower H_{def} compared to cPEVA-based mNPC, which can be explained by the relatively broad ΔH_{rec} of the amorphous nanocomposite at high H_{def}. In the strain-controlled recovery, H_{def} correlates with $H_{\sigma max}$ linearly as shown in Figure 4b for the TMPU-based and the cPEVA-based mNPC. Here, no significant differences for both systems could be determined.
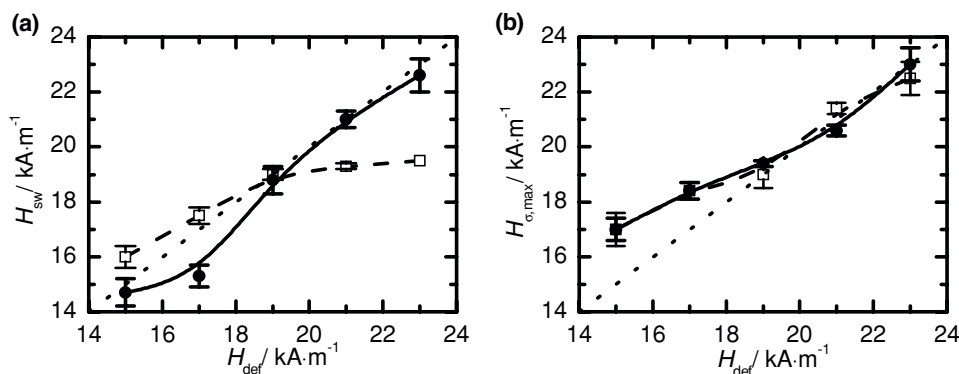

Figure 4. a) H_{sw} versus H_{def} plots for □ TMPU(15.1) and ● cPEVA(13.6) with dotted line indicating linear correlation and solid and dashed guidelines for the eye. b) $H_{\sigma\ max}$ versus H_{def} plots.

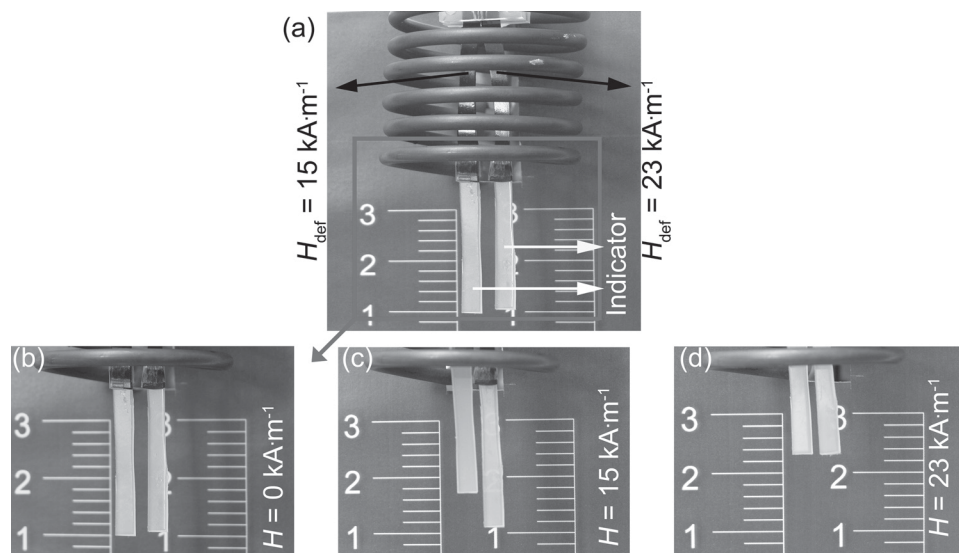**Figure 5.** Macroscopic demonstration of MME in TMPU(15.1): a) Samples after deformation at H_{def} = 15 kA m^{-1} (left) and H_{def} = 23 kA m^{-1} (right) with pure TMPU strip acting as an indicator. b) Closer view of the indicator. c) Shape change of left sample at H_{def} = 15 kA m^{-1}. d) both samples recovered at H_{def} = 23 kA m^{-1}.

A macroscopic demonstration of the MME for two TMPU(15.1) samples is shown in **Figure 5**. Both samples were deformed to ε_m = 50%, the first at H_{def} = 15 kA m^{-1} and the second at H_{def} = 23 kA m^{-1}. The deformation of samples was fixed by reducing H_{def} to 0 kA m^{-1}. A parallel shaped plain TMPU was attached to the TMPU(15.1) mNPC samples acting as an indicator to visualize the recovery outside the inductor. When the magnetic field of H = 15 kA m^{-1} was applied, the sample programmed at H_{def} = 15 kA m^{-1} was recovering, resulting in an upward movement of the indicator. When H was subsequently increased to H = 23 kA m^{-1}, both samples were recovered completely.

3. Conclusion

A series of PEVA- and TMPU-based mNPCs with different mNP content were prepared by processing from the melt. Both matrices displayed a broad T_{trans}, which was ΔT_m = 100 °C in case of cPEVA-based mNPCs and $\Delta T_{g,mix}$ between 20 and 90 °C for TMPU-based mNPCs. For the exploration of MME in an alternating magnetic field, cPEVA(13.6) and TMPU(15.1) were selected as the magnetic field strengths, which could be realized in the experimental set-up resulted in T_{max} in the range of ΔT_m or $\Delta T_{g,mix}$ for these mNPCs. A CMME was designed to investigate the effects of different H_{def} on the recovery of the mNPCs under stress-free or strain-controlled conditions. Samples deformed to ε_m = 50% displayed a decrease of T_{max} between 20 °C for H_{def} = 23 kA m^{-1} and 7 °C for H_{def} = 15 kA m^{-1}. However, these changes in the surface temperature did not significantly influence the magnetic memory behavior in both nanocomposites as cooling takes more time than the shape fixation. In both mNPCs a MME with an almost linear correlation between H_{def} and H_{sw} or $H_{\sigma,max}$ was observed. A small deviation from the linear relationship was observed for the amorphous thermoplastic system under stress-free recovery conditions at high H_{def}. Finally, the MME was demonstrated in a magneto-sensitive, programmable double switch.

4. Experimental Section

Materials: PEVA9 and PEVA40 (DuPont, US), dicumyl peroxide (DCP) (Aldrich), TMPU with the trade name of Tecoflex EG72D Noveon (Wilmington, MA, USA) were used as received. Nanoscaled particles AdNano® MagSilica 50 were provided by Degussa Advanced Nanomaterials (Degussa AG, Hanau, Germany). The particles consist of an iron(III) oxide (Fe_2O_3, CAS Number: 1309-37-1) core in a silica matrix (SiO_2, CAS Number: 112945-52-5, 7631-86-9). The mean aggregate size (Photon correlation spectroscopy of an aqueous dispersion) is 90 nm, the mean domain size (X–ray diffraction) is 20–26 nm, and the domain content (X-ray fluorescence analysis) is 50-60 wt%. The particles have a surface area of 50–65 m$^2 \cdot$g^{-1} and a saturation magnetization of 22–32 A·m^2·kg^{-1}. The density is in the range of 2.5-3.5 g·cm^{-3} .[24]

Preparation of mNPCs: PEVA9, PEVA40 and mNP were mixed by extrusion with a HAAKE PolyLab system (PTW 16/25; Thermo Electron Corporation) co-rotating twin extruder in the presence of 1 wt% DCP. The extrusion was performed at 100 °C with a screw speed between 100 and 150 rpm. The crosslinking of the nanocomposites was achieved by press molding (200 E, Dr. Collin, Ebersberg, Germany) the compound for 30 min at 150 °C and pressure of 100 bar.

TMPU mNPCs were prepared similarly by extrusion with the processing temperature between 165 and 170 °C without subsequent curing.[24]

Characterization Methods: Scanning electron microscopy (SEM) was performed on a Zeiss Gemini, Supra 40VP (Zeiss, Jena Germany) at an accelerating voltage of 10 kV. Ultra thin sections of 70 nm were cut on a Leica FC6 cryo ultra-microtome at 130 °C (Leica Microsystems GmbH Wetzlar, Germany).

Differential scanning calorimetry (DSC) experiments were conducted on a Netzsch DSC 204 Phoenix (Selb, Germany) in the temperature range from –100 °C to 200 °C with a heating and cooling rate of 10 k min^{-1} and with a waiting period of 2 min at the maximum and minimum temperature.

www.MaterialsViews.com

ADVANCED
FUNCTIONAL
MATERIALS
www.afm-journal.de

FULL PAPER

Dynamic mechanical analysis at varied temperature (DMTA) was performed on a Gabo (Ahlden, Germany) Eplexor 25 N using standard test specimen (ISO 527-2/1BB) in temperature sweep mode with a heating rate of 2 K min^{-1} at an oscillation frequency of 10 Hz. PEVA samples were investigated in the temperature interval from −100 °C to 100 °C. TMPU-based samples were investigated from -100 °C to 150 °C.

Wide angle X-ray scattering (WAXS) measurements were performed on a X-ray diffraction system Bruker D8 Discover with a two dimensional detector from Bruker AXS (Karlsruhe, Germany).

Inductive heating was accomplished by positioning the sample in an alternating magnetic field at a frequency of $f = 258$ kHz. The equipment consisted of a high-frequency generator (TIG 5/300; Huettinger Electronic, Freiburg, Germany) and a water-cooled copper coil (6 loops, diameter 4 cm, height 4.5 cm). An IR pyrometer (Metis MY84, Sensortherm; Frankfurt) was used for non-contact measuring of the sample temperature. Additionally, an IR-video camera VarioCAM® HiRes (InfraTec GmbH, Dresden, Germany) was used to visualize the achieved temperatures and to determine the heat distribution.

The magneto-mechanical experiments were conducted with a Zwick Z2.5 (Ulm, Germany) tensile tester, which was combined with the HF generator. The mNPC samples were fixed with plastic clamps in the center of the inductor. The programmed stretching and recovery under the effect of magnetic field was controlled by the tensile tester, the magnetic field strength was manually controlled by adjusting the power output of the generator. The maximum sample length of the elongated sample was limited to 4 cm due to the height of the inductor coil.

Cyclic, magneto-mechanical experiments (CMME) began with a preconditioning step followed by the cyclic test protocol consisting of a magnetic programming procedure followed by a magnetically-stimulated recovery module under stress-free or strain-controlled conditions.

Preconditioning Procedure: Samples were inductively heated at $H_{def} = 23$ kA m^{-1} for 10 min and deformed to $\varepsilon_m = 50\%$. The deformation was fixed by cooling to room temperature at $H_{low} = 0$. Subsequent recovery occurred under stress-free conditions while increasing H from H_{low} to $H_{high} = 27$ kA m^{-1}.

Cyclic test Protocol – Stress-Free conditions: The sample was cooled from H_{high} to H_{def} (step 1) and deformed to $\varepsilon_m = 50\%$ at $H_{def} = 15, 17, 19, 21$ or 23 kA m^{-1} and strain was kept constant for ten minutes to allow relaxation (step 2). H was decreased to $H_{low} = 0$ kA m^{-1} with a rate of 0.2 kA m^{-1}·min^{-1}. After a 10 min waiting period (step 3), the strain was maintained and stress was released to $\sigma = 0$ MPa at H_{low} resulting in the temporary shape characterized by ε_u (step 4). Recovery occurred by increasing the field strength to H_{high} with a rate of 0.2 kA m^{-1} min^{-1} resulting in the recovered elongation ε_p (step 5) under stress-free conditions. H_{sw} was determined as inflection point of the recovery curve.

Cyclic Test Protocol – Strain-Controlled Conditions: The sample was cooled from H_{high} to H_{def} (step 1) and a deformation of $\varepsilon_m = 50\%$ was applied at H_{def} (step 2). The sample was cooled from H_{def} to H_{low} (step 3) keeping the strain constant resulting in the remaining stress σ_u. Afterwards, the stress was released to σ_0 (step 4). The sample was gradually heated at strain-controlled conditions by increasing the field strength from H_{low} to H_{high} with a rate of 0.2 kA m^{-1} min^{-1} while σ_{max} at $H_{\sigma, max}$ was determined as the maximum of the curve (step 5).

Supporting Information

Supporting Information is available from the Wiley Online Library or from the author.

[1] M. Behl, M. Y. Razzaq, A. Lendlein, *Adv. Mater.* **2010**, *22*, 3388.
[2] P. T. Mather, X. F. Luo, I. A. Rousseau, *Ann. Rev. Mater. Res.* **2009**, *39*, 445.
[3] D. Ratna, J. Karger-Kocsis, *J. Mater. Sci.* **2008**, *43*, 254.
[4] I. A. Rousseau, *Polym. Eng. Sci.* **2008**, *48*, 2075.
[5] M. Behl, J. Zotzmann, A. Lendlein, *Adv. Polym. Sci.* **2010**, *226*, 1.
[6] W. Small, P. Singhal, T. S. Wilson, D. J. Maitland, *J. Mater. Chem.* **2010**, *20*, 3356.
[7] Q. H. Meng, J. L. Hu, *Compos. A: Appl. Sci. Manuf.* **2009**, *40*, 1661.
[8] X. F. Luo, P. T. Mather, *Soft Matter* **2010**, *6*, 2146.
[9] I. Bellin, S. Kelch, A. Lendlein, *J. Mater. Chem.* **2007**, *17*, 2885.
[10] S. Kelch, N. Y. Choi, Z. Wang, A. Lendlein, *Adv. Eng. Mater.* **2008**, *10*, 494.
[11] P. R. Buckley, G. H. McKinley, T. S. Wilson, W. Small, W. J. Benett, J. P. Bearinger, M. W. McElfresh, D. J. Maitland, *IEEE Trans. Biomed. Eng.* **2006**, *53*, 2075.
[12] M. Behl, A. Lendlein, *J. Mater. Chem.* **2010**, *20*, 3335.
[13] I. Bellin, S. Kelch, R. Langer, A. Lendlein, *Proc. Nat. Acad. Sci. USA* **2006**, *103*, 18043.
[14] M. Behl, I. Bellin, S. Kelch, A. Lendlein, *Adv. Funct. Mater.* **2009**, *19*, 102.
[15] J. Zotzmann, M. Behl, D. Hofmann, A. Lendlein, *Adv. Mater.* **2010**, *22*, 3424.
[16] Z. He, N. Satarkar, T. Xie, Y.-T. Cheng, J. Z. Hilt, *Adv. Mater.* **2011**, *23*, 3192.
[17] I. S. Kolesov, H.-J. Radusch, *Express Polym. Lett.* **2008**, *2*, 461.
[18] L. Sun, W. M. Huang, *Soft Matter* **2010**, *6*, 4403.
[19] J. Cui, K. Kratz, A. Lendlein, *Smart Mater. Struct.* **2010**, *19*, 065019.
[20] P. Miaudet, A. Derre, M. Maugey, C. Zakri, P. M. Piccione, R. Inoubli, P. Poulin, *Science* **2007**, *318*, 1294.
[21] T. Xie, K. A. Page, S. A. Eastman, *Adv. Funct. Mater.* **2011**, *21*, 2057.
[22] D. M. Feldkamp, I. A. Rousseau, *Macromol. Mater. Eng.* **2010**, *295*, 726.
[23] K. Kratz, S. Madbouly, W. Wagermaier, A. Lendlein, *Adv. Mater.* **2011**, *23*, 4058.
[24] R. Mohr, K. Kratz, T. Weigel, M. Lucka-Gabor, M. Moneke, A. Lendlein, *Proc. Nat. Acad. Sci. USA* **2006**, *103*, 3540.
[25] T. Weigel, R. Mohr, A. Lendlein, *Smart Mater. Struct.* **2009**, *18*, 025011.
[26] G. Vialle, M. Di Prima, E. Hocking, K. Gall, H. Garmestani, T. Sanderson, S. C. Arzberger, *Smart Mater. Struct* **2009**, *18*.
[27] U. N. Kumar, K. Kratz, W. Wagermaier, M. Behl, A. Lendlein, *J. Mater. Chem* **2010**, *20*, 3404.
[28] Q. A. Pankhurst, J. Connolly, S. K. Jones, J. Dobson, *J. Phys. D: Appl. Phys.* **2003**, *36*, R167.
[29] J. Cui, K. Kratz, M. Heuchel, B. Hiebl, A. Lendlein, *Polym. Adv. Technol.* **2011**, *22*, 180.

FULL PAPER

Sub-Picosecond Processes of Ferroelectric Domain Switching from Field and Temperature Experiments

An Quan Jiang,* Hyun Ju Lee, Cheol Seong Hwang,* and James F. Scott*

After calculations of various domain-switching current transients under the pulse from electrical circuit parameters, the field dependence of domain-switching speeds is accurately estimated over five orders of magnitude in a wide temperature range of 5.4–280 K from the height of domain-switching current in $Pb(Zr_{0.4}Ti_{0.6})O_3$ thin films. These estimations are extended following Merz's equation [W. J. Merz, *Phys. Rev.* 1954, 95, 690] and an ultimate domain-switching current density of 1.4×10^8 A cm^{-1} is extracted at the highest field of 0.20 MV cm^{-1}. From classical domain-nucleation models with thermal fluctuations, an ultimate (asymptotic high-field) nucleation time of 0.47 ps is derived when the domain sideways motion is kink-nucleation-rate limited.

1. Introduction

The switching time of ferroelectric polarization in response to ultrafast electric, magnetic, or optical stimuli is vital to the high-speed operation of ferroelectric data-storage devices.[1] This time is limited by the speeds of thermally fluctuating domain nucleation and subsequent growth. Ultimately, polarization reversal may be limited by optical phonon frequencies with reciprocal times of $\tau_0 \approx 10^{-13}$ s.[2–6] The terahertz emission occurring under laser illumination suggests that depolarization occurs within 1–2 ps in ABO_3 ferroelectric oxides.[7] For an ultrathin film thickness comparable to the critical size (h) of the reverse nucleus above which they grow rapidly, domain nucleation transits into a continuous switching mechanism under an

ultrahigh intrinsic coercive field (E_0).[8–10] However, experimental measurements of τ_0, h, and E_0 from the direct electrical characterization are very difficult because of instrumental limits: The fastest such time reported is about 220 ps.[11]

Experimental observations using electrical pulses on platelike ferroelectric capacitors have shown that the time- and space-averaged speed, v, of domain wall motion under a field, E, follows Merz's equation (1):[12–14]

$$v = v_0 \exp(-\delta/E) \tag{1}$$

where δ is the activation field and v_0 is the ultimate nucleation speed in thin films. Alternatively, when thermal fluctuations are considered an explicit exponential in temperature, T, the expression may be written as $v \propto \exp(-\Delta U/k_B T)$, where k_B is the Boltzmann constant and ΔU is the energy barrier for the reversed domain nucleation.[12–16] Initially, polarization switching is believed to occur via the nucleation of an oppositely polarized domain at a defect such as a dislocation or inclusion,[6] where the local barrier is reduced, followed by domain-wall forward expansion from the embryonic domain. Later, the wall moves laterally via a mechanism of kink nucleation. Miller and Weinreich suggested the possibility that the random formation of a critical kink nucleus during the wall sideways motion involves a large-aspect-ratio atomically thin triangular plate near the nascent domain wall before its lateral expansion on the same atomic plane, and that the domain growth speed is limited by nucleation rate instead of by subsequent plate expansion.[16] In this way, Merz's equation is theoretically predicted.

A large number of experimental works involving piezoresponse force microscopy (PFM) images and X-ray reflections have shown the evolution of switched-domain-wall sideways motion over time.[3,17,18] This process is dominant during the steady-state domain switching. Otherwise, the films will be partially switched only at a small portion of regions near defect centers, and a large amount of domains away from these regions are never switched without the wall sideways motion.

From low-temperature Raman scattering studies the E(TO) soft mode (vibrational normal mode) in the $PbTiO_3$ family is known to be nearly independent of T between 8–300 K.[19,20] Therefore, all ln v versus E^{-1} plots at different temperatures should cross at one point according to Equation (1), under the assumption that optical phonon frequencies asymptotically limit high-field switching. From this conclusion the asymptotic high-field domain velocity (v_0) can be obtained.

Prof. A. Q. Jiang
State Key Laboratory of ASIC & System
Department of Microelectronics
Fudan University
Shanghai, 200433, China
E-mail: aqjiang@fudan.edu.cn

Dr. H. J. Lee, Prof. C. S. Hwang
Department of Materials Science and Engineering and Inter-university
Semiconductor Research Center
Seoul National University
Seoul, 151-744, S. Korea
E-mail: cheolsh@snu.ac.kr

Prof. J. F. Scott
Department of Physics
University of Cambridge
Cambridge CB3 0HE, United Kingdom
E-mail: jfs32@hermes.cam.ac.uk

DOI: 10.1002/adfm.201101521

Materials
Views
www.MaterialsViews.com

ADVANCED
FUNCTIONAL
MATERIALS
www.afm-journal.de

FULL PAPER

However, Maksymovych et al. argued against the classical thermal nucleation model for the intrinsic domain nucleation mechanism. Their arguments were based on a PFM study of domain switching in 50–200 nm thick $BiFeO_3$ films, where the coercive field E_c changes by less than 20% over the range $T = 50$–300 K.[21] Moreover, domain nucleation at 0 K is not permitted in the model of $\nu \propto \exp(-\Delta U/k_B T)$, but in reality several ferroelectrics do exhibit such "quantum critical points".[22,23] Several other explanations have also been suggested: disorder-controlled creep wall motion in lead zirconate titanate (PZT) that is governed by a characteristic dynamic exponent μ ($\nu \propto \exp[(-\delta/E)^{\mu}]$);[17,24] and a $k_B T$-power-law decay of the dimensional exponent in the Kolmogorov–Avrami–Ishibashi (KAI) model in capacitor-type $BaTiO_3$ thin films.[25] Currently, the challenge is to reconcile all these experimental observations and theoretical models using different characterization techniques.

In regard to the previous characterizations, PFM makes use of the piezoelectric effect to image the evolution of switched domains over time.[17,21] However, the calculated area used in the determination is inaccurate because it neglects domains that do not fully penetrate the film thickness (e.g., periodically poled $LiNbO_3$ or $KTiOPO_4$ domains penetrate only 10%–20% of the thickness), besides the difficulty of accurately defining local inhomogeneous switching fields.[26,27] In this sense, a technique to study domain-switching response using platelike capacitors could be better. Such a system is shown schematically in **Figure 1**a. The domain-switching time t_0 for a given voltage V can be estimated either from the peak position of domain-current transient or from time dependence of the switched polarization fraction, $p = 1-(t/t_0)^{\nu}$.[3,4,11–13] Unfortunately, the acquired data are also incomplete in describing domain-switching kinetics because of the involvement of circuit parasitic effects, e.g., the circuit RC (resistance-capacitance) time constant, the rise time of input pulse, and charging time that depends on the capacitor area.[11] Additionally, the voltage drop across ferroelectric thin films during domain switching remains at V_c rather than V ($V > V_c$), and thus, the voltage (V_R) across the total resistance R_t in the circuit is $V-V_c$.[28] Therefore, the switching current is V_R/R_t, and the I_{sw}–V_c dependence is more informative than the t_0–V plot.

2. Results and Discussion

2.1. Calculations of Domain-Switching Currents in Ferroelectric Thin-Film Capacitors from Circuit Parasitic Parameters

Generally, the domain-switching response for the ferroelectric capacitor C_f under a square pulse with the voltage $V(t)$ is measured through in-series resistors with the total resistance R_t in the circuit, as shown in Figure 1a. Before the switching pulse, a presetting pulse of –8 V with a width far larger than the domain-switching time is applied to set the film polarization oppositely. The voltage transient V_R across R_t is guarded by the oscilloscope, and the switching current is given by:

$$I_{sw} = V_R/R_t \tag{2}$$

However, the input pulse has the rising time t_r for most commercial pulse generators, as shown by the inset in Figure 1b. If
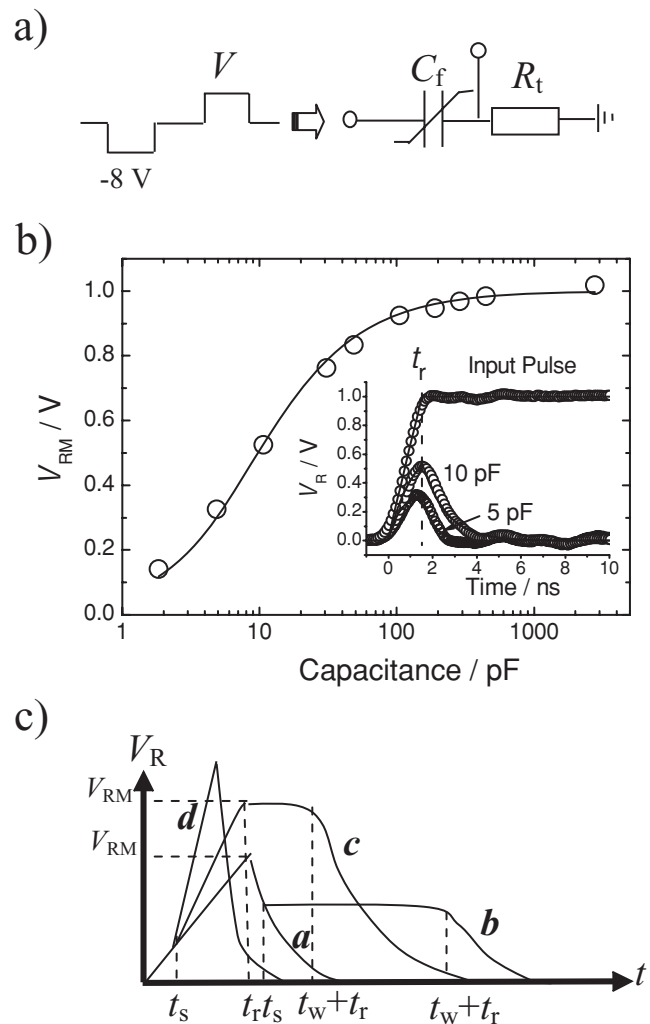

Figure 1. a) The configuration of domain-switching pulses and equivalent circuit description for the pulse performance. b) The input capacitance dependence of the voltage maximum across R_t [solid line is fit to Equation (6)]. The inset shows voltage transients across R_t with different values of C under the input pulse with $V = 1.0$ V, where the solid lines are the best fit of the data to Equation (5). c) The variation of voltage transients across R_t with different t_s and t_w values during the domain-switching time of a ferroelectric capacitor.

the input voltage of $V(t)$ from the pulse generator increases linearly from 0 to the aimed voltage V, we have:

$$V(t) = \begin{cases} V \cdot t/t_r & (t \leq t_r) \\ V & (t > t_r) \end{cases} \tag{3}$$

If C_f is replaced by a linear capacitor C in Figure 1a, we have:

$$Q/C + R_t dQ/dt = V(t) \tag{4}$$

where Q is the charge within C. The voltage transient across R_t is:

$$V_R(t) = \begin{cases} \frac{V}{t_r} R_t C \left[1 - \exp\left(-\frac{t}{R_t C}\right)\right] & (t \leq t_r) \\ \frac{V}{t_r} R_t C \left[\exp\left(\frac{t_r}{R_t C}\right) - 1\right] \exp\left(-\frac{t}{R_t C}\right) & (t > t_r) \end{cases} \tag{5}$$

**ADVANCED
FUNCTIONAL
MATERIALS**

www.afm-journal.de

Materials
Views

www.MaterialsViews.com

The inset in Figure 1b shows voltage transients across R_t with different values for C under $V = 1.0$ V and $t_r = 1.55$ ns, where the solid lines are the best fit for the data in accordance with Equation (5). The voltage is at its maximum at $t = t_r$ with:

$$V_{RM} = \frac{V R_t C}{t_r} \left[1 - \exp\left(-t_r/R_t C\right) \right] \qquad (6)$$

The validity of this equation is proved by the consequent solid-line fitting to the measured V_{RM}–C dependence (open symbols) plotted in Figure 1b.

For an ideal ferroelectric thin film [$C \to C_f$ in Figure 1a], we assume that the V_c distribution over the film is narrow enough, and that the total polarization charge under $V > V_c$ is:

$$Q = 2 P_s S + C_f V \qquad (7)$$

where P_s is the saturation polarization and S is the capacitor area. Here, C_f is assumed to be constant against V to simplify the consequent I_{sw} derivation. The voltage transient across C_f is:

$$V_f(t) = V(t) - V_R(t) \qquad (8)$$

As $t = t_s$ and $V_f = V_c$, the domains within C_f start to switch. After that, V_f is constant with time until $t = t_w + t_s$, when the domain switching completes.[28] The appearance of the current plateau is due to the maximum domain-switching current $I_{sw} = (V-V_c)/R_t$ limited by R_t ($\neq 0$), and a lasting period of domain switching time of t_w is required for the completion of domain screening charge flow (the dissipation of $2P_s S$ charge) in the circuit. After the completion of domain switching, the previous capacitor-charging process is rejuvenated until V is fully dropped across C_f.

The shape of domain-switching current transient changes with t_s, as sketched by the curves b, c, and d in Figure 1c, in comparison to the pure capacitor charging of the curve a. All these voltage transients, along with t_s and t_w, can be accurately resolved by Equation 9 and following equations.

$$\begin{cases} \frac{V}{t_r} R_t C_f \left[1 - \exp\left(-\frac{t_r}{R_t C_f}\right) \right] \exp\left(-\frac{t_s - t_r}{R_t C_f}\right) = V - V_c \\ \frac{1}{R_t} \int_{t_s}^{t_s + t_w} (V - V_c)\, dt = 2 P_s S \end{cases} \qquad (10)$$

we got

$$\begin{cases} t_s = t_r - R_t C_f \ln \dfrac{(V - V_c)\, t_r}{R_t C_f V \left[1 - \exp\left(-\frac{t_r}{R_t C_f}\right) \right]} \\ t_w = \dfrac{2 P_s S R_t}{V - V_c} \end{cases} \qquad (11)$$

Case 2 $t_s \leq t_r$:
If $t_s + t_{sw} > t_r$ (curve c), we have:

$$V_R(t) = \begin{cases} \frac{V}{t_r} R_t C_f \left[1 - \exp\left(-\frac{t}{R_t C_f}\right) \right] & (t < t_s) \\ \frac{V}{t_r} t - V_c & (t_s < t \leq t_r) \\ V - V_c & (t_r \leq t \leq t_s + t_w) \\ (V - V_c) \exp\left(-\frac{t - t_s - t_w}{R_t C_f}\right) & (t_s + t_w < t) \end{cases} \qquad (12)$$

From the equations given in (13):

$$\begin{cases} \frac{V}{t_r} R_t C_f \left[1 - \exp\left(-\frac{t}{R_t C_f}\right) \right] \exp\left(-\frac{t_s - t_r}{R_t C_f}\right) = \frac{t_s}{t_r} V - V_c \\ \frac{1}{R_t} \int_{t_s}^{t_r} \left(\frac{V}{t_r} t - V_c \right) dt + \frac{V - V_c}{R_t} [t_{sw} - (t_r - t_s)] = 2 P_s S \end{cases} \qquad (13)$$

we derived:

$$\begin{cases} t_s \approx \sqrt{\dfrac{2V_c R_t C_f t_r}{V}} & (t_s << R_t C_f) \\ t_{sw} = t_r - t_s + \dfrac{4 P_s S R + (2V_c - V) t_r + V t_s^2 / t_r - 2V_c t_s}{2(V - V_c) R_t} \end{cases} \qquad (14)$$

Otherwise, $t_s + t_{sw} \leq t_r$ (curve d) leads to Equation 15:

$$V_R(t) = \begin{cases} \frac{V}{t_r} R_t C_f \left[1 - \exp\left(-\frac{t}{R_t C_f}\right) \right] & (t < t_s) \\ \frac{V}{t_r} t - V_c & (t_s \leq t \leq t_s + t_w) \\ \frac{V}{t_r} R_t C_f + \left(V \frac{t_s + t_w}{t_r} - V_c - \frac{V}{t_r} R_t C_f \right) \exp\left(-\frac{t - t_s - t_w}{R_t C_f}\right) & (t_s + t_w < t \leq t_r) \\ \left[\frac{V}{t_r} R_t C_f + \left(V \frac{t_s + t_w}{t_r} - V_c - \frac{V}{t_r} R_t C_f \right) \exp\left(-\frac{t_r - t_s - t_w}{R_t C_f}\right) \right] \exp\left(-\frac{t - t_r}{R_t C_f}\right) & (t_r < t) \end{cases} \qquad (15)$$

Case 1 $t_s > t_r$ (curve b):

$$V_R(t) = \begin{cases} \frac{V}{t_r} R_t C_f \left[1 - \exp\left(-\frac{t}{R_t C_f}\right) \right] & (t \leq t_r) \\ \frac{V}{t_r} R_t C_f \left[1 - \exp\left(-\frac{t_r}{R_t C_f}\right) \right] \exp\left(-\frac{t - t_r}{R_t C_f}\right) & (t_r < t < t_s) \\ V - V_c & (t_s \leq t \leq t_s + t_w) \\ (V - V_c) \exp\left(-\frac{t - t_s - t_w}{R_t C_f}\right) & (t_s + t_w < t) \end{cases} \qquad (9)$$

From the equations:

From the Equation 16:

$$\frac{1}{R_t} \int_{t_s}^{t_s + t_w} \left(\frac{V}{t_r} t - V_c \right) dt = 2 P_s S \qquad (16)$$

we derived:

$$t_{sw} = \left(\frac{V_c}{V} + \sqrt{\frac{V_c^2}{V^2} + \frac{t_s^2}{t_r^2} - \frac{2 V_c t_s}{V t_r} + \frac{4 P_s S R_t}{V^2 t_r}} \right) t_r - t_s \qquad (17)$$

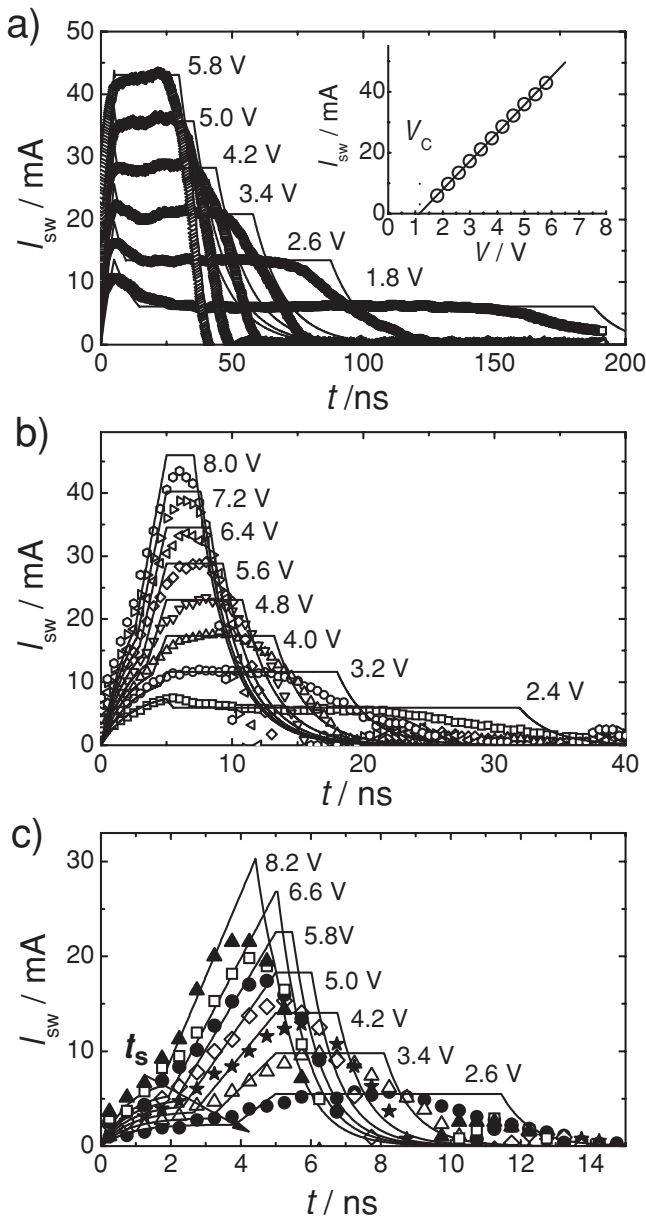where t_s is also given by Equation (14).

www.MaterialsViews.com

ADVANCED
FUNCTIONAL
MATERIALS
www.afm-journal.de

FULL PAPER

Figure 2. The variation of domain-switching current transients for Pt/PZT/Pt with the capacitor area of a) 2.5×10^{-5}, b) 4.0×10^{-6}, and c) 1.0×10^{-6} cm^2 under different values for V. The solid lines are the calculations of the data according to Equation (9–17) without invoking any domain-switching models. The inset in (a) shows the I_{sw}–V dependence fitted linearly by the solid line to Equation (18).

To calculate different domain-switching current transients of a real ferroelectric capacitor under V, the parameters for t_r, R_t, C_f, P_s, V_c and S in Equation (9)–Equation (17) are required. Here we choose $S = 2.5 \times 10^{-5}$ cm^2, $2P_s = 40.6$ μC cm^{-1}, $C_f = 85$ pF (near V_c), and $V_c = 1.14$ V (at $R_t = 100$ Ω) for the typical Pt/PZT/Pt capacitor fabricated via a sol-gel technique. The rise time for the input pulse is $t_r = 5$ ns.

Figure 2 shows the evolution of the domain-switching current transient from the curves b → c → d with shrinkage of the capacitor area from $2.5 \times 10^{-5} → 4.0 \times 10^{-6} → 1.0 \times$

10^{-6} cm^2 under different values for V. Indeed, the switching-current transient shows a plateau in Figure 2a, which degenerates into a peak as $t_s + t_w < t_r$ in Figure 2c. As $t_s > t_r$, the plateau height in Figure 2a obeys Equation (18):

$$I_{sw} = (V - V_c)/R_t \qquad (18)$$

in accord with Equation (2), and I_{sw} has a linear dependence with V so long as V_c is constant, as proved by the plot in the inset of Figure 2a. The extended linear plot intercepts with the voltage axis at V_c, and the reversal of the line slope is R_t. It is experimentally found that R_t is always higher than 100 Ω in the circuit. This result is due to the neglect of the in-series contact resistance R_c between the ferroelectric layer and electrodes, for example, the presence of interfacial non-ferroelectric passive layers (the layers are leaky at high fields during the domain-switching time), which nevertheless increases with the reduction of the capacitor area. Therefore, the accurate estimation of V_c is from the interception of the extraction of the linear I_{sw}–V plot with the V axis, rather than from the plateau height by using the formula $V_c = V–V_R$ directly. From the plateau widths under different values of V in Figure 2a, we estimate only 65% volume fraction of the domains has $V_c = 1.14$ V. This result is due to the broad V_c distribution in a genuine film. For the simplicity of this simulation, we chose the average value of $2P_s = 26$ μC cm^{-2} to fit the maximum current plateau with $V_c = 1.14$ V. The domains with the coercive voltages beyond $V_c = 1.14$ V were neglected in this model. Furthermore, V_c varies nonlinearly with the domain-switching current and thus, with V. But, if the range for the V change is narrow enough, the V_c variation (<3%) is almost negligible within our measured voltage range, and the above-linear dependence between I_{sw} and V in Equation (18) is always correct. Additionally, the maximum capacitance around V_c from the fast pulse measurement is always higher than the capacitance determined from the static capacitance–voltage loop at a slow voltage sweep; this is due to the dielectric degradation. From our fit, we found that $C_f/S = 4.4$ μF cm^{-2} is more reasonable.

The solid lines in Figure 2a–c are calculations of the domain-switching current transients under different S and V with the aforementioned corrected parameters in accord with Equation (2) and Equation (9)–Equation (17), without invoking any domain-switching models. On the whole, the computational curves agree with the experimental data except near the apexes. This apex deviation is due to the broad V_c distribution that smooths these curves. Moreover, the oversimplified parameters in our equations also affect the fitting accuracy, such as the neglects of nonlinear C_f–V dependence, the rounding of the input pulse at around t_r (shown in the inset in Figure 1), and the transmission wave reflection in the circuit, especially for small capacitors under high voltages.

Figure 3 shows switching-current transients with different capacitor areas under $V = 4.0$ V. All current transients with difference capacitor sizes can be generated from this calculation with all parameters except S fixed.

In the literature, the domain-switching speed under different V has mostly been fitted using the KAI (Kolmogordov–Avrami–Ishibashi) model with a switched-domain fraction:[29–31]

$$p(t) = 1 - \exp\left[-(t/t_0)^n\right] \qquad (19)$$

without consideration of the circuit parasitic effect, where t is time and n is the dimension of domain growth, for example,
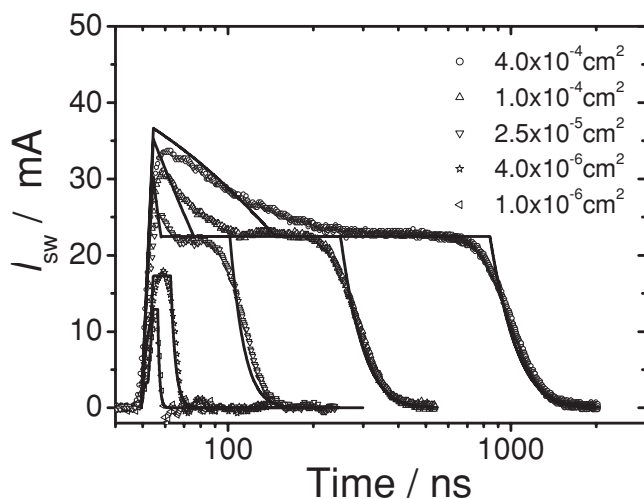
Figure 3. The variation of domain-switching current transients for Pt/PZT/Pt with different capacitor areas under $V = 4.0$ V. The solid lines are calculations of the data according to Equation (9–17).

$n = 3$ for 3D growth and $n = 2$ for 2D growth if the domains grow from pre-existing nuclei. Otherwise, n is enlarged by 1 for the stochastic nucleation throughout the whole switching process. In our case, this method is inaccurate, since domain-switching speed at V is limited by the maximum current flow through R_t in the circuit.

2.2. Estimations of Highest Domain-Switching Current Density and Field

For the description of domain-switching speed under the field correctly, we used the coercive-field dependence of the domain-switching current density rather than the t_0–V dependence. Two sequential square pulses with opposite polarities were applied to the top electrode of platelike Pt/IrO$_2$/PZT/IrO$_2$/Pt thin-film capacitors with a thickness of 140 nm. $I_{sw} \propto v$ can be changed by more than five orders of magnitude by adjusting R_t from 100 Ω to 11 MΩ in accord with Equation (2). The capacitor area, $S = 1.0 \times 10^{-4}$ cm^2, is large enough for the observation of a switching-current plateau (curve b in Figure 1c) across R_t at $V \approx 2V_c$ for I_{sw} and V_c estimations. **Figure 4** shows examples of the voltage transients across R_t. From the plateau height, V_R, we estimated V_c and I_{sw}. As R_t increased from 100 to 100 kΩ, i.e., I_{sw} decreased over three orders of magnitude, and the plateau height slightly increased. This result suggests that there was a slight reduction in V_c with increasing R_t in accord with Equation (18). The variation of I_{sw} versus E_c can be estimated using this method at various values T. This variation is large above about 70 K but small as $T \rightarrow 5.4$ K. Additional polarization–voltage (P–V) hysteresis loop measurements corroborate this observation, as shown by the inset in Figure 4.

For an accurate determination of V_c, we extrapolated the nearly linear V_R–V plot to the V axis in accord with Equation (18), where the intercept corresponds to the V_c value. This extrapolation eliminates the adverse interference of circuit parasitic effects, such as the unknown contact resistance between film and electrodes.[32] If the voltage plateau is tilted because of
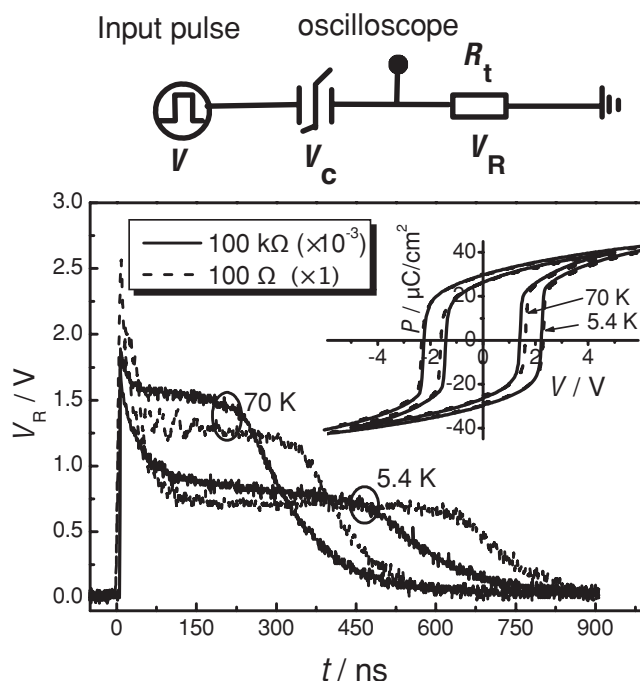

Figure 4. Voltage transient versus time for various values of Rt under $V = 3.0$ V at two different temperatures. The value in parentheses shows the magnification factor of time in the plot. The inset shows the corresponding P–V hysteresis loops at frequencies of 1 Hz (in solid lines) and 1 kHz (in dashed lines).

the presence of interfacial passive layers with capacitance C_i in the films, we use the formula $V_R(t) = V_R^0 \exp\left(\frac{t - t_s}{R_t C_i}\right)$ to determine the plateau height, V_R^0, at the start time, t_s, of domain switching.[33] After applying these corrections we calculated the dependence of $\ln J_{sw}$ on E_c^{-1} for various values of T, as shown in **Figure 5**, where $J_{sw} = I_{sw}/S$.
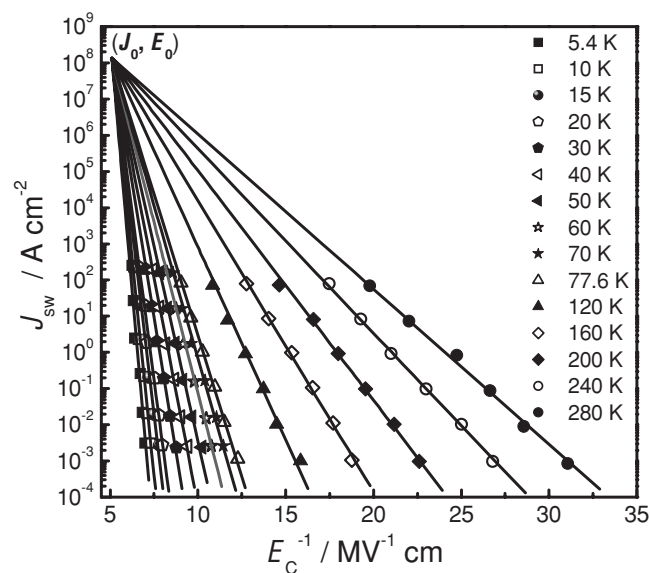

Figure 5. Dependence of domain-switching current density on the inverse coercive field at different temperatures. The solid lines that converge at point (J_0, E_0) are the best fits of the data according to Equation (20).

www.MaterialsViews.com

**ADVANCED
FUNCTIONAL
MATERIALS**
www.afm-journal.de

FULL PAPER

Note that all $\ln J_{sw}$–E_c^{-1} plots which can be fitted linearly intercept at one point (J_0, E_0) with $J_0 = 1.4 \times 10^8$ A cm^{-1} and $E_0 =$ 0.20 MV cm^{-1}. This result is in good accordance with a modified version of Merz's equation:

$$J_{sw} = J_0 \exp\left[-\delta\left(\frac{1}{E_c} - \frac{1}{E_0}\right)\right]$$
$$= J_0 \exp\left(-\frac{\Delta U + \Delta U^*}{k_B T}\right) \tag{20}$$

where $\Delta U^* = (-\delta k_B T / E_0)$ is the reduction in energy of the nucleation barrier in the one-dimensional system when the value of E_c approaches that of E_0, because of the equilibrium domain wall energy which becomes zero at the instability. The E_0 value is very plausible: it agrees within experimental uncertainty with 0.27 MV cm^{-1} reported previously[14] and is much less than the highest field ever sustained by a ferroelectric of 13 MV cm^{-1}.[34]

There are typically three or more characteristic threshold fields for switching domains in ferroelectrics: In PZT Scott et al. found that the coercive field and activation field differ by about a factor of two (typical of perovskite oxide ferroelectrics);[14] in LiNbO$_3$ a very detailed study over ten decades of domain wall velocity (ca. 0.3 nm s^{-1} to 3 m s^{-1}) revealed three threshold fields; a coercive field at 20 MV m^{-1} plus two distinct activation fields of ca. 15 and 17 MV m^{-1}; the latter resulted in a sharp change of slope for domain wall velocity.[35] Identification of these critical fields is model-dependent; for the purposes of this work the important point is that they are all within a factor of two, so for empirical fitting of our data they can be considered together without significant error.

2.3. Nucleation Rate-Limited Domain Switching in Thin Films

According to the classical domain nucleation models,[4,6,12,13,15,16,36] the domain nucleation probability is high near the sites of the preexisting defect centers during the initial stage of domain forward motion. However, the steady-state domain switching in Figure 4 is dominated by the subsequent wall sideways movement. The wall sideways motion occurs through inhomogeneous nucleation of the kink domains near the preexisting and newly formed domain walls. This kink nucleation is a stochastic process of the growth and contraction of reverse domains, and the nuclei often vanish unless the initial nanodomains reach a critical size before the statistical time $<\tau>$, above which they rapidly grow at the speed of sound (a few km s^{-1}).[36] Therefore, domain sideways motion is nucleation-rate limited if the kink nucleation time is much longer than its forward expansion time, which is about 40 ps for a 140 nm-thick PZT with $v_0 \approx 3.5$ km s^{-1} ($v_0 = 2.2$–2.8 or 4.2–4.8 km s^{-1} along the a/b or c axis). For these assumptions we have the nucleation-rate controlled current density of $J_{sw} = 2P_s/<\tau>$ in thin films for the wall sideways motion. This current is proportional to v and stable over time if the density of nucleation sites depending on the total wall area are constant. For the coalescence of two neighboring domains with radii of r_1 and r_2 into one with radius of r_1+r_2 during their sideways motion, the total wall area of about $2\pi(r_1+r_2)d$ is almost

unchanged, where d is the film thickness. Thus, the density of the nucleation centers in proportion to the wall area is roughly constant. This assumption of stable nucleation sites is also in agreement with our experimental observations. For $P_s = 32$ μC cm^{-2} inferred from the P–V loops in Figure 4, the ultimate domain nucleation time is $<\tau_0> = 2P_s/J_0 = 0.47$ ps, in agreement with the soft mode frequency of E(TO) at $\omega_0 =$ 75 cm^{-1}.[19] Each nucleus at E_0 has a very high probability to grow in excess of the critical length, and the waiting time for the hatching of the next kink nucleus can be almost neglected, i.e., τ_0 approaches the full time of domain growth, where the domain nucleation and continuous growth models merge together.[8–10] Therefore, the critical nucleus size approaches (at least is not higher than) $h \approx v_0 \tau_0 = 1.6$ nm at E_0. This is the first estimation of the ultimate kink domain nucleation time/critical length directly from electrical measurements that is consistent with both optical and structural predictions and other reports (1–2 ps time; 1–1.2 nm length).[1,3,8,7,36]

From the Miller–Weinreich model of the wall sideways motion,[16] the inverse of the activation field in Merz's equation is given by Equation (21):

$$\frac{1}{\delta} = \frac{3\sqrt{3}k_B \varepsilon^{1/2}}{16 a^{3/2}\sigma_w^{3/2}\left(\ln\frac{2l}{a}\right)^{1/2}}T \tag{21}$$

where a is the lattice constant, ε is the dielectric permittivity, σ_w is the wall energy, and $l = \frac{2}{3}\frac{\sigma_w}{P_s E_c}$ is the half-hemline length of the critical triangular nucleus, which has the height, $h = 2\sqrt{3}P_s l\left(\frac{a}{\varepsilon\sigma_w}\ln\frac{2l}{a}\right)^{1/2}$ ($h \gg l$), along one domain wall. $1/\delta$ can be experimentally obtained from the slope of $\ln J_{sw}$ versus E_c^{-1}. **Figure 6** shows a plot of δ^{-1} versus T. Although the curve has a roughly linear behavior to obey Equation (21), the deviation in the low T region is apparent, where δ^{-1} saturates below the quantum temperature, T_0. This result is because of the existence of the zero-point energy of the lattice vibrations (neglected in classical models), which sustains the domain nucleation
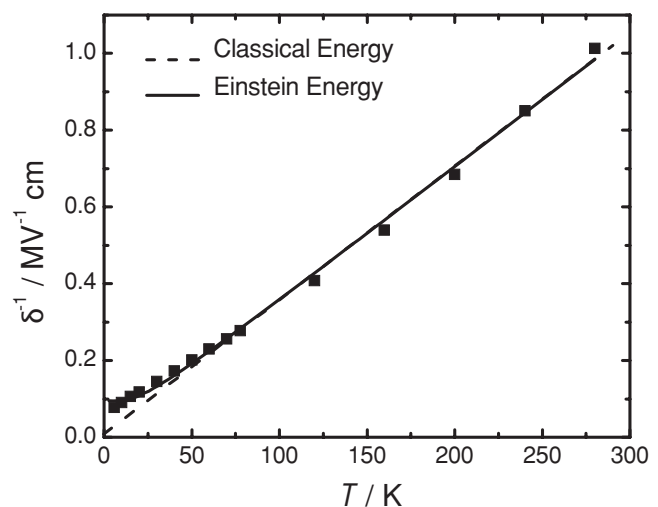

Figure 6. Temperature dependence of the activation field for the domain reversal. The dashed and solid lines are the best fits of the data before and after the zero-point energy correction according to Equation (22).

FULL PAPER

even if $T \rightarrow 0$ K. The reversed domain nucleation needs to overcome one energy barrier for the stabilization at positions of two minimum energy states, but this energy barrier is lowered with both increased temperature and zero-point energy accoding to the effective-field simulation,[37] which is zero at Curie point of ferroelectric–paraelectric phase transition. We then use the Einstein energy with a reduced temperature T^q in replacement of T in Equation (20) and Equation (21):[37,38]

$$k_B T^q = \hbar \omega_0 \left(\frac{1}{2} + \frac{1}{e^{\hbar \omega_0 / k_B T} - 1} \right) \qquad (22)$$

where $\hbar \omega_0 / 2 = k_B T_0 / 2$ is the zero-point energy. This energy approaches $k_B T$ at room temperature. Using this fact, the data can be fitted by the solid line in Figure 6 with $T_0 = 54$ K. This is a reasonable value for the temperature at which nonclassical behavior sets in, usually taken as ca. 15–35 K in quantum paraelectric $SrTiO_3$.[38,39] However, the minor deviation of the fitting below T_0 still exists due to various domain orientations in a polycrystalline film, which is hopefully improved in a single crystal. If T_0 is high enough, the V_c variation at low temperatures is small.[21] When $a \approx 4.0$ Å, $\varepsilon \approx 327$ and $P_s \approx 32$ μC cm^{-2} are assumed to be constant over T from 5.4–280 K (far away from the Curie point at 675 K),[40,41] the 180° domain wall energy along the low-index (100) lattice plane was estimated to be 13 mJ m^{-2} for $2l \times h = 36 \times 39$ nm^2 at $E_c = 150$ kV cm^{-1}. Atomistic calculations at finite temperatures produced a theoretical wall energy of 7.2 mJ m^{-2} for $BaTiO_3$, 132 mJ m^{-2} for $PbTiO_3$, and 168 mJ m^{-2} for $Pb(Zr_{0.5}Ti_{0.5})O_3$ with the Ba, Pb, and Zr centered 180° walls, respectively.[42–44] Our value that agrees to within 2 with that for $BaTiO_3$ and is much smaller than that for $Pb(Zr_{0.5}Ti_{0.5})O_3$ for the following reasons: 1) the $h \gg 2l$ condition is not satisfied in the approximation of the ln J_{sw} vs. E_c^{-1} dependence using the Miller–Weinreich model; 2) the effect of interfacial passive layers on E_c is not considered;[45] and 3) this model assumes a sharp polarization reversal from P_s to $-P_s$ near the edges of the nucleus, but the atomistic model considers the diffuseness of the polarization change across the wall.[36] According to the atomistic dynamics and coarse-grained Monte Carlo simulations, the nucleus is square and limited to one atomic plane with an area of 1.2×1.2 nm^2 at $E_c = 500$ kV cm^{-1}, where the calculated lnJ_{sw} vs. E_c^{-1} plots exactly cross at $v_0 = 4.4$ km s^{-1} at $E_0 = 0.84$ MV cm^{-1} in a highly c-axis oriented PZT film.[36]

3. Conclusions

In conclusion, we estimated sub-picosecond kink-domain nucleation time (0.47 ps) and critical length (1.6 nm) from the ln$J_{sw} - E_c^{-1}$ plots at different temperatures with a nearly sonic domain-growth velocity. These were in agreement with the predictions corresponding to the E(TO) soft-mode frequency in the Raman spectra and in situ synchrotron X-ray scattering observations of domain sideways growth.[8,19] The Merz thermal activation model describes the domain-switching kinetics at low temperatures when the zero-point vibrational lattice energy is considered.

4. Experimental Section

$Pb(Zr_{0.4}Ti_{0.6})O_3$ (PZT) thin films were prepared using sol-gel spin coating on $Pt/TiO_2/SiO_2/Si$ and $IrO_2/Pt/TiO_2/SiO_2/Si$ substrates with the thicknesses of 170 and 140 nm, respectively. Pt and Pt/IrO_2 top electrodes were sputtered on the films annealed at 750 °C for 15 min. Finally, the films were integrated into squares with the side lengths of 1–200 μm, and all capacitors were reannealed at 750 °C for 10 min after photolithographic patterning and dry etching.

Function-step voltage pulses with the nominal rising time of 2.5/5 ns were supplied by an Agilent 81150A/33250A pulse generator with the internal resistance of 50 Ω. Domain-switching response after a presetting pulse was monitored by an LC WR 6200A oscilloscope with the internal resistance of 50 Ω in series with the ferroelectric capacitor. The samples were cooled down by nitrogen/helium liquid flowing through a cryogenic LakeShore probe station interfaced with a Model 332 temperature controller. Capacitance-voltage curves were collected using an Agilent E4980A Precision LCR meter with the voltage amplitude of 0.05 V at 100 kHz. Polarization–voltage (P–V) hysteresis loops were recorded using a Radiant Materials Precision Analyzer with a triangular wave at frequencies of 1–10 kHz.

[1] J. F. Scott, C. A. P. de Araujo, *Science* **1989**, *246*, 1400.
[2] X. F. Du, I. W. Chen, *J. Am. Ceram. Soc.* **1998**, *81*, 3253.
[3] A. Gruverman, D. Wu, J. F. Scott, *Phys. Rev. Lett.* **2008**, *100*, 097601.
[4] A. K. Tagantsev, I. Stolichnov, N. Setter, J. S. Cross, M. Tsukada, *Phys. Rev. B* **2002**, *66*, 214109.
[5] M. Molotskii, A. Agronin, P. Urenski, M. Shvebelman, G. Rosenman, Y. Rosenwaks, *Phys. Rev. Lett.* **2003**, *90*, 107601.
[6] S. Jesse, B. J. Rodriguez, S. Choudhury, A. P. Baddorf, I. Vrejoiu, D. Hesse, M. Alexe, E. A. Eliseev, A. N. Morozovska, J. Zhang, L. Q. Chen, S. V. Kalinin, *Nat. Mater.* **2008**, *7*, 209.
[7] D. S. Rana, I. Kawayama, K. Mavani, K. Takahashi, H. Murakami, M. Tonouchi, *Adv. Mater.* **2009**, *21*, 2881.
[8] M. J. Highland, T. T. Fister, M. I. Richard, D. D. Fong, P. H. Fuoss, C. Thompson, J. A. Eastman, S. K. Streiffer, G. B. Stephenson, *Phys. Rev. Lett.* **2010**, *105*, 167601.
[9] L. Zhang, *Europhys. Lett.* **2010**, *91*, 47001.
[10] J. F. Scott, *Adv. Mater.* **2010**, *22*, 2106.
[11] J. Li, B. Nagaraj, H. Liang, W. Cao, C. H. Lee, R. Ramesh, *Appl. Phys. Lett.* **2004**, *84*, 1174.
[12] W. J. Merz, *Phys. Rev.* **1954**, *95*, 690.
[13] R. C. Miller, A. Savage, *Phys. Rev.* **1959**, *115*, 1176.
[14] J. F. Scott, L. Kammerdiner, M. Parris, S. Traynor, V. Ottenbacher, A. Shawabkeh, W. F. Oliver, *J. Appl. Phys.* **1988**, *64*, 787.
[15] R. Landauer, *J. Appl. Phys.* **1957**, *28*, 227.
[16] R. C. Miller, G. Weinreich, *Phys. Rev.* **1960**, *117*, 1460.
[17] T. Tybell, P. Paruch, T. Giamarchi, J.-M. Triscone, *Phys. Rev. Lett.* **2002**, *89*, 097601.

Materials
Views

www.MaterialsViews.com

ADVANCED
FUNCTIONAL
MATERIALS

www.afm-journal.de

FULL PAPER

[18] A. Grigoriev, D. H. Do, D. M. Kim, C. B. Eom, B. Adams, E. M. Dufresne, P. G. Evans, *Phys. Rev. Lett.* **2006**, *96*, 187601.

[19] J. F. Meng, R. S. Katiyar, G. T. Zou, X. H. Wang, *Phys. Status Solidi A* **1997**, *164*, 851.

[20] M. R. Joya, P. S. Pizani, *Appl. Phys. Lett.* **2010**, *97*, 031903.

[21] P. Maksymovych, S. Jesse, M. Huijben, R. Ramesh, A. Morozovska, S. Choudhury, L. Q. Chen, A. P. Baddorf, S. V. Kalinin, *Phys. Rev. Lett.* **2009**, *102*, 017601.

[22] T. Hikita, T. Maruyama, N. Yamada, *Jpn. J. Appl. Phys.* **1990**, *29*, 2519.

[23] T. Hikita, T. Maruyama, *J. Phys. Soc. Jpn.* **1992**, *61*, 2840.

[24] W. Kleemann, *J. Mater. Sci.* **2006**, *41*, 129.

[25] J. Y. Jo, D. J. Kim, Y. S. Kim, S. B. Choe, T. K. Song, J. G. Yoon, T. W. Noh, *Phys. Rev. Lett.* **2006**, *97*, 247602.

[26] S. Hong, B. Ecabart, E. L. Colla, N. Setter, *Appl. Phys. Lett.* **2004**, *84*, 2382.

[27] S. Hong, N. Setter, *Appl. Phys. Lett.* **2002**, *81*, 3437.

[28] A. Q. Jiang, Y. Y. Lin, T. A. Tang, *J. Appl. Phys.* **2007**, *101*, 104105.

[29] Y. Ishibashi, Y. Takagi, *J. Phys. Soc. Jpn.* **1971**, *31*, 505.

[30] Y. Ishibashi, *J. Phys. Soc. Jpn.* **1990**, *59*, 4148.

[31] S. Hashimoto, H. Orihara, Y. Ishibashi, *J. Phys. Soc. Jpn.* **1994**, *63*, 1601.

[32] H. J. Lee, G. H. Kim, M. H. Park, A. Q. Jiang, C. S. Hwang, *Appl. Phys. Lett.* **2010**, *96*, 212902.

[33] A. Q. Jiang, H. J. Lee, G. H. Kim, C. S. Hwang, *Adv. Mater.* **2009**, *21*, 2870.

[34] F. D. Morrison, P. Zubko, D. J. Jung, J. F. Scott, P. Baxter, M. M. Saad, R. M. Bowman, J. M. Gregg, *Appl. Phys. Lett.* **2005**, *86*, 152903.

[35] G. D. Miller, Ph. D. thesis, Stanford (USA), **1998**.

[36] Y.-H. Shin, I. Grinberg, I.-W. Chen, A. M. Rappe, *Nature* **2007**, *449*, 881.

[37] C. L. Wang, J. C. Li, M. L. Zhao, J. L. Zhang, W. L. Zhong, C. Arago, M. I. Marques, J. A. Gonzalo, *Physica A* **2008**, *387*, 115.

[38] W. Kleemann, J. Dec, B. Westwánski, *Phys. Rev. B* **1998**, *58*, 8985.

[39] W. Zhong, D. Vanderbilt, *Phys. Rev. B* **1996**, *53*, 5047.

[40] S. Yokoyama, Y. Honda, H. Morioka, S. Okamoto, H. Funakubo, T. Iijima, H. Matsuda, K. Saito, T. Yamamoto, H. Okino, O. Sakata, S. Kimura, *J. Appl. Phys.* **2005**, *98*, 094106.

[41] D. I. Woodward, J. Knudsen, I. M. Reaney, *Phys. Rev. B* **2005**, *72*, 104110.

[42] J. Padilla, W. Zhong, D. Vanderbilt, *Phys. Rev. B* **1996**, *53*, R5969.

[43] B. Meyer, D. Vanderbilt, *Phys. Rev. B* **2002**, *65*, 104111.

[44] S. P. Beckman, X. Wang, K. M. Rabe, D. Vanderbilt, *Phys. Rev. B* **2009**, *79*, 144124.

[45] L. J. Sinnamon, R. M. Bowman, J. M. Gregg, *Appl. Phys. Lett.* **2001**, *78*, 1724.

FULL PAPER

Highly Efficient Organic THz Generator Pumped at Near-Infrared: Quinolinium Single Crystals

Pil-Joo Kim, Jae-Hyeok Jeong, Mojca Jazbinsek, Soo-Bong Choi, In-Hyung Baek, Jong-Taek Kim, Fabian Rotermund, Hoseop Yun, Yoon Sup Lee, Peter Günter, and O-Pil Kwon*

A novel highly efficient ionic electro-optic quinolinium single crystals for THz wave applications is reported. Acentric quinolinium derivatives, HMQ-T (2-(4-hydroxy-3-methoxystyryl)-1-methylquinolinium 4-methylbenzenesulfonate) and HMQ-MBS (2-(4-hydroxy-3-methoxystyryl)-1-methylquinolinium 4-methoxybenzenesulfonate) exhibit high order parameters $\cos^3\theta_p = 0.92$ and $\cos^3\theta_p = 1.0$, respectively, as well as a large macroscopic optical nonlinearity, which is in the range of the benchmark stilbazolium DAST (N,N-dimethylamino-N'-methylstilbazolium 4-methylbenzenesulfonate) and phenolic polyene OH1 (2-(3-(4-hydroxystyryl)-5,5-dimethylcyclohex-2-enylidene) malononitrile) crystals. As-grown unpolished bulk HMQ-T crystals with a side length of about 6 mm and thickness of 0.56 mm exhibit 3.1 times higher THz generation efficiency than 0.37 mm thick OH1 crystals and about 8.4 times higher than 1 mm thick inorganic standard ZnTe crystals at the near-infrared fundamental wavelength of 836 nm. Therefore, HMQ crystals with high order parameter obviously have a very high potential for high power THz-wave generation and its applications.

1. Introduction

Recently, terahertz (THz) wave applications such as THz time-domain spectroscopy and THz imaging[1,2] became important due to the unique interactions of these electromagnetic waves with frequencies in the range of 0.3–30 THz, which can intersect with optical phonons due to molecular rotations and vibrations. Other features include high absorbance of semi-conducting and conducting materials, low absorbance of dielectric materials and harmlessness for biological systems.[3,4] Up to now, a limited number of efficient THz generators have been reported,[3] therefore one of most important aims in THz wave technology is the development of broad-band and highly efficient nonlinear optical materials for THz generation.

Electro-optic crystals[5] are promising materials for broadband THz generation by employing either optical rectification (OR)[6] or difference frequency generation (DFG).[7] Presently, inorganic crystals such as ZnTe and GaAs are the most popular THz sources for these techniques.[3,8] Recently, using organic electro-optic crystals, a great improvement in THz generation and detection has been demonstrated.[9–15] The state-of-the-art ionic organic crystals based on dimethylamino-stilbazolium[16,17] and non-ionic configurationally locked polyene (CLP) groups[4,12,13,18,19] exhibit a large macroscopic nonlinearity with largest diagonal electro-optic coefficients of up to $r = 53$ pm V^{-1} at 1.3 μm,[20,21] while inorganic ZnTe crystals have $r_{41} = 4.1$ pm V^{-1}.[12] The larger macroscopic nonlinearities of organic stilbazolium and CLP crystals, compared to inorganic crystals, result in significantly larger THz generation efficiency, with over one order of magnitude larger figure of merit for THz generation: 4200 (pm V^{-1})^2 for DAST (N,N-dimethylamino-N'-methylstilbazolium 4-methyl-benzenesulfonate), 4300 (pm V^{-1})^2 for DSTMS (N,N-dimethyl-amino-N'-methylstilbazolium 2,4,6-trimethylbenzenesulfonate), 5300 (pm V^{-1})^2 for OH1 (2-[3-(4-hydroxystyryl)-5,5-dimethylcy-clohex-2-enylidene]malononitrile), 370 (pm V^{-1})^2 for ZnTe and 86 (pm V^{-1})^2 for GaAs.[12,19]

The characteristics of organic crystals, including the non-linear optical properties, can still be improved or optimized for THz applications. In particular, the benchmark OH1, DSTMS, and DAST crystals exhibit their best THz generation efficiency at the fundamental wavelength in the infrared (IR) region in the range of 1.0–1.6 μm.[10a,11b,12] Below this pump wavelength region, i.e., in the near-infrared (NIR) region 0.7–1.0 μm, which is an important wavelength region for commercial high-power

P.-J. Kim, J.-H. Jeong, Prof. O-P. Kwon
Department of Molecular Science and Technology
Ajou University
Suwon 443-749, Korea
E-mail: opilkwon@ajou.ac.kr
Dr. M. Jazbinsek, Prof. P. Günter
Rainbow Photonics AG and Nonlinear Optics Laboratory
ETH Zurich, CH-8093 Zurich, Switzerland
Dr. S.-B. Choi, I.-H. Baek, Prof. F. Rotermund, Prof. H. Yun
Division of Energy Systems Research
Ajou University
Suwon 443-749, Korea
J.-T. Kim, Prof. Y. S. Lee
Department of Chemistry
Korea Advanced Institute of Science and Technology (KAIST)
Daejeon 305-701, Korea

www.MaterialsViews.com

ADVANCED
FUNCTIONAL
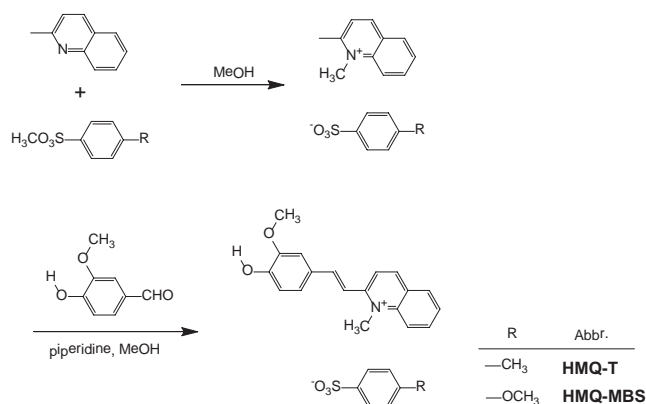MATERIALS
www.afm-journal.de

FULL PAPER

Figure 1. Synthetic route of the investigated methylquinolinium HMQ-T and HMQ-MBS.

femto-second Ti:sapphire laser sources, most of these crystals show a lower THz generation efficiency resulting from non-optimal phase matching.[10a,11b,12] In addition, high photochemical stability and large wavelength range are also important, which are related to the linear absorption of the crystals. Therefore, the development of new organic crystals with highly efficient THz generation and good phase-matchability in the NIR region is a challenging topic.

Here, we report on a series of novel highly efficient ionic electro-optic quinolinium single crystals well-suited for THz wave applications. Acentric quinolinium derivatives, HMQ-T (2-(4-hydroxy-3-methoxystyryl)-1-methylquinolinium 4-methylbenzenesulfonate) and HMQ-MBS (2-(4-hydroxy-3-methoxystyryl)-1-methylquinolinium 4-methoxybenzenesulfonate) exhibit high order parameters and large macroscopic optical nonlinearities, which are in the range of the benchmark DAST, DSTMS, and OH1 crystals. We show that as-grown bulk HMQ-T crystals with a side length of about 6 mm exhibit 3.1 times higher THz generation efficiency than benchmark best OH1 crystals and about 8.4 times higher than inorganic ZnTe crystal at the fundamental wavelength of 836 nm.

2. Results and Discussion

2.1. Design and Molecular Optical Nonlinearity

The chemical structure of the investigated quinolinium derivatives, HMQ-T and HMQ-MBS are shown in **Figure 1**. While benchmark ionic electro-optic crystals showing large optical nonlinearities, such as DAST,[16,20] DSTMS[11] and DAPSH[17a,b] use 1-methylpyridinium or 1-phenylpyridinium salts, HMQ-T and HMQ-MBS use 1-methylquinolinium salt for the electron acceptor group. However, up to now the electron-accepting characteristics of 1-methylquinolinium derivatives have been only scarcely investigated.[22] By electric-field induced second harmonic generation (EFISH) experiments with the non-polar solvent chloroform, in which ionic cations and anions were not dissociated thus allowing such measurements for ionic molecules, the electron-accepting ability of 1-methylquinolinium

iodide with (dialkylamino)-bithiophene electron donor group was measured[22b] to be $\mu\beta_z = 1250 \times 10^{-48}$ esu, similar to 1-methylpyridinium salt (β_z is the vector component of the hyperpolarizability tensor β_{ijk} along the direction of the dipole moment μ).[22b]

In order to investigate the electron accepting characteristics of 1-methyl quinolinium with the 4-hydroxy-3-methoxybenzene electron donor, we calculated the molecular hyperpolarizability tensor β_{ijk} of 2-(4-hydroxy-3-methoxystyryl)-1-methyl-quinolinium (HMQ) cation by quantum chemical calculations with finite field (FF) density functional theory (DFT)[23] using B3LYP/6-311+G∗.[24] The direction of the –O–H group can strongly influence the characteristics of molecular optical non-linearities, including the main direction and the maximal amplitude of the first hyperpolarizability tensor β_{ijk}.[25] In many cases, the C–O–H plane practically coincides with the plane of phenyl and methoxy groups.[12,19,25] In addition, the expected direction of the O–H group in the gas phase is such that the hydrogen is close to the methoxy group, as shown in Figure 1. This is due to the high tendency to form strong intramolecular hydrogen bonds of O–H···O–CH₃.[25] Therefore, for the quantum chemical calculation of the optimized molecular conformation (OPT) of the HMQ cation, the molecular arrangement illustrated in Figure 1 was used. For the optimized HMQ cation, denoted HMQ (OPT), we then calculated the zero-frequency hyperpolarizability tensor β_{ijk} by FF method and evaluated the maximal first-order hyperpolarizability β_{max}.[23] The results are listed in **Table 1** and further details in Table S1 in the Supporting Information (SI).

Although the HMQ cation possesses relatively weaker phenolic and methoxy electron donors compared to conventional dimethylamino electron donor,[5,26] the HMQ (OPT) cation with 1-methylquinolinium electron acceptor exhibit a large maximal first-order hyperpolarizability β_{max} of 145 $\times10^{-30}$ esu, which is similar as for DAST (159 $\times10^{-30}$ esu)[27] with 1-methylpyridinium electron acceptor and dimethylamino electron donor, and is higher than in OH1 molecules (104 $\times10^{-30}$ esu).[12a] 1-Methylquinolinium derivatives having the dimethylamino group as electron donor as in DAST exhibit a larger maximal first-order hyperpolarizability β_{max} (184 $\times 10^{-30}$ esu). This means that the electron accepting strength of 1-methylquinolinium is larger than the one of the widely used 1-methylpyridinium acceptor. Therefore, HMQ and its derivatives with 1-methylquinolinium as acceptor can be interesting materials for nonlinear optical applications, including THz wave generation.

2.2. Synthesis and Characterization

The methathesized synthesis and the resulting crystal structures of HMQ-T and HMQ-MBS have been published previously.[28,29] Here, we report on the optimization of the synthesis procedure, as well as on the relevant physical properties including the linear and the nonlinear optical properties, bulk crystal growth and THz wave generation with these materials.

In this work, the HMQ derivatives were synthesized by two methods: i) metathesization of 2-(4-hydroxy-3-methoxystyryl)-1-methylquinolinium iodine (HMQ-I) with silver(I) methyl-benzenesulfonate for HMQ-T as reported previously;[28] and,

Table 1. Physical and structural data of HMQ crystals in comparison with benchmark DAST[27] and OH1[12a] crystals: the wavelength of the maximum absorption λ_{max} in methanol solution, the melting temperature T_m, the thermal weight-loss temperature T_i, the maximal first-order hyperpolarizability β_{max} determined by quantum chemical calculations considering OPT cation and EXP cation molecules, order parameter $\cos^3(\theta_p)$, where the angle θ_p between the main charge-transfer axis of the crystal and hyperpolarizabilities β of the molecules, the diagonal component of the effective hyperpolarizability tensor $\beta_{ijk}^{eff} \propto \chi_{ijk}^{(2)}$. $N^2\langle(\beta^{eff})^2\rangle$ is the calculated figure of merit for non-resonant powder SHG generation relative to DAST. Powder SHG efficiency was measured at a fundamental wavelength of 1.9 μm relative to DAST powder.

	λ_{max} [nm]	T_m/T_i [°C]	β_{max} (OPT) [10^{-30} esu]	β_{max} (EXP) [10^{-30} esu]	Order parameter $\cos^3(\theta_p)$	$\|\beta_{iii}^{eff}\|$ [10^{-30} esu]	$N^2\langle(\beta^{eff})^2\rangle$	Powder SHG	Crystal structure (point group) symmetry
HMQ-T	439	273/297	145	169	0.92	155	0.77	0.63	monoclinic Pn (m)
HMQ-MBS	441	265/291	145	178	1.0	178	0.94	0.23	monoclinic Pc (m)[29]
DAST[27]	475	250/250	159	194	0.83	161	1	1.0	monoclinic Cc (m)
OH1[12a]	426	212/325	104	93	0.69	63	0.3	0.5	orthorhombic $Pna2_1$ (mm2)

ii) condensation reactions of vanillin with dimethylquinolinium 4-methylbenzenesulfonate for HMQ-T and with dimethylquinolinium 4-methoxybenzenesulfonate for HMQ-MBS (see Figure 1 and the Experimental Section). We encountered few limitations for bulk crystal growth and optical experiments using the previously reported methathesization method. We observed a relatively low solubility of HMQ-I in the reaction solvent methanol (0.14 g per 100 g methanol at 40 °C). Due to the low solubility of HMQ-I in the reaction solvent, the methathesization of larger amounts, which are needed for bulk crystal growth, is relatively hard. Additionally, in many cases the physical properties of phenolic π-conjugated materials are highly sensitive to impurities and environmental conditions.[12a,25] The residual silver(I) iodide accompanying from the methathesization can lead to variations of the physical and optical properties in solution and in the solid state. In inductively coupled plasma (ICP) analysis of our HMQ-T materials synthesized by methathesizations, we observed up to 24 ppm silver, while silver has not been detected for materials synthesized by condensation. In addition, the color of crystalline materials from methathesization is dark brown, while the one from the condensation method is brighter orange. Moreover, we found polymorphism in HMQ-T: the dark brown HMQ-T material recrystallized from methanol after the synthesis of methathesizations exhibit different powder X-ray diffraction (XRD) patterns compared to the reported crystal structure in the literature.[28] Therefore, for further characterization and crystal growth we used the HMQ-T and HMQ-MBS materials synthesized by condensation as shown in Figure 1.

The physical and structural data of HMQ derivatives are listed in Table 1. For comparison, two of the best organic crystalline materials, ionic DAST and non-ionic OH1 crystals, are also listed.[12a,27] According to the well known nonlinearity-transparency trade-off,[5] a similar and a higher maximal first-order hyperpolarizability β_{max} of the HMQ cation than the one of DAST and OH1 crystals, respectively, can be expected to correlate with a similar and a higher wavelength of maximum absorption λ_{max} of the HMQ derivatives as compared to the ones found in DAST and OH1 crystals. We measured the absorption properties of HMQ derivatives in methanol solution. As listed in Table 1, HMQ-T and HMQ-MBS have a larger wavelength of maximum absorption λ_{max} than OH1 as expected, but much lower than DAST: 439 nm for HMQ-T, 440 nm for HMQ-MBS, 426 nm for OH1, and 475 nm for DAST. In a different solvent,

acetonitrile, the wavelength of the maximum absorption λ_{max} (427 nm for HMQ-T and HMQ-MBS, see Figure S1 in the SI) is still considerably lower than for DAST (471 nm). The low absorption of HMQ derivatives combined with a relatively large molecular nonlinearity may be an advantage considering the photochemical stability and larger transparency range. While DAST crystals having dimethylamino electron donor shows only one absorption peak at the wavelength of the maximum absorption λ_{max} of about 475 nm, both HMQ-T and HMQ-MBS crystals having phenolic electron donor show additional absorption peaks at higher wavelength in the range of 500–700 nm in both methanol and acetonitrile solutions (see in Figure S1 in the SI). This may be due to the phenolic electron donor, which is highly sensitive to the environmental condition, allowing the co-existence of various resonance states, benzenoid and quinoid forms.

We also investigated the thermal properties of HMQ materials by differential scanning calorimetry (DSC) and thermal gravimetric analysis (TGA) at a scanning rate of 10 °C min⁻¹. As shown in **Figure 2**, HMQ-T crystals exhibit a high thermal stability with thermal weight-loss temperature T_i up to more than 290 °C, which is higher than that for DAST crystals of
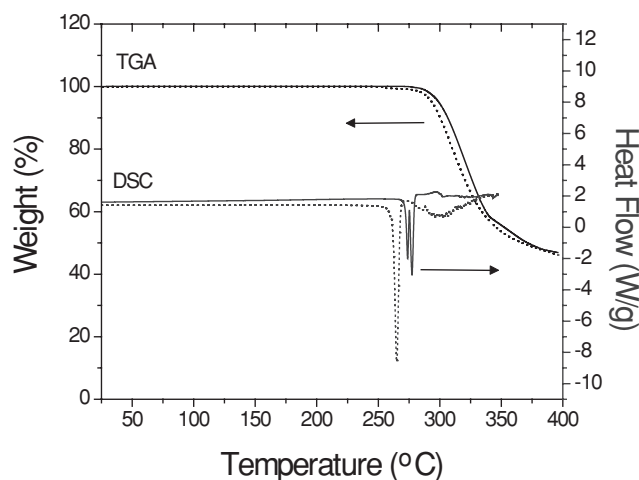

Figure 2. TGA and DSC thermodiagram of HMQ-T (solid line) and HMQ-MBS (dotted line) crystals.

www.MaterialsViews.com

ADVANCED
FUNCTIONAL
MATERIALS
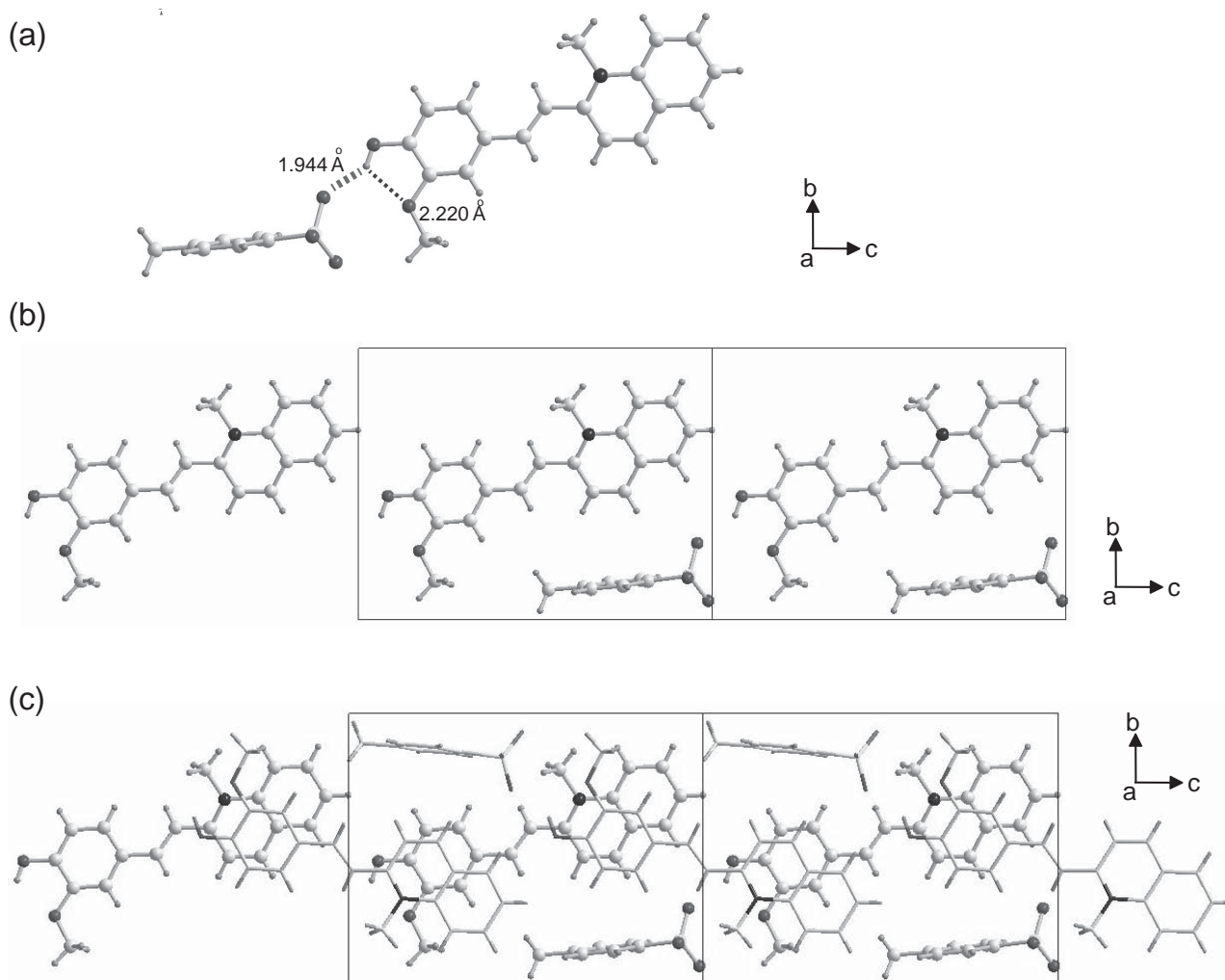www.afm-journal.de

FULL PAPER

Figure 3. Molecular conformation (a) and crystal packing diagram (top view of an acentric chain (b) and the stack of two acentric chains (c)) projected along the *a*-axis of HMQ-T crystals.

260 °C.[16c] The melting temperature T_m is 273 °C for HMQ-T and 265 °C for HMQ-MBS, which are also higher than that for DAST (T_m = 256 °C).[16c]

2.3. Macroscopic Optical Nonlinearity in Crystals

To examine the macroscopic optical nonlinearities, we first analyzed the single X-ray structures of HMQ-T and HMQ-MBS crystals. The crystal structure for HMQ-T crystals has been analyzed newly here, but was found to be identical to that reported in the literature,[28] and for HMQ-MBS crystals the crystal structure reported elsewhere[29] wasused. The molecular conformation and crystal packing diagram of HMQ-T and HMQ-MBS crystals are shown in **Figure 3** and **Figure 4**. The HMQ-T and HMQ-MBS crystals exhibit monoclinic *Pn* and *Pc* space groups, respectively, with point group symmetry *m*.

The main supramolecular interactions in the HMQ-T and HMQ-MBS crystals are strong Coulomb forces between 1-methylquinolinium cations and sulfonate anions, as well as strong

hydrogen bonds between phenolic OH group and sulfonate group[28,29]: –O–H···O–S– groups with O···O distances of about 2.66 Å for HMQ-T and about 2.65 Å for HMQ-MBS (see Figure 3a and Figure 4a). The molecular conformation of HMQ cation in HMQ-T and HMQ-MBS crystals is different.[28,29] In both HMQ-T and HMQ-MBS crystals, the phenolic group (i.e., 4-hydroxy-3-methoxyphenyl group) and the –CH=CH– group are practically in the same plane. However, in both crystals the quinolinium group is not in same plane as the HO–Ph–CH=CH– group due to steric hindrance between the hydrogen atoms on the *N*-substituted methyl group of the quinolinium group and the hydrogen atom on the –CH=CH– group: the twisted angle between the plane of the phenyl ring on the phenolic group and the plane of the pyridinium ring including the nitrogen atom (N[+]) on the quinolinium group is about 17° for HMQ-T[28] and about 27° for HMQ-MBS,[29] while 29° for HMQ (OPT) cations. In addition, the O–H electron-donor group has a different direction in these crystals: in the HMQ-T crystals the O–H direction is toward the neighboring O–CH₃ group with strong intramolecular hydrogen bond with the oxygen
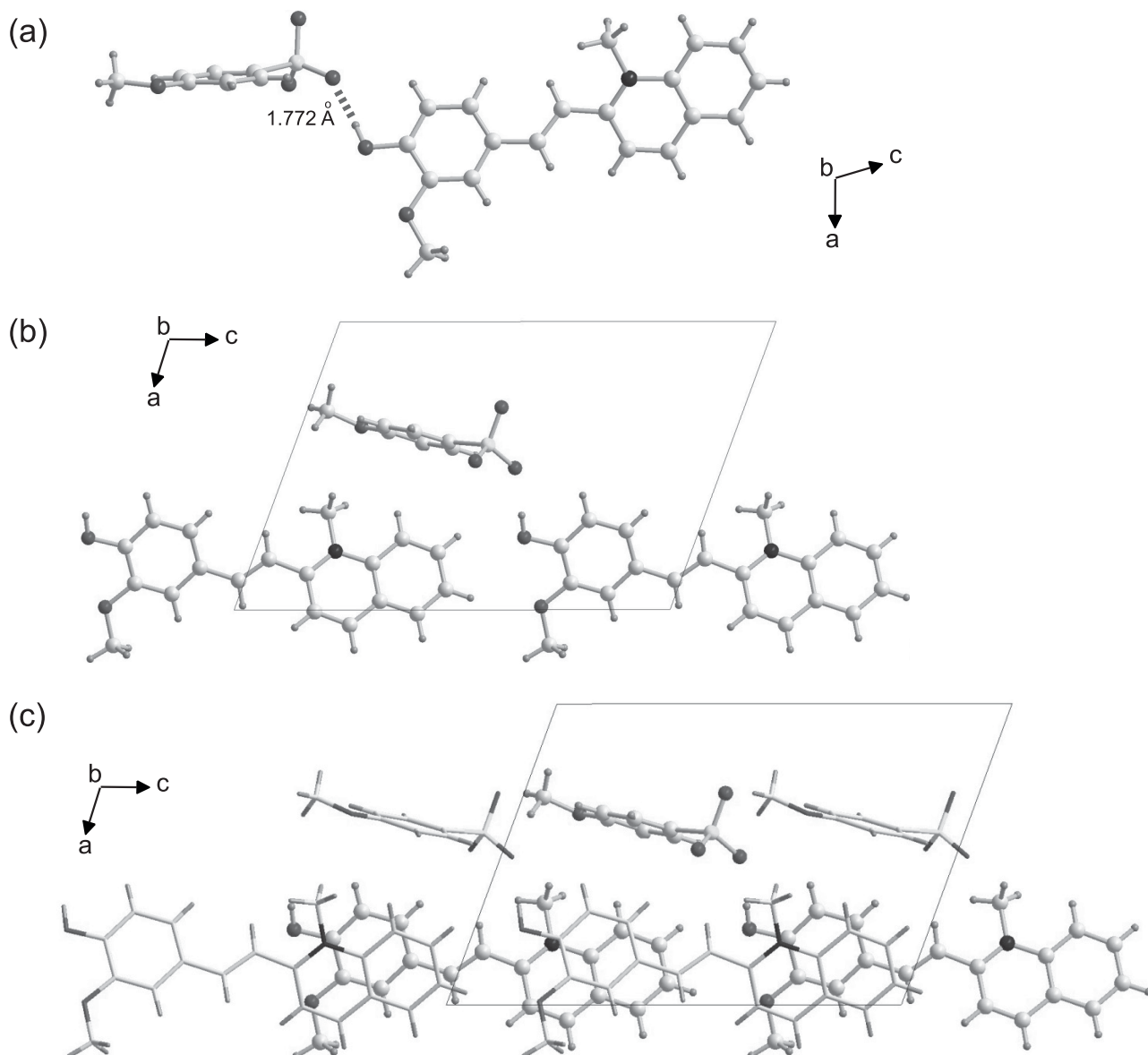
ADVANCED
FUNCTIONAL
MATERIALS
www.afm-journal.de

Materials
Views
www.MaterialsViews.com

FULL PAPER

(a)

1.772 Å

(b)

(c)

Figure 4. Molecular conformation (a) and crystal packing diagram (top view of an acentric chain (b) and the stack of two acentric chains (c)) projected along the *b*-axis of HMQ-MBS crystals.

atom on the neighboring O–CH$_3$ group with H···O distance of 2.22 Å,[28] similarly as in the OPT molecule with H···O distance of 2.12 Å, while the opposite direction appears in HMQ-MBS[29] (see Figure 3a and Figure 4a). We attribute this difference to different positions of the counter anions, which determines the direction of the OH group, forming strong hydrogen bonds with the sulfonated group as discussed above, which outweighs the intramolecular hydrogen bond with the oxygen atom. As shown in Figure 3b and Figure 4b, the pairs of the HMQ cation and anion form an acentric polar layer, which are stacked one by one (see Figure 3c and Figure 4c).

We calculated the microscopic nonlinearity of HMQ cations (EXP), determined by single X-ray structural analysis in each crystal, by density functional theory using the finite filed (FF)

method,[23] in order to investigate the influence of different molecular geometry with a different tilt angle in the π-conjugated bridge[30] and the different direction of the O–H group in the solid state.[25] The resulting maximal first-order hyperpolarizability β_{max} is listed in Table 1 and more details are given in Table S1 in the SI. For both EXP conformations in the crystal, the maximal first-order hyperpolarizability β_{max} slightly increases compared to optimized molecules of HMQ (OPT), 169 ×10^{-30} esu for HMQ-T (EXP) and 178 ×10^{-30} esu for HMQ-MBS (EXP) compared to 145 ×10^{-30} esu for OPT molecules, and the difference between the two crystalline conformations is relatively small. Although the HMQ cation possesses a different direction of the electron-donor OH group in the solid state, still in the same plane as the phenyl ring, the microscopic optical nonlinearities are maintained.
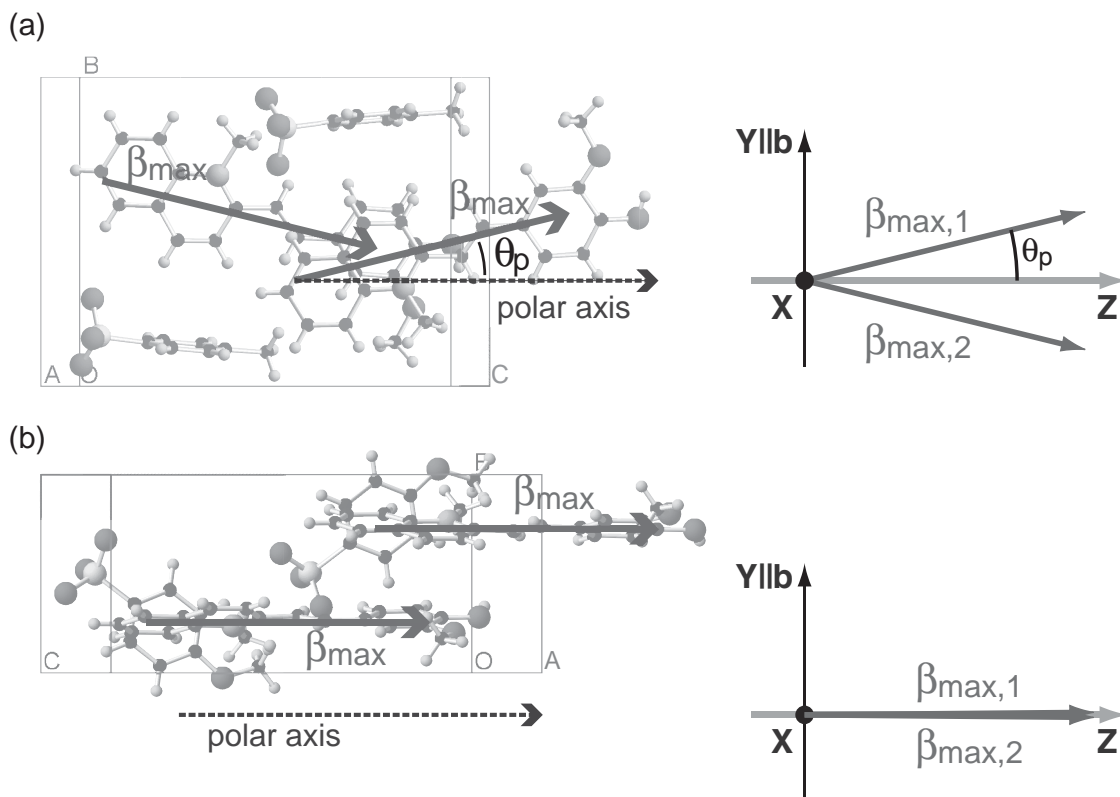
www.MaterialsViews.com

ADVANCED
FUNCTIONAL
MATERIALS
www.afm-journal.de

FULL PAPER

(a)

(b)

Figure 5. Orientation of the molecules within one unit cell in the crystallographic *abc* system and the Cartesian *XYZ* system (the angle between the crystallographic *c* axis and *Z* is $\psi = 1.3°$ for HMQ-T and 7.0° for HMQ-MBS). The dotted and the solid vectors present the polar axis and the direction of the hyperpolarizabilities β of the chromophores, respectively. The angle between the main charge-transfer axis of the crystal *Z* and hyperpolarizabilities β of the molecules is $\theta_p = 13.8°$, leading to an order parameter of $\cos^3\theta_p = 0.92$ for HMQ-T and $\theta_p = 0.5°$, leading to an order parameter of $\cos^3\theta_p = 1.0$ for HMQ-MBS.

When nonlinear optical chromophores possess an asymmetric shape or the position of electron donor and acceptor is not exactly at each end of the long axis of a molecule, we cannot simply assume that the long axis of molecule is the main direction of the first-order hyperpolarizability β_{max},[31] which is an important information for the evaluation of macroscopic optical nonlinearities. Because the position of the nitrogen atom (N+) in the quinolinium acceptor of the HMQ cation is not at the end, but at a side of the long axis of the molecule, we evaluated the direction of the maximal first-order hyperpolarizability β_{max} of HMQ cation based on the FF calculation details reported in Table S1 of the SI. The resulting directions are indicated in **Figure 5**, which shows the projections to the *YZ* plane of the Cartesian *XYZ* system. The Cartesian *XYZ* system was chosen so that the *Y* axis is parallel to the crystallographic (symmetry) *b* axis and the *Z* axis in the *ac* crystallographic plane is along the polar axis of the crystal, or more precisely along the main charge transfer axis of the crystal. For both crystals the polar axis *Z* is almost parallel to the *c* crystallographic axis, as shown in Figure 5.

The angle θ_p between the main charge-transfer axis of the crystal and the maximal first-order hyperpolarizability β_{max} of the molecules is close to zero: $\theta_p = 13.8°$ for HMQ-T and 0.5° for HMQ-MBS. This means that in both crystals the chromophores align almost perfectly parallel with the order parameter

close to 1.0: $\cos^3(\theta_p) = 0.92$ for HMQ-T and 1.0 for HMQ-MBS, which is higher than for both DAST and OH1 crystals as listed in Table 1. Such an alignment optimizes the diagonal susceptibility element and is very favorable for THz-wave generation.

We evaluated the diagonal and off-diagonal component of the effective hyperpolarizability tensor $\beta_{ijk}^{eff} \propto \chi_{ijk}^{(2)}$ in the Cartesian *XYZ* system, considering all hyperpolarizability tensor components β_{mnp} calculated by the FF method and the orientation of the chromophores in the crystallographic system.[23] The diagonal component of the effective hyperpolarizability tensor β_{iii}^{eff} is listed in Table 1 and other non-zero off-diagonal component in Table S2 in the SI. Due to the high order parameter $\cos^3\theta_p$, close to 1.0, the off-diagonal component of HMQ-T and HMB-MBS can be ignored. HMQ-T and HMQ-MBS crystals exhibit a large diagonal component of the effective hyperpolarizability tensor, $\beta_{333}^{eff} = 155 \times 10^{-30}$ esu and 178×10^{-30} esu, respectively, which is larger than for DAST (161×10^{-30} esu) and OH1 (63×10^{-30} esu) crystals. DAST and OH1 have been evaluated previously using analogous calculation methods.[12,27]

In order to screen the macroscopic optical nonlinearity, we performed powder second harmonic generation (SHG) tests[32] at a non-resonant fundamental wavelength of 1.9 μm. The SHG efficiency was measured relative to that of the well-characterized ionic DAST crystals. HMQ-T and HMQ-MBS crystalline powders exhibit a large macroscopic nonlinearity with SHG
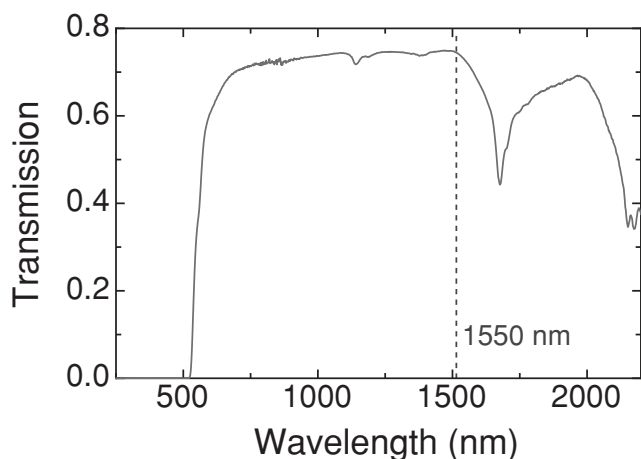
**ADVANCED
FUNCTIONAL
MATERIALS**

www.afm-journal.de

FULL PAPER

*Materials
Views*

www.MaterialsViews.com

Figure 6. Transmission spectra of an unpolished HMQ-T crystal (*b*-plate) with a thickness of 0.32 mm using un-polarized light.

efficiencies of about 0.63 and 0.23 times that of DAST powder, respectively. The SHG efficiency of HMQ-MBS reported previously[29] was considerably lower, only about 0.45 times that of urea (note that DAST exhibits a 3 orders of magnitude higher SHG efficiency with respect to urea at 1.9 μm[16]); Unfortunately the authors did not disclose the wavelength, at which their efficiency was measured.[29] Presumably, when using a commonly employed 1.064 μm fundamental wavelength, the generated SHG signal at 0.532 μm is mostly absorbed by HMQ-T powder (see **Figure 6**), which can explain this discrepancy.

We can estimate the theoretically expected powder test efficiency from the effective hyperpolarizability tensor elements β_{ijk}^{eff} by considering the number density of chromophores N and the averaged contribution over different orientation of crystallites by considering the corresponding point group symmetry.[32] The resulting figure of merit, $N^2 \langle (\beta^{\text{eff}})^2 \rangle$, neglects the contributions of the intermolecular interactions in the crystals as well as possible phase matching enhancements, but usually gives a good first-order estimation for the expected macroscopic nonlinear optical properties.[12,18,19,25] The values of $N^2 \langle (\beta^{\text{eff}})^2 \rangle$ relative to OH1 are for HMQ-T 2.6 times OH1 and for HMQ-MBS 3.2 times OH1, which is for both considerably more than experimentally measured. However, the chromophores with the OH group may be extremely sensitive to environmental conditions, e.g., the microscopic hyperpolarizability of OH1 chromophores may differ by a factor of 2 in different solvents.[12a] Note that the $N^2 \langle (\beta^{\text{eff}})^2 \rangle$ figure of merit for OH1 is about 30% of DAST, while the experimentally measured powder test almost twice larger. Relative to DAST, $N^2 \langle (\beta^{\text{eff}})^2 \rangle$ of HMQ-T is 76%, which is in a very good agreement with the experimental powder test efficiency for DAST. For HMQ-MBS on the other hand, the experimental and theoretical values differ by a factor of 3.7 relative to DAST. These discrepancies may point to a large environmental influence of the microscopic nonlinearity of HMQ chromophores to the environment. Still we can conclude that the new HMQ crystals exhibit excellent second-order nonlinear optical properties in the range of the presently best materials DAST and OH1. This is furthermore confirmed by the THz generation measurements described in Section 2.5.

2.4. Bulk Single Crystals

The solubility of HMQ-T and HMQ-MBS in methanol is shown in **Figure 7**a. The solubility of HMQ-T is higher than for HMQ-MBS: 0.89 g per 100g methanol for HMQ-T and 0.56 g per 100g methanol for HMQ-MBS at 50 °C. The solid line in Figure 7a is according to the well-known van't Hoff thermodynamic equilibrium equation assuming an ideal solution.[11a,33]

We grew bulk HMQ-T and HMQ-MBS single crystals by the slow cooling method in methanol starting at 40 °C and a cooling rate of 1 °C per day. In both crystals first nucleates appeared at about 25–26 °C. Typical as-grown HMQ-T and HMQ-MBS crystals are of yellow color as shown in Figure 7b and Figure 7c, respectively, which are brighter than orange-red OH1 crystals, as well as dark-red DAST crystals. The as-grown HMQ-T crystals have flat and parallel surfaces with a good optical quality, while HMQ-MBS crystals have a more complex morphology.
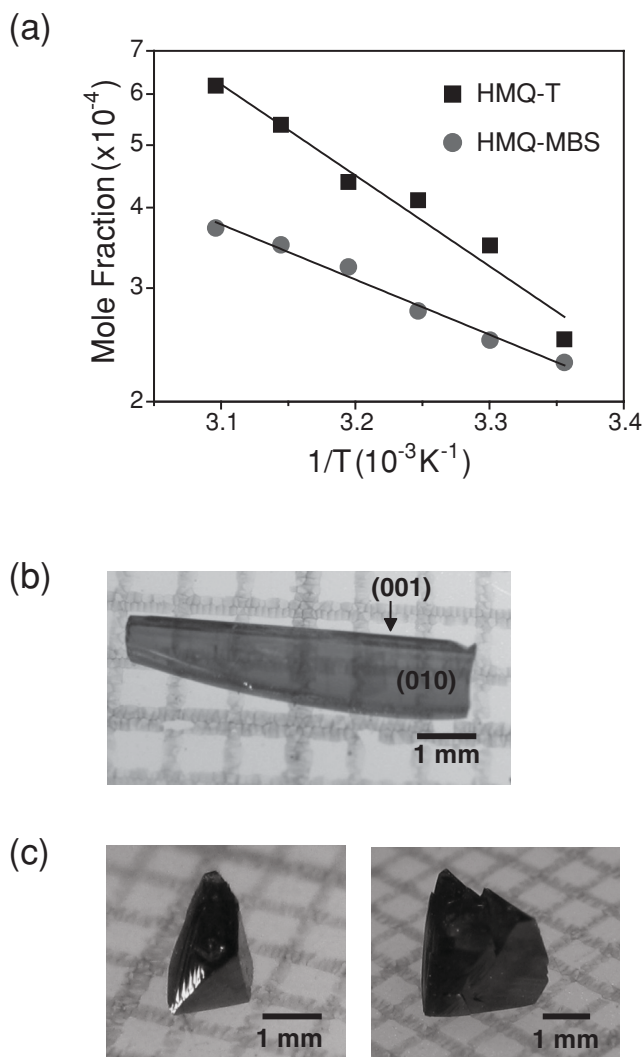
(a)

(b)

(c)

Figure 7. a) Solubility of HMQ-T and HMQ-MBS crystals in methanol: mole fraction *x* in logarithmic scale vs. inverse temperature (*T*⁻¹). Photographs of as-grown (b) HMQ-T and (c) HMQ-MBS crystals by slow cooling method in methanol.

www.MaterialsViews.com

ADVANCED
FUNCTIONAL
MATERIALS
www.afm-journal.de

FULL PAPER

We investigated the morphology of the as-grown HMQ-T crystals by X-ray diffraction. The parallel surfaces are along the *b* crystallographic planes, which means that the polar *c*-axis is in the plane as shown in Figure 7b. Therefore, compared to the morphology of HMQ-MBS crystals with non-parallel surfaces, as-grown HMQ-T crystals are more suitable for THz wave generation.[13]

According to the crystal characteristics, including the morphology, the HMQ-T crystals were chosen here for the characterization of the physical properties and for THz wave generation. Figure 6 shows the transmission spectrum of an unpolished HMQ-T crystal (*b*-plate) with a thickness of 0.32 mm using unpolarized light incident normal to the sample. The cut-off wavelength $\lambda_{cut-off}$ of HMQ-T is about 595 nm, which is considerably shorter than for OH1 (around 640 nm) and DAST (around 680 nm) crystals. The lower cut-off wavelength $\lambda_{cut-off}$ can be advantageous: i) photochemical stability; and, ii) a larger transparency range and therefore a wider range of possible operation wavelengths. The HMQ-T crystals possess an absorption peak at about 1675 nm, but low absorption at 1550 nm, while a relatively strong absorption at about 1550 nm of OH1 crystals[12a] limits its application possibilities at this technologically very important wavelength. Therefore, HMQ-T crystals possess larger transparence range from 595 nm 1550 nm than OH1 from 640 nm to 1400 nm. In addition, the allowance of the fundamental wavelength of 1550 nm may be useful for using widely available laser pump sources at this wavelength, e.g., femtosecond lasers for THz-wave generation and CW telecommunication lasers for electro-optic applications.

2.5. THz-Wave Generation

We generated THz waves by using optical rectification (OR) using femtosecond-laser pump pulses in various nonlinear optical crystals, and detected these waves by the electro-optic sampling (EOS) method.[13] We used fundamental optical pulses with a duration of 170 fs at 836 nm with repetition rate of 1 kHz from a regenerative amplified Ti:sapphire laser. For all nonlinear optical materials the same THz electro-optic detector crystal (ZnTe) was used. The measurements were performed at room temperature in air with a humidity of 28%. The details of our experimental setup for the generation and detection of THz waves are given in the SI.

A HMQ-T crystal with (010) surfaces and a thickness of 0.56 mm was used for THz generation. For comparison we also used a ZnTe crystal with polished (110) surfaces and a thickness of 1.0 mm, which is the most widely used inorganic THz generator material,[8] and organic OH1 crystal with (100) surfaces and a thickness of 0.37 mm, which is one of the state-of-the-art electro-optic crystals with very attractive properties for THz-wave generation.[12] Note that for OH1 crystals a larger thickness is not expected to result in a higher THz generation efficiency at this pump wavelength, since the coherence length for 836 nm pump fs lasers at 1 THz is only about 0.2 mm.[12b] Due to the relatively good optical quality of the crystals with flat surfaces, as-grown HMQ-T and OH1 crystals were used without polishing.

Figure 8a shows time traces of the generated THz waves from nonlinear optical crystals in our experiment. The spectra

of the generated THz fields are shown in Figure 8b, which were obtained by fast Fourier transform (FFT) of the THz time traces of Figure 8a. The amplitude THz-wave generation efficiency of HMQ-T crystals is 8.4 and 3.1 times larger than for ZnTe and OH1 crystals, respectively: the peak-to-peak amplitude of the THz field is 20.2 kV cm^{-1} for HMQ-T, 2.4 kV cm^{-1} for ZnTe, and 6.5 kV cm^{-1} for OH1 crystals. Even though the conditions of phase matching and thickness have not yet been optimized, HMQ-T crystals obviously have a very high potential for high power THz generation and its applications.

3. Conclusions

We have reported on novel highly efficient ionic electro-optic quinolinium single crystals for nonlinear optics, in particular for THz wave applications. Acentric quinolinium derivatives, HMQ-T and HMQ-MBS exhibit a high order parameter $\cos^3\theta_p$
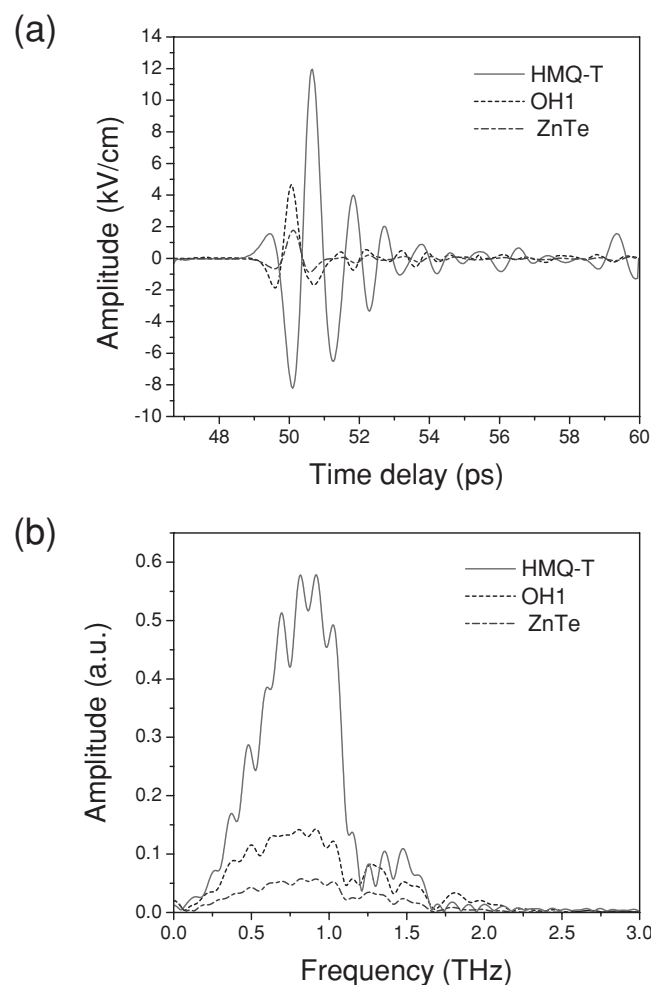

Figure 8. Terahertz pulses generated in single crystals of 0.56 mm-thick HMQ-T (solid line), benchmark 0.37 mm-thick OH1 crystal (dotted line) and inorganic 1 mm thick ZnTe (dashed line) at a fundamental wavelength of 836 nm with the pulse duration of 170 fs. a) Time-trace of the terahertz electric field $E_{THz}(t)$. b) The spectra of $E_{THz}(\nu)$.

FULL PAPER

close to 1.0 and a large macroscopic optical nonlinearity, which are in the range of the benchmark ionic stilbazolium DAST and non-ionic phenolic polyene OH1 crystals. Bulk HMQ-T crystals with good optical quality, a side length of about 6 mm and thickness of 0.56 mm, without polishing procedure, exhibit 3.1 times higher THz generation efficiency than the 0.37 mm thick OH1 crystal and about 8.4 times higher than 1 mm thick inorganic ZnTe crystal at the fundamental wavelength of 836 nm. Therefore, HMQ crystals with high order parameter are very attractive materials for THz wave technology.

4. Experimental Section

Synthesis: All chemicals were purchased from commercial suppliers. 2-Methylquinoline and vaniline for the synthetic route with condensation, as shown in Figure 1, were purchased from Sigma–Aldrich and used without further purification. ^{1}H-NMR spectroscopy data were recorded on a Varian 400 MHz. All chemical shifts are reported in ppm (δ) relative to $(CH_3)_4Si$.

2-(4-Hydroxy-3-Methoxystyryl)-1-Methylquinolinium 4-Methylbenzenesulfonate (HMQ-T): Methyl p-toluenesulfonate (32.34 mL, 0.21 mol (98%)) and 2-methylquinoline (29.8 mL, 0.21 mol (95%)) were dissolved in methanol (50 mL) and the solution was stirred at 50 °C for 1 d. The solution color changed from colorlessness to light pink. After cooling the solution to room temperature, a precipitate was obtained by evaporating methanol and adding 1,2-dimethoxyethane. A white-pink powder of 1,2-dimethoxyquinolinium 4-methylbenzenesulfonate was obtained by filtration and dried in vacuum oven at 60 °C (yield = 76%). 1,2-Dimethylquinolinium 4-methylbenzenesulfonate (40 g, 0.121 mol) and vanillin (18.5 g, 0.121 mol) were dissolved in methanol (100 mL). The catalyst piperidine (2.4 mL, 0.0242 mol) was added by stirring under reflux for 3 d. After cooling to room temperature, an orange crystalline powder was obtained. The final product was obtained by recrystallization in methanol and dried in vacuum oven at 60 °C for 1 h (yield = 22%). ^{1}H-NMR (400 MHz, CD$_3$OD, δ): 8.83 (d, 1H, J = 8.8, C$_5$H$_2$N), 8.44 (d, 1H, J = 9.2, C$_6$H$_4$), 8.40 (d, 1H, J = 8.8, C$_5$H$_2$N), 8.24 (d, 1H, J = 8.0, C$_6$H$_4$), 8.15 (m, 1H, C$_6$H$_4$), 8.06 (d, 1H, J = 15.6, CH), 7.90 (m 1H, C$_6$H$_4$), 7.69 (d, 1H, J = 15.2, CH), 7.68 (d, 2H, J = 6.4, C$_6$H$_4$SO$_3^-$), 7.52 (s, 1H, C$_6$H$_3$), 7.39 (dd, 1H, C$_6$H$_3$), 7.20 (d, 2H, J = 8.4, C$_6$H$_4$SO$_3^-$), 6.91 (d, 1H, J = 8.0, C$_6$H$_3$), 4.57 (s, 3H, OMe), 4.00 (s, 3H, Me), 2.36 (s, 3H, NMe). Elemental analysis for C$_{26}$H$_{25}$NO$_5$S, Calcd C 67.37, H 5.43, N 3.02, S 6.92; Found: C 67.40, H 5.53, N 3.02, S 7.02.

2-(4-Hydroxy-3-Methoxystyryl)-1-Methylquinolinium 4-Methoxybenzenesulfonate (HMQ-MBS): HMQ-MBS was synthesized in a similar manner as HMQ-T, by the condensation reactions of vanillin with dimethylquinolinium 4-methoxybenzenesulfonate (yield = 40%). ^{1}H-NMR (400 MHz, CD$_3$OD, δ): 8.81 (d, 1H, J = 8.8, C$_5$H$_2$N), 8.42 (d, 1H, J = 8.8, C$_6$H$_4$), 8.38 (d, 1H, J = 9.2, C$_6$H$_4$), 8.22 (d, 1H, J = 8.0, C$_5$H$_2$N), 8.13 (m, 1H, C$_6$H$_4$), 8.05 (d, 1H, J = 15.6, CH), 7.88 (m 1H, C$_6$H$_4$), 7.72 (m, 2H, C$_6$H$_4$SO$_3^-$), 7.66 (d, 1H, J = 16.0, CH), 7.50 (s, 1H, C$_6$H$_3$), 7.38 (dd, 1H, C$_6$H$_3$), 6.91 (m, 2H, C$_6$H$_4$SO$_3^-$), 6.89 (m, 1H, C$_6$H$_3$), 4.55 (s, 3H, NMe), 4.00 (s, 3H, OMe), 3.80 (s, 3H, OMe). Elemental analysis for C$_{26}$H$_{25}$NO$_6$S, Calcd. C 65.12, H 5.25, N 2.92, S 6.69; Found: C 65.19, H 5.21, N 2.94, S 6.78.

X-ray Crystal Structure Analysis of HMQ-T: C$_{26}$H$_{25}$NO$_5$S, M_r = 463.55, monoclinic, space group Pn, a = 6.9304 (3) Å, b = 11.1154 (5) Å, c = 14.7594 (5) Å, β = 100.3072 (9)°, V = 1118.62 (7) Å^3, Z = 2, T = 290(1) K, μ(MoK) = 0.18 mm^{-1}. Of 10 740 reflections collected in the θ range 3.4°–27.4° using ω scans on a Rigaku R-axis Rapid S diffractometer, 4492 were unique reflections (R_{int} = 0.025, completeness = 99.1%). The structure was solved and refined against F^2 using SHELX97,[34] 299 variables, wR_2 = 0.098, R_1 = 0.033 (3370 reflections having $F_o^2 > 2\sigma(F_o^2)$), GOF = 1.09, Flack parameter x = −0.08(8), and max/min residual electron density 0.25/−0.21 eÅ^{-3}. Further details of the crystal structure investigation(s) may be obtained from the Cambridge Crystallographic Data Centre (CCDC, 12 Union Road, Cambridge CB2 1EZ, UK; tel.: +44 (1223) 336408, fax: +44 (1223) 336033, e-mail: deposit@ccdc.cam.ac.uk) on quoting the depository number CCDC-824804 for HMQ-T.

X-ray Crystal Structure Analysis of HMQ-MBS:[29] C$_{26}$H$_{25}$NO$_6$S, M_r = 479.54, monoclinic, space group Pc, a = 10.9895(1) Å, b = 7.1363(1) Å, c = 15.6341(2) Å, β = 110.300(1)°, V = 1149.94(3) Å^3, Z = 2, T = 297(2) K, CCDC 629589.

Supporting Information

Supporting Information is available from the Wiley Online Library or from the author.

Acknowledgements

[1] a) Special issue on "T-ray Imaging, Sensing & Detection", *Proceed. IEEE.* **2007**, *95*, 1514–1704; b) R. M. Woodward, V. P. Wallace, R. J. Pye, B. E. Cole, D. D. Arnone, E. H. Linfield, M. Peppern, *J. Invest. Dermatol.* **2003**, *120*, 72; c) T. Loffler, K. Siebert, S. Czasch, T. Bauer, H. G. Roskos, *Phys. Med. Biol.* **2002**, *47*, 3847; d) Z. D. Taylor, R. S. Singh, M. O. Culjat, J. Y. Suen, W. S. Grundfest, H. Lee, E. R. Brown, *Opt. Lett.* **2008**, *33*, 1258.

[2] a) K. L. Nguyen, T. Friscic, G. M. Day, L. F. Gladden, W. Jones, *Nat. Mater.* **2007**, *6*, 206; b) P. Knobloch, C. Schildknecht, T. Kleine-Ostmann, M. Koch, S. Hoffmann, M. Hofmann, E. Rehberg, M. Sperling, K. Donhuijsen, G. Hein, K. Pierz, *Phys. Med. Biol.* **2002**, *47*, 3875; c) J. F. Federici, B. Schulkin, F. Huang, D. Gary, R. Barat, F. Oliveira, D. Zimdars, *Semicond. Sci. Technol.* **2005**, *20*, S266; d) M. C. Beard, G. M. Turner, C. A. Schmuttenmaer, *J. Phys. Chem. B* **2002**, *106*, 7146.

[3] a) M. Tonouchi, *Nat. Photonics* **2007**, *1*, 97; b) B. Ferguson, X. C. Zhang, *Nat. Mater.* **2002**, *1*, 26; c) C. Sirtori, *Nature* **2002**, *417*, 132; c) A. M. Sinyukov, L. M. Hayden, *J. Phys. Chem. B* **2004**, *108*, 8515; d) X. Zheng, C. V. Malaughlin, P. Cunningham, L. M. Hyden, *J. Nanoelectron. Optoelectron.* **2007**, *2*, 1; e) M. Walther, B. M. Fischer, A. Ortner, A. Bitzer, A. Thoman, H. Helm, *Anal. Bioanal. Chem.* **2010**, *397*, 1009.

[4] O. P. Kwon, S. J. Kwon, M. Stillhart, M. Jazbinsek, A. Schneider, V. Gramlich, P. Günter, *Cryst. Growth Des.* **2007**, *7*, 2517.

[5] a) M. Jazbinsek, O. P. Kwon, Ch. in *Handbook of Organic Electronics and Photonics* (Ed: S. H. Nalwa), American Scientific Publishers, Los Angeles **2008**, Ch. 1; b) Ch. Bosshard, M. Bösch, I. Liakatas, M. Jäger, P. Günter, in *Nonlinear Optical Effects and Materials* (Ed: P. Günter), Springer-Verlag, Berlin **2000**, Ch. 3; c) *Introduction to Organic Electronic and Optoelectronic Materials and Devices* (Ed: S. S. Sun, L. R. Dalton), CRC Press, Boca Raton, USA **2008**.

[6] X. C. Zhang, X. F. Ma, Y. Jin, T. M. Lu, E. P. Boden, P. D. Phelps, K. R. Stewart, C. P. Yakymyshyn, *App. Phys. Lett.* **1992**, *61*, 3080.

[7] a) K. Suizu, K. Miyamoto, T. Yamashita, H. Ito, *Opt. Lett.* **2007**, *32*, 2885; b) K. Miyamoto, H. Minamide, M. Fujiwara, H. Hashimoto, H. Ito, *Opt. Lett.* **2008**, *33*, 252.

[8] a) T. Löffler, T. Hahn, M. Thomson, F. Jacob, H. G. Roskos, *Opt. Express* **2005**, *13*, 5353; b) X. Wang, W. Sun, Y. Zhang, *Optik* **2010**, *121*, 1148.

www.MaterialsViews.com

ADVANCED
FUNCTIONAL
MATERIALS
www.afm-journal.de

FULL PAPER

[9] a) P. Y. Han, M. Tani, F. Pan, X. C. Zhang, *Opt. Lett.* **2000**, *25*, 675; b) T. Taniuchi, S. Okada, H. Nakanishi, *J. Appl. Phys.* **2004**, *95*, 5984; c) K. Kuroyanagi, K. Yanagi, A. Sugita, H. Hashimoto, H. Takahashi, S. Aoshima, Y. Tsuchiya, *J. Appl. Phys.* **2006**, *100*, 043117; d) T. Matsukawa, Y. Mineno, T. Odani, S. Okada, T. Taniuchi, H. Nakanishi, *J. Cryst. Growth.* **2007**, *299*, 344.

[10] a) A. Schneider, M. Neis, M. Stillhart, B. Ruiz, R. U. A. Khan, P. Günter, *J. Opt. Soc. Am. B* **2006**, *9*, 1822; b) A. Schneider, M. Stillhart, P. Günter, *Opt. Express.* **2006**, *14*, 5376; c) A. Schneider, P. Günter, *App. Opt.* **2006**, *45*, 6598; d) A. Schneider, I. Biaggio, P. Günter, *Appl. Phys. Lett.* **2004**, *84*, 2229.

[11] a) Z. Yang, L. Mutter, M. Stillhart, B. Ruiz, S. Aravazhi, M. Jazbinsek, A. Schneider, V. Gramlich, P. Günter, *Adv. Funct. Mater.* **2007**, *17*, 2018; b) M. Stillhart, A. Schneider, P. Günter, *J. Opt. Soc. Am. B.* **2008**, *25*, 1914.

[12] a) O. P. Kwon, S. J. Kwon, M. Jazbinsek, F. D. J. Brunner, J. I. Seo, Ch. Hunziker, A. Schneider, H. Yun, Y. S. Lee, P. Günter, *Adv. Funct. Mater.* **2008**, *18*, 3242; b) F. D. J. Brunner, O. P. Kwon, S. J. Kwon, M. Jazbinsek, A. Schneider, P. Günter, *Opt. Express* **2008**, *16*, 16496.

[13] J. Y. Seo, S. B. Choi, M. Jazbinsek, F. Rotermund, P. Günter, O. P. Kwon, *Cryst. Growth Des.* **2009**, *9*, 5003.

[14] a) J. J. Carey, R. T. Bailey, D. Pugh, J. N. Sherwood, F. R. Cruickshank, K. Wynne, *Appl. Phys. Lett.* **2002**, *81*, 4335; b) H. Hashimoto, H. Takahashi, T. Yamada, K. Kuroyanagi, T. Kobayashi, *J. Phys.: Condens. Matter* **2001**, *13*, L529; c) V. Krishnakumar, R. Nagalakshmi, *Cryst. Growth Des.* **2008**, *8*, 3882.

[15] F. D. J. Brunner, A. Schneider, P. Günter, *Appl. Phys. Lett.* **2009**, *94*, 061119.

[16] a) S. R. Marder, J. W. Perry, W. P. Schaefer, *Science* **1989**, *245*, 626; b) S. R. Marder, J. W. Perry, C. P. Yakymyshyn, *Chem. Mater.* **1994**, *6*, 1137; c) F. Pan, M. S. Wong, Ch. Bosshard, P. Günter, *Adv. Mater.* **1996**, *8*, 592.

[17] a) B. J. Coe, J. A. Harris, I. Asselberghs, K. Wostyn, K. Clays, A. Persoons, B. S. Brunschwig, S. J. Coles, T. Gelbrich, M. E. Light, M. B. Hursthouse, K. Nakatani, *Adv. Funct. Mater.* **2003**, *13*, 347; b) H. Figi, L. Mutter, Ch. Hunziker, M. Jazbinsek, P. Günter, B. J. Coe, *J. Opt. Soc. Am. B* **2008**, *25*, 1786; c) J. Ogawa, S. Okada, Z. Glavcheva, H. Nakanishi, *J. Cryst. Growth.* **2008**, *310*, 836.

[18] a) O. P. Kwon, B. Ruiz, A. Choubey, L. Mutter, A. Schneider, M. Jazbinsek, P. Günter, *Chem. Mater.* **2006**, *18*, 4049; b) O. P. Kwon, S. J. Kwon, M. Jazbinsek, V. Gramlich, P. Günter, *Adv. Funct. Mater.* **2007**, *17*, 1750.

[19] a) O. P. Kwon, S. J. Kwon, M. Jazbinsek, J. Y. Seo, J. T. Kim, J. I. Seo, Y. S. Lee, H. Yun, P. Günter, *Chem. Mater.* **2011**, *23*, 239; b) O. P. Kwon, M. Jazbinsek, H. Yun, J. I. Seo, J. Y. Seo, S. J. Kwon, Y. S. Lee, P. Günter, *CrystEngComm* **2009**, *11*, 1541.

[20] F. Pan, G. Knopfle, Ch. Bosshard, S. Follonier, R. Spreiter, M. S. Wong, P. Günter, *Appl. Phys. Lett.* **1996**, *69*, 13.

[21] Ch. Hunziker, S. J. Kwon, H. Figi, F. Juvalta, O. P. Kwon, M. Jazbinsek, P. Günter, *J. Opt. Soc. Am. B* **2008**, *25*, 1678.

[22] a) B. J. Coe, J. J. Hall, J. A. Harris, B. S. Brunschwig, S. J. Coles, M. B. Hursthouse, *Acta Crystallogr. E* **2005**, *61*, o464; b) C. G. Fortuna, C. Bonaccorso, F. Qamar, A. Anu, I. Ledouxb, G. Musumarra, *Org. Biomol. Chem.* **2011**, *9*, 1608.

[23] S. J. Kwon, O. P. Kwon, J. I. Seo, M. Jazbinsek, L. Mutter, V. Gramlich, Y. S. Lee, H. Yun, P. Günter, *J. Phys. Chem. C* **2008**, *112*, 7846.

[24] a) A. D. Becke, *J. Chem. Phys.* **1993**, *98*, 5648; b) J. P. Perdew, *Phys. Rev. B* **1986**, *33*, 8822.

[25] O. P. Kwon, M. Jazbinsek, J. I. Seo, E. Y. Choi, H. Yun, F. D. J. Brunner, P. Günter, Y. S. Lee, *J. Chem. Phys.* **2009**, *130*, 134708.

[26] O. Kwon, S. Barlow, S. A. Odom, L. Beverina, N. J. Thompson, E. Zojer, J. L. Bredas, S. R. Marder, *J. Phys. Chem. A* **2005**, *109*, 9346.

[27] P. J. Kim, J. H. Jeong, M. Jazbinsek, S. J. Kwon, H. Yun, J. T. Kim, Y. S. Lee, I. H. Baek, F. Rotermund, P. Günter, O. P. Kwon, *CrystEngComm* **2011**, *13*, 444.

[28] S. Chantrapromma, B. Jindawong, H. K. Fun, *Acta Cryst. E* **2007**, *E63*, o4928.

[29] S. Chantrapromma, B. Jindawong, H. K. Fun, P. S. Patil, *Anal. Sci.* **2007**, *23*, x81.

[30] a) O. P. Kwon, M. Jazbinsek, H. Yun, J. I. Seo, E. M. Kim, Y. S. Lee, P. Günter, *Cryst. Growth Des.* **2008**, *8*, 4021; b) O. P. Kwon, M. Jazbinsek, J. I. Seo, P. J. Kim, H. Yun, Y. S. Lee, P. Günter, *J. Phys. Chem. C* **2009**, *113*, 15405.

[31] O. P. Kwon, M. Jazbinsek, J. I. Seo, P. J. Kim, E. Y. Choi, Y. S. Lee, P. Günter, *Dyes Pigm.* **2010**, *85*, 162.

[32] K. Kurtz, T. T. Perry, *J. Appl. Phys.* **1968**, *39*, 3798.

[33] J. R. Brice, in *Crystal Growth Processes*, John Wiley and Sons, New York **1986**, Ch. 2.

[34] G. M. Sheldrick, *Acta Crystallogr.* **2008**, *A64*, 112.

FULL PAPER

Novel Approach for Alternating Current (AC)-Driven Organic Light-Emitting Devices

Ajay Perumal,* Markus Fröbel, Sandeep Gorantla, Thomas Gemming, Björn Lüssem, Jürgen Eckert, and Karl Leo*

A novel approach for alternating current (AC)-driven organic light-emitting devices is reported, which uses the concept of molecular doping in organic semiconductors. Doped organic charge-transport layers are used to generate charge carriers within the device, hence eliminating the need for injecting charge carriers from external electrodes. Bright luminance of up to 1000 cd m^{-2} is observed when the device is driven with an AC bias. The luminance observed is attributed to charge-carrier generation and recombination, leading to the formation of excitons within the device, without injection of charge carriers through external electrodes. A mechanism for internal charge-carrier generation and the device operation is proposed.

1. Introduction

Inorganic alternating current (AC) thin-film electroluminescence (TFEL) display devices are well established.[1] AC-TFEL devices consist of a polycrystalline phosphor layer doped with a luminescent impurity (e.g., Mn or Cu) that is enclosed between a pair of insulating layers.[1,2] The device is robust due to the use of inorganic materials and simple in fabrication. However, challenges remain for these devices, as the fabrication consists of different deposition steps and some phosphors require additional annealing.[1] The complex processing procedure involving annealing at different temperatures and narrow spectral distribution of inorganic dyes makes it difficult to obtain white light with a balanced red, green, and blue (RGB) contribution.[3]

Previously, there have been efforts to fabricate hybrid organic–inorganic AC electroluminescence (AC-EL) devices by sandwiching organic molecules Alq$_3$ (tris(8-hydroxy-quinolinato)aluminum) between silicon dioxide (SiO$_2$) layers. Blue emission instead of the normal green Alq$_3$ molecule emission

was observed when the device was driven with AC.[4,5] Hot electron impact i.e., band to band excitation or solid state cathodoluminescence (CL) like emission was proposed as origin for blue emission.[4,5]

Recently, there have been also efforts to fabricate organic AC-EL devices suggesting the possibility of providing the charge carriers (the holes and electrons) within the organic layers without the need for injecting them from external electrodes, while driving the device with AC voltage.[6,7] Nanoparticles were employed as symmetrical bipolar charge-generating centers in these devices. The mechanism with which the nanoparticles generate the electrons and holes is not known. The processing of ITO nanoparticle layers with ethanol dispersion formed by spin coating is also tedious, as the nanoparticles tend to cluster. Moreover, the light intensities were rather low in these devices.

We report on a new concept for the AC organic light-emitting devices, which are robust and bright. They are organic–inorganic hybrid devices. A luminance of up to 1000 cd m^{-2} is observed, when the device is driven with an AC bias. AC organic light-emitting devices can be used for efficient light generation without the need to inject charge carriers into the device. We exploit the mechanical strength and chemical stability of inorganic insulators and combine it with the excellent optical properties of organic materials whose emission color can be chemically tuned so that it covers the entire visible spectrum.

The AC organic light-emitting device concept reported in this work is similar to AC-TFEL device with the double-insulating structure,[1,2] but with a simpler device fabrication procedure. The whole device is processed at room temperature eliminating the complex processing and annealing steps. In this device, an organic emission layer doped with organic dye acts as luminescent center, having the advantage of an efficient emission over the entire visible spectrum.[8] We also employ the concept of molecular doping for small molecule organic semiconductors, allowing for an efficient transport as well as for generation of charge carriers.[9,10] The light generation is due to the formation of excitons by recombination EL, unlike the mechanism of hot electron impact excitation of phosphor emissive centers in case of inorganic AC devices.

To our knowledge to date there is no convincing evidence for controlled charge-carrier generation within the device, without injecting charge carriers either in organic or inorganic AC driven light-emitting devices. With time-resolved AC-EL

A. Perumal, M. Fröbel, Dr. B. Lüssem, Prof. Dr. K. Leo
Institut für Angewandte Photophysik (IAPP)
Technische Universität Dresden (TUD)
01062 Dresden, Germany
E-mail: ajay.perumal@iapp.de; leo@iapp.de
S. Gorantla, Dr. T. Gemming, Prof. Dr. J. Eckert
IFW Dresden, Institut für Komplexe Materialien
PO Box 270116, 01171 Dresden, Germany
S. Gorantla, Dr. T. Gemming, Prof. Dr. J. Eckert
Institut für Werkstoffwissenschaft
Technische Universität Dresden (TUD)
01062 Dresden, Germany

measurements, we demonstrate the evidence of charge-carrier regeneration within the device. We propose the regeneration of charge carriers to be due to Zener tunneling at high AC bias applied to the device in the negative cycle. The fabrication of multicolor display devices or white large-area lighting panels would be far simpler with this technique in comparison to AC-TFEL devices.

Organic light-emitting diodes (OLEDs) driven by a direct current (DC) bias are well established.[11,12] The light generated in DC devices is due to injection of charge carriers, leading to current and the generation of excitons, while the light generated by driving the device with an AC bias is due to internal charging of the device. AC drive also avoids the charge accumulation in the device due to frequent reversal of the applied bias. We believe that the new concept for AC-driven light-emitting devices might offer the path towards future plug and play, flat, and flexible light sources.

2. Results and Discussion

The devices consist of an organic EL layer composed of unipolar/ambipolar charge-transport material as a host matrix, which is doped with an organic dye (5–10 wt%) with or without an electron and a hole generation layers, enclosed between a pair of transparent metal-oxide insulating dielectric layers. A transparent ITO acts as a bottom electrode for light out-coupling and aluminum (Al) as a top-reflective electrode (**Figure 1**). We have chosen silicon oxide (SiO_2) as the transparent dielectric insulating material in our devices.

The AC-EL spectra for all the device structures in Figure 1 are shown in **Figure 2**a. Orange-red emission from the phosphorescent dopant $Ir(MDQ)_2(acac)$, which peaks at approximately 610 nm, is observed in all devices. Spectra are recorded for all the devices driven with different AC voltages and frequencies. The AC-EL peak shows no shift with an increase in applied voltage or with frequency for all the devices. Due to a nonoptimized optical cavity, the spectra broaden for device B, C, and D.

For the device A with only a single EL layer enclosed between insulating layers, we observe a very weak luminance with an increasing AC bias applied to the device. The luminance levels are below the detection limit of the luminance meter. However, the luminance level is sufficient to record the spectra with very high integration times.

With the addition of intrinsic charge-transport layers on either side of the EL layer (device B), the luminance is strongly enhanced. The *L–V* response at different frequencies is shown in Figure 2b. We observe an increase in light output as a function of increasing AC voltage across the device. The threshold voltage for the onset of luminance is approximately 39 V for this device; beyond the threshold voltage the luminance increases
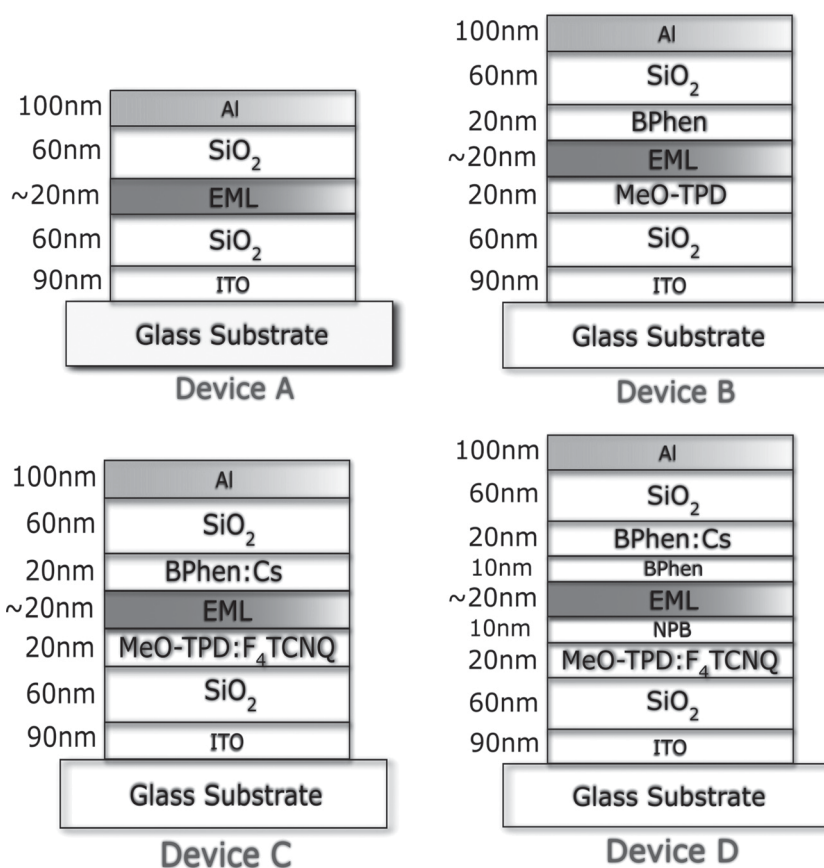

Figure 1. Device structures: A) Single layer device; B) intrinsic or undoped charge-transport layer device; C) PN-doped device without blockers; D) PIN-doped device with blockers.

as a function of the applied AC bias at any fixed frequency. We achieve a maximum luminance of approximately 100 cd m^{-2} at frequency of 10 kHz with this device.

For the devices A and B with the intrinsic or undoped organic layers the observed luminance when driven with an AC bias is due to the presence of charge carriers existing within the device due to ionized impurities.[13] The concentration of charge carriers due to ionized impurities in intrinsic or undoped organic layers is known to be low, thus the luminance levels achieved in these devices are also low.

We introduced asymmetrically doped charge-transport layers on both sides of the EL layer (device C) to increase the number of charge carriers within the device and thereby enhance the luminance and the performance of the device. The *L–V* curves for this device recorded as a function of frequency are shown in Figure 2b. We observe an increase in the luminance output in comparison to devices A and B and a decrease in the threshold AC bias of approximately 10 V. Due to the doping of transport layers, a higher number of free charge carriers is available in the layer.[9,14] When the AC bias is applied, more free charge carriers are available for the formation of excitons at the EL, which leads to the reduction in the threshold voltage. The observed luminance for the device C with doped charge-transport layers on both sides of EL layer is highest in comparison to device A and B with intrinsic organic layers. For all the devices A, B,
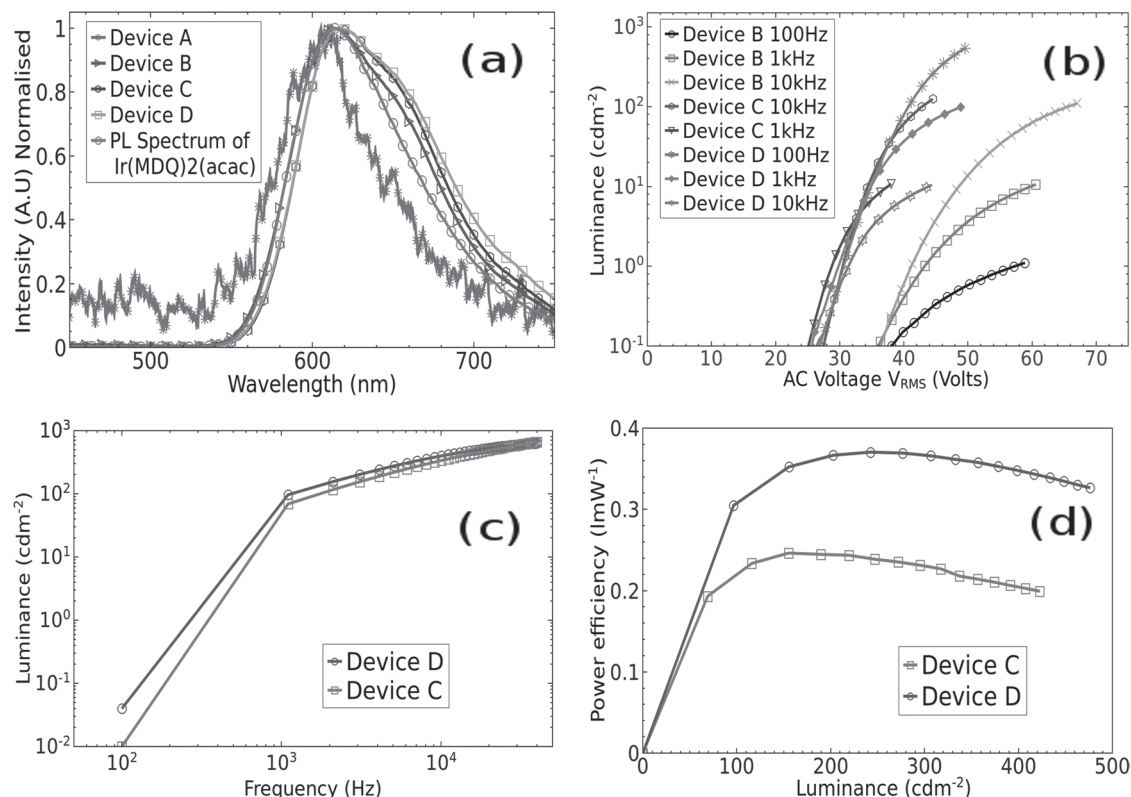
Figure 2. a) AC-EL spectra of all the devices shown in Figure 1, recorded at different applied AC voltages. Orange-red emission from phosphorescent dopant Ir(MDQ)2(acac) peaked at approximately 610 nm is observed in all the devices. The photoluminescence spectrum of the phosphorescent Ir dye Ir(MDQ)2(acac) is shown for reference. b) Luminance–voltage (L–V) characteristics of the devices B, C, and D, shown in Figure 1, at different frequencies. c) Luminance–frequency (L–f) characteristics of the devices C and D shown in Figure 1. d) Power efficiency as a function of luminance of the devices C and D shown in Figure 1.

and C, after the initial increase in luminance output from the device with increasing AC bias, the luminance tends towards saturation at higher voltages due to the availability of a limited number of charge carriers within the device to form excitons and generate light. The applied AC bias can be increased up to the breakdown voltage limit of the insulating layer. We stop collecting the data just below the breakdown voltage for all the above devices. Beyond the breakdown voltage the device is irreversibly damaged.

On application of AC bias to the device, the dielectric gets polarized and the charge carriers move to the luminescent centers. The applied AC bias is divided across the device depending on the capacitances of the insulating dielectric layers (C_{it} and C_{ib}), and the organic layer (C_o). Up to a certain minimum AC bias the device does not emit any light, as can be seen in Figure 2b, we term it as the threshold AC bias for light emission. Below the threshold AC bias, all of the above-mentioned capacitive elements are contributing to the total capacitance of the device. During this time the voltage, which drops across the organic layers is not sufficient to move the charge carriers to form excitons and generate light. Above the threshold AC bias, the field-assisted drift and diffusion of charge carriers moves the charge carriers towards the emissive zone, where they are trapped on the emissive dye to form excitons leading to emission of light. Due to the movement of the charge carriers in the organic layer above the threshold voltage, the layer becomes

conductive and the capacitive contribution from the organic layer (C_o) becomes negligible. Beyond this point, the applied AC bias can be increased up to the dielectric breakdown field strength of the insulating metal oxide dielectric layer.

Further, thin blocking layers are introduced for device D as in the case of DC-OLEDs, which confine the emission zone and reduce quenching of excitons.[15] This device shows the same voltage and frequency dependence as device C, except the observed luminance at any fixed applied bias and fixed frequency is higher compared to the device without blockers, as shown in Figure 2b. We expect this to be due to an effective confinement of the emission zone and reduced quenching of the excitons. The luminance also saturates earlier for the devices without blockers.

For the L–V curves recorded as a function of the increasing frequency, we observe steeper L–V curves and an increase in luminance (Figure 2b). The luminance variation as a function of frequency at a fixed AC bias (L–f response) for device C and D is shown in Figure 2c. The steady increase of luminance with frequency is related to capacitive reactance of the device, which is inversely proportional to the frequency. As the frequency increases the capacitive reactance decreases and the current flowing through the device increases (Supporting Information, Figure S2). More charge carriers are available for recombination, leading to higher luminance. However the luminance does not increase indefinitely. The charge-carrier response to the applied field at high frequencies is limited by the mobility in

Materials Views
www.MaterialsViews.com

ADVANCED
FUNCTIONAL
MATERIALS
www.afm-journal.de

FULL PAPER

amorphous organic semiconductors. Although, as a function of frequency, the impedance decreases and the intern the current increases, the charge carriers appear to be static at very high frequencies. As a result the number of charge carriers available in the EL layer is reduced at high frequencies, and the luminance tends towards saturation or even may decrease. We observe that the luminance tends towards saturation at high frequencies in our devices. We are limited by the amplifier bandwidth to frequencies lower than 30 kHz. The light emission is frequency dependent in our devices and the increase in luminance as a function of frequency is not merely due to increase in light-emitting cycles. The decrease of luminance as a function of the decreasing frequency (ultimately DC), clearly indicates that the device does not respond to the DC bias.

Another important parameter of the device is efficiency. Efficiency is defined as the ratio of photometric power emitted from the device to the electrical input power. This ratio is given in lumen per watt (lm W^{-1}). The power efficiency is measured by inserting a series resistor to the device. The power input per sample area is calculated as,

$$P\left(W/m^2\right) = \frac{1}{AT} \int_0^T V_{RMS}(t) . I_{RMS}(t) . dt \qquad (1)$$

$$P\left(W/m^2\right) = \frac{1}{A} . V_{RMS} . I_{RMS} . \cos(\varphi) \qquad (2)$$

where φ is the phase angle (in degrees) between sinusoidal voltage and current.

The power efficiency is given by (assuming Lambertian emission),

$$\eta_P \left[lm/W\right] = \pi . \frac{L[cd/m^2]}{P[W/m^2]} \qquad (3)$$

The power efficiency is plotted in Figure 2d as a function of luminance for device C and D. A maximum power efficiency of 0.37 lm W^{-1} was achieved for device D, which also showed the best power efficiency values at higher luminance. Since the organic active layer is sandwiched between the metal oxide dielectric insulating layers, large displacement currents flow in the insulating layers during AC operation. We estimate the power efficiency with contributions included from the power dissipation on ITO. DC tests were made on these devices to verify if we observe luminance due to injected charge carriers. We observe no luminance in this case and the currents measured in the device are very low (**Figure 3**). This is obvious from the capacitive nature of the device. When a DC bias is applied to a capacitor, it blocks the flow of current through the capacitor, the charge builds up on the plates of the capacitor. The dielectric break down occurs for insulating metal oxide layer when the applied voltage is sufficiently high. This builds conduction paths in the dielectric. The spikes observed in Figure 3 are due to a dielectric breakdown of the metal oxide insulating layer. The breakdown fields for the sputtered silicon oxide insulating dielectric layers are of the order of 7–10 MV cm^{-1}. This unambiguously demonstrates that the charge carriers are not injected in these devices but they are either intrinsic or generated due to the doping process.[9,10,14]

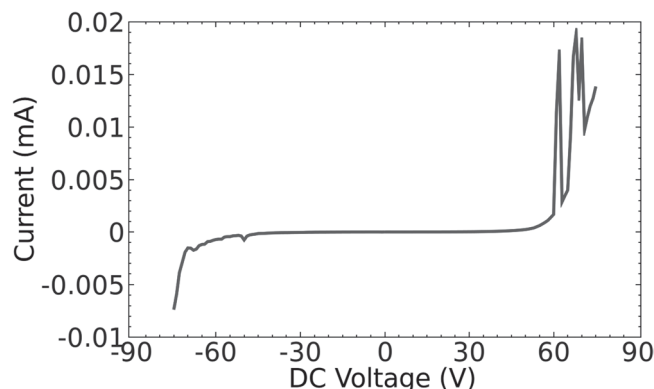Our choice of sputter deposition of insulating metal oxide dielectric layer on top of an organic layer demands sputter

Figure 3. Current–Voltage (I–V) curve with DC voltage applied to the device. We observe AC-EL in our devices at ~40 V_{RMS}. Equivalent DC voltage does not lead to any luminance from our devices; we have performed DC tests up to ±70 V. Even for very high DC voltages (70 V), the current is of the order of microamperes (μA) in our devices.

deposition to be performed carefully without causing significant damage to the underlying organic layer which affects the performance of the device. The processing parameters were carefully chosen. **Figure 4**a shows a cross-sectional bright-field transmission electron microscopy (TEM) image of the complete device. The individual layers of the complete device are clearly identified and the TEM image shows no visible damage to the layers. The determined thickness values are consistant with the measured layer thickness from quartz crystal microbalance (QCM). In general the organic layers are composed of carbon, hydrogen, oxygen, and nitrogen. The dominant carbon content and the amorphous nature of all organic layers exhibits no distinguishable contrast for different organic layers. For this reason, the entire organic layer stack appears as a single unit of approximately 80 nm, which is the total thickness of all the organic layers as shown in Figure 4b, with relatively brighter contrast due to the weaker scattering events. The different layers shown in Figure 4b are labeled in the corresponding schematic Figure 4c. The observed interface between the organic layer and the insulating oxide layers is sharp and continuous. No gaps or voids are observed along the interface. The EDX analysis of the top sputtered silicon oxide layer and the organic layers showed that there is 2 atomic% silicon penetration into the organic layers (Supplementary info-Figure S3).

The cross-sectional TEM studies of an OLED device, with TEM specimens prepared by focused ion beam (FIB) technique has been already shown to be a valuable technique for structural and analytical characterization of organic layers.[16,17]

The energy-filtered TEM (EFTEM) analytical imaging method is used for mapping the chemical distribution of elements in the layers.[18–21] Since the individual organic layers in complete device could not be distinguished in TEM, we have used EFTEM to map the chemical distribution of elements in the bi-layer consisting of the sputter deposited silicon oxide on top of the electron transporting 4,7-diphenyl-1,10-phenanthroline (BPhen) layer prepared on a glass-substrate. Figure 4d shows the EFTEM image formed by electrons with zero energy loss, which is identical to a normal bright-field TEM image and serves as a reference image to compare with the silicon
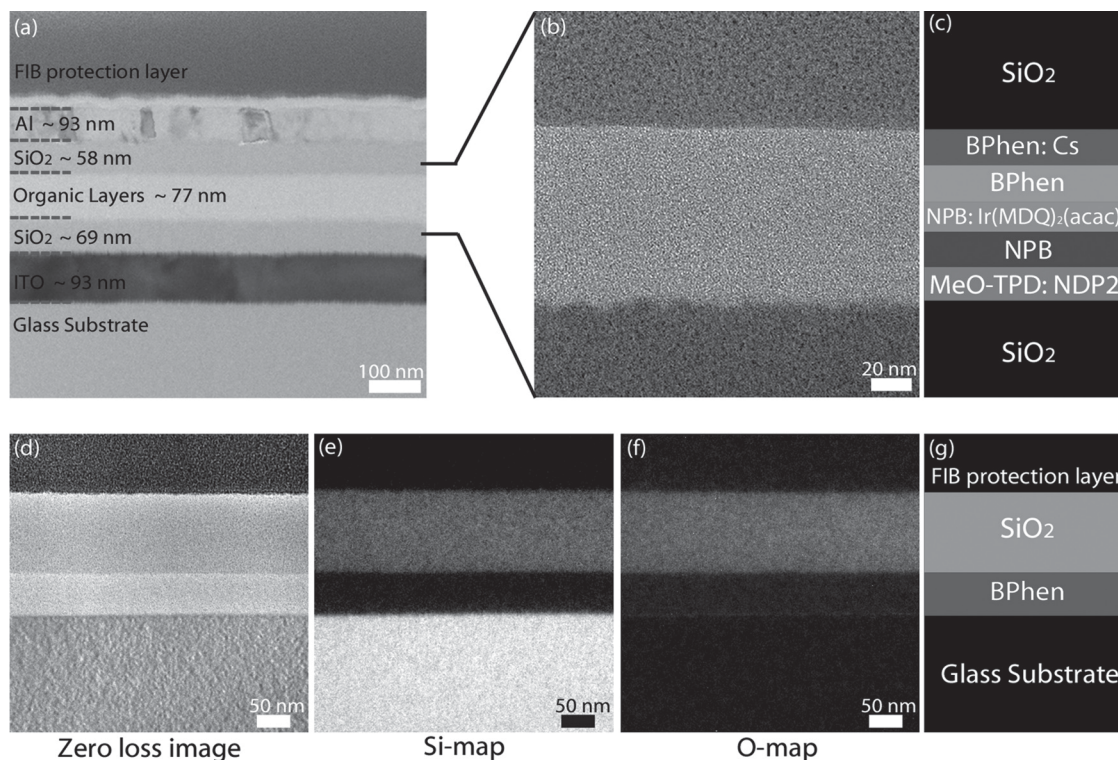
ADVANCED
FUNCTIONAL
MATERIALS
www.afm-journal.de

Materials
Views
www.MaterialsViews.com

Figure 4. (a) Bright field TEM image showing the cross-section of the complete device. (b) The HR-TEM image of silicon oxide-organic layers- silicon oxide interface, the individual organic layers showed no distinct contrast in the TEM due to the predominant carbon content. We could not resolve the individual organic layers but the interface between oxide and organic layers is observed to be sharp and continuous one. The different layers imaged in (b) are labeled in the corresponding scheme (c). The images (d–f) show the cross-section of a sample with neat BPhen layer with a sputtered layer on top in the energy-filtered imaging mode. d) EFTEM image at zero energy loss, which is comparable to a bright-field TEM image of the cross-section. e) EFTEM elemental map of silicon. The bright contrast corresponds to silicon. f) EFTEM elemental map of oxygen. The bright contrast corresponds to oxygen. The Si and O maps also show that the sputtered layer is silicon oxide. The different layers in the images (d–f) are labeled in the scheme (g).

and oxygen elemental maps shown in Figure 4e and f, respectively. The different layers imaged in Figure 4d–f are labeled in the corresponding scheme Figure 4g. In Figure 4e, the bright contrast in the image corresponds to the Si signal. The abrupt damping of the Si signal at the silicon oxide/BPhen interface and the absence of any bright contrast in the BPhen layer indicates the penetration of Si during sputtering is not significant under the sputter deposition conditions we have employed. The distribution of Si and O signals in Figure 4e and f also confirms the sputtered layer being silicon oxide.

Sputtering could cause physical damage to the organic molecules or by the silicon penetration in to organic, UV radiation exposure or the oxidation the organic ligands at the top oxide interface. However, in contrast to standard injection devices, there is no current flow across this interface and therefore we assume that it has no major influence.

The AC operation of the device is confirmed by the time resolved AC-EL measurements performed to record the luminance vs. time response of the device. The luminance-time

response is measured at a constant frequency of 10 kHz and as a function of the applied voltage shown in **Figure 5**. The luminance time response is similar at other frequencies.
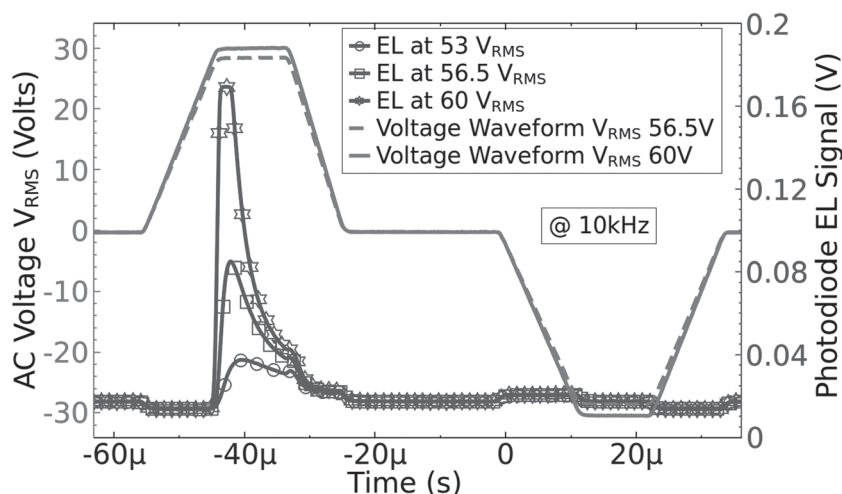

Figure 5. The time-resolved measurements of the alternating voltage pulse at 10 kHz (left axis) and the corresponding AC-EL as recorded by the photodetector (V) (right axis). The device emits light only in the forward cycle.

Materials
Views
www.MaterialsViews.com

ADVANCED
FUNCTIONAL
MATERIALS
www.afm-journal.de

FULL PAPER

Only in the forward cycle (one half of the AC cycle), the applied field assists in the drift of the charge carriers to form excitons and light is generated. We also observe that if we increase the applied voltage to the device, the photodetector records a higher signal due to an increase in the luminance output from the device. If we keep the AC bias at high level for a longer time and record the luminance output as a function of time, after the luminance onset there is initially a steep increase and later on the luminance decreases even though the applied AC bias is kept high. This indicates that there are no more charge carriers within the device to form excitons to generate light.

The novelty of this concept is in the regeneration of charge carriers within the device, without injecting them as done in DC devices. If we do not inject the charge carriers into the device we need to regenerate them by some means within the device to sustain the luminance. We propose the following mechanism for the regeneration of charge carriers within the device. At equilibrium, the Fermi levels of metal, insulator, and the organic layer are aligned. For the case of low positive applied AC bias (less than the built-in potential), the built-in potential gets reduced by an amount equal to the externally applied bias, which is depicted in **Figure 6**a. In the extreme forward bias case where the applied AC bias is exceeding the built-in potential, the band alignment is shown in Figure 6b. The cathode Fermi level moves relative to the anode Fermi level depending on the external applied AC bias. The charge carriers (holes and electrons) are injected into the emission layer and excitons are generated, which decay radiatively. Since the charge carrier drift forms excitons in the positive half of the AC cycle, the charge carriers leave behind ionized dopants on the p- and n- side.

In the opposite cycle at high negative AC bias, the charge carriers can tunnel directly from the HOMO of the p- side to the LUMO of the n-layer through the intrinsic layer due to band level alignment. The energy levels between the transport and intrinsic layer are spread in such a way that there is stepwise staircase like distribution (ladder like states) (Figure 6c),[22] which assists in the charge carrier tunneling from one ladder state to another at large applied negative AC bias. Thus charge carriers (holes and electrons) are generated and drift towards the insulators and neutralize the ionized dopants. This brings the system back to the original state. By this process, free charges are generated that are used in the subsequent forward cycle to generate excitons again. The device does not emit light in the negative cycle. This is also confirmed in a reference DC device with just the emission layer sandwiched between ITO and Al. The device only emits in the forward direction and does not emit in the reverse bias. This clearly demonstrates that our AC devices behave similar to diodes, which generate light only in one cycle.

To add further evidence to the device operating mechanism, we increase the doping concentration of the charge-transport layers and thus increase the number of free charge carriers.[9,14] Intrinsic organic layers have a typical charge-carrier density of 10^{14} cm^{-3}.[13] By doping we can increase the charge-carrier density by orders of magnitudes to typically 10^{18}–10^{19}cm^{-3}.[9,14] If the charges are regenerated within the device as we propose, an increase in charge-carrier density should also increase the luminance. To prove this we varied the doping concentration
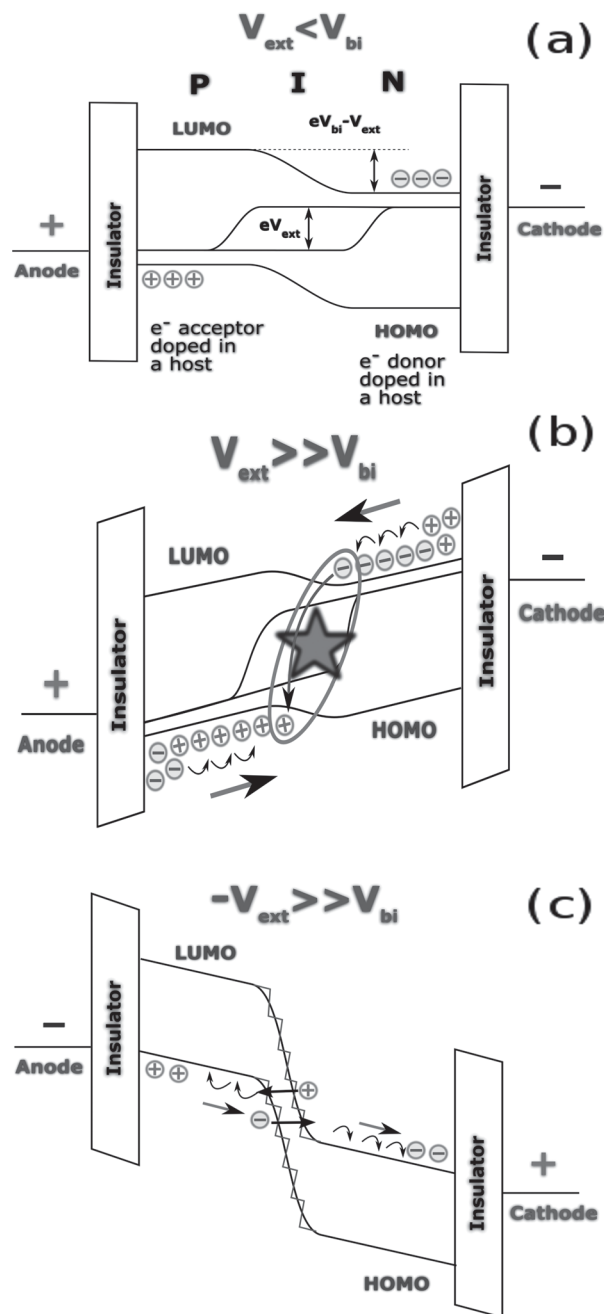

Figure 6. Schematic of energy level alignment with the applied bias, shown for forward and reverse AC bias. For the case of low positive applied AC bias (less than the built-in potential), the built-in potential is reduced by an amount equal to external applied bias as shown in (a). In the extreme forward bias case where the applied AC bias is exceeding the built-in potential, the band alignment is shown in (b). In the opposite cycle at high negative AC bias the energy levels between the transport and intrinsic layer are spread in such a way that there is stepwise staircase such as distribution (ladder-like states), which assist in the charge-carrier tunneling from one ladder state to another, as shown in (c).

on the p-side and simultaneously measure the conductivity for the corresponding molar ratio (MR). For this experiment we have chosen MeO-TPD doped with NDP2. The F_4TCNQ
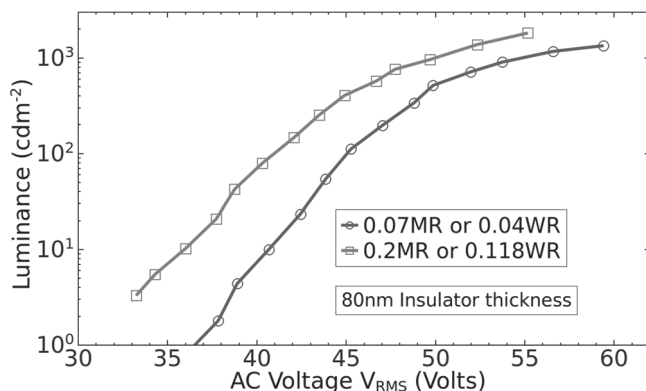
Figure 7. Luminance voltage response for two different doping concentrations of NDP2 (4 wt% and 14 wt%) for the device C shown in Figure 1, with 80 nm SiO_2 on both sides.

molecules have a low evaporation temperature of ~75 °C and are thus very volatile, while NDP2 is a commercial proprietary material with a low-lying LUMO comparable to F_4TCNQ, but is very stable and has a higher evaporation temperature avoiding tool contamination. F_4TCNQ and NDP2 dopants on the p-side are interchangeable, which lead to a comparable performance of our devices.[14]

We have chosen two MR of NDP2 doped in MeO-TPD that differ significantly for a more pronounced observation of this effect, for the same thickness of insulating layers. We adjusted the same conductivity for p-doped (MeO-TPD doped with NDP2) and n-doped (BPhen doped with Cs) layers. This was done after checking the doping efficiency[14] for the p- and n-doped side to be almost the same at around 5%. The number of charge carriers is also approximately the same and amounts to 10^{19} cm^{-3} on both sides. The luminance observed at any voltage is higher for higher doping concentration (**Figure 7**), which confirms the working principle that we have discussed above.

3. Conclusions

In conclusion, we have demonstrated a novel approach for an AC driven organic light-emitting devices with a simple device fabrication procedure using the concept of molecular doping in organic semiconductors. Doped organic charge-transport layers are successfully utilized for the generation of charge carriers within the device, hence eliminating the need for injecting charge carriers from external electrodes. The AC driven organic light-emitting devices demonstrated in this contribution emit bright luminance of up to 1000 cd m^{-2} and show a maximum power efficiency of 0.37 lm/W for non optimized devices.

4. Experimental Section

The devices are prepared on a glass substrate with a pre-coated and structured ITO film of 90 nm thickness and a sheet resistance of approximately 25 Ω square^{-1}. The substrates are subsequently cleaned in an ultrasonic bath with acetone followed by ethanol and iso-propanol.

The SiO_2 insulating layers are coated via planar radio frequency (RF) magnetron sputtering using a SiO_2 sputter target of 5 cm in diameter,

obtained from MaTeK GmbH. During the sputter deposition an argon pressure of 2×10^{-3} mbar is maintained in the sputtering chamber. The RF power supply with impedance matching network is used at 150 W. Typical deposition rates are 1–2 Å s^{-1}. The organic layers are deposited by a thermal vapor deposition process. The devices are completed with the top Al contact deposited by thermal evaporation. The whole processing of the device is done in a cluster tool under ultrahigh vacuum (UHV) conditions. The base pressure of the cluster tool is 10^{-8} mbar. The devices are encapsulated with an additional glass and epoxy resin in a nitrogen atmosphere for further characterization without breaking the vacuum.

Doped organic charge-transport layers serve as charge-generating centers as well as for better transport of these carriers. MeO-TPD (N,N′-tetrakis(4-methoxyphenyl)-benzidine) doped with F_4TCNQ (2,3,5,6-tetrafluoro-7,7,8,8,-tetracyanoquino dimethane) acts as hole generating p-doped transport layer while BPhen (4,7-diphenyl-1,10-phenanthroline) doped with *Cesium* (Cs) acts as electron generating n-doped transport layer. The emission layer consists of α-NPD (N,N′-di(naphthalen-2-yl)-N,N′-diphenylbenzidine) as a host and $Ir(MDQ)_2(acac)$ [Iridium(III)bis(2-methyldibenzo-[f,h] quinoxaline) (acetylacetonate)] as orange phosphorescent dye dopant, with 10 wt% doping in all devices. Doping is achieved by co-evaporation of the host and the dopant molecule while the evaporation rates are being monitored independently by two different quartz crystal microbalances (QCM). The thickness of the layers is also monitored via QCM. The device area is 6.7 mm^2.

The device A consists of a 20-nm-thick single EL layer sandwiched between SiO_2 dielectric insulating layers of 60 nm in thickness. Device B is similar to Device A except for the addition of intrinsic or undoped charge-transport layers, MeO-TPD and BPhen (20 nm each) on both sides of the EL layer. Device C is the same as Device B, except for the doped charge-transport layers (p-doped MeO-TPD:F_4TCNQ and n-doped BPhen:Cs) of 20 nm each. Device D is similar to Device C except for the addition of charge-blocking layers α-NPD and BPhen (10 nm each). For all the devices we have chosen the same thickness of the EL layer for comparison. The EL layer with an emitting system of α-NPD:$Ir(MDQ)_2(acac)$ allows for an effective energy transfer from the host to the guest dopant molecules.[23–25]

For the AC-EL device characterization, AC sinusoidal voltages are applied from an arbitrary function generator (Agilent 33210A) connected to a bipolar linear power amplifier (Apex Micro-technology). The electro-luminescence (EL) spectra are recorded with a USB-2000 mini spectrometer (OceanOptics, Dunedin). The luminance is recorded with a luminance meter (KonicaMinolta, CS-100A). The luminance is recorded as a function of either the AC bias applied to the device (at a fixed frequency) (L–V) or as a function of the frequency of the applied AC bias (keeping the applied AC bias constant) (L–f).The complete measurement setup is fully automated with computer control. All measurements are performed at room temperature.

The time resolved AC electroluminescence response is detected using a fast photo diode (Thorlabs). The power input to the device is calculated by measuring the voltage drop across the device and a series resistor (100 Ω) and the phase angle between the two signals using a single phase precision power meter (LMG-95 ZES Zimmer GmbH).

The cross-sectional transmission electron microscopy (TEM) specimens are prepared using the focused ion beam (FIB) preparation technique on a Zeiss 1540XB cross beam FIB- scanning electron microscope. The TEM investigations are carried out on a FEI Tecnai F30 TEM/STEM microscope operating at 300 kV accelerating voltage. The microscope is equipped with a field emission gun, and Si(Li) energy dispersive X-ray (EDX) spectrometer for spectroscopic compositional analysis of the specimen and a GATAN imaging filter GIF200 for energy-filtered TEM (EFTEM) imaging for elemental mapping. The high-angle annular dark field (HAADF-STEM) imaging mode is used for EDXS analysis, which allows for location-specific acquisition of X-ray spectra. Bright-field TEM and high-resolution TEM imaging modes are used for thickness measurement of different layers in the multi layer device cross-section and also to investigate the interface quality between the organic layers and the insulating SiO_2 layers.

www.MaterialsViews.com

ADVANCED
FUNCTIONAL
MATERIALS
www.afm-journal.de

FULL PAPER

Supporting Information

Acknowledgements

[1] P. D. Rack, P. H. Holloway, *Mater. Sci. Eng.* **1998**, *R21*, 171–219.
[2] J. C. Hitt, J. P. Bender, J. F. Wager, *CRC Crit. Rev. Solid State Mater. Sci.* **2000**, *25*, 29–85.
[3] V. Wood, M. J. Panzer, J. Chen, M. S. Bradley, J. E. Halpert, M. G. Bawendi, V. Bulovic, *Adv. Mater.* **2009**, *21*, 2151–2155.
[4] X. L. Xu, X. H. Chen, Y. B. Hou, Z. Xu, X. H. Yang, S. G. Yin, Z. J. Wang, X. R. Xu, S. P. Lau, B. K. Tay, *Chem. Phys. Lett.* **2000** *325*, 420–424.
[5] S. Y. Yang, L. Qian, F. Teng, Z. Xu, X. R. Xu, *J. Appl. Phys.* **2005**, *97*, 126101–126103.
[6] T. Tsutsui, S. B. Lee, K. Fujita, *Appl. Phys. Lett.* **2004**, *85*, 2382–2384.
[7] S. B. Lee, K. Fujita, T. Tsutsui, *Jpn. J. Appl. Phys.* **2005**, *44*, 6607–6611.
[8] Y. Kawamura, K. Goushi, J. Brooks, J. J. Brown, H. Sasabe, C. Adachi, *Appl. Phys. Lett.* **2005**, *86*, 071104.
[9] M. Pfeiffer, K. Leo, X. Zhou, J. S. Huang, M. Hofmann, A. Werner, J. Blochwitz-Nimoth, *Org. Electron.* **2003**, *4*, 89–103.
[10] K. Walzer, B. Maennig, M. Pfeiffer, K. Leo, *Chem. Rev.* **2007**, *107*, 1233–1271.
[11] C. W. Tang, S. A. VanSlyke, *Appl. Phys. Lett.* **1987**, *51*, 913–915.
[12] S. Reineke, F. Lindner, G. Schwartz, N. Seidler, K. Walzer, B. Lüssem, K. Leo, *Nature* **2009**, *459*, 234–238.
[13] N. Hayashi, H. Ishii, Y. Ouchi, K. Seki., *J. Appl. Phys.* **2002**, *92*, 3784–3793.
[14] S. Olthof, W. Tress, R. Meerheim, B. Lüssem, K. Leo, *J. Appl. Phys.* **2009**, *106*, 103711.
[15] X. Zhou, M. Pfeiffer, J. Blochwitz, A. Werner, A. Nollau, T. Fritz, K. Leo, *Appl. Phys. Lett.* **2001**, *78*, 410–412.
[16] J. Loos, J. K. J van Duren, F. Morrissey, R. A. J. Janssen, *Polymer* **2002**, *43*, 7493–7496.
[17] B. Schaffer, C. Mitterbauer, A. Schertel, A. Pogantsch, S. Rentenberger, E. Zojer, F. Hofer, *Ultramicroscopy* **2004**, *101*, 123–128.
[18] F. Hofer, P. Warbichler, W. Grogger, *Ultramicroscopy* **1995**, *59*, 15–31.
[19] F. Hofer, P. Warbichler, W. Grogger, G. Kothleitner, *Ultramicroscopy* **1997**, *67*, 83–103.
[20] F. Hofer, W. Grogger, P. Warbichler, I. Papst, *Mikrochim. Acta* **2000**, *132*, 273–288.
[21] G. Kothleitner, F. Hofer, *Micron* **1998**, *29*, 349–357.
[22] H. Kleemann, R. Gutierrez, F. Lindner, S. Avdoshenko, P. D. Manrique, B. Lüssem, G. Cuniberti, K. Leo, *Nanoletters* **2010**, *10*, 4929–4934.
[23] M. A. Baldo, D. F. O. Brien, M. E. Thompson, S. R. Forrest, *Phys. Rev. B* **1999**, *60*, 14422–14428.
[24] J. S. Huang, M. Pfeiffer, A. Werner, J. Blochwitz, K. Leo, S. Y. Liu, *Appl. Phys. Lett.* **2002**, *80*, 139–141.
[25] R. Meerheim, S. Scholz, S. Olthof, G. Schwartz, S. Reineke, K. Walzer, K. Leo, *J. Appl. Phys.* **2008**, *104*, 014510–014518.

FULL PAPER

Arrays of Cone-Shaped ZnO Nanorods Decorated with Ag Nanoparticles as 3D Surface-Enhanced Raman Scattering Substrates for Rapid Detection of Trace Polychlorinated Biphenyls

Haibin Tang, Guowen Meng,* Qing Huang,* Zhuo Zhang, Zhulin Huang, and Chuhong Zhu

A new, highly sensitive and uniform three-dimensional (3D) hybrid surface-enhanced Raman scattering (SERS) substrate has been achieved via simultaneously assembling small Ag nanoparticles (Ag-NPs) and large Ag spheres onto the side surface and the top ends of large-scale vertically aligned cone-shaped ZnO nanorods (ZnO-NRs), respectively. This 3D hybrid substrate manifests high SERS sensitivity to rhodamine and a detection limit as low as 10^{-11} M to polychlorinated biphenyl (PCB) 77—a kind of persistent organic pollutants as global environmental hazard. Three kinds of inter-Ag-NP gaps in 3D geometry create a huge number of SERS "hot spots" that mainly contribute to the high SERS sensitivity. Moreover, the supporting chemical enhancement effect of ZnO-NRs and the better enrichment effect ascribed to the large surface area of the substrate also help to achieve a lower detection limit. The arrays of cone-shaped ZnO-NRs decorated with Ag-NPs on their side surface and large Ag spheres on the top ends have potentials in SERS-based rapid detection of trace PCBs.

1. Introduction

Surface-enhanced Raman scattering (SERS) spectroscopy has been developed rapidly for its tremendous potentials in chemical and biological sensing applications due to its high sensitivity, rapid response, and fingerprint effect.[1–4] Various approaches to regular substrates with two-dimensional (2D) and three-dimensional (3D) "hot spots" for SERS detection have been presented.[5–7] For many years SERS substrates were primarily restricted to noble metal (Au, Ag, and Cu) structures. Recently, it has been found that various semiconductors, such as ZnO,[8] ZnS,[9] TiO₂,[10] Cu₂O,[11] and CuO,[12] can also generate weak SERS activity with typical prominent enhancement factors ranging from 10^1 to 10^3. Therefore, composites or heterostructures between semiconductors (Si, ZnO, and TiO₂) and noble metals (Au and Ag) have attracted attention, as a much higher SERS effect could be achieved due to the contributions from both the electromagnetic enhancement (excited by the localized surface plasmon resonance of noble metals) and the semiconductor supporting chemical enhancement (caused by the charge transfer between the noble metal and the adjacent semiconductor).[13–20] ZnO, a versatile semiconductor material with a direct band gap of 3.37 eV, has received special attention due to its excellent performance in supporting chemical enhancement of SERS substrates.[21,22] Several methods have thus been developed to fabricate this new type of ZnO/noble metal hybrid SERS substrate. For example, electroless plating was employed to assemble Ag nanoparticles (Ag-NPs) onto the surface of ZnO nanorods (ZnO-NRs) by sensitizing and activating with Sn^{2+} or by irradiation with UV light.[22,23] Interestingly, the Ag-NPs could also be located on the tips of the ZnO-NRs via a photodeposition method or galvanic reduction.[24,25] Alternatively, with the help of surface modification with amino or mercapto groups, Au-NP/ZnO-particle and Au- or Ag-NPs/ZnO-multipods hybrid structures were achieved.[21,26] However, the spatial gaps between these small noble metal particles on the ZnO supporter were too large to work efficiently as SERS "hot spots" and, moreover, the complicated coupling agents for linking the metal NPs onto the ZnO surface, such as (3-aminopropyl) triethoxysilane, may bring extra interferential bands in the SERS measurements, especially if the target analytes have similar Raman spectral response with the coupling agents. To tackle this problem, physical sputtering was exploited. For example, a SERS substrate called "3D hybrid Ag-nanocluster-decorated ZnO nanowire arrays" was fabricated

Dr. H. Tang, Prof. G. Meng, Dr. Z. Zhang, Dr. Z. Huang, Dr. C. Zhu
Key Laboratory of Materials Physics and Anhui Key Laboratory of Nanomaterials and Nanostructures
Institute of Solid State Physics
Chinese Academy of Sciences
P. O. Box 1129, Hefei 230031, P. R. China
E-mail: gwmeng@issp.ac.cn
Prof. Q. Huang
Key Laboratory of Ion Beam Bioengineering
Hefei Institutes of Physical Science
Chinese Academy of Sciences
Hefei 230031, P. R. China
E-mail: huangq@ipp.ac.cn

www.MaterialsViews.com

ADVANCED
FUNCTIONAL
MATERIALS
www.afm-journal.de

FULL PAPER
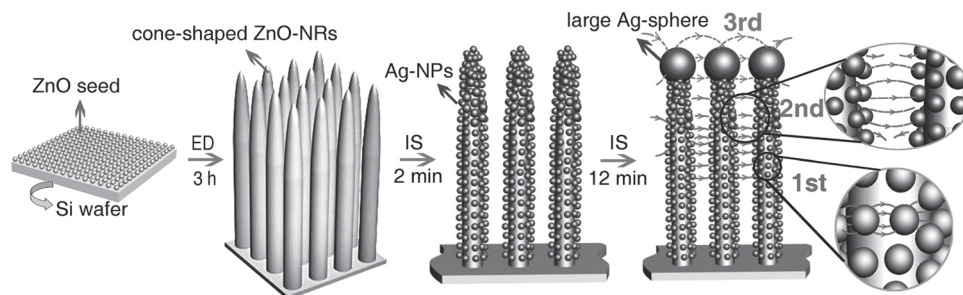
Scheme 1. Schematic image of the fabrication of an arrays of ZnO-NRs decorated with Ag-NPs (on the NRs side surface) and Ag spheres (on the NRs tops) on Si wafers. There are three kinds of "gaps" between the Ag-NPs to form 3D "hot spots" as indicated as 1st, 2nd, and 3rd schematically. "1st" stands for the gaps between the Ag-NPs located on the side surface of the same NR; "2nd" stands for the gaps between the two Ag-NPs located on the side surface of two neighboring NRs; and "3rd" stands for the gaps between the two large Ag spheres located on the tops of two neighboring NRs.

via depositing Ag nanoclusters onto ZnO nanowire arrays by using a gas-aggregation-type nanocluster beam source.[27] However, as the authors claimed themselves, the ZnO nanowire arrays were not perfectly aligned, and the Ag nanoclusters were randomly distributed over the wires with a finite size distribution, which could not create sufficient uniformly distributed "hot spots" for highly sensitive and uniform SERS activity.

Herein, we report a synthetic approach to large-scale arrays of vertically aligned cone-shaped ZnO-NRs decorated with Ag-NPs in different dimensions on their side surface and top ends as highly sensitive and uniform 3D SERS substrate, as shown schematically in **Scheme 1**. Firstly, homogeneous crystalline ZnO seeds on planar Si wafer were achieved via thermal decomposition of zinc acetate pre-dispersed on the Si wafer.[28] Then, arrays of vertically aligned cone-shaped ZnO-NRs were grown on the ZnO-seeds-coated Si wafer via electrodeposition (denoted as "ED"). To achieve arrays of cone-shaped ZnO-NRs, instead of using Zn plate as anode in our previous work,[29] here, we purposly used a graphite plate as the anode and a given volume of electrolyte with lower concentration in the electrodeposition. With the electrodeposition growth of the ZnO-NRs from the bottom to the top, the Zn^{2+} concentration in the electrolyte decreases continuously and, accordingly, the diameter of the ZnO-NRs decrease from the bottom to the top, resulting in cone-shaped ZnO-NRs. Finally, small Ag-NPs were assembled onto the side surface of the cone-shaped ZnO-NRs via top-view ion-sputtering (denoted as "IS") Ag with a short duration, and then a large Ag sphere was further decorated onto the top end of each cone-shaped ZnO-NR by elongation of the ion-sputtering duration, to achieve a more sensitive SERS substrate loaded with high-density "hot spots" in 3D geometry. The resulting new hybrid 3D substrate shows such a high SERS activity that rhodamine (R6G) of a concentration as low as 10^{-12} M could still be identified. We tried to use this 3D highly sensitive SERS substrate to detect trace polychlorinated biphenyls (PCBs), a class of highly toxic persistent organic pollutants that have been causing global environmental hazard.[30,31] Conventionally, trace PCBs could be detected by using phosphorimetry,[32] chromatographic analysis,[33] or gas chromatography-isotope dilution time-of-flight mass spectrometry.[34] However these methods have some fatal shortcomings: they require sophisticated instruments and are time-consuming. Using our

3D hybrid SERS substrate, a low detection limit of 10^{-11} M for PCB-77 (3,3′,4,4′-tetrachlorobiphenyl, one congener of PCBs) has been achieved. Thus our highly sensitive hybrid SERS substrate with sufficient 3D "hot spots" shows a very promising and practical solution to the rapid trace detection of PCBs.

2. Results and Discussion

Large-area uniform arrays of vertically aligned and cone-shaped ZnO-NRs on a Si wafer are shown in the scanning electron microscopy (SEM) image of **Figure 1**a. As large-area uniformly distributed ZnO seeds could be achieved on the Si wafer, wafer-scaled (1.5 cm × 2.5 cm) arrays of vertically aligned cone-shaped ZnO-NRs could be achieved via ZnO-seed-induced electrodeposition. The insets in Figure 1a reveal that the as-electrodeposited ZnO-NRs are vertically aligned with cone-shaped morphology and an average height of about 1.2 μm; the estimated average diameter near the half height of the cone-shaped ZnO-NRs is about 60 nm. As for the electrodeposition of ZnO, our previous work reveals that current density and electrolyte concentration are critical to the morphologies of the resultant products as follows:[29] 1) A much lower (such as 0.01 mA cm^{-2}) current density would lead to ZnO films consisting of ZnO nanoparticles rather than ZnO-NRs regardless of the change of Zn^{2+} concentration in the electrolyte; 2) A moderate (0.2–3.0 mA cm^{-2}) current density would lead to arrays of ZnO-NRs with planar ends (due to the dynamic equilibrium of the electrolyte concentration caused by the continuous electro dissolution of the Zn anode to form Zn^{2+} into the solution) as the ZnO growth direction is dominated along the electric field, and the diameter of the ZnO-NR is proportional to the Zn^{2+} concentration in the electrolyte; 3) a high (5.0 mA cm^{-2}) current density would lead to conglutinated ZnO-NRs as the growth of the ZnO-NRs along the a-axis becomes obvious. To achieve cone-shaped ZnO-NRs, in this work, we applied a moderate current density (0.5 mA cm^{-2}) and used a graphite plate as the working electrode in a given volume (100 mL) of electrolyte with a low concentration of 0.05 M Zn^{2+}. There would be no new Zn^{2+} to complement the consumption resulted from the ZnO-NR growth, resulting in a gradual decrease in Zn^{2+} concentration in the electrolyte during the whole electrodeposition and, accordingly, the diameter of

ADVANCED
FUNCTIONAL
MATERIALS
www.afm-journal.de

Materials
Views
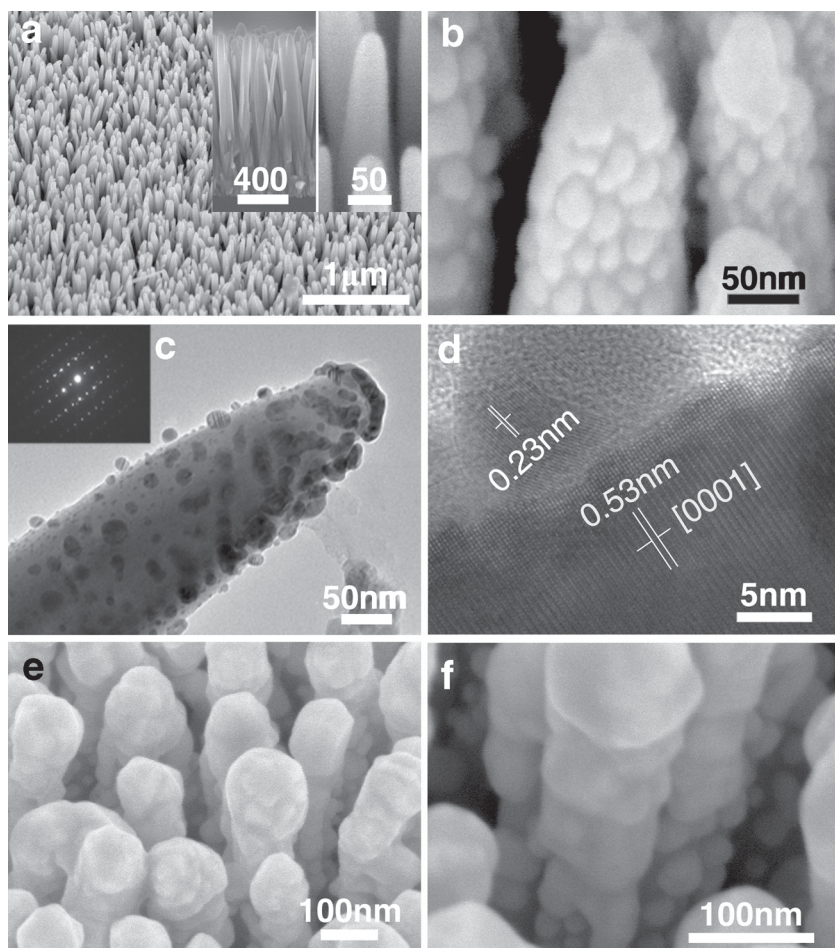www.MaterialsViews.com

FULL PAPER

Figure 1. a) SEM image of the wafer-scale arrays of cone-shaped ZnO-NRs. Left inset: side view; right inset: enlarged image of the tapered ZnO-NRs. b) SEM and c) TEM image of the ZnO-NRs after an Ag-sputtering for 135 seconds. The inset is the selected-area electron diffraction (SAED) pattern taken from the ZnO-NR. d) A lattice-resolved TEM image of the ZnO-NR and Ag-NP adjacent surface. e) SEM image of ZnO-NRs with large Ag spheres on their tops. f) SEM image of small Ag-NPs on the side surface of the ZnO-NRs after an Ag-sputtering for 12 min.

diameter are sputtered onto the side surface of the cone-shaped ZnO-NRs (Figure S1(a), Supporting Information); with an increase of the sputtering duration to 1 min, Ag-NPs with a slightly larger size of about 8 nm are formed on the side surface of the cone-shaped ZnO-NRs (Figure S1(b), Supporting Information). For longer sputtering durations, not only the number and size of the Ag-NPs growing on the side surface of the cone-shaped ZnO-NRs increase, but bigger Ag-NPs are formed also on the top ends of the cone-shaped ZnO-NRs, as shown in the SEM image (Figure 1b) of a sample sputtered for 135 s (see also Figure S1(c) in the Supporting Information for the sample sputtered with Ag for 2 min). Detailed SEM observations further verify the two kinds of NPs (the small ones and the big ones) as follows: 1) Small Ag-NPs are distributed randomly but uniformly on the whole side surface of the cone-shaped ZnO-NRs. The size of these small Ag-NPs is about 20 nm in diameter, with an average separation of less than 5 nm between adjacent small Ag-NPs, which is critical to create high SERS activity excited by the surface plasmon coupling between the narrow gaps of the neighboring Ag-NPs growing on the same ZnO-NR. 2) Big Ag-NPs, about 50 nm in diameter, are formed on the top ends of the cone-shaped ZnO-NRs, as can be seen in the transmission electron microscopy (TEM) image in Figure 1c. The big Ag-NP looks like a "hat" on the top end of the cone-shaped ZnO-NR, whose formation is attributed to Ostwald ripening of top-end NPs in the later period of Ag sputtering.[36] Lattice-resolved TEM (Figure 1d) reveals the good crystalline nature of both the cone-shaped ZnO-NRs and the Ag-NPs sputtered onto the ZnO-NRs. The measured spacing of lattice planes of the ZnO-NRs is about 0.53 nm, being assigned to the (0001) plane of ZnO; while the measured spacing of lattice planes of the Ag-NPs is about 0.23 nm, being assigned to the (111) plane of Ag. These are consistent with the X-ray diffraction (XRD) results (Figure S1(d), Supporting Information).

With a further increase in the Ag-sputtering duration, the separation between the top ends of the neighboring ZnO-NRs decreases gradually as the big Ag-NPs on top ends of the NRs grow laterally, and consequently less and less Ag can reach the side surface of the cone-shaped ZnO-NRs. When the sputtering duration increases to 12 min, the big Ag-NPs on the top ends of the ZnO-NRs become spheres with large diameters of up to about 100 nm, as shown in Figure 1e. The average gap between the Ag spheres on the top ends of two neighboring ZnO-NRs is estimated to be about 50–60 nm, although the minimum can be several nanometers and the maximum can reach 100 nanometers. In order to show the small Ag-NPs on the side surface of the well-aligned and uniformly distributed

the ZnO-NRs decreases gradually from the bottom to the top end. Therefore large-scale arrays of vertically aligned cone-shaped ZnO-NRs are formed on the Si wafer. In contrast to those previously reported ZnO-NRs achieved via hydrothermal synthesis[25] or chemical vapor deposition (CVD),[35] our ZnO-NRs are cone-shaped and well-vertically-aligned, with a high distribution density, narrow-diameter distribution and an aspect ratio of about 20. As every ZnO-NR is cone-shaped with sharp top, a wider separation exists between the neighboring top ends of NRs. Therefore, with these vertically aligned cone-shaped ZnO-NRs arrays as a substrate it will be very easy to sputter a large number of Ag-NPs onto the side surface and the top ends of the cone-shaped ZnO-NRs via top-view Ag ion-sputtering and, further, to achieve a large quantity of efficient SERS "hot spots" in the focused region of an incident laser-light spot during Raman spectroscopy measurement.

Then ion-sputtering has been performed to assemble Ag-NPs onto the cone-shaped ZnO-NRs. With a very short sputtering duration of 0.5 min, only a few small Ag-NPs of about 5 nm in

www.MaterialsViews.com

ADVANCED
FUNCTIONAL
MATERIALS
www.afm-journal.de

FULL PAPER

cone-shaped ZnO-NRs, we tried very hard to find an abnormal wide gap of two neighboring ZnO-NRs, as shown in Figure 1f. Through the gaps among the ZnO-NRs, it can be seen clearly that the whole side surface of the cone-shaped ZnO-NRs are coated with small Ag-NPs, about 30 nm in diameter. If the sputtering duration keeps increasing, the Ag spheres on the top ends of the ZnO-NRs will consequently keep growing and finally aggregate to form a film (Figure S1(e), Supporting Information). In contrast to the previously reported fabrication strategies and the corresponding structures, in which only Ag-NPs of one dimension were formed on the surface of the ZnO-NRs or on the top ends,[22,24] here our ZnO-NRs are cone-shaped (resulting from the continuous decrease of Zn^{2+} in the electrolyte during the electrodeposition), vertically aligned, and homogeneously distributed on the Si wafer with a high density (resulting from the ZnO-seeds assisted electrodeposition). More importantly, for our 3D hybrid SERS substrates, not only small Ag-NPs (about 30 nm) are uniformly sputtered onto the whole side surface of the cone-shaped ZnO-NRs, but also large Ag spheres (about 100 nm) are sputtered onto the top ends of the cone-shaped ZnO-NRs. It should also be noted that the Ag-NPs and Ag spheres with different dimensions are assembled simultaneously, merely by simple physical ion-sputtering without using any reagents. Thus our work presents a clean and green method that circumvents potential Raman spectral interference caused by the chemical modification agents.[21,26]

Then, R6G dye was used as a probe molecule to reveal the sensitivity of the as-prepared 3D hybrid SERS substrates. **Figure 2**a shows that the SERS activity of the as-prepared substrate improves with the increase of the Ag-sputtering duration from 1 min to 10 min, but decreases for the substrates with sputtering duration of 15 min, 20 min, and 25 min. For a detailed study of the SERS activity of the substrates with different Ag-sputtering durations from 8 min to 14 min, we used a low concentration of R6G solution (5.0×10^{-9} M) for the Raman spectroscopy measurements and a data acquisition time of

4 s; the results are shown in Figure 2b. It can be seen that the Raman activity of the as-prepared substrates improved sharply with the increase of the sputtering durations from 1 min to 12 min and diminished for longer Ag-sputtering durations.

The above SERS sensitivity variations with different Ag-sputtering durations can be ascribed to the particular structural development of the as-prepared substrate. For substrates with short Ag-sputtering duration (1 min for example) only a few efficient gaps are present between the neighboring Ag-NPs on the side surface of the same ZnO-NR (first kind of SERS "hot spots", denoted as the "1st" in Scheme 1); thus, the SERS activity is not high enough. When the Ag-sputtering duration is increased to 2 min, the size of the Ag-NPs on the side surface of the cone-shaped ZnO-NRs increases, as shown in Figure 1b (see also Figure S1(c), Supporting Information). Not only the first kind of "hot spots" contribute to the higher SERS intensity, but also the "hot spots" that stemmed from the Ag-NPs on two neighboring ZnO-NRs (second kind of SERS "hot spots", denoted as the "2nd" in Scheme 1) become more efficient. Once the sputtering duration is increased from 2 min to 12 min, the Raman intensity from the corresponding substrates increases sharply. During these sputtering periods, the growth of the Ag spheres on the top ends of the ZnO-NRs, with a dimension approaching 100 nm, is dominant, accompanied by a growth of the Ag-NPs located on the side surface of the NRs, approaching 30 nm. Therefore, it is concluded that a new kind of "hot spots", originated from the large Ag spheres on the top ends of two neighboring ZnO-NRs (the third kind of "hot spots", denoted as the "3rd" in Scheme 1), make a great contribution to the high SERS enhancement. For substrates with Ag-sputtering durations for more than 12 min, especially for 20 min or 25 min, the Raman activity decreases rapidly. The continuous growth of the large Ag spheres on the top ends of the ZnO-NRs with the elongation of Ag-sputtering duration results in the aggregation of the Ag spheres (or even in the formation of a layer of Ag on the top ends of the ZnO-NRs arrays) and consequently the
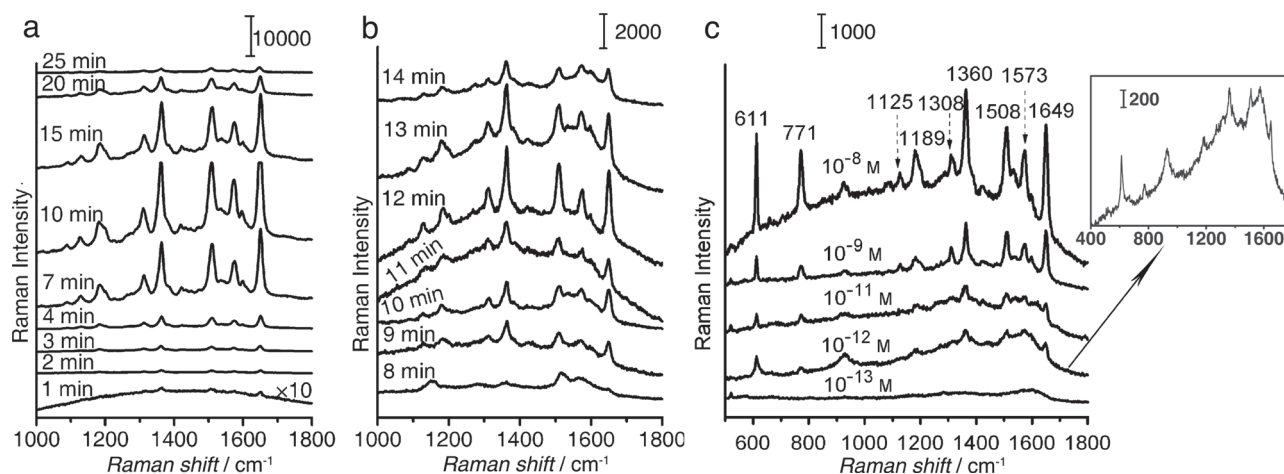

Figure 2. The SERS spectra of R6G collected on the substrates with different Ag-sputtering durations (indicated on the upper-left of each spectrum). a) Exposed to a 5.0×10^{-7} M R6G solution with a data acquisition time of 0.2 s; b) Exposed to a 5.0×10^{-9} M R6G solution with a data acquisition time of 4 s; c) collected on the same substrates with Ag-sputtering for 12 min, and exposed to different R6G concentrations (indicated in the upper middle position of each spectrum). The inset in (c) is the enlarged SERS spectrum of R6G collected on the substrate exposed to 10^{-12} M R6G solution with a data acquisition time of 4 s.

efficiency of "hot spots" is removed. Thus, from the comparison of the Raman spectra it can be concluded that the as-prepared arrays of the cone-shaped ZnO-NRs decorated with Ag-NPs with an Ag-sputtering duration for 12 min has the strongest SERS activity.

The observed high SERS enhancement from the as-prepared substrate with an Ag-sputtering duration of 12 min can be explained by the electromagnetic enhancement mechanism as a result of surface plasmon resonance excitation of Ag-NPs and chemical enhancement effects of ZnO. Theoretical calculation and experiments have shown that the narrow inter-particle gaps induce "hot spots" that provide a giant electromagnetic SERS enhancement.[37–40] Especially, when the interparticle separation decreases to less than 10 nm, the electromagnetic coupling between two neighboring Ag-NPs creates extremely high SERS activity. With an increase in the Ag-sputtering duration to 12 min, not only the number, but also the size of the Ag-NPs increases. With the size increment, the gaps between the Ag-NPs decrease correspondingly, as shown in Figure 1 and Figure S1 in Supporting Information, followed by the increment of the SERS activity, as shown in Figure 2. For Ag-sputtering longer than 12 min, the gaps between the Ag-NPs disappear as a result of the further size increment and aggregation of the Ag-NPs. Consequently, the SERS activity decreases significantly, as shown in Figure 2b. In addition, for the Ag spheres on the tops of the ZnO-NRs, a size-dependent SERS enhancement effect may also exist. It has been reported that the most effective NPs for SERS at 514.5 nm (the excitation wavelength we use) excitation have a narrow size distribution of 80–100 nm.[41,42] For Ag-sputtering of 12 min, large Ag spheres of 100 nm are formed on the tops of the ZnO-NRs, which also contributes to the best SERS detection sensitivity. This result is further confirmed by the surface plasmon absorption measurement shown in Figure S2 in the Supporting Information, where the surface plasmon absorption of the substrates with Ag-sputtering for 2 min merely centers at 430 nm but becomes wider (including 514.5 nm) for the substrate with an Ag-sputtering duration of 12 min. This surface plasmon absorption band broadening is ascribed to the size and shape variations of the Ag-NPs, and is helpful to improve the SERS activity at 514.5 nm excitation via surface plasmon resonance.[43]

Additionally, the supporting chemical enhancement effect of the semiconducting ZnO-NRs also contributes to the high SERS sensitivity of our hybrid substrates.[8,13,21] As the work function of ZnO (5.2 eV vs. NHE) is larger than that of Ag (4.26 eV vs. NHE), the Fermi energy level of ZnO is lower than that of Ag.[44] Once the Ag-NPs are sputtered onto the surface of the ZnO-NRs, electron transfer from Ag-NPs to ZnO-NRs occurs until their level of Fermi energy attains equilibrium. As a consequence of the charge redistribution, Ag is positively charged, while ZnO is negatively charged, and the highest charge-density region is located on the adjacent face of Ag-NPs and ZnO-NRs. This local electric field can enhance the localized electromagnetic field excited by the surface plasmon resonance to improve the Raman scattering of the analytes.[26,45,46] To further prove the supporting chemical enhancement effect of the ZnO-NRs, we compared the Raman activities of three substrates: an Ag film growing on a ZnO film (ZnO/Ag film), a bare ZnO film, and a bare Ag film. The resulting Raman

spectroscopy measurements of these substrates, after being immersed in 10^{-6} M R6G solution, are shown in Figure S3 in the Supporting Information. The chemical enhancement effect of bare ZnO is too weak to reveal the characteristic bands of R6G at such low concentration. However, the Raman intensity of R6G bands at 611 and 1360 cm^{-1} collected on the ZnO/Ag film are about twice as high as those collected on the bare Ag film. Due to the interaction of ZnO and Ag, the SERS activity of the ZnO/Ag substrate is higher than that of the bare Ag substrate, demonstrating that the supporting semiconducting ZnO in the hybrid structure really does have chemical enhancement effect on the SERS activity of the noble metal.

To further reveal the good SERS enhancement effect of the 3D hybrid substrate with Ag-sputtering for 12 min, SERS spectra collected from this substrate, after being immersed in different concentrations (from 10^{-8} to 10^{-13} M) of R6G solution, are shown in Figure 2c. The spectral feature characteristics of R6G can be identified clearly, even at a concentration as low as 10^{-12} M, where sharp peaks at 611, 771, and 1125 cm^{-1} are associated with C–C–C ring in-plane, out-of-plane bending, and C–H in-plane bending vibrations, respectively, while the bands at 1189, 1360, 1508, and 1649 cm^{-1} are assigned to symmetric modes of in-plane C–C stretching vibrations.[22,27,47] We believe that not only the high SERS activity of this substrate contributes to the high detection sensitivity, but also the sorption effect of the as-prepared 3D hybrid substrate helps to improve the detection sensitivity. It should be mentioned that the arrays of the vertically aligned cone-shaped ZnO-NRs decorated with Ag-NPs have a large surface area, which will lead to a better enrichment of the analyte molecules. Our simple calculations (Part S4, Supporting Information) reveal that about four times more analyte molecules are absorbed on this 3D hybrid substrate than on a normal surface, with the same area of the projected spot of the incident laser, i.e., much more analytes can be captured by our 3D hybrid substrate, which will lead to the improvement of detection limit in trace detection applications. We estimated the SERS enhancement factor (EF) of our 3D hybrid substrate, which is about 3.58×10^7 (Part S5, Supporting Information).

The good uniformity of the as-prepared 3D hybrid SERS substrate was also tested. All the Raman spectra of R6G, obtained from 10 random points on the same piece of SERS substrate, show almost the same intensity for each characteristic band of R6G (Figure S6, Supporting Information). The reason for the good uniformity of the Raman signals can be attributed to our fabrication procedure and the morphological characteristics of the resultant 3D hybrid substrate. Firstly, with the help of a layer of uniformly distributed ZnO seeds on the Si wafer, vertically aligned and cone-shaped ZnO-NRs are uniformly electrodeposited on the Si wafer in high density. Then, a large number of Ag-NPs is uniformly sputtered not only on the whole side surface but also onto the top ends of the cone-shaped ZnO-NRs. The resultant three kinds of nanometer-scale gaps, or SERS "hot spots", are homogeneously distributed in the projected area of the incident laser.

Lastly, the uniform and highly sensitive hybrid SERS substrate with Ag-sputtering for 12 min is used to identify PCB-77, one of 209 congeners of PCBs. The PCB-77 Raman spectra collected from the substrates after being immersed in different PCB-77 concentrations of 10^{-6}, 10^{-8}, 10^{-10}, 10^{-11}, and 10^{-12} M

www.MaterialsViews.com

ADVANCED
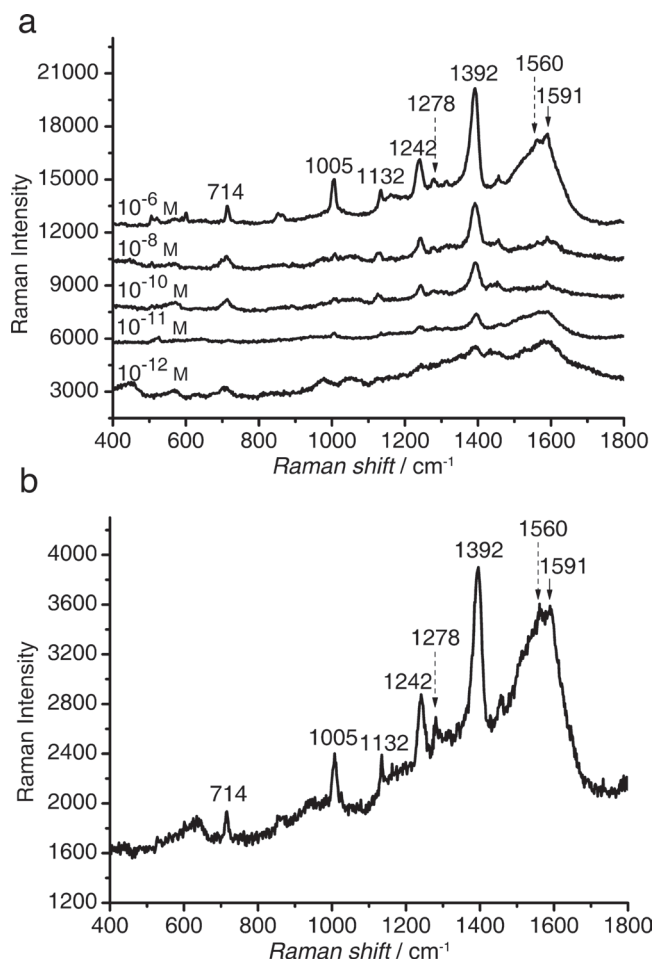FUNCTIONAL
MATERIALS
www.afm-journal.de

FULL PAPER

Figure 3. a) SERS spectra of PCB-77 collected on the as-prepared substrates with Ag-sputtering for 12 min after being exposed to different concentrations of PCB-77 in *n*-hexane solution; the data acquisition time was 50 s. b) Enlarged SERS spectrum of PCB-77 collected on the substrate after being exposed to 10^{-11} M solution and dried.

3. Conclusions

In summary, with the help of a uniform layer of ZnO seeds on planar Si wafer, large-scale vertically aligned cone-shaped ZnO-NRs were fabricated on Si wafers by electrodeposition with a graphite plate as an anode in electrolyte with a limited volume. Small Ag-NPs and large Ag spheres were simultaneously assembled uniformly onto the side surface and the top ends of the cone-shaped ZnO-NRs, respectively, via simple physical ion-sputtering. The sharp top ends of the cone-shaped ZnO-NRs are essential to form the special morphology of the particles and thus the high SERS activity: small Ag-NPs (30 nm) and large Ag spheres (100 nm) could be sputtered onto the side surface and the top ends of the cone-shaped ZnO-NRs. The following three kinds of inter-particle nano-scaled gaps contribute to the high SERS sensitivity as "hot spots": 1) gaps between the small Ag-NPs growing on the same cone-shaped ZnO-NR; 2) gaps between the Ag-NPs growing on the two neighboring ZnO-NRs; 3) gaps between the large Ag spheres on the top ends of two neighboring ZnO-NRs. Moreover, the supporting chemical enhancement effect of ZnO also makes a contribution to the SERS sensitivity. Additionally, as a 3D hybrid substrate, we believe that the better enrichment effect ascribed to the large surface area of the arrays of the vertically aligned NRs decorated with Ag-NPs may also help to achieve a lower detection limit. The 3D hybrid substrate manifests high SERS sensitivity to R6G and a detection limit as low as 10^{-11} M for PCB-77. Therefore the as-prepared arrays of vertically aligned and cone-shaped ZnO-NRs decorated with small Ag-NPs on the side surface and large Ag spheres on the top ends have great potentials as effective SERS substrates for rapid trace detection and monitoring of PCBs.

4. Experimental Section

Fabrication of Cone-Shaped ZnO-NRs Arrays: A layer of ZnO seeds was firstly developed onto Si wafer by wetting the Si wafer with zinc acetate ethanol solution (20 μL, 20 mM), rinsing the substrate with droplets of ethanol, and then drying in a nitrogen stream. The zinc acetate on the Si wafer was subsequently decomposed into ZnO at 350 °C for 20 min. These processes were performed again to provide uniform seeds layer. Then, on the ZnO-seed-coated Si wafer, arrays of cone-shaped ZnO-NRs were electrodeposited with a graphite sheet as anode at a constant current density (0.5 mA cm^{-2}) for 3 h in Zn(NH$_3$)$_4$(NO$_3$)$_2$ aqueous solution (100 mL, 0.05 M), which was prepared by gradually dropping ammonia water into zinc nitrate hexahydrate aqueous solution until the solution became clear. The electrochemical cell was put into a water bath at 80 °C during the whole electrodeposition. Finally, the substrate was cleaned with de-ionized water and dried with high-purity flowing nitrogen gas.

Assembly of Ag-NPs and Ag Spheres: Ion sputtering was applied using a JFC1100 ion sputter to assemble Ag-NPs on the surface of the ZnO-NRs. Arrays of vertically aligned ZnO-NRs grown on the Si wafer were placed up-side down, 2 cm away from the Ag target. The sputtering was operated for different periods of durations (1.3 kV, 2.5 mA). The as-prepared samples were cut into pieces (2 mm × 2 mm) as SERS substrates. These SERS substrates were soaked in R6G and PCB-77 solutions of different concentrations for 10 h. The pieces were taken out and dried before the subsequent characterization.

Characterization: The wafer-scale arrays of vertically aligned ZnO-NRs with and without Ag-NPs and Ag spheres were characterized by using field-emission SEM (SIRION 200, Toshiba S4800) and TEM

in *n*-hexane are shown in **Figure 3**a. It can be seen that the Raman intensity of PCB-77 decreases with the PCB-77 concentration decrease. The SERS sensitivity of the as-prepared 3D hybrid substrate is so high that the characteristic Raman bands of PCB-77 collected on the substrate exposed to a low 10^{-11} M concentration can be clearly identified (Figure 3b) and assigned as follows: the band at 714 cm^{-1} belongs to the C–Cl stretching mode, the bands at 1005, 1132, 1242 and 1278 cm^{-1} are attributed to the aromatic vibration modes, and the bands at 1560 and 1591 cm^{-1} are assigned to the C–C bridge stretching mode.[48–51] It should be mentioned that the peak at 1392 cm^{-1} in the Raman spectra is attributed to the amorphous carbon.[52] The EF of this substrate for detecting PCB-77 is estimated to be 3.24×10^7 (Part S7, Supporting Information). Taken together, it is therefore reasonable to conclude that the as-prepared arrays of large-scale vertically aligned cone-shaped ZnO-NRs, in which each NR is decorated with small Ag-NPs on its side surface and large Ag-sphere on its top end, have uniform and very high SERS activity with potentials as effective SERS substrate for rapid detection of trace PCBs.

FULL PAPER

(JEM-2010) instruments and an X-ray diffractometer (X'Pert Pro MPD). All SEM images were taken with 30 degrees tilt. UV–vis spectra of the ZnO-NR arrays and the as-prepared arrays of ZnO-NRs decorated with Ag-NPs hybrid structures were measured with a UV–vis–near-infrared spectrophotometer (Hitachi, U-4100) with diffusion reflection spectroscopy accessories. The Raman scattering spectra were recorded on a confocal microprobe Raman system (LABRAM-HR, France; Renishaw, inVia). The excitation wavelength was 514.5 nm from an air-cooled argon ion laser with an effective power of 2 mW.

Supporting Information

Supporting Information is available form the Wiley Online Library or from the author.

Acknowledgements

[1] S. Shanmukh, L. Jones, J. Driskell, Y. Zhao, R. Dluhy, R. A. Tripp, *Nano Lett.* **2006**, *6*, 2630.

[2] K. Kneipp, H. Kneipp, *Accounts. Chem. Res.* **2006**, *39*, 443.

[3] M. Mulvihill, A. Tao, K. Benjauthrit, J. Arnold, P. Yang, *Angew. Chem.* **2008**, *120*, 6556; *Angew. Chem. Int. Ed.* **2008**, *47*, 6456.

[4] K. Lee, V. P. Drachev, J. Irudayaraj, *ACS Nano* **2011**, *5*, 2109.

[5] M. K. Hossain, Y. Kitahama, G. G. Huang, X. Han, Y. Ozaki, *Anal. Bioanal. Chem.* **2009**, *394*, 1747.

[6] M. Fan, G. F. S. Andrade, A. G. Brolo, *Anal. Chim. Acta.* **2011**, *693*, 7.

[7] P. Xu, N. H. Mack, S.-H. Jeon, S. K. Doorn, X. Han, H.-L. Wang, *Langmuir* **2010**, *26*, 8882.

[8] Y. Wang, W. Ruan, J. Zhang, B. Yang, W. Xu, B. Zhao, J. R. Lombardi, *J. Raman Spectrosc.* **2009**, *40*, 1072.

[9] Y. Wang, Z. Sun, H. Hu, S. Jing, B. Zhao, W. Xu, C. Zhao, J. R. Lombardi, *J. Raman Spectrosc.* **2007**, *38*, 34.

[10] A. Musumeci, D. Gosztola, T. Schiller, N. M. Dimitrijevic, V. Mujica, D. Martin, T. Rajh, *J. Am. Chem. Soc.* **2009**, *131*, 6040.

[11] A. Kudelski, W. Grochala, M. Janik-Czachor, J. Bukowska, A. Szummer, M. Dolata, *J. Raman Spectrosc.* **1998**, *29*, 431.

[12] Y. Wang, H. Hu, S. Jing, Y. Wang, Z. Sun, B. Zhao, C. Zhao, J. R. Lombardi, *Anal. Sci.* **2007**, *23*, 787.

[13] X. Wang, X. Kong, Y. Yu, H. Zhang, *J. Phys. Chem. C* **2007**, *111*, 3836.

[14] J. G. Fan, Y. P. Zhao, *Langmuir* **2008**, *24*, 14172.

[15] X. Li, G. Chen, L. Yang, Z. Jin, J. Liu, *Adv. Funct. Mater.* **2010**, *20*, 2815.

[16] S. M. Morton, L. Jensen, *J. Am. Chem. Soc.* **2009**, *131*, 4090.

[17] B. Zhang, H. Wang, L. Lu, K. Ai, G. Zhang, X. Cheng, *Adv. Funct. Mater.* **2008**, *18*, 2348.

[18] C. Cheng, B. Yan, S. M. Wong, X. Li, W. Zhou, T. Yu, Z. Shen, H. Yu, H. J. Fan, *ACS Appl. Mater. Interfaces* **2010**, *2*, 1824.

[19] M.-L. Zhang, X. Fan, H.-W. Zhou, M.-W. Shao, J. A. Zapien, N.-B. Wong, S.-T. Lee, *J. Phys. Chem. C* **2010**, *114*, 1969.

[20] J.-S. Hwang, K.-Y. Chen, S.-J. Hong, S.-W. Chen, W.-S. Syu, C.-W. Kuo, W.-Y. Syu, T. Y. Lin, H.-P. Chiang, S. Chattopadhyay, K.-H. Chen, L.-C. Chen, *Nanotechnology* **2010**, *21*, 025502.

[21] L. Yang, W. Ruan, X. Jiang, B. Zhao, W. Xu, J. R. Lombardi, *J. Phys. Chem. C* **2009**, *113*, 117.

[22] X. Zhao, B. Zhang, K. Ai, G. Zhang, L. Cao, X. Liu, H. Sun, H. Wang, L. Lu, *J. Mater. Chem.* **2009**, *19*, 5547.

[23] W. Song, Y. Wang, H. Hu, B. Zhao, *J. Raman Spectrosc.* **2007**, *38*, 1320.

[24] W. Song, X. Han, L. Chen, Y. Yang, B. Tang, W. Ji, W. Ruan, W. Xu, B. Zhao, Y. Ozaki, *J. Raman Spectrosc.* **2010**, *41*, 907.

[25] C. Pacholski, A. Kornowski, H. Weller, *Angew. Chem.* **2004**, *116*, 4878; *Angew. Chem. Int. Ed.* **2004**, *43*, 4774.

[26] P. Chen, L. Gu, X. Xue, Y. Song, L. Zhu, X. Cao, *Mater. Chem. Phys.* **2010**, *122*, 41.

[27] S. Deng, H. M. Fan, X. Zhang, K. P. Loh, C. L. Cheng, C. H. Sow, Y. L. Foo, *Nanotechnology* **2009**, *20*, 175705.

[28] L. E. Greene, M. Law, D. H. Tan, M. Montano, J. Goldberger, G. Somorjai, P. Yang, *Nano Lett.* **2005**, *5*, 1231.

[29] Z. Zhang, G. Meng, Q. Xu, Y. Hu, Q. Wu, Z. Hu, *J. Phys. Chem. C* **2010**, *114*, 189.

[30] G. Andrea, L. Manodori, R. Zangrando, A. Cincinelli, G. Capodaglio, P. Cescon, *Environ. Sci. Technol.* **2005**, *39*, 9406.

[31] B. R. DeCastro, S. A. Korrick, J. D. Spengler, A. M. Soto, *Environ. Sci. Technol.* **2006**, *40*, 2819.

[32] A. F. Arruda, H. C. Goicoechea, M. Santos, A. D. Campiglia, A. C. Olivieri, *Environ. Sci. Technol.* **2003**, *37*, 1385.

[33] V. Schurig, S. Reich, *Chirality* **1998**, *10*, 316.

[34] J.-F. Focant, J. W. Cochran, J.-M. D. Dimandja, E. DePauw, A. Sjödin, W. E. Turner, J. Donald G. Patterson, *Analyst* **2004**, *129*, 6.

[35] H. He, W. Cai, Y. Lin, B. Chen, *Langmuir* **2010**, *26*, 8925.

[36] K. Morgenstern, G. Rosenfeld, G. Comsa, *Surf. Sci.* **1999**, *441*, 289.

[37] E. Hao, G. C. Schatz, *J. Chem. Phys.* **2004**, 357.

[38] W. Li, P. H. C. Camargo, X Lu, Y Xia, *Nano Lett.* **2009**, *9*, 485.

[39] J. A. Fan, C. Wu, K. Bao, J. Bao, R. Bardhan, N. J. Halas, V. N. Manoharan, P. Nordlander, G. Shvets, F. Capasso, *Science* **2010**, *328*, 1135.

[40] H. Im, K. C. Bantz, N. C. Lindquist, C. L. Haynes, S-H. Oh, *Nano Lett.* **2010**, *10*, 2231.

[41] S. R. Emory, W. E. Haskins, S. Nie, *J. Am. Chem. Soc.* **1998**, *120*, 8009.

[42] S. Nie, *Science* **1997**, *275*, 1102.

[43] Q. Zhang, W. Li, C. Moran, J. Zeng, J. Chen, L.-P. Wen, Y. Xia, *J. Am. Chem. Soc.* **2010**, *132*, 11372.

[44] Z. Sun, C. Wang, J. Yang, B. Zhao, J. R. Lombardi, *J. Phys. Chem. C* **2008**, *112*, 6093.

[45] G. Shan, L. Xu, G. Wang, Y. Liu, *J. Phys. Chem. C* **2007**, *111*, 3290.

[46] K. Bhatt, S. Tan, S. Karumuri, A. K. Kalkan, *Nano Lett.* **2010**, *10*, 3880.

[47] Z. Huang, G. Meng, Q. Huang, Y. Yang, C. Zhu, C. Tang, *Adv. Mater.* **2010**, *22*, 4136.

[48] Y. Yang, G. Meng, *J. Appl. Phys.* **2010**, *107*, 044315.

[49] Q. Zhou, Y. Yang, J. Ni, Z. Li, Z. Zhang, *Physica. E* **2010**, *42*, 1717.

[50] Q. Zhou, Y. Yang, J. Ni, Z. Li, Z. Zhang, *Nano Res.* **2010**, *3*, 423.

[51] *Infrared and Raman Characteristic Group Frequencies: Tables and Charts*, (Ed: G. Socrates), 3rd Ed., Wiley, New York **2001**.

[52] A. C. Ferrari, J. Robertson, *Phys. Rev. B* **2000**, *61*, 14095.

ADVANCED FUNCTIONAL MATERIALS

www.afm-journal.de

Editor in Chief:	David Flanagan
Deputy Editor:	Timothy Adams
Managing Editor:	Lisa Wylie
Deputy Managing Editor:	Sibylle Meyer
Editorial Staff:	Lianne Beltran
	Angelika Böer
	Mary Farrell
	Hilary Gallagher
	Viola Küstner
	Eliza-Beth Lerch
	Duoduo Liang
	Adrian Miller
	Sjef Öllers
	Martin Ottmar
	Eva Rittweger
	Lisa Smith
	Lorna Stimson
	John Uhlrich
	Elizabeth Wilson
	Guangchen Xu
Founding Editor:	Peter Gregory
Administration:	Ursula Damm
	Melanie Rettenmaier
	Anke Osterland
Production:	Christine Herth
Marketing:	Sonja Hoffmann

Annual subscription rates 2012:

		Institutional*
Europe	EUR	4854/5582
Switzerland	SFr	7678/8830
Outside Europe	US $	5861/6740

* Print or electronic delivery/print + electronic delivery

Postage and handling charges included.
Prices are subject to local VAT/sales tax.
Prices are subject to change without notice.

Materials Views
http://MaterialsViews.com

Manuscript Submission & Personal Homepage

manuscriptXpress
www.manuscriptxpress.com

Full text:	wileyonlinelibrary.com
Homepage:	www.afm-journal.de